D   ADB224215

Development of the MAMA Detectors for the Hubble Space Telescope Imaging Spectrograph.

NAS5-29389

IN-89-CR

053032

STANFORD UNIV CA

APR 1997

I   つ

UNCLASSIFIED / LIMITED

Redistribution Of DTIC-Supplied Information Notice

As a condition for obtaining DTIC services, all information received from DTIC that is not clearly marked for public release will be used only to bid or perform work under a U.S. Government contract or grant or for purposes specifically authorized by the U.S. Government agency that sponsored the access. Furthermore, the information will not be published for profit or in any manner offered for sale.

Reproduction Quality Notice

We use state-of-the-art, high-speed document scanning and reproduction equipment. In addition, we employ stringent quality control techniques at each stage of the scanning and reproduction process to ensure that our document reproduction is as true to the original as current scanning and reproduction technology allows. However, the following original document conditions may adversely affect Computer Output Microfiche (COM) and/or print reproduction:

- Pages smaller or larger than 8.5 inches x 11.0 inches.

- Pages with background color or light colored printing.

- Pages with smaller than 8 point type or poor printing.

- Pages with continuous tone material or color photographs.

- Very old material printed on poor quality or deteriorating paper.

If you are dissatisfied with the reproduction quality of any document that we provide, particularly those not exhibiting any of the above conditions, please feel free to contact our Directorate of User Services at (703) 767-9066/9068 or DSN 427-9066/9068 for refund or replacement.

Do Not Return This Document To DTIC

UNCLASSIFIED / LIMITED

CENTER FOR SPACE SCIENCE AND ASTROPHYSICS

STANFORD UNIVERSITY

Development of the MAMA Detectors for

the *Hubble* Space Telescope Imaging Spectrograph

Final Report for NASA Contract NAS5-29389

April 1997

19970528 055

J. Gethyn Timothy
CSSA, ERL 314
Stanford University
Stanford, CA 94305

DTIC QUALITY INSPECTED 3

Contents

1. Introduction

The development of the Multi-Anode Microchannel Array (MAMA) detector systems started in the early 1970's in order to produce multi-element detector arrays for use in spectrographs for solar studies from the Skylab-B mission. Development of the MAMA detectors for spectrographs on the *Hubble* Space Telescope (HST) began in the late 1970's, and reached its culmination with the successful installation of the Space Telescope Imaging Spectrograph (STIS) on the second HST servicing mission (STS-82 launched 11 February 1997). Under NASA Contract NAS5-29389 from December 1986 through June 1994 we supported the development of the MAMA detectors for STIS, including complementary sounding rocket and ground-based research programs. This final report describes the results of the MAMA detector development program for STIS.

2. STIS Development Program

The STIS instrument was proposed to NASA in May 1985 and selected for development by NASA in November 1985 (see Woodgate et al., SPIE Instrumentation in Astronomy VI, 627, 350, 1986). Development of STIS was severely impacted by two significant events, first the loss of the space shuttle Challenger in February 1986, and, second, the discovery of the spherical aberration in the HST primary mirror after launch in April 1990. After the Challenger disaster it was hoped that STIS would be installed in HST on the first servicing mission in the 1992 to 1995 time frame. However, the spherical aberration problem forced the installation of STIS to be deferred to the second HST servicing mission, allowing COSTAR, the corrective optics package, to be installed in HST on the first servicing mission.

In March 1991, STIS was descoped in response to budget problems within the HST project. As originally proposed, STIS incorporated two CCD detectors with formats of 2048 x 2048 pixels for the visible and near IR spectral regions, and two MAMA detectors with formats of 2048 x 2048 pixels for the near- and far-ultraviolet spectral regions. After descope, STIS incorporated one CCD detector with a format of 1024 x 1024 pixels and two MAMA detectors with formats of 1024 x 1024 pixels. This configuration of STIS was accepted by NASA in October 1991.

Development continued and STIS was finally installed in HST on the second servicing mission in February 1997. As of this date STIS, and the MAMA detectors are being commissioned for science operations. Details of the STIS instrument configuration and the on-orbit performance can be found on the Internet on the STIS homepage at http://hires.gsfc.nasa.gov/stis/stispage.html.

3. STIS MAMA Detector Systems

When STIS was proposed the MAMA detector systems had already reached a high level of maturity with MAMA detectors having formats as large as 256 x 1024 pixels in use at ground-based telescopes and under development for flight on sounding-rocket instruments (see Timothy, Pub. Astron. Soc. Pacific, 95, 810, 1983). However, under the impetus of the STIS program, a number of significant advances were made with the MAMA technology. These advances included:

1. The development of high-gain curved-channel microchannel plates (C-plate MCPs) in formats as large as 50 mm in diameter for use with the (1024 x 1024)-pixel MAMAs. C-plate MCPs with 12-micron-diameter channels on 15-micron centers, and with 10-micron-diameter channels on 12-micron centers were successfully fabricated. In a parallel development C-plate MCPs with 8-micron-diameter channels on 10-micron centers were also fabricated.

2. The initial development of C-plate MCPs in formats as large as 85 mm in diameter for use with the (2048 x 2048)-pixel MAMAs.

3. The development of new MCP geometries, including MCPs with curved front faces to match spectrometer focal surfaces and planar output faces to match the readout arrays, and MCP structures with very-high dynamic ranges.

4. The development of the capacitatively- and inductively-balanced fine-fine anode-array geometry for the MAMA readout arrays. This geometry greatly improved the uniformity of response from pixel to pixel.

5. The fabrication and test of fine-fine MAMA readout arrays with formats of 1024 x 1024 pixels (pixel dimensions of 25 x 25 microns^2), and formats of 2048 x 2048 pixels (pixel dimensions of 25 x 25 microns^2). The arrays with formats of 2048 x 2048 pixels were fabricated as four contiguous (1024 x 1024)-pixel arrays for redundancy and to increase the total array count rate capability. In a parallel development fine-fine anode arrays with pixel dimensions as small as 14 microns have been fabricated.

6. The development of the high-resolution ("hi-res") decode algorithm for the MAMA readout arrays. This increases the resolution by a factor of two in each axis with the ultimate resolution set by the center-to-center- spacing of the channels in the MCP. The (1024 x 1024)-pixel array with 25 x 25 microns^2 pixels in standard ("lo-res") readout mode, for example, becomes a (2048 x 2048)-pixel array with 12.5 x 12.5 microns^2 pixel in "hi-res" mode.

7. The development of a flight-quality image decoding ASIC for the MAMA readout system. This ASIC can decode pixel addresses from arrays with formats of 224, 360, 960, and 1024 pixels and can provide data in both "lo-res" and "hi-res" modes of operation under electronic control.

8. The development of flight-quality ASIC amplifier and discriminator circuits for the MAMA detector system.

9. The development of flight quality open and sealed MAMA detector tubes for operation at wavelengths from the far ultraviolet to the near IR.

10. The flight of far ultraviolet MAMA detector systems on sounding rockets.

11. The operation of visible-light MAMA detector systems on ground-based telescopes, particularly for high-time-resolution applications including speckle interferometry and speckle imaging.

Details of these different development activities are described in the representative publications attached to this report, and in the references contained therein.

The STIS MAMA detectors are now being brought into operation on orbit. Simultaneously, STIS-format MAMA detectors are being prepared for use in a number of other instruments, including the High-Resolution EUV Spectroheliometer (HiRES) sounding rocket payload (Timothy et al., Opt. Eng. 30, 1142, 1991). Observations at ground-based telescopes with the visible-light MAMA detector systems are also continuing, with coordinated observations anticipated in support of the STIS science program, e.g., observations of flare stars.

The MAMA technology has the capability for even further improvement in areas such as detective quantum efficiency, local and global dynamic range, and the reduction of weight, volume, and power, while retaining the unique capabilities for fast timing and photon-limited noise observations. Developments in all of these areas are continuing.

Recent developments with VUV and soft x-ray detector systems

J. Gethyn Timothy

Center for Space Science and Astrophysics, Stanford University, ERL 314,
Stanford, CA 94305 USA

ABSTRACT

Recent developments with detector systems for use at vacuum ultraviolet (VUV) and soft x-ray wavelengths have emphasized improvements in the detective quantum efficiencies and the capability for high-resolution imaging while retaining a high photometric accuracy. This paper compares and contrasts the performance characteristics of the three principal classes of imaging detector systems currently under active development, namely, the bare Charge-Coupled Device (CCD), the intensified CCD, and the microchannel plate (MCP) coupled to different imaging electronic readout systems.

1. INTRODUCTION

The vacuum ultraviolet (VUV) and soft x-ray spectral region from about 2000 Å down to about 1 Å can be divided into a number of different domains based on practical limitations, as shown in Figure 1. Between about 1050 Å (the short wavelength cut off for LiF) and about 20 Å (the long wavelength cut off for an Al window that can withstand a pressure of 1 atmosphere) no rugged window materials are available and open-structure detector systems must typically be employed. Further, until the recent development of synthetic multilayer coatings,[1] grazing-incidence optical systems were required in order to produce a high reflectivity at wavelengths below about 300 Å. For the purposes of this review paper, the wavelength range from about 300 Å to 2000 Å will be considered the VUV, and the wavelength range from about 1 Å to 300 Å will be considered the soft x-ray region. However, it should be noted that the term EUV (extreme ultraviolet) is usually used to describe the wavelength range from about 300 Å to 1200 Å, and the term XUV is often used to describe the wavelength range from about 100 Å to 300 Å. Because of the recent developments of synchrotron and storage-ring radiation sources and high-power short wavelength lasers, and also because of access to this wavelength region for astrophysical studies in space, there is currently a major thrust to develop new types of VUV and soft x-ray detector systems. Particular emphasis is being placed on increasing the data collection efficiency, first, by improving the detective quantum efficiency (DQE), and, second, by adding an imaging capability while retaining the photometric accuracy of the detector systems. This paper describes the three principal classes of imaging detector systems currently under active development, namely the bare Charge-Coupled Device (CCD), the intensified CCD, and the microchannel plate (MCP) with different imaging electronic readout systems, and compares and contrasts their performance characteristics.

2. BARE CCDs

The Si CCD is being used for a wide variety of scientific applications, principally because of its imaging capability, linear response and very high quantum efficiency at visible and near infrared wavelengths (see Figure 2).[2] At high light levels, thick, front-side illuminated CCDs can be employed. However, for very low light level applications, such as astronomical imaging, thinned, back-side illuminated CCDs must be employed to minimize background events caused by cosmic rays and radioactive sources. Another factor affecting the low light level operation of CCDs is the readout noise. At slow readout rates (~10 to 100 KHz) read noise levels in the range from 5 to 15 electrons rms have been achieved. However, at these rates, it takes many seconds to read out a large-format imaging CCD with the order of 800 x 800 pixels.[3] A further source of background noise in CCDs is the instrinsic dark current of Si. Cooling to the order of -90°C is typically required to reduce the dark current to levels of less than 10^{-2} electrons pixel^{-1} s^{-1}, in order to permit long integration times.[4]

The absorption path length for photons in Si has a maximum between 2500 and 3000 Å.[5] VUV photons are absorbed close to the surface of the device, and thinned back-side illuminated CCDs must be employed. In order to obtain a high DQE at VUV wavelengths, a number of techniques are currently being investigated. The first is to use a downconverting phosphor such as coronene, which absorbs the VUV photon and emits a visible-light photon at wavelengths near 5000 Å.[6] A more effective technique is to bend the band structure near the surface of the CCD in order to drive the electron-hole pairs into the depletion region. Various techniques are currently being employed to induce this effect, namely, ultraviolet flooding,[5] coating the surface of the CCD with a platinum flashgate,[2,7] and ion implantation.[8,9]

At soft x-ray wavelengths below about 100 Å, the absorption path length for a photon in Si increases significantly and thick

Publications.
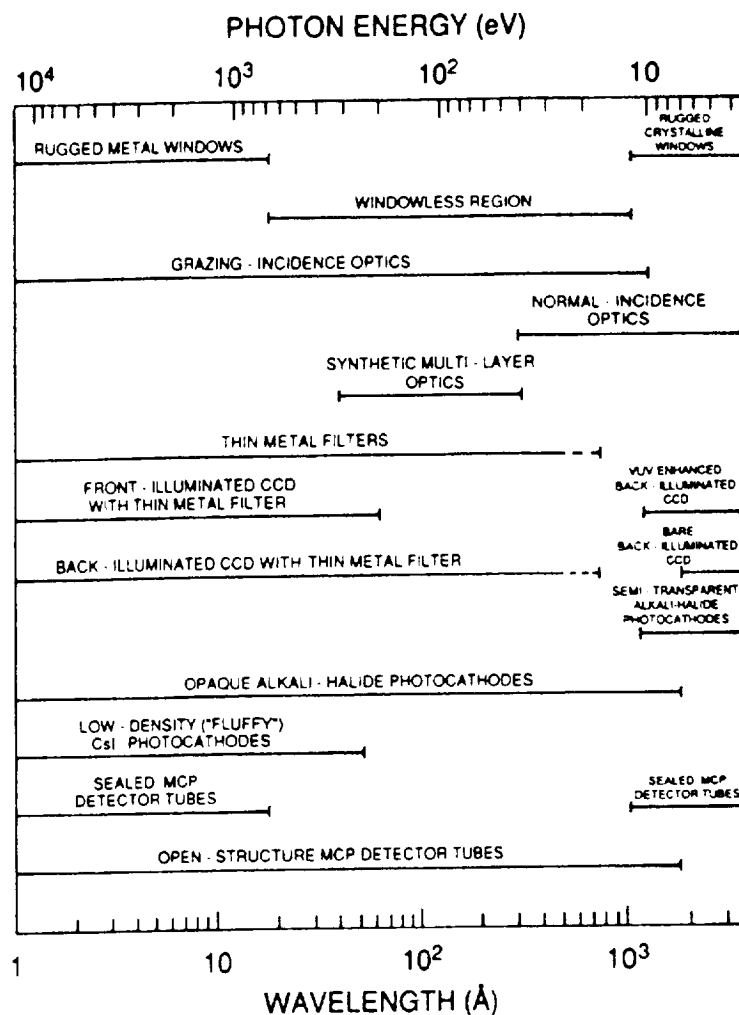
PHOTON ENERGY (eV)

Figure 1. Operating ranges for optical components and detectors in the VUV and soft x-ray spectral region.

front-side illuminated CCDs can again be employed. Further, since one electron-hole pair is produced for approximately every 3.5 eV deposited in the depletion region, multiple electron-hole pairs are produced and the CCD can be used in a pulse-counting mode at soft x-ray wavelengths.[10] At wavelengths below about 10 Å (~1 keV), sufficient electron-hole pairs are produced to allow a high degree of energy resolution. At wavelengths longer than about 10 Å, the energy resolution is currently limited by the readout noise. Resolutions significantly better than 200 eV have been obtained at soft x-ray energies above about 1 keV (~13 Å).[11] One problem with the operation of CCDs at soft x-ray wavelengths is that the photon is sufficiently energetic to pass through the thin depletion layer. For this reason, the development of "deep depletion" CCDs is now in progress in order to improve the DQE at soft x-ray energies above about 5 keV.[12,13] The energy resolution is also degraded if the electron-hole pairs are divided between two or more pixel sites.[10]

Another factor that must be taken into consideration is the very wide wavelength response of the CCD. Many VUV and soft x-ray sources, particularily astrophysical sources, emit significantly more strongly at longer wavelengths. The elimination of this "red leak" is mandatory if the VUV or soft x-ray image is not to be obscured by longer wavelength scattered light. The filter that has the best transmission at soft x-ray wavelengths, but is opaque to longer wavelength radiation, is a thin Al foil.[14] A 1500 Å thick, freestanding Al foil which has a visible light rejection of the order of 10^8 to 10^9, has a long wavelength cut off near 500 Å. Sn filters, although less rugged, can be used to efficiently transmit radiation at longer wavelengths to about 750 Å,[15] although the level of visible light rejection will be lower than that of Al. The exact level of
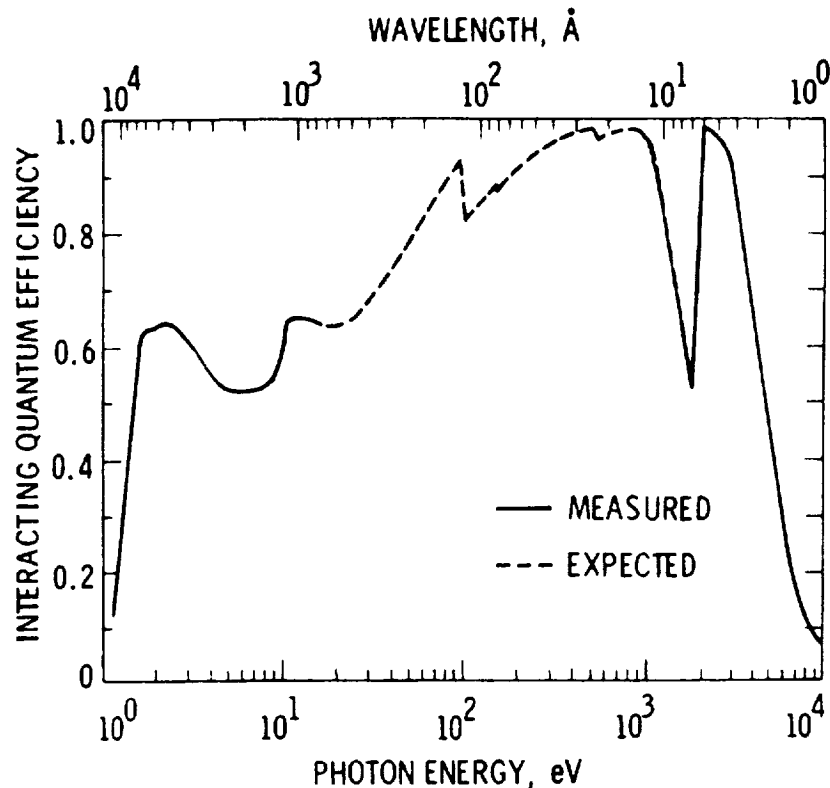
Figure 2. Measured and expected interacting quantum efficiency for a VUV enhanced back-illuminated CCD (courtesey J. Janesick[2]).

VUV and visible-light rejection required for an x-ray CCD will depend on the specific application. However, until efficient short pass VUV filters are developed (for example, an alkali metal filter[16]) the use of CCDs for direct imaging at wavelengths between about 750 Å and 3000 Å will not be practical for many applications. For spectroscopy, even if long wavelength radiation is effectively suppressed by means of a double pass spectrometer, detectors employing conventional photoemissive cathodes such as CsI, KBr and Cs_2Te, and operating with zero readout noise, will often prove to have higher DQEs, particularly for low signal level applications.[17] The largest format CCDs in use today at VUV and soft x-ray wavelengths are, first, the Texas Instruments Corp. thinned, back-side illuminated three-phase (800 x 800)-pixel chip[3] and the front-side illuminated uniphase (800 x 800)-pixel chip,[18] both with 15 x 15 microns[2] pixels, and, second, the front-side illuminated uniphase (1024 x 1024)-pixel chip with 18 x 18 microns[2] pixels.[19] Tektronix Inc. are working towards a thinned, back-side illuminated (2048 x 2048)-pixel chip with pixel dimensions of 27 x 27 microns[2], and currently have devices with formats of (512 x 512)-pixels under evaluation.[20]

3. INTENSIFIED CCDs

For studies at VUV and soft x-ray wavelengths, where a high level of rejection of longer wavelength radiation is required, "solar blind" photoemissive cathodes are commonly used.[21] These can be incorporated into an image intensifier and optically coupled to a solid state array such as a CCD. This type of detector can be operated either in an analog mode with the charge integrated in the CCD prior to readout, or, at low signal levels, in the pulse-counting mode where the CCD is read out at a fast enough rate to identify each detected photon. Although a number of different types of image intensifier and solid state array combinations are currently in use,[22] the proximity-focussed MCP intensifier tube (Generation II wafer tube[23]) coupled to a CCD is becoming the most popular imaging system because of the lack of image distortion, and because it can be used in an open-structure mode at VUV and soft x-ray wavelengths between about 1050 Å and 20 Å. The structure of this type of intensified CCD is shown in the schematic in Figure 3. A high-gain MCP, which can be either a "chevron" or "Z-plate" stack,[24,25] or a single curved-channel MCP,[26] is used to amplify the photoelectron to produce a charge cloud of 10^4 to 10^6

electrons. This charge cloud is then accelerated into a phosphor which emits visible-light photons and provides an additional gain of the order of a factor of 10. The photons from the phosphor are then optically coupled by means of a fiber-optic faceplate into the pixel sites of the CCD.
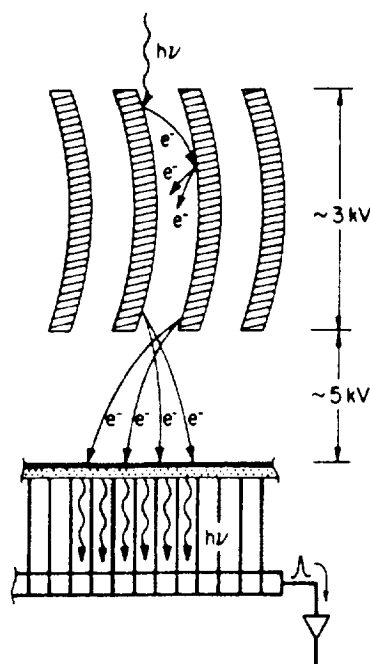

Figure 3. Schematic of MCP-intensified CCD detector system.

The advantages of the MCP-intensified CCD are its modular construction, relatively low operating voltages, and the elimination of the requirement for the CCD to survive the environmental conditions required for photocathode processing, particularly bake at temperatures in excess of 300°C. In addition, a very-large-format MCP can be optically coupled to a mosaic of smaller CCDs to produce a detector with a larger active area than can be obtained with a single CCD.[27,28] The principal limitation of this type of image intensifier is the relatively long decay time of the phosphor. In the pulse-counting mode, corrections must be made for the photons detected on more than one readout cycle of the CCD. Also, at high gain levels the light spot from the MCP intensifier tube is many pixels in diameter. Prior-frame-subtraction and centroiding techniques are accordingly required to obtain both a high photometric accuracy and the full spatial resolution of the CCD. Even with these techniques, the maximum output count rate is scene dependent, i.e., much lower for flat fields than for isolated point or line emission sources, and is typically limited to the order of 1 to 5 counts s^{-1} $pixel^{-1}$ (random).[29]

The optimum photocathodes for use at VUV and soft x-ray wavelengths at this time are the alkali halides; opaque CsI from about 1800 Å to about 10 Å [30,31,32] and low-density "fluffy" CsI from about 1 to 50 Å [33] (see Figure 4), KBr from about 1400 Å to below 50 Å,[34,35] and MgF$_2$ and LiF from about 1200 Å to below 20 Å.[30,36] An opaque Cs$_2$Te photocathode protected by a MgF$_2$ window in a sealed tube can also be used at wavelengths between 1150 Å and about 3000 Å.

Because it was originally feared that high quantum efficiencies would not be obtained when an alkali halide photocathode was directly deposited on the front face of an MCP, an alternative form of direct-bombardment intensified CCD with an oblique focused opaque photocathode[37] has been employed. A system of this type (see Figure 5) has recently been flown in a high-resolution VUV sounding-rocket spectrometer (E. B. Jenkins, private communication). However, recent results with thick (~15000 Å) alkali-halide photocathodes on MCPs suggest that high quantum efficiencies at VUV wavelengths can be obtained with high-gain MCPs having channel input bias angles of 15° or greater,[32,34] although the quantum efficiencies are still lower than those reported for planar photocathodes.[38] At soft x-ray wavelengths, the MCP channel input bias angle should be selected to take advantage of the strong increase of the quantum efficiencies of the alkali-halide photocathodes at high angles of incidence.[39]
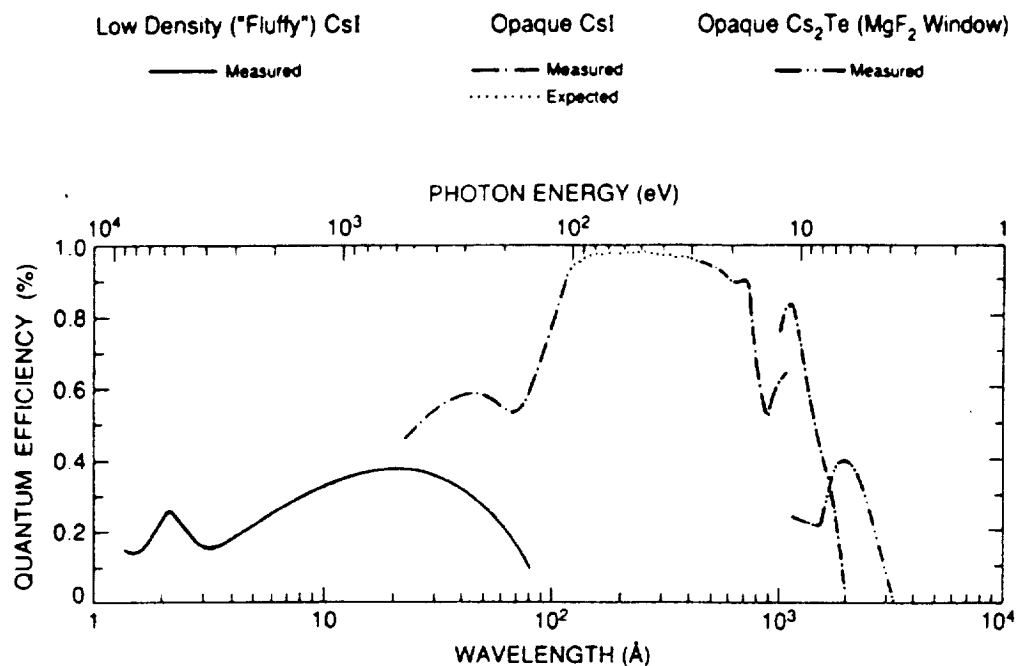
Low Density ("Fluffy") CsI — Measured

Opaque CsI — · — Measured ········ Expected

Opaque Cs$_2$Te (MgF$_2$ Window) — ·· — Measured

Figure 4. Cs$_2$Te and CsI photocathode quantum efficiencies at VUV and soft x-ray wavelengths.
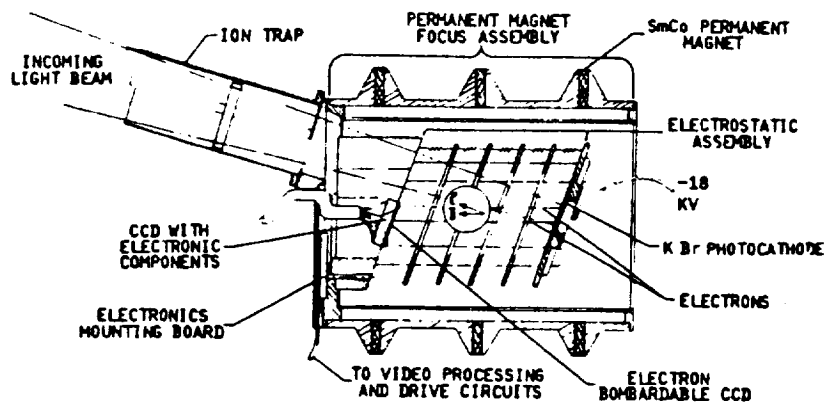

Figure 5. Schematic of direct-bombarded intensified CCD detector system with an oblique-focussed opaque photocathode (courtesy E. B. Jenkins).

4. MCPs WITH IMAGING ELECTRONIC READOUT SYSTEMS

A number of different electronic readout systems are in use with high-gain MCPs or are under development at this time.[22,40] These include the discrete-anode array[31], the resistive-anode array (RANICON),[41,42] the wedge-and-strip (WS) array,[43,44] the crossed-wire array (High Resolution Imager),[45] the coded anode-array (CODACON),[46] the coincidence-anode multi-anode array (MAMA),[31,47] and delay-line arrays.[48] All of these arrays have the general form shown in the schematic in Figure 6. A high-gain MCP with an opaque photocathode on the front face, or a semi-transparent photocathode mounted in proximity focus with the front face, is mounted in proximity focus with the readout array of electrodes.
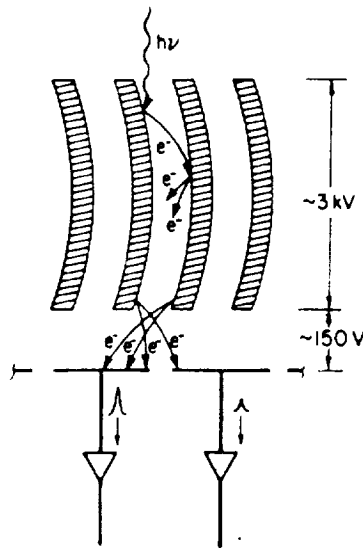

Figure 6. Schematic of high-gain MCP electronic imaging detector system.

In the discrete-anode array the output charge cloud from the MCP is collected on a metallic anode which is directly connected to an amplifier and discriminator circuit. The dimensions of the anode define the pixel dimensions, anodes as small as 100 microns in width have been fabricated to date. This type of readout array has a very-high dynamic range but the total number of pixels is limited by practical considerations of connector and electronic technologies to the order of 500 or less. Output count rates as high as 10^6 counts mm^{-2} s^{-1} (random) have been achieved with a coincidence loss of less than 10% with MCPs having gains of the order of 10^6 electrons pulse^{-1}.

The resistive-anode array or RANICON uses a resistive sheet as the anode, and charge-division- or rise-time-encoding techniques to determine the spatial location of the detected photon. Formats as large as 500 x 500 pixels with a spatial resolution of the order of 40 microns have been achieved to date. Because the resistive-anode array employs an analog-interpolation technique to determine the spatial location of a detected photon, MCP gains in excess of 10^7 electrons pulse^{-1} are required to obtain the optimum spatial resolution and the maximum array count rate is currently limited to the order of about 4 x 10^4 counts s^{-1} (random).

The wedge-and-strip (WS) array operates in a similar manner to the resistive anode array, but employs specially shaped conducting electrodes to effect the charge division for determining the spatial location of the detected photon (see Figure 7). The WS array has very similar performance characteristics to the resistive-anode array, but a better spatial resolution for a given MCP gain because of the elimination of shot noise in the resistive sheet.
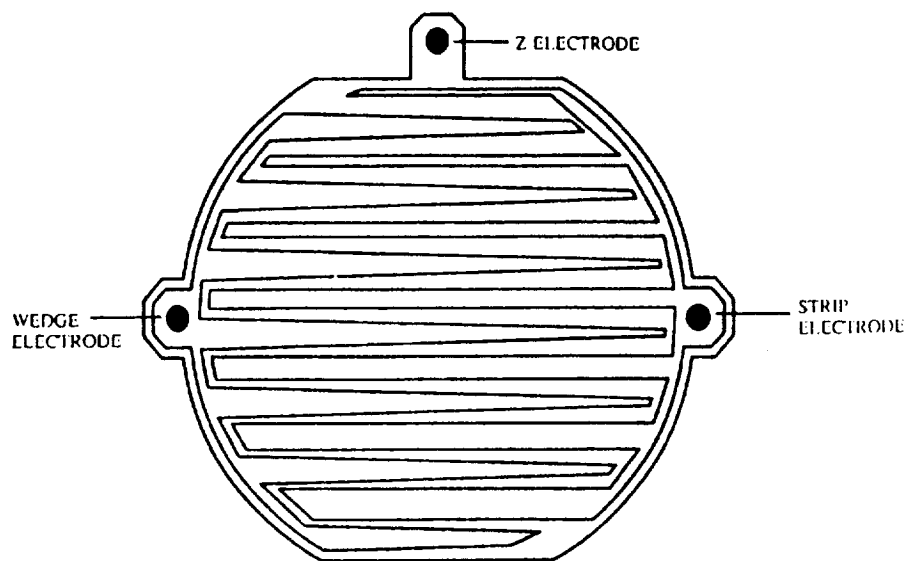
Figure 7. Schematic of a three-electrode wedge-and-strip array
(courtesy O. Siegmund).

The crossed wire-array or High Resolution Imager (HRI) is a more complex version of the resistive anode array, employing a series of discrete anode wires linked by resistive coupling electrodes. Although the HRI employs an analog interpolation technique to determine the spatial location, it has a higher dynamic range and spatial resolution than the RANICON or WS arrays because of the larger number of amplifiers employed in each axis. The Advanced HRI,[49] which employs 65 amplifiers in each axis, is planned to have an active area of 100 x 100 mm^2 and a spatial resolution of about 25 x 25 microns^2.

The coded-anode array (CODACON) employs a gray-code electrode configuration to determine the spatial location of the detected photon on a set of discrete pixel electrodes. Because the CODACON employs a capacitive coupling technique to transfer charge to the encoding electrodes, it produces a lower signal-to-noise than the all conducting electrode readout systems and has not yet been operated efficiently in a two-dimensional imaging configuration.
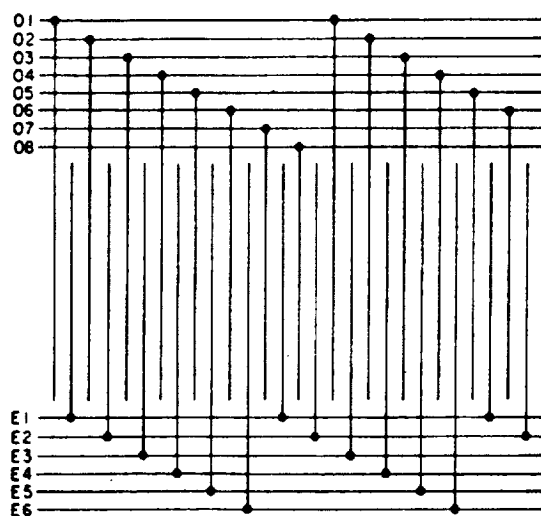
Figure 8. Schematic of a one-dimensional coarse-fine coincidence anode array .

The coincidence-anode multi-anode array (MAMA), which has been designed from the outset to provide the maximum spatial resolution and dynamic range, employs a set of discrete pixel electrodes linked in an all conducting $2\sqrt{N}$ coarse-fine encoding system (see Figure 8) to determine the position of the detected photon. In a (1 x 1024)-pixel linear array a total of 64 amplifiers are required to determine the location of the detected photon. A two-dimensional imaging array is constructed using two orthogonally oriented arrays, fabricated by means of a multi-layer technique, with the two sets of conducting electrodes insulated from each other by a SiO_2 dielectric layer. A (1024 x 1024)-pixel imaging array (see Figure 9) requires a total of 128 amplifiers (64 in each axis). The MAMA readout array geometry is currently being optimized in the (256 x 1024)-pixel format with 25 x 25 microns^2 pixels.[50] The theoretical spatial resolution of 25 microns FWHM and a position sensitivity of better than 1 micron have been demonstrated. The (1024 x 1024)-pixel array with 25 x 25 microns^2 pixels will be under test in the second quarter of 1988 and a (2048 x 2048)-pixel array with 25 x 25 microns^2 pixels is expected to be completed by end of 1989. Arrays with 14 x 14 microns^2 pixels will also be fabricated later in 1988. The current MAMA electronics system has a pulse-pair resolution of 100 ns, giving a total array count rate of 10^6 counts s^{-1} (random) with a 10% coincidence loss.

Delay-line anode arrays are currently in a very early stage of development, but have already demonstrated the capability to produce a spatial resolution of better than 100 microns.
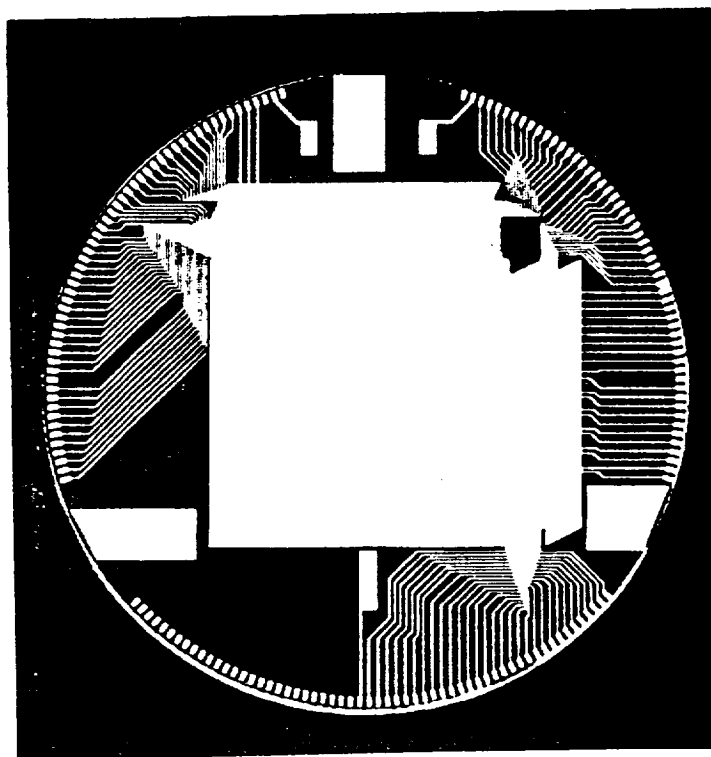

Figure 9. (1024 x 1024)-pixel coincidence-anode MAMA array with 25 x 25 microns^2 pixels.

5. SUMMARY

High-resolution imaging detector systems with high DQEs are currently under active development for use at VUV and soft x-ray wavelengths. Bare CCDs can provide simultaneously high-spatial and high-energy resolutions and can operate in the pulse-counting mode at soft x-ray wavelengths, but VUV enhancement techniques are still in an early stage of development.

The largest format CCDs that can be forseen in the near future have active areas of about 55 x 55 mm^2. MCP-intensified CCDs and MCPs with electronic readout systems can provide a high level of visible-light rejection and a high DQE at VUV and soft x-ray wavelengths through the use of "solar blind" photocathodes. MCPs with active areas of up to 140 mm in diameter are currently available, and imaging systems with active areas of up to 100 x 100 mm^2 are under development. Both the MCP-intensified CCDs and the MCPs with electronic readout systems can be used in the pulse-counting mode at all VUV and soft x-ray wavelengths.

6. ACKNOWLEDGEMENTS

7. REFERENCES

1.   T. W. Barbee Jr., "Multilayers for x-ray optics," Opt. Eng. 25 (8), 898-915 (1986).
2.   J. R. Janesick, T. Elliot, S. Collins, M. M. Blouke and J. Freeman, "Scientific charge-coupled devices," Opt. Eng. 26 (8), 692-714 (1987).
3.   J. E. Gunn and the "Four-shooter" team, "Four-shooter: a large format charge-coupled device for the Hale telescope," Opt. Eng. 26 (8), 779-787 (1987).
4.   M. M. Blouke, J. R. Janesick, T. Elliott, J. E. Hall, M. W. Cowens and P. J. May, "Current status of the 800 x 800 charge-coupled device image sensor," Opt. Eng. 26 (9), 864-874 (1987).
5.   J. R. Janesick, T. Elliott, S. Collins, H. Marsh, M. M. Blouke and J. Freeman, "The future scientific CCD," in State of the Art Imaging Arrays and Their Applications, K.N. Prettyjohns, ed., Proc. SPIE 501, 2-31 (1984).
6.   M. M. Blouke, M. W. Cowens, J. E. Hall, J. A. Westphal and A. B. Christiansen, "Ultraviolet downconverting phosphors for use with silicon CCD imagers," Applied Optics 19 (19), 3318-3321 (1980).
7.   J. R. Janesick, D. Campbell, T. Elliott and T. Daud, "Flash technology for charge-coupled device imaging in the ultraviolet," Opt. Eng. 26 (9), 852-683 (1987).
8.   R. A. Stern, R. C. Catura, R. Kimble, A. F. Davidsen, M. Winzenread, M. M. Blouke, R. Hayes, D. M. Walton and J. L. Culhane, "Ultraviolet and extreme ultraviolet response of charge-coupled-device detectors," Opt. Eng. 26 (9), 875-883 (1987).
9.   J. T. Bosiers, N. S. Saks, D. McCarthy, M. C. Peckerar and D. J. Michels, "CCDs for high resolution imaging in the near and far UV," in Ultraviolet Technology, R. E. Huffman, ed., Proc. SPIE 687, 126-135 (1986).
10. G. A. Lupino, N. M. Ceglio, J. R. Doty, G. R. Ricker and J. V. Vallerga, "Imaging and nondispersive spectroscopy of soft x-rays using a laboratory x-ray change-coupled device system," Opt. Eng. 26 (10), 1048-1054 (1987).
11. G. P. Garmire and the AXAF CCD imaging spectrometer team, "The AXAF CCD imaging spectrometer," in X-ray Instrumentation in Astronomy, J. L. Culhane, ed., Proc. SPIE 597, 261-266 (1985).
12. M. W. Bautz, G. E. Berman, J. P. Doty and G. R. Ricker, "Charge-coupled-device x-ray detector performance model," Opt. Eng. 26 (8), 757-765 (1987).
13. D. H. Lumb, E. G. Chowanietz and A. Wells, "X-ray measurements of charge diffusion effects in EEV Ltd. charge-coupled devices," Opt. Eng. 26 (8), 773-778 (1987).
14. W. R. Hunter, D. W. Angel and R. Tousey, "Thin films and their uses for the extreme ultraviolet," Applied Optics 4 (8), 891-898 (1965).
15. J. H. Vallerga, O. H. W. Siegmund, P. Jelinsky and M. Hurwitz, "The calibration of thin film filters to be used on the extreme ultraviolet Explorer satellite," X-ray calibration: Techniques, Sources, Detectors," P. Rockett and P. Lee, eds., Proc. SPIE 689, 138-143 (1986).
16. R. W. Wood, "Physical Optics," Dover Publications, Inc., New York, 561 (1967).
17. J. Vallerga and M. Lampton," Charge coupled devices vs. microchannel plates in the extreme and far ultraviolet: a comparison based on the latest laboratory measurements," to appear in Proc. SPIE 868, (1988).
18. K. P. Klaasen, M. C. Clary and J. R. Janesick," Charge-coupled device television camera for NASA's Galileo mission to Jupiter," Opt. Eng. 23 (3), 335-342 (1984).

19. E. J. Rhodes, Jr., T. K. Bursch, R. K. Ulrich and S. Tomczyk, "A one megapixel image acquisition and processing system for solar oscillation studies," in Instrumentation for Astronomy VI, D. L.Crawford, ed., Proc. SPIE 627, 256-267 (1986).

20. M. M. Blouke, B. Corrie, D. C. Heidtmann, F. H. Yang, M. Winzenread, M. C. Lust and H. H. Marsh IV, "Large format, high resolution image sensor," Opt. Eng. 26 (9), 837-843 (1987).

21. J. A. R. Samson, "Techniques of Vacuum Ultraviolet Spectroscopy, " John Wiley and Sons, Inc., New York, 224 (1967).

22. J. G. Timothy, "Optical detectors for spectroscopy," Pub. Astron. Soc. Pacific 95 (573), 810-834 (1983).

23. I. P. Csorba, "Image Tubes," Howard Sams and Co., Inc., Indiana, 37 (1985).

24. J. L. Wiza, "Michrochannel plate detectors," Nucl. Instr. and Methods 162, 587-601 (1979).

25. O. H. W. Siegmund, M. Lampton, J. Bixler, S. Chakrabarti, J. Vallerga, S. Bowyer and R. F. Malina, "Wedge and strip image readout systems for photon counting detectors in space astronomy," J. Opt. Soc. Amer. 3 (12), 2139-2145 (1986).

26. J. G. Timothy, "Curved-channel microchannel array plates," Rev. Sci. Instrum. 52 (8), 1131-1142 (1981).

27. D. Weistrop, J. T. Williams, A. Boggess, K. L. Hallam, D. A. Klinglesmith III and R. W. O'Connel, "Mosaic, a large area, photon-counting detector for the space ultraviolet," AAS Photo bulletin No. 35, 3-5 (1984).

28. E. Roberts, T. Stapinski and A. Rogers, "Photon-counting array detectors for the FUSE/Lyman satellite telescope," J. Opt. Soc. Amer. 3 (12), 2146-2150 (1986).

29. T. E. Stapinski, A. W. Rodgers and M. J. Ellis, "A two-dimensional photon counting array, " Pub. Astron. Soc. Pacific 93 (552), 242-246 (1981).

30. J. A. R. Samson, "Techniques of vacuum utraviolet spectroscopy," John Wiley and Sons, Inc., New York, 233-236 (1967).

31. J. G. Timothy, G. H. Mount and R. L. Bybee, "Multi-anode microchannel arrays," IEEE Trans. on Nucl. Sci. NS-28 (1), 689-697 (1981).

32. O. H. W. Siegmund, E. Everman, J. V. Vallerga, S. Labov J. Bixler and M. Lampton, "High quantum efficiency opaque CsI photocathodes for the extreme and far ultraviolet," in Ultraviolet Technology, R. E. Huffman, ed., Proc. SPIE 687, 117-124 (1986).

33. M. P. Kowalski, G. G. Fritz, R. G. Cruddace, A. E. Unzicker and N. Swanson, "Quantum efficiency of cesium iodide photocathodes at soft x-ray and extreme ultraviolet wavelengths, " Applied Optics 25 (14), 2440-2445 (1986).

34. O. H. W. Siegmund, E. Everman, J. V. Vallerga, J. Sokolowski and M. Lampton, "Ultraviolet quantum detection efficiency of potassium bromide as an opaque photocathode applied to microchannel plates," Applied Optics 26 (17), 3607-3614 (1987).

35. O. H. W. Siegmund, E. Everman, J. V. Vallerga and M. Lampton, "Soft x-ray and extreme ultraviolet quantum detection efficiency of potassium bromide layers on microchannel plates," to appear in Applied Optics (1988).

36. L. B. Lapson and J. G. Timothy, "Use of MgF_2 and LiF photocathodes in the extreme ultraviolet," Applied Optics 12 (2), 388-393 (1973).

37. C. B. Johnson and K. L. Hallam,"The oblique image converter," Advances in Electronics and Electron Physics 40 A, 69-82 (1976).

38. G. R. Carruthers, "Further developments of electrographic image detectors," in Ultraviolet and Vacuum Ultraviolet Systems, W. R. Hunter, ed., Proc. SPIE 279, 112-122 (1981).

39. G. W. Fraser, M. J. Whiteley and J. F. Pearson, "Developments in microchannel plate detectors for imaging x-ray astronomy," in X-ray Instrumentation in Astronomy, J. C. Culhane, ed., Proc. SPIE 597, 343-351 (1985).

40. M. Lampton, "Readout techniques for photon-counting microchannel image systems," to appear in Proc. SPIE 868 (1988).

41. M. Lampton and F. Paresce, "The RANICON, a resistive anode image connector," Rev. Sci. Instrum. 45 (9), 1098-1105 (1974).

42. C. Firmani, E. Ruiz, C. W. Carlson, M. Lampton and F. Paresce, "High-resolution imaging with a two-dimensional resistive anode photon counter," Rev. Sci. Instrum. 53 (5), 570-574 (1982).

43. C. Martin, P. Jelinsky, M. Lampton, R. F. Malina and H. O. Anger, "Wedge-and-strip anodes for centroid-finding position-sensitive photon and particle detectors," Rev. Sci. Instrum. 52 (7), 1067-1074 (1981).

44. O. H. W. Siegmund, S. Clothier, J. Thornton, J. Lemen, R. Harper, I. M. Mason and J. L. Culhane, "Application of the wedge-and-strip anode to position sensing with microchannel plates and proportional counters," IEEE Trans. on Nucl. Sci. NS-30 (1), 503-507 (1983).

45. E. Kellogg, P. Henry, S. Murray, L. Van Speybroek and P. Bjorkholm, "High-resolution imaging x-ray detector," Rev. Sci. Instrum. 47 (3), 282-290 (1976).

46. W. E. McClintock, C. A. Barth, R. E. Steele, G. M. Lawrence and J. G. Timothy, "A rocket-borne instrument with a high-resolution microchannel plate detector for planetary ultraviolet spectroscopy," Applied Optics 21 (7), 3071-3079 (1982).

47. J. G. Timothy, "Multianode microchannel array detector systems: performance characteristics," Opt. Eng. 24 (6), 1066-1071 (1985).

48. M. Lampton, O. H. W. Siegmund and R. Raffani, "Delay line anodes for microchannel plate spectrometers," to appear in Rev. Sci. Instrum. (1988).

49. S. S. Murray and J. H. Chappell, "The advanced x-ray astrophysics facility high-resolution camera," in X-ray Instrumentation in Astronomy, J. L. Culhane, ed., Proc. SPIE 597, 274-281 (1985).

50. J. G. Timothy and R. L. Bybee, "High-resolution pulse-counting array detectors for imaging and spectroscopy at ultraviolet wavelengths," in Ultraviolet Technology, R. E. Huffman, ed., Proc. SPIE 687, 109-116 (1986).

Status of the MAMA Detector Development Program

J.S. Morgan and J.G. Timothy

Abstract

Large format 2048 x 2048-pixel Multi-Anode Microchannel Array (MAMA) detectors are being developed for use in the Hubble Space Telescope. The first of these large format MAMA detectors is scheduled to be built by spring of 1989. Other flight and ground-based programs using MAMA detectors include a rocket flight in 1988, speckle imaging, and astrometry. Improvements in the detector design continue to be made. Initial tests have shown that fixed pattern sensitivity variations have been greatly reduced by the use of a redesigned anode array. Laboratory measurements are being made to quantify the performance of MAMA detectors. The stability of flat fields taken with a bialkali MAMA is shown to vary with exposure time. These variations are attributable solely to problems with the photocathode. Measurements are presented which show that centroid positions may be computed from MAMA data to an accuracy of at least 0.01 pixels.

Users of imaging detectors for scientific applications are typically characterized by strong interests in the sensitivity, pixel format, dynamic range, stability, and cost of such detector systems. Projects like the MAMA detector development program exist in attempts to placate the properly insatiable desires for better imaging detectors. The Multi-Anode Microchannel Array (MAMA) detectors are zero read-noise, photon-counting imaging arrays with random read-out electronics. As such these detectors excel

in applications that require detection of very low intensity signals which would be swamped by the presence of detector read noise. They also are good detectors for applications which require high time resolution because unlike serial read-out detectors like CCDs, the detection of individual photons may be sampled and recorded at megahertz rates independent of where on the array the photons may arrive. Currently the lack of suitable blocking filters makes MAMA detectors an attractive choice over CCDs in the ultraviolet because UV MAMAs can be made completely insensitive to visible radiation by the choice of a suitable photocathode.

At Stanford University we are involved in the construction, evaluation, and the application of these detectors. Working MAMA detectors are currently available in formats as large as 256 x 1024-pixels with pixel dimensions of 25 μm square. However, a major effort is being made both at Stanford and at Ball Aerospace in Boulder, Colorado to construct 2048 x 2048-pixel UV MAMA detectors for use in the Space Telescope Imaging Spectrograph (STIS). WOODGATE et al. [1] give a detailed description of the STIS instrumentation. Two 2048 x 2048-pixel MAMA detectors will be flown on board STIS. One will have CsI deposited directly on the microchannel plate and will be sensitive to light of wavelengths between 1050 and 1700 A and a second will have a Cs_2Te photocathode with high sensitivity between 1700 and 3000 A. Figure 1 shows the rough design of the array layouts and window structures planned for these two detectors. Owing to the lack of materials with high transparencies at the shortest of these wavelengths, the window for the CsI detector is of a thin domed design. The tilt of the window is required by the multiple modes of operation of the STIS. The anode arrays for the 2048 x 2048-pixel detectors are to consist of four 1024 x 1024-pixel subarrays constructed on the same quartz substrate with a single pixel dead space between each subarray. A major milestone on the way to producing the 2048 x 2048-pixel device is the construction of an independent 1024 x 1024-pixel array. Each of the subarrays will have its own set of decoding and amplifying electronics and may be operated independently of the other three. The STIS project requires the miniaturization of the amplifier and decode circuitry for the flight systems. This design was chosen to minimize single point failures of the detectors through redundancy of components, to increase the dynamic range of the full 2048 x 2048-pixel device to approximately 4×10^6 counts s^{-1} through multiplexing, and to permit the development of the detector to proceed in a modular fashion by allowing the development of the electronics to take place at the

time that the 1024 x 1024-pixel arrays are being built and tested. The project is currently on schedule for the completion of the first 1024 x 1024-pixel detector by the end of 1987. Plans have been made to assemble the first 2048 x 2048-pixel detector by spring of 1989.

Telescopic observations using MAMA detectors represent the practical application of the detector system. In addition to the development work being done for the space telescope, ground- and rocket-based observations are being made. A program with Professor Burton Jones at Lick Observatory is underway to evaluate the detector for use in astrometry both with Ronchi ruling instrumentation and through direct imaging. The direct imaging observations have been motivated by the results of recent laboratory measurements that suggest that MAMA detectors may have very fine
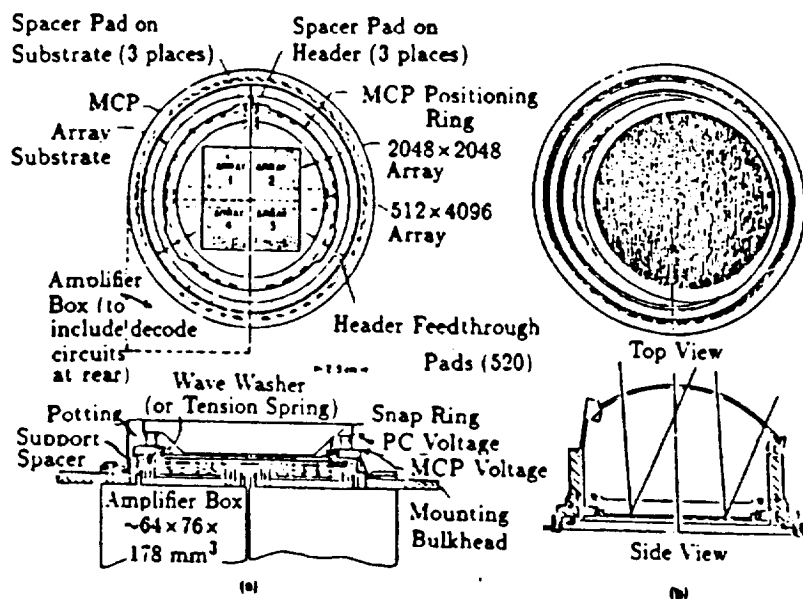

Figure 1. (a) Schematic of 2048 x 2048-pixel anode arrays and the re-entrant window for the Cs_2Te MAMA detector for STIS. (b) The thin, domed LiF window for the CsI MAMA detector.

position sensitivity. The results of some of these laboratory measurements are discussed below. A MAMA detector is scheduled to fly on a rocket flight in May of 1988 in an effort to obtain an ultraviolet image of M82 and an edge-on spiral galaxy. This project is headed by Dr. Andrew Smith of the NASA Goddard Space Flight Center.

In collaboration with Dr. Keith Hege of Steward Observatory speckle observations of the asteroid Vesta and several binary stars were made late in 1986 with a 256 x 1024-pixel bialkali MAMA in order to evaluate the performance of the MAMA detector in this demanding application. Initial evaluation of these data indicate that the point spread function of MAMA detectors is very stable and independent of count rate. Figure 2 shows laboratory measurements of the point spread function of a bialkali MAMA detector. The measurements were made by shining a spot of light with subpixel dimensions on the detector. A logarithmic scale is used on the ordinate of the graph. The pixels adjacent to the illuminated pixel show approximately 10% crosstalk. Past efforts to do speckle imaging with other detectors have been severely limited by variations in their point spread function which induce artifacts in the data reduction. The initial analysis of the MAMA speckle data indicates that the noise level in the power spectrum caused by variations in the detector point spread function is at least an order of magnitude smaller in the MAMA data than that seen in either intensified vidicons or in the PAPA detector. An S-20 MAMA has been constructed for use on speckle imaging applications. The increased red response of the S-20 photocathode is important for speckle observations because the atmospheric correlation time increases with wavelength. A red sensitive detector is extremely valuable for this application for it allows longer integration times which effectively increases the signal to noise ratio available in each image.

The rest of this paper will focus on the progress we have made in the construction and evaluation of MAMA detectors. Besides expanding the format of the arrays our current efforts have focused on improving the anode read-out of the detectors and incorporating third generation, GaAs photocathode technology into the tubes. Our interest in the speckle imaging applications for the MAMA detector is currently motivating our efforts to build a GaAs MAMA; the increased quantum efficiency and red sensitivity of the GaAs photocathode make it even more desirable than the S-20 MAMA for the speckle application. However, the astrometric program would also
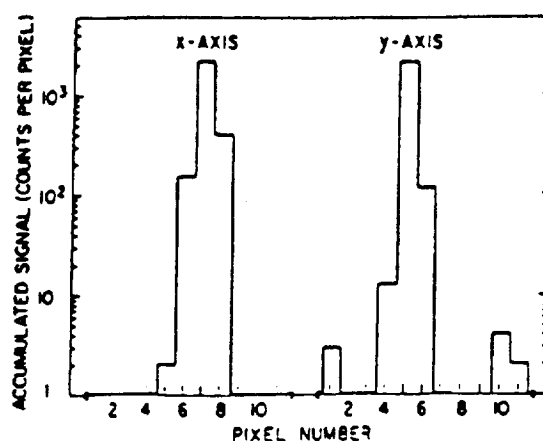
Figure 2. The point spread function of a bialkali MAMA detector. The logarithmic scale on the ordinate enhances the appearance of the signal in pixels adjacent to the peak.

benefit greatly by the availability of such a device. We have made preliminary designs for a 244 x 960-pixel GaAs detector with 14 μm square pixels and are currently in the proposal stage seeking funds for its construction.

We have recently made major improvements in the performance of MAMA detectors by utilizing a new geometry in the anode array. Until recently all MAMA anode arrays have been based on a series of "coarse" position anodes interleaved with anodes which encode the "fine" position information. A description of the "coarse-fine" arrays is given by TIMOTHY [2]. These "coarse-fine" arrays suffer from a fixed pattern sensitivity variation which is caused by uneven inductive or capacitive coupling between anodes in the array. While this fixed pattern sensitivity is easily and completely removed by flat-fielding, this is difficult to do with some applications such as speckle imaging. The new generation of anode arrays has eliminated the capacitive and inductive imbalances present in the older arrays by incorporating only "fine" anodes in the arrays. Figure 3 shows raw measurements of a uniformly illuminated field taken with a "coarse-fine" detector and similar measurements taken with a "fine-fine" detector The data for the "fine-fine" detector were taken at Ball Aerospace by Mr. R.L. Bybee

and Mr. H.E. Culver. Almost all of the variations seen in the "coarse-fine" data are attributable to the fixed pattern variations in the detector. In contrast, the variations seen in the "fine-fine" data are mostly due to shot noise of the input photon flux.

In addition to improving the flat-field response of the detector, the "fine-fine" arrays may enable us to use stacked microchannel plates in place of the single curved channel plates currently used in the detectors. In the past chevrons could not be used in MAMA detectors owing to incompatibilities between the anode arrays and the spatial size of the output pulses in chevron plates. No such incompatibilities exist with the "fine-fine" arrays. Use of a two-stage MCP configuration in the tubes could improve the amplification of the input signal and the dynamic range of the device. The point spread functions of the "fine-fine" arrays have not yet been measured, but it is expected to be significantly improved over that seen for the coarse-fine arrays (Fig. 2) owing to the decreased level of cross-talk between anodes.
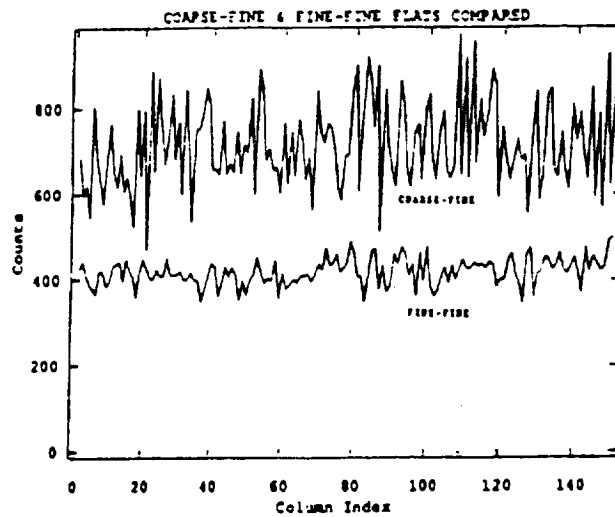

Figure 3. A comparison of raw flat field data using MAMA detectors equipped with coarse-fine and fine-fine generation anode arrays. The variations in the coarse-fine array are fixed pattern sensitivity variations caused by cross-talk between anodes. The variations in the fine-fine array are mostly due to photon shot noise.

Lately our evaluations of the detectors have centered on determining the flat
field stability and position sensitivity of these devices. The detector used for these
measurements was the bialkali tube previously mentioned. This tube is known to have
a poorly processed photocathode. The quantum efficiency of this device is negligible in
the upper left corner of the array. Figure 4 shows a trace through a central row of the
detector. The fine structure in the trace is the fixed pattern sensitivity variation caused
by the cross-coupling between adjacent pixels. Figure 5 shows evidence that the low
sensitivity corner of the array is a result of low sensitivity in the photocathode. Figure
5a shows an 8 hour dark integration with the photocathode biased on. Figure 5b shows
a similar dark with the photocathode back-biased. The dark counts with the cathode
biased off are uniform while the counts with the cathode biased on show structure simi-
lar to that seen in flat fields taken with this device.

The flat field response of the bialkali detector is seen to vary with exposure
time. The sensitivity of the detector's upper left corner decreases by approximately 20%
if the high voltage is left off or the detector is left unilluminated for several tens of
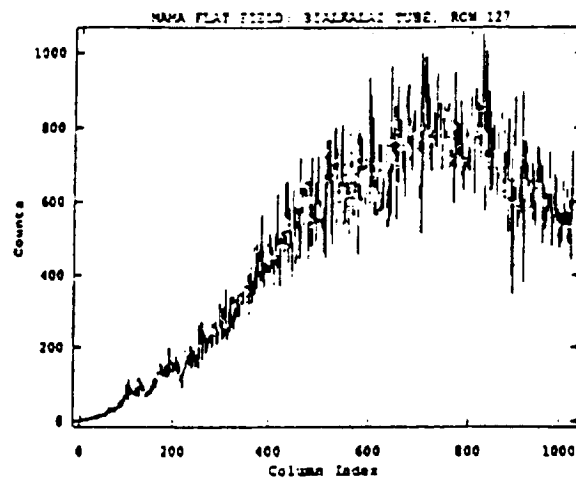

Figure 4. A row trace is shown through the middle of a raw flat field image taken with
a 256 x 1024-pixel bialkali MAMA. The decrease of detector sensitivity to the left is
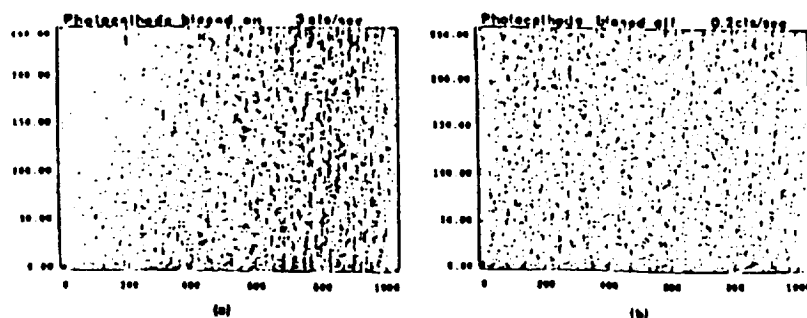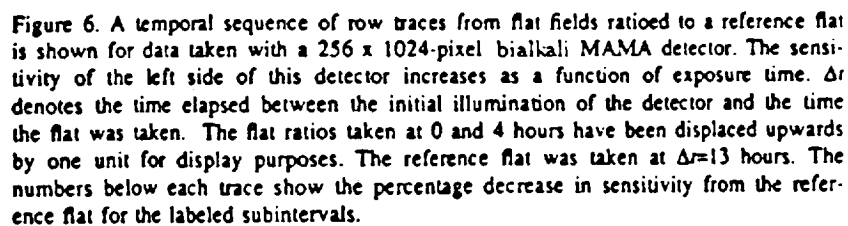attributed to an improperly processed photocathode.

Figure 5. Two eight hour darks are shown. (a) Dark taken with the photocathode at its normal operating potential. (b) Dark taken with the photocathode back biased. The dark count rate over the entire array is given for each exposure in the figure.

days. The sensitivity of this region is restored by several hours of uniform illumination at the normal operating voltage. Figure 6 illustrates this effect. The detector was first left unilluminated for 58 days. A series of 1 hour flat fields were then taken. Each flat field was ratioed to a flat field taken after 13 continuous hours of illumination. Row traces through some of these flat field ratios are shown in Fig. 6. The time elapsed from the initial illumination of the detector is given for each trace by Δt. Photon shot noise causes the high frequency structure. The magnitude of the high frequency structure increases to the left owing to the decreasing sensitivity of the detector as shown in Fig. 4. If the flat fields were completely stable, then the slope of each trace should be zero. This is not the case and the percentage departures from a straight line averaged over the subintervals shown are labeled below each trace. The magnitude of the departure increases to the left and decreases with exposure time. We interpret the measurements shown in Figs. 4 through 6 as indications that the photocathode has a gradient in its cesium concentration which is affected by cesium migration caused by long term flat field exposures.

We have measured the position sensitivity of the detector by illuminating the detector with a 3 μm (FWHM), movable spot of light. The light source is mounted on a stepper motor driven X-Y translation table. The spot was moved across the detector in

Figure 6. A temporal sequence of row traces from flat fields ratioed to a reference flat is shown for data taken with a 256 x 1024-pixel bialkali MAMA detector. The sensitivity of the left side of this detector increases as a function of exposure time. Δr denotes the time elapsed between the initial illumination of the detector and the time the flat was taken. The flat ratios taken at 0 and 4 hours have been displaced upwards by one unit for display purposes. The reference flat was taken at Δr=13 hours. The numbers below each trace show the percentage decrease in sensitivity from the reference flat for the labeled subintervals.

1 μm steps and an image of the spot was taken at each step. These images were flat fielded and then centroid positions were computed for each image. A linear fit was then made to a plot of the centroid vs. stepper motor positions. This fit was then subtracted

from the data to produce the residual plot shown in Fig. 7. The ordinate units are in fractions of a pixel. The abscissa shows the stepper motor position and is labeled in microns. The plotted measurements span two 25 μm pixels. The residual plot of a detector with perfect position sensitivity would be a horizontal line at a residual of zero. Oscillations about this line are caused by the convolution of a finite pixel dimension with the size of the input source. These digitization errors can be modeled if the source size is known. The dashed line in Fig. 9 shows the digitization errors calculated from a model of the pixel response function of the detector and a gaussian profile of the input spot. The standard deviation of the measured residuals from the dashed line is 0.005 pixels. The current measurement is limited by the statistics of the flat field and by uncertainties in the movement of the stepper motors. We are in the process of acquiring higher precision translation tables and longer flat field integrations in order to find the intrinsic limitations of the device. Measurements over larger areas are being made to determine if this accuracy can be maintained over several pixels.
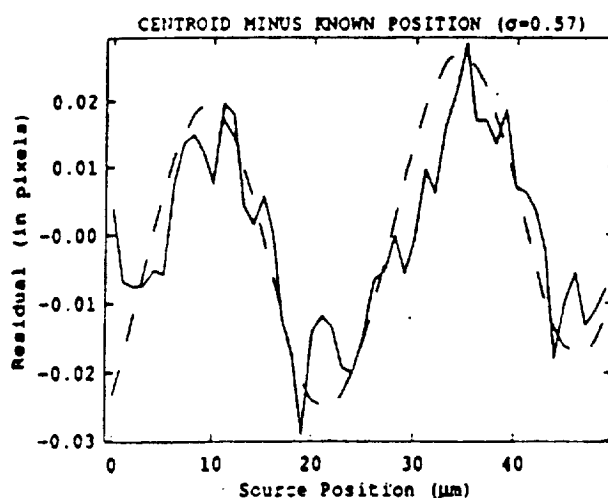

Figure 7. A measurement of the position sensitivity of a MAMA detector with 25 μm square pixels is shown. A 3 μm spot of know position is moved across the detector in 1 μm increments. Centroid positions are calculated at each position. The ordinate residual is the centroid position subtracted from the known spot position. The dashed line shows the expected residuals from a model of a 3 μm spot convolved with an estimate of the pixel response function of the detector.

Acknowledgements

References

1. B.E. Woodgate, A. Boggess, T.R. Gull, S.R. Heap, et al., "Second generation spectrograph for the Hubble Space Telescope," *SPIE Instrumentation in Astronomy VI, 627*, 350-362 (1986).

2. J.G. Timothy, "Imaging at soft X-ray wavelengths with high-gain microchannel plate detector systems," *SPIE X-Ray Imaging II, 691*, 35-42 (1986).

Very-large-format pulse-counting UV detectors

J. Gethyn Timothy

Center for Space Science and Astrophysics
Stanford University, ERL314
Stanford, CA 94305

ABSTRACT

Multi-anode Microchannel Array (MAMA) detector systems with formats of 2048 x 2048 pixels and pixel dimensions of 25 x 25 μm^2 are being developed for use in the NASA Goddard *Hubble* Space Telescope Imaging Spectrograph (STIS). This paper describes the current state of development of these detector systems.

1. INTRODUCTION

The Multi-anode Microchannel Array (MAMA) detector systems are high-resolution pulse-counting imaging systems designed specifically for use in space. The MAMA readout technique produces the highest dynamic range (~10^6 counts s^{-1} (random) with a 10% coincidence loss), spatial resolution (25 μm FWHM) and position sensitivity (<1 μm) of any currently available pulse-counting imaging detector system.[1] Very-large-format MAMA detector systems are currently under development for use at ultraviolet wavelengths in the NASA Goddard *Hubble* Space Telescope Imaging Spectrograph (STIS).[2]

This paper describes the current state of development of these detector systems.

2. MAMA DETECTOR SYSTEMS

The detailed evaluation of the MAMA detectors is being undertaken using the (256 x 1024)-pixel systems with 25 x 25 μm^2 pixels. Systems of this type with a coarse-fine and a balanced coarse-fine encoding electrode geometry are currently under intense evaluation in the laboratory and at ground-based telescopes[3,4] and (224 x 960)-pixel arrays with a capacitively-balanced and inductively-decoupled fine-fine encoding electrode geometry have undergone a preliminary evaluation[5,6]. A (256 x 1024)-pixel balanced coarse-fine detector system is currently being prepared for flight on a NASA Goddard astronomy sounding rocket. This detector has an opaque CSI photocathode deposited on the front face of the MCP and was fabricated by EMR Photoelectric, Inc.[7] Since the MAMA employs a step and repeat encoding-electrode geometry, the size can be increased without degrading the spatial resolution or position sensitivity. The capacitance of the readout array will increase with size, but even in the 1024 x 1024 pixel format remains small compared with the dynamic input capacitance of the charge-sensitive amplifiers used in the current generation of electronics.

The critical requirement for a stable, long-life MAMA detector tube, used in the open-structure mode at extreme ultraviolet (EUV) and soft x-ray wavelengths, and sealed for use with activated photocathodes at near ultraviolet and visible wavelengths, is a properly conditioned high-gain Microchannel Plate (MCP). To date, all of the MCPs used in the MAMA detector tube have been curved-channel MCPs,[8] which produce a high gain and a narrow output pulse-height distribution with a very low level of ion-feedback in a single plate. In order to evaluate these MCPs, in the 25-mm format for use with the (256 x 1024)- and (224 x 960)-pixel arrays, and in the 40-mm format for use with the (1024 x 1024)-pixel arrays we have fabricated the (1 x 100)-pixel and (1 x 76)-pixel discrete-anode arrays, shown in Figure 1.

The evaluation of the MCPs is carried out in a high-vacuum, hydrocarbon-free environment in a demountable MAMA detector tube of the type shown in Figure 2. Only molecular absorption and ion pumps are used on these systems and the evaluation is typically carried out at pressures below 10^{-7} Torr. Conditioning of a curved-channel MCP consists typically of a bake at a temperature of 300°C or greater and a "scrub" with the MCP stimulated either by high energy (600 eV or greater) electrons or by a ultraviolet photons from a mercury "Penray" lamp to a total signal level of not less than 0.4 C cm^{-2}.

The (2048 x 2048)-pixel MAMA detector (75-mm-format) for STIS will have 25 x 25 μm^2 pixels and an active area of 52 x 52 mm^2. To increase the dynamic range and to provide redundancy for a five-year flight mission, the detector will be constructed from four contiguous (1024 x 1024)-pixel arrays with a single-pixel dead space, as shown in Figure 3.
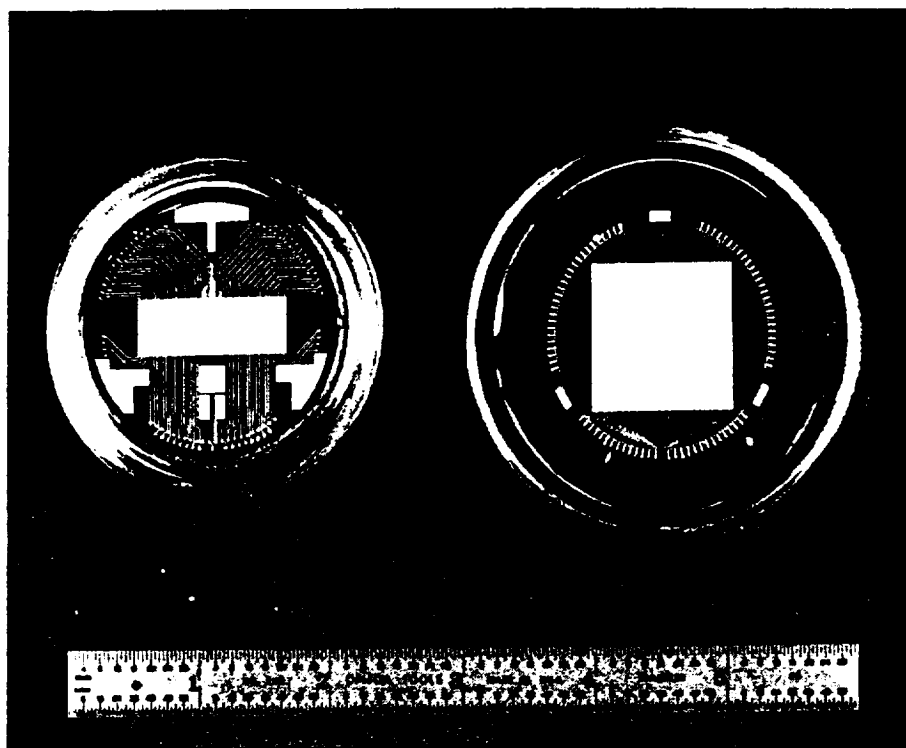
Figure 1. (1 x 100)-pixel and (1 x 76)-pixel discrete-anode arrays for the evaluation of the 25-mm and 40-mm-format high-gain MCPs respectively.

As the first step in the fabrication of this detector, Ball Aerospace Systems Division (BASD)[9] have fabricated and now have under test the first (1024 x 1024)-pixel detector system. The readout array for this system (see Figure 4) is identical to one quadrant of the STIS array. All of the encoding electrodes are on only two sides of the array, although some of the output electrodes have been brought into the other two quadrants because of substrate area limitations inside the 40-mm-format detector tube. This array employs a capacitively-balanced and inductively-decoupled fine-fine encoding electrode structure. The performance of the first 40-mm-format curved channel MCP, fabricated by Galileo Electro-Optics Corp (GEOC)[10] was nominal.

3. FUTURE DEVELOPMENTS

We see no technological roadblocks to prevent the fabrication of the (2048 x 2048)-pixel MAMA detector systems. A number of other papers in these proceedings underscore the power of this technology. With the improvements in high-gain MCPs using the "long life" glass, recently introduced by GEOC, and with the BASD anode-array fabrication facility in operation we see no problems in fabricating MAMA detectors in any format that can be accommodated on a 140-mm-diameter substrate. Spatial resolution and positive sensitivity will be independent of the size of the active area. Work has now started on the design of the 75-mm-format ceramic header and tube body, and the first detector tube is expected to be under test in the Fall of 1989 if the current rate of funding by NASA is not reduced. BASD is also sufficiently confident of the accuracy of their lithography that we have initiated the fabrication of a set of MAMA detectors with 224 x 960 pixels and pixel dimensions of 14 x 14 μm^2. Speed improvements in the electronics with pulse-pair resolutions of better than 10 ns can also be foreseen, and improvements to the high-gain MCPs should allow a linear response to greater than 10^3 counts pixel^{-1} s^{-1} (25 x 25 μm^2 pixels).
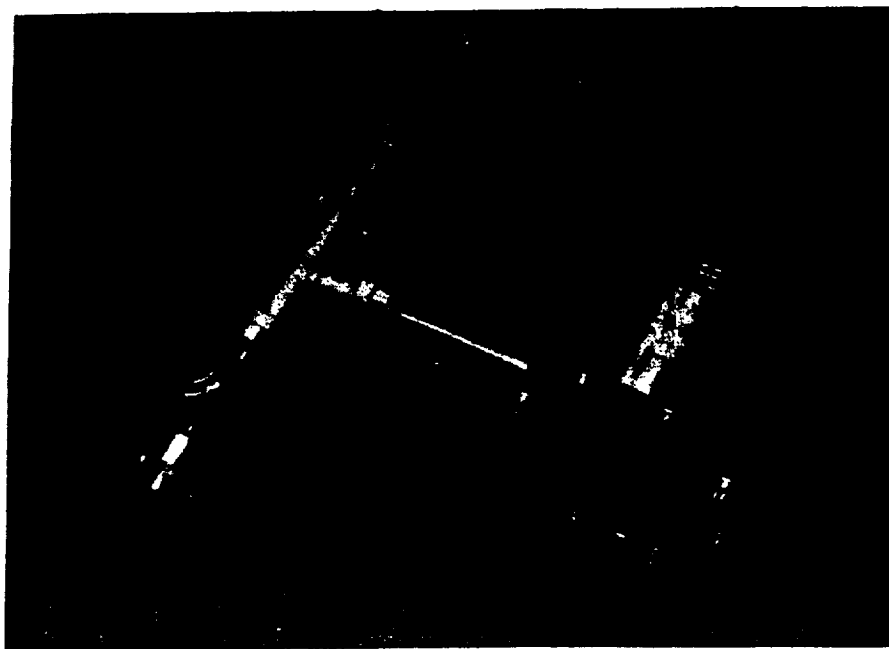
(a)
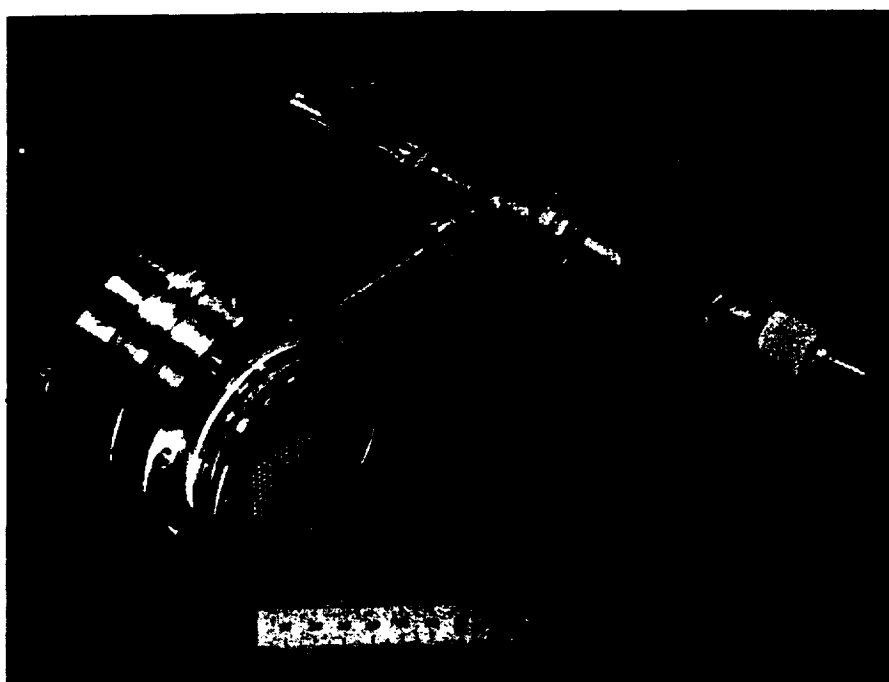
(b)

Figure 2. Demountable MAMA detector tube for the evaluation of 40-mm-format high-gain MCPs.
a. Front view.
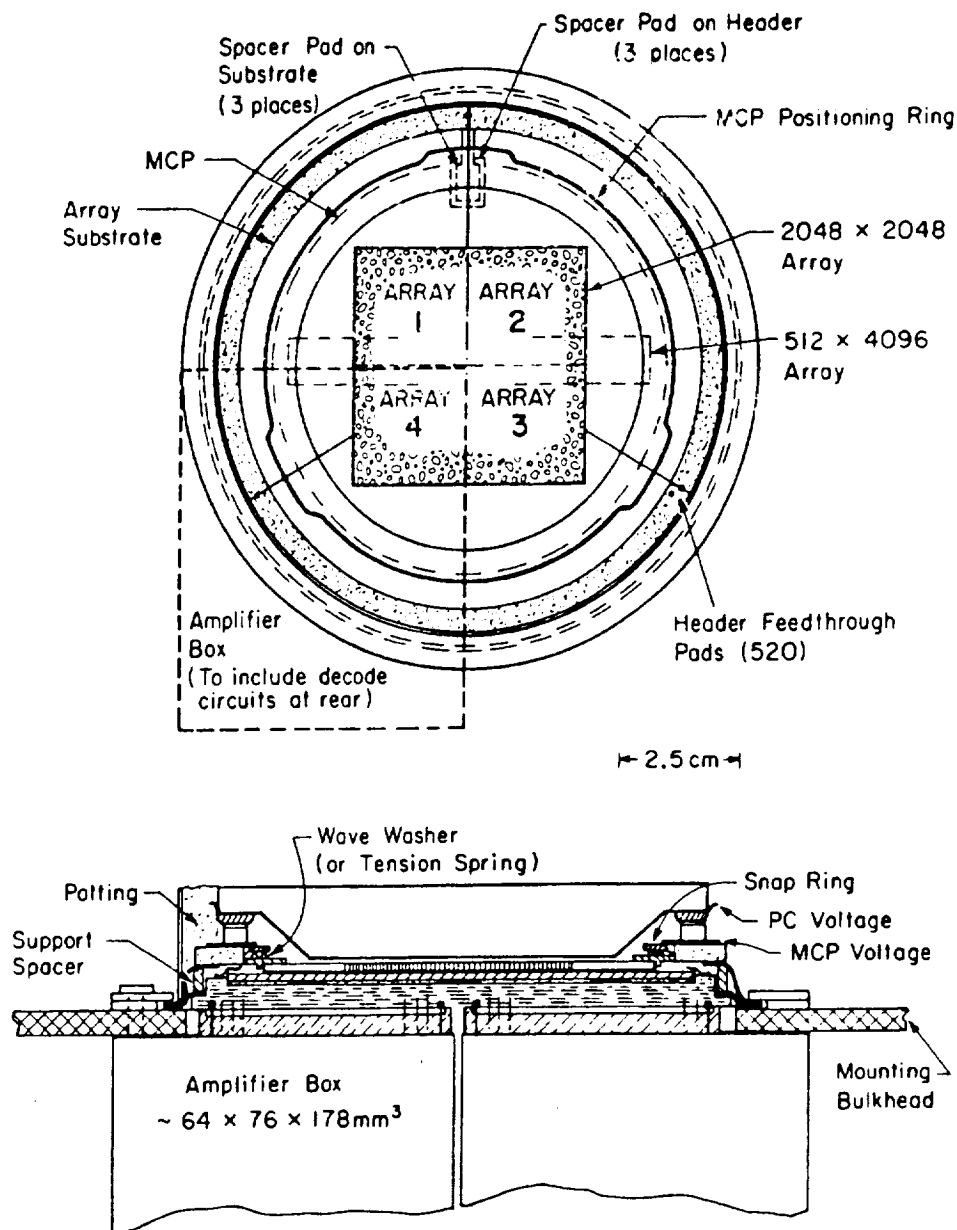b. Rear view showing the 170-pin multi-layer ceramic header.

Figure 3. Configuration of the (2048 x 2048)-pixel MAMA detector for the NASA Goddard *Hubble* Space Telescope Imaging Spectrograph (STIS).
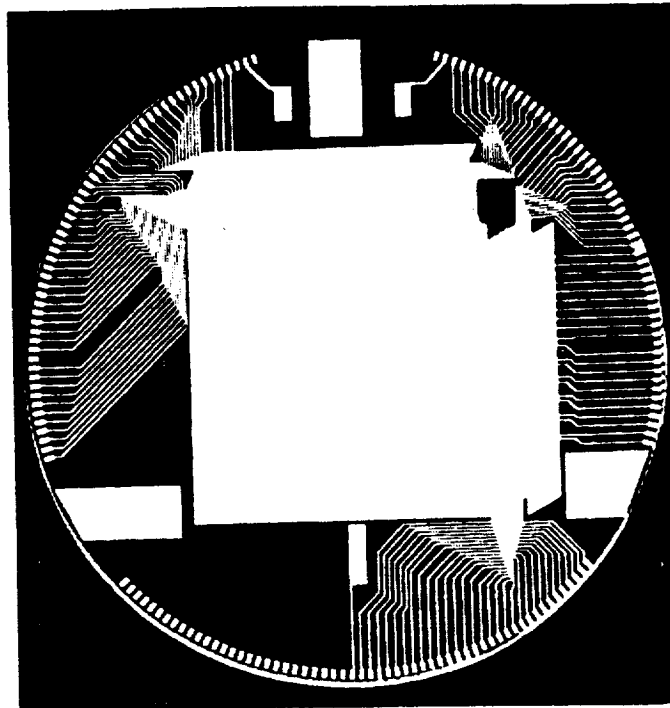
4. ACKNOWLEDGEMENTS

Figure 4. (1024 x 1024)-pixel MAMA readout array with 25 x 25 μm^2 pixels.

5. REFERENCES

1. J. G. Timothy, "Photon counting detector systems", in Instrumentation for Ground Based Optical Astronomy, L. B. Robinson, ed., Springer Verlag, 516-527 (1988).

2. B. E. Woodgate and the STIS science team," Second generation spectrograph for the *Hubble* Space Telescope", in Instrumentation in Astronomy VI, D. L. Crawford, ed., Proc. SPIE 627, 350-362 (1986).

3. J. S. Morgan and J. G. Timothy, "Status of the MAMA detector development program", in Instrumentation for Ground Based Optical Astronomy, L. B. Robinson, ed., Springer Verlag, 557-567 (1988).

4. M. Cullum, "Experience with the MAMA detector", in Instrumentation for Ground Based Optical Astronomy, L. B. Robinson, ed., Springer Verlag, 568-573 (1988).

5. J. S. Morgan, D. C. Slater, J. G. Timothy and E. B. Jenkins, "Position sensitivity of MAMA detectors", these proceedings (1988).

6. D. B. Kasle, "Decoding techniques for fine-fine geometry multi-anode microchannel arrays", these proceedings (1988).

7. EMR Photoelectric, Inc., P. O. Box 44, Princeton, NJ 08540.

8. J. G. Timothy, "Curved-channel microchannel array plates", Rev. Sci. Instrum. 52 (8), 1131-1142 (1981).

9. Ball Aerospace Systems Division, P. O. Box 1062, Boulder, CO 80306.

10. Galileo Electro-Optics Corp., Galileo Park, Sturbridge, MA 01518.

Centroid position measurements and subpixel sensitivity variations with the MAMA detector

Jeffrey S. Morgan, D. C. Slater, John G. Timothy, and E. B. Jenkins

Initial measurements of the position sensitivity of a visible-light multi-anode microchannel array (MAMA) detector show that centroid calculations for image spots are accurate to better than 0.04 pixels even with sources that are essentially delta functions at the photocathode. Subpixel sensitivity variations of 10–15% are typically found for pixels in the array. Variations as large as 30% are possible in the worst conditions. These variations limit the photometric accuracy of the detector when very small scale features are observed. The photometric accuracy and the position sensitivity of the detector appear to be limited by cross-coupling effects within the anode array. Initial measurements with more recent designs of the detector show that most or all of this cross-coupling has been eliminated. We will report on the position sensitivity of the newer detectors when they become available for testing.

I. Introduction

The precision to which one is able to define the spatial position of an object on the focal plane of an imaging detector is important for many applications. In astrometry one is interested in obtaining the relative positions of stars. In spectroscopy the precise location of spectral lines is of interest for many reasons. In image processing some commonly needed image manipulations such as rotation and alignment require a knowledge of the positions of common features within images. In such applications it is common practice to compute the centroid positions of image features in an effort to obtain positions to an accuracy of a fraction of a pixel.

A detector's position sensitivity is intimately associated with its photometric accuracy. This point will become evident throughout the course of this article. In some important situations the photometric accuracy and the position sensitivity of a detector are determined by the subpixel response of the detector. It is therefore highly appropriate to consider these detector characteristics together.

Some theoretical work and numerical simulations have been published concerning the accuracy of position measurements. Bobroff[1] presents a maximum likelihood analysis of position measurements errors assuming a known point spread function (PSF) for the detector. He evaluates the position errors by computing the χ^2 fit of data to the PSF. His analysis includes a treatment of detector noise. Bulau[2] reports on numerical simulations of several centroid algorithms. The purpose for his simulations is to choose a rapid algorithm which may be computed in real time and implemented cheaply in hardware. Gatewood et al.[3,4] and KenKnight[5] discuss the positional accuracy obtainable with photographic imaging and the use of Ronchi rulings. The focus of this paper is to delineate and to define the limitations of position sensitivity inherent within a class of imaging detectors known as the Multianode Microchannel Arrays (MAMAs).

In practical use the accuracy of computed centroid positions can be limited by the performance of the detector used rather than the statistics or spatial width of the input signal. Two relevant parameters to consider are detector noise and the detector's uniformity of response across a single pixel. It is difficult to estimate the effects of subpixel variations in the response of the detector. In addition, users are often lacking such detailed knowledge of the detector response. For detectors which utilize microchannel plates (MCPs) for the amplification of the input signal, the issue of subpixel variations in the detector response is important and nontrivial.

We show that, despite these practical difficulties, highly accurate centroiding may be carried out with MAMA detectors. Our results show that centroid po-

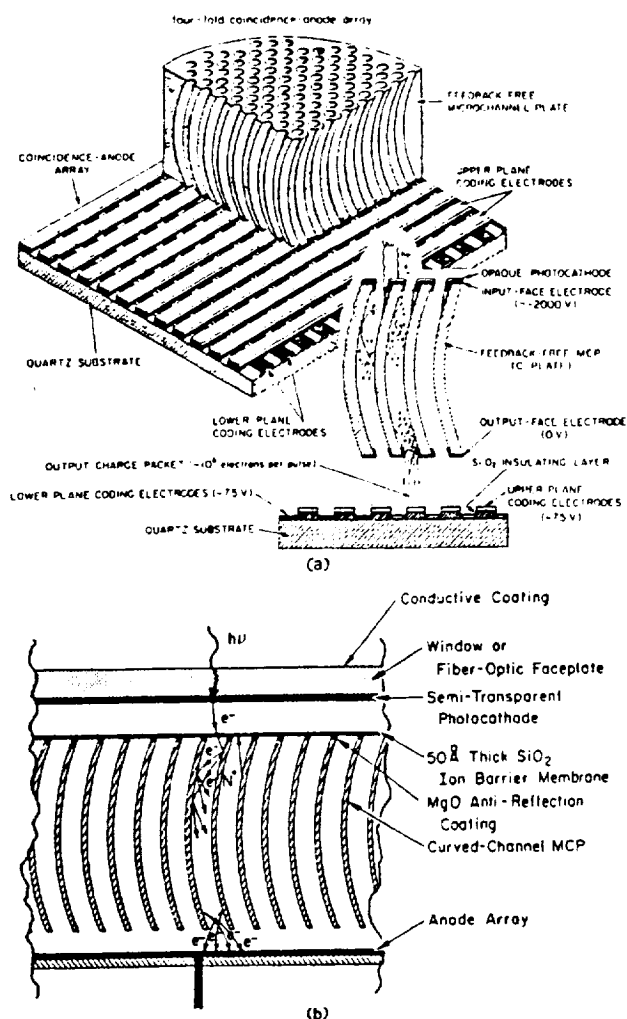Fig. 2. Microphotograph of the pores in a microchannel plate. The pore diameters are 12 μm on 15-μm centers.

Fig. 1. (a) Schematic of a typical MAMA detector for use at EUV and soft x-ray wavelengths. (b) Schematic of a visible-light MAMA detector with a semitransparent, proximity focused photocathode.

sitions may be determined with visible-light MAMA detectors to an accuracy of better than 0.04 pixels, with modest signal levels and with features smaller than one pixel. We also address here the issue of subpixel sensitivity variations in the MAMA detector. We show that for MAMA tubes utilizing proximity focused, semitransparent photocathodes, these variations are typically of the order of 10–15%. We consider changes to the detector which should result in considerably improved centroid detection and smaller subpixel sensitivity variations.

II. The MAMA Detector

An understanding of the characteristics and operating principles of the MAMA detector is essential for following the discussion in subsequent sections of this article. Figure 1(a) shows the basic configuration of a MAMA detector. There are two basic types of MAMA detector, those with opaque photocathodes deposited on the front face of the MCP for use at extreme ultraviolet and soft x-ray wavelengths and those with semitransparent photocathodes deposited on a window
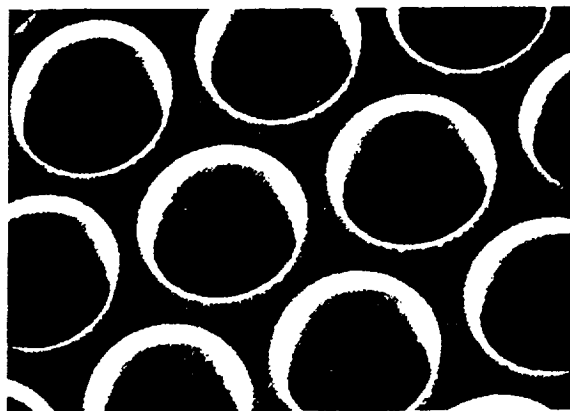
that is mounted in proximity focus with the front face of the MCP [see Fig. 1(b)] for use at near ultraviolet and visible wavelengths. A potential difference of ~500 V accelerates the electrons which emerge from the photocathode and the smallness of the gap limits their lateral spread. This configuration is usually called a proximity focus. Visible-light detectors fabricated to date utilize proximity focused photocathodes to convert the incident photon flux to photoelectrons. A potential of several hundred volts between the photocathode and the front face of the MCP is required so that the photoelectrons can penetrate the ion-barrier membrane covering the channels in the MCP. The detector used in this study contains a blue sensitive, bialkali photocathode on a 7056 glass window with a separation of ~300 μm between the window and the front fact of the MCP.

A potential of a few thousand volts is applied between the front and rear surfaces of the MCP. As an electron hits the semiconducting layer on the glass surface, an average of about two secondary electrons is emitted. An avalanche develops as the electrons are accelerated down the channel and hit the channel walls. The channels in the MCPs used in MAMA detectors are curved to inhibit the feedback of ions which are liberated by the electron cascade from moving toward the front of the channels where they can cause after pulses by stimulating secondary cascades. The amplification achieved is a function of the L/D ratio of the plate where L and D are, respectively, the length and diameter of the channels. A modal gain of ~10^6 is achieved without significant ion feedback in a single curved channel MCP. The geometry and uniformity of the channel packing for a typical MCP is shown in Fig. 2. The channels in this MCP have diameters of 12 μm and are spaced on 15-μm centers.

Two crossed anode grids are mounted in proximity focus ~50 μm behind the output face of the MCP at an attractive potential of 80 V. Electron avalanches from the MCP pores are collected by the crossed anode grids, amplified, and then sent to coincidence decoding circuitry which determines the spatial position of each pulse.[6] The geometry of the anode array determines

the pixel size and image format of the detector. The detector evaluated has 25 × 25-μm^2 pixels in a (256 × 1024)-pixel format.

An assumption that is normally made in centroid detection is that the detector sensitivity is uniform from pixel to pixel. Violation of this assumption or improper flat-field corrections for a nonuniform response can result in large errors in the derived centroid positions. Figure 3 illustrates that MAMA detectors have good temporal stability. The figure shows the results of dividing one flat field by another taken 58 days later. A 200-point section from a single row in the ratio image is plotted. The row and section shown were chosen to coincide with the region in the array in which the position sensitivity measurements were made. The intensity of the flat-field lamp was not constant, as indicated by an average ratio less than unity, but the image is uniform to within the photon statistics of the flat-field exposures. This is indicated by the ratio of the expected statistical errors given by $\sqrt{2\bar{n}}$, where $\bar{n}$ is the average number of counts in each pixel, with the standard deviation, σ_r, of points in the ratio image. For the data in Fig. 3, $\bar{n}$ = 800 and $\sqrt{2\bar{n}}/\sigma_r$ = 1.05. At the 3% level there are no temporal variations in the flat-field corrections. Several exposures with $\bar{n}$ = 800 were coadded for the flat field used on the centroid data. No statistically significant differences were found between individual flat fields or between coadded subsets of these flat fields.

In a subsequent section we show that our position measurements are not currently limited by the statistics of the flat field. However, we also show that, despite the temporal stability of the detector's flat-field response, problems were encountered in applying these flat-field corrections to the position sensitivity measurements. The cause of these problems is a topic discussed at the conclusion of this paper.

Subpixel sensitivity variations can also create errors in centroid positions. We define here the pixel response as the relative probability of photon detection as a function of position within a single pixel. Perfect pixels have a uniform response. We will often loosely refer to a nonuniform pixel response as a sensitivity variation. The pixel response of MAMA detectors is a function of the proximity focus on both sides of the MCP and the performance of the anode arrays in detecting the output charge cloud. Because MAMA detectors come with directly deposited and proximity focused photocathodes, it is desirable to define the pixel response of the detector in terms of the interaction of the anode array with the output pulses from the MCP.

At some spatial scales the channel spacing of the MCP should cause sensitivity variations. This is especially true if the input face of the MCP has a thin film on its front surface to block ions which could bombard and degrade the photocathode. Owing to the film, photoelectrons impinging on the interstitial area between the channels are absorbed without producing secondary emission. The detector used here employed a filmed MCP. For input beams with spatial
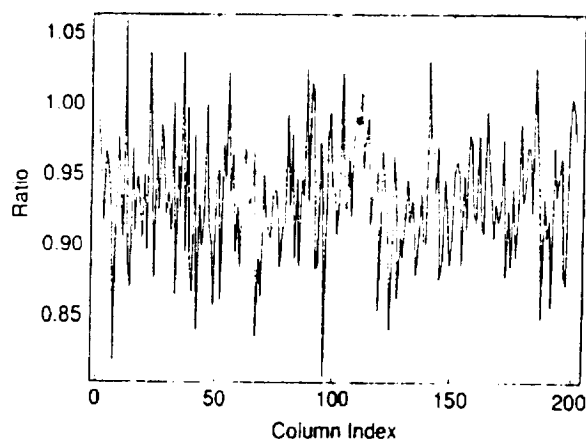

Fig. 3. Ratio of two flat fields taken 58 days apart. The flat-field exposures are reproducible to within the statistical errors of the exposures. For each flat field $\bar{n}$ = 800 counts.

widths of the order of, or smaller than, the diameter of a single channel, the channel spacing of the MCP will induce significant subpixel sensitivity variations. However, numerical simulations show that these variations fall off rapidly with input beamwidth. For Gaussian input beams with widths of 1 and 1.3 channel diameters (FWHM) the channel spacing will induce sensitivity variations of 50% and 15%, respectively.

The size of the smallest spot of electrons that can be received by the MCP input face is limited by the wavelength of the detected photon, photocathode type, and the photocathode-to-MCP spacing. For monoenergetic emission from a photocathode with a Lambertian phase function ($\cos\theta$), a point source on the photocathode will be spread to a uniform disk of radius r on the MCP given by

$$r = 2D\sqrt{\overline{V_e}/\overline{V_d}}, \qquad (1)$$

where D is the distance between photocathode and MCP, V_d is the gap voltage, and V_e is the initial energy of the emitted photoelectrons. For visible photocathodes V_e is typically 1 eV.[7] V_d and D for our detector were 500 V and 305 ± 25 μm, respectively. For these conditions Eq. (1) gives r = 27.3 μm, corresponding to a full spot width of 54.6 μm. This is far too large to be consistent with the total point spread function (PSF) of the detector. The detector pixels are 25 μm wide. Pixels on either side of one whose center is illuminated by a delta function source show a response <5% of the total intensity. An approximation roughly consistent with the photoelectron energy distributions measured by retarding potential techniques is given by assuming a Maxwellian dispersion of emission energies about a most probable value of 1 eV. However, this only decreases the spot size to a Gaussian profile with 42-μm FWHM.[8] Our measurements of the total detector PSF require the spreading from the photocathode to be <20-μm FWHM. Later we present measurements that show that there are no subpixel sensitivity variations attributable to the channel spacing with amplitudes greater than ~2% of the peak pixel sensitivity. From such measurements a lower limit of 16-μm

FWHM can be derived for the width of the input spot. Monte Carlo calculations of the beam spreading from the proximity focus show that our constraints on the input spot size imply an emission phase function that is approximately proportional to $\cos^5\theta$. This is quite consistent with Eberhardt's measurements of the transfer properties of proximity focused tubes.[9] For blue light ($\sim$4100 Å) on an S-20 photocathode he measured beam spreading consistent with an average radial emission energy of 0.3 eV. The filter used in our measurements had a central wavelength of 4500 Å. A phase dependence of $\cos^5\theta$ and emission energies of 1 eV give an average radial emission energy of 0.34 eV. Eberhardt points out that evidence indicates that the multialkalai photocathodes (e.g., S-20) have smaller average emission energies than bialkalai photocathodes. We adopt here 18-μm FWHM as an estimate of the spot size on the input face of the MCP in the proximity focused tube.

An understanding of the array layout and coincidence logic is necessary to understand what shapes the spatial response of a single pixel. What follows is a description of the array layout in the MAMA detectors and a discussion of some aspects of the current coincidence logic. Interested readers are referred to an article by Timothy[10] for more detail on the array layouts and coincidence logic used in MAMA detectors.

The anode array consists of two sets of electrodes. One axis of the pulse coordinates is encoded by each level. Figure 1 shows how the orientation of the electrodes in one level are crossed with respect to that of the electrodes in the second level to simultaneously encode both x and y coordinates of the detected charge pulses. The method of position encoding is the same for each level; only the number of electrodes in each level differs according to the lengths of the x and y axes of the image format. Figure 4 shows the layout for one level of the anode array.

Each level consists of an alternating sequence of fine and coarse electrodes. The center-to-center spacing of the electrodes is 25 μm. Pixel centers lie halfway between adjacent anodes. Twofold and threefold events are photoevents which trigger pulses above a predetermined threshold level on two and three adjacent anodes, respectively. Onefold events are disallowed by properly configuring the gap and gap voltage between the MCP and the anode array. Twofold and threefold events have unique addresses in the current array layout. Events triggering pulses on four or more adjacent electrodes do not and are therefore rejected by the coincidence logic.

The method in which twofold and threefold events are coadded in current versions of the MAMA detectors gives rise to an asymmetric pixel response curve. Each anode lies at the edge of a 25-μm pixel. It is therefore fairly obvious how to assign a pixel location for any twofold event. It is less obvious how this is done with threefold events since these events appear to be centered on the edge of two adjacent pixels. If all the pulses from the MCP were uniform with an amplitude such that each pulse was capable of generating a
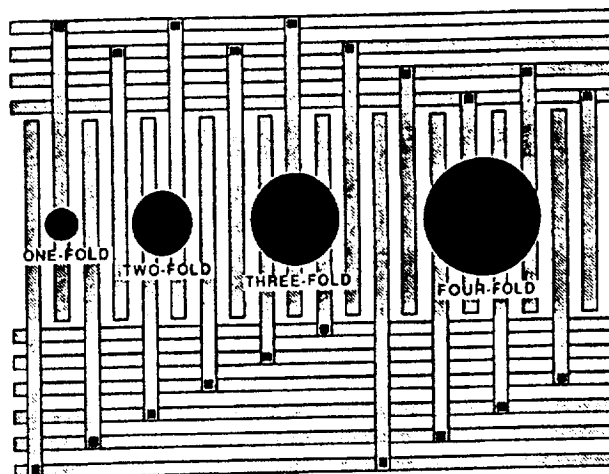

Fig. 4. Simplified layout of one level of the anode array. The spots denote the size of charge clouds from the MCP. Coarse electrodes are at the top of the diagram and fine electrodes are at the bottom.

threefold event, one could safely assign all events into 12.5-μm rather than 25-μm pixels. In this case pixel centers would lie both between adjacent anodes and on the anodes themselves. Twofold events would include all pulses that fell between adjacent anodes and threefolds would include all pulses that fell on an anode. This situation is perfectly symmetric and would not lead to an asymmetric pixel response curve. However, the pulse height distribution from the MCP includes a spread of pulse amplitudes and a significant number of twofold events come from small amplitude pulses incapable of producing threefold events. The circuitry in current MAMA detectors sums the twofold events in a single 12.5-μm bin with the threefold events in the next highest 12.5-μm bin to form a single 25-μm pixel. The result is a more uniform pixel-to-pixel response which is less sensitive to fluctuations of the bias voltages applied to the anode arrays. This is done at the expense of the pixel response function which becomes asymmetric owing to the unequal number of twofold and threefold events. By carefully tuning the bias and threshold voltages it is possible to equalize the number of twofold and threefold events and to therefore restore the symmetry of the pixel response curve, but this can only be done at the expense of the overall detective quantum efficiency.

III. Poisson Statistics

Poisson statistics of the incoming photoevents represent the most fundamental limitation of centroiding accuracy. Gatewood et al.[4] showed that for the Ronchi grating technique errors in stellar positions are proportional to $S^{-1/2}$, where S is the total number of counts recorded. We derive here the positional errors in centroid calculations which arise from the shot noise of the detected photons and show that the errors are proportional to $S^{-1/2}$ in this case also. In addition, the errors are proportional to the width of the input spot size. We also derive here error equations appropriate for situations where either detector noise, a uniform

background signal, or the flat-field statistics are significant contributors to the positional uncertainties.

A centroid position is given by the following expressions for x_c and y_c:

$$x_c = \frac{\sum\limits_{ij}^{N} x_j n_{ij}}{\sum\limits_{ij}^{N} n_{ij}} \text{ and } y_c = \frac{\sum\limits_{ij}^{N} y_i n_{ij}}{\sum\limits_{ij}^{N} n_{ij}}, \qquad (2)$$

where x_j, y_i, and n_{ij} are the coordinates and counts associated with the pixel in row i and column j of the output array. The expressions for the errors in x_c and y_c will be identical except that y_i will substitute for x_j in the final equation. We will therefore focus only on the expression for the errors in x.

For formulas of the form $x = u/v$, the generalized law of error propagation may be used to derive that s_x, the errors in x, are given by

$$\frac{s_x^2}{x^2} = \frac{s_u^2}{u^2} + \frac{s_v^2}{v^2} - \frac{2s_{uv}}{uv}, \qquad (3)$$

where s_u^2 and s_v^2 are the variance in the measurements of u and v, respectively, and s_{uv} is the covariance of these quantities.[11] The variance and covariance are defined by the equations

$$s_u^2 = \overline{(u - \bar{u})^2} = \overline{u^2} - \bar{u}^2, \qquad (4)$$

$$s_{uv} = \overline{(u - \bar{u})(v - \bar{v})} = \overline{uv} - \bar{u}\bar{v}, \qquad (5)$$

where $\bar{u}$ and $\bar{v}$ are the average values of u and v.[12]

From Eq. (2) we make the following substitutions for u and v:

$$u = \sum\limits_{ij}^{N} x_j n_{ij} \text{ and } v = \sum\limits_{ij}^{N} n_{ij}. \qquad (6)$$

Using Eqs. (4)–(6) we have derived the following relations:

$$s_u^2 = \sum\limits_{ij}^{N} s_{ij}^2 x_j^2 + \sum\limits_{ij \neq kl}^{N} s_{ijkl} x_j x_k, \qquad (7)$$

$$s_v^2 = \sum\limits_{ij}^{N} s_{ij}^2 + \sum\limits_{ij \neq kl}^{N} s_{ijkl}, \qquad (8)$$

$$s_{uv} = \sum\limits_{ij}^{N} s_{ij}^2 x_j + \sum\limits_{ij \neq kl}^{N} s_{ijkl} x_j, \qquad (9)$$

where s_{ij}^2 is the variance of n_{ij}, the counts in the ijth pixel and s_{ijkl} is the covariance of the counts between pixels at coordinates i,j and k,l. We show in Sec. V that for MAMA detectors the covariance between pixels is negligible compared to the other terms in Eqs. (7)–(9) and we are therefore justified in setting $s_{ijkl} = 0$. However, even if s_{ijkl} were comparable to s_{ij}^2 this would remain a fair approximation since Eq. (3) shows that the effects of the increase it causes in the terms s_u^2 and s_v^2 are approximately canceled by the increase in s_{uv}.

We need to define the source and character of the noise that causes s_{ij}^2 to be nonzero in Eqs. (7)–(9). Data numbers in a flat-fielded image are given for each pixel by the formula

$$n_{ij} = \bar{n}_f \frac{(n_{ij})_o}{(n_{ij})_f}, \qquad (10)$$

where $(n_{ij})_o$ and $(n_{ij})_f$ are the data numbers in the object and flat-field recordings, respectively, and the normalization factor, n_f, is the average data number in the flat-field measurement. Using Eq. (3) we can determine the variance of n_{ij} if the variances of the object and flat-field recordings are known. We assume that detector read noise characterized by a variance σ_r^2 and Poisson shot noise contribute to the variance of both the flat-field and the object recordings. With the approximations we use below, the variance σ_r^2 can also represent noise present only in the object recording which is presumably caused by a uniform background signal. We investigate two special cases. First, when either read noise or a uniform background signal is present, we have

$$s_{ij}^2 = n_{ij} + \sigma_r^2. \qquad (11)$$

Second, when the flat-field statistics contribute significant noise we find

$$s_{ij}^2 = n_{ij}\left(1 + \frac{n_{ij}}{\bar{n}_f}\right), \qquad (12)$$

where $\bar{n}_f$ is the mean level of the flat field. In Eq. (12) σ_r^2 is assumed to be negligible, but its inclusion is a straightforward combination of Eqs. (11) and (12).

We first derive the position errors in the presence of detector noise or a background signal. We assume Eq. (11) and substitute Eqs. (7)–(9) into Eq. (3) to find

$$s_x^2 = \frac{1}{\sum\limits_{ij}^{N} n_{ij}} (\sigma_x^2 + \sigma_r^2 f), \qquad (13)$$

where σ_x is the width of the spot given by

$$\sigma_x = (\overline{x^2} - \bar{x}^2)^{1/2}, \qquad (14)$$

$$\bar{x} = \frac{\sum\limits_{ij}^{N} n_{ij} x_j}{\sum\limits_{ij}^{N} n_{ij}}, \qquad (15)$$

$$\overline{x^2} = \frac{\sum\limits_{ij}^{N} n_{ij} x_j^2}{\sum\limits_{ij}^{N} n_{ij}}, \qquad (16)$$

$$f = \frac{\sum\limits_{ij}^{N} x_j^2 + N\bar{x}^2 - 2\bar{x}\sum\limits_{ij}^{N} x_j}{\sum\limits_{ij}^{N} n_{ij}}. \qquad (17)$$

If the read noise σ_r^2 is negligible, Eq. (13) shows that Poisson noise alone causes position errors that are proportional to the width of the object and inversely proportional to the square root of the total number of counts in the feature.

Equation (13) is considerably simplified when each pixel in the object has approximately the same intensi-

ty. This is a reasonable approximation to use when trying to obtain a quick estimate of the position errors. If we assume that for all pixels

$$n_{ij} \approx a = \frac{\sum\limits_{ij}^{N} n_{ij}}{N} . \tag{18}$$

we find Eq. (13) reduces to

$$s_x^2 = \frac{\sigma_x^2}{\sum\limits_{ij}^{N} n_{ij}} \left(1 + \frac{\sigma_r^2}{a} \right) . \tag{19}$$

Read noise or a background signal is therefore insignificant if its variance is significantly less than the average data number in the object (i.e., if $\sigma_r^2 \ll a$).

An expression similar to Eq. (13) may be derived for the case where the flat-field statistics contribute significant noise. We start with Eq. (12) and follow a similar procedure to obtain

$$s_x^2 = \frac{1}{\sum\limits_{ij}^{N} n_{ij}} \left[\sigma_x^2 + \frac{1}{\bar{n}_f} (\overline{nx^2} + \bar{n}\bar{x}^2 - 2\bar{x}\,\overline{nx}) \right] , \tag{20}$$

where again the barred terms are weighted averages similar to the expression

$$\overline{nx^2} = \frac{\sum\limits_{ij}^{N} n_{ij}^2 x_j^2}{\sum\limits_{ij}^{N} n_{ij}} . \tag{21}$$

It is again useful to simplify Eq. (20) by considering the case where every pixel in the object has approximately the same data number. For this case we find that Eq. (20) reduces to

$$s_x^2 = \frac{\sigma_x^2}{\sum\limits_{ij}^{N} n_{ij}} \left(1 + \frac{a}{\bar{n}_f} \right) , \tag{22}$$

where a is still defined by Eq. (18). From Eq. (22) it becomes clear that the flat-field statistics become significant only when the data level in the object becomes comparable with that in the flat field (i.e., $a \geq \bar{n}_f$). For Gaussian distributions Eq. (22) overestimates the errors, but not badly. Simulations we have run show this estimate to be within a factor of 2 of the errors calculated by Eq. (20).

IV. Sampling Errors

The results from the preceding section show that it is advantageous to work with the smallest spot sizes possible if high accuracy positional information is desired. Unfortunately, the pixel dimensions of the detector usually limit the size of usable spots. If the spot size is of the order of a pixel, the positional errors are dominated by errors induced by the discrete sampling of the image rather than by the Poisson errors given by Eq. (19) or Eq. (22). In this section we show how the sampling errors may be calculated and we indicate the

magnitude of these errors as a function of spot size for the case of a Gaussian spot.

For simplicity of notation we consider here the 1-D centroid. The extension to two dimensions is obvious. For the 1-D case the centroid position of the spot on the photocathode is given by the equation

$$x_c = \frac{\int x f(x) dx}{\int f(x) dx} , \tag{23}$$

where $f(x)$ is the spot profile. This position is independent of the detector response function. The interval of integration is assumed to be over the whole spot profile for integrals without expressly given limits. The detector centroid, x_d, is influenced by two additional factors, the discrete nature of the sampling and nonuniformities in the sensitivity across a single pixel. By necessity we assume that all pixels have the same sensitivity variations given by the pixel response function $g(x)$. To calculate x_d we first define the pixel boundaries of the ith pixel to be x_i and x_{i+1}. We then define the pixel center $\bar{x}_i$ to be given by the expression

$$\bar{x}_i = \left(\frac{x_{i+1} + x_i}{2} \right) . \tag{24}$$

The digital centroid is then given by the equation

$$x_d = \frac{\sum\limits_{i} \bar{x}_i \int_{x_i}^{x_{i+1}} g(x) f(x) dx}{\sum\limits_{i} \int_{x_i}^{x_{i+1}} g(x) f(x) dx} . \tag{25}$$

We wish to compute the difference between the true centroid position, x_c, and that given by the detector. We define

$$\Delta x \equiv x_c - x_d. \tag{26}$$

Δx is the deviation of the detector centroid from the true centroid position, however we often call Δx the residual because in practice we estimate Δx by assuming that the true motion of the spot on the detector is linear and then subtracting a linear fit to the data from the data itself. The motion from our stepper motors was not perfectly linear, but we show corrections that we have applied that make these errors negligible. Under these circumstances the experimental residual differs from Δx only in that the least-squares fitting algorithm we used induces some systematic effects which we point out below.

For the case of perfect pixels where $g(x) = 1$, Eqs. (23)–(26) may be combined to give

$$\Delta x = \frac{\sum\limits_{i} \int_{x_i}^{x_{i+1}} f(x)(x - \bar{x}_i) dx}{\int f(x) dx} . \tag{27}$$

In Fig. 5 we show the results of assuming Gaussians of various widths for the input spot profile, $f(x)$, and calculating Δx from Eq. (27). The Gaussian widths (FWHM) are given in units of a pixel width. The plots
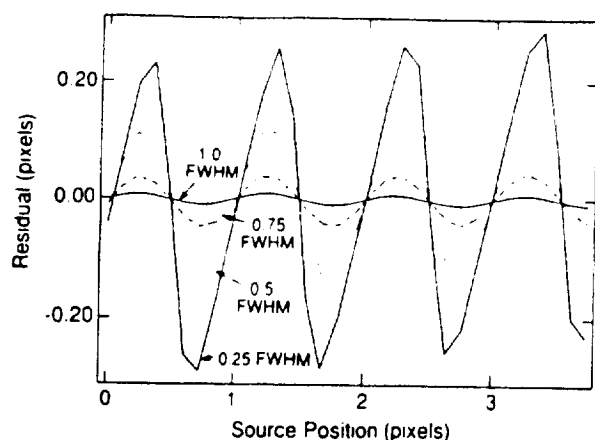
Fig. 5. Theoretical calculations of the sampling errors as a function of input spot width. Gaussian spots are assumed. The FWHM spot widths are given in units of a pixel. A uniform pixel response is assumed.
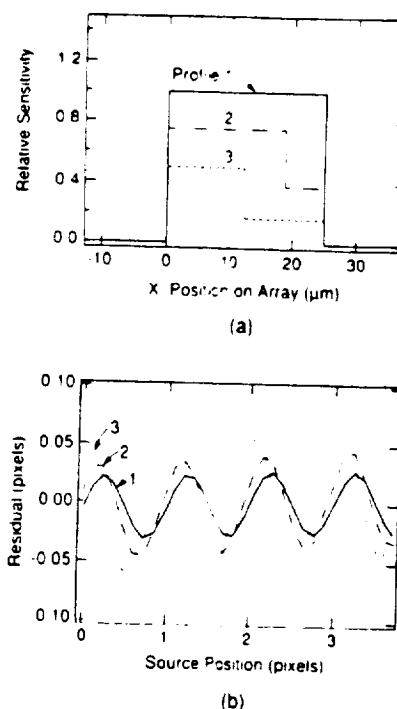

(a)

Source Position (pixels)

(b)

Fig. 6. Effects of a nonuniform pixel response on the sampling errors. (a) Various profiles of $g(x)$ assumed. The peak sensitivity of profiles 2 and 3 have been decreased from 1 to more clearly illustrate their shapes. (b) Sampling errors calculated by assuming the pixel response curves shown in (a) and a Gaussian input spot of 1-pixel FWHM.
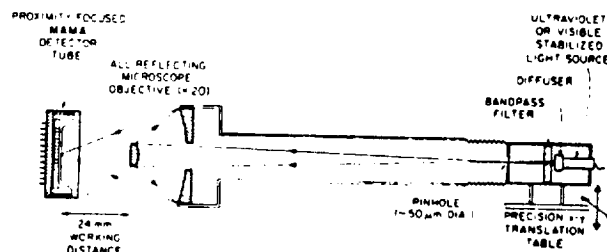

Fig. 7. Schematic of the experimental setup.

in Fig. 5 cover several pixel widths to emphasize the cyclical nature of the errors. It can be seen that the magnitude of the errors decreases sharply as a function of input spot width. The systematic errors shown in Fig. 5 become comparable with the Poisson errors at even moderate signal levels. For example, the Poisson error for a spot of 1-pixel width and a total signal of 1000 counts is 0.03-pixel widths. This error is similar to the magnitude of the sampling errors given by the curve in Fig. 5 for an input spot width of 0.75-pixels (FWHM).

In Figs. 6(a) and (b) we show the effects of an imperfect pixel response curve on the calculation of Δx. Numerical integrations of Eq. (25) were done for these calculations. We assumed a Gaussian $f(x)$ with a FWHM of 1 pixel. Changes in $g(x)$ can induce changes in both the amplitude and the phase of the sampling errors. This emphasizes the fact that for measurements of small spots it is imperative that the function $g(x)$ must be well known for every pixel. In the worst case, complex pixel-to-pixel variations in $g(x)$ could be caused by variations in the sensitivity of the amplifiers attached to each anode. Practically speaking, if $g(x)$ varies significantly between pixels, this variation becomes a fundamental limitation of the detector for the task of measuring and cataloging $g(x)$ for each pixel is overwhelming for a raster size of reasonable proportions.

The small slope imposed on the largest amplitude residual curve shown in Fig. 6(b) is caused by using a simple linear least-squares algorithm to fit the oscillating curve of centroid positions. This is not an intrinsic feature of the sampling errors. This slope can be reduced by doing the fit over a larger number of oscillations or by using a more sophisticated fitting algorithm.

V. Measurements

Measurements of the position sensitivity of a (256 × 1024)-pixel visible-light MAMA detector were made with the apparatus shown in Fig. 7. A power-stabilized incandescent lamp was placed behind a 50-μm diam pinhole and a filter with a 500-Å bandpass centered at a wavelength of 4500 Å.

The lamp and pinhole were mounted on an XYZ stage whose position was controlled by stepper motors with a step resolution of 20 μm. An inverted all reflecting objective with a working distance of 24 mm was used to minify the image of the pinhole by a factor of 20. With this demagnification, the gearing of the stepper motors allows the pinhole image to be moved in 1-μm increments on the photocathode. The accuracy and reproducibility of the image motion were checked by the use of a micrometer on the XYZ stage. Figure 8 shows the results of the micrometer measurements in the x direction after a least-squares solution for the linear trend was removed from the data. An

asymmetric oscillation with a peak-to-peak magnitude of 11.5 μm was observed near the frequency of the stepper motor gearing of 200 steps/revolution. With the objective's minification this represents a peak-to-peak position error of 0.6 μm or 0.02 pixels on the detector.

Measurements of the covariance of error fluctuations between pixels were made by taking a series of flat-field exposures and computing from these images the covariance between pixels within the array. The covariance between nearest neighbor pixels was computed and compared with the variance of the measurements within a single pixel. Within the errors of the measurements the covariance was found to be close to zero and no larger than one-tenth the variance within a pixel. A similar result was found between pixels which were not nearest neighbors.

We have been able to produce a spot width of 3.1 μm on the detector photocathode in spite of the aberrations produced in the detector window. This is quite close to the diffraction limit of the telescope objective which is limited in this configuration by the size of the secondary rather than the primary. Figure 9 shows the results from a knife-edge test for this setup. As shown by the dashed curve in Fig. 9(a) the spot profile is close to being Gaussian within a few hundred steps of best focus. Near best focus the x and y axes profiles are similar. Larger spot widths are made by either defocusing the image or by increasing the size of the pinhole. The second technique is preferable because defocusing the beam produces an asymmetric profile. Figure 9(b) shows the spot profile for an out-of-focus image. For large, out-of-focus spots the x and y profiles have significant differences.

Focusing for subpixel spots may be done by three methods with the MAMA detectors. The first method is to find the best focus by use of a knife-edge in the beam and then construct a focusing curve by moving the beam out of focus and measuring the spot diameter with the knife-edge at several positions until the spot width is >1 pixel. Best focus is then achieved without the knife-edge in the beam by interpolating between points where the spot diameter can be measured directly on the array. It was necessary to place a spare window identical to that used in the detector in the beam before the knife-edge in order to make the optical paths equivalent for the knife-edge and small spot measurements.

The second focusing method is to use the saturation of the MCP to determine the best focus. As best focus is approached the light intensity per unit area increases on the detector. If the light source is bright enough the smaller spot sizes will drive the illuminated MCP channels into saturation and the count rate from the detector will decrease. The minimum count rate will indicate best focus. A third technique is to simply plot the counts in the central or maximum pixel as a function of focus position. This differs from the second technique where the total number of counts across the array was used. This technique is less sensitive to the behavior of the wings of the spot distribution.
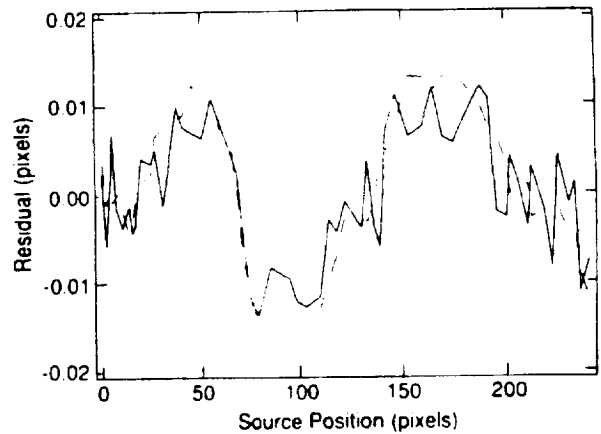

Fig. 8. Micrometer measurements of errors in the stepper motor motions. The stepper motor is geared to 1-μm steps on the detector with 200 steps/revolution. The dashed line shows the corrections for the gear motion errors that were applied to the position measurements.
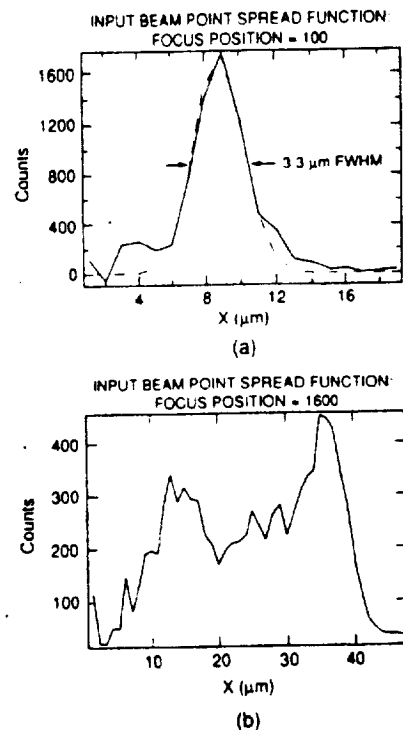

(a)

(b)

Fig. 9. Results of a knife-edge test with a pinhole of 50-μm diameter. (a) The x profile of a spot is shown 100 steps from best focus. The dashed line shows a Gaussian profile with 3.3-μm FWHM. (b) The asymmetric profile of an out-of-focus spot is shown. The doughnut structure of the beam is clearly visible. Its FWHM is 29 μm.

Owing to the minification of the objective, the focus position was extremely sensitive to the distance between the objective and the detector. Focus was therefore achieved by setting and locking the microscope and detector positions with a crude focus and then refining the focus by moving the light source under stepper motor control. This required large mo-

tions of the light source and caused a significant $1/r^2$ fall-off of the light intensity as the focus changed. A 1/r^2 correction was therefore required for both the second and third focusing techniques. In practice we employed all three techniques and estimated the errors in our spot diameter by the dispersion of the focus positions so obtained. Figure 10 shows our focusing curve derived from the knife-edge measurements. The three techniques yielded best focus positions that were within a 400-step interval. Figure 10 can be used to estimate that this represents an error of <1 μm in the width of the input beam. Traces of the spot across a single pixel give a check on the spot diameter since such traces consist of a convolution of the spot diameter with the pixel response curve. Crude estimates of the pixel response curves and the assumed spot diameters are consistent with these measured traces. A final check on the focus was made after our centroid measurements were made. The focus was displaced 400 steps from the best focus position and a scan across a single pixel was made. Any significant change in the width of this scan compared with those taken at best focus is an indication of errors in the best focus position. No changes were observed.

Most of the results reported here come from measurements made with a small aperture (50 μm) at best focus. This produced a FWHM spot diameter of 3.5 ± 1 μm on the detector. Figure 11(a) shows the results obtained from a trace across the detector with this small spot. In this figure we plot the known position of the spot as measured by the stepper motor position vs the derived centroid position. At each stepper motor position a flat-field correction was applied to the spot image before the centroid was calculated. The solid line in the figure is a linear least-squares fit through the data. Figure 11(b) shows the same data as Fig. 11(a) with the linear trend subtracted. The crosses in Fig. 11(b) show the locations of the pixel centers as determined by the centroid calculations.

The Poisson errors were calculated by applying Eq. (22), and the resulting 2σ error bar is shown in the corner of Fig. 11(b). MAMA detectors have no read noise, but there was a background signal owing to scattered light in the optics. The signal from the scattered light was small (~75 counts) and negligible if the centroid calculations were truncated below a threshold of 100 counts. By using this threshold level we can effectively remove the background error terms describable by Eq. (19). A large number of counts (~70,000) were recorded at each stepper motor position. The average number of counts in the coadded flat-field exposure was considerably less (~10,000). Therefore the Poisson errors in this exposure are limited by the shot noise of the flat field.

It is clear that the variations observed in Fig. 11 are larger than can be attributed to the Poisson statistics and furthermore, they are not random. The oscillations of the data about the line are caused in part by the sampling errors discussed in Sec. IV. This is expected for the spot size used and is evidenced by the fact that the errors show a rough periodicity at the frequency of
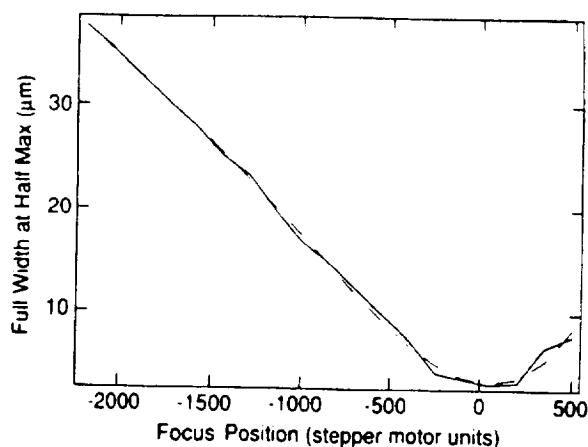

Fig. 10. Our focus curve. The plot shows the spot diameter (FWHM) as determined from knife-edge measurements as a function of distance from best focus.
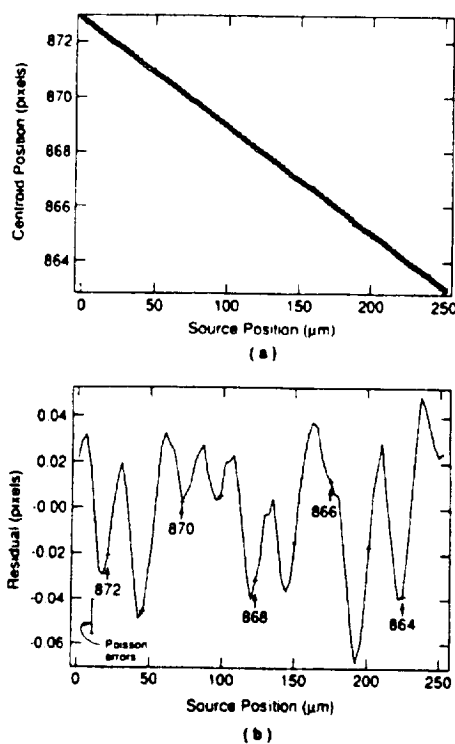

(a)

(b)

Fig. 11. (a) Plot of known position vs derived centroid position for a spot of 3.5-μm diameter. A linear least-squares fit is shown superimposed on the data. (b) The data from (a) are shown with the linear trend subtracted. The bar in the corner indicates the magnitude of the Poisson errors for these data.

the pixel spacing. The effective spot width determines the magnitude of the peak-to-peak variations caused by the sampling. Figure 5 shows that amplitude variations as large as 0.03 pixels indicate an input spot width of ~0.75 pixels or 18-μm FWHM.

The irregularities of the variations shown in Fig. 11 are of considerable interest. These irregularities currently limit the position sensitivity of the detector. The nature of this positional noise is made clearer by a

Fourier analysis of the residual data. The power spectrum of the data in Fig. 11(b) is shown by the solid line in Fig. 12 and the wavelength of the prominent peaks in the residual power spectrum are labeled. The dashed curves in Figure 12 show the power spectra of synthetic residual curves constructed by adding Poisson noise with a standard deviation of 0.015 pixels to sampling errors similar to those shown in Fig. 5. As expected, 0.015 is approximately twice the observed Poisson noise. The long and short dashed curves had sampling errors with amplitudes of 0.04 and 0.02 pixels, respectively. The peaks in the synthetic curves clearly mark the spatial frequency of the pixels. The peak amplitudes in the synthetic curves show that the amplitude of the sampling errors is smaller than 0.03 pixels. An amplitude of 0.02 pixels is consistent with an input spot size of ~20 μm and indicates that our 18-μm estimate of the spot size may be slightly in error.

Substantial power exists at spatial frequencies lower than the pixel frequency. The distribution of power at the low frequencies is not random. The largest peak in the residuals' power spectrum is at a wavelength of 76 μm cycle^{-1}. The peak at 38 μm cycle^{-1} is a harmonic of this peak. The decrease in power at high spatial frequencies is caused by the finite size of the input spot. The spot size limits the frequency response of the measurements to frequencies below $\frac{1}{18}$ cycle μm^{-1}, which corresponds to a normalized frequency of 0.33 in Fig. 12. This spatial structure is not present in the ratio between two flats.

Flat-field corrections are normally used to eliminate low spatial frequency variations, but Fig. 12 shows that these corrections were not adequate to remove all the low frequency noise. Simulations show that the entire power spectrum in Fig. 12 can be reproduced quite well if the flat-field corrections for every third pixel are off by 10%. We show below that the photometry of the small spot measurements in inaccurate, which also implies that improper flat-field corrections have been applied. Flat-field corrections use a single number to describe the pixel-to-pixel variations of $g(x)$, the pixel response function. For each pixel a number is assigned which represents the average sensitivity across that pixel relative to other pixels. If $g(x)$ is not constant across a pixel, errors in the photometry and position sensitivity can result when objects of subpixel extent are imaged. The results presented so far appear consistent with these expectations. However, if the position and photometric errors are caused only by a structure in $g(x)$ across a pixel, these errors are extremely sensitive to the size of the object which is imaged. We illustrate this point later in this section. Next we show position measurements done with a large spot which are inconsistent with this sensitivity to image size. The large spot measurements have driven us to the conclusion that the observed errors are not primarily the result of subpixel variations in $g(x)$ but are instead caused by cross-coupling between pixels which is clearly not a subpixel phenomenon and is less sensitive to the input spot size. We discuss this topic in greater detail in Sec. VI.
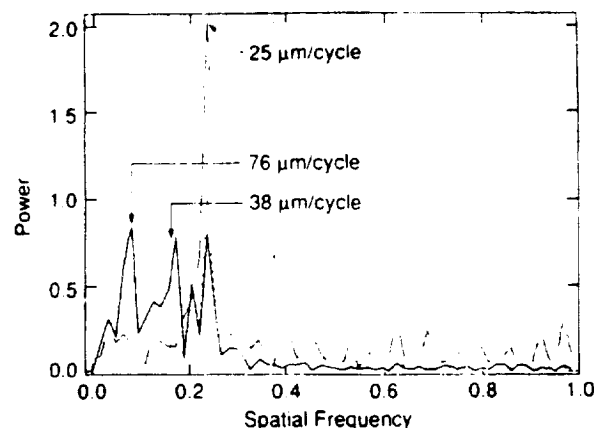

Fig. 12. Solid line shows the power spectrum of Fig. 11(b). The spatial frequency scale is normalized to the Nyquist frequency of the measurements ($f_{Nyquist} = \frac{1}{2}$ cycle μm^{-1}). The dashed curves show the power spectra of synthetic residual curves which were constructed by adding Poisson noise ($\sigma = 0.015$ pixels) to sampling errors with amplitudes of 0.04 pixels (long dashed curve) and 0.02 pixels (short dashed curve). The absolute spatial frequencies of the prominent peaks in the spectra of the measured residuals are labeled.
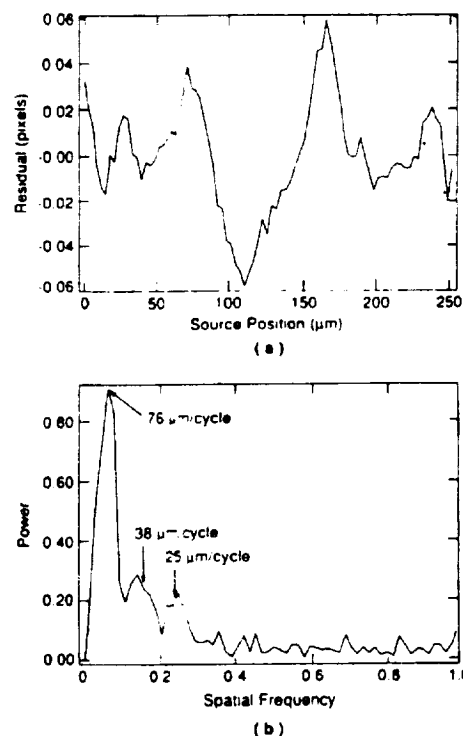

Fig. 13. (a) Centroid residuals are shown for a spot size of 40-μm diameter. The format of the plot is identical to Fig. 11. (b) The power spectrum of the residuals shown in (a) is plotted.

Figure 13 shows centroid measurements from a scan of a large spot across the detector. Figure 13(a) shows the centroid residuals and Fig. 13(b) shows the power spectrum of (a). Both the small and large spot measurements were taken across the same region of the detector. The large spot was formed by defocusing the microscope objective and had a width of 40-μm

FWHM. Knife-edge measurements show that this spot consisted of an asymmetric doughnut with some high frequency structure. One side of the large spot profile was approximately twice the intensity of the opposite side. It is immediately evident from the power spectrum that the 76-μm cycle^{-1} peak and its overtone are still present and that the sampling errors at the pixel frequency are substantially reduced. The magnitude of the peak at 76 μm cycle^{-1} is virtually unaltered by the large change in the input spot. These measurements support the conclusion that errors in the centroid residuals are not caused by the optical system nor by temporal variations in the detector and confirm that the noise power at the pixel frequency is caused primarily by sampling errors.

The largest peak in the power spectrum is at the frequency of the moire pattern caused by the beating between the 25-μm spacing between pixel anodes and the 15-μm spacing between MCP pores. The pores and the anodes line up every 75 μm. The difference between this and a wavelength of 76 μm cycle^{-1} is insignificant. Some of the fine structures present in Figs. 11–13 may be the result of other beat patterns within the detector, but we have done initial calculations which indicate that these are at most a minor contribution to the observed position errors.

We have constructed a simplified model of the MCP–anode interaction to estimate the variations in $g(x)$ that might be expected to arise from moire patterns within the detector. We calculate simulated position errors from this model to use as a common reference to compare with the observations. A Gaussian input spot of photoelectrons is assumed to illuminate the front of the MCP. We then assume that the intensity at the center of each pore is proportional to the electron flux through the pore entrance. At the back of the MCP we assume that each pore generates a Gaussian pulse of electrons with an amplitude proportional to its entrance flux of electrons. This simulates the integrated signal generated by that pore for a large number of events. Each pore then delivers a charge cloud on the anode array which is distributed as a 2-D Gaussian. The signal on a given anode is the integrated signal from each stimulated pore. The anode signals were then used to compute a perceived centroid. This was subtracted from the original position of the assumed photoelectron flux to derive a simulated residual curve. This model completely ignores the complexity of thresholding and the coincidence logic within the detector electronics, but we use it here primarily to better understand the qualitative behavior of the system. Since the size of the input spot is fairly well determined, the major free parameter of the model is the width of the output pulse from each MCP pore. We varied the output pulse width over a wide range to understand its role in the final results.

For the model parameters that we consider most realistic (an input spot width of 18 μm and output pulse width of ~30 μm) we find a fairly complex residual curve with maximum errors as large as 0.008 pixels. The major spectral components in these curves lie at

the pixel frequency, the pore frequency, and the sum and difference of these terms. In addition, if the principal axes of the pores are inclined to the direction of the anodes, another component is present. If rows of pores on the MCP are inclined to the anodes, pixels in a given row do not equally sample pores in a given row on the MCP. In the detector used for these measurements we have determined the orientation of the pores with respect to the anodes by observing the diffracted light of a laser shining on the detector. The angle between the principal axes of the pores and the direction of the anodes was observed to be small (~6°). In the model, a small inclination between the anodes and rows of pores on the MCP results in a low frequency (~125 μm cycle^{-1}) modulation of the previously mentioned spectral components. The large output pulse width is likely despite the close proximity of the anodes to the MCP (~50 μm) owing to the small MCP-anode bias potential (80 V) and to the effects of space charge repulsion in the saturated output pulse.

The spectral signature of the model does not closely resemble that observed in Figs. 12 and 13. No spectral component is found near a wavelength of 76 μm cycle^{-1} and the amplitudes of the model residual errors are smaller than those observed. For the unlikely case of extremely small output pulses (15 μm), the amplitude of the residual errors can reach as large as 0.04 pixels. However, in all cases the residual errors decrease dramatically (<0.00005 pixels) as the input spot size is increased to 40 μm. These results illustrate how inconsistent the large spot measurements are with the hypothesis that the position errors are caused only by subpixel variations in $g(x)$, the pixel response function.

We now turn to the issue of photometry of small spot measurements. We have used the spots to map small scale variations in the relative detective quantum efficiency (DQE) of the detector. The characterization of such variations is important for an understanding of the intrinsic limitations of centroid detection and of the photometric accuracy of the detector.

Figure 14 shows a DQE map with subpixel resolution of a 50-$\times$ 50-μm region of our detector. This map is a contour plot of the total counts recorded at each position of a raster scan of our 3.5-μm spot. At each raster position an image of the spot was taken, a flat-field correction was applied, and the total counts recorded in the flat-corrected image were stored in the appropriate position of the DQE map. The map is therefore an image of the detector's DQE after flat-field corrections have been applied. The spot was stepped across the array in 2-μm increments. This map is highly oversampled. Its resolution is set to ~18 μm by the dispersion of the photoelectrons as they travel between the photocathode and the front face of the MCP.

The heavy lines in Fig. 14 show contours of the spot's centroid positions. The centroid position contours are labeled on the x and y axes of the map. The x-axis contours are jagged and appear noisy while the y-axis contours are relatively smooth. The deviations from straight lines in the x contours have a maximum amplitude of ~0.05 pixel which corresponds to approximate-
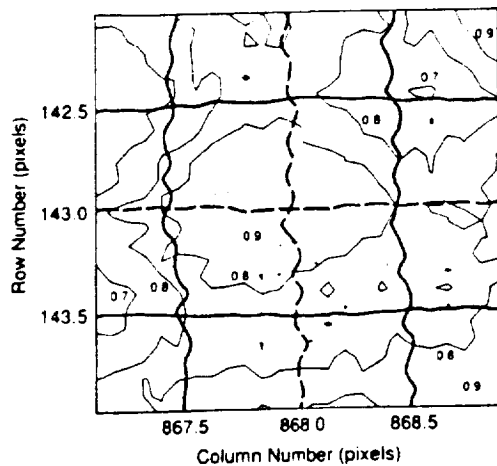
Fig. 14. A 50- × 50-μm map of the subpixel variations in the detector's detective quantum efficiency (DQE). Light lines show contours of the detector DQE. Heavy lines show contours of the pixel centers and boundaries as determined by centroid measurements. The DQE contours are labeled in percentage of the peak efficiency seen near the pixel center. The coordinates of the pixel boundaries are labeled at the sides of the figure.

ly one step of the stage motor. These deviations are not random. A comparison of the x-axis contours reveals a high correlation between the deviations observed in one contour and those observed on another at the same y position. The x-axis contour deviations are attributable to slippage of the translation stage during the backscan between raster rows. This occurred despite our efforts to remove gear backlash by overscanning during the raster backscans. The y axis was never backscanned during the raster measurements and was moving in the direction of gravity. We are in the process of installing higher resolution translation stages to eliminate these errors.

The accuracy of these DQE measurements depends on the stability of our lamp over a period of several days. The stability of the light source was tested by taking many exposures with the spot at a fixed location on the array. Five-minute exposures were taken over a period of 2 h at count rates comparable with those used for these measurements. These tests were sufficient to show that the lamp variability was less than ~1% during this time interval. The stability of the light source and the repeatability of these measurements were confirmed by rescanning a row in the raster shown in Fig. 14. The rescan agreed to within 1% of the original data.

Figure 14 shows that there are small scale sensitivity variations within MAMA detectors. The maximum and minimum count rates in Fig. 14 differ by ~30%. The variations are smooth with a peak sensitivity centered between pixel anodes. These variations are asymmetric with the width along the x axis being larger than that along the y axis. The position of peak sensitivity is offset from the pixel center determined by the centroid calculations. The x-axis centroid contours are slightly offset from the anode positions owing to asymmetrics caused by the addition of threefold

events to the pixel response. The lack of such an offset in the y axis is an indication that very few threefold events are detected on the y-axis anodes. A lack of threefold events may be caused by obscuration by the x-axis anodes which overlay those for the y axis. No evidence for the existence of sensitivity variations owing to the hexagonal MCP pore structure is seen. The count rates used for the raster scan measurements were low (6 and 15 counts s^{-1} for the small and large spots, respectively). In Sec. VI we show that this is significantly below the count rates at which evidence for MCP saturation is seen. It is therefore unlikely that the lack of pore structure in the DQE map can be attributed to a decrease in contrast owing to saturation.

We have used our small spot measurements to derive a crude estimate of the detector's pixel response function. This estimate ignores the MCP channel separation and assumes a linear transformation between the distribution of photoelectrons on the input face of the MCP and the distribution of avalanche electrons at the MCP output. This is probably a poor estimate of the true transformation but it is simple and will serve as a reference for future work. By assuming a Gaussian shape with 18-μm FWHM for the input spot from the photocathode we can use Fig. 14 to estimate the pixel response. Figure 15(a) shows the pixel response along the x axis required to match the DQE variations observed in Fig. 14. The pixel response curve was assumed to consist of contributions from twofold and threefold events. As shown in Fig. 15(a) the contribution from twofold events was assumed to peak near the pixel center while that from threefolds peaked near the pixel boundary. The relative ratio of these two components was constrained by independent measurements of their count rates during our small spot measurements. Figure 15(b) shows a synthetic DQE map constructed by assuming the pixel profile in Fig. 15(a) and the 18-μm FWHM input spot size. The general shape and magnitude of the sensitivity variations in the synthetic DQE map match those seen in the data of Fig. 14. The asymmetry of the synthetic sensitivity variations was created by assuming that no threefold events were detected on the y-axis anodes. The y-axis pixel response was therefore assumed to be just the twofold curve shown in Fig. 15(a). The asymmetry of the pixel response curve along the x axis is responsible for displacing the centroid contours slightly away from the pixel center which is at the position of peak sensitivity. Single row spot scans through the center of several pixels confirms that this asymmetry is a consistent feature of pixels throughout the detector array.

The single row scans appear to indicate that the small scale sensitivity variations shown in Fig. 14 are not highly reproducible across the array. They also illustrate the typical magnitude of the photometric errors when point sources are observed. Figure 16 shows the integrated intensity of the small and large spot scans as a function of position across the array. The general shapes of the curves are similar owing to effects of vignetting as the spot is scanned across the
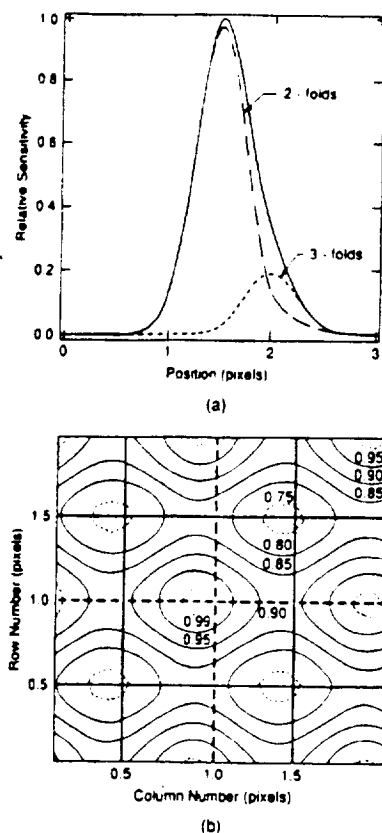
(a)

(b)

Fig. 15. (a) Pixel response curve derived from Fig. 14. The dashed curves show the assumed contributions of twofold and threefold events to the total response curve which is shown by the solid line. (b) A synthetic DQE map derived from assuming an effective input spot size of 18-μm FWHM and the response curve shown in (a).

(a)

(b)
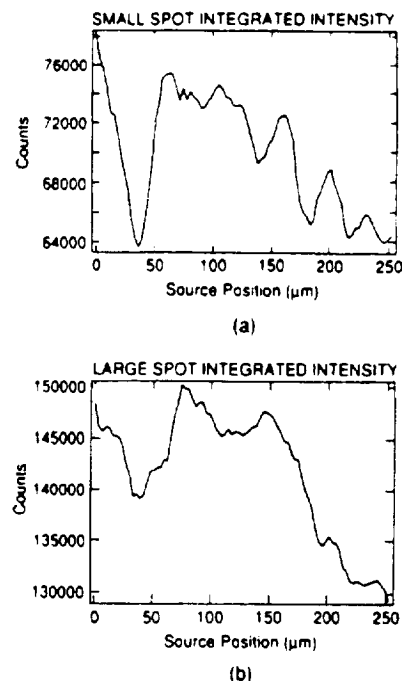
Fig. 16. Photometric response of the detector when spots are moved across the detector. The small and large spots were 3.5- and 40-μm FWHM, respectively. The decreasing counts toward large source positions were due to vignetting in the microscopic objective.

telescope's field of view. The small spot scan has variations that are clearly associated with small scale variations in the detector. As the size of the spot is increased, these variations decrease as the averaging approaches that used for the flat-field measurements. For point sources Fig. 16 shows that the small scale variations can cause photometric errors as large as ~15%. Figure 14 shows that errors as large as 30% are possible in the worst conditions. The large sensitivity decrease near the source position of 25 μm in Fig. 16 implies that the small scale variations may vary considerably from pixel to pixel.

Like the position measurements, the variations of the integrated counts in Fig. 16 are also inconsistent with the hypothesis that they are caused only by subpixel variations in $g(x)$. The observed variations are ~10% and ~3% for the small and large spot measurements, respectively. The statistical errors of the integrated counts are <0.3% for the large spot measurements. When the pixel profile of Fig. 15(a) is used to compute the integrated counts in the detector, variations of ~10% are found when the input spot size is 18 μm. However, with the same pixel profile the integrated counts vary by <0.01% when the spot size is increased to 40 μm. The observed variations in Fig. 16(b) are over 2 orders of magnitude larger than ex-

pected and are 1 order of magnitude larger than the statistical errors. This calculation illustrates how photometric errors caused by subpixel variations in $g(x)$ are also extremely sensitive to the input spot size.

VI. Conclusions

We have shown that centroid measurements with an accuracy of 0.04 pixels are easily obtainable with a visible-light MAMA detector. Owing to the proximity focus photocathode, this can be done with features far smaller than a pixel dimension. This is an important point for applications such as astrometry where it is often desirable to have both high position sensitivity and a large field of view. Typically these are conflicting requirements because of the limited formats of available detectors and the commonly perceived need to oversample the point spread function of the imaging system. Our measurements show that for MAMA detectors oversampling may be unnecessary in many applications.

The position sensitivity of the detector is apparently limited by the lack of an appropriate flat field. The position errors observed here are caused by ~10% errors in the flat-field corrections. We have shown that flat fields are consistent with other flat fields. We desire to understand why the sensitivity of the detector differs when uniformly illuminated as opposed to illumination with a small spot. One difference between the small spot measurements and the flat-field measurements is the per pixel count rate. The per pixel count rates of the spot and flat-field measurements were ~15 and 0.2 counts s^{-1}, respectively. Plate

saturation at a count rate as low as 15 counts s^{-1} pixel^{-1} is inconsistent with previous determinations of MCP performance characteristics. For our MCP with an operating resistance of 80 MΩ, an applied voltage of 1850 V, and a total area of 1.75 cm^2, we have wall current densities of 1.3 $\times$ 10^{-5} C cm^{-2} s^{-1}. For a plate gain of 10^6 and a count rate of 15 counts s^{-1} pixel^{-1} the avalanche current density through a single pixel is $\sim$4 $\times$ 10^{-7} C cm^{-2} s^{-1}. The avalanche current density is therefore only 3% of the wall current density. Timothy[13] showed that saturation effects begin to take place in curved channel MCPs made of Corning 8161 glass only when the avalanche current density is close to 20% of the standing wall current density.

Another indication that MCP saturation is not the cause of the anomalous position errors is that the quantitative nature of the errors is not sensitive to the size of the input spot. The small spot measurements had an input width of $\sim$18 μm on the MCP while the width of the large spot was $\sim$40 μm. The count rates for the large and the small spot measurements were within a factor of 2 of each other, but the area of the plate sampled differed by a factor of 4. The large spot measurements had a significantly lower input intensity and yet the power spectrum of the position errors was virtually unchanged.

The occurrence of the position errors at the moire frequency between the MCP channels and the array electrodes suggests that the errors are derived from a pixel-to-pixel variation in the ratio of twofold to threefold events. It is clear that threefolds are favored by a configuration where the MCP channels lie directly above an electrode. The simulations show that the contribution of threefolds is sufficient to shift the centroid contours by the required amount. This can be seen in Fig. 15 where threefold events were included in the x anodes but not in the y anodes. The result was an x shift from the pixel center in the sensitivity contours of $\sim$0.1 pixels. A variation in the twofold to threefold ratio would therefore appear to be a likely explanation if the position errors were sensitive to the size of the input spot. Because this sensitivity is not observed we favor a second explanation. The moire pattern varies the ratio of twofold to threefold events in each pixel which in turn modulates the level of cross-coupling between pixels in the array. Cross-coupling in the array is responsible for a scene dependent sensitivity of each pixel which is less dependent on the image size than subpixel variations in the pixel response function. The details of cross-coupling in the array are discussed below.

Cross-coupling in the array causes a significant number of counts generated in one pixel to be improperly recorded in an adjacent pixel. For small spots this significantly distorts the photoevent distribution. This distortion is not properly corrected by a flat field because the relative sensitivity of a pixel as measured by a flat field includes contributions from adjacent pixels. Cross-coupling therefore causes the relative sensitivity of pixels in a detector to be scene dependent.

It is known that cross-coupling takes place between adjacent pixels in the array. MAMA flat-field exposures exhibit a pattern of alternating high and low sensitivity pixels which is produced in the following manner. We explained in Sec. II how a single pixel consists of contributions from both twofold and threefold events. Half of the pixels have twofolds which are received by a fine–coarse (fc) combination of anodes. We call these fc pixels. Similar logic leads us to call the other pixels cf pixels. Along a row or column cf and fc pixels are in alternate order. The coadded threefolds in fc pixels are received on a fine–coarse-fine (fcf) anode combination while threefolds in cf pixels are received by a coarse–fine–coarse (cfc) combination. Owing to their physical layout on the array, adjacent coarse anodes experience some capacitive cross-coupling and a high level of inductive cross-coupling. Pulses received on one coarse anode are likely to induce a pulse on an adjacent coarse anode. This coupling causes many of the twofolds in fc pixels to appear to the coincidence circuitry as a cfc threefold in the adjacent lower cf pixel. For cf pixels this coupling does not matter because the cfc threefolds that are generated by the cross-coupling are coadded into the same cf pixel.

The magnitude of the cross-coupling observed in MAMA flat fields is that required to explain the improper flat-field corrections in the small spot measurements. Flat-field corrections were applied to both the position and photometric sensitivity measurements. The 20–30% pixel-to-pixel variation of counts observed in a MAMA flat field implies that $\sim$10–15% of the counts in an fc pixel are improperly distributed to the adjacent lower cf pixel. This coincides with the magnitude of the photometric errors observed in the small spot measurements. Errors of this magnitude were also sufficient to reproduce the power spectrum of the position errors.

The moire beating of anodes and pores can have a direct impact on the strength of the cross-coupling. The cross coupling between adjacent pixels is initiated by twofold pulses in fc pixels. The position of the MCP channels relative to a pixel's electrodes will influence the relative number of twofolds and threefolds generated within that pixel. Pixels with channels directly over the electrodes will favor the generation of threefolds and will therefore have a smaller amount of cross-coupling. This argument also implies that the cross-coupling between pixels can depend on very small scale structure in the illumination. A pixel illuminated only at its edge will have few twofolds whereas a pixel illuminated by a small central spot will favor twofolds. It is therefore impossible for a single flat field to properly correct for the relative sensitivities of pixels for the small spot measurements. The relative amount of cross-coupling varies as the spot moves across the detector.

These results indicate that the position sensitivity of current versions of the MAMA detector is superior to that of any other currently available pulse-counting MCP detector system. In addition to this, a recent
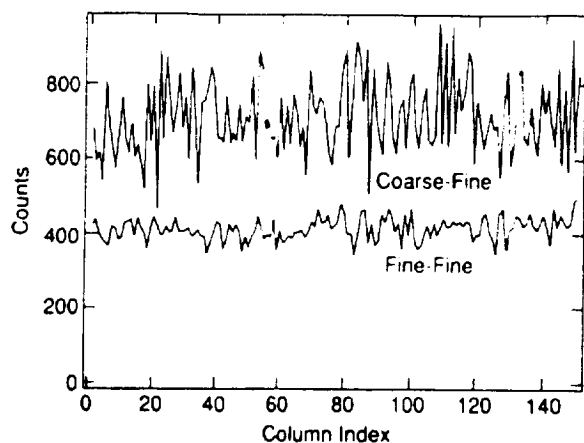
Fig. 17. Comparison of the flat fields from MAMA detectors employing course-fine and fine-fine anode arrays. The pixel-to-pixel variations in the coarse-fine detector are dominated by cross-coupling effects while the data from the fine-fine detector are dominated by the photon shot noise.

change in the design of the MAMA anode array offers significant hope that major improvements in both the position sensitivity and the subpixel photometric accuracy have already been accomplished. The tube used in these experiments employed a first generation anode array which we now designate as a coarse-fine array. The anodes in the new fine-fine arrays have been designed to decrease the cross-coupling between pixels and to allow the coincidence circuitry to handle events larger than threefolds. Figure 17 shows a comparison between flat fields taken with this tube and a flat field taken from a prototype fine-fine MAMA tube which was assembled at Ball Aerospace by Richard Bybee, Ed Culver, and Max Hedges. For the old, coarse-fine array the pixel-to-pixel variations shown are primarily due to cross-coupling between pixels. In contrast, the variations in the fine-fine flat field are dominanted by the Poisson statistics of the exposure. This encouraging result implies that the prime limitation of the MAMA detector's position sensitivity has been eliminated in more recent versions of the detec-

tor. We plan to conduct small spot measurements on detectors utilizing the new arrays as soon as they become available for testing.

References

1. N. Bobroff, "Position Measurement with a Resolution and Noise-Limited Instrument," Rev. Sci. Instrum. 57, 1152 (1986).
2. S. E. Bulau, "Simulations of Various Centroding Algorithms," Proc. Soc. Photo-Opt. Instrum. Eng. 627, 680 (1986).
3. G. Gatewood, L. Breakiron, R. Goebel, S. Kipp, J. Russel, and J. Stein, "On the Astrometric Detection of Neighboring Planetary Systems, II," NASA Conf. Publ. 2124 (1980), pp. 77-118.
4. G. Gatewood, J. Stein, C. Difatta, K. DeJonge, and L. Breakiron, "A Preliminary Look at Astrometric Accuracy as a Function of Photon Counts," Astron. J. 90, 2397 (1985).
5. C. KenKnight, "Limit Posed for Astrometry by Earth's Atmosphere," NASA Conf. Publ. 2124 (1980), pp. 55-60.
6. J. G. Timothy and R. L. Bybee, "Photon-Counting Array Detectors for Space and Ground-Based Studies at Ultraviolet and Vacuum Ultraviolet (VUV) Wavelengths," Proc. Soc. Photo-Opt. Instrum. Eng. 279, 129 (1981).
7. W. E. Spicer, "The Production of Pairs in Semiconductors by Low Energy Electrons," J. Phys. Chem. Solids 22, 365 (1961).
8. J. M. Grant, "Note on the Proximity Focusing of Electron Images," Proc. IEEE 54, 801 (1966).
9. E. H. Eberhardt, "Image Transfer Properties of Proximity Focused Image Tubes," Appl. Opt. 16, 2127 (1977).
10. J. G. Timothy, "Imaging at Soft X-Ray Wavelengths with High-Gain Microchannel Plate Detector Systems," Proc. Soc. Photo-Opt. Instrum. Eng. 691, 35 (1986).
11. X. X. Bevington, Data Reduction and Error Analysis for the Physical Sciences (McGraw-Hill, New York, 1969).
12. S. Brandt, Statistical and Computational Methods in Data Analysis (North-Holland, Amsterdam, 1983).
13. J. G. Timothy, "Curved-Channel Microchannel Array Plates," Rev. Sci. Instrum. 52, 1131 (1981).

MAMA Detector Systems: A Status Report

J. Gethyn Timothy, Jeffrey S. Morgan and David C. Slater
Center for Space Science and Astrophysics
Stanford University, ERL 314
Stanford, CA 94305-4055, USA

David B. Kasle
Code 683
NASA Goddard Space Flight Center
Greenbelt, MD 20771, USA

and

Richard L. Bybee and H. Ed Culver
Ball Aerospace Systems Group
P.O. Box 1062
Boulder, CO 80306-1062, USA

ABSTRACT

A number of different MAMA detector systems are now in use at both ultraviolet and visible wavelengths. MAMA detectors with formats of 256 x 1024 pixels and with pixel dimensions of 25 x 25 microns^2 are being used in the laboratory and at ground-based telescopes and an ultraviolet version has recently been flown on a Black Brant sounding rocket. Third-generation (224 x 960)-pixel MAMA detectors with 25 x 25 microns^2 pixels are also being used in the laboratory and at ground-based telescopes and a (224 x 960)-pixel detector with 14 x 14 microns^2 pixels is currently under test in the laboratory. Third-generation MAMA detectors with formats of 360 x 1024 pixels are under development for use at extreme ultraviolet (EUV) wavelengths on the European Space Agency/NASA Solar and Heliospheric Observatory (SOHO) mission and detectors with 1024 x 1024 and 2048 x 2048 pixels are under development for use at ultraviolet and far ultraviolet (FUV) wavelengths on the NASA Goddard Space Flight Center's *Hubble* Space Telescope Imaging Spectrograph (STIS). Both of these detectors have pixel dimensions of 25 x 25 microns^2. This paper describes the configurations, modes-of-operation and some of the latest performance data for the different detector systems.

1. Introduction

The Multi-Anode Microchannel Array (MAMA) detector system has been designed from the outset to provide the high spatial resolution, very large number of image elements, geometric fidelity and photometric dynamic range to satisfy the demanding requirements of high-resolution imaging and spectroscopy at ultraviolet, FUV and EUV wavelengths for a number of applications in modern space astronomy. Since the MAMA employs a random readout technique, the arrival time of a detected photon can be determined with high accuracy. For this reason, MAMA detectors are also being employed for high-time-resolution applications such as speckle imaging, astrometry, and image reconstruction at both ultraviolet and visible wavelengths. Further, since the FUV and EUV MAMA detectors employ "solar blind" photocathodes and the noise level with the MAMA readout system is defined solely by the photon statistics and the photocathode dark current, the MAMAs have a significantly higher DQE than CCDs at this time for many low signal level applications at FUV and EUV wavelengths. In developing the MAMA, special efforts were taken to ensure that it will operate with maximum reliability in the space environment. For this reason, the MAMA detector system uses a minimum number of components in the detector tube and employs

conservatively-rated, low-power analog and digital electronics.

The MAMA detector system is now becoming highly developed as the result of its selection for use in both the NASA Goddard Space Flight Center's *Hubble* Space Telescope Imaging Spectrograph (STIS)[1] and in a number of instruments on the European Space Agency (ESA)/NASA Solar and Heliospheric Observatory (SOHO) mission [2]. In addition, the MAMA has been baselined for use in the prime spectrograph of the *Lyman* Far Ultraviolet Spectroscopic Explorer (FUSE) mission and in two instruments on the Space Station. The recent successful flight of a (256 x 1024)-pixel FUV MAMA detector on the NASA Goddard astronomy sounding rocket payload is a further step in the ongoing program of laboratory and flight tests of the MAMA detectors in preparation for these long-duration space missions.

In this paper we describe the configurations and modes-of-operation of the different MAMA detector systems. We also present some recent

data which demonstrate the capabilities of the detector systems and outline the key tasks of the MAMA detector development program for the next few years, in particular the fabrication of the very-large-format (2048 x 2048)-pixel detector systems and the fabrication of compact high-speed and low-power hybrid amplifier, discriminator and event address-decoding circuits.

2. MAMA Detector Systems

The components of a MAMA detector consist of the tube assembly, which can be sealed with a window or used in the open-structure configuration, containing a single, high-gain, curved-channel microchannel plate (MCP) electron multiplier with the photocathode material deposited on, or mounted in proximity focus with the front surface. To detect and measure the positions of the electron clouds generated by single photon events, the MAMA detector employs two layers of precision electrodes which are mounted in proximity focus with the output surface of the MCP (see Figures 1 and 2).
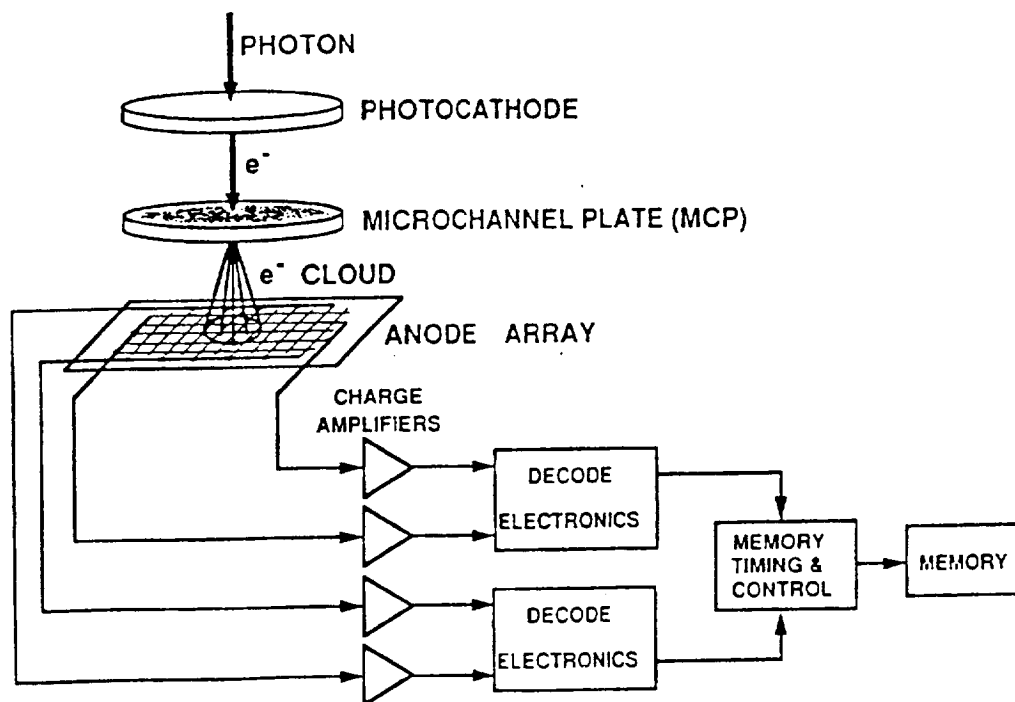

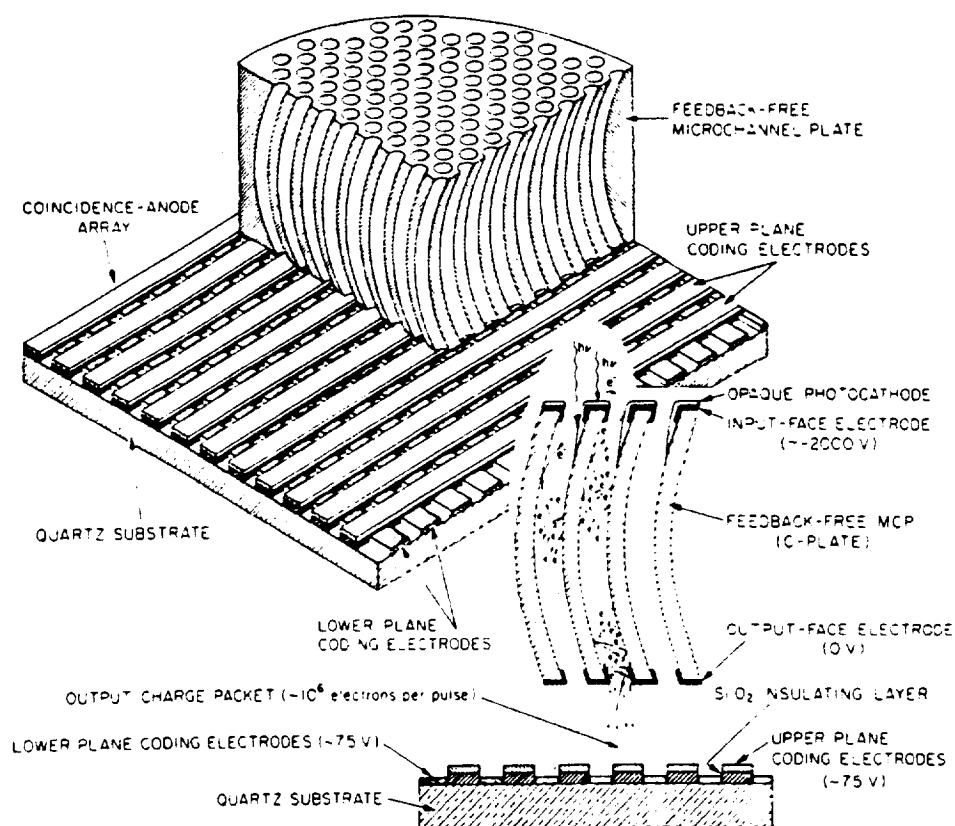Figure 1. Schematic of the imaging MAMA detector system.

Figure 2. Schematic showing details of the curved-channel MCP and the imaging multi-layer anode array used in the MAMA detector tubes.

Digital logic circuits respond to the simultaneous arrivals of signals from several of these electrodes in each axis, which are arranged in groups to uniquely identify a x b pixels in one dimension with only a + b amplifier and discriminator circuits. For example, a total of 32 x 32, i.e. 1024, pixels in one dimension can be uniquely identified with 32 + 32, i.e. 64, amplifier and discriminator circuits. In the imaging MAMA detector tube, the arrays are mounted in tandem with orthogonal orientations, so that positions can be sensed in two dimensions. In this configuration (a x b)^2 pixels can be uniquely identified with only 2 x (a + b) amplifier and discriminator circuits. The (1024 x 1024)-pixel array thus requires a total of only 128 amplifier and discriminator circuits. The two layers of anode electrodes in the imaging arrays are insulated from each other by a SiO$_2$ dielectric layer. This dielectric between the upper layer

electrodes is etched away to allow the low energy (~30 eV) electrons in the charge cloud from the MCP to be collected simultaneously on both arrays.

The encoding-electrode geometry has been refined as the MAMA technology has become more mature. Three different encoding-electrode geometries are currently under evaluation, as shown in the schematics in Figure 3. These are, in order of development, the coarse-fine, balanced coarse-fine and fine-fine configurations. All the configurations encode the position of the detected photon in a similar manner. A charge pulse detected on a fine-encoding electrode (e.g. output F1 in Figure 3a or b) could have originated on one of a number of pixel electrodes connected to this output electrode along one axis of the array. This positional ambiguity is removed by the detection of a simultaneous output pulse on one
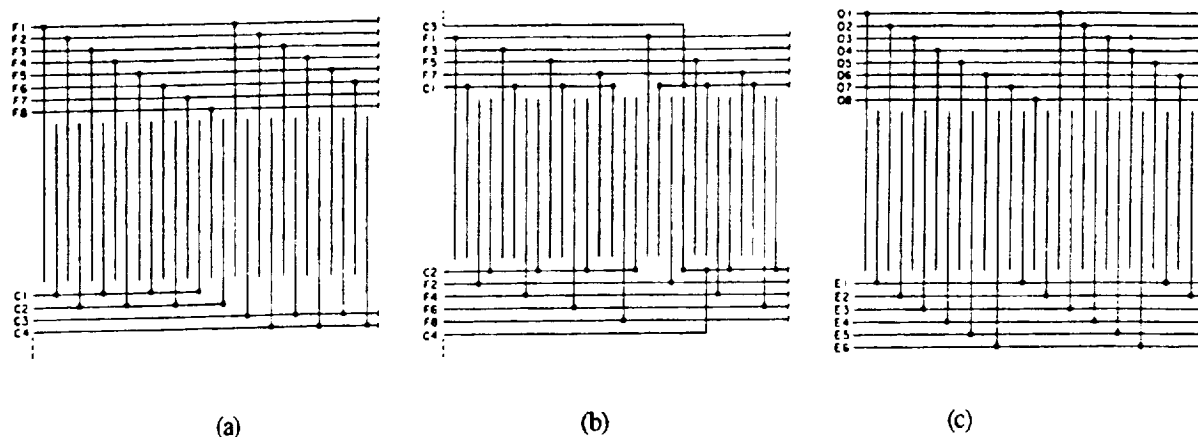
Figure 3. Configurations of the different MAMA anode array encoding geometries.
a. Coarse-fine array.　　　　b. Balanced coarse-fine array.　　　　c. Fine-fine array.

of the coarse-encoding electrodes (e.g. output C1 in Figure 3a or b). There is only one position along the array where a particular pair of fine- and coarse-encoding electrodes are adjacent. The fine-fine configuration (Figure 3c) operates in an identical manner with the simultaneous detection of pulses on the odd and even sets of electrodes. In the imaging arrays, this position-encoding technique is implemented simultaneously in the two axes.

In practice, it is not possible to exactly align a channel in the MCP with a particular pair of pixel electrodes. Also, in order to obtain a uniform response across the active area, the dimensions of the channels are smaller than the separation between the pixel electrodes. Typically, 10- or 12-micron-diameter channels on 12- or 15-micron centers are used in the MAMA detectors with 25 x 25 microns^2 pixels. Furthermore, the high-gain MCP produces a space-charge saturated electron cloud which expands rapidly when leaving the channel (see Figure 4a.)

In order to maintain the inherent high spatial resolution of the MAMA readout array, the spreading of the charge cloud is controlled by keeping the distance from the output surface of the MCP to the anode array as small as possible (typically of the order of 50 to 100 microns) and

by applying an accelerating potential of the order of +50 to +150 V between the output surface of the MCP and the anode electrodes. A small differential voltage in the range 1 to 5 V is applied between the upper and lower sets of electrodes in order to ensure that the charge cloud divides uniformly between the electrodes in the two layers.

In the coarse-fine and balanced coarse-fine arrays, the position of a charge cloud collected on two or three adjacent electrodes in each axis is uniquely encoded. The positions of adjacent two-fold and three-fold events in each axis are determined by the digital address-decode circuits. Since the nominal pixel size in the MAMA is determined by the center-to-center spacing of the anode electrodes, the positions of adjacent two-fold and three-fold events differ by about one half of a pixel i.e. about 12.5 microns in the arrays with 25 x 25 microns^2 pixels. In the present MAMA systems adjacent two-fold and three-fold events are co-added to produce the nominal pixel resolution with a good uniformity of response. However, in these two array configurations a charge cloud collected on four or more electrodes produces a positional ambiguity (see Figure 4b). Furthermore, we have determined that the imbalance in the inter-electrode capacitance between the different groups of encoding electrodes in the coarse-fine array produces a fixed

pattern in the flat field response and slightly degrades the point spread function[3]. These effects are significantly reduced by interlacing the coarse- and fine-encoding electrodes in the balanced coarse-fine array but inductive coupling caused by the very fast (<500 ps) charge pulses from the MCP still affects the pixel-to-pixel uniformity of response. For these reasons the fine-fine array, in which the electrodes are capacitively balanced and inductively decoupled,

is now the configuration of choice. In addition, as shown in Figure 4c, four-fold and higher-fold events can be encoded without positional ambiguity. The present systems of decode electronics fabricated at Stanford University are designed to accept up to six-fold events in each axis. The key characteristics of the different encoding-electrode geometries are summarized in Table 1.

Figure 4. Modes-of-operation of the different MAMA encoding-electrode geometries. a. Schematic showing the spreading of the space-charge saturated electron cloud from the high-gain MCP. b. Schematic showing the positional ambiguity introduced when the charge cloud is collected on four or more electrodes in one axis of a coarse-fine or balanced coarse-fine array. c. Schematic showing the unique position encoding when the charge cloud is collected on more than three electrodes in one axis of the fine-fine array.
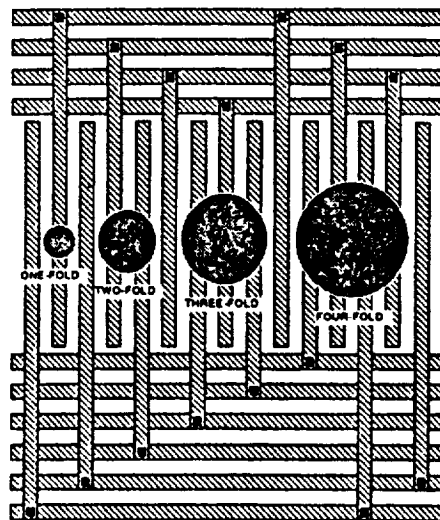
(a)

FINE-FINE ARRAY WITH MULTI-FOLDS

(b)
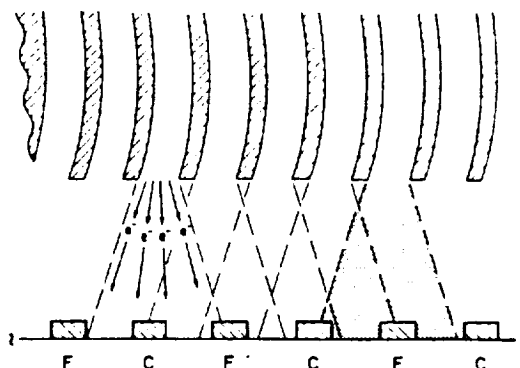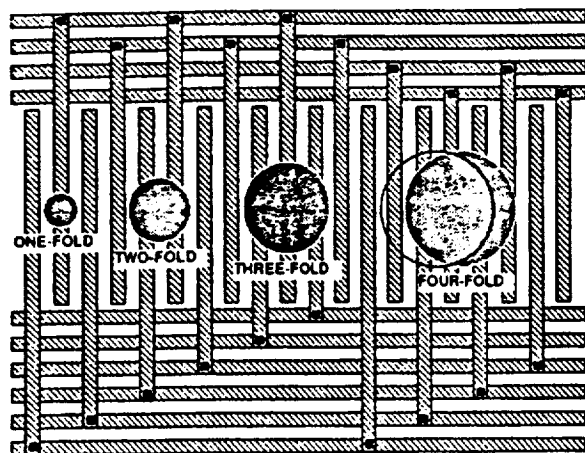
(c)

Table 1. Characteristics of the MAMA encoding-electrode geometries

Coarse-fine array -

- n + m outputs encode n x m pixels in one-dimensional array
- 2 (n + m) outputs encode (n x m)^2 pixels in two-dimensional array
- position ambiguity for four-fold and higher-fold events in each axis
- imbalance in capacitive coupling between coarse- and fine-encoding electrodes
- inductive coupling between different groups of electrodes

Balanced coarse-fine array -

- n + m outputs encode n x m pixels in one-dimensional array
- 2 (n + m) outputs encode (n x m)^2 pixels in two dimensional array
- position ambiguity for four-fold and higher-fold events in each axis
- coarse- and fine-encoding electrodes capacitively balanced
- inductive coupling between different groups of electrodes

Fine-fine array -

- 2(n + 1) outputs encode n x (n +2) pixels in one-dimensional array
- 4(n +1) outputs encode [n x (n +2)]^2 pixels in two-dimensional array
- no position ambiguity for up to (n - 1)-fold events in each axis
- n must be even to avoid position ambiguities in last group of electrodes in each axis
- capacitively balanced
- inductively decoupled

It is of importance to note that the simultaneous arrival of pulses on non-adjacent electrodes in each axis is declared a non-valid event and rejected by the address-decode circuits. The spatial resolution and geometric fidelity of the MAMA detector is accordingly independent of position on the array or of signal level, a unique characteristic which has been verified in a number of laboratory and ground-based telescope tests. A schematic of one of the decode circuits is shown in Figure 5 and described in detail by David Kasle in a separate paper in these proceedings.
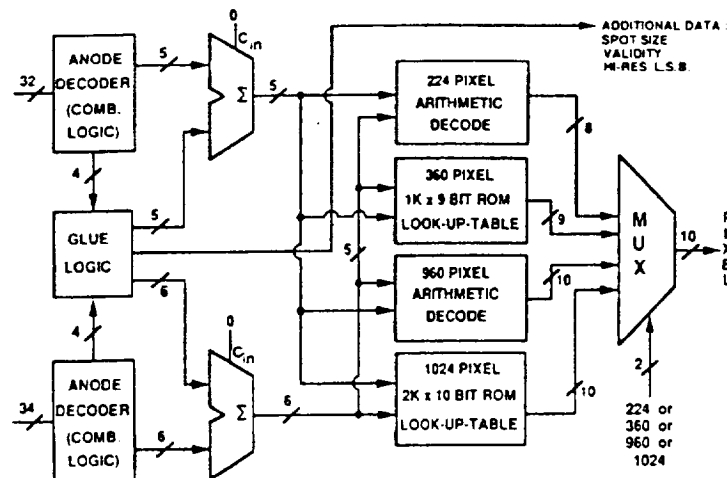

Figure 5. Schematic of MAMA fine-fine address-decode circuit.

A number of different photocathodes are currently being utilized in the MAMA detector tubes. At FUV and EUV wavelengths below about 1500 Å opaque alkali-halide photocathodes deposited directly on the front surface of the MCP provide the best detective quantum efficiencies (DQEs). In this configuration, photoelectrons produced in the photocathode on the web area between the

channels can be collected by means of appropriate focusing potentials, as shown in Figure 6a. The pulse-counting DQE can accordingly be greater than 80% of the intrinsic photocathode quantum efficiency. However, the lateral drift of the photoelectrons will be energy dependent and the focusing voltage required to maintain the desired point spread function will depend on both the
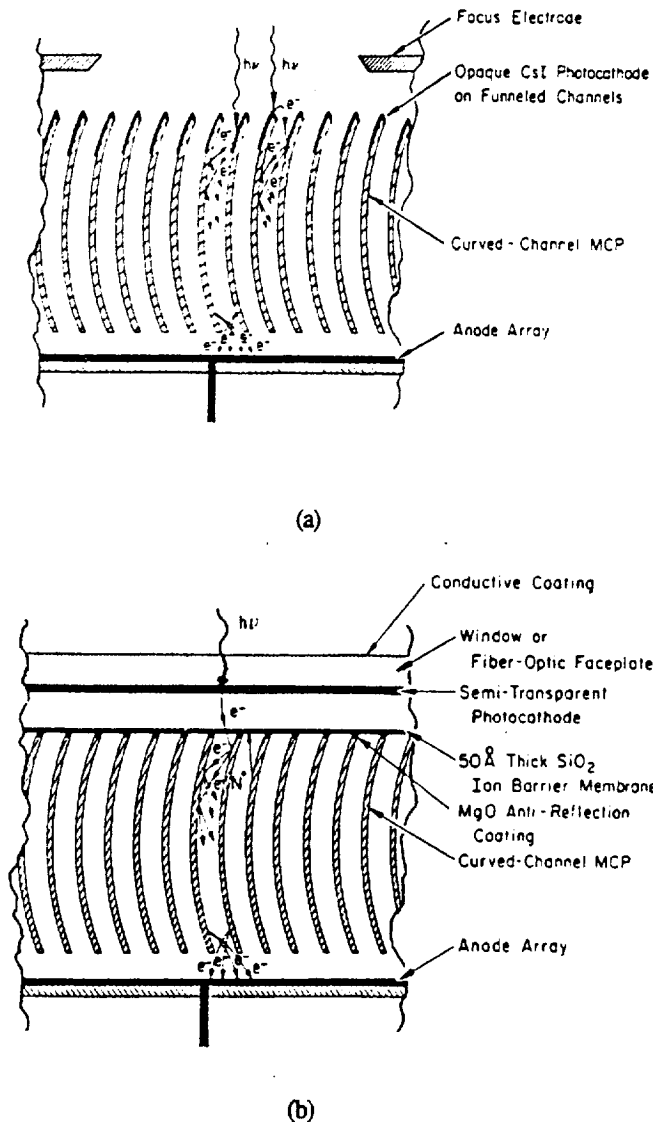

(a)

(b)

Figure 6. Schematics of MAMA photocathode configurations.
a. Opaque photocathode for use at FUV and EUV wavelengths.
b. Semi-transparent, proximity-focused photocathode for use at ultraviolet and visible wavelengths.

photocathode material and on the wavelength [4]. The best photocathode materials available at this time are CsI, KBr and MgF_2[5]. All can be used in the open-structure configuration at EUV wavelengths, but CsI, and to a lesser extent, KBr will degrade rapidly if exposed to humidity.

At ultraviolet and visible wavelengths, where activated photocathodes such as Cs_2Te, K_2CsSb, and $(Cs)Na_2KCsSb$ must be employed, the MAMAs utilize the semi-transparent, proximity-focused photocathode structure shown in Figure 6b. In this configuration, the input surface of the MCP is typically covered with a thin (of the order of 50 to 100 Å thick) SiO_2 film which inhibits photocathode degradation caused by back-bombardment with positive ions produced within the channels. Since the SiO_2 film prevents photoelectrons landing on the web area from

reaching the MCP channels the pulse-counting DQE is reduced by a factor proportional to the channel open-area ratio of the MCP (typically 50 to 65%). This reduction in the DQE is highly undesirable and we are currently investigating techniques to eliminate the film while at the same time ensuring the long-term stability of the photocathode quantum efficiency.

3. Performance Characteristics

The configurations of representative imaging MAMA detector systems now under evaluation are shown in Figure 7. All of the imaging MAMA anode arrays have been fabricated by Ball Aerospace Systems Group (BASG), Boulder CO and units of all arrays have been fabricated with zero defects.
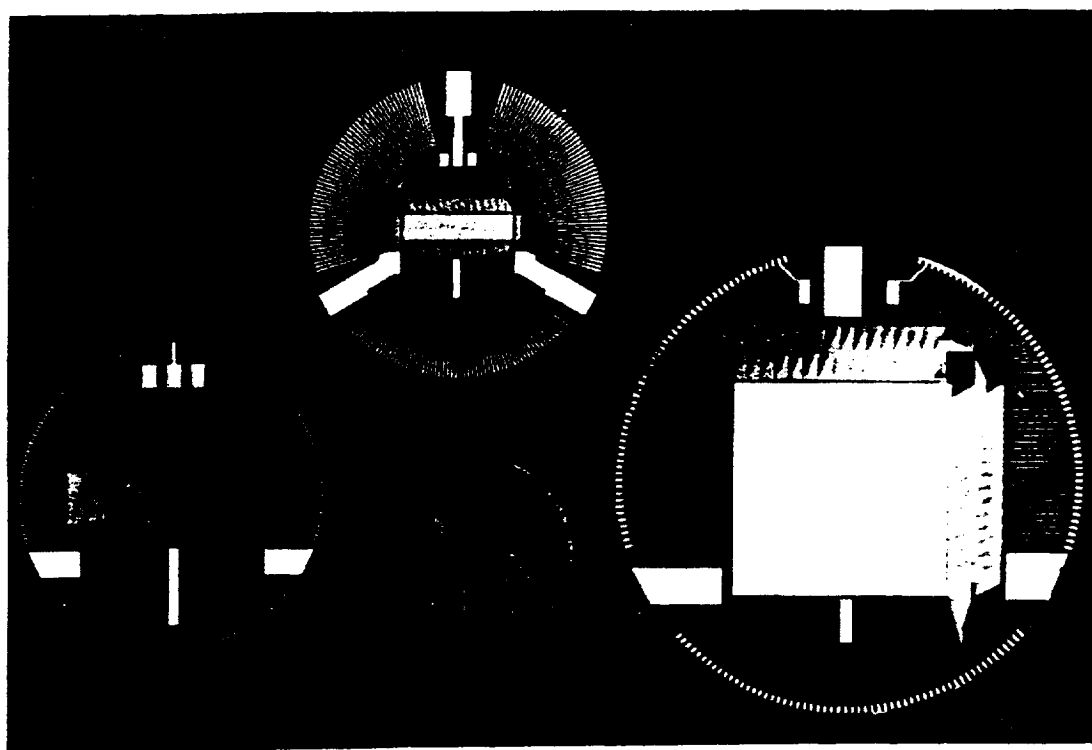

Figure 7. Configurations of representative imaging MAMA arrays.
Left: (256 x 1024)-pixel balanced coarse-fine array with 25 x 25 microns^2 pixels.
Center: (224 x 960)-pixel fine-fine array with 14 x 14 microns^2 pixels.
Right: (1024 x 1024)-pixel fine-fine array with 25 x 25 microns^2 pixels.

The (256 x 1024)-pixel balanced coarse-fine detector system with 25 x 25 microns^2 pixels (left array in Figure 7) was flown successfully on the NASA Goddard astronomy sounding rocket on 26 June 1989. The detector was used in the time-tag imaging mode and recorded ultraviolet images of the galaxy NGC 6240. The time-tagged data stream is being used to correct the image blurs caused by drifts in the rocket pointing system. Analyses of these data are currently being carried out by Dr. Andrew Smith at the NASA Goddard Space Flight Center.

The (224 x 960)-pixel fine-fine detector system with 14 x 14 microns^2 pixels (center array in Figure 7) is being used in the laboratory to verify the capability of the MAMA to provide the spatial resolution required for the prime spectrograph of the *Lyman* FUSE mission. This detector utilizes a curved-channel MCP with 8-micron-diameter channels fabricated by Galileo Electro-Optics Corp., Sturbridge, MA (see Figure 8).

In the initial imaging tests, the first (224 x 960)-pixel detector, which is defect free, has demonstrated the theoretical imaging performance at 2537 Å. The images of positive and negative USAF test targets recorded at this wavelength are shown in Figure 9. A cut through the image of a 20-micron-diameter spot of light and a row from a rectified flat-field image are shown in Figure 10. The spot image has the expected profile, and the deviations in the flat field are in perfect agreement with the Poisson statistics of the original exposure.

The (1024 x 1024)-pixel fine-fine array with 25 x 25 microns^2 pixels (right array in Figure 7) has been configured with the encoding electrodes on only two sides of the active area. This permits four of these arrays to be fabricated on a single substrate to produce a (2048 x 2048)-pixel array with a dead space between the four quadrants of three pixels or less. An array with this configuration is currently being fabricated for STIS. Imaging tests of the (1024 x 1024)-pixel detector system (i.e. one quadrant of the STIS detector) are currently being carried out at both ultraviolet and visible wavelengths. The arrays currently installed in both the 40-mm-format ultraviolet demountable tube and the .
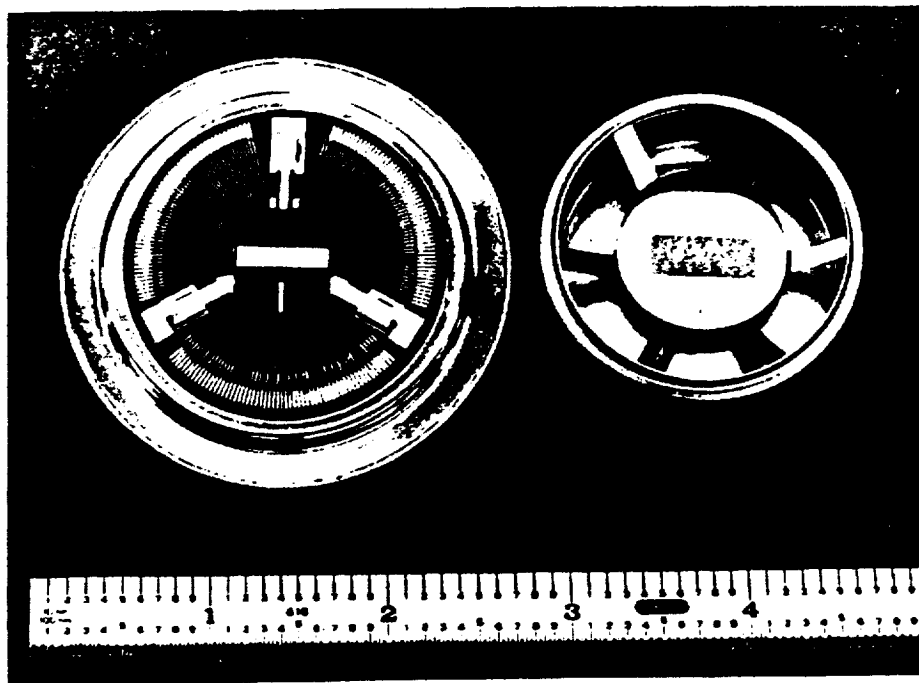

Figure 8. (224 x 960)-pixel fine-fine MAMA detector components.
Left: anode array mounted on the ceramic header.
Right: curved-channel MCP with 8-micron-diameter channels.
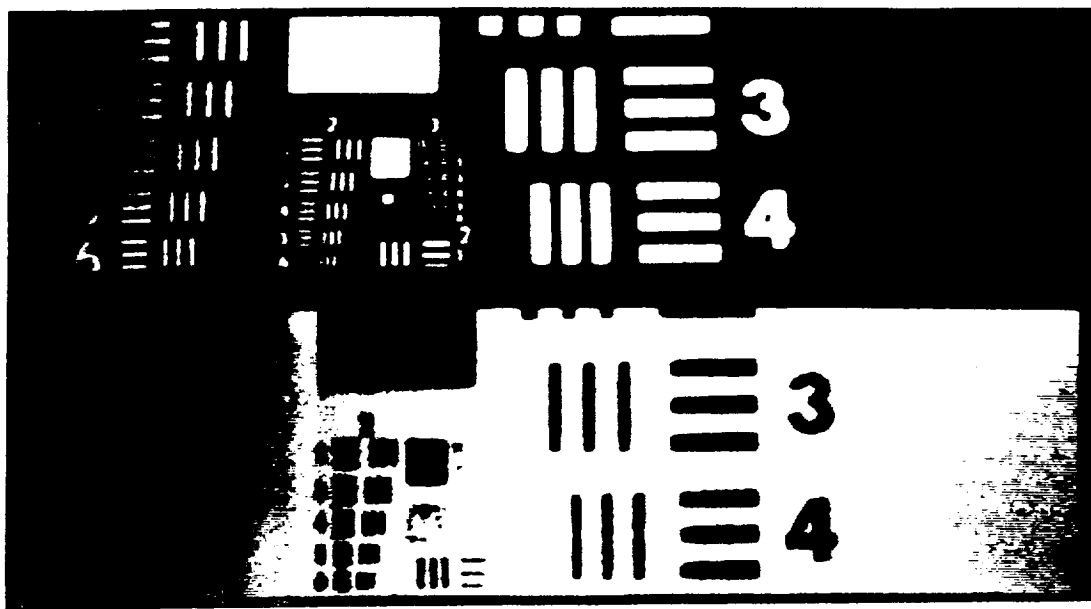
Figure 9. Positive and negative images of a USAF test target taken at ultraviolet wavelengths with a (224 x 960)-pixel fine-fine array with 14 x 14 microns^2 pixels and a curved channel MCP with 8-micron-diameter channels. The sequence of bars in these images starts with a resolution of 2.51 line-pairs mm^{-1} (Group 0, element 3 on the right side of the images). The closest bars in the image have a resolution of 113.6 line-pairs mm^{-1} (Group 5, element 6 to the left of the image centers).

(a)

(b)
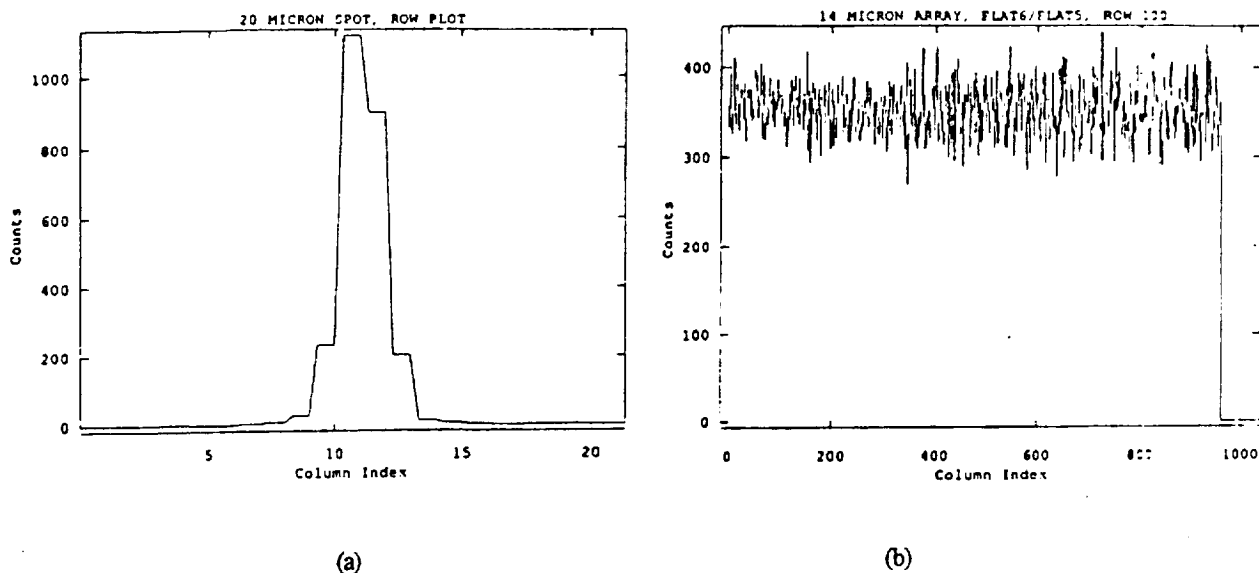
Figure 10. Data recorded with the 14-micron-pixel MAMA detector. a) A cut through an ultraviolet image of a 20-micron spot of light at 2537 Å. b) A row from a rectified flat field image. Here one flat field image has been rectified by another and then renormalized to its original count rate. The data illustrated show deviations which are in perfect agreement with the Poisson statistics of the original exposures (7.6%).
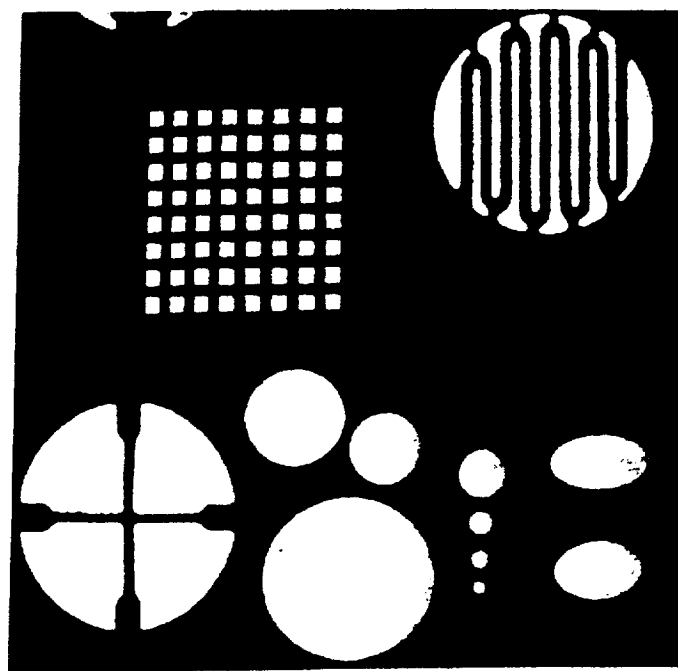
(a)
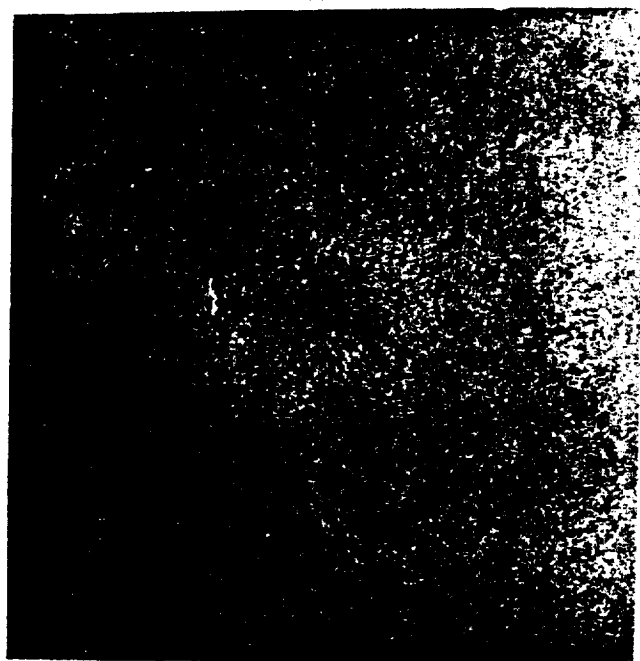
(b)

Figure 11. Images recorded with the (1024 x 1024)-pixel MAMA detector at 2537 Å.
a. Test mask.
b. Rectified flat field.

40-mm-format sealed visible-light tube are defect free. As examples of the type of data currently being recorded with these detectors, an image of a test mask and a rectified flat field recorded at 2537 Å are shown in Figure 11. We plan to fly the ultraviolet version of this detector on the NASA Goddard astronomy sounding rocket late in 1990.

Detailed studies of the performance characteristics of all of the detector systems are now in progress.

4. Future Developments

In addition to the laboratory evaluations, the primary tasks of the MAMA program at this time are the detailed design and fabrication of the (360 x 1024)-pixel flight detectors for the SOHO mission and the fabrication of the prototype (2048 x 2048)-pixel detectors for STIS.

A number of breadboard units of the SOHO detectors are now in fabrication. The detectors will operate in different scientific instruments over the wavelength range from about 400 to 1600 Å. Open detector tubes, sealed detector tubes and sealed detector tubes with openable covers will be employed. All will be based on the standard 25-mm-format demountable tube body fabricated by EMR Photoelectric, Princeton, NJ (see Figure 12).
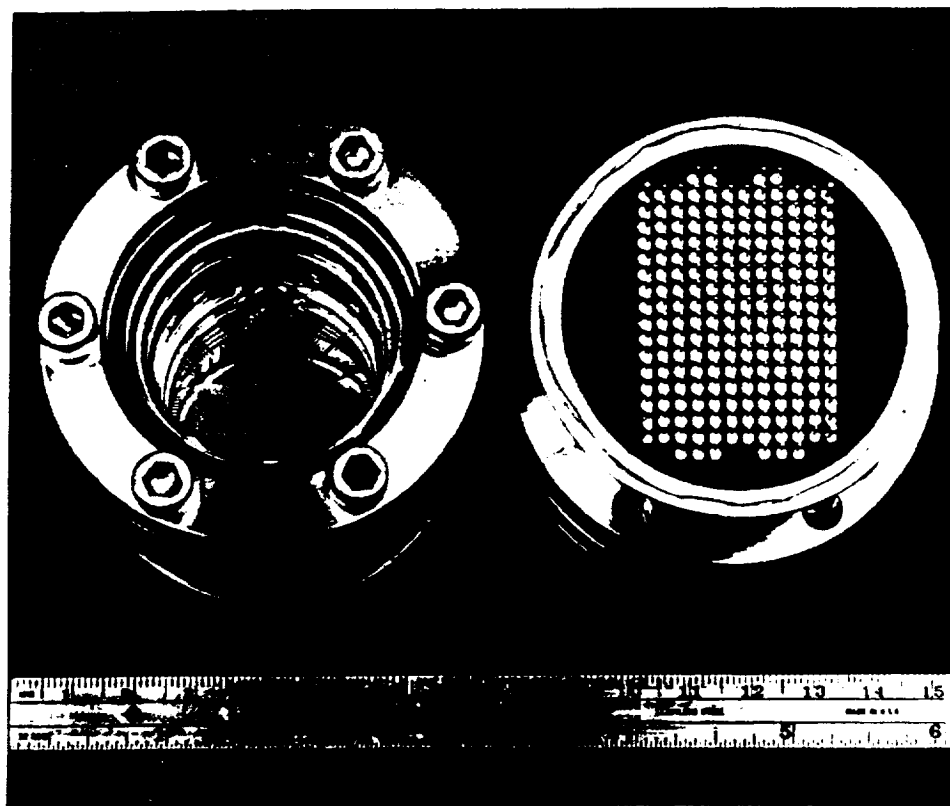

Figure 12. (360 x 1024)-pixel MAMA detector for SOHO.
Left: anode array mounted in the 25-mm-format demountable tube.
Right: rear view of tube body showing electrical outputs from the multi-layer ceramic header.

A major effort is underway at Stanford and at BASG to miniaturize the MAMA electronics through the development of custom chips for the amplifier and discriminator and address-decode circuits. The hybrid MAMA electronics systems will be used on both the SOHO and STIS programs. The requirements for SOHO are for a detector head assembly incorporating the amplifier, discriminator and address-decode circuits, together with the detector high-voltage power supplies, with dimensions no greater than $130 \times 85 \times 180$ mm^3 and a mass no greater than 4.0 kg. This low volume and mass must be achieved without compromising the requirements of high system speed (~175 ns pulse-pair resolution) and low power (<7 W), coupled with the ability to operate for several years in the radiation environment in low earth orbit and at the L1 libration point. Details of the technologies being employed for the custom chips are given in the papers by David Kasle and Ed Cole in these proceedings.

The principal task on the STIS program is the fabrication of the prototype (2048 x 2048)-pixel detector system with 25 x 25 microns^2 pixels. The first batch of anode arrays (see Figure 13) are currently being fabricated at BASG. Because of the need for redundancy in a detector to be used for over five years in space, we have chosen to configure the array as four independent (1024 x 1024)-pixel arrays separated by a three-pixel dead space. The size of this dead space permits a total failure in the anode-electrode bias voltages in any one quadrant without affecting the performance characteristics of the remaining three quadrants. Four totally independent electronics systems are employed.
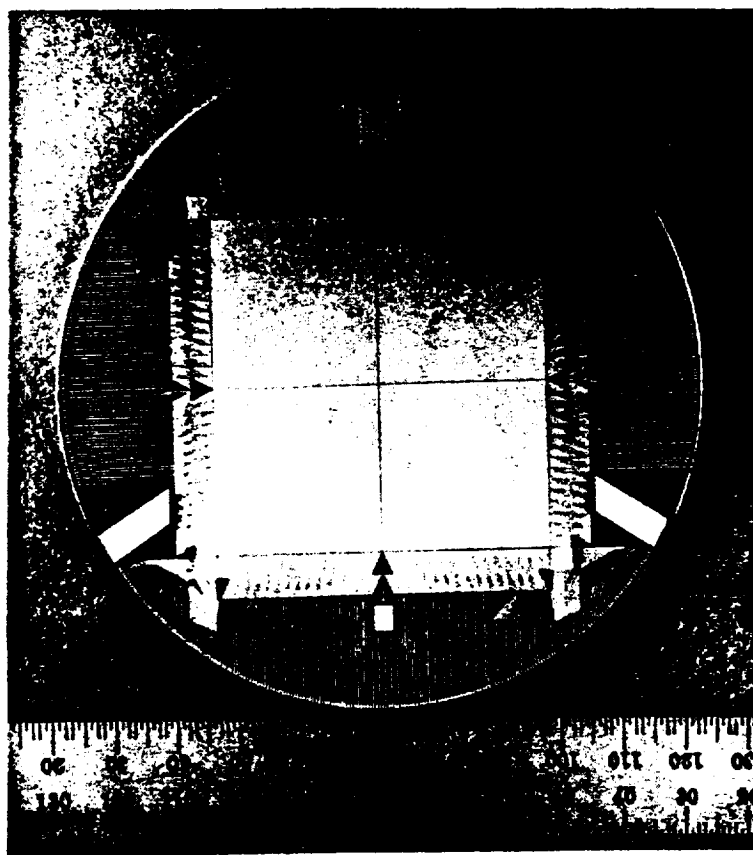

Figure 13. (2048 x 2048)-pixel fine-fine MAMA array with 25 x 25 microns^2 pixels for STIS.

Because of the size of this array, we are fabricating a new 75-mm-format MAMA detector tube. The key component of this tube, the 540-pin multi-layer ceramic header, is currently being fabricated by Advanced Packaging Systems, San Diego, CA. 75-mm-format curved-channel MCPs are being fabricated by Galileo Electro-Optics and 75-mm-format "chevron" MCP stacks have been received from Amperex Inc., Smithfield, RI. First turn-on of this detector is expected to take place in December 1989.

5. References

1. B. E. Woodgate and the Space Telescope Imaging Spectrograph Science Team, "Second Generation Spectrograph for the *Hubble* Space Telescope, "*SPIE vol. 627 Instrumentation in Astronomy VI*, pp. 350 - 362, 1986.

2. "The SOHO Mission: Scientific and Technical Aspects of the Instruments, "European Space Agency *SP-1104*, November 1988.

3. J. S. Morgan, D. C. Slater, J. G. Timothy and E. B. Jenkins, "Centroid Position Measurements and Sub-pixel Sensitivity Variations with the MAMA Detector," *Applied Optics vol 28*, pp. 1178 - 1192, 1989.

4. R. C. Taylor, M. C. Hettrick and R. F. Malina, "Maximizing the Quantum Efficiency of Microchannel Plate Detectors: The Collection of Photoelectrons from the Interchannel Web using an Electric Field," *Rev. Sci. Instrum. vol. 54*, pp. 171 - 176, 1983.

5. O. H. W. Siegmund, E. Everman, J. Vallerga and M. Lampton, "Extreme Ultraviolet Quantum Efficiency of Opaque Alkali Halide Photocathodes on Microchannel Plates" *SPIE vol. 868 Optoelectronic Technologies for Remote Sensing from Space*, pp. 18 - 24, 1988.

Performance characteristics of a curved-channel microchannel plate with a curved input face and a plane output face

David C. Slater, Jeffrey S. Morgan, and J. Gethyn Timothy
Center for Space Science and Astrophysics
Stanford University, ERL 327, Stanford, CA 94305-4055

ABSTRACT

The performance of a high-gain curved-channel microchannel plate (C^2MCP) with a spherical concave input face and a plane output face has been evaluated in the laboratory. This format allows the input face of the MCP to match a curved focal surface, such as in a Rowland circle spectrometer mounting, and, at the same time, permits the use of a high-resolution plane readout array in proximity focus with the output face. The MCP was evaluated in a discrete-anode Multi-Anode Microchannel Array (MAMA) detector system. The MCP tested had channel diameters of 12 μm, a rectangular active area of 9 x 27 mm^2, and a front face radius-of-curvature of 250 mm. The length-to-diameter (L/D) ratio of the channels varied from 136:1 at the edges of the active area to 106:1 at the center. The variation of the L/D ratio across the active area of the MCP allowed the relationship between the saturated modal gain of the pulse-height distribution and the L/D ratio to be examined from modal gain measurements. The saturated modal gain was found to be inversely proportional to the L/D ratio and directly proportional to the applied MCP voltage. The measured performance characteristics are described and compared with gain models based upon the geometric parameters of the MCP.

1. INTRODUCTION

With the development of imaging EUV spectrometers that utilize reflective concave diffraction gratings,[1,2] there has been a need to further develop the imaging capability of detectors commonly used with these spectrometers. Most detectors have planar focal surfaces, however, the surface of best focus for imaging spectrometers using reflective concave gratings lies on the Rowland circle[3]. Therefore for optimum focus, the focal surface of the detector must conform to the curvature of the Rowland circle. The imaging capability of pulse-counting detectors that use microchannels plates (MCPs) would thus be improved if the input surface of the MCP matched the radius of curvature of the reflective diffraction grating. This paper describes the performance of such a high-gain curved-channel MCP[4] with a spherically curved input face and a plane output face. This MCP, called the curved-front-face MCP, employed channels with diameters of 12 μm and a rectangular active area of 9 x 27 mm^2. The MCP was made of Corning 8161 glass with a plate resistance of ~200 MΩ. The radius of curvature of the input face was 250 mm. The MCP was manufactured by Galileo Electro-Optics Corporation.

The MCP was tested in a ceramic/stainless steel demountable Multi-Anode Microchannel Array (MAMA) detector tube with a linear 1 x 100 discrete anode array in proximity focus to the MCP[5]. Each anode in the array represented a pixel with dimensions of 270 μm in width by 8 mm in length. The demountable tube allowed the MCP to operate under ultra-high vacuum conditions necessary for minimal ion-feedback (< 10^{-8} torr). Inside the MAMA tube the MCP was mounted directly above the linear anode array with a gap between the anode array and the output face of the MCP of 100 μm. The top and bottom surfaces of the MCP were electrically connected to an external power supply necessary to bias the MCP for operation. The input face of the MCP was biased negative with respect to the output face which was held at ground. In addition, a positive bias of 50 volts was applied to the anodes themselves to attract the output electrons from the MCP to the array and to keep the electron clouds from radially dispersing due to coulomb repulsion.

The curvature of the input face of the curved-front-face MCP enabled the effects of channel length on output gain to be studied. The gain is defined as the number of electrons in each output pulse emitted from a single channel in the MCP for every input photon that enters the top of the channel. Not all output pulses from the MCP are of the same size. This is due to the random distribution of energies and collision parameters of the electrons inside the channels. The statistical distribution in the size of the output pulses can be characterized by creating a histogram of their magnitudes. The resultant histogram is called the pulse-height distribution (PHD) which is important in characterizing the performance of an MCP.

The shape and mean gain of the PHD depend on the geometry of the channels and the applied voltage across the MCP. Curved-channel plates that operate under low gain conditions ($\leq 10^4$ electrons/pulse) have PHDs that are negative exponential in shape. As the applied voltage is increased, the size of the output charge pulses become nearly constant in size due to space-charge saturation[6]. When this occurs, the PHD becomes quasi-Gaussian in shape with a peak in the distribution occurring at an output gain corresponding to the size of the majority of the pulses. The gain at the position of this peak is called the modal gain. The modal gain is a function of the diameter of the channels, D, and the ratio of the length of the channels L to its diameter - an expression known as the length-to-diameter ratio (L/D). The modal gain also depends on the applied voltage across the MCP. Loty[7] has derived an expression for the maximum modal gain of an MCP operating under space-charge saturated conditions. His expression for the maximum modal gain $\bar{G}$, in units of the number of electrons is given by

$$\bar{G} = \frac{\pi \epsilon}{4e} \frac{V}{(L/D)} D ,$$ (1)

where V is the applied MCP voltage in volts; ϵ is the dielectric constant of the MCP glass in farads $meter^{-1}$; D is the diameter of a single channel in meters; and e is the charge on the electron (1.6×10^{-19} coulomb). The most important feature of equation (1) is not the absolute value of $\bar{G}$, but rather the dependence of $\bar{G}$ with respect to V and L/D.

Figure 1 is a schematic of the geometry of the curved-front-face MCP showing a cross cut of the MCP along the length of the active area. Since the input face of the MCP is a spherical concave surface, the thickness, or length of the channels is a function of the position on the input surface. If x is the position along the length of the active area measured from the origin at the center of the active area, and y is the orthogonal position along the width of the active area, the thickness L of the plate at the position (x, y) is given by

$$L(x, y) = L_o + R(1 - \cos \theta),$$ (2)

where

$$\theta(x, y) = \sin^{-1}\left[\frac{\sqrt{x^2 + y^2}}{R}\right].$$ (2a)

The angle θ is measured from the center of the plate with respect to the plate's normal direction. R is the radius of curvature of the MCP and L_o is the thickness of the MCP at the center of the plate. Equation (2) can be used with equation (1) to derive how the output gain should vary as a function of position on the MCP. The values for L_o and R for the curved-front-face MCP was 1.272 mm and 250 mm, respectively. The ratios of measured modal gain values taken at various spatial locations on this MCP were compared to the expected ratios using equations (1) and (2), and will be discussed in detail below.

Curved-Front-Face MCP Geometry
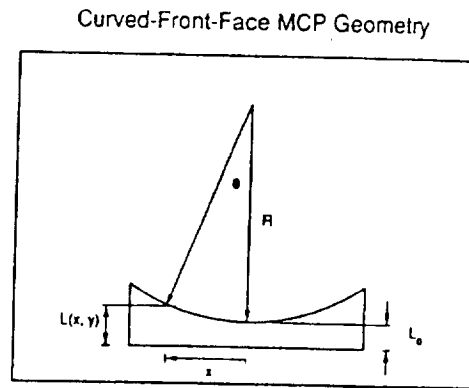
Figure 1. Schematic showing the geometry of the curved-front-face MCP. The input face of the MCP has a spherical surface of radius R. The thickness of the MCP at the center of the plate is L_o, and the thickness measured at a position (x, y), where x is the distance measured along the length of the active area from the center of the plate, and y is the orthogonal distance measured along the width of the active area from the center of the plate, is given by $L(x, y)$. The angle θ is measured from the plate normal. This figure only shows the cross cut of the plate along $y = 0$.

2. BAKE AND UV SCRUB PROCEDURES

High-gain MCPs must operate under high vacuum conditions to minimize ion-feedback. To ensure a high vacuum environment, the MCP must first be subjected to a high temperature bake while installed in the MAMA tube assembly. The bake allows contaminants that are commonly found adsorbed onto the internal surfaces of the MCP after manufacture (e.g. moisture), to outgas from these surfaces. The MAMA tube assembly is typically baked to a maximum temperature of 300° C for a minimum of 6 hours. During the bake, the MAMA tube is attached to a vacuum chamber which is equipped with a 30 liter/second ion pump for continuous removal of the outgassed products. A residual gas analyzer is also attached to the chamber and is used to monitor the quantity and species of the outgassed products.

Not all of the adsorbed contaminants are removed during the bake. To further clean the channels of the MCP, the MAMA tube assembly is subjected to a "UV scrub" session which immediately follows the bake. The MAMA tube assembly is isolated and removed from the vacuum chamber and attached to its supporting electronics to begin the UV scrub procedure. During this procedure, high voltage is gradually applied to the MCP while exposed to ultraviolet light that is directed onto its front surface from a mercury (Hg) penray lamp. The strong emission line at 2537 Å from the Hg lamp provides the necessary stimulus for the MCP to start the secondary electron cascade process through the channels. The high number of electrons released in each output avalanche effectively "scrubs" away any adsorbed substances which the bake did not eliminate. During the UV scrub, the voltage applied to the MCP is gradually raised at an average rate of 50 volts per day until the maximum operational voltage is reached. The pulse-height distribution, spatial uniformity, dark noise, and total number of output events are all carefully monitored during the entire UV scrub session.

The curved-front-face MCP was first installed into a 1 x 100 discrete anode MAMA tube and then baked to 300° C for a period of 6 hours. Following the bake, the MCP was subjected to a UV scrub session which lasted a period of 45 days at which time 1.0×10^{10} counts mm^{-2} were accumulated. The scrub began at an applied voltage across the MCP of 1200 volts, and ended at 2100 volts. The pulse-height distributions were monitored for two pixels - pixel 12, located 10.25 mm from the center of the array, and pixel 49 located at the center.

The channels in the center of the active area first began to show a peak in the PHD at an applied MCP voltage of 1300 volts. The peak, which was just above the threshold set in the electronics (1.5×10^5 electrons/pulse), indicated that the center channels were in space-charge saturation at this voltage. The peak for the channels above pixel 12, however, did not appear above threshold until the MCP voltage reached 1400 volts.

The center channels possessed the smallest L/D ratios in the plate and hence were the first to show space-charge saturation. In this region the magnitude of the electric field across the channels was stronger than in the surrounding channels causing the electrons to strike the channel walls with greater force. Consequently the output gain was higher for the center channels, high enough to become space-charge saturated. As the voltage across the MCP was further increased, space-charge saturation began to progressively occur in the channels further and further from the center.

Figure 2 is a plot showing the modal gain of pixel 12 ($\overline{G}_{12}$) shown with circles and 49 ($\overline{G}_{49}$) shown with triangles as a function of the accumulated output counts per square millimeter during the UV scrub. Also shown in this figure are the values of the applied MCP voltage during the scrub. The first point evident in the figure is that the modal gain of pixel 49 is always greater than that for pixel 12. This is a consequence of the inverse relationship of the modal gain to the length of the channels. The second point is that in the intervals of constant applied MCP voltage where the number of accumulated counts increased the modal gain for both pixels dropped as the electrons, colliding against the channel walls, scrubbed away heavier adsorbed ions. The heavier ions created output pulses which, on average, were of higher gain than those pulses created by the electrons. Thus as the number of ions decreased during the scrub, the gain dropped.

Figure 3 shows the ratio of the modal gain of pixel 49 to that of pixel 12 ($\overline{G}_{49}/\overline{G}_{12}$) as a function of the accumulated output counts per square millimeter during the UV scrub. The figure also shows the magnitude of the applied MCP voltage during the scrub. The modal gain values are those plotted in Figure 2. The basic shape of the curve plotted in this figure indicates that the ratio $\overline{G}_{49}/\overline{G}_{12}$ drops with increasing values of the applied MCP voltage. As the voltage approached 2000 volts, the ratio approached the value predicted by equation (1) - namely the inverse ratio of the lengths of the channels over pixel 12 to those over pixel 49 (L_{12}/L_{49}) which is 1.17 for this plate and is shown by the dashed horizontal line in the figure. This result demonstrates that the modal gain across the MCP is inversely proportional to the lengths of the channels as equation (1) predicts, but only over a range of applied MCP voltages above ~2000 volts. Below this, the ratio is somewhat larger than predicted indicating a more complex relationship of modal gain to the L/D and applied MCP voltage V. The figure also shows that in the intervals where the plate was
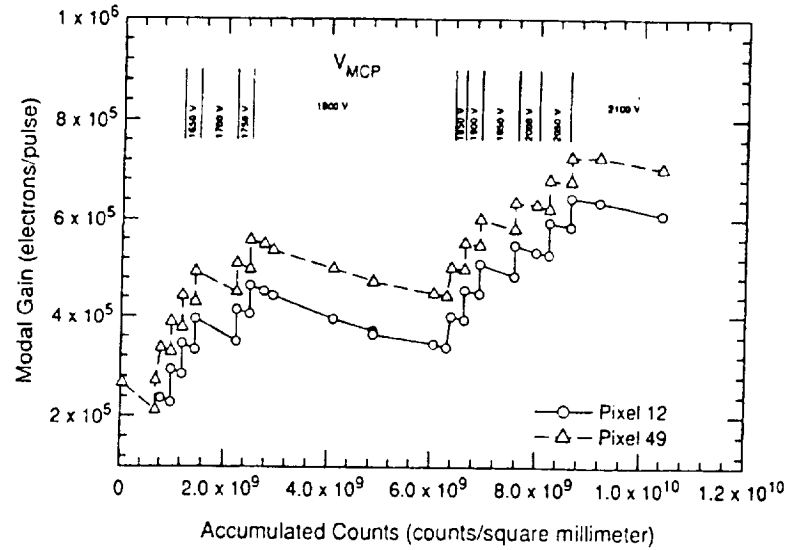
Figure 2. Modal gain versus the accumulated number of output counts mm^{-2} during the UV scrub. The circles denote the gain values for pixel 12, and the triangles for pixel 49. Also shown in this figure are the values of the MCP voltage applied during the scrub. MCP illuminated with 2537 Å photons.
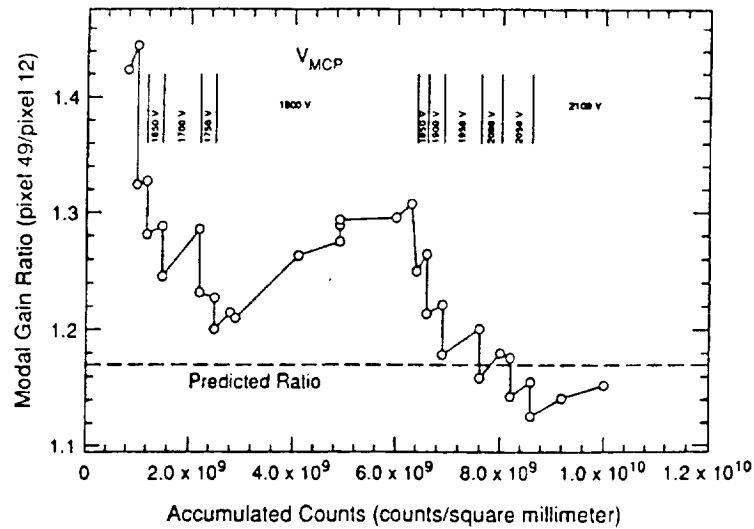
Figure 3. The ratio of the modal gains of pixel 49 to pixel 12 versus the accumulated number of output counts mm^{-2} during the UV scrub. The modal gain values of pixel 12 and 49 are shown in Figure 2. Also shown in this figure are the values of the MCP voltage applied during the scrub. The predicted ratio given by the inverse ratio of the lengths of the channels over pixel 49 to pixel 12 is shown with the dashed line. MCP illuminated with 2537 Å photons.

accumulating counts (at constant MCP voltage), the ratio $\overline{G}_{49}/\overline{G}_{12}$ most often increased and at the applied MCP voltages of 1800 volts and 2100 volts it appears to approach an asymptotic value. Since $\overline{G}_{49}$ and $\overline{G}_{12}$ were both decreasing in these intervals, $\overline{G}_{12}$ must have dropped faster than $\overline{G}_{49}$. This could have occurred in either of two ways: 1) the channels over pixel 12 with the larger L/D ratios were cleaning up faster than those over pixel 49; or 2) the shorter channels over pixel 49 did not require as much cleanup as the longer channels over pixel 12, making $\overline{G}_{12}$ drop a greater amount than $\overline{G}_{49}$. The second explanation seems more plausible since it is hard to imagine shorter channel lengths taking longer to clean up. When the channels over pixel 12 finally became as clean the MCP voltage allowed, the drop in gain slowed down and stopped so that the ratio approached a constant value.

3. PERFORMANCE CHARACTERISTICS

After completion of the UV scrub, the PHD and spatial uniformity as a function of the applied MCP voltage were measured. Figures 4a and b show the modal gain and PHD resolution, respectively, for pixels 12 and 49 as a function of the applied MCP voltage. Both pixels 12 and 49 showed modal gains that increased linearly with MCP voltage. The PHD resolution for both pixels, however, was found to decrease with increasing MCP voltage. Pixel 49 showed an upward trend in the PHD resolution as the voltage was increased beyond 1950 volts. This is a result of the onset of ion-feedback which started in the center of the MCP where the L/D ratio was smallest. The PHD resolution of pixel 12, on the other hand, stayed relatively constant as the MCP voltage increased beyond 1950 volts. This is consistent with the fact that larger L/D ratios generally provide better ion-feedback suppression due to the longer lengths of the channels and the lower effective electric field magnitude which reduces the impact energy of the ions against the channel walls. Because of this, longer L/D ratio plates are generally preferred since they can maintain higher gain output at higher applied MCP voltages with much less ion-feedback than smaller L/D plates. Pixel 12 and 49 reached a maximum modal gain of 6.09×10^5 electrons/pulse, and 7.10×10^5 electrons/pulse, respectively, at the maximum applied MCP voltage of 2100 volts. The PHD resolution measured at this voltage was 29.2% for pixel 12 and 42.8% for pixel 49.
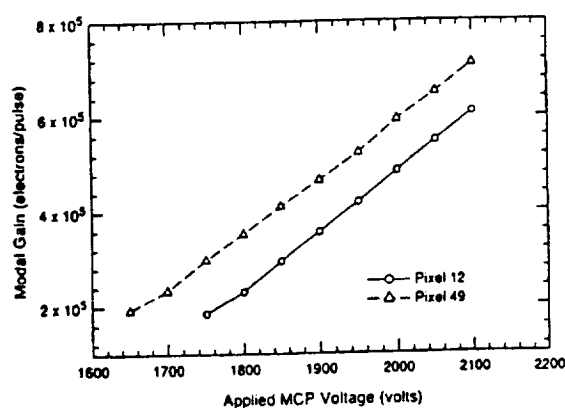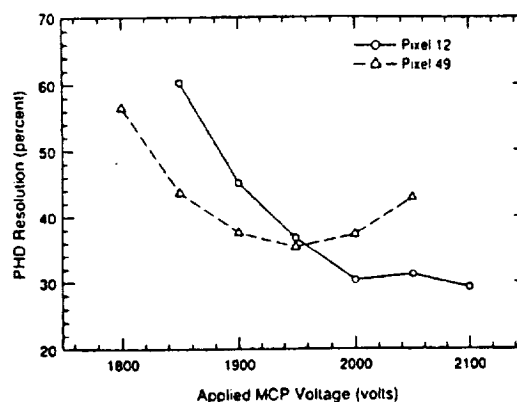

Figure 4. (a) The modal gain versus the applied MCP voltage for pixels 12 (circles) and 49 (triangles). The data shows the linear relationship of the modal gain with applied MCP voltage. (b) The PHD resolution versus applied MCP voltage for pixels 12 (circles) and 49 (triangles).
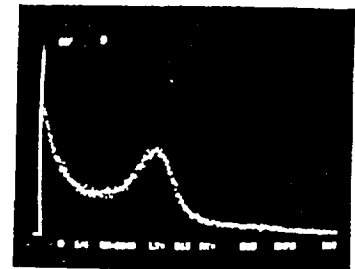
Figures 5a - c show a sequence of PHDs of pixel 49 at applied MCP voltages of 1700, 1900, and 2100 volts, respectively. At 1700 volts (Figure 5a) the PHD is peaked indicating that the channels in the center of the plate are in space-charge saturation. The modal gain at this voltage was 2.34×10^5 electrons/pulse, a value just above the threshold set in the electronics at 1.5×10^5 electrons/pulse (the solid vertical line at the left edge of the figure is located at the electronic threshold level). At 1900 volts (Figure 5b) the peak of the distribution has moved towards the right to higher levels of gain. At this voltage the modal gain was 4.66×10^5 electrons/pulse. The distribution is quasi-Gaussian in shape except for the high level shoulder to the left of the peak. This high level shoulder indicates the presence of an excessive number of lower gain output pulses. These lower gain pulses are caused by the presence of ion-feedback. Figure 5c shows the PHD at 2100 volts. Here again the peak of the distribution has moved out to a still higher level of gain (7.1×10^5 electrons/pulse), but there is an increase in ion-feedback with the low gain tail to the left of the peak rising above the peak itself. This regime is clearly beyond the level at which one would want to operate. Figure 6 shows the PHD of pixel 12 at 2100 volts for comparison. Pixel 12 exhibited a much lower level of ion-feedback than pixel 49. For this reason, larger L/D ratios in MCPs are more desirable because of the greater amount of ion-feedback suppression provided by these plates.
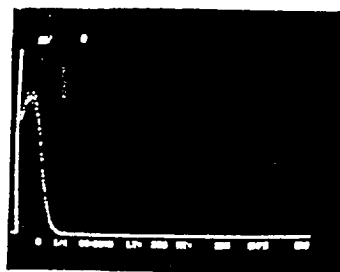
V_{MCP} = 1700 volts
$\bar{G}$ = 2.34 x 10^5 electrons/pulse
R = 55.6%
(a)
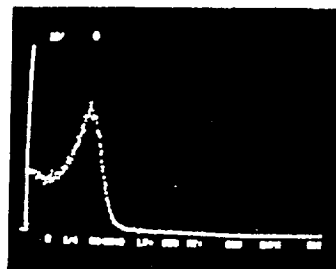
V_{MCP} = 1900 volts
$\bar{G}$ = 4.66 x 10^5 electrons/pulse
R = 37.6%
(b)

V_{MCP} = 2100 volts
$\bar{G}$ = 7.10 x 10^5 electrons/pulse
R = 42.8%
(c)

Figure 5. A sequence of photos showing the PHDs of pixel 49 with increasing applied MCP voltage: (a) 1700 volts - $\bar{G}_{49}$ = 2.34x10^5 electrons/pulse, R = 55.6%; (b) 1900 volts - $\bar{G}_{49}$ = 4.66x10^5 electrons/pulse, R = 37.6%; (c) 2100 volts - $\bar{G}_{49}$ = 7.10x10^5 electrons/pulse, R = 42.8%. The vertical line on the left side of the photos is the position of the electronic threshold set at 1.5x10^5 electrons. MCP illuminated with 2537 Å photons.
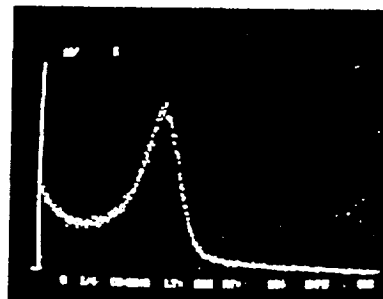

Figure 6. The PHD of pixel 12 at an applied MCP voltage of 2100 volts. The modal gain $\bar{G}_{12}$ = 6.09x10^5 electrons/pulse, R = 29.2%. MCP illuminated with 2537 Å photons.

Figures 7a-d show the spatial output count rate as a function of position along the length of the MCP for applied MCP voltages of 1600, 1700, 1800, and 1900 volts, respectively. At low applied voltages, only the channels in the center portion of the plate responded as is evident in Figure 7a. As the voltage was increased, the channels at the edges of the plate began to respond. This again is a result of the dependence of the modal gain to the L/D ratio and the applied MCP voltage described by equation (1). Equation (1) predicts that channels with smaller L/D ratios should begin to saturate at lower applied MCP voltages compared to channels with larger L/D ratios. This is exactly what was observed - the channels in the center of the plate with the smaller L/D ratios were the first to respond. As the MCP voltage was increased, the response moved outwards from the center to those channels with increasing L/D ratios as is evident in Figures 7b, c, and d.

Figure 8 shows the output count rate of four representative pixels in the array as a function of the applied MCP voltage. Pixel 2 represents the output from channels on the extreme left side of the MCP. Pixels 25 and 75 represent the output from channels about 1/4 and 3/4 of the distance across the length of the plate, respectively. Finally, pixel 50 represents the output from the center of the MCP. Figure 8 shows that pixel 50 was the first to detect output pulses as the MCP voltage was increased. Pixels 25 and 75 were not far behind as they began to rise rapidly at an applied MCP voltage of ~1600 volts. Finally, pixel 2 began to respond at 1700 volts.

Again, this shows the inverse relationship of the modal gain to the L/D ratio at constant applied MCP voltages. Each curve in Figure 8 shows a steep rise followed by a region where the output count rate began to level off. The steep rise is due to the rise in output gain as the voltage was increased. With increased gain, the number of pulses that exceeded the electronic threshold level increased until the majority of the pulses were well above threshold. When this occurred, the output count rate leveled out to a constant value. This is the ideal region in which to operate because the output is rather insensitive to changes in the supply voltage to the MCP and to variations in the threshold setting. Beyond this region, the output count rate again began to increase due to the onset of ion-feedback at the higher MCP voltages. At these higher voltages additional scrubbing action in the channels caused the release of additional adsorbed substances. These substances became ionized by collisions with the output electron clouds and wandered back up the channels to hit the walls releasing additional electrons which were then detected. Because of the large mass of these ions compared to the electron's mass, the ions do not make it very far up the channel before striking the channel wall. Hence, the output pulses from these events are generally of low gain.

4. CONCLUSIONS

The continuously varying channel lengths from the center of the curved-front-face MCP to its edge has allowed a look at how the shape and modal gain of the PHD depend on the channel length. The performance data shows a definite inverse relationship of modal gain with the L/D ratio, as equation (1) predicts. This was born out of the measurements of the PHDs as well as the spatial uniformity of the output counts across the active area of the MCP. In addition, the amount of ion-feedback suppression was found to be a function of the length of the channels. Greater ion-feedback suppression was found for channels of longer length. It was also found that the UV scrub is more effective in cleaning the walls of channels that are of shorter length, since these channels have smaller surface area, and the effective electric field across these channels is greater for a constant applied MCP voltage across the plate.

The spatial response of the curved-front face MCP was found to be quite uniform as the applied MCP voltage was raised to a level of 1900 volts. In addition, at an applied MCP voltage of ~1950 volts all the channels in the plate were in space-charge saturation without excessive ion-feedback. This, the relatively high output gain of ~4 x 10^5 electrons/pulse, and the PHD resolution of ~35% indicate that the curved-front-face MCP is more than adequate for its intended use in a spectrometer that utilizes a Rowland circle type mounting.

Future plans in the evaluation of curved-front-face MCPs are to measure the modal gain as a continuous function of position across the entire active area of the MCP. This would provide a more accurate way to measure the $(L/D)^{-1}$ dependence of the modal gain. In addition, we hope to make use of such an MCP in a MAMA imaging detector attached to an EUV spectrometer that utilizes a Rowland circle mounting to allow detailed measurements of the imaging performance.
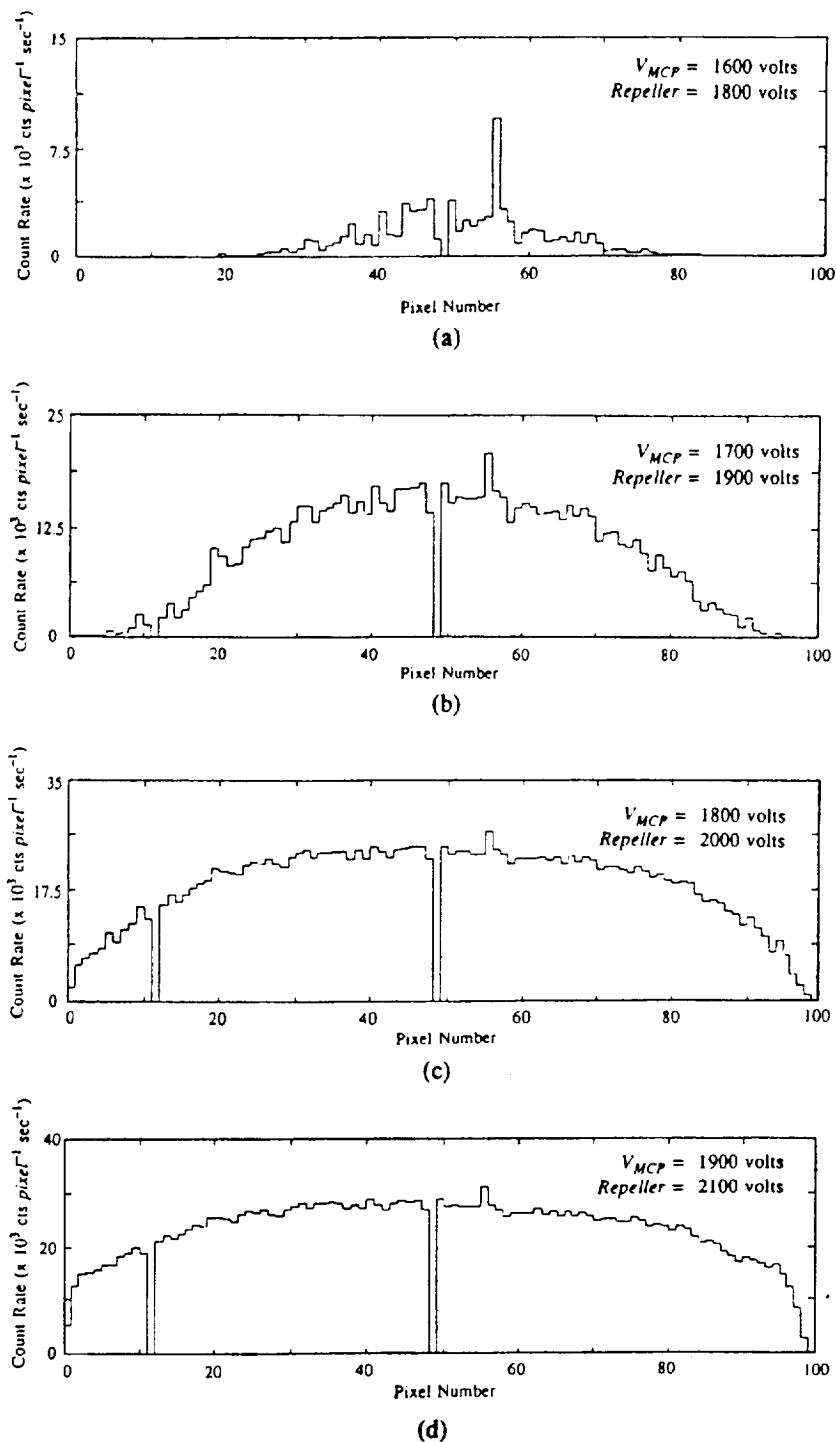
Figure 7. The output count rate as a function of spatial position along the 1x100 linear pixel array. The applied MCP voltages are (a) 1600 volts, (b) 1700 volts, (c) 1800 volts, and (d) 1900 volts. As the voltage is raised, the center of the plate is first to respond, followed by the edges of the plate as the voltage is further increased. Pixels 12 and 49 have zero counts because they are connected to different output circuitry for pulse-height distribution analyses.

5. ACKNOWLEDGEMENTS

6. REFERENCES

1. Huber M.C.E., J.G. Timothy, J.S. Morgan, G. Lemaitre, G. Tondello, E. Jannitti, and P.Scarin, "Imaging extreme ultraviolet spectrometer employing a single toroidal diffraction grating: the initial evaluation," *Appl. Opt.*, Vol. 27, No. 16, pp 3503-3510, 1968.

2. Huber M.C.E. and G. Tondello, "Stigmatic performance of an EUV spectrograph with a single toroidal grating," *Appl. Opt.*, Vol. 18, No. 23, pp 3948-3953, 1979.

3. Born and Wolf, *Principles of Optics*, Pergamon Press, 1975.

4. Timothy J. G., "Curved-channel microchannel plates," *Rev. Sci. Instrum.*, No. 52 (8), 1981.

5. Timothy J. G., "Performance characteristics of multi-anode microchannel array detector systems," SPIE Vol. 501, pp 89-97, 1984.

6. Wiza J.L., "Microchannel Plate Detectors," *Nucl. Instrum. and Meth.*, 162, pp 587-601, 1979.

7. Loty C., "Saturation effects in channel electron multipliers," *Acta Electronica*, Vol. 14, No. 1, pp 107-109, 1971.
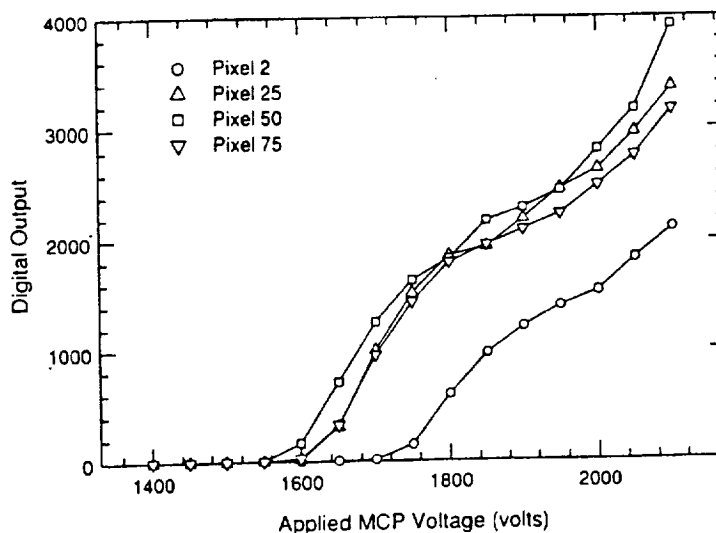
Figure 8. The output count rate of four representative pixels (pixels 2, 25, 50, and 75) versus the applied MCP voltage. The first pixel to respond at low MCP voltages samples channels with the smallest *L/D* ratios (i.e. pixel 50 in the center of the MCP). Pixel 2 has the longest channels over it so it is the last to respond. The curves all begin to roll over above 1900 volts, then show a rise due to increasing ion-feedback at the higher voltages.

High resolution decoding techniques and single-chip decoders for multi-anode microchannel arrays

David B. Kasle

NASA Goddard Space Flight Center
ERL Room 327, Stanford University
Stanford, California 94305

ABSTRACT

The multi-anode microchannel array (MAMA) is a photon counting detector which decodes the position of an event through coincidence discrimination. The decoding algorithm which associates a given event with the appropriate pixel is determined by the geometry of the array. In a standard MAMA detector, the pixel size is determined by the spacing of the anode array; however, the actual limiting factor to the pixel resolution is the spacing of the channels in the microchannel plate. The analog amplitude of charge amplifier pulses can be converted to digital quantities and employed for increasing the resolution of the detector by calculating the centroid position of each event in real time. This centroiding procedure can be implemented as an independent module of the decoder, operating in parallel with the standard digital decoding circuitry and providing the least significant bit(s) of the pixel address. Decoding hardware and techniques for enhanced pixel resolution are discussed in light of speed and complexity issues. A space-based realization of the MAMA detector requires that the decoding circuit be a single-chip monolithic or hybrid integrated circuit because of power, size and weight constraints. A single-chip CMOS gate array version of the decoder is discussed and contrasted with existing multi-chip decoders in terms of size, speed and power.

1. INTRODUCTION

The multi-anode microchannel array (MAMA) employs a photocathode for photon/electron conversion, a microchannel plate (MCP) for electron multiplication and an anode array combined with charge amplifiers for event detection. Decode electronics interpret the charge amplifier outputs to determine the pixel position of an event. The integration over time of a number of events results in a two-dimensional image which is stored in memory. The block diagram of a MAMA detector is shown in figure 1.

The current generation of MAMA detectors employ fine-fine anode arrays, each of which consists of two sets of interleaved fine discrimination anodes in a repeating series. The first set consists of n anodes (which repeats for n+2 cycles) and the second set consists of n+2 anodes (which repeats for n cycles), resulting in a total of $n*(n+2)$ pixels, where n must be even to insure unique decoding over the entire array. The interleaving of the two sets of anodes is analogous to two waves of slightly different frequency beating against each other for one complete cycle.

The spread of the electron cloud due to a single photon event varies according to bias voltages applied to the photocathode, MCP and anode array, as well as to MCP characteristics. The size of an electron cloud is quantized by the number of anodes illuminated, also referred to as the order of the fold, i.e., a three-fold designates the situation in which three contiguous anodes are struck by sufficient numbers of electrons to have voltages greater than some user-specified threshold. A scaled-down version of a fine-fine anode array (n=4) with one-, two-, three-, and four-folds is shown in figure 2. The electron cloud spread must be sufficient to illuminate at least two anodes, i.e. a two-fold, in order to allow for the unique decoding of the position of the event; however, the decoding algorithm must be capable of coping with higher order folds. Determining the pixel position of a two-fold is relatively straight forward, but this is not the case for higher order folds. Thus event decoding is divided into anode encoding, which is the process of converting an m-fold into the equivalent two-fold for arbitrary m, and pixel decoding, which is the process of translating the resultant two-fold into the correct pixel position.

The anode encoding process is demonstrated for three- and four-folds in figure 2. The equivalent two-folds are indicated by the smaller black circle outlines contained within the shaded areas of the three-fold and four-fold. Note that the three-fold has two possible equivalent two-folds, a property of all odd-ordered folds. For odd-ordered folds, the decoder has three options: always choose the left equivalent two-fold, always choose the right or dither between the two. Dithering between left and right makes the pixel sensitivity profiles more symmetric, but introduces a small amount of noise in the image.

The pixel decoding process involves the translation of the two encoded anode numbers which make up the current equivalent two-fold into the corresponding pixel number. Pixel decoding admits either look-up table or arithmetic algorithm solutions.
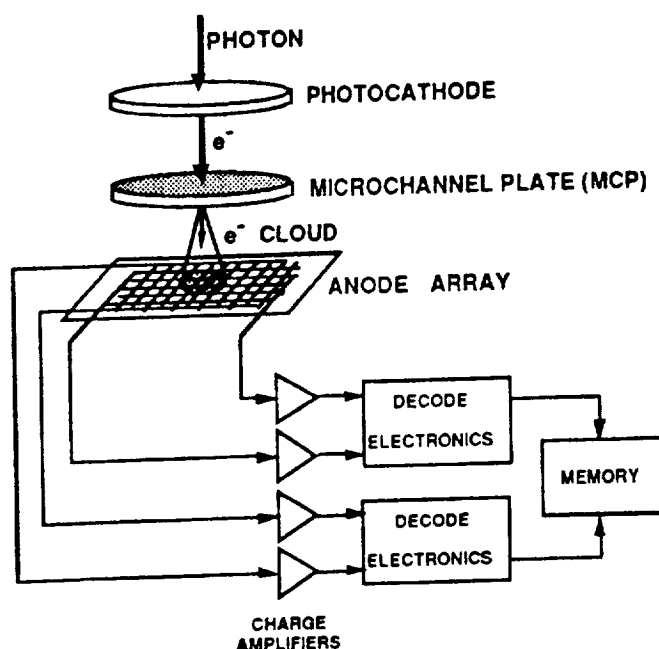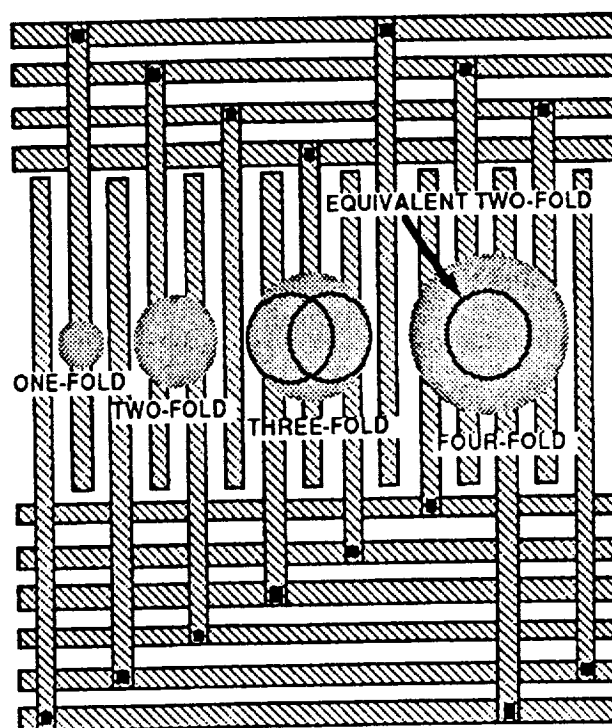

Figure 1. MAMA block diagram

Figure 2. fine-fine array with multi-folds

2. HIGH RESOLUTION DECODING

In a standard MAMA detector pixel size is equal to the spacing of the anodes; however the ultimate limiting factor in the resolution of the detector is the spacing of the pores in the microchannel plate. The resolution of the MCP is generally about twice that of the anode array. This leads to the question : Is it possible to increase the resolution of the detector without changing the detector itself but only by altering the readout electronics? The answer is yes, and there are several ways to do this. The simplest technique is called even-odd discrimination and involves discriminating between even and odd folds to generate a single least significant bit (LSB). The LSB is then concatenated at the end of the most significant bits (MSB's), thereby doubling the detector resolution. This operation can be performed in parallel with the standard decoding procedure and necessitates the addition of minimal hardware to the standard decoding circuitry (although the memory size must be quadrupled). Figure 3 illustrates normal resolution (top) versus even-odd discrimination (bottom). Standard pixels are twice the size and span from the center of one anode to the next, whereas the even-fold pixels are centered betweeen the anodes and the odd-fold pixels are centered on the anodes themselves. The value of the least significant bit depends on whether the throw left or the throw right option is used for handling odd-ordered folds. In the case of throw left, the LSB is high if the event is an odd-fold, whereas in the case of throw right, the LSB is high if the event is an even-fold and is low otherwise. Notice that the dither option for odd-ordered folds cannot be used when performing even-odd discrimination. The performance of this algorithm depends in part on the number of even-folds being comparable to the number of odd-folds. The additional hardware required to perform even-odd discrmination in parallel with the standard decoding circuitry incurs no loss of decoder speed.

Greater accuracy can be obtained at the expense of increased circuitry if the analog voltage values of the anodes are made available as digital quantities through the addition of analog-to-digital (A/D) converters to the charge amplifier outputs. There are several ways to use this addditional data to generate the LSB(s) in parallel with the standard decoding of the MSB's. The simplest of these is called the anode voting algorithm and involves subdividing each standard size pixel in half, then generating the LSB which selects in which half of the pixel to bin the event by "voting" between the two anodes which make up the equivalent two-fold; i.e., if the right hand anode has a greater magnitude signal than the left hand anode, then

the LSB is one and the event is binned in the right half. Otherwise the LSB is zero and the event is binned in the left half. A slightly more complex version of this algorithm uses all anodes of the multi-fold, not just the equivalent two-fold. For example, in the case of a five-fold, the central anode would be ignored while the two left side anodes would be summed and compared to the sum of the two right side anodes to generate the LSB and determine in which side the event should be binned. Very fast flash A/D converters of eight bits or less would be ideal for this purpose. Either of the two high resolution voting schemes requires a minimal penalty in the speed of the decoder. Figure 4 compares even-odd discrimination (top) with the voting algorithm (bottom). Both have double the resolution of standard decoding, but they are skewed with respect to each other by one half of a pixel, and in each case the voting algorithm must choose between two adjacent pixels. Figure 5 illustrates the hardware required for equivalent two-fold voting in block diagram form.
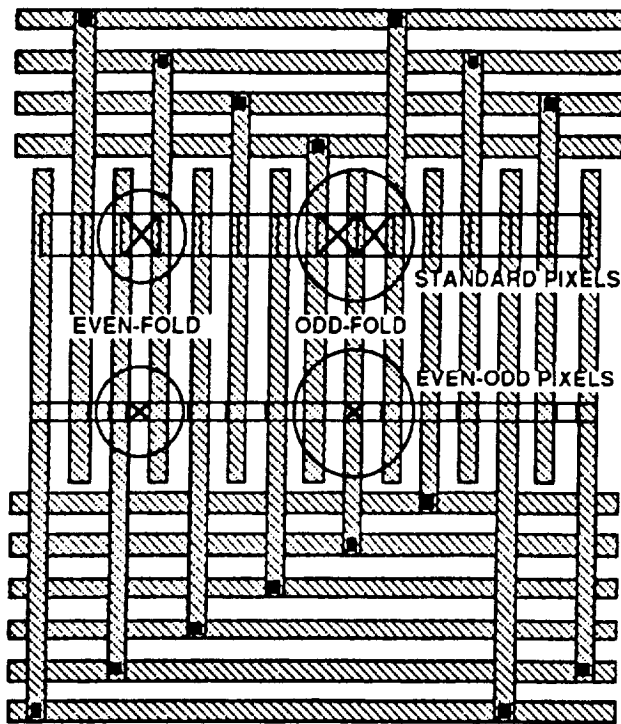
Figure 3. high resolution : even-odd discrimination
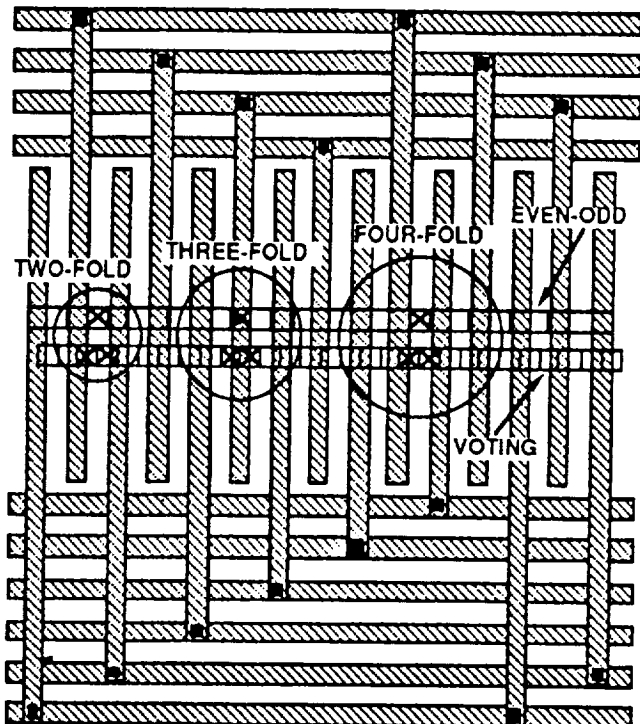
Figure 4. even-odd discrimination vs. voting algorithm

A considerably more complex utilization of A/D converters is anode centroiding. This technique can be employed with either the equivalent two-fold or the full multi-fold and can be used to generate an arbitrary number of LSBs to any desired accuracy, although it is probably only useful to centroid to the resolution of the MCP. The centroid is described by the equation :

$$\overline{X} = \frac{\Sigma X_i \cdot A_i}{\Sigma A_i} \qquad (1)$$

where X_i is the position of anode i with respect to the standard pixel position and A_i is the digital value of the analog voltage of anode i. The pixel position is then given by

$$\text{pixel \# = standard pixel \# +} \boxed{\frac{2^n - 1}{2} + \overline{X}} \longleftarrow \text{LSB's} \qquad (2)$$

where n is the number bits included in the LSBs. This algorithm suffers a significant penalty in terms of speed because it requires addition, multiplication and division. While adders are quite fast and Booth algorithm multipliers are relatively fast, division is a slow process involving reciprocal approximation followed by multiplication. Because these operations must be performed in serial fashion, the speed penalty can be quite significant.

All of the high resolution decoding algorithms described above produce data which can be flat fielded for purposes of normalizing pixel responsivity. In addition, all of the algorithms can be implemented in parallel to the standard decoding circuitry to produce the LSB(s).
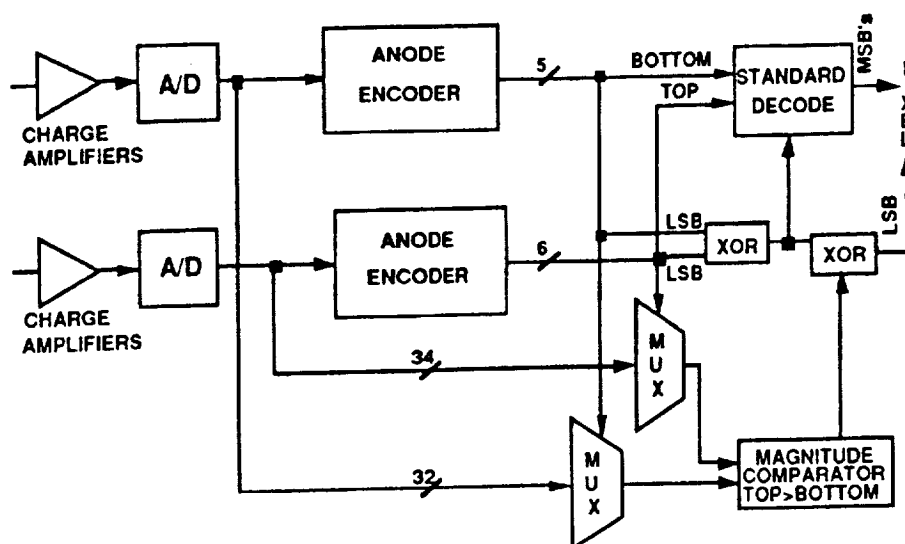
Figure 5. equivalent two-fold voting hardware block diagram

3. SINGLE CHIP DECODERS

To date, all MAMA detector systems have had circuitry composed of discrete parts, suitable for ground-based astronomy or use on sounding rockets. However, in the near future MAMA detectors will be employed in satellite systems such as the Solar Heliospheric Observatory and the Space Telescope Imaging Spectrograph. Space-based MAMA detectors require (relatively) radiation hard decoding circuitry with lower power, weight, and size and higher reliability than their ground-based counterparts, preferably in the form of a single chip. The obvious solution to this problem is an Application Specific Integrated Circuit (ASIC). ASICs are single chips which can contain massive amounts of combinational and sequential logic, a feature which allows for designs with significant parallelism and therefore significant speed advantages. ASIC's can be easily upgraded or modified without any weight or size penalty, and a design composed of ASIC parts will have fewer components and therefore higher reliability than the the same circuitry constructed with discrete parts. Power constraints dictate that the ASIC be of the Complementary Metal Oxide Semiconductor (CMOS) variety.

The simplest ASIC's are Field Programmable Logic Devices (FPLDs), which can be programmed by the user by either burning fusable links or storing static charges within the device. While this capability of instant turn-around is useful in the design phase, FPLDs have a much smaller device capacity and tend to be slower than other forms of ASIC. FPLDs are inexpensive in terms of the cost per package basis, but more expensive in terms of the cost per gate. In addition, no radiation hard FPLDs are currently available, making them undesirable for space-based applications.

Gate arrays offer an ASIC technology with considerably greater speed and dramatically greater functional capacity. A gate array usually consists of numerous unconnected CMOS gates (although BiCMOS and ECL technology arrays are also available). The design process consists of deciding how to interconnect the gates and fabrication consists of applying two layers of metal according to the design masks. Gate arrays are less expensive on a per gate basis, being able to accommodate designs of over 50,000 gates. Fabrication time depends on the vendor, but is generally around a month after final design submission. Circuit speed depends largely on layout efficiency and fan-out, but is approaching that of full custom designs thanks to channel-free compacted arrays and shrinking device sizes. Radiation hard gate arrays are available which are hardened to 500 Krads and can tolerate over 10^8 rads/sec without upset and up to 10^{12} rads/sec without latch up. The current generation of high performance CMOS gate arrays are as fast as standard Transistor-Transistor Logic (TTL) discrete parts but use much less power, and they have a high rate of first time success without requiring repeated design iterations.

Standard cells are pre-designed and optimized combinational and sequential circuit blocks which make up a library of functions available to the designer. The standard cell ASIC design process consists of selecting the appropriate functions and determining their interconnections. Thanks in part to variable transistor sizes, cell-based designs tend to be somewhat denser and faster than array-based designs. Cell-based designs also tend to be more expensive than array-based designs and typically require a month and a half to two months to fabricate after final design submission. Read Only Memories and Random Access Memories (ROMs and RAMs) are two to four times denser in cell-based technologies than in array-based technologies, and the smaller die sizes required by cell-based ASICs generally lead to greater flexibility in packaging. Cell-based designs typically require longer times for testing, production and design iteration. Radiation hardness and functional capacity of cell-based technology are comparable to those of array-based technology.

Full custom ASIC designs provide the ultimate in small size, low power and high speed performance. Unfortunately, since they must be laid out by hand, one transistor at a time, they are also the most expensive and require typically a year or more to produce. A variety of technologies are available, including CMOS, Bipolar and Gallium Arsenide (GaAs). Functional capacity is limited only by die size and density is limited only by minimum device size and designer ingenuity. Radiation hard technology is readily available, but the high cost and slow turn around time of radiation hard full custom ASIC's makes them undesirable for all but the most demanding of applications.

Because of their relatively low cost, massive functional capacity and fast production time, CMOS gate arrays were selected as the target technology for space-based MAMA decoders, and LSI Logic was selected as the vendor by virtue of their high performance and high capacity radiation hard gate arrays. The decoder has been designed and is currently being simulated at Stanford University.

The design process was unique because Olympus, the Stanford University Logic Synthesis System was employed for generating the entire circuit. Olympus actually consists of a number of independent software packages which pass data via standard file formats, as shown in figure 6. Typically a gate array is designed by using a schematic editor to lay out the circuit, gate by gate; this is a rather tedious process for any substantial circuitry. However, Olympus allows the user to describe the behavior of a circuit with a hardware description language called Hardware C (which resembles the C programming language). This is very much like writing a functional simulation of the circuit, a much easier task than using a schematic editor to lay out each gate. Olympus then performs all the tasks necessary to convert the high level description into an actual circuit design.
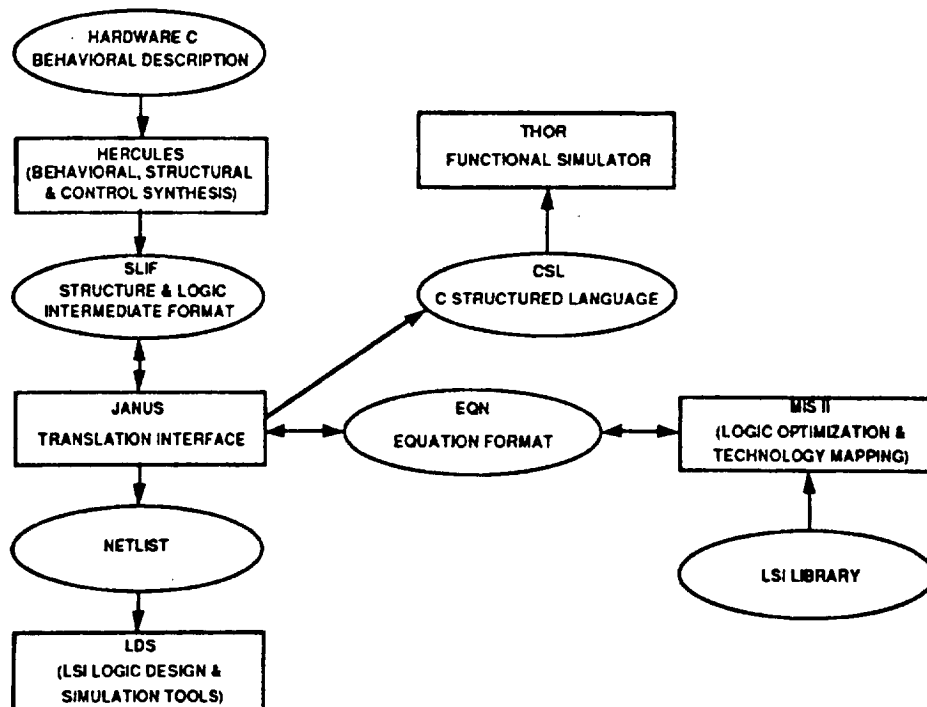

Figure 6. Stanford University Logic Synthesis System and LSI Design and Simulation tools

Hercules, the high level synthesis package of Olympus, performs behavioral, structural and control synthesis to convert the Hardware C description into a register transfer level (RTL) description consisting of combinational and sequential equations. The RTL description is then written out in Structure and Logic Intermediate Format (SLIF) form. If the user wishes to perform functional simulation at this juncture, the SLIF file is translated into C Structured Language (CSL) format and the THOR simulator performs functional (but not electrical) simulation. Next the Janus translation interface program translates the SLIF description into Equation (EQN) format. The EQN format file is then logically optimized and mapped into the LSI technology by the MIS II program. Janus translates the output of MIS II into a standard netlist in the LSI Logic format. At this point the design process is complete. Finally the LSI Logic Design and Simulation tools (LDS) are used for gate level simulation and electrical evaluation of the circuit. LDS also performs placement and routing of the gates and handles chip finishing tasks such as placing bond wires from the die to the pad frame. The design is now ready for fabrication.

A block diagram of the gate array realization of the MAMA decoder is shown in figure 7. Input latches are required to store transient inputs which are not always precisely coincident in time due to timing jitter in the charge amplifiers. Massively parallel combinational logic encodes the inputs into an equivalent two-fold. So called "glue logic" adjusts the equivalent two-fold for degenerate cases, such as wrap-around, when an event spans the transition from one cycle of the anodes to the next. The equivalent two-fold is then simultaneously decoded in parallel into the pixel location for array sizes of 224, 360, 960 and 1024 pixels. All four pixel outputs are multiplexed into the correct pixel address according to the actual MAMA detector anode array size in use. A pipelined output latch maintains a valid pixel output while new inputs are propagating through the circuit, thereby improving pulse pair resolution. The equivalent two-fold to pixel address decoding can be performed with either ROM Look-Up Tables (LUTs) or arithmetic algorithm logic blocks, and the gate array contains both. ROM LUT's require four to six times the number of gates required by arithmetic algorithm pixel decoders, but they have the advantage of operating more than twice as fast.
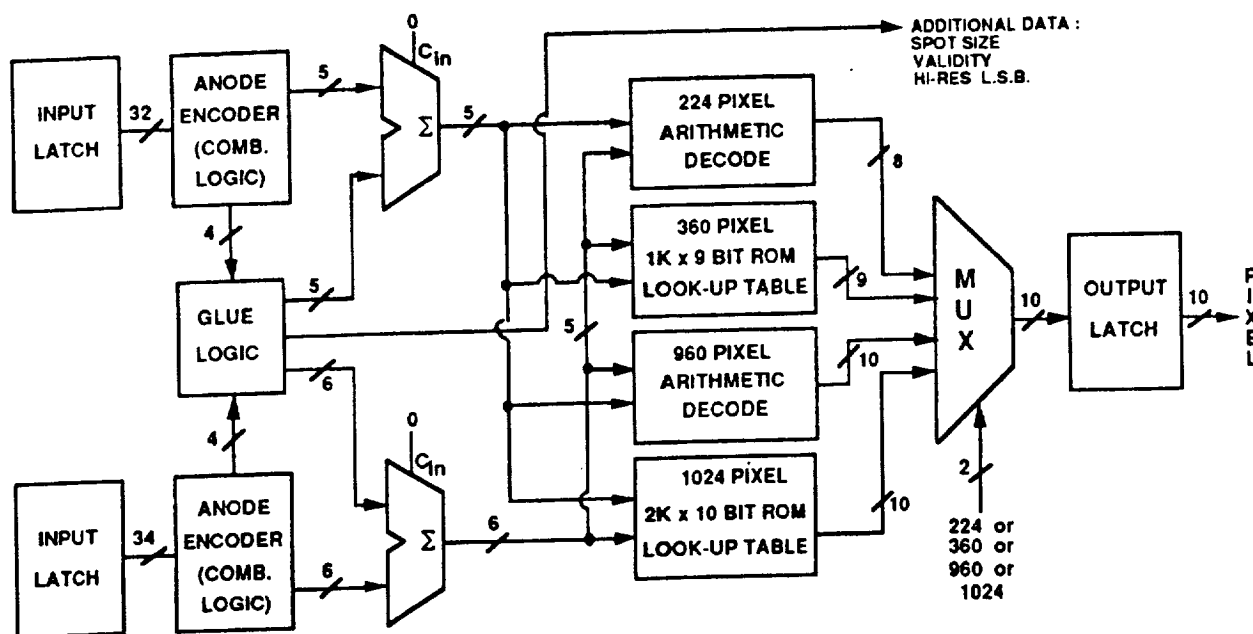
Figure 7. MAMA decoder gate array block diagram

The gate array design can accommodate active high or active low charge amplifier inputs, and decodes any user selected combination of two-, three-, four-, five- or six-folds. High resolution even-odd discrimination is provided as an option, and under normal resolution odd-ordered folds can be handled by throwing left, throwing right or dithering between the two. Inputs and outputs are latched and the timing jitter window which defines whether charge amplifier outputs are coincident in time is user controllable. The gate array can decode a single axis of 224, 360, 960 or 1024 pixels; for example, two gate arrays would be required to decode the output of a 360 by 1024 pixel MAMA detector. Normal commercial fabrication will be used for initial evaluation of the gate array, but the design will eventually be fabricated in radiation hardened technology. The gate array chip can be put in a variety of packages, including pin grid arrays and surface

mount packages; however, leadless chip carriers are not suitable for this application, because of the high number of inputs and outputs exceeds the current limits of leadless chip carriers.

A ceramic pin grid array (CPGA) package which will house the gate array is shown in figure 8. By way of contrast a pair of fine-fine decoders constructed from discrete parts for a ground-based MAMA detector are shown in figure 9. The more densely populated circuit board decodes 960 pixels and the other board decodes 224 pixels. The CPGA has an area of 17 cm^2, while each discrete part decoder circuit board occupies 331 cm^2. The gate array is projected to require less than 0.25 watts to perform decodes in less than 175 nanoseconds (including input and output latching time), as opposed to the discrete part decoders which require 12 watts to decode events in 75 nanoseconds (without any latching).
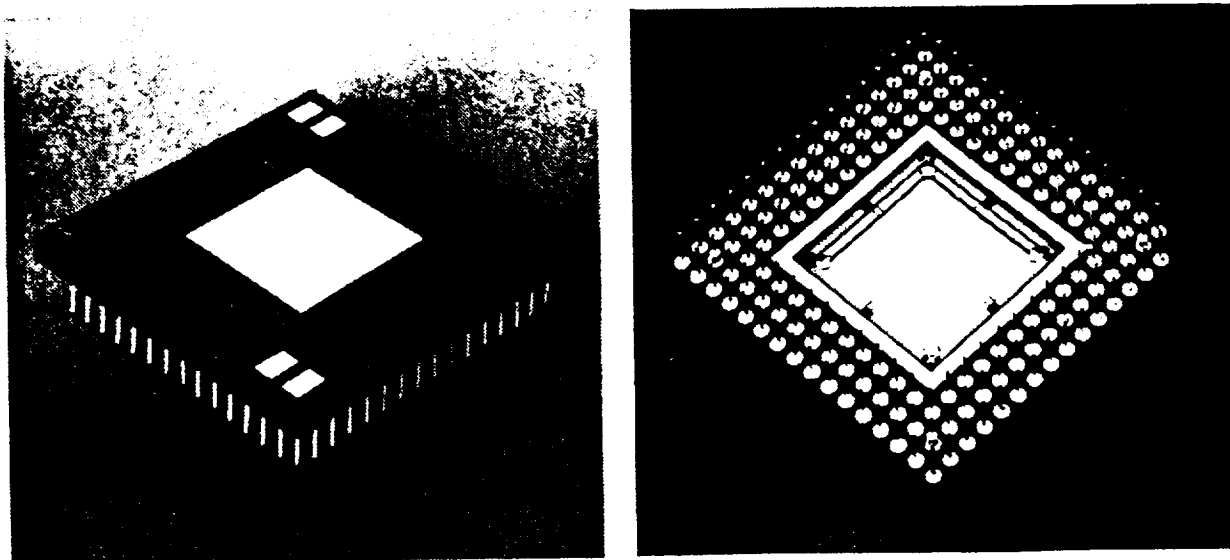
Figure 8. Ceramic pin grid array package for housing gate array MAMA decoder
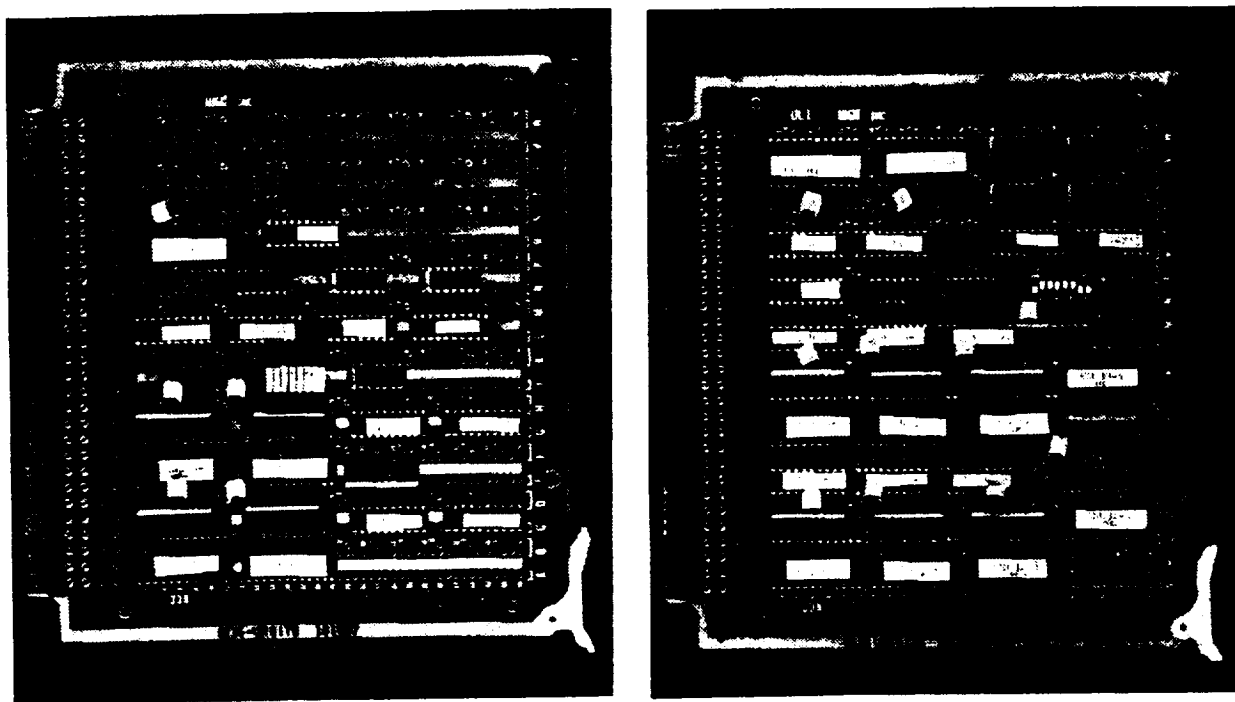
Figure 9. MAMA discrete part decoder circuit boards : 224 and 960 pixels

4. CONCLUSIONS

The resolution of a MAMA detector can be increased without changing the detector itself, simply by altering the readout electronics. Resolution can be doubled by even-odd discrimination, and the addition of A/D converters to the charge amplifiers allows more complex high resolution decoding techniques such as anode voting and anode centroiding. Space-based MAMA applications require decoders of low power, small size, high reliability and radiation hardness. These requirements are satisfied by a CMOS technology gate array ASIC currently under developement at Stanford University. The circuit was designed using Olympus, the Stanford University Logic Synthesis System. The gate array handles active high or active low inputs, has latched inputs and outputs, performs even odd discrimination for high resolution, interprets two-through six-folds and decodes 224, 360, 960 or 1024 pixels. The gate array can be fabricated in standard commercial technology or radiation hardened technology.

5. ACKNOWLEDGMENTS

6. REFERENCES

1. D.B. Kasle , "Decoding Techniques for fine-fine-geometry multi-anode microchannel arrays", SPIE Ultraviolet technology II Vol. 932, pp. 280-284, 1988.
2. D.C. Ku and G. De Micheli, "HERCULES - A System for High-Level Synthesis", Proceedings of the ACM/IEE 25th Design Automation Conference, 1988
3. J.S. Morgan, D.C. Slater, J.G. Timothy and E.B. Jenkins, "Centroid position measurements and subpixel sensitivity variations with the MAMA detector", Applied Optics Vol 28, No. 6, pp. 1178-1192, March 1989.
4. J.G. Timothy, "Electronic readout systems for microchannel plates," IEEE Transactions on Nuclear Science Vol. NS-32, No. 1, pp. 427-432, 1985.
5. J.G. Timothy and R.L. Bybee, "High-resolution pulse-counting array detectors for imaging and spectroscopy at ultraviolet wavelengths," SPIE Ultraviolet technology Vol. 687, pp. 109-116, 1986.

Imaging MAMA Detector Systems

David C. Slater, J. Gethyn Timothy and Jeffrey S. Morgan
Center for Space Science and Astrophysics
Stanford University, ERL 314
Stanford, CA 94305-4055, USA

and

David B. Kasle
Code 683
NASA Goddard Space Flight Center
Greenbelt, MD 20771, USA

ABSTRACT

Imaging MAMA detector systems with formats as large as 1024 x 1024 pixels are now being used at ultraviolet and visible wavelengths. In addition, MAMA detectors with 2048 x 2048 pixels are under construction for use on NASA Goddard Space Flight Center's *Hubble* Space Telescope Imaging Spectrograph (STIS). These detector systems operate with zero readout noise and are optimized for low signal level studies on the ground and in space. The ultraviolet versions of the MAMAs utilize "solar blind" photocathodes and have significantly higher detective quantum efficiencies than currently available CCDs for many applications at far ultraviolet (FUV) and extreme ultraviolet (EUV) wavelengths.

In this paper, we describe the configurations and performance characteristics of the latest versions of the MAMA detectors and discuss the development of the hybrid electronic circuits needed for forthcoming space missions. We also briefly present data recorded with the MAMA detectors on a recent sounding rocket flight. In addition, we report on the performance characteristics of several different types of high-gain microchannel plate (MCP) configurations currently under evaluation with the MAMA detector systems: specifically curved-channel, "chevron", "Z-plate", and helical-channel MCPs. The gain, uniformity, dark noise and dynamic range characteristics of these plates are compared and contrasted with particular emphasis given to their effect on MAMA detector system performance.

1. INTRODUCTION

The Multi-Anode Microchannel Array (MAMA) detector systems are state-of-the-art photon counting imaging detectors currently under development in the laboratory for use in a number of space astrophysics missions. These detectors are designed to provide high spatial and temporal resolution for applications in low-light level imaging and spectroscopy at ultraviolet, FUV and EUV wavelengths. Large-format versions of these devices (2048 x 2048 pixels) are currently under development as the prime detectors for the *Hubble* Space Telescope Imaging Spectrograph (STIS), and high-spatial-resolution versions of the detectors have been baselined for the prime spectrograph on board the Far Ultraviolet Spectroscopic Explorer (FUSE)/*Lyman*. In addition to these astronomy missions, (360 x 1024) - pixel MAMA detectors have been selected for use in several instruments on board the European Space Agency (ESA)/NASA Solar and Heliospheric Observatory (SOHO) mission and in the Ultra-high-resolution XUV Spectroheliograph (UHRXS) to be built for the Space Station *Freedom*.

As part of the development of the MAMA detectors we are gathering astronomical data from both ground based observations and sounding rocket flights. Because of the random readout capability of the MAMA system, it lends itself to imaging applications which require high time resolution, such as speckle interferometry, speckle imaging, astrometry, and image motion compensation at both visible and ultraviolet wavelengths. In addition, the thresholding techniques employed in the system electronics result in zero readout noise so that the residual noise in the output signal is just the Poisson noise from the incoming light signal and the dark noise from the MCP.

In this paper we describe the configurations and performance characteristics of the latest versions of the MAMA detector systems. We also present recent sounding rocket data recorded with a MAMA detector showing the galaxy

NGC 6240 imaged in the ultraviolet at wavelengths around 1450 Å. In addition to these imaging results, we present some performance data recorded with a MAMA detector utilizing a number of different high-gain MCP configurations. In particular, we compare and contrast the gain characteristics, dark noise, spatial uniformity, and dynamic range.

2. MAMA DETECTOR SYSTEMS

The MAMA detector system is composed of the tube assembly, the charge amplifiers, discriminators, and the decode electronics followed by the memory, timing, and control circuitry. Figure 1 shows a schematic block diagram of the MAMA detector system. The tube assembly contains a single high-gain curved-channel microchannel plate (MCP) in proximity focus with a two dimensional anode array. The MAMA can operate with either a semi-transparent photocathode deposited on the back surface of an input window in proximity focus with the front face of the MCP or in the open tube configuration with an opaque photocathode deposited directly on the input face of the MCP. Figure 2 shows a three-dimensional cutaway of the MCP and anode array in an open tube configuration. The anode array is a two-dimensional array of gold electrodes deposited in two orthogonal layers separated by a thin layer of silicon dioxide. The top layer encodes one axis of the two dimensional array and the bottom layer encodes the orthogonal axis. The output charge clouds from the MCP must strike two or more anodes simultaneously in each direction to allow the position of the event to be encoded correctly. The anode center-to-center spacing determines the pixel size. Anode arrays with both 25 x 25 μm^2 pixels and 14 x 14 μm^2 pixels have been fabricated and tested to date[1].

The charge pulses from the anodes are first amplified with the charge-sensitive amplifiers and are then sent to a discriminator which creates a digital pulse only if the input pulse is above a set threshold level. The threshold is set above the system electronic noise yet remains well below the level of the output signal pulses from the MCP. The digital output pulses are then fed into the decode logic circuitry which determines, from the particular group of anodes that have been simultaneously hit with signal charge, the location of the event. This method of encoding allows a x b pixels in each dimension to be decoded with a + b amplifier and discriminator circuits. The orthogonal axis encodes pixel locations in the same way. Hence, to encode an array of 1024 x 1024 pixels, only 2 x 64, or 128 amplifier and discriminator circuits are required. After the address of each photo-event is decoded, it can either be tagged with the time of arrival and stored to tape
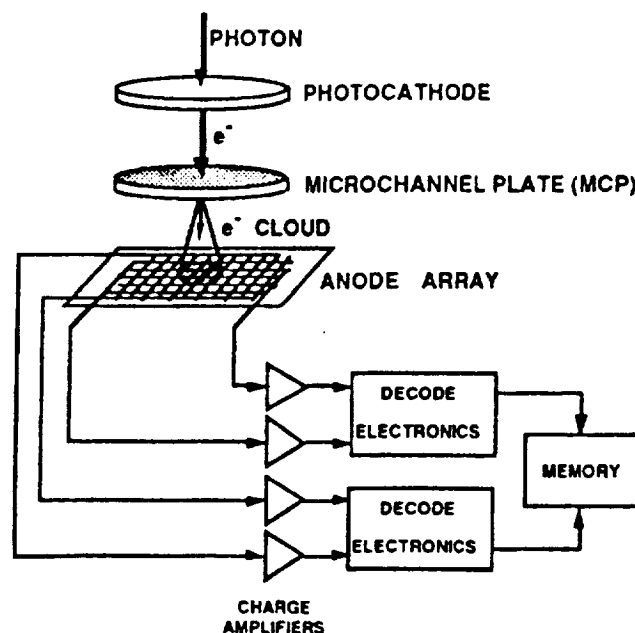
Figure 1. Schematic of the imaging MAMA detector system.
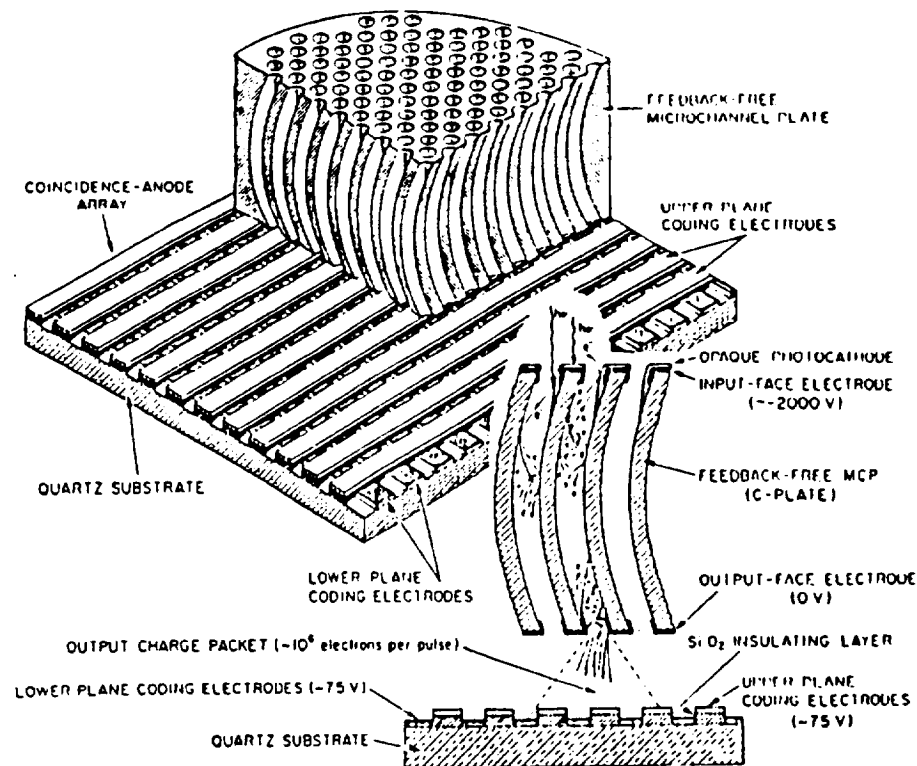
Figure 2. Schematic showing a cutaway of the MAMA imaging detector system with the single high-gain curved-channel MCP and the two dimensional anode array.

(referred to as the time-tag mode), or the events can be integrated in memory over a period of time and read out as an integrated image. The time-tag mode is used if temporal resolution is required, such as in applications involving speckle imaging and motion compensation. More detailed information on the time-tag mode of operation is given by Timothy, et al.[2,3]

Three different anode array geometries have been designed, built, and tested using the above method of pixel encoding. The first generation of these arrays were called the coarse-fine arrays. The output pixel-to-pixel uniformity of these arrays suffered from capacitive imbalances between the coarse and fine anodes which introduced a fixed pattern in the flat field response. This was somewhat remedied in the second generation design, which rearranged the anode geometry to reduce the capacitive coupling. These arrays, called balanced coarse-fine arrays, still suffered output nonuniformities from the inductive coupling between anodes resulting from the fast risetime of the output pulses from the MCP (< 500 ps).

A third generation of anode arrays have now been fabricated and tested which utilize a slightly different encoding geometry. This new array geometry, called the fine-fine array, was designed to capacitively balance and inductively decouple the anodes to provide improved pixel-to-pixel output uniformity. These arrays allow the encoding of $[n \times (n + 2)]^2$ pixels in a two dimensional array with $4 \times (n + 1)$ amplifier and discriminator circuits. (224 x 960) - pixel, (360 x 1024) - pixel and (1024 x 1024) - pixel fine-fine arrays have already been fabricated and tested. Figure 3 shows the (2048 x 2048) - pixel fine-fine array, which is comprised of four contiguous (1024 x 1024) - pixel arrays butted up against each other with less than a 3 pixel dead space between arrays. The (2048 x 2048) - pixel arrays have been fabricated but not yet tested in a complete MAMA system. We are currently waiting the delivery of the 75-mm-format MCPs required for this size array. We plan to start testing these arrays in April, 1990. More detailed information on the configurations and performance characteristics of these arrays is given by Timothy, et al.[1,4] and by Morgan, et al.[5]
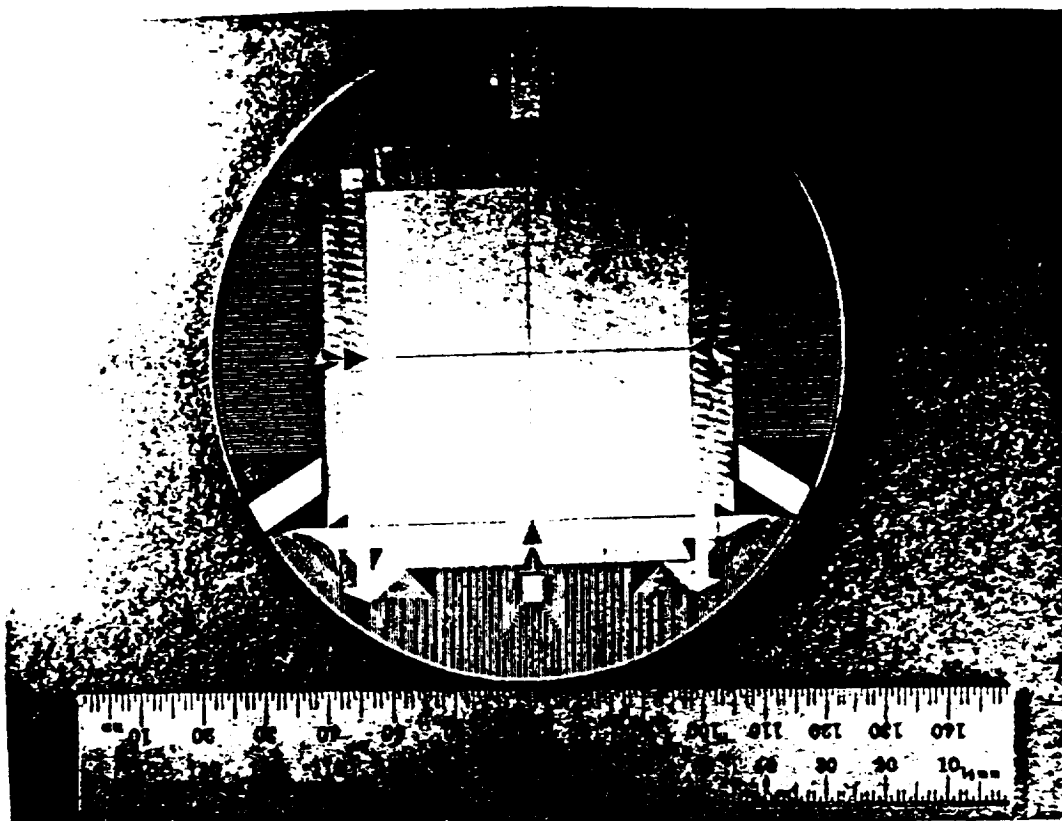
Figure 3. (2048 x 2048) - pixel fine-fine array with 25 x 25 μm^2 pixels.

3. MAMA HYBRID ELECTRONIC DEVELOPMENT STATUS

To date, all MAMA detector systems have had circuitry composed of discrete parts, suitable for ground-based astronomy or use on sounding rockets. However, in the near future MAMA detectors will be employed in satellite systems such as the Solar and Heliospheric Observatory and the Space Telescope Imaging Spectrograph. Space-based MAMA detectors require relatively radiation-hard decoding circuitry with lower power, weight, and size and higher reliability than their ground-based counterparts, preferably in the form of a single chip. The obvious solution to this problem is an Application Specific Integrated Circuit (ASIC). ASICs are single chips which can contain massive amounts of combinational and sequential logic, a feature which allows for designs with significant parallelism and therefore significant speed advantages. ASIC's can be easily upgraded or modified without any weight or size penalty, and a design composed of ASIC parts will have fewer components and therefore higher reliability than the the same circuitry constructed with discrete parts.

Because of their relatively low cost, massive functional capacity and fast production time, CMOS gate arrays were selected as the target technology for space-based MAMA decoders, and LSI Logic was selected as the vendor by virtue of their high performance and high capacity radiation hard gate arrays. The decoder has been designed and is currently being simulated at Stanford University. The decoder can interpret the outputs of 224, 360, 960 or 1024 pixel arrays. Fabrication of the decoder chip in commercial technology is scheduled for June of 1990. After testing, the decoder chip can also be fabricated in radiation resistant technology able to tolerate over 10^8 rads/sec without upset and up to 10^{12} rads/sec without latch up.

Ball Aerospace currently has plans to submit a design to Tektronics for an integrated version of the amplifier/discriminator electronics. Test versions of the integrated amplifier chips are scheduled for delivery by the end of this summer. By using both the integrated decode and amplifier chips, the SOHO tube, amplifiers, and decode circuitry will be

able to fit within a box of approximately 25 x 15 x 10 cm^3 dimensions. This represents a miniaturization by about a factor of 14 over current implementations of the detector.

4. GODDARD ROCKET FLIGHT RESULTS

In June 1989, under the direction of Dr. Andrew Smith at the NASA Goddard Space Flight Center, a (256 x 1024) - pixel balanced coarse-fine MAMA detector with an opaque CsI photocathode was flown aboard a Boosted Terrier Black Brant Sounding Rocket to record ultraviolet imaging data of the irregular galaxy NGC 6240. This galactic object is thought to be two gas-rich galaxies in collision. The purpose of this flight was to collect imaging data necessary to study the spatial morphology of the UV emissions in this object.

The MAMA tube assembly and supporting electronics flown on this rocket flight are shown in Figure 4. Figure 5a shows 220 seconds of raw data taken in the time-tag mode. The data were taken at a central wavelength of 1450 Å with a passband of $\Delta\lambda = 500$ Å. The field-of-view of this image is 6.4 x 25.6 arc min^{-2}. The raw image is smeared due to pointing drifts during the flight (note the 3 star trails on the left side of the image). The galaxy itself is smeared beyond recognition. Figure 5b shows the reconstructed image with the smear motion removed. This was obtained by using the time-tagged photo-events in the star trails to determine the time history of the pointing drifts. These corrections were then applied to the entire set of time-tagged data. The widths of the reconstructed star images are approximately two pixels (3 arcsec). NGC 6240 now shows up clearly in the reconstructed image. Further information on the results of this experiment is given by Morgan, et al.[3]
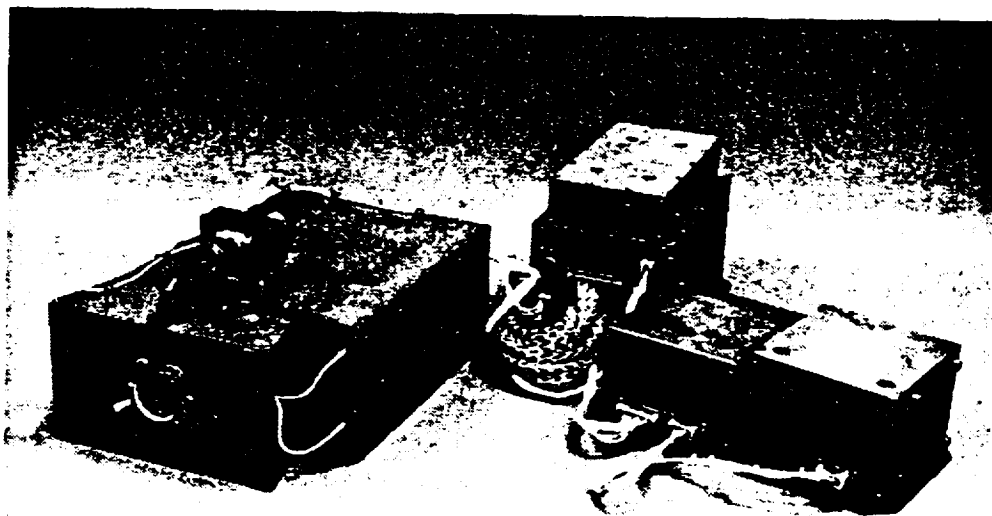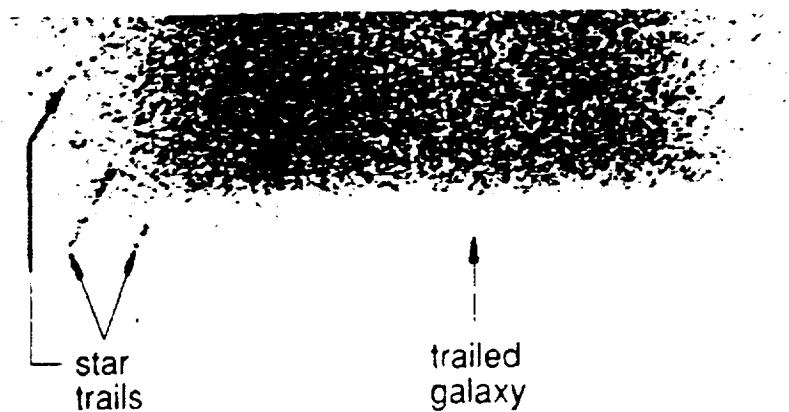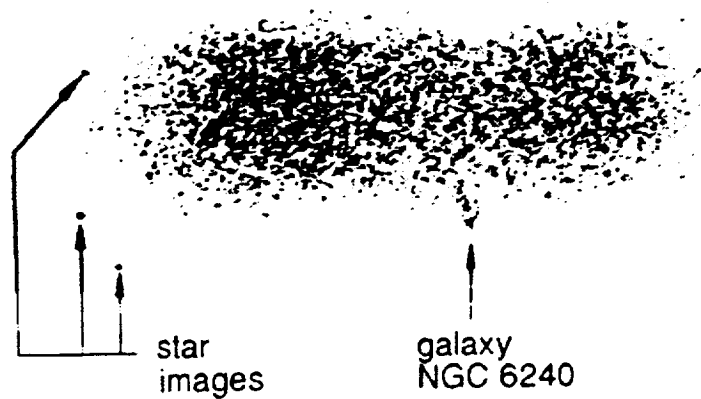

Figure 4. (256 x 1024) - pixel MAMA imaging system flown on the rocket flight to collect UV data of NGC 6240.

Raw Image: $\lambda = 1450$ Å

star
trails

trailed
galaxy

(a)

Reconstructed Image: $\lambda = 1450$ Å

star
images

galaxy
NGC 6240

(b)

Figure 5. Raw (a) and reconstructed (b) UV images of NGC 6240.

5. MCP DEVELOPMENT TESTING

5.1 High-Gain MCP Configurations

The MCP used in the MAMA detector is a thin semiconducting glass plate composed of 10^5 to 10^7 small pores or channels which provide amplification of incoming radiation or particles by means of secondary electron emission. MCPs have been made with channel diameters as small as 4 μm [6], however, most of the high-gain MCPs that we have tested to date have channel diameters of 12 μm on 15 μm centers. Amplification is accomplished when a negative high voltage (a few KV) is applied to the input face of the MCP with the output face at ground. When a photo-generated electron from a photocathode strikes the top inside surface of a channel, two or more electrons are emitted from the channel surface. The applied voltage across the MCP pulls each of these electrons further into the channel where they again strike the channel wall liberating two or more additional electrons per impact. This multiplication process continues until the cloud of liberated electrons, which generally contains 10^5 to 10^6 electrons, exits the output end of the channel. The number of electrons in the output electron cloud is called the gain. The gain is determined by the physical size of the channels, the physical characteristics of the MCP glass, and the magnitude of the applied MCP voltage.

The output electron clouds are not all uniform in size because of the random nature of the electron collisions inside the channels. The size of the output clouds are therefore statistically distributed. Such a distribution, generally referred to as the pulse-height distribution (PHD), is important in characterizing the performance of the MCP in an imaging detector. When an MCP is operated under low gain conditions, the PHD is negative exponential in shape [7]. As the gain is increased by increasing the applied MCP voltage, the sizes of the electron clouds become more uniform due to space-charge saturation effects and changes in the electrostatic field at the output end of the channels. These effects cause the PHD to become quasi-Gaussian in shape [7]. The peak in the distribution is called the modal gain, and the FWHM divided by the modal gain is called the PHD resolution. Amplifiers with discriminator thresholds set to the low gain "valley" of a space-charge saturated PHD are less sensitive to changes in MCP gain performance and therefore are more photometrically stable when operating in the "pulse-counting" regime.

We, at Stanford, are currently conducting an investigation of the performance characteristics of four types of high-gain MCP configurations with the MAMA detector system. These four configurations include the curved-channel ("C-plate"), the "chevron", the "Z-plate", and the helical-channel MCP. The curved-channel MCPs were made by Galileo Electro-Optics Corporation, the "chevron" by Hamamatsu Corporation, the "Z-plate" by Amperex Corporation, and the helical-channel plates by Detector Technology Inc. The gain, output uniformity, and dark count rate were measured for each of the above configurations using a demountable MAMA detector system. The purpose of this investigation was to determine which of the four high-gain MCP configurations are best suited to allow the MAMA detector system to meet the design goals of the STIS and the SOHO space programs.
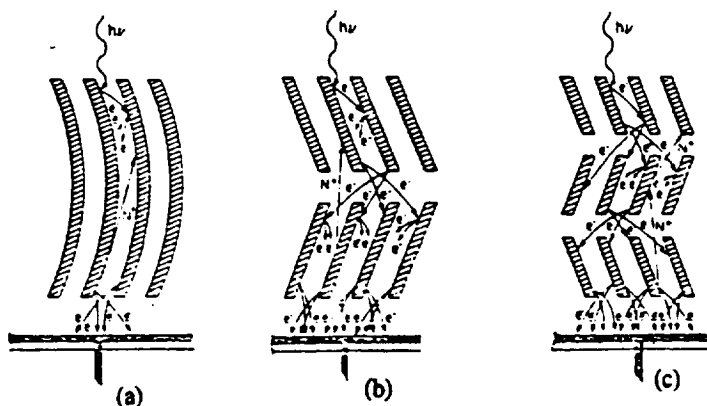

Figure 6. High-gain MCP configurations. (a) curved-channel, (b) "chevron", and (c) "Z-plate".

The MCP in the MAMA detector system must be capable of high-gain output in the "pulse-counting" regime for proper operation. This requires that the MCP operate under high applied voltage conditions sufficient to provide space-charge saturated pulse-height distributions with high modal gain and low ion-feedback. Ion-feedback is an undesirable condition in which residual gas molecules in the path of the output electron cloud are positively ionized by the impact with the cloud and are then pulled back up the channel by the applied MCP voltage. These ions strike the channel wall liberating additional electrons which then cascade down the channel creating noise pulses following the main signal pulse.

Figure 6 is a schematic showing the cross-sectional view of three of the four high-gain MCP configurations that are under evaluation. These are the curved-channel (Figure 6a), the "chevron" (Figure 6b), and the "Z-plate" configurations (Figure 6c). The curved-channel configuration is composed of a single plate with the channels curved in a "C" shape to suppress ion-feedback. The other two configurations utilize two ("chevron") or three ("Z-plate") MCPs stacked together, each set with their angled straight channels opposing each other to provide ion-feedback suppression.

Figure 7 shows the channel configuration for the fourth high-gain MCP under evaluation — the helical-channel MCP. This figure shows an early version of a helical fiber configuration with four channels twisted together[8]. The helical-channel MCP is built up by fusing as many of these twisted elements together as necessary to make the desired plate size. Since no shearing is required to construct these plates (unlike the curved-channel MCP which requires shearing to construct the C-shape of the channels), the yield of good usable plates is theoretically much greater than for curved-channel MCPs. With only four channels per twisted element, the open-area-ratio (OAR), defined as the ratio of the total open area of all the channels to the total active area of the plate, was only about 12% with channel diameters of 50 μm. Later versions that we have tested contain up to 91 channels per twisted element with 25 μm diameter channels. These MCPs have improved OARs of approximately 45%.

5.2 Testing Results

The characterization of the four MCP configurations was conducted utilizing a MAMA demountable tube with a linear output array of 100 anodes. A photograph of the (1 x 100) - anode tube assembly is shown in Figure 8. The tube consists of a ceramic and stainless steel rear body which houses the anode array, the MCP, and a repeller plate used to focus electrons emitted from the MCP's intrachannel web regions down into the MCP channels for improved detection efficiency. The anode array output pulses are conducted through a ceramic header at the rear of the MAMA tube to the output pins at the back of the tube. The anodes are metallized gold on a ceramic substrate with a separation distance between anodes of 270 μm and a length of 8 mm. The MCP is held in proximity focus above the anode array with a gap of approximately 100 μm. Two high voltage feedthrough rings make contact with the input surface of the MCP and the repeller plate above the MCP. A negative voltage is applied to the input surface of the MCP with the output side resting on three gold pads at ground potential spaced 120 degrees from each other. The anodes are typically biased 50 to 150 V positively with respect to ground to attract the electron charge clouds from the MCP and to reduce their radial dispersion.

Before the MCP is characterized it undergoes a bakeout followed by a UV "scrub" procedure to eliminate as much residual gas and adsorbed contaminants as possible on the MCP and on the surrounding tube surfaces. The bakeout of the MCP and tube assembly is conducted under high-vacuum conditions at a temperature of 300 degrees C for a period of at least 8 hours. Following the bakeout, the tube is then turned on electrically with high voltage gradually applied to the MCP while being illuminated with 2537 Å photons from a mercury penray lamp. This UV "scrub" procedure is designed to further clean up the internal surfaces of the channels by electron impact. The scrubbing action takes place as the voltage on the MCP is gradually raised and the avalanche electron clouds which impact the output end of the channels "scrub" away adsorbed material from the channel surfaces. This scrubbing action also lowers the secondary electron yield which in turn causes the modal gain to slowly decrease as the accumulated number of pulse events increase. During this "scrub" phase the MCP voltage is raised on average 50 volts per day until the full operational voltage is reached. The "scrub" continues at full voltage until the modal gain plateaus at a constant value. After reaching this plateau, the MCP is ready for characterization.

To date we have tested over 20 curved-channel MCPs with active-area diameters of 25 mm and channel diameters of 12 μm with 15 μm pitch. Of this large group, the best results have come from a set of plates with channel length-to-diameter ratios (L/D) of 120:1 and with input channel bias angles greater than 12 degrees. These plates have demonstrated well saturated pulse-height distributions at applied MCP voltages around 2000 volts with modal gains ranging from 3 x 10^5 to 5 x 10^5 electrons pulse^{-1} and with PHD resolutions of 35 to 45%. The gain uniformity measured across the MCPs was generally better than ± 10% peak-to-peak. Figure 9 shows the PHD of one curved-channel MCP in this group at 2000 volts
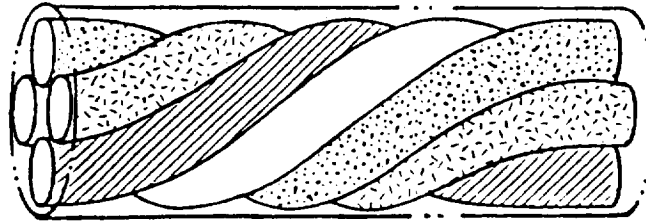
Figure 7. Helical-channel fiber configuration showing four fibers per twisted element.
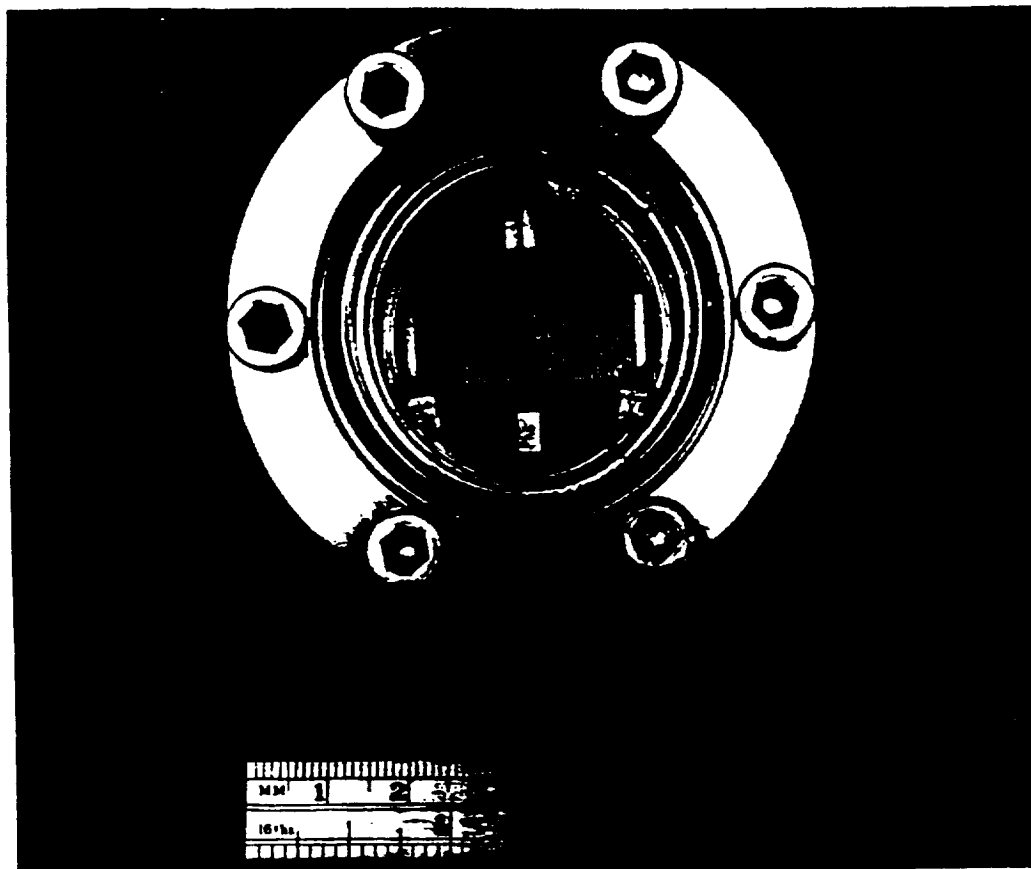
Figure 8. 1 x 100 - anode array used to evaluate 25 mm diameter MCPs.

applied MCP voltage. The modal gain was measured at 4.1×10^5 electrons pulse^{-1} with a PHD resolution of 36%. The peak-to-valley ratio (defined as the ratio of the output count rate at the peak in the PHD to the output count rate in the valley at the low gain side of the PHD) was greater than 10. There is evidence of some ion-feedback which shows up in the PHD as a broad tail extending beyond the "knee" on the high gain side of the peak. The ratio of this ion-feedback tail at 1.5 times the modal gain to the peak in the PHD is greater than 10 indicating excellent feedback suppression.
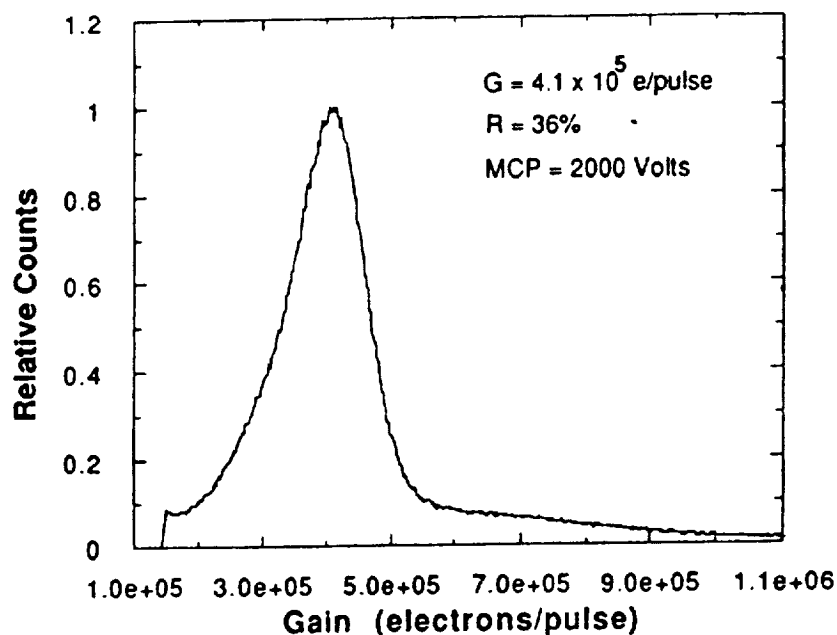
Figure 9. Pulse-height distribution of curved-channel MCP at 2000 volts. Modal gain was 4.1×10^5 electrons pulse^{-1} and the PHD resolution was 36%.
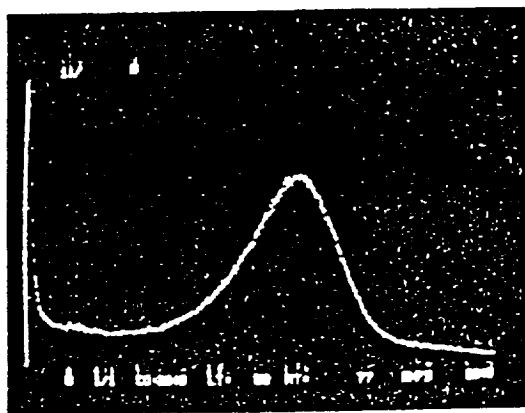
Figure 10. Pulse-height distribution of "chevron" MCP at 3200 volts. Modal gain was 1.2×10^7 electrons pulse^{-1} and the PHD resolution was 38%.

We have also tested two 40-mm-diameter curved-channel MCPs with 12-μm-diameter channels. The modal gains of these two plates were 4 x 10⁵ electrons pulse⁻¹ and 5 x 10⁵ electrons pulse⁻¹, respectively, with one plate exhibiting 30% PHD resolution and the other 50% at 2000 volts of applied MCP voltage. These plates have since been placed into imaging (1024 x 1024) - pixel MAMA detector tubes, one with an S-20 photocathode for further image testing and for ground-based astronomical observations[1], and the second with an opaque CsI photocathode for future use on the Goddard Astronomy sounding rocket.

We have tested to date one pair of 25-mm-diameter Hamamatsu "chevron" plates (two MCPs stacked against each other with no gap between) with 10-μm-diameter channels and a combined L/D ratio of 200:1. This set of plates showed excellent space-charge saturation with a peak modal gain of 1.2 x 10⁷ electrons pulse⁻¹ and a PHD resolution of 38% at 3200 volts of applied MCP voltage (see Figure 10). Again, the peak-to-valley ratio was better than 10 and the ion feedback tail at 1.5 times the modal gain was a factor of 10 lower than the peak of the PHD.

We have also tested one fused "Z-plate" stack from Amperex Corporation. This plate was a 36 mm diameter format plate with 12 μm diameter channels and an overall L/D ratio of 120:1. Figure 11 shows the PHD at an applied MCP voltage of 2600 volts. At this voltage the plate exhibited a modal gain of 2 x 10⁶ electrons pulse⁻¹ with a PHD resolution of 63%, and a peak-to-valley ratio of 3. The ratio of the peak count rate to the high-gain feedback tail count rate at 1.5 times the modal gain was better than 25 suggesting that the suppression of ion-feedback was greater for this plate than that measured for both the curved-channel and "chevron" configurations.
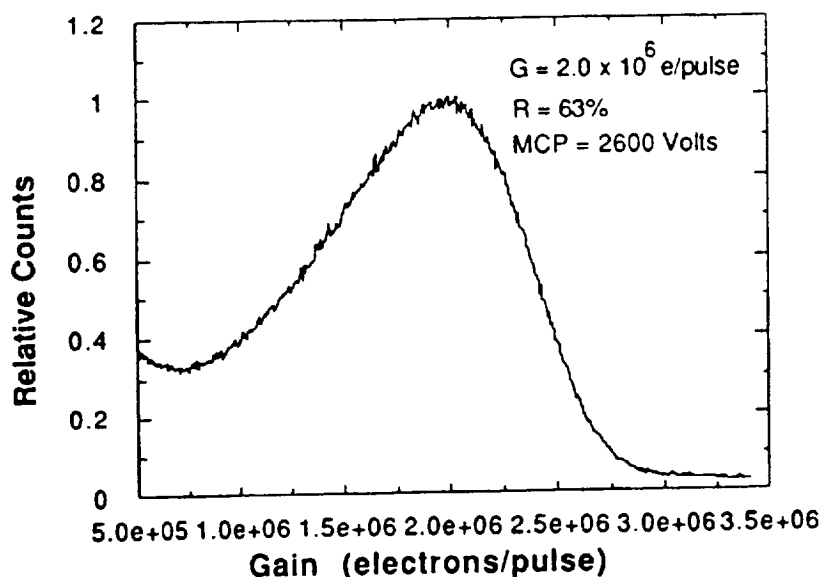
Figure 11. Pulse-height distribution of "Z-plate" at 2600 volts. Modal gain was 2.0 x 10⁶ electrons pulse⁻¹ and the PHD resolution was 63%.

Finally, we have tested a number of helical-channel MCPs from Detector Technology, Inc with plate diameters of 25 mm. The best results to date were from a plate with 25 μm diameter channels (91 channels per twisted element) and an L/D ratio of 125:1. Figure 12 shows the recorded PHD of this plate at an applied MCP voltage of 3000 volts. At this voltage, the modal gain was 1.1 x 10⁶ electrons pulse⁻¹ with a PHD resolution of 79%. The peak-to-valley ratio was 2.3 but the ion-feedback high-gain tail was well suppressed with a smooth decrease in the output count rate from the peak out to the high-gain end of the distribution. The ion-feedback tail was lower than the peak in the distribution by a factor of 55 at a gain value 2.25 times the modal gain. Future tests with these MCPs will include imaging tests in a (224 x 960) - pixel fine-fine MAMA system.
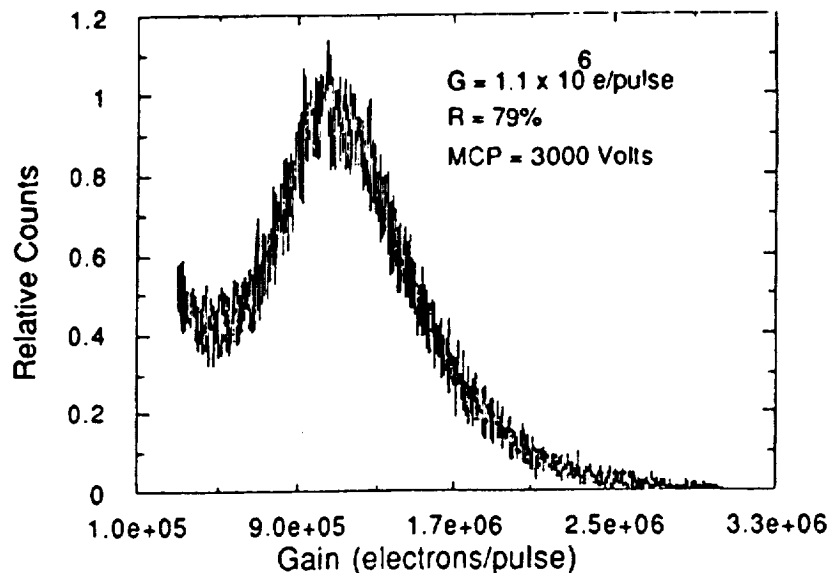
Figure 12. Pulse-height distribution of a helical-channel MCP at 3000 volts. Modal gain was 1.1×10^6 electrons pulse[-1] and the PHD resolution was 79%.

The dark count rate for the above MCPs were also measured during the characterization procedure. The curved-channel MCPs were generally quiet with dark count levels of around 0.01 to 0.1 counts sec^{-1} mm^{-2}. The "chevron" and helical-channel plates also exhibited fairly low dark count rates in the range of 0.03 to 0.08 counts sec^{-1} mm^{-2}. The "Z-plate" showed the highest dark count rate of 0.7 counts sec^{-1} mm^{-2}. The higher dark count rates were generally associated with plates which contained a number of isolated "hot spots" caused by field emission from sharp points on the MCP surface. This was evident from the shape of the PHD, which was quasi-Gaussian, indicating that the dark events originated from the top surface. The low dark count plates exhibited negative exponential shaped PHDs indicating the dark was most probably due to internal radioactive decay in the MCP glass[9].

Figure 13 is a plot of the modal gain as a function of the applied MCP voltage for each of the four MCP configurations. The curved-channel MCPs have demonstrated the tightest (lowest PHD resolution) distributions of any of the four tested MCP configurations. In addition, they have the further advantage of being able to operate at the lowest applied MCP voltages of any of the four configurations. The modal gain values, however, are the lowest of the four configurations. For the MAMA imaging system, the curved-channel MCPs are still a good choice, especially for systems which utilize 25 mm diameter format MCPs. The gain uniformity, however, may begin to degrade with larger format MCPs due to the increased difficulty in maintaining good uniform shear across the entire active area of the MCP. The choice of MCP for the larger diameter formats remains to be seen. It will be determined by which configuration provides the best gain uniformity over the large active area with the best pulse-height distribution characteristics.

The "chevron" and "Z-plate" MCPs both showed high modal gains with excellent spatial uniformity. Larger format MCPs of these configurations (i.e. 75 mm diameter plates) will be tested in the near future and compared to the performance of the 75 mm diameter curved-channel plates which have also not yet been tested in an imaging MAMA system.
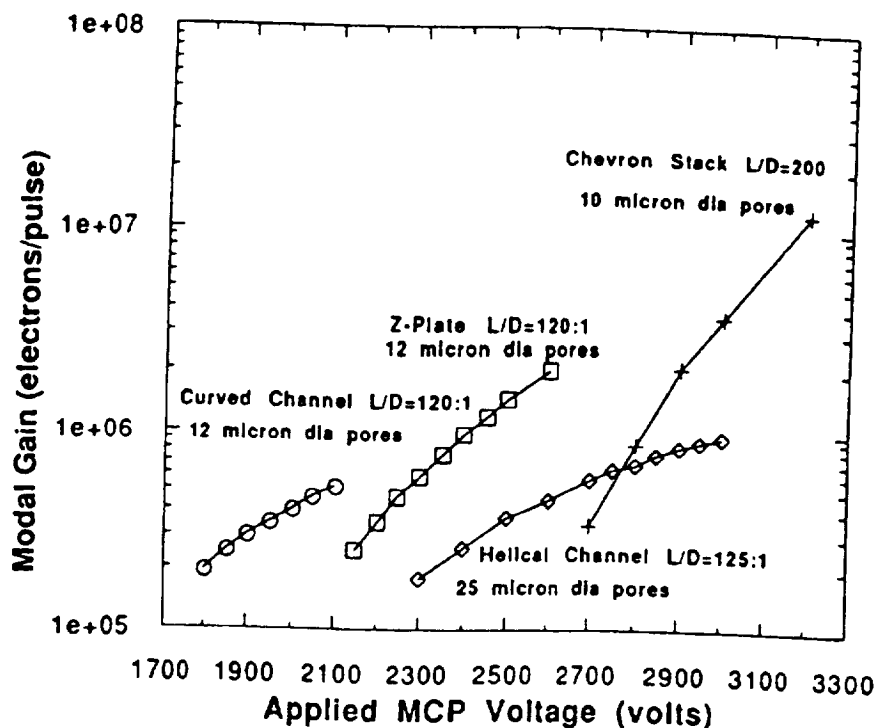
Figure 13. Modal gain versus applied MCP voltage for the curved-channel (circles), "Z-plate" (squares), helical-channel (diamonds), and "chevron" (crosses) MCPs.

In addition to measuring the gain and dark count characteristics of the above MCPs, we are also conducting measurements to determine the maximum count rate an MCP can sustain before it begins to saturate. The channels of an MCP require a certain finite amount of time, called the dead time, to recharge after passage of an output pulse. The dead time, τ_d, is a function of both the channel resistance and the channel capacitance[7]. Typically, the dead time is on the order of a few milliseconds to tens of milliseconds. Therefore, as the input count rate per channel approaches $1/\tau_d$, the channel output gain begins to drop. Not only does the modal gain drop, but the shape of the pulse-height distribution changes as well. Figure 14 shows the PHD of a curved-channel MCP with a channel resistance of $4 \times 10^{13}\Omega$. At an input count rate of 0.3 counts sec^{-1} channel^{-1} the PHD has a modal gain of 3.9×10^5 electrons pulse^{-1} and a PHD resolution of 37%. At 24 counts sec^{-1} channel^{-1} the modal gain has dropped 10% to a value of 3.5×10^5 electrons pulse^{-1}, and the PHD resolution has increased to 57%. At 42 counts sec^{-1} channel^{-1} the modal gain has dropped 25% to a value of 3×10^5 electrons pulse^{-1}, and the PHD resolution has risen to 115%. As the count rate further increases, the pulse-height distribution eventually becomes negative exponential in shape as the amount of output charge is no longer enough to cause space-charge saturation. It is also evident from the figure that the relative number of counts at the peak in the distribution decreases with increasing input count rate. In addition, the relative number of counts at low gain values below the peak and at high gain values above the peak increase with input count rate. The relative number of low gain counts increases because the output end of the channels are no longer able to contribute electrons to the pulse cloud and therefore a larger majority of the pulses are of lower gain. The high gain tail also increases with input count rate relative to the peak indicating that a greater percentage of output counts are due to ion-feedback at the higher count rates. The higher count rates are effectively causing additional scrubbing of the channels which desorbs additional contaminants from the channel walls.
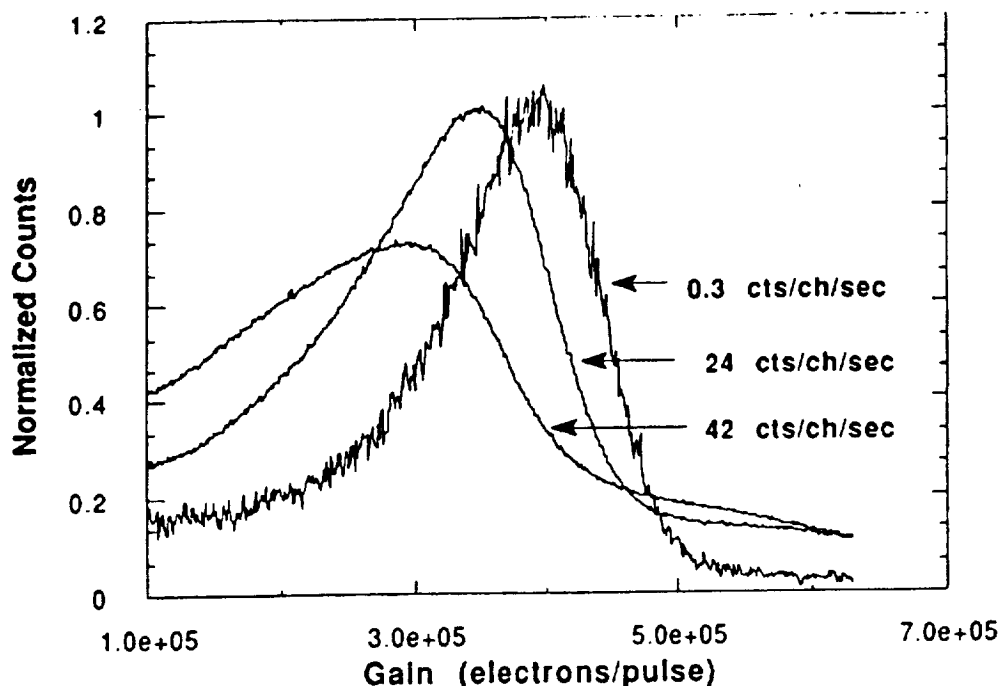
Figure 14. Pulse-height distributions at different input count rates per channel for a curved-channel MCP.

The effective drop in the output gain of the MCP at increased input count rates will cause a corresponding drop in the detective quantum efficiency (DQE) of the MAMA imaging detector system. The amount of DQE loss is both related to how the pulse-height distribution function changes with input count rate and at what level the electronic discriminator threshold is set. The highest input count rates measured for curved-channel MCPs show a drop in the modal gain of 10% at count rates of 30 to 50 counts sec^{-1} channel^{-1}. This corresponds to a 10% drop in DQE at an input count rate of 30 to 50 counts sec^{-1} channel^{-1} with a threshold set in the MAMA electronics at a value that is half the effective unsaturated modal gain of the MCP per anode. For imaging MAMA detector arrays with 25 μm square pixels, the 10% loss in DQE occurs at input count rates of 120 to 200 counts sec^{-1} pixel^{-1}. These results have been measured with an imaging MAMA detector array by Vic Argabright at Ball Aerospace Systems Division.

6. FUTURE TASKS

The principal task at this time is the testing of the 75 mm diameter format MCPs which will be utilized in the STIS (2048 x 2048) - pixel MAMA system. We have received two 75 mm curved-channel MCPs from Galileo Electro-Optics Corporation and two sets of 75 mm "chevron" MCPs from Amperex Inc. These plates will first be tested in a 1 x 100 anode MAMA tube to evaluate gain characteristics, dark noise, and dynamic range. They will then be further evaluated for imaging performance in a demountable (2048 x 2048) - pixel fine-fine MAMA imaging array. We plan to start testing these MCPs when the first 75-mm-format tube is available in March 1990.

In addition to the large 75-mm-format MCPs, we will also continue to evaluate 25-mm-format curved-channel MCPs required for the SOHO program. In particular, we will be testing the imaging quality of these plates using the (360 x 1024) - pixel fine-fine SOHO MAMA detector breadboard system that is scheduled for delivery to Stanford in March 1990.

We will also continue to evaluate the helical-channel MCPs. To date we have not yet conducted imaging tests with these plates, but we now have one installed in a (224 x 960) - pixel fine-fine MAMA tube that we will begin testing in

March, 1990. At this time the helical-channel MCPs are being successfully constructed with 25 μm diameter channels and with open-area-ratios of 45%. The goal is to construct such an MCP with 10 to 12 μm diameter channels with an OAR approaching 60%. Further work to reach this goal is currently underway at Detector Technology in collaboration with our group at Stanford University.

Work continues to miniaturize the charge amplifier/discriminator circuitry and the logic decode circuitry with custom built integrated circuits. The first engineering units of the chips will be available for test in July 1990.

7. ACKNOWLEDGEMENTS

8. REFERENCES

1. Timothy J.G., J.S. Morgan, D.C. Slater, D.B. Kasle, R.L. Bybee and H.E. Culver, "MAMA Detector Systems: A Status Report," *SPIE Vol. 1158*, pp. 104-117, 1989.

2. Timothy J.G. and J.S. Morgan, "Imaging by time-tagging photons with the Multianode Microchannel Array detector systems," *Instrumentation in Astronomy VI, SPIE Vol. 627*, pp. 654-659, 1986.

3. Morgan J.S., J.G. Timothy, A.M. Smith, B. Hill, and D.B. Kasle, "High time-resolution imaging with the MAMA detector systems," to appear in *SPIE Instrumentation in Astronomy VII*, 1990.

4. Timothy J.G., "Electronic readout systems for microchannel plates," *IEEE Transactions on Nuclear Science, NS-32*, pp. 427-432, 1985.

5. Morgan J.S., D.C. Slater, J.G. Timothy, and E.B. Jenkins, "Centroid position measurements and subpixel sensitivity variations with the MAMA detector," *Applied Optics, 28*, pp. 1178-1192, 1989.

6. Laprade B.N. and S.T. Reinhart, "The Ultra Small Pore Microchannel Plate," *SPIE Vol. 1072*, pp. 119-129, 1989.

7. Wiza J.L., "Microchannel Plate Detectors," *Nuclear Instruments and Methods, 162*, pp. 587-601, 1979.

8. Slater D.C., J.G. Timothy, P.W. Graves, T.J. Loretz, and R.L. Roy, "Performance characteristics of a new helical-channel microchannel plate," *SPIE Vol. 932*, pp. 124-131, 1988.

9. Fraser G.W., J.F.Pearson, and J.E. Lees, "Dark Noise In Microchannel Plate X-Ray Detectors," *Nuclear Instruments and Methods in Physics Research, A254*, pp. 447-462, 1987.

Imaging pulse-counting detector systems for space ultraviolet astrophysics missions

J. Gethyn Timothy

Center for Space Science and Astrophysics
Stanford University, ERL 314
Stanford, California 94305-4055

ABSTRACT

A family of imaging, pulse-counting, photoelectric detector systems, the Multi-Anode Microchannel Arrays (MAMAs), are now under active development for use on a number of space ultraviolet astrophysics missions at far-ultraviolet (FUV) and extreme-ultraviolet (EUV) wavelengths between about 300 and 28 nm. Specifically, MAMA detectors are being fabricated and tested for use in two instruments on the ESA/NASA Solar and Heliospheric Observatory (SOHO) mission, for the NASA Goddard Space Flight Center's *Hubble* Space Telescope Imaging Spectrograph (STIS), and for the prime FUV spectrograph of the Far Ultraviolet Spectroscopic Explorer FUSE/*Lyman* mission. The construction and performance characteristics of the different MAMA detector systems are described, and techniques for improving the spatial resolution of each of the detector systems by the use of custom Application-Specific Integrated Circuits (ASICs) in the electronics are discussed.

1. INTRODUCTION

A family of imaging, pulse-counting, photoelectric detector systems, the Multi-Anode Microchannel Arrays (MAMAs), are now under active development for use on a number of space ultraviolet astrophysics missions at far-ultraviolet (FUV) and extreme-ultraviolet (EUV) wavelengths between about 300 and 28 nm. Open, open with openable cover, and sealed (360 x 1024)-pixel MAMA detector systems, with pixel dimensions of 25 x 25 microns^2 and MgF$_2$, KBr, and CsI photocathodes, are now under construction for use in the Solar Ultraviolet Measurements of Emitted Radiation (SUMER)[1] and the Ultraviolet Coronagraph Spectrometer (UVCS)[2] instruments on the ESA/NASA Solar and Heliospheric Observatory (SOHO) mission.[3] Very-large-format (2048 x 2048)-pixel MAMA detector systems, with pixel dimensions of 25 x 25 microns^2 and CsI and Cs$_2$Te photocathodes, are currently under test for the NASA Goddard Space Flight Center's *Hubble* Space Telescope Imaging Spectrograph (STIS).[4] Proof-of-concept sealed and open (224 x 960)-pixel MAMA detector systems, with pixel dimensions of 14 x 14 microns^2, are also under test as part of the Far Ultraviolet Spectroscopic Explorer (FUSE)/*Lyman* Phase B study.[5] An open (728 x 2024)-pixel MAMA detector system with 22 x 16 microns^2 pixels, which is one quadrant of the proposed (728 x 8096)-pixel MAMA detector for the FUSE/*Lyman* prime spectrograph, will be fabricated and tested in 1991 as part of the continuing Phase B study. Finally, an open (728 x 2808)-

pixel MAMA detector system, with pixel dimensions of 14 x 14 microns^2, will be fabricated in 1991 for use in our sounding rocket High-Resolution EUV Spectroheliometer (HiRES).[6] An overview of the status of the development program and descriptions of the different MAMA detector systems are given in the following sections of this paper.
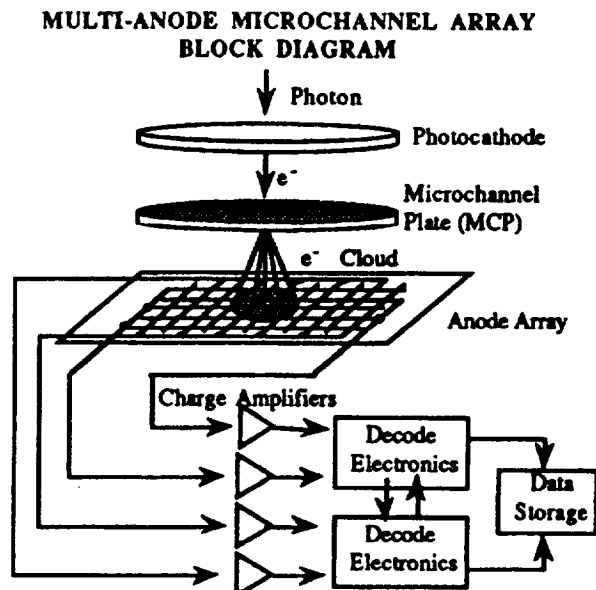
**MULTI-ANODE MICROCHANNEL ARRAY
BLOCK DIAGRAM**

Fig. 1. Schematic of the imaging MAMA detector system.

MULTI-ANODE MICROCHANNEL ARRAY

four-fold coincidence-anode array
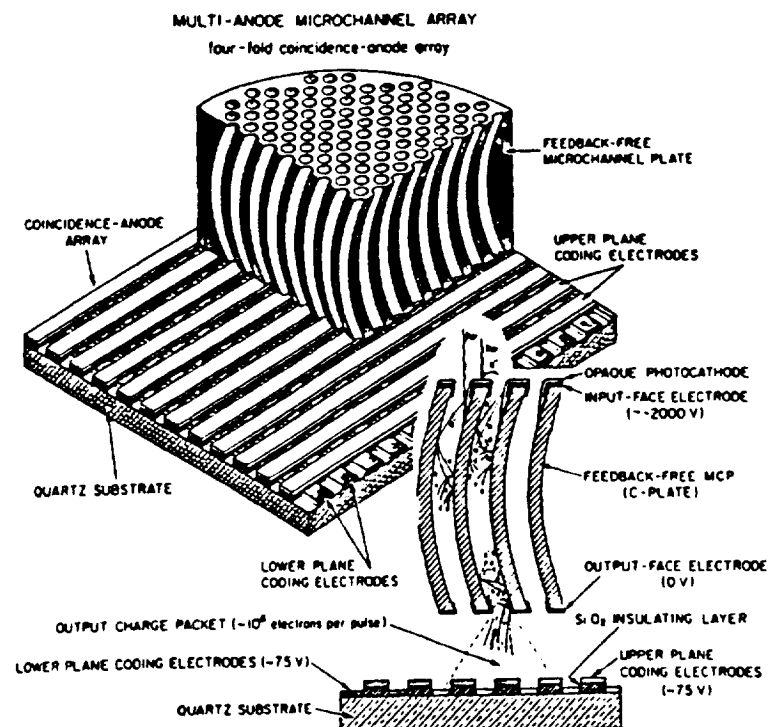
Fig. 2. Schematic showing details of the curved-channel MCP and the imaging multi-layer anode array used in the MAMA detector tubes.

2. MAMA DETECTOR SYSTEMS

The construction and mode-of-operation of the MAMA detector system has recently been described in some detail in the literature.[7] The components of a MAMA detector consist of the tube assembly, which can be sealed with a window or used in the open-structure configuration, containing a single, high-gain, curved-channel microchannel plate (MCP) electron multiplier with the photocathode material deposited on, or mounted in proximity focus with the front surface. To detect and measure the positions of the electron clouds generated by single photon events, the MAMA detector employs two layers of precision electrodes which are mounted in proximity focus with the output surface of the MCP (see Figs. 1 and 2).

Digital logic circuits respond to the simultaneous arrivals of signals from several of these electrodes in each axis, which are arranged in groups to uniquely identify a x b pixels in one dimension with only a + b amplifier and discriminator circuits. For example, a total of 32 x 32, i.e. 1024, pixels in one dimension can be uniquely identified with 32 + 32, i.e. 64, amplifier and discriminator circuits. In the imaging MAMA detector tube, the arrays are

mounted in tandem with orthogonal orientations, so that positions can be sensed in two dimensions. In this configuration (a x b)^2 pixels can be uniquely identified with only 2 x (a + b) amplifier circuits. The (1024 x 1024)-pixel array thus requires a total of only 128 amplifier and discriminator circuits. The two layers of anode electrodes in the imaging arrays are insulated from each other by a SiO_2 dielectric layer. This dielectric between the upper layer electrodes is etched away to allow the low energy (~30 eV) electrons in the charge cloud from the MCP to be collected simultaneously on both arrays.

The arrangements of the electrodes in one axis of the original "coarse-fine" configuration array and in one axis of the latest "fine-fine" configuration array are shown in Fig. 3. The "fine-fine" configuration provides a structure in which the electrodes are capacitively balanced and inductively decoupled in order to maximize the uniformity of the flat-field response.

In addition, as shown in Fig. 3, the "fine-fine" configuration permits the location of large charge clouds from MCP "chevron" or "Z-plate" stacks to be encoded without ambiguity.[8] The electronic decode circuits designed at Stanford University and fabricated by LSI
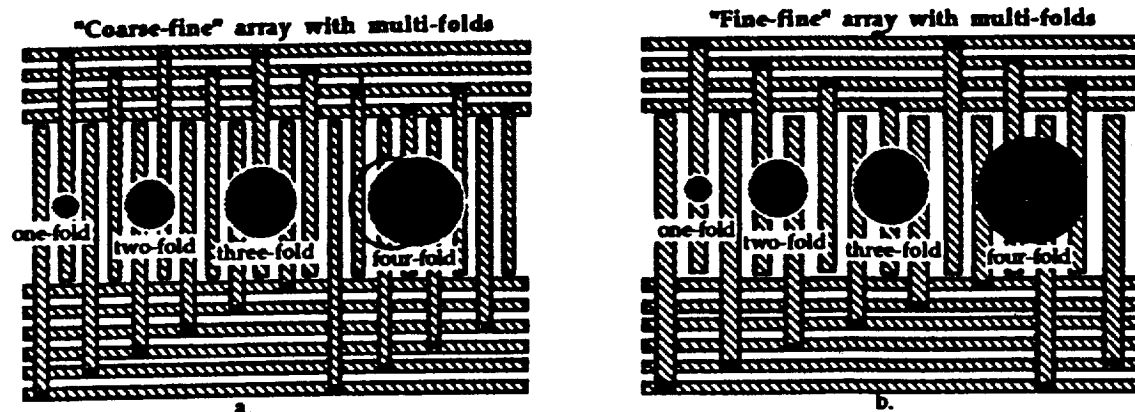
Fig. 3. Configurations of MAMA "coarse-fine" and "fine-fine" anode arrays.

a. "Coarse-fine" configuration. A positional ambiguity is introduced when the charge cloud is collected on four or more electrodes in one axis of the array.

b. "Fine-fine" configuration. Position encoding is unique, even when the charge cloud is collected on four or more electrodes in one axis of the array.

Logic Inc., San Jose, CA, have been configured to accept up to six simultaneous events in each axis.[9] The digital data from the MAMA detector system are either integrated in a Random Access Memory (RAM) or, for high-time-resolution studies, the x-y coordinates and the arrival time of each detected photon are stored on a recording medium such as magnetic tape. The current MAMA time-tag data system has an absolute accuracy of 10 μs.[10]

3. FLIGHT MAMA DETECTOR SYSTEMS

The key parameters of the MAMA detectors for SOHO, STIS and FUSE/*Lyman* are listed in Table 1.

The SOHO format of 360 x 1024 pixels (see Fig. 4) is designed for use in the SUMER and UVCS imaging spectrometers. Spatial information along the length of the spectrometer entrance slit is recorded in the 360-pixel direction while, simultaneously, spectral information is recorded along the 1024-pixel direction. The pixel dimensions are 25 x 25 microns[2]. The SOHO array mounted in the 25-mm-format demountable breadboard detector tube is shown in Fig. 5. The STIS (2048 x 2048)-pixel array is designed for multi-mode operation, specifically, echelle spectroscopy, long-slit spectroscopy, slitless spectroscopy, photon time-tagging and direct imaging. The array is fabricated from four contiguous

TABLE 1

Key Parameters of the MAMA Detectors for SOHO, STIS, and FUSE/*Lyman*

	SOHO	STIS	FUSE
Pixel Format:	360 x 1024	2048 x 2048 [4 x 1024 x 1024]	728 x 8096 [4 x 728 x 2024]
Pixel Dimensions:	25 x 25 μm²	25 x 25 μm²	22 x 16 μm²
Anode Array Active Area:	9.0 x 25.6 mm²	51.2 x 51.2 mm²	16.0 x 32.4 mm² (x 4)
MCP Active Area:	10 x 27 mm²	52 x 52 mm²	17 x 33 mm² (x 4)
MCP Pore Size:	10 microns	10 microns	8 microns
Number of Amplifiers: (including analog output)	105 (104+1)	529 ([4 x 32] + 1)	577 ([4 x 144] + 1)
Photocathode Material:	CsI, KBr & MgF₂	CsI and Cs₂Te	KBr
Hybrid Amplifier and Discriminator:	Yes	Yes	Yes
Gate Array Decode Circuits	Yes	Yes	Yes
Openable Cover:	Yes	No	Yes
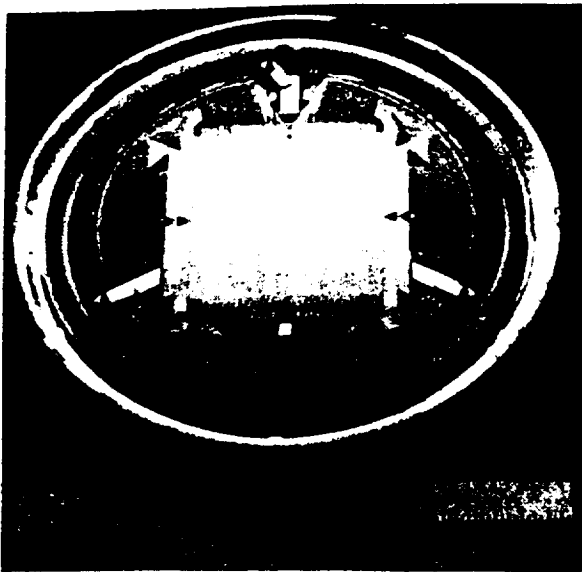
Fig. 7. STIS MAMA "fine-fine" (2048 x 2048)-pixel array with 25 x 25 microns^2 pixels. The array is constructed from four contiguous (1024 x 1024)-pixel arrays with a 3-pixel dead space.

Two versions of the STIS array have been fabricated. A (1024 x 1024)-pixel array, i.e. one quadrant of the full array, has been fabricated in a 40-mm-format tube, as shown in Fig. 6, and is now under test in both the demountable ultraviolet and the sealed visible-light detector tubes.

The first units of the complete STIS (2048 x 2048)-pixel array (see Fig. 7) have been completed in the dedicated anode array fabrication facility at Ball Electro-optics and Cryogenics Division (BECD), Boulder, CO, and fabrication of the first 75-mm-format evaluation tube is nearing completion. A 75-mm-format demountable tube with a (1 x 100)-pixel discrete-anode evaluation array has been completed and tests of the first 75-mm-format high-gain MCP's are about to start. The 25-mm-, 40-mm-, and 75-mm-format demountable MAMA detector tubes are shown in Fig. 8. The multi-layer ceramic headers in the 25-mm- and 40-mm-format tubes each contain a total of 170 electrical feedthroughs, while the 75-mm-format tube has a total of 640 electrical feedthroughs, plus additional high-voltage feedthroughs.

As part of the FUSE/Lyman Phase A study, an array with a format of 224 x 960 pixels and pixel dimensions of 14 x 14 microns^2 (see Fig. 9) was fabricated and tested in both demountable ultraviolet and sealed visible-light detector tubes. The high-gain MCP used with this array is a C-plate MCP fabricated by Galileo Electro-Optics Corp., Sturbridge, MA with a channel diameter of 8 microns.
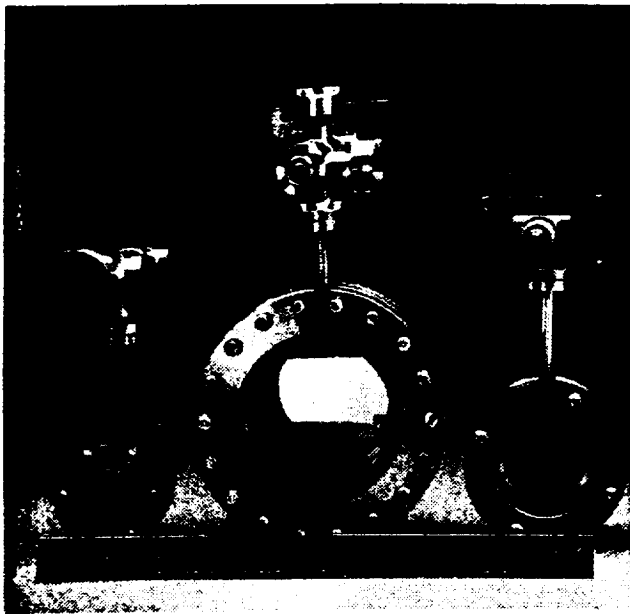
a.
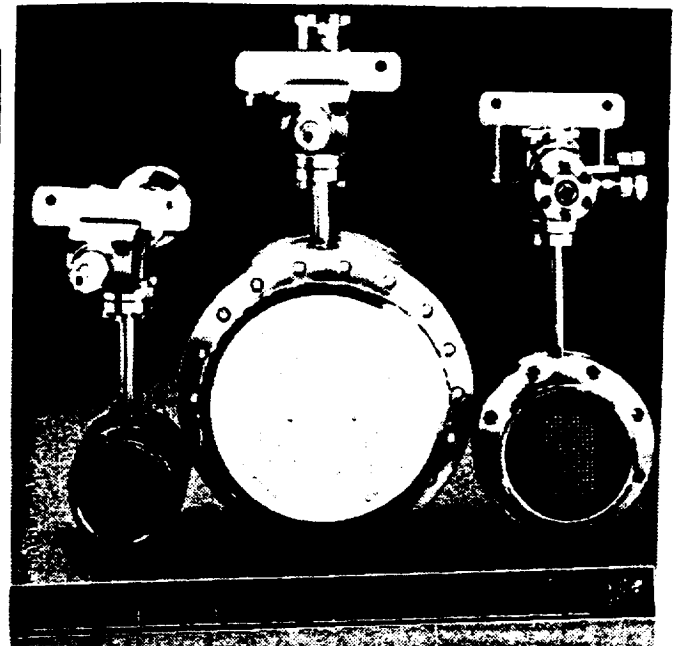
b.

Fig. 8. Demountable MAMA detector tubes. From left to right: 25-mm-format, 75-mm-format, and 40-mm-format tubes.

a. Front view.

b. Rear view showing electrical feedthroughs in the multi-layer ceramic headers.
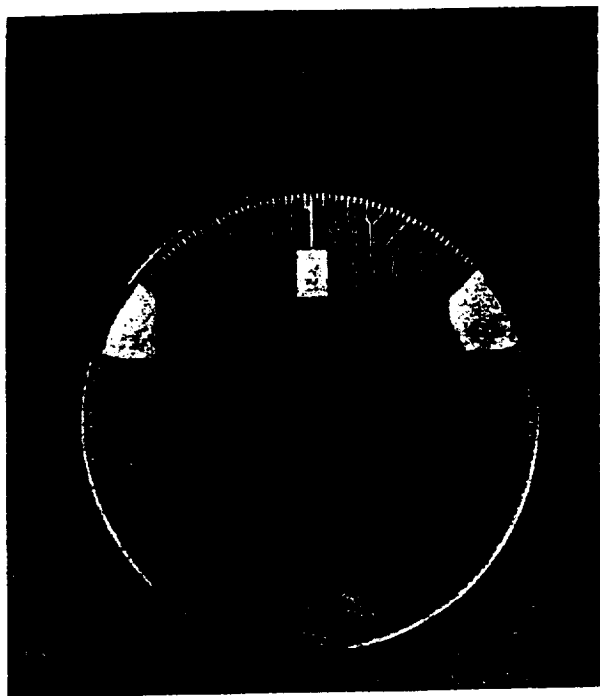
Fig. 4. SOHO MAMA "fine-fine" array with a format of 360 x 1024 pixels and pixel dimensions of 25 x 25 microns^2.

Fig. 6. STIS MAMA "fine-fine" (1024 x 1024)-pixel array with 25 x 25 microns^2 pixels.

(1024 x 1024)-pixel arrays with a 3-pixel dead space. This configuration provides redundancy; total electronics failure in one quadrant will not affect the performance of the remaining three quadrants. In addition, the total array count rate is increased, each quadrant can deliver ~2 x 10^6 counts s^{-1} with a loss of detective quantum efficiency (DQE) of less than 30%.
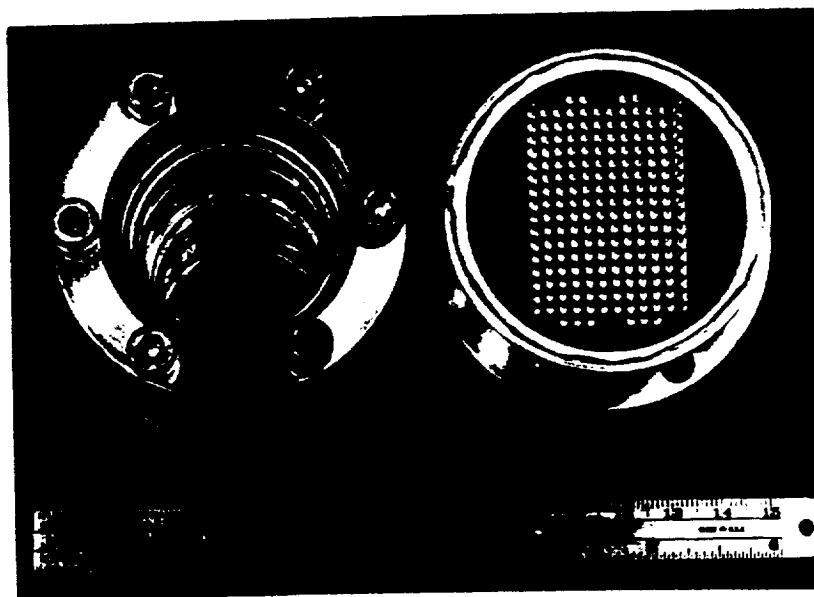
Fig. 5. SOHO MAMA breadboard demountable detector tube.
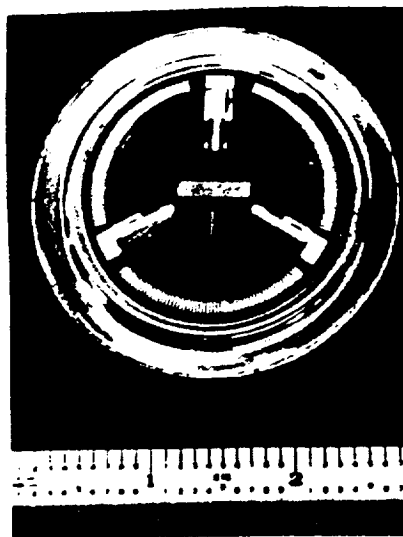
Fig. 9. FUSE/*Lyman* Phase A "fine-fine" evaluation array with a format of 224 x 960 pixels and pixel dimensions of 14 x 14 microns^2.

The proposed FUSE/*Lyman* prime FUV spectrograph detector will have a format of 728 x 8096 pixels and pixel dimensions of 22 x 16 microns^2. Spatial information will be obtained along the entrance slit of the spectrometer in the 728-pixel direction and, simultaneously, spectral information will be obtained along the Rowland circle of the spectrometer in the 8096-pixel direction. The array will be fabricated from four contiguous (728 x 2024)-pixel arrays each with an independent MCP for maximum reliability on the long-duration space mission (see Fig. 10).

Detailed design and fabrication of one quadrant of this array will be started later this year as part of the FUSE/*Lyman* Phase B program.

The last array that is currently being designed and fabricated is the (728 x 2808)-pixel array with 14 x 14 microns^2 pixels for the high-resolution stigmatic EUV spectroheliometer on the HiRES sounding rocket payload. This array will be used for very-high spatial, spectral and temporal resolution studies of the solar outer atmosphere.

REPELLER PLATE STUD
6 PL

0-80 x .12 SHCS
30 PL

MCP STUD (H.V.)
12 PL

REPELLER PLATE
(TOP HALF SHOWN)

ARRAY POS. WEDGE
4 PL

MCP
4 PL

728 x 2024 ARRAY
4 PL

CERAMIC HEADER ASSY

DOOR ATTACH FLANGE

ARRAY STUD SCREW (GND.) 12 PL

BOND PAD .009 X .150 .015 C.-C.
876 PL

MCP POS. FRAME 4PL

MCP ACTIVE AREA 16 X 32.4 MM
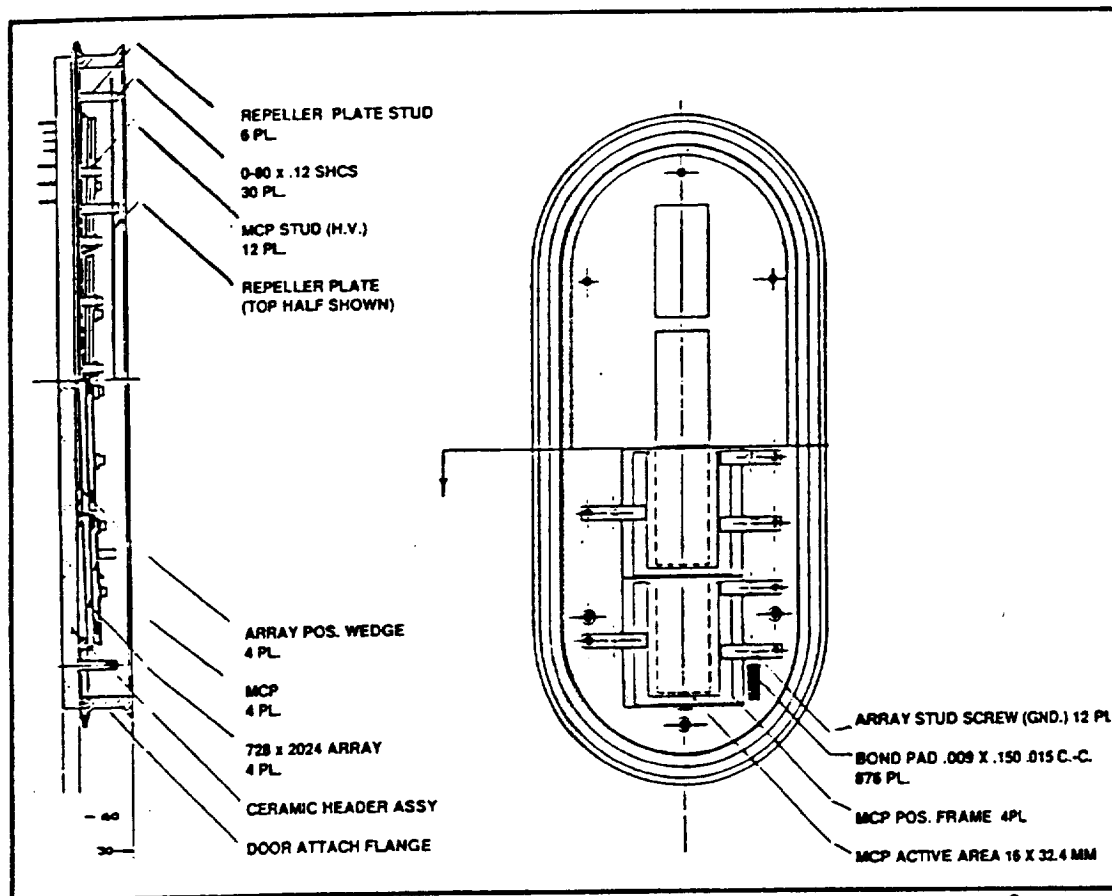
Fig. 10. Proposed configuration of the (728 x 8096)-pixel MAMA detector with 22 x 16 microns^2 pixels for the FUSE/*Lyman* prime FUV spectrometer. The array consists of four contiguous (728 x 2024)-pixel arrays, each with an independent MCP.

4. SUMMARY OF DEVELOPMENT PROGRAM STATUS

As a result of the impetus of the SOHO, STIS and FUSE/*Lyman* flight programs, a number of key development milestones have been achieved:

1. Units of all of the readout array formats have been fabricated free of defects and with a high yield in the dedicated facility at BECD.

2. The development of the "fine-fine" anode array geometry permits the MAMA to utilize any of the high-gain MCP configurations currently available, including "chevron" and "Z-stack" MCPs.

3. The use of MCPs with channel diameters significantly smaller than the pixel dimensions eliminates Moiré patterns in the flat field response of the MAMA.

4. The custom gate-array decode ASIC chip (see Fig. 11) has recently been used for imaging tests with a demonstrated pulse-pair resolution of better than 160 ns. The ASIC is significantly more compact than the discrete component decode circuits and requires a total power of only 0.5 W, as opposed to the discrete decoder power of 2.3 W.

5. The SOHO breadboard detector systems have demonstrated a single pixel count rate (25 x 25 microns^2 pixels) of >400 counts pixel^{-1} s^{-1} with a 10% loss of DQE (see Fig. 12) and the theoretical fall off of DQE of 30% at 9 x 10^5 counts s^{-1} (random) total array count rate with a system pulse-pair resolution of 350 ns (Fig. 13).

6. Both the 25 micron-pixel and 14-micron-pixel arrays have demonstrated their theoretical spatial resolutions.

7. A first-generation MAMA detector with the "coarse-fine" anode geometry has demonstrated a position sensitivity of better than 0.04 pixels (<1 micron).[11] Significantly better performance (limited only by the signal-to-noise ratio) is expected for the arrays with the "fine-fine" anode geometry.

8. Quantum efficiencies of better than 32% have so far been achieved at FUV wavelengths near 1200 Å with both CsI and KBr photocathodes. Photocathode optimization is still in progress.

9. The first units of the Tektronix amplifier/discriminator ASIC have been fabricated and are now under test at
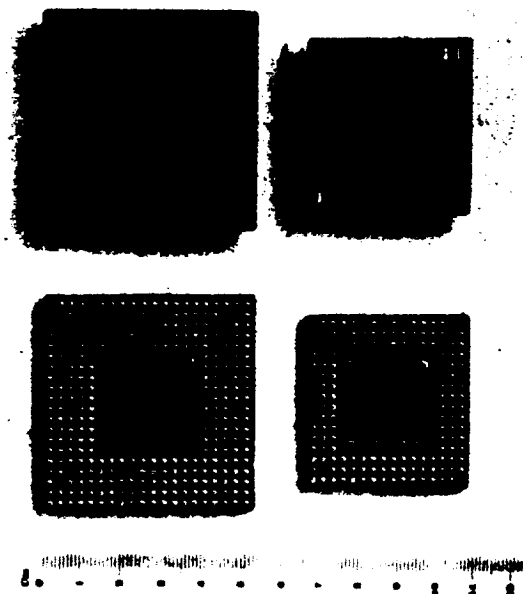
Fig. 11. Custom MAMA gate-array decode ASIC.
Left: 299-pin laboratory evaluation chip.
Right: 155-pin flight chip.

BECD. All indications are that the design characteristics of speed and power will be met.

10. The 256 x 1024-pixel "coarse-fine" FUV MAMA detector flown on the NASA Goddard Astronomy Sounding Rocket payload (ASRP), successfully recorded an image of the galaxy NGC 6240, probably the faintest extended ultraviolet image recorded prior to HST observations. The time-tag imaging capability of the MAMA was successfully used to correct for drifts in the sounding rocket attitude control system.[10] A second successful flight recorded an image of the galaxy NGC 4449 on 22 March 1991.

11. We have successfully operated a curved-channel MCP with a curved front face and a planar output face.[12] Imaging tests of this MCP in a MAMA detector tube are now in progress.

12. The MAMA position-encoding scheme intrinsically provides spatial information at a higher resolution than the nominal "pixel".[13] Initial laboratory tests have shown that the 25-micron-pixel detectors can provide a spatial resolution of 12.5 microns and the 14-micron-pixel detectors can provide a spatial resolution of 7
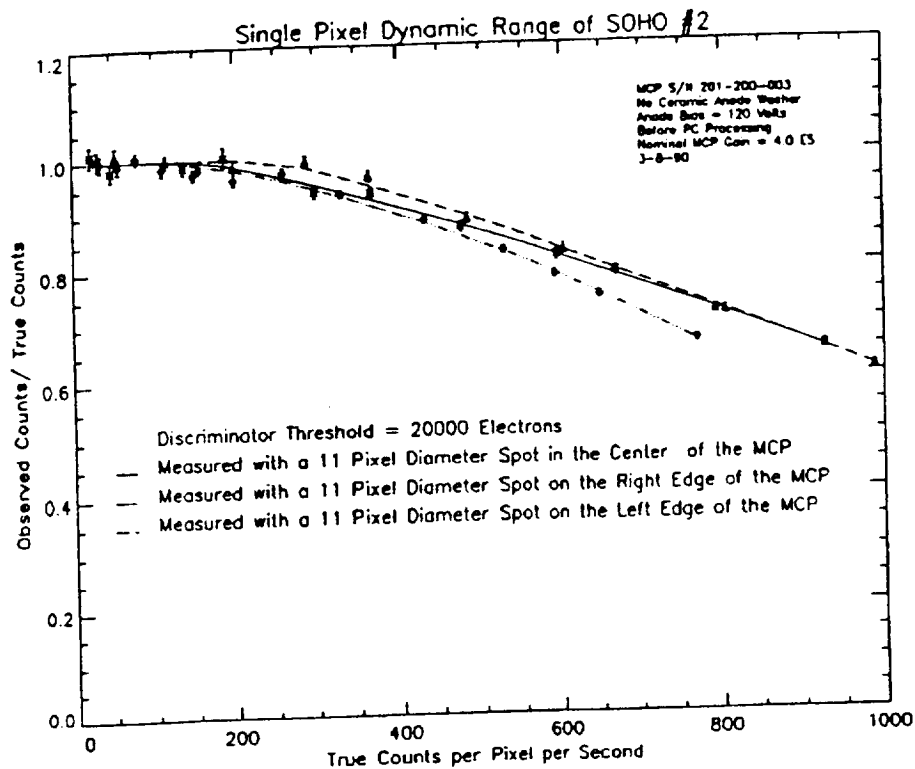
Fig. 12. Variation of DQE of SOHO breadboard detector system as a function of single pixel count rate.
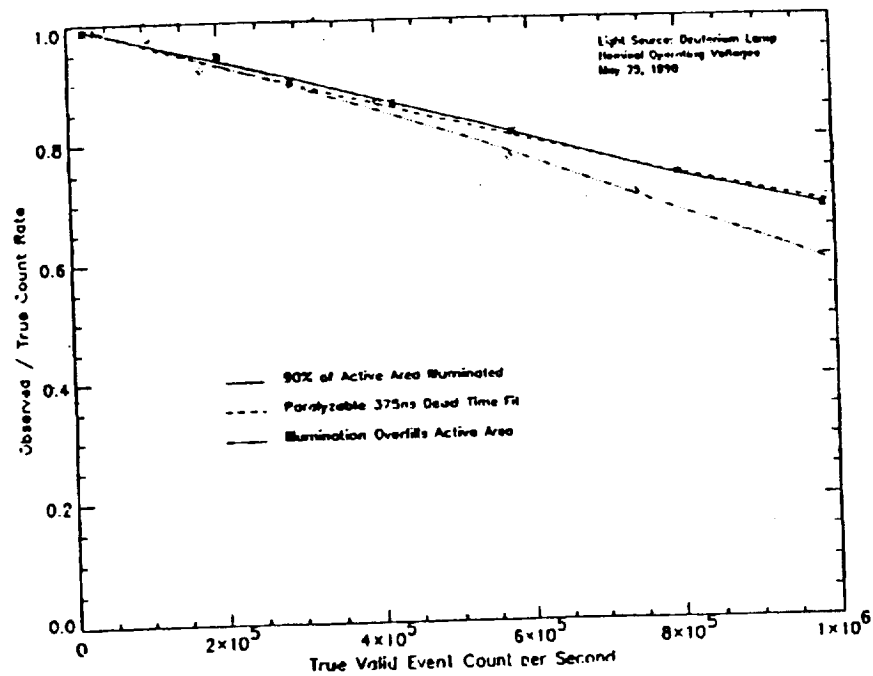
Fig. 13 Variation of DQE of SOHO MAMA breadboard detector system as a function of total array count rate (system pulse-pair resolution 350 ns).

microns, provided that an MCP with appropriate channel dimensions is utilized.

13. A custom imaging MAMA detector tube has been fabricated and is now being used for the evaluation of two-stage MCP structures.

14. The first SOHO flight-configuration engineering model MAMA detector system is in fabrication and will be delivered from BECD in July of this year.

In summary, at this time the MAMA anode array fabrication is a proven technology and the development of the advanced analog and digital electronics circuits is essentially complete. Further significant improvements in the MAMA performance characteristics are possible with the current technology through improvements to the high-gain MCP structures and the MCP/photocathode interface. These will be pursued with NASA support over the next two years.

5. ACKNOWLEDGEMENTS

6. REFERENCES

1. K. Wilhelm and the SUMER Investigation Team, "SUMER - Solar Ultraviolet Measurements of Emitted Radiation", European Space Agency *SP-1104*, pp. 31-37, November 1988.

2. J. Kohl and the UVCS Investigation Team, "UVCS - An Ultraviolet Coronagraph Spectrometer for SOHO", European Space Agency *SP-1104*, pp. 49-54, November 1988.

3. V. Domingo and A. I. Poland, "SOHO - An Observatory to Study the Solar Interior and the Solar Atmosphere", European Space Agency *SP-1104*, pp. 7-12, November 1988.

4. B. E. Woodgate and the Space Telescope Imaging Spectrograph Science Team, "Second Generation Spectrograph for the *Hubble* Space Telescope", *SPIE vol. 627 Instrumentation in Astronomy VI*, pp. 350-362, 1986.

5. "*Lyman* - The Far Ultraviolet Spectroscopic Explorer", NASA Phase A Study Final Report *NAS5-30339*, July 1989.

6. "HiRES - A High-Resolution Stigmatic EUV Spectroheliometer", J.G. Timothy and the HiRES Science Team, *SPIE vol. 1343 X-Ray/EUV Optics for Astronomy*, pp. 350-358, 1990.

7. J. G. Timothy, "MAMA Detector Systems: A Status Report", *SPIE vol. 1158 Ultraviolet Technology III*, pp. 104-117, 1989.

8. D. B. Kasle, "Decoding Techniques for "fine-fine" Geometry Multi-Anode Microchannel Arrays", *SPIE vol. 932 Ultraviolet Technology II*, pp. 280-284, 1988.

9. D. B. Kasle and G. DeMicheli, "An Image Decoding ASIC for Space-Based Applications", to appear in *Proceedings of EURO ASIC 91*, IEEE Computer Society Press, 1991.

10. J. S. Morgan, J. G. Timothy, A. M. Smith, B. Hill, and D. B. Kasle, "High-Time-Resolution Imaging with the MAMA Detector Systems", *SPIE vol. 1235 Instrumentation in Astronomy VII*, pp. 347-357, 1990.

11. J. S. Morgan, D. C. Slater, J. G. Timothy and E. B. Jenkins, "Centroid Position Measurements and Sub-pixel Sensitivity Variations with the MAMA Detector", *Applied Optics vol. 28*, pp. 1178-1192, 1989.

12. D.C. Slater, J. S. Morgan and J. G. Timothy, "Performance Characteristics of a Curved-Channel Microchannel Plate with a Curved Input Face and a Plane Output Face", *SPIE vol. 1158 Ultraviolet Technology III*, pp. 118-126, 1989.

13. D. B. Kasle, "High-resolution Decoding Techniques and Single-chip Decoders for Multi-anode Microchannel Arrays", *SPIE vol. 1158 Ultraviolet Technology III*, pp. 311-318, 1989.

High-dynamic-range MCP structures

David C. Slater and J. Gethyn Timothy

Center for Space Science and Astrophysics
Stanford University, HEPL 172
Stanford, CA 94305-4055, USA

ABSTRACT

We report on the development of a new high-dynamic-range two-stage Multi-Anode Microchannel Array (MAMA) imaging tube designed for improved high count rate performance at FUV and EUV wavelengths. The new two-stage MAMA tube employs two 25-mm-diameter format MCPs placed in tandem with a small gap between the plates. The front (input) MCP is designed to be a low-gain converter plate that supports an opaque photocathode and converts the detected photons to electrons, while the second (output) MCP is of higher conductivity and thus maintains the overall gain of the multiplier at high count rates. The second MCP is mounted in proximity focus with a (224 x 960) - pixel fine-fine coincidence MAMA array for high-spatial-resolution imaging studies. The applied voltage across each MCP can be controlled independently. We report on the gain and dynamic range performance characteristics of the two-stage MAMA tube in two different configurations: first, with the output MCP having moderate conductivity (~100 MΩ); and second, with the output MCP having very high conductivity (~2 MΩ). These results are compared and contrasted with those of the more conventional MAMA tube configuration which employs a single high-gain curved-channel MCP.

1. INTRODUCTION

1.1 The MAMA Detector

The Multi-Anode Microchannel Array (MAMA) detector systems are state-of-the-art photon counting imaging detectors currently under development in the laboratory for use in a number of space astrophysics missions.[1-5] MAMA detectors are designed to provide high spatial and temporal resolution for applications in low-light-level imaging and spectroscopy in the visible (4000 – 7000 Å), ultraviolet (2000 – 4000 Å), far ultraviolet (FUV) (1000 – 2000 Å) and extreme ultraviolet (EUV) (100 – 1000 Å) wavelengths. Large-format versions of these devices (2048 x 2048 pixels) are currently under development as the prime detectors for the *Hubble* Space Telescope Imaging Spectrograph (STIS).[6] High-spatial-resolution versions of the detectors have also been baselined for the prime spectrograph on board the Far Ultraviolet Spectroscopic Explorer (FUSE)/*Lyman*.[7] In addition to these astronomy missions, (360 x 1024) - pixel MAMA detectors have been selected for use in several instruments on board the European Space Agency (ESA)/NASA Solar and Heliospheric Observatory (SOHO) mission[8] and in the Ultra-high-resolution XUV Spectroheliograph (UHRXS) to be built for the Space Station *Freedom*. Furthermore, a sounding rocket High-Resolution EUV Spectroheliometer (HiRES), designed to obtain very high spatial, spectral and temporal resolution images of the outer solar atmosphere, is slated to employ a (728 x 2808)-pixel MAMA imaging detector system.[9]

A schematic block diagram showing the principal components of the MAMA imaging detector system is shown in Figure 1. Individual photons focussed onto the front surface of the detector are first converted to single electrons by the photo-emissive material which makes up the photocathode. The photocathode can either be deposited onto a window in proximity focus with the microchannel plate (MCP) as depicted in Figure 1 (a semi-transparent photocathode), or deposited directly onto the input surface of the MCP (an opaque photocathode). The electrons that are emitted by the photocathode impinge on the input surface of a single high-gain curved-channel (C²) MCP.[10] The MCP is a semiconducting glass plate composed of millions of tiny hollow pores or channels with diameters of 10 to 12 μm and center-to-center spacings of 15 μm. These channels provide the necessary amplification to allow for the detection of single photon events by the electronics. The MCP accomplishes this amplification through the process of secondary electron emission within each of the channels. Each electron that enters a channel at the input stimulates the creation of an output pulse of 10^5 to 10^6 electrons.[5] The channels are curved to limit ion-feedback.

PHOTON

PHOTOCATHODE

e⁻

MICROCHANNEL PLATE (MCP)

e⁻ CLOUD

ANODE ARRAY

DECODE ELECTRONICS

MEMORY

DECODE ELECTRONICS

CHARGE AMPLIFIERS
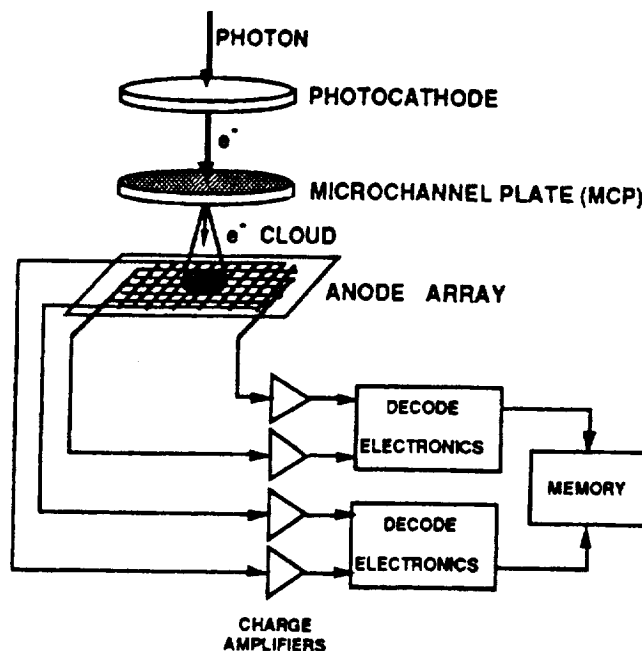
Figure 1. Schematic block diagram of the imaging MAMA detector system. [Courtesy of D. B. Kasle].

In proximity focus with the output of the MCP is a two-dimensional array of anodes that intercept each of the output pulses, and which generate current pulses that are fed to amplification and decoding circuitry. The decoding circuitry computes the (x, y) position, or pixel location, of each detected event and increments the unique address for the given location in memory by one count.

1.2 Dynamic Range Limitations of the MAMA Detector

The dynamic range of a photon detector is defined to be the ratio of the maximum to minimum detectable light intensity levels over which the output of the detector remains linear with input. The maximum detectable light intensity is typically defined to be that which causes a deviation in output linearity by more than 10%. This level can either be defined in terms of the light flux at a given wavelength (for a given photocathode), or in terms of the input count rate to the MCP—referred to as the maximum upper level count rate. The minimum detectable light intensity is defined to be the detector dark noise level.

The MAMA system has two sources of dark noise: 1) the inherent dark noise of the MCP resulting from radioactive beta decay, emission points, cosmic rays, etc.[11, 12]; and 2) that due to thermionic emission from the photocathode. Cooling the photocathode can lower the thermionic emission level below the dark noise of the MCP thus making the MCP the limiting noise contributor. Typical dark noise levels of well conditioned MCPs are on the order of 0.1 - 1 counts cm⁻² sec⁻¹.[5, 13]

The maximum upper level count rate of the MAMA system is governed by the MCP for image fields composed of discrete point sources. For small spots imaged onto the array, conventional MCPs composed of channels with resistances > 10^{14} Ω begin to show signs of temporal saturation at input count rates of less than 10^7 counts cm⁻² sec⁻¹, which corresponds to a count rate per MCP channel of < 20 counts channel⁻¹ sec⁻¹.[14] At these count rates there is ~10% loss in the overall detective quantum efficiency (DQE) of the MAMA due to temporal saturation of the MCP. With larger fields of illumination (greater than ~10% of an array composed of 10^6 pixels), the dynamic range is limited, not by the saturation level of the MCP, but by the pulse-pair resolution of the analog amplifier/discriminator electronics and the digital decoding circuitry. The speed of the fastest MAMA electronics allows resolution between two input pulses that are separated by a minimum of ~100 ns. This sets the upper total array count rate for a 30% loss in DQE at ~3.6 x 10^6 counts sec⁻¹ (random). Because the size of the imaged object determines whether the MCP or the electronics limits the dynamic range, one must specify two dynamic ranges — the *pixel* dynamic range for small discrete imaged objects, and the *global* dynamic range for

spatially extended imaged objects. For the MAMA detector, the *pixel* dynamic range is on the order of 10^8, and the *global* dynamic range is on the order of 10^6. In this paper, we shall focus on the pixel dynamic range performance.

Currently, the MAMA detector can easily achieve the dark count rate levels that have been specified for each of the space programs mentioned above using conventional high-gain C^2 MCPs. The maximum count rate capability of the MAMA utilizing conventional MCPs with channel resistances of $\sim 10^{14}$ Ω, however, is well shy of the desired count rate goals for the above mentioned space missions. Most of these missions require an upper level count rate capability at least 5 times the rate currently obtainable with conventional MCP resistances (> 100 counts channel^{-1} sec^{-1}). HiRES is the most stringent, with a desired upper count rate goal nearly 2 orders of magnitude greater than currently achievable.

The upper level count rate capability of the MCP is limited by the finite time it takes to replenish charge that has been extracted from each MCP channel that is stimulated by an input event.[15] The time it takes to recharge a previously stimulated channel is governed by the channel recharge time constant, τ_{ch}, which is, to zeroth order, proportional to the product of the channel resistance, R_{ch}, and capacitance, C_{ch}. A finite τ_{ch} implies a dependance of the output gain of the MCP to the input count rate level. At low input count rates, there is enough time between input events to allow each of the stimulated channels to fully recharge before the next event occurs. At higher count rates, however, the channels have not had enough time to fully recharge before the next event; hence, the output gain from the following events are decreased. The drop in gain with increasing input flux is called *gain sag*.[14]

Since the MCP is normally operated in the high-gain mode, it displays a quasi-Gaussian shaped pulse-height distribution (PHD). The gain value at the peak of this distribution, called the *modal gain*, is a quantity that can be easily measured as a function of the average input count rate per MCP channel, Λ. Monte Carlo simulations of how the PHD changes with Λ were performed to determine how the modal gain varies with Λ, assuming a pure Gaussian PHD at very low count rates ($\Lambda\tau_{ch} \ll 1$). The modal gain, $\bar{g}$, was found to vary with Λ in the following manner[14]:

$$\bar{g} = \frac{\bar{G}_o}{1 + k(R_o)\Lambda\tau_{ch}}$$

(1)

$\bar{G}_o$ is the modal gain measured at very low input count rates ($\Lambda\tau_{ch} \ll 1$); and $k(R_o)$ is a constant that depends on the PHD resolution, R_o, measured again at very low count rates. The PHD resolution is defined to be the full-width-at-half-maximum (FWHM) of the PHD divided by the modal gain, $\bar{G}_o$, and is commonly expressed as a percentage. For values of R_o between 0 and 100%, $k(R_o)$ is a linear function of R_o of the form $k(R_o) \approx 0.011R_o$. The drop in modal gain values as a function of increasing input flux is called *modal gain sag*.

Gain sag measurements made with a variety of single high-gain C^2 MCPs with channel resistances between 10^{12} Ω to 10^{14} Ω show a strong linear correlation between τ_{ch} and R_{ch} as one would expect with each MCP channel behaving as an RC circuit.[14] For channels with resistances of 10^{14} Ω, the τ_{ch} is ~ 15 msec. High conductivity MCPs with channel resistances of 10^{12} Ω demonstrate τ_{ch} values in the range of 0.1 - 0.2 msec. The main problem with using low conductivity MCPs is their high operational temperatures resulting from joule heating. The joule heating is caused by the very high strip currents through the MCP resulting from the high voltages required to achieve adequate output gain performance. MCPs with $R_{ch} < 10^{13}$ Ω, and that require ~ 2000 volts for proper high-gain operation, will reach operating temperatures in excess of 100° C.[14] At these elevated temperatures, the MCP is essentially under a continual bake. MCPs operating at temperatures exceeding 200° C have shown drops in R_{ch} over time resulting from continual H_2 reduction occurring inside the tube. This can lead to eventual thermal runaway if operated for an extended period of time.

For improved signal-to-noise performance, the MAMA's detection circuitry includes a discriminator so that only output pulses from the MCP that exceed a threshold gain level are counted. Pulses with gains below threshold are discarded. Thus, when the output gain of the MCP begins to drop with increasing input flux, the ratio of detected counts that exceed the threshold to the total number of output counts begins to drop. This quantity, termed the *saturation detection efficiency* (*SDE*), is defined as[14]

$$SDE\,(\Lambda\tau_{ch}) = \frac{\displaystyle\int_A^\infty f_g\,(\xi;\,\Lambda\tau_{ch})\,d\xi}{\displaystyle\int_A^\infty f_g\,(\xi;\,\Lambda\tau_{ch} \ll 1)\,d\xi}$$

(2)

where $f_g(g; \Lambda\tau_{ch})$ represents the functional dependance of the PHD with gain, g, for a given product $\Lambda\tau_{ch}$; th is the threshold level set in the discriminator electronics; and ξ is a dummy integration variable. The rate at which the SDE drops with Λ depends on τ_{ch} as well as on how the shape of the PHD changes for a given modal gain-to-threshold ratio, $\overline{G_o}/th$. The predicted behavior of the SDE was simulated with the Monte Carlo model described above and was found to be exponentially dependant on Λ in the following way[14]:

$$SDE\ (\Lambda\tau_{ch}) = C_o\ \exp\ (-a\Lambda\tau_{ch})$$

(3)

The constant a is inversely proportional to $\overline{G_o}/th$; C_o is approximately unity for $\overline{G_o}/th > 2$ and $R_o < 60\%$.

1.3 The 2-Stage Configuration

The upper count rate performance of the MAMA detector system depends critically on how the PHD is affected by increasing input count rates. One way to improve the upper count rate performance is to employ MCPs with lower channel resistances. Another way is to seek a detector configuration that minimizes the broadening of the PHD that occurs at high count rates, so that a proportionally fewer number of output counts fall below threshold. To maximize the improvement, a combination of both of these improvement factors should be incorporated into a detector design.

In this paper we describe our attempt to improve the upper count rate performance of the MAMA detector by employing a newly designed MAMA detector tube that utilizes two MCPs in a cascaded configuration similar to a "chevron" configuration. This tube, called the 2-Stage MAMA tube, employs two MCPs stacked together with a 150-μm thick ceramic spacer placed in between the two plates. Each MCP can be independently biased with separate high-voltage D.C. power supplies.

The dynamic range performance of the 2-Stage MAMA tube was found to exceed the performance of the single MCP MAMA design. The improved performance resulted primarily from the improved PHD characteristics associated with the operation of this tube under certain conditions that are spelled out in further detail below. The PHD characteristics were optimized when the top MCP was operating as a low-gain plate converting incoming photons to electrons, with the bottom MCP operating as a high-gain plate.

Ainbund and Maslenkov[16] carried out an investigation involving the performance characterization of a "chevron" stack of MCPs and found that the PHD performance improved with the application of a *retarding* field within the interplate gap between the two MCPs. They tested a variety of "chevron" stack configurations with interplate gap distances ranging from 0.1 mm up to 1 mm. All of these configurations showed a drop in the PHD resolution, R_{PHD}, as V_{gap} dropped below 0 volts, with a minimum in R_{PHD} occurring for all the tested configurations within -50 to -100 volts. R_{PHD} also showed improvement with the application of a positive V_{gap}, but the minimum in R_{PHD} with $V_{gap} > 0$ was always substantially higher than the minimum in R_{PHD} with $V_{gap} < 0$. They also reported that the modal gains were lower with $V_{gap} < 0$ (comparable to a single high-gain MCP).

Fraser et al.[17] carried out a similar investigation involving a "chevron" stack with a gap distance of 160 μm and found the same behavior—improved PHD resolutions and modal gain values comparable with single high-gain curved-channel MCPs with $V_{gap} < 0$. Both Fraser et al. and Ainbund and Maslenkov attribute the improved PHD resolution performance to the smaller and more tightly packed electron clouds emanating from the top MCP. The repulsive field allows only those electrons that have sufficient energy to reach the bottom MCP. These higher energy electrons generally come from regions within the top MCP channels that are further from the output than those of lesser energy, since they have had more time to gain energy from the applied electric field. Consequently, the higher energy electrons that do arrive at the bottom MCP emerge from the top MCP within a smaller solid angle compared with those electrons of lower energy that emerge from the channel output with rather large angles with respect to the channel normal. The lower modal gain values with $V_{gap} < 0$ results from the smaller number of electrons that are able to reach the bottom MCP.

Figure 2 is a schematic showing a cross cut view of the rear body of the 2-Stage MAMA imaging detector tube. This tube was designed to test the gain, dynamic range, and imaging performance characteristics of a cascaded two-stage high-gain MCP configuration utilizing two 25-mm-diameter format MCPs. The 2-Stage rear body assembly was constructed out of Kovar and ceramic and was designed to operate under high vacuum conditions ($< 10^{-7}$ torr). The back surface of the tube is made up of a ceramic header which contains feedthrough pins that are used to electrically connect the anode array within the tube body to the external MAMA electronics. The anode array, which is itself constructed on a glass substrate and epoxyed to the inside surface of the header, is connected electrically to the header with gold ribbon. The bottom MCP rests above the anode array, supported by three gold pads spaced 120° apart. On top of the bottom MCP lies a specially designed ceramic washer that electrically isolates the bottom MCP from the top MCP. The top MCP is mounted on the upper surface of the
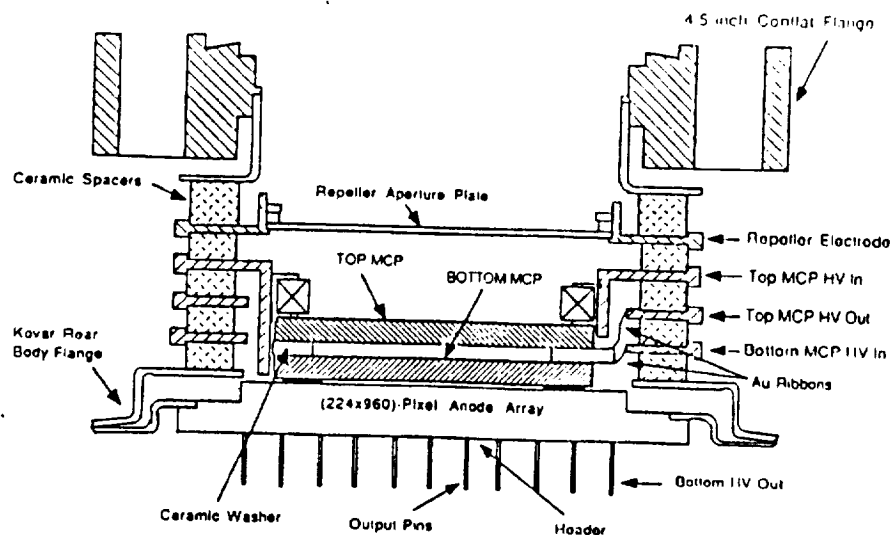
Figure 2. Cross sectional view of the 2-Stage MAMA imaging detector.

washer. The interplate gap distance is set by the thickness of the washer, which for the measurements reported here was 150 μm.

A total of four high-voltage feedthrough electrodes made of Kovar are sandwiched between ceramic rings that are bonded to the top surface of the header's Kovar flange. The first high-voltage feedthrough electrode from the bottom is used to bias the top surface of the bottom MCP. Three gold ribbons attached to the bottom surface of the ceramic washer, and spaced 120° apart, are used to make the electrical connection from the washer to the first feedthrough. The three gold pads on which the bottom MCP rests serve as the high-voltage output. The second high-voltage feedthrough electrode is the high-voltage output for the top MCP. It is connected to the top surface of the ceramic washer with gold ribbons spaced 120° apart in the same manner as the first electrode is to the bottom surface of the washer. The input surface of the top MCP is, in turn, connected to the third feedthrough electrode. The three electrodes allow independent biasing of both the bottom and top MCPs. The fourth feedthrough electrode provides biasing to the repeller aperture plate mounted above the top MCP. This plate is used to improve the detection efficiency by repelling those electrons that are photo-generated within the interchannel regions of the top MCP back down into the MCP channels.

2. EXPERIMENTAL SETUP & PROCEDURE

The 2-Stage tube was operated and tested using two separate MCP configurations—designated configuration I and II. Table I lists the MCP characteristics of both the top and bottom MCPs for both configurations. In configuration I, both top and bottom MCPs were high-gain C^2 plates with channel diameters, D, of 12.5 μm on 15-μm centers. Both MCPs had rectangular active areas measuring 7.5 mm by 27 mm. The channel length-to-diameter ratio (L/D) for the top and bottom MCPs were, respectively, 140 and 130. The average channel resistance for the bottom MCP was 1.1×10^{14} Ω at an applied MCP voltage of 2300 volts. In configuration II, the top MCP was composed of 10-μm diameter straight channels, with an L/D ratio of 40 and a circular active area with a diameter of ~27 mm. The bottom MCP was again a high-gain C^2 plate with a rectangular active area of 7.5 mm by 27 mm, 12.5-μm diameter channels, and an L/D ratio of 136, but with a very low plate resistance of only 10 MΩ at room temperature (20° C). The average channel resistance of this high-conductivity MCP was ~2 x 10^{12} Ω at an applied MCP voltage of 2100 volts.

The MCPs of configuration I were chosen to test whether or not the SDE performance of the MAMA would improve using MCPs of conventional resistance (R_{ch} ~10^{14} Ω) with the 2-Stage tube. Configuration II was chosen to determine the maximum SDE performance improvement possible with the 2-Stage tube operating with an MCP which had already demonstrated a τ_{ch} value that was about two orders of magnitude smaller than that of MCPs with conventional resistance.

Figure 3 shows, schematically, the equipment and its setup used to conduct the modal gain sag and SDE measurements performed with the 2-Stage tube operating in both configurations I and II. The setup consisted primarily of two combined systems—the MAMA detector system and its associated supporting electronics, and the optical system used to direct ultraviolet photons to the front surface of the top MCP.

-5-

Table I. Tested 2-Stage tube MCP Configurations

Configuration	R_{top} (MΩ)	R_{bot} (MΩ)	D_{top} (μm)	D_{bot} (μm)	$(L/D)_{top}$	$(L/D)_{bot}$
I	141	111	12.5	12.5	140	130
II	50	1.7	10	12.5	40	136

The optical system was designed to provide a uniformly illuminated circular spot of light onto the input surface of the top MCP, which could be varied in relative intensity by the use of calibrated neutral density (ND) filters. Two light sources were used in these measurements—a BHK Analamp Model 81-1057-01 mercury (Hg) "penray" lamp, which provided ultraviolet photons from its strong 2537Å emission line, and a Hamamatsu Model L1636 high intensity deuterium (D_2) lamp that output a continuum ultraviolet emission spectrum between 2000 Å and 3000 Å. The Hg "penray" lamp was used to characterize the gain performance of both tested configurations; the D_2 lamp was used to measure the dynamic range performance in terms of modal gain sag and *SDE* measurements. A UV diffuser was placed in front of the lamp source to create a more uniform "lambertian" exitance across the aperture mask containing the circular area, which was focussed onto the MCP. The lens used to focus the aperture mask was an 85-mm focal length, f/4.5 - 22 achromatic camera lens with high transmission in the UV, manufactured by Asahi Optical Company. A special fixture was built to hold the camera lens, aperture mask, diffuser, and lamp source together with a fixed distance between the lens and mask of 300 mm, giving a demagnification factor of 2.53 to the imaged object. This optical assembly was mounted onto a translational stage which itself was attached to an optical rail. The translational stage allowed lateral movement of the optical assembly perpendicular to the optical axis.

The MAMA electronics used for these tests only supported analog output for PHD analysis. Imaging performance data has not yet been acquired with the 2-Stage tube. The (224 x 960)-pixel array at the back end of the 2-Stage tube was configured as one large anode by tying all the anodes together. The pulses collected by this one large anode was output to a single analog channel consisting of a charge amplifier, whose output was sent directly to the pulse-height analyzer (PHA) for PHD data acquisition. The PHA used was a Tracor Northern TN-7200 Multichannel Analyzer. An HP-85 computer was used to extract PHD data from the PHA for further data manipulation and storage. The pulse-pair resolution of the analog
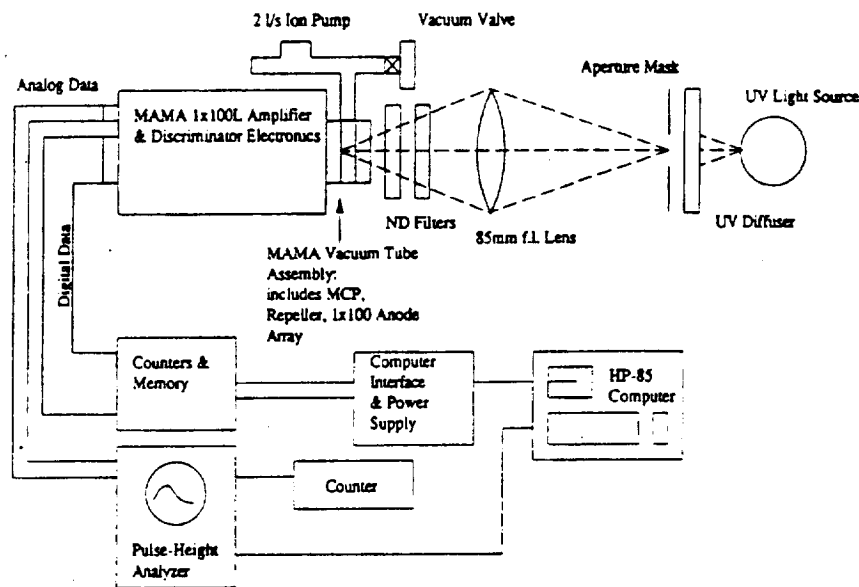

Figure 3. Schematic showing experimental setup for high input count rate measurements.

channel/PHA was measured to be ~550 ns, giving a maximum input count rate capability of the electronics of ~2 x 10^5 counts sec^{-1} with a 10% coincident loss. Also shown in Figure 3 is a digital data path that is used to acquire imaging data. This path was not operational for the set of measurements discussed in this paper.

The dynamic range data was measured in the form of modal gain sag and *SDE* data. The modal gain sag data was acquired by measuring the peak position of the PHD as a function of the true input count rate, Λ. Λ was varied by assuming that the true input count rate was that measured at very low input light flux, so that the MCPs were not in temporal saturation ($\Lambda \tau_{ch} << 1$). This low count rate was measured by integrating the total number of accumulated counts within the acquired PHD from the threshold gain value set with the PHA. This low rate became the baseline rate which was used to calculate the succeeding higher input count rates based on the changes in the calibrated optical density values of the various ND filters used.

3. GAIN CHARACTERISTICS OF THE 2-STAGE TUBE

The 2-Stage MAMA tube was operated and characterized for both configurations I and II. Before operation, the tube with both MCPs installed was baked under vacuum to a temperature of 180° C. Following the bake, the tube was attached to the MAMA electronics to begin the UV "scrub" procedure. This procedure entailed exposing the tube to UV radiation (2537 Å) from a Hg "penray" lamp while slowly increasing the applied MCP voltages until the desired operational voltages were reached. In so doing, the channel surfaces were cleaned from any adsorbed condensates by the "scrubbing" action of the electron cascades within the channels. This material was then pumped out of the tube with the attached ion pump. The UV "scrub" procedure has proved effective in lowering both dark noise and ion feedback. Following the UV scrub, each configuration was characterized and tested for gain and output behavior as a function of the applied voltages to both top and bottom MCPs.

Figures 4a, b show the PHD recorded with the 2-Stage tube operating in configuration I with V_{top} at 1200 volts (Figure 4a), and at 1400 volts (Figure 4b), with with the bottom MCP held at 2300 volts. These PHDs have an excellent quasi-Gaussian shaped peak with a modal gain value of ~5 x 10^5 electrons pulse^{-1}, a low PHD resolution of ~41%, and a peak-to-valley ratio[†] (PVR) greater than 10. The PHD with V_{top} = 1400 volts shows a secondary peak at ~9.5 x 10^5 electrons pulse^{-1} which is believed to result from lateral spreading of the charge cloud within the interplate gap causing a number of output pulses from the top MCP to hit two channels in the bottom MCP.

The modal gain and PHD resolution as a function of V_{bot}, with V_{top} held fixed at 1200 volts, is shown in Figure 5 for configuration I. The behavior of both these quantities with MCP voltage is qualitatively identical to that of a single MCP. The minimum PHD resolution was found to occur with V_{bot} at 2300 volts and was thus chosen as the optimum voltage. Beyond 2300 volts, the PHD resolution is shown to rise resulting from increased ion-feedback.

Figures 6a and b show how the output count rate varied with V_{bot} (Figure 6a) and V_{top} (Figure 6b). As Figure 6a demonstrates, the behavior of the output count rate with V_{bot} (V_{top} was held fixed at 1200 volts) is qualitatively identical to that for a single high-gain MCP—that is, the output shows the characteristic rollover with increasing V_{bot} followed by a rise in count rate above 2300 volts resulting from increased ion-feedback.

The behavior of the output count rate as a function of V_{top} (with V_{bot} held fixed), however, was quite different as evident in Figure 6b. The output count rate was found to rise nearly exponentially with V_{top}, starting off slowly for V_{top} below 1200 volts, and steadily rising as V_{top} was increased. Since the modal gain was not changing appreciably as V_{top} was increased, the rise in the output count rate was a result of an increase in the detective quantum efficiency (DQE). As V_{top} was increased, the exit energy and the output gain from the top MCP rose. This, in turn, increased the probability that electrons reached the bottom MCP for eventual detection. The exponential rise in the output count rate with increasing voltage to the top MCP is a consequence of the Maxwellian shape of the energy distribution of the exiting electrons. The repelling interplate gap acts to eliminate electrons with energies below a fixed threshold energy located far out in the wings of the Maxwellian distribution where the number of electrons of increasing energy fall off exponentially. As V_{top} increased, the distribution moved towards higher energy allowing the number of electrons exceeding the energy threshold to rise exponentially.

[†] The peak-to-valley ratio is defined to be the ratio of the amplitude of the PHD at the modal gain or peak of the distribution to the amplitude of the "valley" on the low-gain side of the peak.
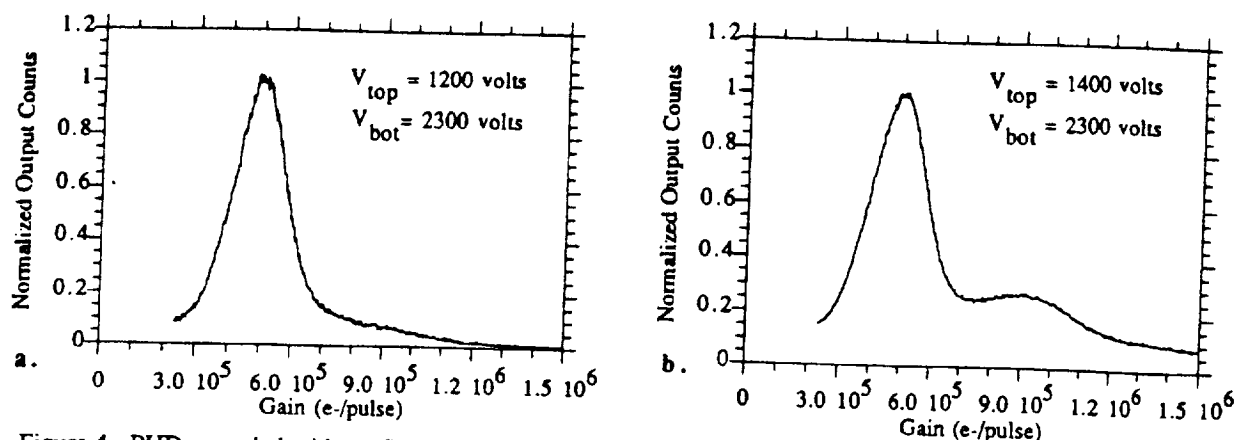
Figure 4. PHD recorded with configuration I with the bottom MCP at 2300 volts, and the top MCP at 1200 volts (a), and 1400 volts (b). Data taken with 2537 Å photons.

The gain and output count rate performance of the 2-Stage tube operating in configuration II was qualitatively the same as that measured for configuration I. The optimum voltages for this configuration with a V_{gap} of -100 volts was a V_{top} of 500 volts and a V_{bot} of 2100 volts. The PHD displayed a nice quasi-Gaussian shape with a modal gain of 2.4×10^5 electrons pulse[-1]; a PHD resolution of 35%; and a PVR of 8. Because of the very low resistance of the bottom MCP (1.7 MΩ at 2100 volts), the excessively high strip current (>600 μA cm^{-2}) led to a rather high operating temperature as a result of joule heating. The operating temperature was in excess of 200° C. This so called "Hot Plate" was found to remain in stable operation over many hours after turn-on; however, over a sustained period of operation exceeding more than a day, the strip current began to slowly increase indicating a further drop in plate resistance. This drop in resistance may be the result of the process used to lower the MCP glass resistance during manufacture—the process known as hydrogen reduction.[18] During this step, which occurs after the MCP channels have been etched out, the MCP is placed in a furnace at an elevated temperature (> 350° C) in the presence of hydrogen gas. The hydrogen diffuses into the glass matrix reducing the lead oxide in the glass to metallic lead. The newly altered glass matrix now allows for electronic conduction to occur with much lower resistivity. Hence, if the "Hot Plate" were allowed to continue to operate, there is the chance that eventually the resistance will begin a precipitous drop leading to a thermal "runaway" condition which would destroy the plate and most probably the anode array directly behind it.

Figure 5. Modal gain (solid curve) and PHD resolution (dashed line) as a function of the applied bottom MCP voltage for the 2-Stage MAMA tube operating in configuration I. The top MCP voltage for these measurements was 1200 volts. Data taken with 2537 Å photons.
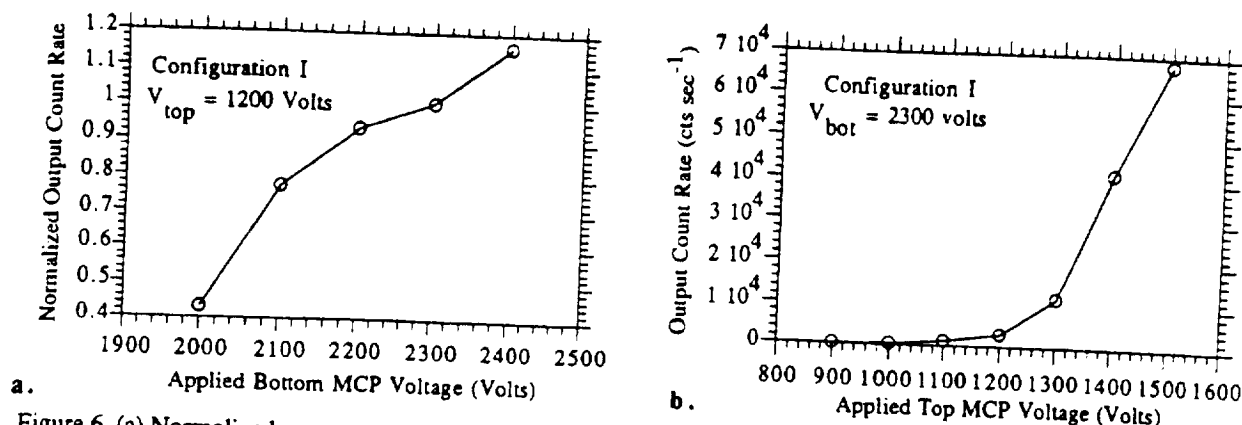
Figure 6. (a) Normalized output count rate of the 2-Stage MAMA tube operating in configuration I as a function of the applied voltage to the bottom MCP with 1200 volts applied to the top MCP. (b) The output count rate as a function of the applied voltage across the top MCP, with the bottom MCP held at 2300 volts. Data taken with 2537 Å photons.

4. HIGH COUNT RATE PERFORMANCE OF THE 2-STAGE TUBE

The high count rate performance of the 2-Stage MAMA tube was evaluated for both configurations I and II by measuring the modal gain sag and *SDE* as a function of the true input count rate, *A*. The experimental setup for these measurements is shown in Figure 3. The aperture mask was a circular pinhole 600 μm in diameter. The spot was demagnified to a diameter of 237 μm by the 85-mm focal length lens. The channel recharge time constant, τ_{ch}, was inferred through least-squares fitting of the modal gain versus *A* data with Equation 1. In addition, the PHDs at each *A* value were recorded for PHD resolution, PVR, and modal gain analyses. Table II summarizes the results of these measurements in terms of τ_{ch} and the measured value of *A* for which the *SDE* = 0.9 (10% loss in DQE). In addition, Table II also lists the gain performance at the optimum operating voltages used for these measurements.

4.1 Gain Sag Data

The operational conditions that were chosen for these measurements were based on those that gave the best PHD performance. For MCP configuration I, V_{top} and V_{bot} were set at 1200 volts and 2300 volts, respectively, with the interplate gap at -100 volts. Figure 7a shows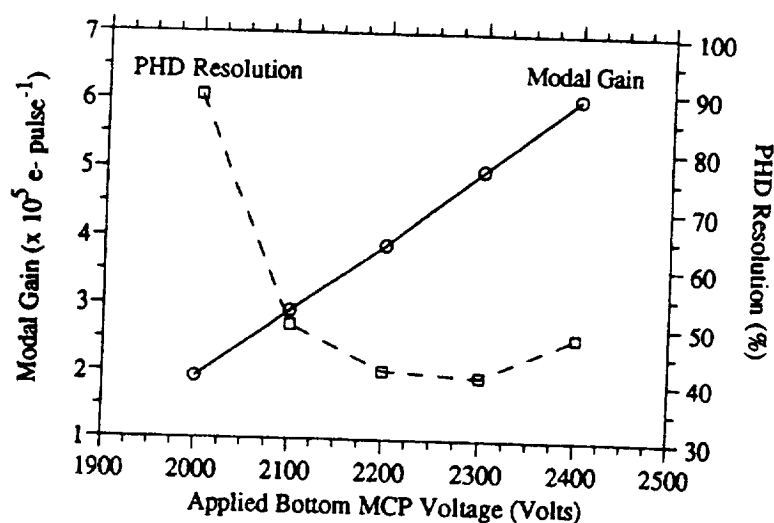 the measured modal gain as a function of the true input count rate, *A*. The modal gain was found to drop 10% at ~30 counts channel[-1] sec^{-1}. The dashed curve through the data points is the least-squares fit of the data with Equation 1. The resulting data fit gave a $k(R_o)\tau_{ch}$ value of 5.4 ± 0.1 msec. With a PHD resolution, R_o, of 37%, the value of $k(R_o)$ was 0.40, for a τ_{ch} of 13.5 ± 0.2 msec. This measured value for τ_{ch} is about what is expected for the given channel resistance of the bottom MCP (~10[14] Ω), based on previously measured τ_{ch} versus R_{ch} values of single high-gain MCPs.

Figure 7b shows how the PHD changed with *A* for the three representative *A* values of 5, 65 and 193 counts channel[-1] sec^{-1} with configuration I. Each displayed PHD has been normalized in amplitude to that for *A* = 5 counts channel[-1] sec^{-1}. What is most remarkable about the behavior of these PHDs with *A* is how little the PHD shape degraded as *A* increased. At 5 counts channel[-1] sec^{-1}, the PVR was ~18 with a PHD resolution of 37%. At 65 counts channel[-1] sec^{-1}, the PVR actually increased to the value of 27, with a PHD resolution of 55%. At 193 counts channel[-1] sec^{-1}, the PHD resolution had only increased to 78%. Increased ion feedback at the higher input count rates was present with the rise in the high-gain tail evident at both 65 an 193 counts channel[-1] sec^{-1}.

The gain sag data taken with configuration II was qualitatively similar to that of configuration I except for the rate at which the modal gain dropped with *A*. Figure 8a shows the measured modal gain as a function of *A* with configuration II. Figure 8b shows how the PHD changed with *A* for the three representative *A* values of 14, 555 and 1100 counts channel[-1] sec^{-1} with configuration II. The gain sag measurements were performed with the top MCP at an applied voltage of 500 volts and the bottom at 2100 volts. The modal gain and PHD resolution at these voltages were, respectively, 2.4 x 10^{5} electrons pulse[-1], and 35%. The modal gain dropped 10% at ~625 counts channel[-1] sec^{-1}. The extracted value of τ_{ch} based on the

-9-

Figure 7. (a) Modal gain sag versus Λ made with the 2-Stage MAMA tube operating in configuration I. The dashed curve is the least-squares fit of Equation 1 to the data. (b) Normalized PHDs with the 2-Stage MAMA operating in configuration I taken at three increasing values of the input count rate, Λ.

curve fit of the modal gain sag data with Equation 1 was 0.5 ± 0.1 msec. Again, this value of τ_{ch} is within a factor of two of that expected for the channel resistance of the bottom MCP of $-1.8 \times 10^{12} \, \Omega$. The PHD resolution at low count rates was lower for this MCP operating in the 2-Stage tube compared with its measured value as a single MCP (-65%).

Figure 9 shows how the PHD resolution, R_{PHD}, grew with the product $\Lambda\tau_{ch}$ for both configurations I (squares) and II (triangles); and, for comparison, that measured for an MCP operating in a single plate configuration, using a conventional MAMA detector. Also shown in the figure are the predicted changes in R_{PHD} versus $\Lambda\tau_{ch}$ based on the Monte Carlo model simulating the output gain as a function of Λ for a single MCP channel. Measurements of R_{PHD} as a function of Λ for the single high-gain MCP shows a rather close agreement with the Monte Carlo model. The 2-Stage tube operating in configuration I, however, shows that the R_{PHD} changed much more slowly with Λ. This rather slow increase in R_{PHD} with Λ means that the SDE will not fall off as rapidly with Λ, thus leading to a higher input count rate capability.

The smaller growth of the PHD's resolution with Λ is probably due to the better detection efficiency of MCPs to input electrons than to photons. For the single MCP configuration, many of the input photons make multiple reflections within the channels before being converted to electrons (especially for bare MCPs with no input photocathode). Hence, the upper regions of the channels are not involved with the multiplication process. This leads to a PHD of lower modal gain, lower PVR, and a higher PHD resolution. The top MCP of the 2-Stage tube, however, acts as a "photocathode" which feeds
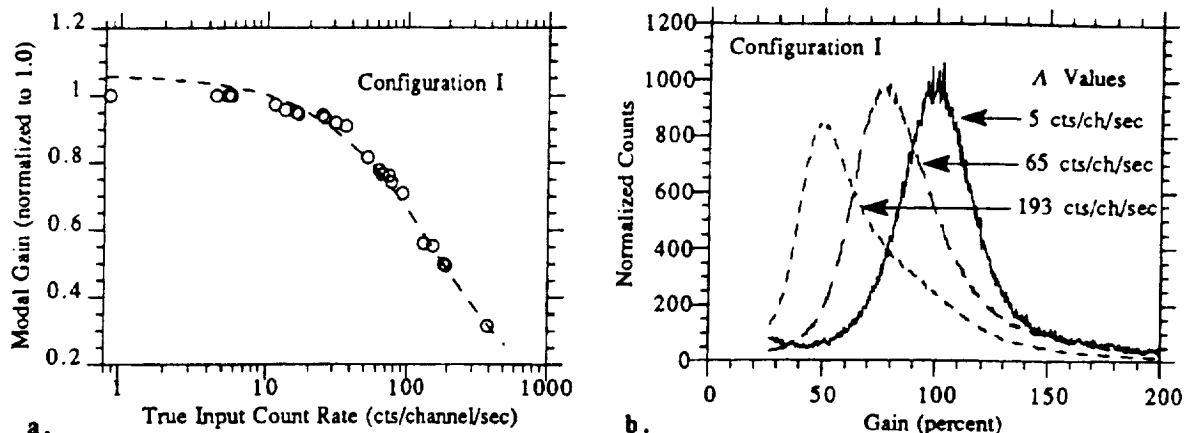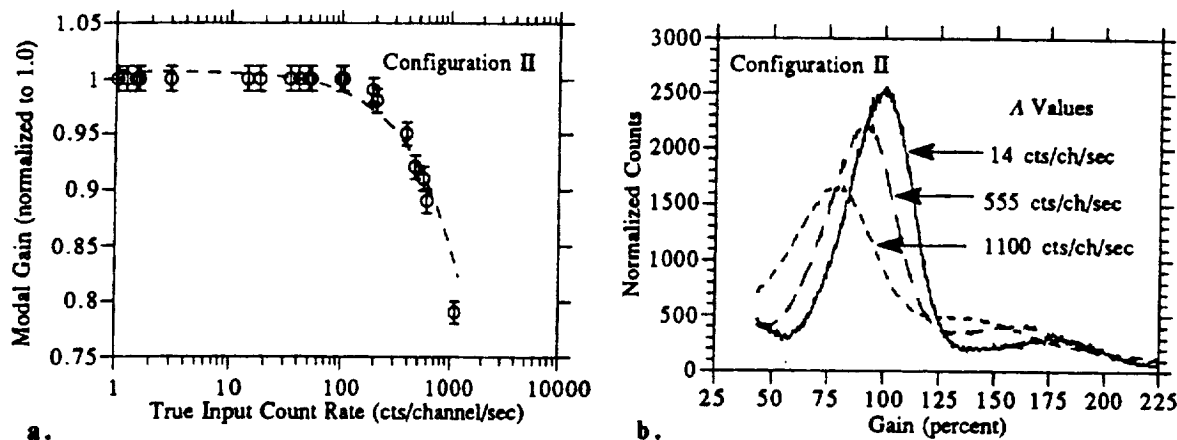

Figure 8. (a) Modal gain sag versus Λ made with the 2-Stage MAMA tube operating in configuration II. The dashed curve is the least-squares fit of Equation 1 to the data. The vertical error bars represent the 1-sigma error in the measured modal gain. (b) Normalized PHDs with the 2-Stage MAMA operating in configuration II taken at three increasing values of the input count rate, Λ.
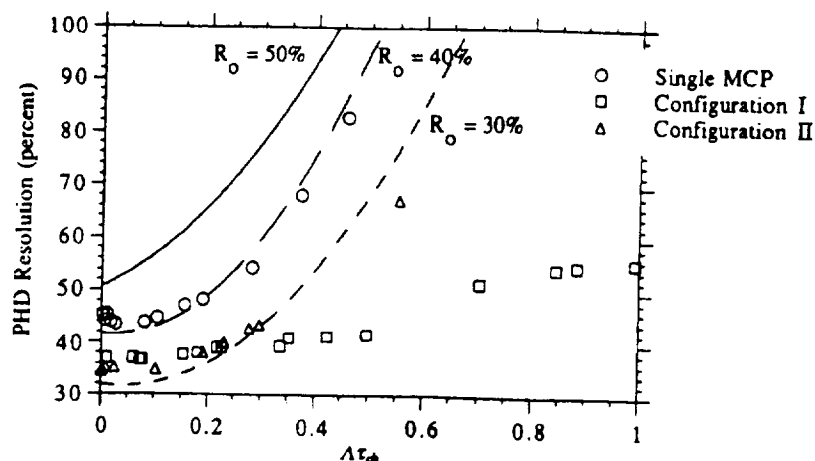
-10-

Figure 9. Measured PHD resolution as a function of $\Lambda\tau_{ch}$ for a single MCP configuration (circles); and for the 2-Stage tube operating in configuration I (squares); and configuration II (triangles). The three curves in the plot are the expected changes in the PHD resolution with $\Lambda\tau_{ch}$, according to the Monte Carlo model for R_o values of 30%, 40% and 50%.

the bottom MCP with "event" electrons. These "event" electrons are converted at the very top of the channels comprising the bottom MCP so that the entire channel length is utilized for electron multiplication. This leads to higher modal gains, higher PVRs, and lower PHD resolutions. The channels can also sustain the PHD's low resolution at higher count rates because there is more effective channel length to work with before temporal saturation begins degrading the PHD's shape. The modal gain still drops at the same rate with Λ as expected for the given channel resistance, but the PHD maintains a fairly constant width.

The PHD resolution measured with configuration II grew more quickly with Λ, almost at the same rate as that predicted by the Monte Carlo model, than that of configuration I. The PVR, however, was higher compared with that measured with the bottom MCP operating as a single MCP, and therefore an improvement in the SDE is expected.

4.2 SDE Data

The SDE was computed for both configurations I and II using the acquired PHDs taken at various values of Λ, and Equation 2. Figure 10a shows the SDE, corrected for the finite pulse-pair resolution of the electronics, as a function of Λ with configuration I. These data were recorded with the threshold set at a gain value of 1.3×10^5 electrons pulse^{-1}, giving a modal gain-to-threshold ratio, $\overline{G_o}/th$, of 3.7. The dashed line through the data points is the least-squares fit of the SDE model, given by Equation 3, with $a\tau_{ch} = 0.8 \pm 0.1$ msec. The vertical error bars represent the computed 1-sigma error of the SDE values. The true input count rate at which the detection efficiency dropped by 10% (Λ@10%-loss) was ~157 counts channel^{-1} sec^{-1}.

In order to make a proper comparison of the Λ@10%-loss value between the 2-Stage configuration I and the single MCP configuration utilizing only the bottom MCP, requires that the values of Λ@10%-loss be calculated for a constant $\overline{G_o}/th$ ratio. For a $\overline{G_o}/th = 3.0$, the value of Λ@10%-loss for the 2-Stage tube operating in configuration I was 117 counts channel^{-1} sec^{-1}. With the bottom MCP operating as a single MCP, the predicted Λ@10%-loss value is ~19 counts channel^{-1} sec^{-1}. This predicted value is based on the measured value of τ_{ch} using Equation 3. The 2-Stage tube results thus represents an improvement in the upper count rate performance over the single MCP configuration by a factor of ~6. This improvement is clearly the result of a PHD that stays relatively constant in width and maintains its high PVR with increasing Λ.

Figure 10b shows the SDE, corrected for the finite pulse-pair resolution of the electronics, as a function of Λ with configuration II. These data were recorded with the threshold set at a gain value of 0.95×10^5 electrons pulse^{-1}, giving a $\overline{G_o}/th$ of 2.5. The dashed line through the data points is again the least-squares fit to the SDE model given by Equation 3, with $a\tau_{ch} = 0.045 \pm 0.026$ msec. Note that the fall-off in the SDE values did not occur with any statistical significance until the last data point at $\Lambda = 1107$ counts channel^{-1} sec^{-1}. The Λ@10%-loss value for this configuration, taking into account the large uncertainty in the measured value of $a\tau_{ch}$, was ~1480 counts channel^{-1} sec^{-1}. For a $\overline{G_o}/th = 3.0$, the value of Λ@10%-loss was ~1900 counts channel^{-1} sec^{-1}.

-11-

Table II. Gain/Dynamic Range Results

Configuration	V_{top}/V_{bot} (Volts)	V_{gap} (Volts)	$\overline{G_o}$ (e- pulse^{-1})	R_o (%)	τ_{ch} (msec)	Λ @ $0.9SDE$ $\overline{G_o}/th = 3$ (cts ch^{-1} sec^{-1})
I	1200/2300	-100	4.9×10^5	37	13.5 ± 0.2	117
II	500/2100	-100	2.4×10^5	35	0.5 ± 0.1	1900

The SDE of the high conductivity bottom MCP was measured in the single MCP configuration to allow comparison with the 2-Stage results. The modal gain, PHD resolution and PVR performance of this plate operating in this configuration was, respectively, 1.3×10^5 electrons pulse^{-1}, 65%, and 1.6. The measured Λ@10%-loss value for this MCP was ~440 counts channel^{-1} sec^{-1} ($\overline{G_o}/th = 3.0$). Hence, the 2-Stage configuration with this high conductivity MCP represents an improvement in SDE performance by a factor of ~4.3 compared with the performance of this high conductivity MCP operating as a single high-gain MCP. Again, this improvement is primarily due to the better PHD performance of this MCP when operated in the 2-Stage configuration.

5. CONCLUSIONS AND FUTURE TASKS

The 2-Stage tube, operating with $V_{gap} < 0$, was found to achieve superior PHD performance characteristics over the single high-gain MCP configuration in both higher values for the PVR, and lower values of R_{PHD}, that did not change appreciably with increasing Λ. Both of these improvements resulted in better upper level count rate performance; i.e., higher values of Λ for a given drop in the SDE by a factor of 4 to 6 over the single MCP MAMA configuration. In addition, it was found this improvement augmented the improvement already achievable with lower resistive MCPs. With the low-resistance bottom MCP in configuration II (the "Hot Plate"), the overall improvement in upper count rate performance over the single MCP version of the MAMA operating with a moderate conductive plate (~10^{14} Ω channel^{-1}) was nearly two orders of magnitude. Hence, maximum achievable upper level count rates are improved with the 2-Stage design.

The drawback discovered with the operation of this tube, however, was the low apparent DQE associated with operating with a repelling interplate gap voltage. Working at higher top MCP voltages improves the DQE, but because the output count rate depends exponentially upon the top voltage, there is lower count rate stability with changes in V_{top}.

Reducing the repelling interplate gap voltage from -100 volts to say -20 to -30 volts should raise the DQE and hopefully maintain the improved PHD performance with increasing input count rate. Further testing of the 2-Stage tube to
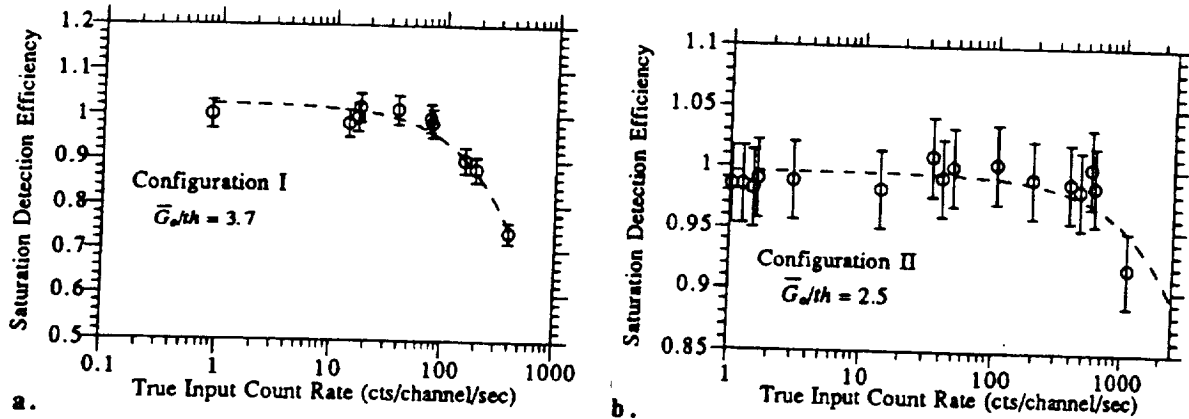

Figure 10. SDE data as a function of the true input count rate, Λ, measured with the 2-Stage tube operating in configuration I (a) and II (b). The vertical error bars represent the 1-sigma uncertainty in the measured SDE values. The dashed curve through the data points is the least-squares fit of the data with Equation 3.

find the best combination of V_{top}, V_{bot}, and V_{gap} which gives the optimum operation in terms of PHD, dynamic range, and DQE performance is therefore necessary. In addition, further testing to determine its imaging characteristics with $V_{gap} < 0$ must be examined.

In addition, other MCPs possessing mid-to-high conductivities at operational MCP voltages ($\sim 10^{13} \Omega$) should be measured for dynamic range performance with the 2-Stage tube. The optimum setup may be that of a mid-to-high conductivity MCP with curved-channels and an L/D ratio greater than 100 for the bottom MCP, and a low conductivity MCP, again with curved-channels and an L/D ratio greater than 100, for the top MCP. This range of conductivities would not suffer from the operational instabilities resulting from the high operational temperatures characteristic of the very high conductivity MCPs such as that demonstrated by the "Hot Plate". This setup running with the top MCP at low gain, and the bottom at high gain, and with a repelling interplate gap voltage should provide high count rate capability exceeding 500 counts channel^{-1} second^{-1} (for 10% loss in *SDE*) with stable operation.

6. ACKNOWLEDGEMENTS

7. REFERENCES

1. J. G. Timothy and R. L. Bybee, "Multi-Anode Microchannel Arrays," *Solid State Imaging Devices*, SPIE Proceedings, **116**, 24 (1977).
2. J. G. Timothy and R. L. Bybee, "Multi-Anode Microchannel Array Detectors for Space Shuttle Imaging Applications," *Shuttle Pointing of Electro-Optical Experiments*, SPIE Proceedings, **265**, 93 (1981).
3. J. G. Timothy and R. L. Bybee, "Multi-Anode Microchannel Arrays: New Detectors for Imaging and Spectroscopy in Space," *AIAA 21st Aerospace Sciences Meeting*, AIAA-83-0105, Reno, Nevada, 1983.
4. J. G. Timothy, J. S. Morgan, D. C. Slater. D. B. Kasle, R. L. Bybee, and H. E. Culver, "MAMA Detector Systems: A Status Report," Ultraviolet Technology III, SPIE Proceedings, **1158**, 104 (1989).
5. D. C. Slater, J. G. Timothy, and J. S. Morgan, "Imaging MAMA Detector Systems," *Electron Image Tubes and Image Intensifiers*, SPIE Proceedings, **1243**, 35 (1990).
6. B. E. Woodgate and the Space Telescope Imaging Spectrograph Science Team, "Second generation spectrograph for the Hubble Space Telescope," *Instrumentation in Astronomy VI*, SPIE Proceedings, **627**, 350 (1986).
7. *Lyman — The Far Ultraviolet Spectroscopic Explorer*, Phase A Study Final Report, NASA, July 1989.
8. *The SOHO Mission — Scientific and Technical Aspects of the Instruments*, ESA Report SP-1104 (ISSN 0379-6566), November 1988.
9. J. G. Timothy, T. E. Berger, J. S. Morgan, A. B. C. Walker Jr., J. C. Bhattacharyya, S. K. Jain, A. K. Saxena, M. C. E. Huber, G. Tondello, and G. Naletto, " HiRES: A High-Resolution Stigmatic EUV Spectroheliometer for Studies of the Fine Scale Structure of the Solar Chromosphere, Transition Region and Corona," *X-Ray/EUV Optics for Astronomy, Microscopy, Polarimetry, and Projection Lithography*, SPIE Proceedings, **1343**, 350 (1990).
10. J. G. Timothy, "Curved-channel microchannel array plates," *Review of Scientific Instruments*, **52**, No. 8, 1131 (1981).
11. J. G. Timothy, "Performance characteristics of multi-anode microchannel array detector systems," *State-of-the-Art Imaging Arrays and Their Applications*, SPIE Proceedings, **501**, 89 (1984).
12. O. H. W. Siegmund, J. Vallerga, and B. Wargelin, "Background Events in Microchannel Plates," *IEEE Transactions on Nuclear Science*, **NS-35**, 524 (1988b).
13. W. B. Feller, L. M. Cook, G. W. Fraser, J. F. Pearson, S. S. Murray, and M. R. Garcia, "Low Noise Microchannel Plates," *Image Intensification*, SPIE Proceedings, **1072**, 138 (1989).
14. D. C. Slater, *Dynamic Range Improvement Study of Multi-Anode Microchannel Array Detector Systems*, Ph.D. Dissertation, Stanford University, 1991.
15. J. L. Wiza, "Microchannel Plate Detectors," *Nuclear Instruments and Methods*, **162**, 587 (1979).
16. M. R. Ainbund and I. P. Maslenkov, "Improving the Characteristics of Microchannel Plates in Cascade Connection," translated from *Pribory i Tekhnika Eksperimenta*, No. 3, 145 (1983).
17. G. W. Fraser, M. J. Whiteley, and J. F. Pearson, "Developments in microchannel plate detectors for imaging X-ray astronomy," *X-Ray Instrumentation in Astronomy*, SPIE Proceedings, **597**, 343 (1985).
18. K. B. Blodgett, "Surface Conductivity of Lead Silicate Glass after Hydrogen Treatment," *Journal of the American Ceramic Society*, **34**, 14 (1951).

Performance Characteristics of the Imaging MAMA Detector Systems for SOHO, STIS, and FUSE/*Lyman*

J. Gethyn Timothy

Center for Space Science and Astrophysics
Stanford University, ERL 314
Stanford, California 94305 USA

ABSTRACT

Imaging Extreme Ultraviolet (EUV) Multi-Anode Microchannel Array (MAMA) detector systems with formats of 360 x 1024 pixels and pixel dimensions of 25 x 25 microns^2 are being fabricated and tested for flight in two instruments on the ESA/NASA Solar and Heliospheric Observatory (SOHO). In addition, very-large-format (1024 x 1024)- and (2048 x 2048)-pixel Far Ultraviolet (FUV) and EUV MAMA detectors with pixel dimensions of 25 x 25 microns^2 are being fabricated and tested for use in the NASA Goddard Space Flight Center's *Hubble* Space Telescope Imaging Spectrograph (STIS), a second-generation instrument scheduled for in-orbit installation in 1997. Finally, FUV MAMA detectors with formats of 224 x 960 pixels and pixel dimensions of 14 x 14 microns^2 are being evaluated as prototypes of the detector for the prime FUV spectrograph of the Far Ultraviolet Spectroscopic Explorer (FUSE/*Lyman*) mission. The configurations and performance characteristics of the different detector systems are described and the plans for further development of the Advanced Technology MAMA detector system discussed.

1. INTRODUCTION

We are currently fabricating and characterizing Multi-Anode Microchannel Array (MAMA) detector systems for use on a number of space ultraviolet astrophysics missions at far-ultraviolet (FUV) and extreme-ultraviolet (EUV) wavelengths between about 300 and 28 nm. Open, open with openable cover, and sealed, (360 x 1024)-pixel MAMA detector systems, with pixel dimensions of 25 x 25 microns^2 and MgF$_2$, KBr, and CsI photocathodes will be used in the Solar Ultraviolet Measurements of Emitted Radiation (SUMER)[1] and the Ultraviolet Coronagraph Spectrometer (UVCS)[2] instruments on the ESA/NASA Solar and Heliospheric Observatory (SOHO)[3], scheduled for launch in 1995. Prototype very-large-format (1024 x 1024)- and (2048 x 2048)-pixel MAMA detector systems, with pixel dimensions of 25 x 25 microns^2 and CsI and Cs$_2$Te photocathodes, are currently under test and in fabrication for the NASA Goddard Space Flight Center's *Hubble* Space Telescope Imaging Spectrograph (STIS),[4] a second-generation instrument scheduled for in-orbit installation in 1997. Proof-of-concept sealed and open (224 x 960)-pixel MAMA detector systems, with pixel dimensions of 14 x 14 microns^2, are also under test as part of the Far Ultraviolet Spectroscopic Explorer (FUSE/*Lyman*) Phase B study.[5]

The performance characteristics of these different detector systems are described in the following sections of this paper in the context of the scientific objectives of each of the instruments.

2. MAMA DETECTOR SYSTEM

Details of the construction and mode-of-operation of the MAMA detector system have recently been presented in the literature.[6,7] The components of a MAMA detector consist of, first, the tube assembly and, second, the associated analog and digital electronic circuits. The MAMA detector tube, which can be sealed with a window or used in an open-structure configuration, contains a single, high-gain, curved-channel microchannel plate (MCP) electron multiplier with the photocathode material deposited on, or mounted in proximity focus with the front surface. Electrodes are mounted in proximity focus with the output surface of the MCP to detect and measure the positions of the electron clouds generated by single photon events (see Figs. 1 and 2).
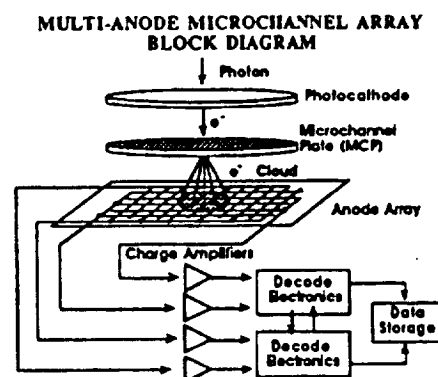
Fig. 1. Schematic of the imaging MAMA detector system.
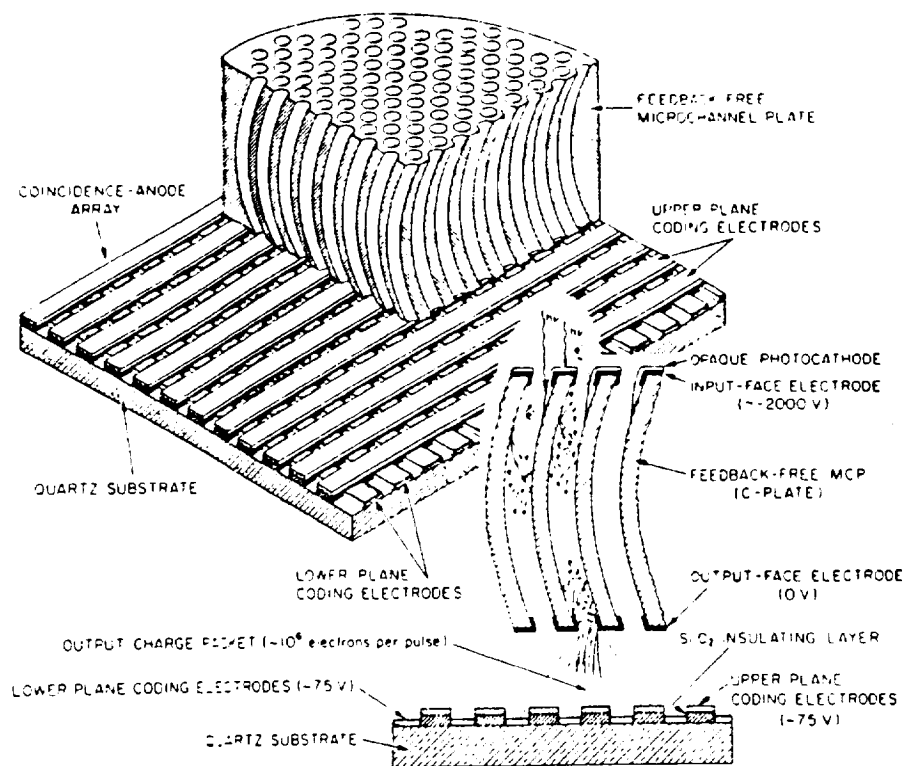
Fig. 2. Schematic showing details of the curved-channel MCP and the imaging multi-layer anode array used in the MAMA detector tubes.

The charge collected on the anode electrodes is amplified and shaped by high-speed amplifier and discriminator circuits.

Digital logic circuits respond to the simultaneous arrival of the shaped signals from several of these electrodes in each axis, which are arranged in groups to uniquely identify a x b pixels in one dimension with only a + b amplifier and discriminator circuits. For example, a total of 32 x 32, i.e. 1024, pixels in one dimension can be uniquely identified with 32 + 32, i.e. 64, amplifier and discriminator circuits. In the imaging MAMA detector tube, two arrays are mounted in tandem with orthogonal orientations, so that the positions of the detected photons can be sensed in two dimensions. In this configuration (a x b)² pixels can be uniquely identified with only 2 x (a + b) amplifier and discriminator circuits. Thus, a (1024 x 1024)-pixel array, for example, requires a total of only 128 amplifier and discriminator circuits. The two layers of anode electrodes in the imaging arrays are insulated from each other by a SiO_2 dielectric layer. The dielectric between the upper layer electrodes is etched away to allow the low energy (-30 eV) electrons in the charge cloud from the MCP to be collected simultaneously on both arrays. Details of the latest MAMA anode-array geometries and position-encoding algorithms can be found in the literature.[8-10]

3. SOHO MAMA DETECTOR SYSTEMS

The MAMA detectors for the SUMER and UVCS instruments on the SOHO mission have a high degree of commonality, but also significant differences dictated by the scientific needs of the two instruments. The definition of the detector systems has accordingly required a great deal of interaction between the MAMA detector development group, the SUMER instrument team at the Max-Planck-Institut für Aeronomie (MPAe), Katlenburg-Lindau, Germany, and the UVCS instrument team at the Smithsonian Astrophysical Observatory (SAO), Cambridge, MA. All of the detectors have formats of 360 x 1024 pixels and pixel dimensions of 25 x 25 microns². The other key parameters are listed in Table 1. The SUMER instrument is designed for spatially-resolved line-profile studies at wavelengths between about 40 and 160 nm. This instrument employs two MAMA detectors for redundancy. The prime detector is designed to be used in an open configuration and has a cover which can be opened on command after the instrument is under high vacuum in a test chamber or in the space environment. The purpose of the cover is to protect the photocathode materials and the high-gain MCP from contamination during the years of the instrument and spacecraft integration and test

Table 1. Key Parameters of the MAMA Detectors for the SUMER and UVCS Instruments
on the SOHO Mission.

| | SUMER | | UVCS | |
	Detector A	Detector B	Detector 1	Detector 2
Pixel Format	360 x 1024	360 x 1024	360 x 1024	360 x 1024
Pixel Dimensions	25 x 25 μm^2	25 x 25 μm^2	25 x 25 μm^2	25 x 25 μm^2
Anode Array Active Area	9.0 x 25.6 mm^2	9.0 x 25.6 mm^2	9.0 x 25.6 mm^2	9.0 x 25.6 mm^2
MCP Active Area	10 x 27 mm^2	10 x 27 mm^2	10 x 27 mm^2	10 x 27 mm^2
MCP Pore Size	12 microns	12 microns	12 microns	12 microns
Number of Amplifiers (including analog output)	105 (104+1)	105 (104+1)	105 (104+1)	105 (104+1)
Photocathode Material	MgF_2 and KBr	MgF_2 and KBr	CsI	KBr
Hybrid Amplifier and Discriminator	Yes	Yes	Yes	Yes
Gate Array Decode Circuits	Yes	Yes	Yes	Yes
Configuration	Openable cover	Open	Sealed	Openable cover

programs. The different subassemblies which make up the openable-cover detector system are shown in Fig. 3 and the detector system block diagram is shown in Fig. 4. The SOHO detector systems are being fabricated at our prime industrial contractor, Ball Electro-Optics and Cryogenics Division (BECD), Boulder, CO. The configuration of the photocathodes on the SUMER detector is shown in Fig. 5. Two photocathode materials are deposited on the front face of the curved-channel MCP: KBr for a high-quantum efficiency at wavelengths between 80 and 160 nm; and MgF_2 for both a high-quantum efficiency at wavelengths between

40 and 80 nm, and also to provide rejection of the strong H Ly α 121.6 nm radiation, since in SUMER the spectral lines at wavelengths below 80 nm are observed in second order. In addition, the detector has two 10% transparency nickel meshes mounted over a 30-pixel area at either end of the array to act as attenuators for the H Ly α 121.6 nm line, permitting this extremely strong emission line to be observed in active regions on the solar disk without saturating the detector system.

The back-up detector in the SUMER instrument (detector B) is open and does not have the openable cover in
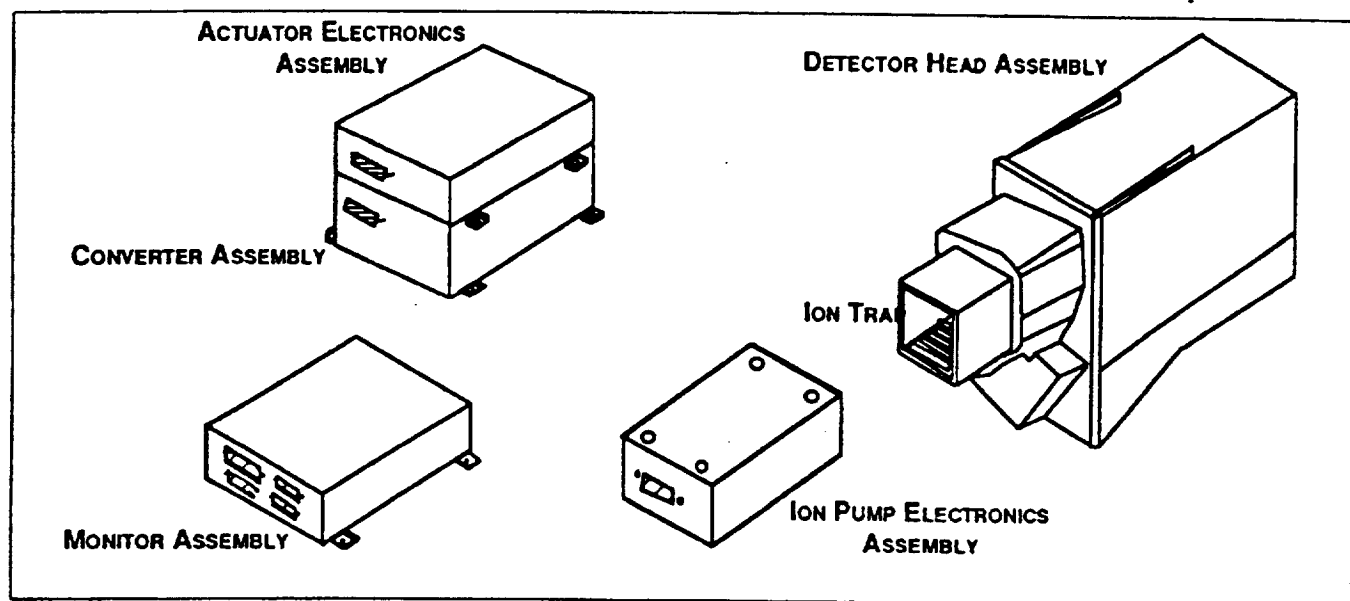
Fig. 3. Openable-cover SOHO MAMA detector system subassemblies.
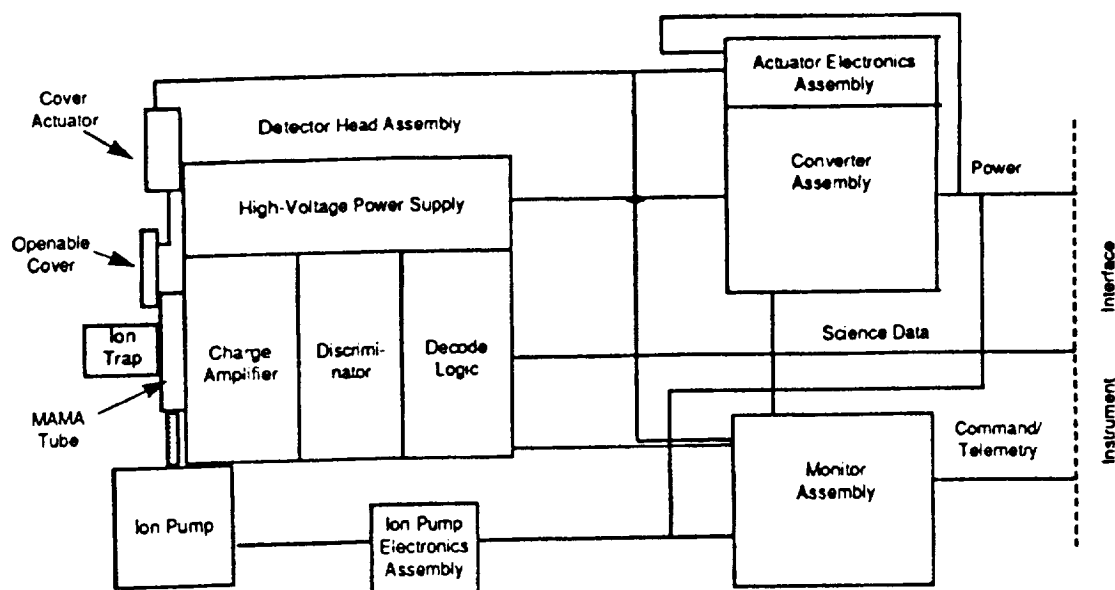
Fig. 4. Openable-cover SOHO MAMA detector system block diagram.

order to eliminate the effects of any systematic design problem in the openable-cover mechanism. The dual photocathode is again used on the back-up detector, even though some degradation of the KBr photocathode is

Fig. 5. SUMER MAMA detector system photocathode configuration.

expected during the several years that the detector must be stored under a dry N_2 purge during instrument and spacecraft integration and test. We originally planned to use solely the MgF_2 photocathode for the open detector, since this material has proved to be highly stable on exposure to dry N_2. However, a loss of sensitivity of even a factor of two in the KBr photocathode prior to launch will still yield significantly higher quantum efficiencies than MgF_2 at wavelengths longer than 80 nm, and will, accordingly, increase the scientific return in the event that the back-up detector has to be employed during the mission.

The UVCS detectors are designed primarily to observe radiation at wavelengths between 103 and 135 nm from the solar corona above the disk, and also to observe radiation at wavelengths between 61 and 135 nm on the solar disk. The sealed detector, designed to observe scattered H Ly α 121.6 nm radiation from the corona, has a MgF_2 window and a CsI photocathode deposited on the front face of the MCP. The sealed detector is sensitive to radiation in the wavelength band from 113 to >135 nm. Because of the optical configuration of the UVCS spectrometer, the UVCS tube must have a thin "wafer" configuration, with the distance from the front surface of the MgF_2 window to the CsI photocathode being no more than 7 mm.

The second detector, which is open with an openable cover and is identical in configuration to the SUMER prime detector, is used to observe radiation at shorter wavelengths. This detector has a KBr photocathode for maximum sensitivity at wavelengths between 93 and 107 nm. The detector is also used to observe radiation at wavelengths between 46 and 63 nm in second order.

Breadboard (360 x 1024)-pixel MAMA detector systems have so far been delivered to the Astronomisches Institut Tübingen (AIT) in Germany and to the University of Padua in Italy to support the SUMER and UVCS development programs, respectively. The SUMER breadboard system has a CsI photocathode deposited on the front face of the MCP, and the Padua breadboard system has a KBr photocathode deposited on the front face of the MCP. A sealed breadboard UVCS detector system with a "wafer" tube having a MgF_2 window and a CsI photocathode deposited on the front face of the MCP will shortly be delivered to SAO. The configuration of the (360 x 1024)-pixel SOHO anode array is shown in Fig. 6a, and the configuration of the breadboard detector system, which employs discrete electronics components and is significantly larger than the flight units, is shown in Fig. 6b.

(a)
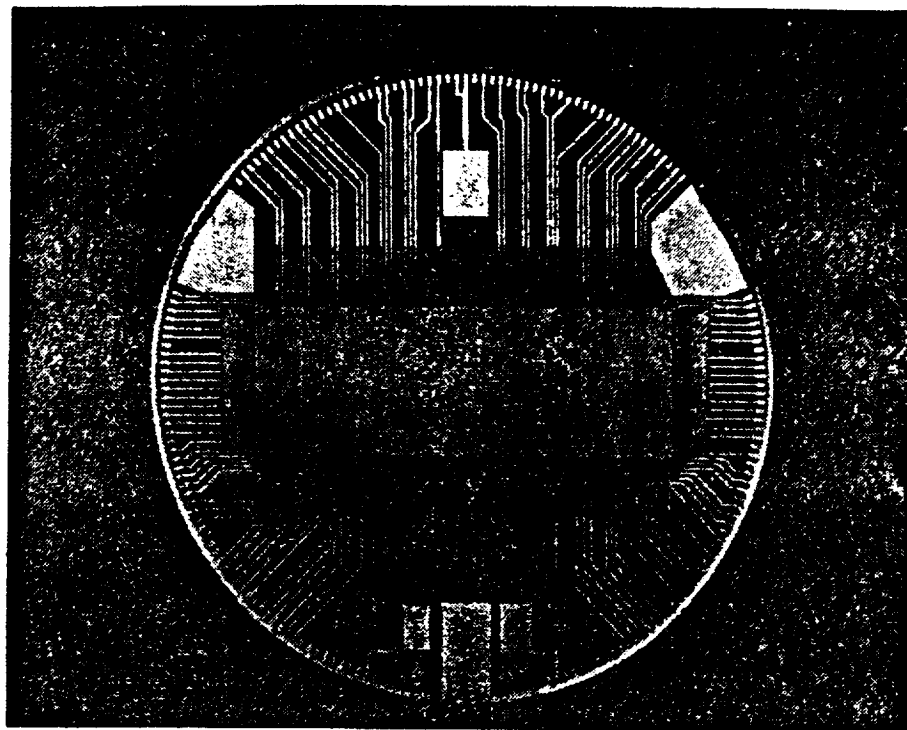
Fig. 6. SOHO MAMA Breadboard Detector System.
(a) (360 x 1024)-pixel anode array with 25 x 25 microns^2 pixels.
(b) Assembled breadboard detector system with laboratory evaluation tube attached.

(b)
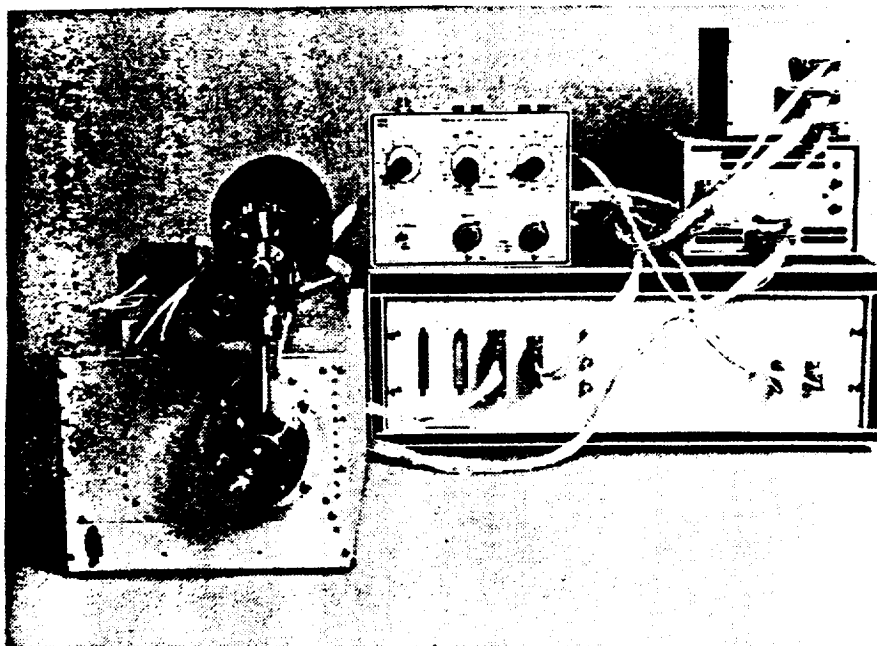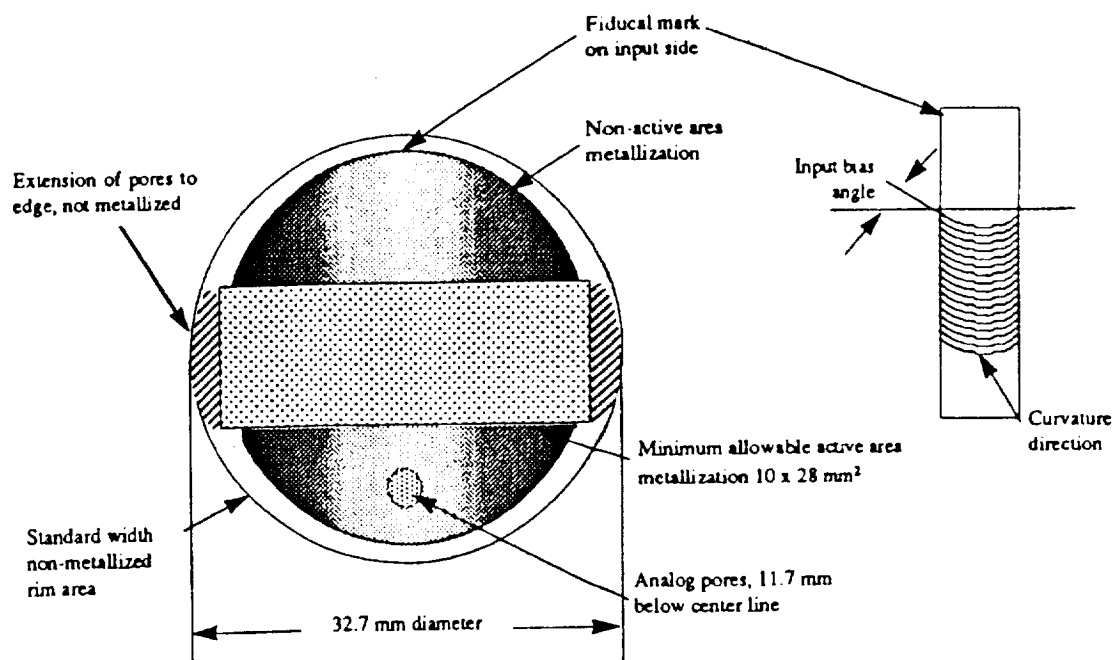
Fig. 7. Configuration of the SOHO Curved-channel MCP.

A prime consideration for the SOHO mission is that the detectors must have a very high dynamic range, both per pixel and from the total array. The optimized MCP configuration (see Fig. 7), which permits the use of a high-conductivity plate, and the new application-specific integrated circuit (ASIC) decode chip will be used in the flight detector systems and will significantly increase the maximum count rate capability from each pixel and from the total array. A 10% loss of detective quantum efficiency (DQE) at a single pixel rate in excess of 100 counts s^{-1} and a

total array rate in excess of 6×10^5 counts s^{-1} are predicted on the basis of measurements to date with the breadboard detector systems. Some of the key performance characteristics for the SOHO flight detector systems are listed in Table 2. Since both instruments will employ the detectors in imaging spectrometers for high-accuracy line profile and line-shift measurements, the geometric fidelity of the detectors is of paramount importance. An image of a US Air Force test target recorded with the SUMER breadboard detector system is shown in Fig. 8. These imaging tests have
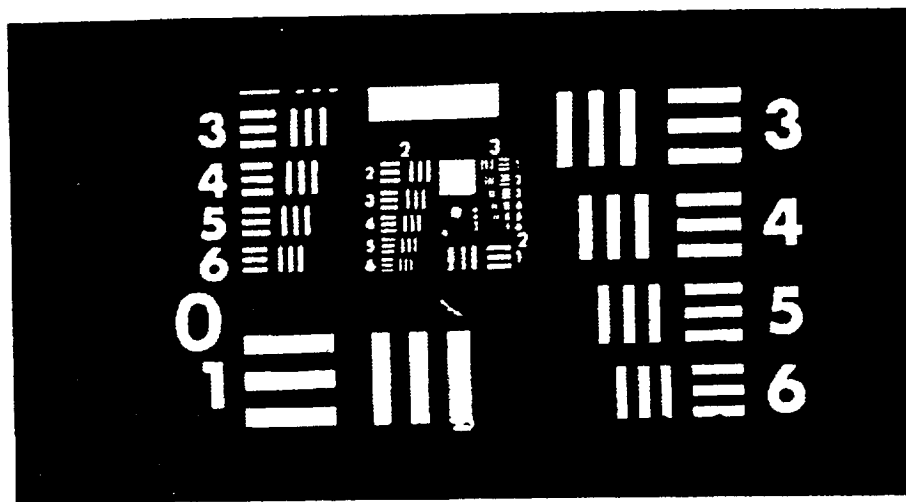
Fig. 8. Image of a test target recorded with (360 x 1024)-pixel SOHO MAMA breadboard detector system.

Table 2. Key SOHO MAMA Detector Performance Characteristics

Parameter	SUMER Detectors A & B	UVCS Sealed	UVCS Open	Units	Comments
Pixel resolution	25	25	25	Microns	FWHM
Crosstalk	< 2 (< 1 goal)	< 1	< 1	Percent Percent	Into pixels adjacent to an illuminated pixel
	4×10^{-2} (< 10^{-2} goal)	< 10^{-2}	< 10^{-2}	Percent Percent	Into a pixel two pixels or more from an illuminated pixel
Position sensitivity	< 2.5 (< 1.0 goal)	< 2.5	< 2.5	Microns Microns	Ability to identify the centroid of a spectral or spatial feature with a diameter of 30 microns FWHM (S/N limited)
Spatial linearity	± 25 per 26 mm (± 5 goal)	± 5.0 per 13 mm ± 5.0 per 4 mm	± 5.0 per 13 mm ± 5.0 per 4 mm	Microns Microns	Maximum variations dependent on curvature uniformity of C-plate MCP. C-plate is curved in 360 pixel direction.
Detective Quantum Efficiency (DQE):					Assumed to be 75 percent of photocathode quantum efficiency
Bare MCP	>7 (>10 goal)			Percent Percent	Windowless at 584 Å
KBr	>20 (>30 goal)			Percent Percent	Windowless at 1066 Å
MgF$_2$	>10 (>15 goal)			Percent Percent	Windowless at 584 Å
CsI		>7 through MgF$_2$ window >10 through MgF$_2$ window		Percent Percent	At 1164 Å At 1216 Å and 1304 Å
KBr			>20	Percent	Windowless at 584 Å and 1048 Å
Long wavelength cutoff: Bare MCP KBr MgF$_2$	1403 1700 1254			Å Å Å	Defined as wavelength where detective quantum efficiency (DQE) < 2 percent (< 1 percent goal)
CsI		< 1 at 2000 < 10^{-1} at 2500 < 10^{-2} at 3000 < 10^{-3} at 4000		Percent at Å Percent at Å Percent at Å Percent at Å	DQE
KBr			< 1 at 1700 < 10^{-1} at 2200 < 10^{-2} at 3200 < 10^{-3} at 4000	Percent at Å Percent at Å Percent at Å Percent at Å	DQE
Dark count rates: Bare MCP	< 0.02 (< 0.01 goal)			Counts mm^{-2}s^{-1} Counts mm^{-2}s^{-1}	At < 30° C ambient temperature
KBr	< 0.2 (< 0.1 goal)			Counts mm^{-2}s^{-1} Counts mm^{-2}s^{-1}	At < 30° C ambient temperature
MgF$_2$	< 0.07 (< 0.03 goal)			Counts mm^{-2}s^{-1} Counts mm^{-2}s^{-1}	At < 30° C ambient temperature
CsI		< 0.1		Counts mm^{-2}s^{-1}	At < 30° C ambient temperature
KBr			< 0.1	Counts mm^{-2}s^{-1}	At < 30° C ambient temperature
Single pixel maximum true count rate	150	35	35	Counts s^{-1} Counts s^{-1}	At 30 percent loss of DQE At 10 percent loss of DQE
Single amplifier maximum count rate	> 2.0 x 10^5 > 6.0 x 10^5			Counts s^{-1} (random) Counts s^{-1} (random)	At 10 percent loss of DQE At 30 percent loss of DQE
		> 2.4 x 10^4	> 2.4 x 10^4	Counts s^{-1} (random)	At 10 percent loss of DQE
Total array maximum count rate	> 3 x 10^5	> 3 x 10^5	> 3 x 10^5	Counts s^{-1} (random)	At 10 percent loss of DQE
Poisson response	5	5	5	Percent statistical significance level	Chi-square test comparing sample distribution to true Poisson distribution.

shown that the theoretical spatial resolution of 25 microns has been achieved and that the position sensitivity and spatial resolution are independent of both signal level and time. Small geometric nonuniformities are observed in the detector systems because of nonuniformities in the locations of the channels of the MCP. New techniques for manufacturing the curved-channel MCPs for the flight detector systems are expected to improve the geometric fidelity; however, the calibration of these spatial nonuniformities will be a major task in the detector characterization program.

4. STIS MAMA DETECTOR SYSTEMS

The NASA Goddard Space Flight Center's *Hubble* Space Telescope Imaging Spectrograph (STIS) is a multi-mode instrument designed for echelle spectroscopy, long-slit spectroscopy, slitless spectroscopy, photon time-tagging, and direct imaging. The instrument, as originally conceived, contains four detectors, each with formats of 2048 x 2048 pixels. Two Tektronix CCD's are used to cover the wavelength range from 300 to 1100 nm, and two MAMA detectors are used to cover the wavelength range from 300 nm down to the short wavelength limit of the MgF_2 window at 115 nm. The D-1 MAMA detector employs a CsI photocathode deposited on the front face of the MCP for optimum sensitivity in the range from 115 to 170 nm, and the

D-2 MAMA detector employs a Cs_2Te photocathode which will either be deposited on the MgF_2 window of the detector tube, or on the front face of the MCP, to cover efficiently the wavelength range from 115 to 300 nm. The format of the STIS detector is 2048 x 2048 pixels, with pixel dimensions of 25 x 25 microns[2], fabricated from four contiguous (1024 x 1024)-pixel arrays with a 3-pixel dead space, as shown in Fig. 9. This arrangement provides redundancy, because an electronics failure in one quadrant will not affect the performance of the remaining three quadrants, and also increases the dynamic range of the detector by a factor of 4, since each quadrant works as an independent detector system. The characteristics of the STIS detector are listed in Table 3.

The "bake and scrub" of the first 75-mm-format "chevron" MCP stack received from Philips Components, Inc. is now in progress in preparation for the first imaging tests with this detector system.

As a precursor to the work with the (2048 x 2048)-pixel detector, we have constructed a number of (1024 x 1024)-pixel detectors in the 40-mm-format MAMA detector tubes, with the anode array configuration shown in Fig. 10. A rectified image recorded with one of these detector systems is shown in Fig. 11.

Recently, the STIS instrument has been forced to descope, and the (1024 x 1024)-pixel MAMA detector system is now baselined for this instrument. As shown in
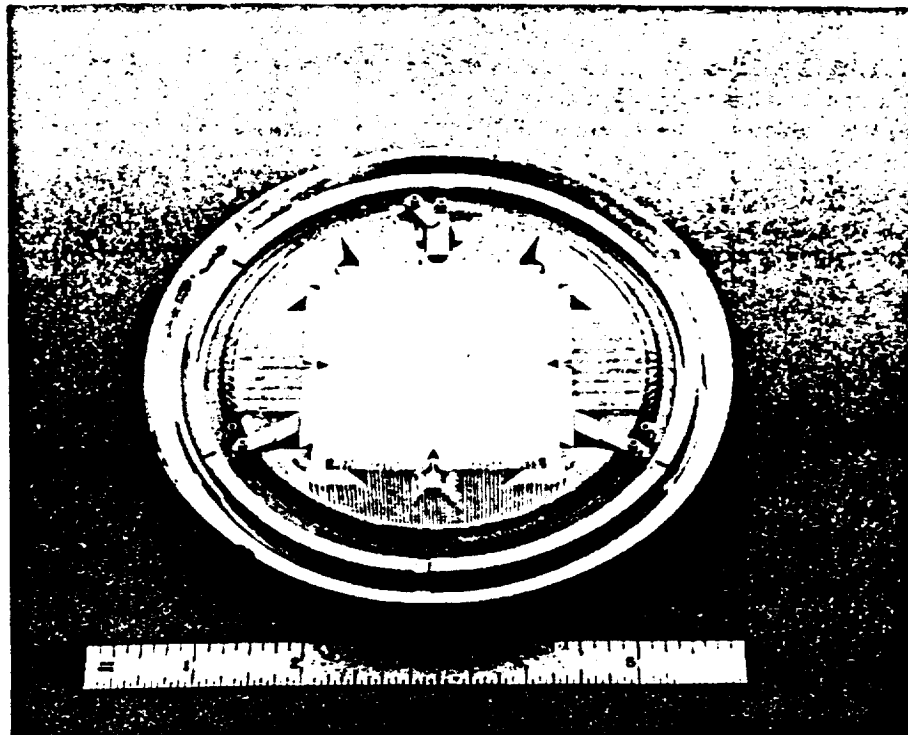
Fig. 9. STIS MAMA (2048 x 2048)-pixel anode array mounted on the 75-mm-format ceramic header. Pixel dimensions are 25 x 25 microns[2] and the dead space between the four (1024 x 1024)-pixel arrays is 3 pixels wide.

Table 3. Key Characteristics of the MAMA Detectors for STIS and FUSE/Lyman.

	STIS	FUSE
Pixel Format:	2048 x 2048 (4 x 1024 x 1024)	728 x 8096 (4 x 728 x 2024)
Pixel Dimensions:	25 x 25 microns^2	22 x 16 microns^2
Anode Array Active Area:	51.2 x 51.2 mm^2	16.0 x 32.4 mm^2 (x 4)
MCP Active Area:	52 x 52 mm^2	17 x 33 mm^2 (x 4)
MCP Pore Size:	10 microns	8 microns
Number of Amplifiers: (including analog output)	529 ([4 x 132] + 1)	577 ([4 x 144] + 1)
Photocathode Material:	CsI and Cs$_2$Te	KBr
Hybrid Amplifier and Discriminator	Yes	Yes
Gate Array Decode Circuits:	Yes	Yes
Openable Cover:	No	Yes

Fig. 10, the encoding electrode structures in the present (1024 x 1024)-pixel array have been located on only two sides of the active area to provide the capability for butting the four arrays together to form the (2048 x 2048)-pixel array. For the demonstration (1024 x 1024)-pixel MAMA detector now being fabricated for STIS, the encoding electrodes will be located on all four sides of the array, as for the SOHO array, in order to provide an optimized (1024 x 1024)-pixel structure for a very-long-duration flight mission.

5. FUSE/*LYMAN* MAMA DETECTOR SYSTEM

The prime EUV spectrograph of the FUSE instrument employs an aspheric concave diffraction grating in a Rowland circle mounting. Accordingly, the detector for this spectrograph must have a long rectangular format to cover the spectral range from 90 to 120 nm, with a spectral resolution ($\lambda/\delta\lambda$) of 30,000. In addition, the pixel size must
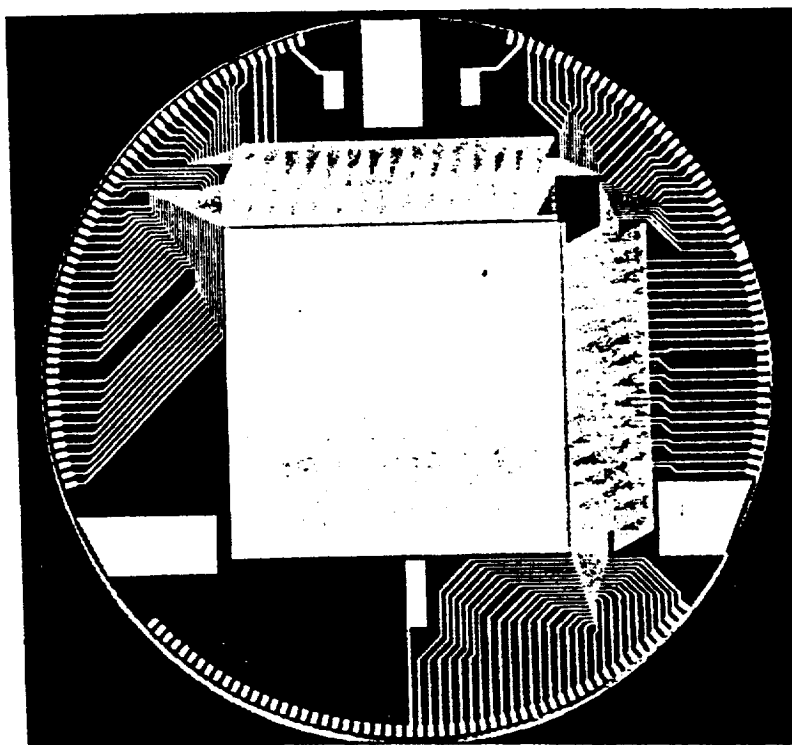
Fig. 10. STIS MAMA (1024 x 1024)-pixel anode array with 25 x 25 microns^2 pixels.
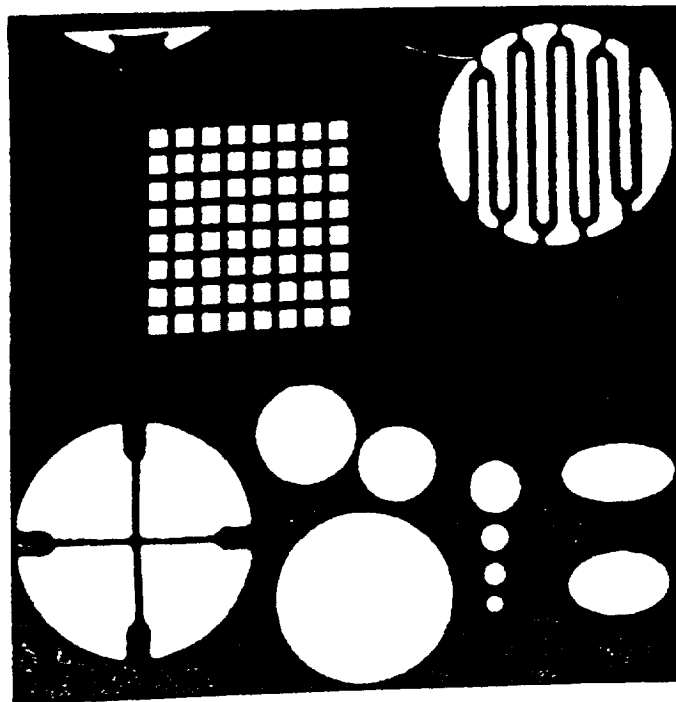
Fig. 11. Image recorded with STIS MAMA (1024 x 1024)-pixel detector system.

be smaller than 25 microns in order to obtain the required spectral resolution in a spectrograph with a size compatible with the limitations of the Explorer-class FUSE payload. The Phase A concept for the MAMA detector system is a (728 x 8096)-pixel detector composed of four contiguous (728 x 2024)-pixel arrays, each with 22 x 16 microns² pixels. The proposed configuration is shown in Fig. 12, and the key characteristics of the detector are listed in Table 3.

In order to validate the smaller pixel size in the MAMA detector system, as part of the FUSE Phase A study two (224 x 960)-pixel MAMA detector tubes with array pixel dimensions of 14 x 14 microns² were fabricated (see Fig. 13). One is a sealed tube with a bialkali visible light photocathode, and the other is an open, demountable tube which will be used for high-resolution studies at EUV wavelengths. The high-gain curved-channel MCP used with this array employs 8-micron-diameter channels on 10-micron centers, as shown in Fig. 13. Images of test targets taken with this detector system are shown in Fig. 14, and as shown in Fig. 15, it can be seen that the theoretical resolution of 14 microns is being achieved. Further evaluations of these detector systems in the open-structure mode at wavelengths below 120 nm will be undertaken later this year, using our toroidal grating imaging EUV spectrograph. High-resolution images will also be recorded using the new decode ASIC chip in order to determine if the resolution can be further improved to the theoretical limit of 10 microns set by the channel spacing of the MCP.
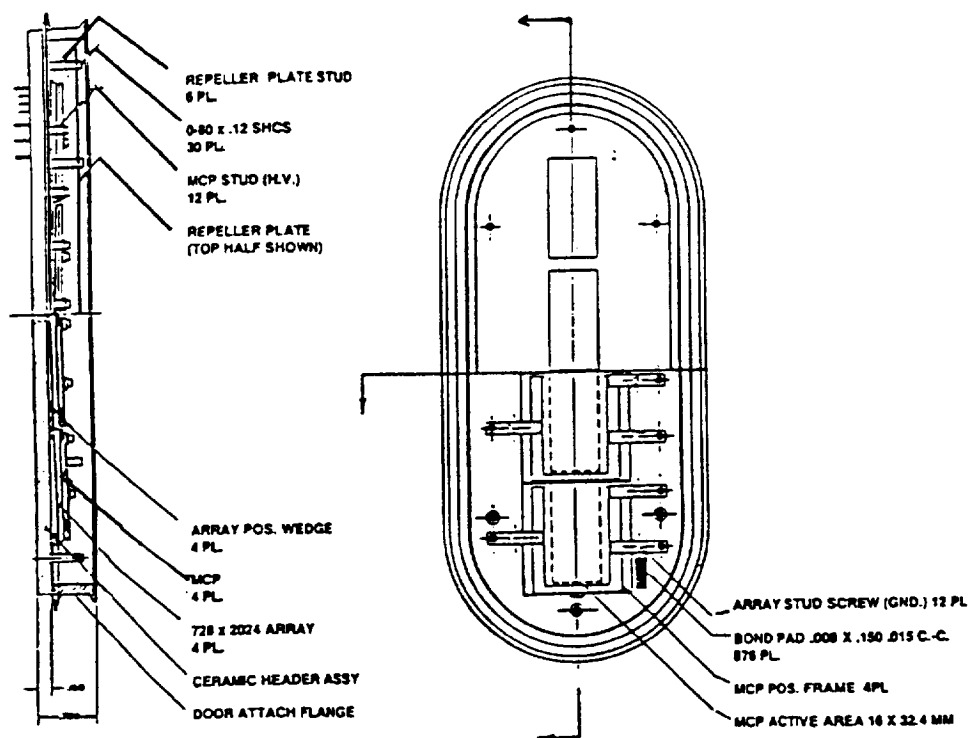
Fig. 12. Schematic of proposed FUSE MAMA detector composed of four contiguous (728 x 2024)-pixel arrays with 22 x 16 microns² pixels.
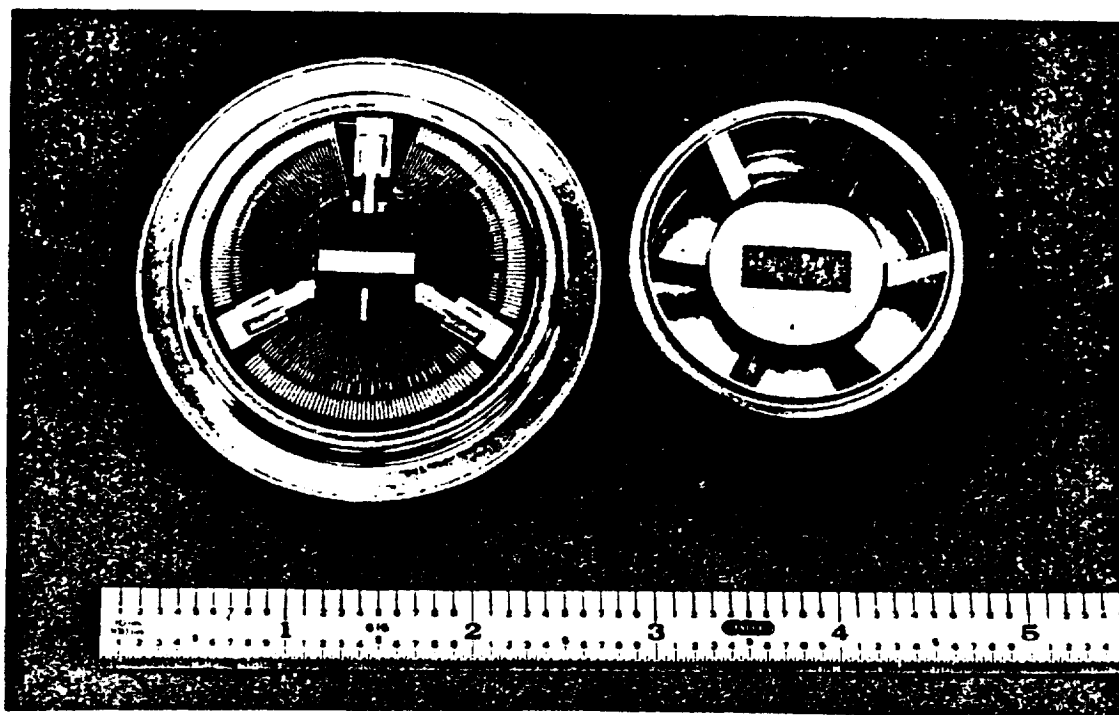
Fig. 13. Proof-of-concept FUSE MAMA (224 x 960)-pixel array with pixel dimensions of 14 x 14 microns^2. The curved-channel MCP has 8-micron-diameter channels on 10-micron centers.

6. THE ADVANCED TECHNOLOGY MAMA DETECTOR SYSTEM

The large amount of data being recorded with the MAMA detector systems, including those in the high-resolution imaging mode, have shown that the imaging characteristics of the detector system are being limited by the performance of the high-gain, curved-channel MCPs. In particular, nonuniformities of curvature and spatial distortions at the multi-fiber boundaries (see Fig. 16) are degrading the geometric fidelity of the MAMA anode array. In addition, the maximum single-pixel count rate of the MAMA is limited by the properties of the MCP. In order to
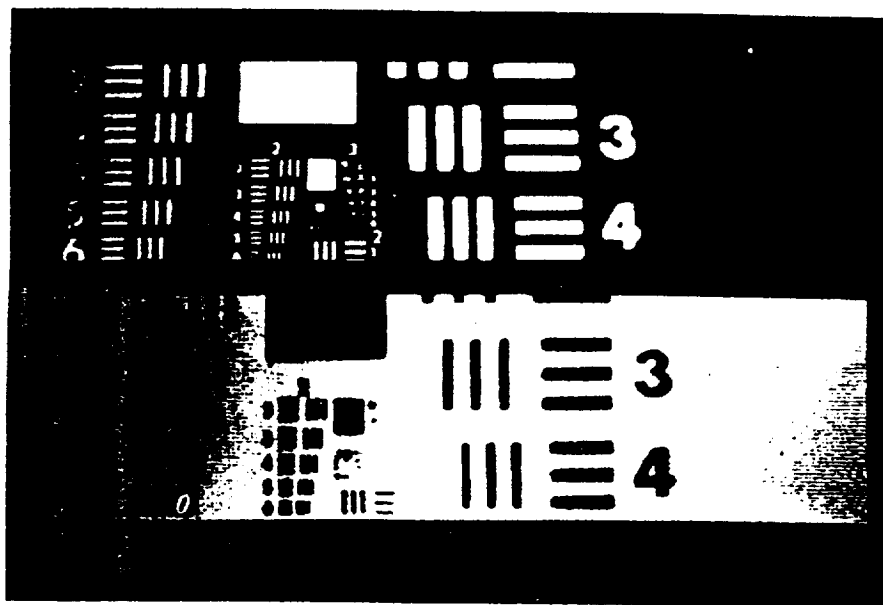
Fig. 14. Positive and negative images of a USAF test target taken at ultraviolet wavelengths with a (224 x 960)-pixel fine-fine array with 14 x 14 microns^2 pixels, and a curved-channel MCP with 8-micron-diameter channels. The sequence of bars in these images start with a resolution of 2.51 line pairs mm^{-1} (Group 0, element 3 on the right side of the images). The closest bars in the image have a resolution of 113.6 line pairs mm^{-1} (Group 5, element 6 to the left of the image centers).
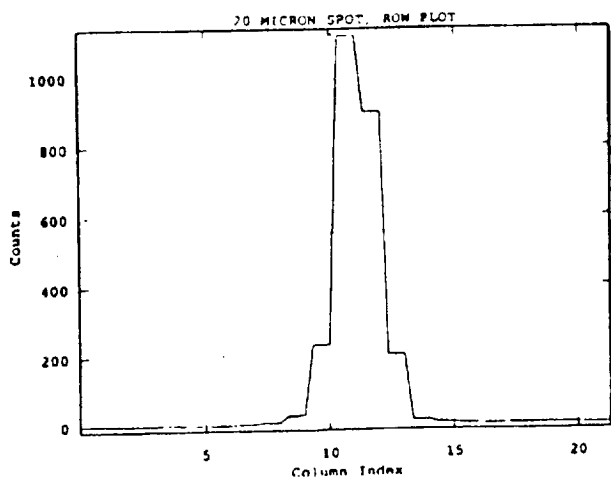
Fig. 15. A cut through an image of a 20-micron-diameter spot of ultraviolet light recorded with the 14 x 14 microns² pixel MAMA detector tube.

overcome these limitations, we have started investigations of improved MCPs fabricated from reduced lead silicate glass (RLSG) and, also, are conducting preliminary investigations into the possibility of fabricating advanced technology (AT) MCPs using silicon lithographic techniques.

For the RLSG MCPs, we plan to continue investigations of very small pore devices, and as part of the SOHO program, we are undertaking a series of developments at both Galileo Electro-Optics Corporation (GEOC) and Detector Technology, Inc., (Detech) in order to improve the degree of curvature and the uniformity of curvature in the present generation of MCPs. The potential advantages of the AT-MCPs are, first, the complete elimination of geometric distortions because of the precision of the lithographic fabrication process, and second, the possibility of producing a very-high-dynamic-range structure by fabrication of an optimized dynode structure. At this point in time, we have just started initial etch-tests with our first wafers in preparation for attempts to fabricate single-element and one-dimensional structures.
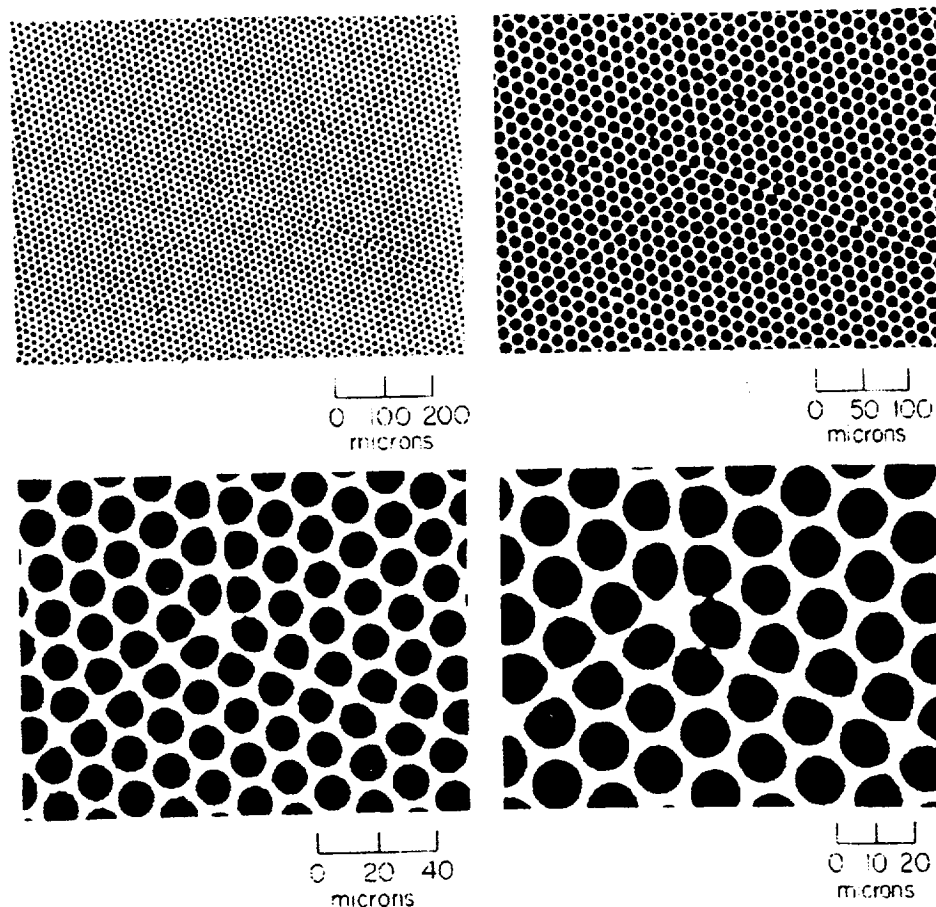
Fig. 16. Distortions of the interfaces of the multi-fibers in a curved-channel MCP.

7. ACKNOWLEDGEMENTS

8. REFERENCES

1. K. Wilhelm and the SUMER Investigation Team, "SUMER - Solar Ultraviolet Measurements of Emitted Radiation", European Space Agency *SP-1104*, pp. 31-37, November 1988.

2. J. Kohl and the UVCS Investigation Team, "UVCS - An Ultraviolet Coronagraph Spectrometer for SOHO", European Space Agency *SP-1104*, pp. 49-54, November 1988.

3. V. Domingo and A. I. Poland, "SOHO - An Observatory to Study the Solar Interior and the Solar Atmosphere", European Space Agency *SP-1104*, pp. 7-12, November 1988.

4. B. E. Woodgate and the Space Telescope Imaging Spectrograph Science Team, "Second Generation Spectrograph for the *Hubble* Space Telescope", *SPIE vol. 627 Instrumentation in Astronomy VI*, pp. 350-362, 1986.

5. "*Lyman* - The Far Ultraviolet Spectroscopic Explorer", NASA Phase A Study Final Report *NAS5-30339*, July 1989.

6. J. G. Timothy, "MAMA Detector Systems: A Status Report", *SPIE vol. 1158 Ultraviolet Technology III*, pp. 104-117, 1989.

7. J. G. Timothy, "Imaging Pulse-Counting Detector Systems for Space Ultraviolet Astrophysics Missions", to appear in *SPIE vol. 1494 Space Astronomical Telescopes and Instruments*, 1991.

8. D. B. Kasle, "Decoding Techniques for "fine-fine" Geometry Multi-Anode Microchannel Arrays", *SPIE vol. 932 Ultraviolet Technology II*, pp. 280-284, 1988.

9. D. B. Kasle, "High-resolution Decoding Techniques and Single-chip Decoders for Multi-anode Microchannel Arrays", *SPIE vol. 1158 Ultraviolet Technology III*, pp. 311-318, 1989.

10. D. B. Kasle and G. DeMicheli, "An Image Decoding ASIC for Space-Based Applications", to appear in *Proceedings of EURO ASIC 91*, IEEE Computer Society Press, 1991.

An Image Decoding ASIC for Space-Based Applications

David B. Kasle
NASA Goddard Space Flight Center
.and Stanford University
Stanford, California 94305

Giovanni DeMicheli
Center for Integrated Systems
Stanford University
Stanford, California 94305

Abstract

The multi-anode microchannel array (MAMA) is a photon counting detector with primarily astronomical applications which decodes the position of an event through coincidence discrimination. The decoding algorithm which associates a given event with the appropriate pixel is determined by the geometry of the anode array. A space-based realization of the MAMA detector requires that the decoding circuit be an Application Specific Integrated Circuit because of power, size and weight constraints. A 1.5 micron CMOS gate array version of the decoder has been fabricated and tested. The chip's development and characteristics are presented, and the ASIC decoder is contrasted with existing discrete component decoders in terms of size, speed, power, reliability, and operational flexibility. A new algorithm incorporated into the ASIC decoder which doubles the pixel spatial resolution is also described.

1. Introduction

The multi-anode microchannel array (MAMA) detector employs a photocathode for photon/electron conversion, a microchannel plate (MCP) for electron multiplication and an anode array combined with charge amplifiers for event detection. Digital decoding electronics interpret the charge amplifier outputs to determine the pixel position of an event. The block diagram of a MAMA detector is shown in Figure 1.

The current generation of MAMA detectors employ arrays which consist of two sets of interleaved anodes in a repeating series (see Figure 2). For historical reasons these are called "fine-fine" anode arrays. The first set of anodes consists of n anodes (which repeats for n+2 cycles) and the second set consists of n+2 anodes (which repeats for n cycles), resulting in a total of n*(n+2) pixels, where n must be even to insure unique decoding over the entire array. The interleaving of the two sets of anodes is analogous to two waves of slightly different frequency beating against each other for one complete cycle. Another pair of anode sets (not shown in Figure 2) of m and m+2 anodes run underneath and perpendicular to the first pair of anode sets, resulting in a total of m*(m+2) pixels in the perpendicular axis.

Figure 1. MAMA block diagram

The spread of the electron cloud due to a single photon event varies depending on the MCP's characteristics as well as bias voltages applied to the photocathode, MCP and anode array. The size of an electron cloud is quantized by the total number of anodes illuminated in a given axis, also referred to as the order of the fold. For example, a three-fold designates the situation in which three contiguous anodes are struck by sufficient numbers of electrons to have voltages greater than some user-specified threshold. A subsection of a scaled-down version of one axis of a fine-fine anode array (n=4) with one-, two-, three-, and four-folds is shown in Figure 2. The electron cloud spread must be sufficiently large to illuminate at least two anodes (a two-fold) in order to allow for the unique decoding of the position of the event. However, owing to size variations in the electron cloud from the MCP, the decoding algorithm must be capable of coping with higher-order folds. As Figure 2 illustrates, every higher-ordered fold can be reduced to an equivalent two-fold (that two-fold which occupies the same pixel as the higher-ordered fold); in the case of an odd-fold there are two possible equivalent two-folds. A decoder's function is to take an arbitrarily ordered fold and infer the correct pixel position of the

86
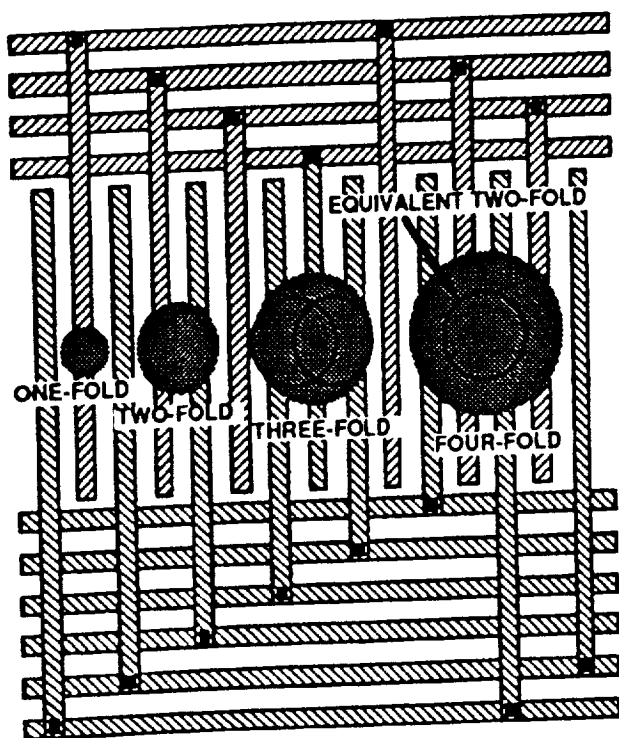
Figure 2. Fine-fine array single axis with multi-folds

event in the anode array. Since there is one decoder input for each anode, a single axis requires 2n+2 inputs. A typical value for n is 32, in which case the decoder must accommodate 66 inputs for a single axis of the detector. Because of the large number of inputs and complicated requirements for legal events, event decoding cannot easily be reduced to a single step process. The algorithm for event decoding is therefore divided into two stages: for anode encoding, which is the process of converting a k-fold into the equivalent two-fold for arbitrary k (see Figure 2); and pixel decoding, which is the process of translating the equivalent two-fold into the correct pixel position. Typically the anode encoding operation reduces the datapath width from 66 bits to 11 bits, thereby simplifying the pixel decoding operation.

To date, all MAMA detector systems have had circuitry composed of discrete parts, suitable for ground-based astronomy or use on sounding rockets. However, in the near future MAMA detectors will be employed in satellite systems such as the Solar Heliospheric Observatory (SOHO) and the Space Telescope Imaging Spectrograph (STIS). Space-based MAMA detectors require (relatively) radiation-hard decoding circuitry with lower power, weight, and size as well as higher reliability than their ground-based counterparts, preferably in the form of a single chip or a pair of chips. The obvious solution to this problem is an Application Specific Integrated Circuit (ASIC). An ASIC-based design has fewer components and therefore higher reliability than the same circuitry constructed with discrete parts. Power constraints dictate that the ASIC be of the CMOS type.

2. Design Methodology

Because of their relatively low cost, massive functional capacity and fast production time, CMOS gate arrays were selected as the target technology for space-based MAMA decoders, and LSI Logic was selected as the vendor by virtue of their high performance and high-capacity commercial and radiation-hard gate arrays. A prototype decoder has been designed and fabricated in commercial technology and has been succesfully evaluated in end-to-end system tests at Stanford University.

Major portions of the MAMA decoder chip were designed with computer-aided synthesis tools which are part of the Olympus system developed at Stanford University. The circuit was modeled in a high level language, called HardwareC, which was compiled into a logic netlist, then optimized and mapped into an interconnection of cells of the chosen target library. Specific blocks like ROMs were explicitly declared in the HardwareC description so that their functionality and modularity were preserved through the synthesis process. The gate level netlist was generated in a format compatible with the LSI Logic Design and Simulation (LDS) tools which were used for gate level simulation and electrical evaluation of the circuit. The LDS tools allowed critical areas of the circuitry to be identified and fine-tuned to optimize performance. In addition, the LDS tools performed the simulation of all legal anode input combinations for two-, three-, four-, five- and six-folds over a wide range of temperature and supply voltage conditions. Finally chip-finishing tasks such as floorplanning and assignment of bonding pads were performed with the LDS tools. The design was then fabricated in 155 pin and 299 pin PGA packages; the larger package incorporates a large number of diagnostic test points for testing and characterization purposes and the smaller package is targeted for satellite flight systems.

3. Circuit Description

A simplified block diagram of the gate array realization of the MAMA decoder is shown in Figure 3. Transient inputs (which are not always precisely coincident in time or of uniform length due to sensitivity and speed variations in the individual charge amplifiers) are stored in edge-triggered flip-flops. Because the decoder inputs are connected directly to the clock pins of the flip-flops, the flip-flops act as edge-triggered latches. The occurrence of an event in any one of the input lines initiates a sequence of actions within the timing and control state machine. The maximum allowed delay between the earliest and latest charge amplifier outputs from a single event is called the amplifier skew. After a user-controlled period corresponding to the amplifier skew, the state machine connects the Q outputs with the D inputs of the input flip-flops, thereby freezing the state

Figure 3. MAMA decoder gate array simplified block diagram

of the flip-flops. Multiple blocks of parallel combinational logic perform the anode encoding (mentioned earlier in Section 1) of the inputs into the equivalent two-fold. After another user-specified period (corresponding to the time required for anode encoding), the state machine then stores the equivalent two-fold in a midpoint pipeline data register, at which time pixel decoding begins and a new event may start the anode encoding process. The pipelined architecture improves pulse-pair resolution, which measures the minimum time between separate detectable events. The pixel decoding process is performed by ROM Look-Up Tables (LUTs) which convert the equivalent two-fold output of the midpoint register into the corresponding pixel location. The equivalent two-fold is simultaneously decoded in parallel for array sizes of 224, 360, 960 and 1024 pixels. All four pixel outputs are multiplexed into the correct pixel address according to the actual MAMA detector anode array size in use. A pipelined output register maintains a valid pixel output while new inputs are propagating through the circuit.

Numerous options and features are incorporated into the MAMA decoder ASIC. The gate array design can accommodate active high or active low charge amplifier outputs, and decodes any user selected combination of two-, three-, four-, five- and/or six-folds. The ability of the user to examine any order of fold individually is important in characterizing detector performance; an example of this is illustrated in Figure 4, which shows the measured frequency of occurrence of the various orders of folds as a percentage of the total event frequency. Since odd-ordered folds have two possible equivalent two-folds and therefore correspond to two possible pixels, they

can be handled by choosing the left pixel, choosing the right pixel, or alternating between the two. Inputs and outputs are latched and the amplifier skew window as well as the number of clock cycles to allow for anode encoding are both user controllable; this allows the decoder ASIC to accommodate a variety of amplifier skews and to tolerate speed degradation due to high temperature, low supply voltage or radiation exposure. The state machine automatically recovers from illegal states. The chip can accommodate clock speeds as high as 50 MHz. The four on-chip ROMs are independent and could be made redundant in a space-qualified system, thereby providing backup ROMs in the event of radiation damage to part of the circuit. The gate array can decode a single axis of 224, 360, 960 or 1024 pixels; the decoder ASIC thus serves as a universal decoder, capable of interpreting the

Figure 4. Distribution of multi-folds

output of any of the currently existing MAMA detectors which utilize the fine-fine anode arrays. For example, a 360 by 1024 pixel MAMA detector would require one decoder chip for the 360 pixel axis and another for the 1024 pixel axis. Although both of these decoder ASICs are identical, one chip would act as the timing master and the other chip would serve as the timing slave, with communication between the two carried out by dedicated handshake lines. In the event that the slave detects an event input when the master does not, the slave can send a handshake signal to the master causing the master to reset itself as well as the slave, leaving both chips ready to accept new event inputs.

There are several error prevention features built into the decoder ASIC. One-folds and simultaneous events are both rejected automatically because they cannot be associated with any given pixel through coincidence discrimination. Similarly, folds whose order is greater than six and occurrences of events containing any non-contiguous anodes are also rejected. Because the inputs are edge-triggered, malfunctioning charge amplifier outputs which are stuck at zero or one are ignored. Metastability protection is designed into both the data path and the state machine; the expected mean time between metastability failures is two billion years given a worst case scenario of a 50 MHz clock and a 6.25 MHz event rate at 125 °C combined with a 4.5 volt supply. Schmitt trigger input buffers are employed wherever possible for improved noise immunity, and control inputs have built-in pull-up or pull-down resistors to force them to a default operational configuration should they somehow be disconnected.

The 155 pin and 299 pin ceramic PGA packages which house the gate arrays are shown in Figure 5. Both of the PGA's are constructed in the cavity downwards configuration to improve heat handling characteristics. A pair of gate arrays requires less than 0.4 watts to perform decodes with a pulse-pair resolution of 160 nanoseconds when clocked at 50 MHz. Each gate array is composed of approximately 23,000 gates, of which 18,000 are ROM LUTs. Normal commercial fabrication was used for initial evaluation of the gate array, and it is not yet clear whether fabrication of the chips in radiation-hardened technology will be necessary. The expected lifetime radiation dose for the STIS and SOHO systems is less than 30 kRad. The spacecraft electronics will be exposed to a wide variety of energetic particles, including a significant number of massive particles such as protons. A 299 pin decoder ASIC was subjected to proton bombardment for a total dose of 30 kRad and survived in good working order. The chip was tested both during and after the proton exposure, and a sample combinational logic path was monitored for variations in propogation delay. After exposure to 30 kRad, the propogation delay had increased by 8%, well within tolerable limits.

In contrast to the ASIC version of the MAMA decoder, an example of the latest generation of decoder constructed at the Ball Aerospace Systems Group from discrete components is shown in Figure 6. The discrete component decoder is more than two times slower and uses more than six times the power of its ASIC counterpart. The discrete component decoder occupies 8.4
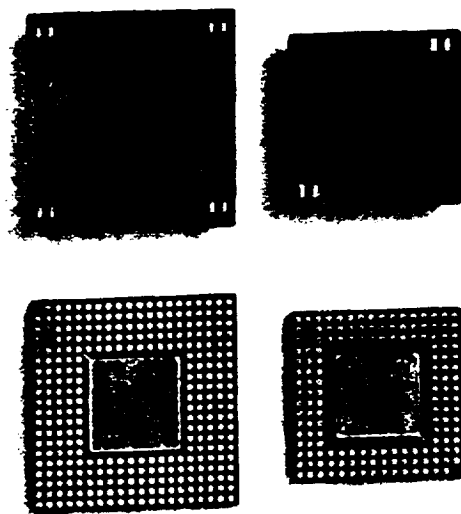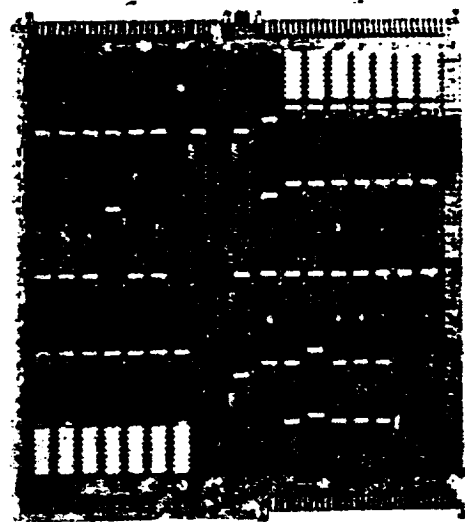

Figure 5. MAMA ASIC decoder PGA packages

Figure 6. Discrete component MAMA decoder

times the area of the ASIC, thereby presenting a larger cross section to radiation and making it less reliable for space-based applications, as well as less desirable from the standpoint of size and weight. In addition the ASIC has greater flexibility in that it can decode any size array and can accommodate either active high (used in older systems) or active low (used in next generation systems) charge amplifier outputs. The discrete component decoder is limited to a single array size and can only be used with active high charge amplifier outputs. Table 1 summarizes the major differences between the ASIC and discrete component decoders.

	ASIC DECODER	DISCRETE DECODER
POWER	0.4W	2.5 W
PULSE-PAIR RESOLUTION	160 nS adjustable	350 nS fixed
SIZE	35 cm2	295 cm2
DECODES	224 x 960 360 x 1024 1024 x 1024	360 x 1024
FOLDS SELECTABLE?	YES	NO
METASTABILITY PROTECTION?	YES	NO
CHARGE AMP OUTPUTS	active high or active low	active high only

Table 1. ASIC decoder vs. discrete component decoder

4. High Resolution Decoding

A special feature incorporated into the MAMA decoder ASIC is high resolution decoding. In a standard MAMA detector pixel size is equal to the spacing of the anodes, but the spatial resolution of the MCP is generally about twice that of the anode array. This implies that the detector is capable of spatial resolution twice as high as that achieved with the original fine-fine decoding scheme. It is possible to increase the resolution of the detector without changing the detector itself, but only by altering the readout electronics. One technique for doubling the spatial resolution is called even-odd discrimination and this algorithm is incorporated into the decoder ASIC; this is the first time it has ever been employed in any decoding circuit. Even-odd discrimination involves discriminating between even-folds and odd-folds to generate a single least significant bit (LSB), thereby doubling the detector's spatial resolution. The value of the least significant bit depends on whether the throw left or the throw right option is used for handling odd-ordered folds. In the case of throw left, the LSB is high only if the event is an odd-

fold, whereas in the case of throw right, the LSB is high only if the event is an even-fold and is low otherwise. This operation can be performed in parallel with the standard decoding procedure with no loss of decoder speed and necessitates the addition of minimal hardware to the standard decoding circuitry (although the memory size must be quadrupled). Figure 7 illustrates normal resolution (top) versus high resolution achieved with even-odd discrimination (bottom). Standard pixels are twice the size, and span from the center of one anode to the next, whereas the even-fold pixels are centered between the anodes and the odd-fold pixels are centered on the anodes themselves. The performance of this algorithm depends in part on the number of even-folds being comparable to the number of odd-folds. MAMA detectors can usually be configured to satisfy this condition, as was illustrated in Figure 4 in which 52% of the events detected were even-folds and 48% were odd-folds. The even-odd discrimination algorithm has been succesfully tested in preliminary imaging experiments at Stanford University. Figure 8 shows two spots, created by placing a mask with two holes in front of an ultraviolet light source, imaged by the decoder ASIC. The smaller pair of spots on the left were imaged in normal resolution mode; the pair of larger spots on the right are the same two spots imaged in high resolution mode with even-odd discrimination. Thus far, higher spatial resolution has clearly been achieved, and more precise tests are being carried out to measure the exact degree of resolution.
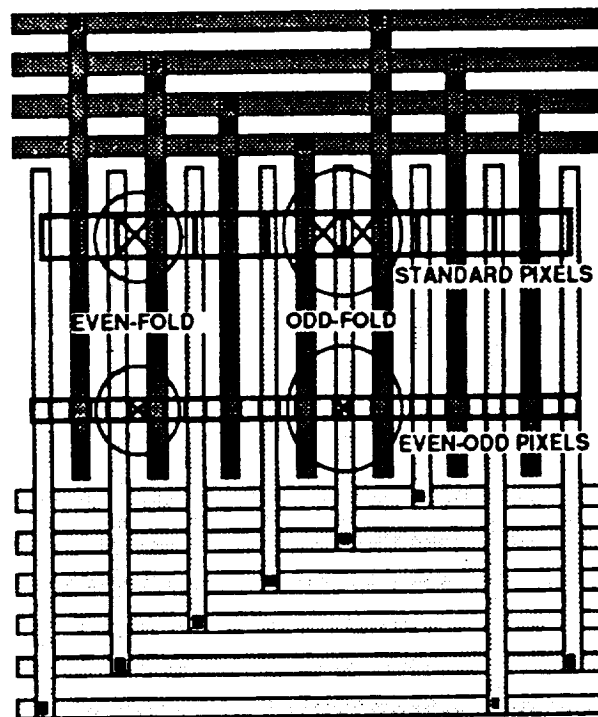

Figure 7. High resolution : even-odd discrimination
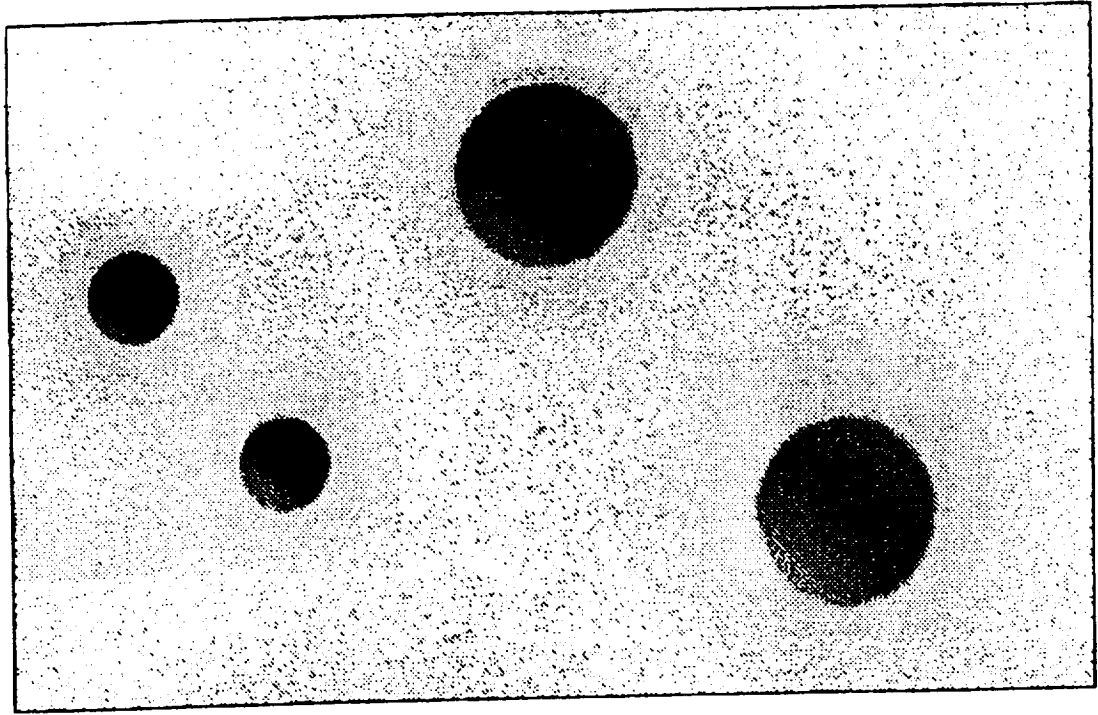
Figure 8. Normal resolution image of two spots combined with high resolution image of the same two spots

5. Summary

An ASIC version of a MAMA digital decoder, suitable for space-based applications, has been designed, fabricated and tested successfully. The design was fabricated in commercial 1.5 micron CMOS gate array technology, and the chip is smaller, faster, incorporates more features and uses less power than previous discrete component decoders. The chip has performed well in preliminary radiation exposure tests and incorporates a new algorithm which doubles the detector spatial resolution.

Acknowledgements

References

1. D.B. Kasle , "Decoding Techniques for fine-fine-geometry multi-anode microchannel arrays", SPIE Ultraviolet Technology II Vol. 932, pp. 280-284, 1988.

2. D.B. Kasle , "High resolution decoding techniques and single chip decoders for multi-anode microchannel arrays", SPIE Ultraviolet Technology III Vol. 1158, pp. 311-318, 1989.

3. G. De Micheli, D. Ku, F. Mailhot, T. Truong, "The Olympus Synthesis System for Digital Design", IEEE Design & Test, October 1990.pp. 37-53

4. J.G. Timothy, "Electronic readout systems for microchannel plates," IEEE Transactions on Nuclear Science Vol. NS-32, No. 1, pp. 427-432, 1985.

5. J.G. Timothy and R.L. Bybee, "High-resolution pulse-counting array detectors for imaging and spectroscopy at ultraviolet wavelengths," SPIE Ultraviolet Technology Vol. 687, pp. 109-116, 1986.

6. J.S. Morgan, et. al., "High Time-Resolution Imaging with the MAMA Detector Systems," SPIE Instrumentation in Astronomy Vol. 1235, No. 7, pp. 347-356, 1990.

Multi-anode microchannel array detector systems for space astrophysics missions

J Gethyn Timothy

Center for Space Science & Astrophysics, Stanford University ERL 314, Stanford, CA 94305, USA

ABSTRACT: The multi-anode microchannel arrays (MAMAs) are now under active development for use on a number of space ultraviolet astrophysics missions at far ultraviolet and extreme ultraviolet wavelengths. Visible-light versions of these detector systems are also being used for high-time-resolution studies, including speckle interferometry, at ground-based telescopes. The configurations of the different MAMA detector systems are described, and the use of custom application-specific integrated circuits (ASICs) in the electronics to improve the performance characteristics is discussed.

1. INTRODUCTION

We are currently fabricating and characterizing a number of different MAMA detector systems for use on space astrophysics missions at far ultraviolet (FUV) and extreme ultraviolet (EUV) wavelengths between about 300 and 28 nm. We are utilizing visible-light versions of these detector systems for scientific studies at ground-based telescopes at wavelengths between about 800 and 300 nm.

Open, open with openable cover, and sealed (360 x 1024)-pixel MAMA detector systems, with pixel dimensions of 25 x 25 microns^2 and MgF$_2$, KBr, and CsI photocathodes will be used in the Solar Ultraviolet Measurements of Emitted Radiation (SUMER) (Wilhelm *et al* 1988) and the Ultraviolet Coronagraph Spectrometer (UVCS) (Kohl *et al* 1988) instruments on the ESA/NASA SOHO mission (Domingo and Poland 1988), scheduled for launch in 1995. Prototype very-large-format (1024 x 1024)- and (2048 x 2048)-pixel MAMA detector systems with pixel dimensions of 25 x 25 microns^2 and CsI and Cs$_2$Te photocathodes are currently under test and in fabrication for the NASA Goddard Space Flight Center's *Hubble* Space Telescope Imaging Spectrograph (STIS) (Woodgate *et al* 1986), a second-generation instrument scheduled for in-orbit installation in 1997. Under this program a (256 x 1024)-pixel MAMA detector system has recently been flown twice on sounding rockets for FUV imaging of galaxies at wavelengths between about 125 and 170 nm. A (1024 x 1024)-pixel prototype FUV detector system will be flown on a sounding rocket in the coming year. Finally, proof-of-concept sealed and open (224 x 960)-pixel MAMA detector systems, with pixel dimensions of 14 x 14 microns^2 are under test as part of the FUSE/Lyman Phase B Study (NASA Final Report 1989). Visible-light versions of the (224 x 960)-pixel detector system and the (1024 x 1024)-pixel detector system are being utilized at ground-based telescopes in a number of high-time-resolution studies, including speckle interferometry.

2. MAMA DETECTOR SYSTEM

Details of the construction and mode-of-operation of the MAMA detector system have recently been presented in the literature (Timothy 1989 and 1991a). Briefly, the components of a MAMA detector consist of, first, the tube assembly and, second, the associated analog and digital electronic circuits. The MAMA detector tube, which can be sealed with a window or used in an open-structure configuration,

contains a single, high-gain, curved-channel microchannel plate (MCP) electron multiplier with the photocathode material deposited on, or mounted in proximity focus with the front surface. Electrodes are mounted in proximity focus with the output surface of the MCP to detect and measure the positions of the electron clouds generated by single photon events (see Figures 1 and 2). The charge collected on the anode electrodes is amplified and shaped by high-speed amplifier and discriminator circuits.

Figure 1. Schematic of the imaging MAMA detector system.

Digital logic circuits respond to the simultaneous arrival of the shaped signals from several of these electrodes in each axis, which are arranged in groups to uniquely identify a x b pixels in one dimension with only a + b amplifier and discriminator circuits. In the imaging MAMA detector tube, two arrays are mounted in tandem with orthogonal orientations, so that the positions of the detected photons can be sensed in two dimensions. In this configuration (a x b)^2 pixels can be uniquely identified with only 2 x (a + b) amplifier and discriminator circuits. Thus, a (1024 x 1024)-pixel array, for example, requires a total of only 128 amplifier and discriminator circuits. The two layers of anode electrodes in the imaging arrays are insulated from each other by a SiO_2 dielectric layer. The dielectric between the upper layer electrodes is etched away to allow the low energy (~30 eV) electrons in the charge cloud from the MCP to be collected simultaneously on both arrays. Details of the latest MAMA anode-array geometries and position-encoding algorithms can be found in the literature (Kasle 1988 and 1989; Kasle and DeMicheli 1991).

3. SOHO MAMA DETECTOR SYSTEMS

Figure 2. Schematic showing details of the curved-channel MCP and the imaging multi-layer anode array used in the MAMA detector tubes.

The MAMA detectors for the SUMER and UVCS instruments on the SOHO mission have a high degree of commonality, but also significant differences dictated by the scientific needs of the two instruments (Timothy 1991b). All of the detectors have formats of 360 x 1024 pixels and pixel dimensions of 25 x 25 microns^2. The other key parameters are listed in Table 1.

The open detector with the openable cover is utilized for both SUMER and UVCS. The purpose of the cover is to protect the photocathode materials and the high-gain MCP from contamination during the years of the instrument and spacecraft integration and test programs. The different subassemblies which make up the openable-cover SOHO MAMA

Table 1. Key Parameters of the MAMA Detectors for the SUMER and UVCS Instruments on the SOHO Mission.

|	SUMER		UVCS	
	Detector A	Detector B	Detector 1	Detector 2
Pixel Format	360 x 1024	360 x 1024	360 x 1024	360 x 1024
Pixel Dimensions	25 x 25 μm^2	25 x 25 μm^2	25 x 25 μm^2	25 x 25 μm^2
Anode Array Active Area	9.0 x 25.6 mm^2	9.0 x 25.6 mm^2	9.0 x 25.6 mm^2	9.0 x 25.6 mm^2
MCP Active Area	10 x 27 mm^2	10 x 27 mm^2	10 x 27 mm^2	10 x 27 mm^2
MCP Pore Size	12 microns	12 microns	12 microns	12 microns
Number of Amplifiers (including analog output)	105 (104+1)	105 (104+1)	105 (104+1)	105 (104+1)
Photocathode Material	MgF$_2$ and KBr	MgF$_2$ and KBr	CsI	KBr
Configuration	Openable cover	Open	Sealed	Openable cover

detector system are shown in Figure 3a, and the detector block diagram is shown in Figure 3b.

The back-up detector in the SUMER instrument is open, and does not have the openable cover in order to eliminate the effects of any systematic design problem in the openable cover mechanism. Great care will need to be taken, however, to ensure that the photocathodes and the MCP in this detector are not contaminated during the prelaunch integration and test programs.
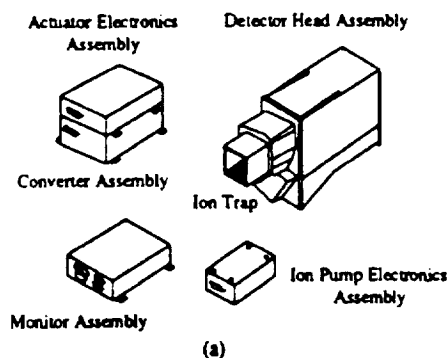
Both of the SUMER detectors employ a dual photocathode structure. Two photocathode materials are deposited on the front face of the curved-channel MCP: KBr for a high quantum efficiency at wavelengths between 80 and 160 nm, and MgF$_2$ for both a high quantum efficiency at wavelengths between 40 and 80 nm and also to provide rejection of radiation at, and around, the wavelength of the strong H Lyman α 121.6 nm emission line.

The UVCS MAMA sealed detector, designed to observe scattered H Lyman α 121.6 nm radiation from the solar corona, has a MgF$_2$ window and a CsI photocathode deposited on the front face of the MCP. The sealed detector is sensitive to radiation in the wavelength band from 113 to > 135 nm. Because of the optical configuration of the UVCS spectrometer, the sealed UVCS MAMA tube must have a thin "wafer" configuration, with the distance from the front surface of the MgF$_2$ window to the CsI photocathode being no more than 7 mm.
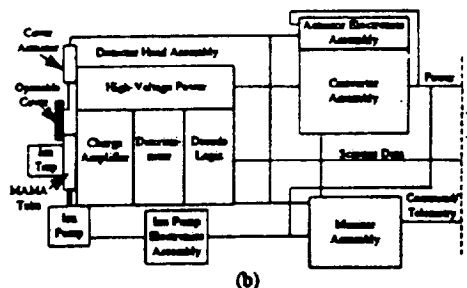
The second UVCS MAMA detector, which is open with an openable cover and is identical in configuration to the SUMER MAMA detector, is used to observe radiation at shorter wavelengths. This detector has a KBr

Figure 3. Openable-cover SOHO MAMA detector system. (a) System subassemblies. (b) System block diagram

photocathode for maximum sensitivity at wavelengths between 93 and 107 nm.

A prime consideration for the SOHO mission is that the MAMA detectors must have a very high dynamic range, both per pixel and from the total array. The active area of the curved-channel MCP is rectangular to match the active area of the anode array which permits the use of a high-conductivity plate in order to increase the maximum count rate limit of each pixel. The dynamic range is further enhanced by the use of the new amplifier/discriminator application-specific integrated circuit (ASIC) which can operate with a discriminator threshold as low as 2 x 10⁴ electrons pulse⁻¹. In addition, the new ASIC decode chip will be used in the flight detector systems to increase the total array count rate capability. A 10% loss of detective quantum efficiency (DQE) at a single pixel rate in excess of 100 counts s⁻¹, and a total array rate in excess of 6 x 10⁵ counts s⁻¹ are now predicted on the basis of measurements to date with the breadboard detector systems. Imaging tests with the breadboard detector systems have shown that theoretical spatial resolution of 25 microns full-width-at-half-maximum (FWHM) has been achieved, and that the position sensitivity and spatial resolution are independent of both signal level and time. New techniques for manufacturing the curved-channel MCPs for the flight detector systems are expected to further improve the geometric fidelity.

4. STIS MAMA DETECTOR SYSTEMS

The STIS is a multi-mode instrument designed for echelle spectroscopy, long-slit spectroscopy, sinless spectroscopy, photon time-tagging, and direct imaging. The instrument, as originally conceived, contains four detectors, each with formats of 2048 x 2048 pixels. Two Tektronix CCDs are used to cover the wavelength range from 300 to 1100 nm, and two MAMA detectors are used to cover the wavelength range from 300 nm down to the short wavelength limit of the MgF₂ window at 115 nm. The short-wavelength MAMA detector employs a CsI photocathode deposited on the front face of the MCP for optimum sensitivity in the range from 115 to 170 nm, and the long-wavelength MAMA detector employs a CsTe photocathode which will either be deposited on the MgF₂ window of the detector tube, or on the front face of the MCP to cover efficiently the wavelength range from 115 to 300 nm.
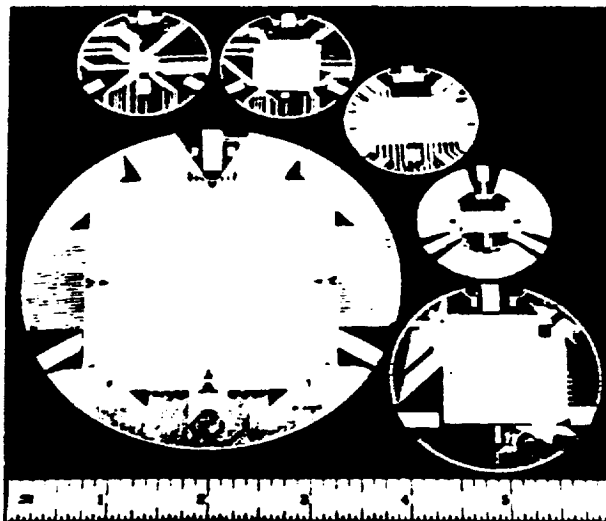
The format of the STIS detector is 2048 x 2048 pixels with pixel dimensions of 25 x 25 microns², fabricated from four contiguous (1024 x 1024)-pixel arrays with a 3-pixel dead space, as shown in Figure 4. This arrangement provides redundancy because an electronics failure in one quadrant of the array will not affect the performance of the remaining three quadrants.

Figure 4. MAMA anode arrays. Clockwise from top left: two high-dynamic-range test arrays: the SOHO (360 x 1024)-pixel array; the FUSE (224 x 960)-pixel evaluation array; and the STIS (1024 x 1024 - and (2048 x 2048)-pixel arrays.

and also increases the dynamic range of the detector by a factor of four, since each quadrant works as an independent detector system.

The key characteristics of the STIS detector are listed in Table 2.

Recently the STIS instrument has been forced to descope and the (1024 x 1024)-pixel MAMA detector system (see Figure 4), which we have fabricated as a precursor to the fabrication of the (2048 x 2048)-pixel system, is now baselined for this instrument. Imaging tests with prototype versions of these detectors are now underway, and preparations are being made for the flight of a (1024 x 1024)-pixel detector system on a sounding rocket in November 1991.

Table 2. Key Characteristics of the MAMA Detectors for STIS.	
Pixel Format:	2048 x 2048 (4 x 1024 x 1024)
Pixel Dimensions:	25 x 25 microns²
Anode Array Active Area:	51.2 x 51.2 mm²
MCP Active Area:	52 x 52 mm²
MCP Pore Size:	10 microns
Number of Amplifiers: (including analog output)	529 ([4 x 132] + 1)
Photocathode Materials:	CsI and Cs₂Te

5. FUSE/*LYMAN* MAMA DETECTOR SYSTEM

The prime EUV spectrograph of the FUSE instrument employs an aspheric concave diffraction grating in a Rowland circle mounting. Accordingly, the detector for this spectrograph must have a long rectangular format to cover the spectral range from 90 to 120 nm, with a required spectral resolution ($\lambda/\Delta\lambda$) of 30,000. In addition, the pixel size must be smaller than 25 microns in order to obtain the required spectral resolution in a spectrograph with a size compatible with the limitations of the Explorer-class FUSE payload. The Phase A concept for the MAMA detector system is a (728 x 8096)-pixel detector composed of four contiguous (728 x 2024)-pixel arrays, each with 22 x 16 microns² pixels. The proposed configuration is shown in Figure 5, and the key characteristics of the detector are listed in Table 3.

In order to validate the smaller pixel size in the MAMA detector system as part of the FUSE Phase A study, two (224 x 960)-pixel MAMA detector tubes with pixel dimensions of 14 x 14 microns² were fabricated (see Figure 4). The high-gain curved-channel MCP used with this array employs 8-micron-diameter channels on 10-micron centers. Images of test targets taken with this detector system have
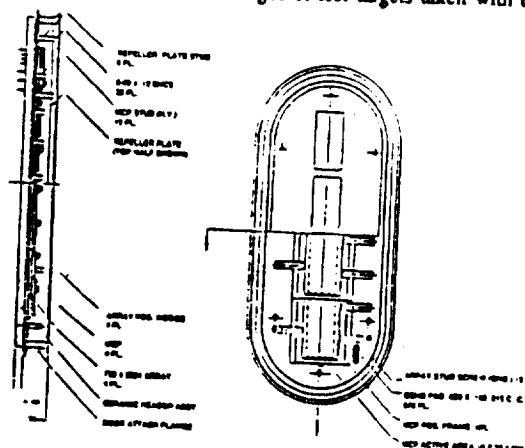

Figure 5. Schematic of proposed FUSE MAMA detector composed of four contiguous (728 x 2024)-pixel arrays with 22 x 16 microns² pixels.

demonstrated the theoretical spatial resolution of 14 microns. Further evaluations of this detector system in the open-structure mode at wavelengths below 120 nm will be undertaken later this year, using our toroidal grating imaging EUV spectrograph. High-resolution images will also be recorded with the visible-light detector tube in the laboratory and at ground-based telescopes using the new decode ASIC chip in order to determine if the resolution can be further improved to the theoretical limit of 10 microns set by the channel spacing of the MCP.

Table 3. Key Characteristics of the MAMA Detector for FUSE Lyman.

Pixel Format:	728 x 8096 (4 x 728 x 2024)
Pixel Dimensions:	22 x 16 microns²
Anode Array Active Area:	16.0 x 32.4 mm² (x 4)
MCP Active Area:	17 x 33 mm² (x 4)
MCP Pore Size:	8 microns
Number of Amplifiers: (including analog output)	577 ([4 x 144] + 1)
Photocathode Material:	KBr

6. IMAGING TESTS WITH THE MAMA DETECTOR SYSTEMS

The visible-light versions of the MAMA detector systems are being used in conjunction with our speckle camera in an ongoing program of speckle interferometry and speckle imaging at ground-based telescopes. The MAMA has a unique capability to identify the time of arrival of each detected photon to an accuracy significantly better than a microsecond. The pulse-pair resolution of the custom ASIC decode chip is better than 160 ns, and the temporal resolution of our time-tag system used for ground-based observations is currently set at 10 μs. The results of deconvolving the images of unresolved binary stars are shown in Figure 6. The advantage of taking this type of data with the MAMA detector system is that the integration time can be optimized for the maximum signal-to-noise ratio during the data-reduction phase of the program, rather than during the observing time at the telescope. A plot of the dependence of the signal-to-noise ratio on the integration time is shown in Figure 7.

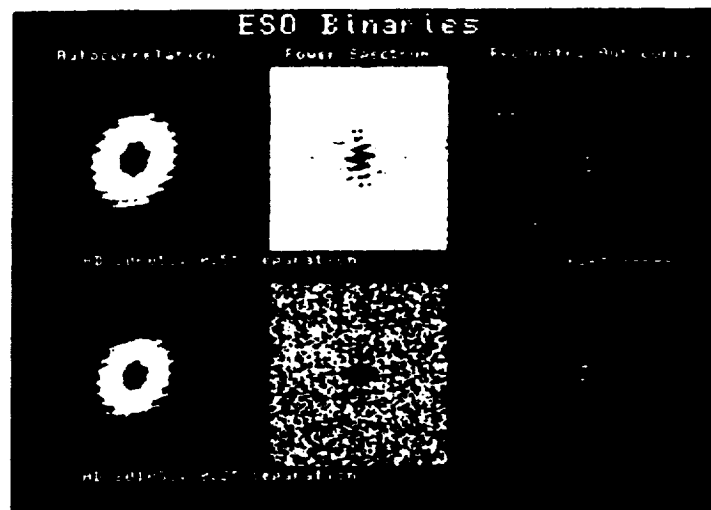An ultraviolet image of the galaxy NGC 4449 recorded on the last flight of the NASA Goddard Astronomy

Figure 6. Deconvolved images of unresolved binary stars recorded with the MAMA detector in the time-tag mode.
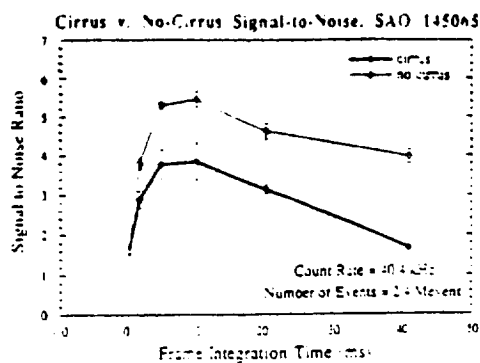
Figure 7. Dependence of the signal-to-noise ratio of the speckle data on the integration time used to bin the time-tag data stream.

Sounding Rocket Payload (ASRP), is shown in Figure 8. Again, the time-tag mode of recording data was used to produce this image and to correct for the effects of the drifts of the sounding rocket pointing system.

As described recently by Kasle (1989) and Kasle and De Micheli (1991), the new custom decode ASIC chip enables us to use more sophisticated algorithms for decoding the positions of the detected photons. In this way, it is possible to double the resolution of the existing 25-micron pixel and 14-micron pixel MAMA detector systems, provided that the center-to-center spacing of the channels in the curved-channel MCP is small enough. The first tests of this technique have been recently undertaken,

using one of the (360 x 1024)-pixel SOHO breadboard detector systems with 25 x 25 microns^2 pixels. The improvement in resolution using the new high-resolution decode algorithm can be seen in the images of a US Air Force test target shown in Figure 9. The measured spatial resolution of this system increased from 25 microns to 16 microns FWHM, which is close to the theoretical limit of 15 microns expected from the spacing of the channels in the curved-channel MCP. Further detailed tests of this high-resolution system are now continuing, with particular emphasis on the stability of the high-resolution imaging point-spread-function as functions of both time and signal level. On the basis of these measurements, we can now foresee the use of MAMA detector systems with spatial resolutions as high as 7 to 8 microns, provided that curved-channel MCPs with channel diameters of 6 microns or less can be successfully fabricated.

Figure 8. Image of the starburst irregular galaxy NGC 4449 in the wavelength range from 125 to 170 nm recorded with a (256 x 1024)-pixel MAMA detector system on the NASA Goddard Astronomy Sounding Rocket Payload. The image has been corrected for drifts in the rocket attitude control system using the MAMA time-tag data stream.

Low Resolution (2x Magnification)   High Resolution
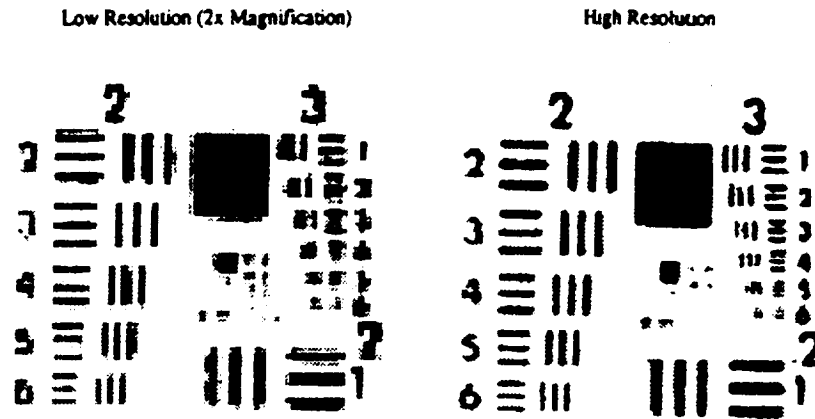

Figure 9. Normal-resolution image of groups 2 through 7 of a US Air Force test target and a high-resolution image of the same target recorded with a SOHO MAMA breadboard detector system.

7. ACKNOWLEDGEMENTS

8. REFERENCES

Domingo and Poland A I 1988 *European Space Agency* SP-1104 7-12

Kasle D B 1988 *SPIE Ultraviolet Technology II*, 932 280-284

Kasle D B 1989 *SPIE Ultraviolet Technology II*, 1158 311-318

Kasle DB and DeMicheli G 1991 *Proceedings of EUROPEAN ASIC 91* (IEEE Computer Soc Press)

Kohl J and the UVCS Investigation Team 1988 *European Space Agency* SP-1104 49-54

NASA Phase A Study Final Report 1989 NAS5-30339

Timothy J G 1989 *SPIE Ultraviolet Technology III* 1158 104-117

Timothy J G 1991a *SPIE Space Astronomical Telescopes and Instruments* 1494 (in press)

Timothy J G 1991b *SPIE EUV, X-Ray & Gamma Ray Instrumentation for Astronomy II* 1549 (in press)

Wilhelm K and the SUMER Investigation Team 1988 *European Space Agency* SP-1104 31-37

Woodgate B and the Space Telescope Imaging Spectrograph Science Team 1986 *SPIE Instrumentation in Astronomy VI* 627 350-362

Photon-counting detector systems: Current status and future prospects

J Gethyn Timothy

Center for Space Science and Astrophysics, Stanford University, ERL 314, Stanford,
CA 94305, USA

ABSTRACT: Imaging photon-counting detector systems are under active development for
a wide range of ground-based and space applications. In particular, the use of imaging
photon-counting detector systems at Far Ultraviolet (FUV) and Extreme Ultraviolet (EUV)
wavelengths is now of great importance in view of the current availability of very-high-
efficiency solar-blind photocathode materials. A critical component of many of these
imaging photon-counting detector systems is the high-gain Microchannel Plate (MCP). In
this paper, the current development status of each of the different imaging photon-counting
detector systems is described, and the prospects for future developments are discussed. The
present development status of the high-gain MCP and the prospects for future developments
of this imaging electron multiplier system are also discussed in some detail.

1. INTRODUCTION

Imaging photon-counting detector systems are under active development for a wide range of
ground-based and space applications. These types of detector systems have important
capabilities which are not available in the integrating solid-state imaging detector systems such
as the Charge Coupled Devices (CCDs). In particular, photon-counting detectors with random
read-out systems operate with zero read noise and have a very-fast event-timing capability
which can be used for many types of image reconstruction and image stabilization. Further,
unlike the CCDs which are sensitive to a very broad range of energies, the response of the
imaging photon-counting detector systems can be tailored to a specific wavelength or energy
range by the use of a suitable photocathode material. For this reason, imaging photon-counting
detector systems are currently the best detectors for use at Far Ultraviolet (FUV) and Extreme
Ultraviolet (EUV) wavelengths since the use of solar-blind photocathodes allows a highly
effective level of discrimination against longer wavelength radiations, which for many
investigations, particularly in the field of astrophysics, have intensities orders of magnitude
higher than those in the short wavelength region. The efficient use of bare CCDs at FUV and
EUV wavelengths will require the development of high-efficiency short-pass ultraviolet filters,
which are currently not available.

In this paper, the current state of development of the different types of imaging photon-
counting detector systems are reviewed, and the prospects for future developments of the
different systems discussed.

2. IMAGING PHOTON-COUNTING DETECTOR SYSTEMS

Three principal types of imaging photon-counting detector systems are under development for
use at ultraviolet and visible-light wavelengths. These are the electron-bombarded solid-state
arrays, the MCP-intensified solid-state arrays, and the direct electronic read-out MCP imaging
arrays (see Figure 1). At higher energies in the soft x-ray region, the bare silicon CCD can
also be used as an imaging photon-counting detector, since sufficient electron-hole pairs are
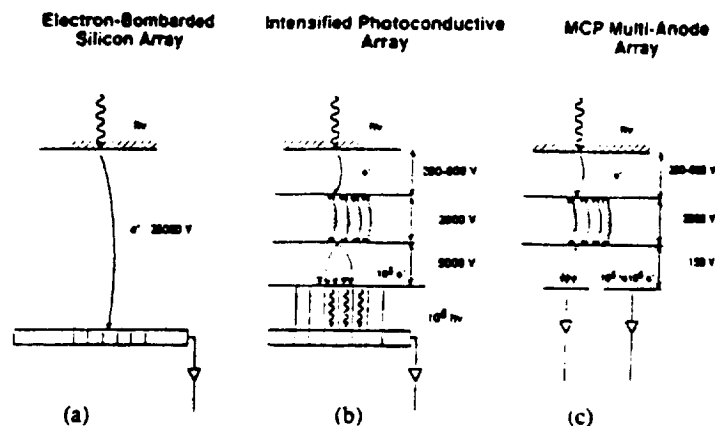produced by the absorption of a high-energy photon to permit single photon detection.

Figure 1. Schematics of the three principal types of photon-counting detector systems.

In the electron-bombarded solid-state arrays (see the schematic in Figure 1a), such as the Digicons currently being used in the Faint Object Spectrograph (FOS) and the Goddard High-Resolution Spectrograph (GHRS) on the *Hubble* Space Telescope (HST) (Brandt *et al.*, 1979), the photoelectron from a semi-transparent photocathode is accelerated to a potential of the order of 25 kV, impacting a solid-state diode array or CCD and producing sufficient electron-hole pairs for single photon detection. A number of problems associated principally with the survival of the solid-state diode array or the silicon CCD during the high temperatures required to condition the detector tube prior to photocathode processing have hampered the development of the visible-light and ultraviolet versions of these detectors. In addition, the magnetic focusing system of the Digicon, which permits the image to be scanned over the diode array, is a bulky and rather complex system for space applications (see Figure 2). Nevertheless, the FOS and GHRS Digicons have excellent performance characteristics (see, for example, Eck, Beaver and Shannon, 1985) and are performing outstandingly well in orbit (Troeltzsch *et al.*, 1991, Harms and Fitch, 1991). Open-structure electron-bombarded CCDs with rugged opaque oblique-focus photocathodes are also now being utilized for space applications at FUV and EUV wavelengths (Carruthers *et al.*, 1988, Lawrence and Joseph, 1988).
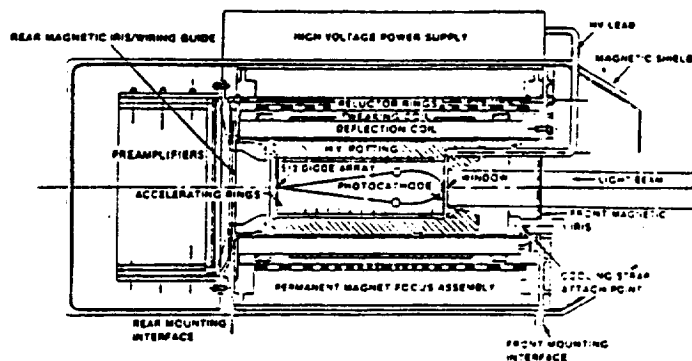

Figure 2. Schematic of the *Hubble* Space Telescope Digicon detector (from Brandt *et al.*, 1979).

Because of the complexities of the electron-bombarded arrays, the major development thrust at this time is, accordingly, on the MCP-intensified solid-state array or CCD array (ICCD), shown in the schematic in Figure 1b. This type of detector is modular in construction and is proving to be highly versatile since a number of different CCD configurations are currently commercially available and proximity-focused MCP image-intensifier tubes (see Figure 3) are readily available from the military night-vision industry (see, for example, Van Geest and Stoop, 1985). A number of groups are also developing special large-format MCP image-intensifier tubes specifically for use with photon-counting ICCD detector systems (see, for example, Norton *et al.*, 1988).
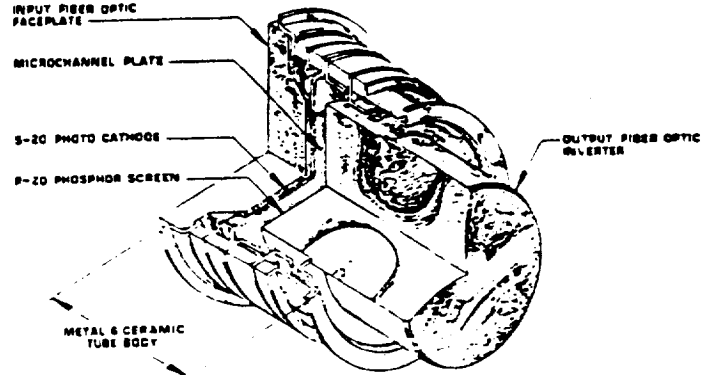

Figure 3. Schematic of a Generation II proximity-focused MCP image intensifier tube
(courtesy of Litton Corp.)

In the ICCD the primary photoelectron is amplified by the MCP and the output cloud of electrons re-converted to visible-light photons by means of a phosphor. These photons are then coupled to the CCD pixels by means of a fiber-optic light guide or by a lens. The principal limitation of this type of detector system as a photon-counting imaging detector is the low dynamic range (< 10 counts pixel^{-1} s^{-1}) caused by the phosphor decay time and the CCD cycle time, together with the need for centroiding and prior frame subtraction to produce a true, high-resolution photon-counting detector system. Nevertheless, this type of imaging photon-counting detector system is currently being widely used at all wavelengths from the near infrared to the extreme ultraviolet and proposals have been made for the fabrication of very-large-format detectors of this type using mosaics of fiber-optics and CCDs, as shown in Figure 4 (Williams and Weistrop 1983, Roberts, Tuohy and Dopita, 1988).

The most actively developed imaging photon-counting detector systems today, particularly for space astrophysics missions, are the direct electronic readout imaging MCP detector systems of the type shown in the schematic in Figure 1c. A number of high-spatial-resolution electronic readout systems are currently under development, with the characteristics listed in Table 1. These fall into two major categories: analog readout systems, in which the position of the detected photon is determined by charge-ratio or electronic-timing techniques, and the discrete-pixel detector systems, in which the output charge from the MCP is collected on a precision array of discrete electrodes. The principal analog readout systems are the Resistive Anode Encoder (RAE), the Wedge-and-Strip Array (WS), the Spiral Anode Array (SPAN) and the Delay Line Array (DADA). These arrays are shown in Figure 5. In the Resistive Anode Encoder (Wiza, 1979, Barstow *et al.*, 1985) (see Figure 5a), the charge from the MCP is collected on a resistive sheet and the position of the detected photon determined either by the ratio of charges collected on four electrodes at the edges of the sheet, or by rise-time discrimination from the coincident detected pulses.
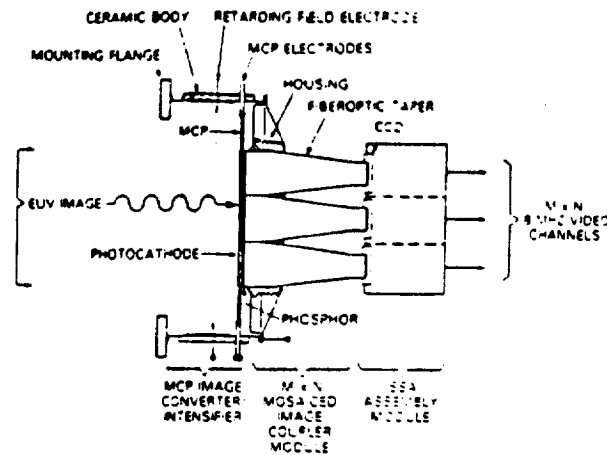
Figure 4. Schematic of a mosaic MCP-intensified CCD detector system (from Williams and Weistrop, 1983).

Table 1. Characteristics of Electronic MCP Readout Systems.

Class	Type	Format (Pixels)	Spatial Resolution	Reference
Analog	Resistive Anode (RAE)	450 x 450	100 x 100	Barstow et al., 1985
	Wedge and Strip (WS)	575 x 575	70 x 70	Siegmund et al., 1988
	Spiral Anode (SPAN)	1000 x 1000	25 x 25	Lapington et al., 1990
	Delay Line (DADA)	4000 x 375	25 x 40	Siegmund et al., 1989
Discrete Electrode	Coded Anode Converter (CODACON)	64 x 1024	100 x 25	Lawrence, 1991
		256 x 256	40 x 40	
	Multi-Anode Microchannel Array (MAMA)	2048 x 2048	25 x 25	Timothy, 1991
		224 x 960	14 x 14	
Hybrid	High-Resolution Imager (HRI)	4000 x 4000	25 x 25	Murray and Chappell, 1985

The resolution of this type of readout system is limited by shot noise in the resistive anode, and it is now being replaced by the Wedge-and-Strip Array (Martin et al., 1981, Siegmund et al., 1988) (see Figure 5b) which operates by dividing charge between conducting electrodes and produces a higher spatial resolution. The Spiral Anode Array (Lapington et al., 1990) is an enhanced derivative of the Wedge-and-Strip Array. The most advanced of all of the analog readout systems under development at this time are single and double Delay-Line Arrays (Siegmund et al., 1989) shown in Figures 5c and d. In the single delay line (Figure 5c) the x position is determined by the difference in the arrival times of the pulses at each end of the delay line while the y position is determined by charge division from the Wedge-and-Strip electrode pattern. The double delay line (Figure 5d) operates in an identical manner but the use of two interleaved delay lines allows the use of all the available charge for both the x and y position identifications.
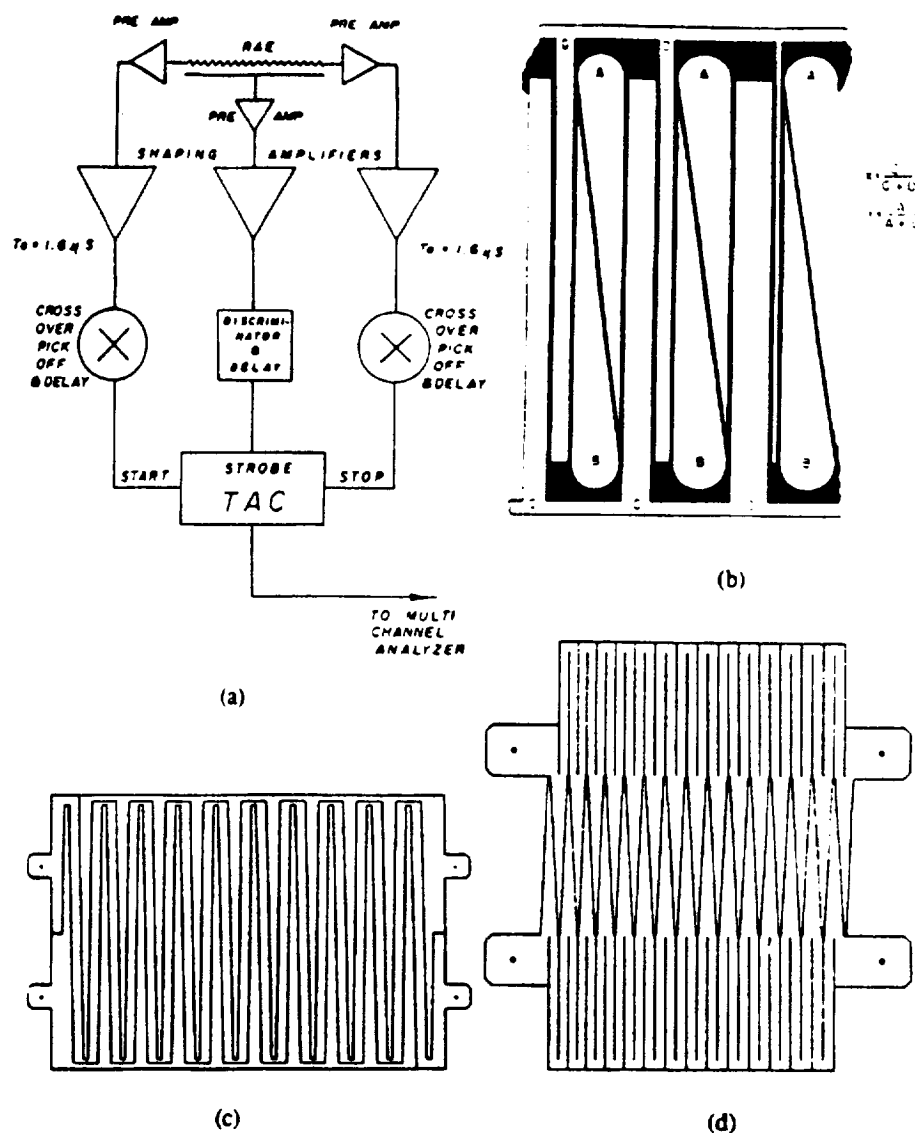
Figure 5. Schematics of analog MCP electronic readout systems.

a. Resistive Anode Encoder (RAE) (from Wiza, 1979).
b. Wedge-and-Strip Array (WS) (from Martin *et al.*, 1981).
c. Single Delay Line Array (DADA) (from Siegmund *et al.*, 1989).
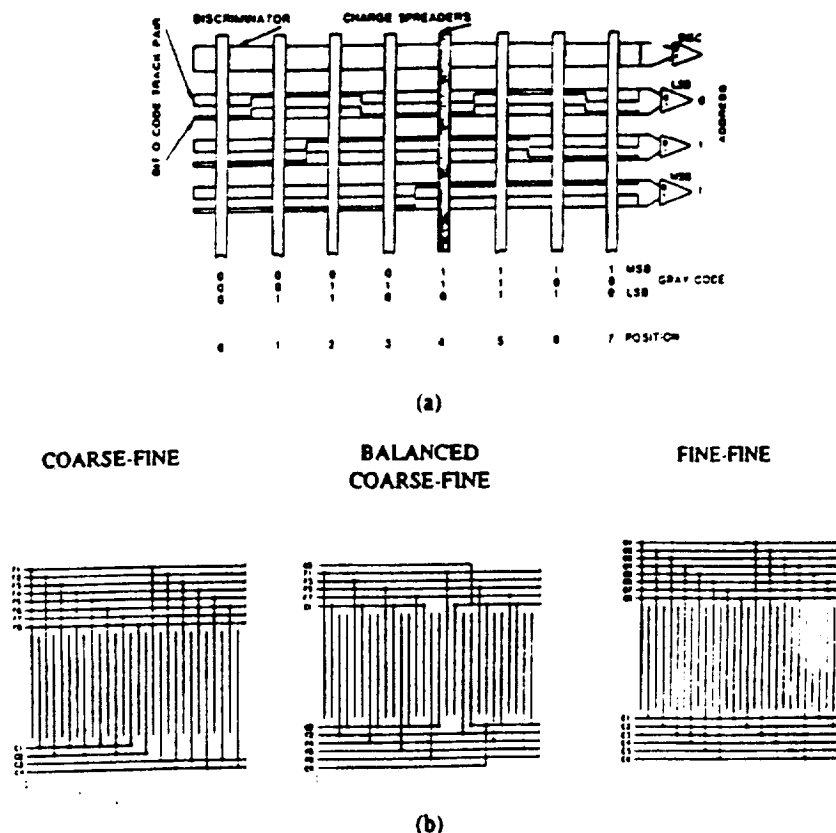d. Double Delay Line Array (DADA) (from Siegmund *et al.*, 1989).

(a)

COARSE-FINE   **BALANCED COARSE-FINE**   **FINE-FINE**

(b)

Figure 6. Schematics of discrete-pixel MCP electronic readout systems.

a. The Coded Anode Converter (CODACON) array shown in one dimension (from McClintock *et al.*, 1982).

b. Coarse-fine, balanced coarse-fine and fine-fine Multi-Anode Microchannel Arrays (MAMAs) shown in one dimension (from Timothy *et al.*, 1989).

Two types of discrete-pixel readout systems are under development at this time: the Coded Anode Convertor (CODACON), under development at the University of Colorado (see Figure 6a), and the Multi-Anode Microchannel Array (MAMA) detector system under development at Stanford University (see Figure 6b). Both one-dimensional and two-dimensional CODACON detectors have been utilized at FUV and EUV wavelengths (see, for example, McClintock *et al.*, 1982). In the CODACON array, charge collected on a pixel electrode is capacitively coupled into output electrodes arranged in a Gray code pattern. The simultaneous detection of coincident pulses on the coded anodes coupled to the amplifiers defines a bit pattern which identifies the spatial location of the detected charge cloud in one dimension. Two orthogonal arrays are utilized in a two-dimensional imaging CODACON detector. The future development of this particular readout system is at present limited to the needs of the EUV spectrometer on the *Cassini* mission to Saturn and Titan (Lawrence, 1991).

The imaging MAMA detector system is currently under active development at this time for a number of flight missions (Timothy *et al.*, 1989, Timothy, 1991). In the MAMA detector two sets of interleaved anodes coupled in groups to each amplifier are used to uniquely identify the position of the charge cloud in one dimension. As for the CODACON, two orthogonal arrays are used in the two-dimensional imaging MAMA detector systems. As shown in Figure 6b, a number of different MAMA anode configurations are in use; the fine-fine configuration providing at this time the optimum performance characteristics.

A hybrid electronic readout detector system which combines the analog and discrete pixel techniques is the High-Resolution Imager (HRI) which was flown on the *Einstein* Observatory (Kellogg *et al.*, 1976) and is now under development in an advanced version for the Advanced X-ray Astrophysics Facility (AXAF) (Murray and Chappell, 1988). This system uses two orthogonal arrays of discrete wires linked by resistors with every eighth wire connected to an amplifier, and employs interpolation algorithms to determine the exact location of the detected charge cloud to a precision of a fraction of the wire spacing (see the schematic in Figure 7).
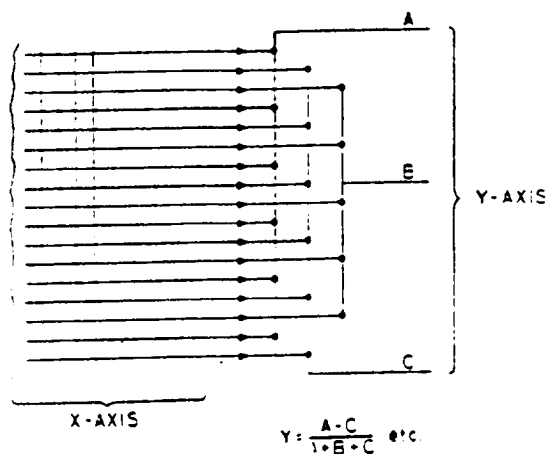

Figure 7. Schematic of the position-encoding technique of the *Einstein* High Resolution Imager. Every eighth wire is connected to an amplifier.

In the soft x-ray region, deep-depletion CCDs which can provide simultaneous position and energy information are currently under active development (see, for example, Janesick *et al.*, 1988, Garmire *et al.*, 1988, Lumb and Holland, 1988). The progress towards the goal of simultaneous high energy resolution and high Detective Quantum Efficiency (DQE) with x-ray CCDs has been reviewed recently by Fraser (1989). The spatial and energy resolutions of the CCDs are potentially significantly superior to those of gas detectors, such as the Imaging Proportional Counter (IPC), and these gas detectors can now be expected to be superseded by the CCDs for future x-ray photon-counting imaging applications.

One ingenious photon-counting detector that falls out of the mainstream of current development programs is the Precision Analog Photon Address (PAPA) detector (see the schematic in Figure 8). This detector utilizes a set of 9 + 9 photomultiplier tubes mounted behind coded masks to provide the spatial information for a format of 512 x 512 pixels (Gonsiorowski, 1986). A conventional image-intensifier tube is used to amplify the signal from the detected photon in order to provide an adequate signal for each of the photomultiplier tubes.
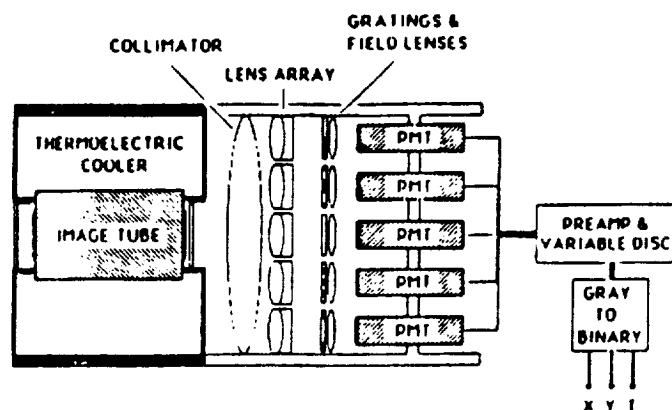
Figure 8. Schematic of the PAPA detector system (from Gonsiorowski, 1986).

3. HIGH-GAIN MICROCHANNEL PLATES (MCPS)

The high-gain microchannel MCP forms the basis of most of the imaging photon-counting detector systems currently under development for use at wavelengths from the near-infrared to the soft x-ray region. Three types of high-gain MCP structures are currently being utilized. These are the chevron MCP stack, the Z-plate MCP stack, and the curved-channel, or C-plate, MCP, as shown in Figure 9. The MCPs in the chevron and Z-stacks are fabricated from conventional straight channels and ion-feedback inhibition takes place at the boundary between the plates.
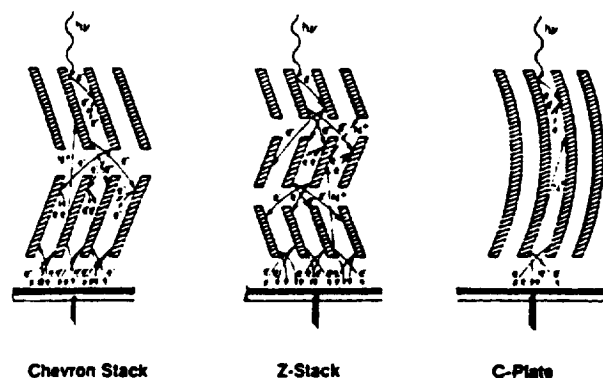
Chevron Stack   **Z-Stack**   **C-Plate**

Figure 9. Schematics of high-gain MCP structures.

Both of these MCP configurations produce gains in excess of 10^7 electrons pulse^{-1}, and resolutions of the output pulse-height distributions of better than 40%, (the resolution is defined as the FWHM of the distribution divided by the modal gain of the distribution). Performance characteristics of this quality have been obtained with both flat (Siegmund *et al.*, 1985, Fraser *et al.*, 1988) and curved plates (Siegmund *et al.*, 1990). MCPs of these configurations are available with active areas of up to 100 x 100 mm^2, and in smaller sizes with channel diameters as small as 8 microns.

A single C-plate MCP is more difficult to fabricate, but produces a more optimum performance for very-high spatial resolution imaging detector systems since the charge spreading at the interfaces of the different plates in the chevron and Z-plate stacks is eliminated. C-plate MCPs with channel diameters of 12 and 10 microns produce gains of the order of 5×10^5 electrons pulse[1] and resolutions of the output pulse-height distribution of better than 40% (see Figure 10). These performance characteristics have also been obtained with both flat (Timothy, 1981) and curved (Slater *et al.*, 1989) plates. C-plate MCPs with pore sizes as small as 8' microns are currently under evaluation and the fabrication of C-plate MCPs with diameters of 40 mm and 75 mm is currently in progress.

Of particular interest for studies at FUV and EUV wavelengths are the very-high DQEs obtained with MCPs with opaque alkali-halide photocathodes deposited on the input faces (Siegmund and Gaines, 1990).
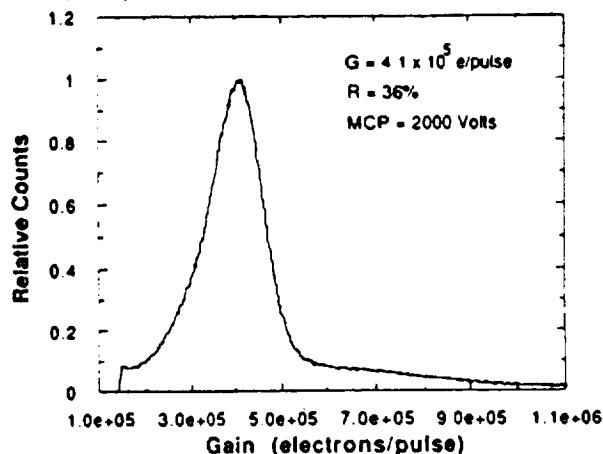

Figure 10. Output pulse-height distribution for a C-plate MCP with 12-micron-diameter channels.

4. PROSPECTS FOR FUTURE DEVELOPMENTS

A number of developments of the imaging photon-counting array technologies are currently in progress. Very-large-format CCDs are under development for a number of space astrophysics missions. As examples of the current state-of-the-art, the Tektronix CCD being developed for the NASA Goddard *Hubble* Space Telescope Imaging Spectrograph has a format of 2048 x 2048 pixels and pixel dimensions of 21 x 21 microns^2 (Woodgate, 1989), while the largest Ford Aerospace (now Loral) CCD has a format of 4096 x 4096 pixels and pixel dimensions of 7.5 x 7.5 microns^2 (Janesick *et al.*, 1989). The potential for very-low (< 1 e- rms) read noise CCDs means that these detectors will probably ultimately replace the current generation of the photon-counting detectors at visible wavelengths for applications not requiring a fast-timing capability.

The development of the high-gain MCPs is also being actively pursued at this time. Curved-channel MCPs fabricated by new proprietary techniques are achieving uniformities of structure of a quality never before achieved. The development of small-pore MCPs with channel diameters as small as 6 microns is currently in progress and exotic fabrication techniques such as fractal geometries for the reduced lead silicate class (RLSG) MCPs, and the use of lithographic solid-state techniques for the fabrication of MCPs in silicon and other materials are

under intensive investigation by a number of groups. MCPs with square channels are also being fabricated and tested.

Looking further into the future, the development of exotic three-dimensional imaging photon-counting detector systems which can provide, simultaneously, a two-dimensional imaging capability and a high degree of energy resolution is being actively pursued for use at soft x-ray wavelengths and studied conceptually for use at EUV and FUV wavelengths.

The needs for the development of ultraviolet and visible-light detector systems have recently been reviewed as part of the Astrotech 21 workshop organized by the Jet Propulsion Laboratory (JPL) (Timothy *et al.*, 1991). The present capabilities and future needs for the high-gain MCPs and MCP readout systems are listed in Tables 3 and 4.

It is clear that the complimentary technologies of the solid-state integrating detectors and the very fast-timing imaging photon-counting detectors now have the potential for revolutionizing scientific investigations in many fields on the ground and in space. The one caveat is that the scientific programs cannot at present, support the financial requirements of the semi-conductor and night-vision industries. Without a source of significant and consistent financial support, the availability of large-format scientific CCDs and MCPs cannot be guaranteed and the scientific programs will continue to be subject to the vagaries of the semi-conductor and night-vision industries, particularly during the present period of budget cutbacks and turmoil in the defense industries.

Table 2. Capabilities and requirements for scientific CCDs (from Timothy *et al.*, 1991).

Development Status	Flown in Space	Developed for Space	Demonstrated in Laboratory	Desired for Future Mission
Sample Mission	HST WF/PC 1	HST WF/PC 2	N/A	NGST
Visible blindness	$< 10^{-4}$	$< 10^{-9}$	$< 10^{-9}$ with filter	$< 10^{-9}$ for imaging
Array size	800 x 800	800 x 800	4k x 4k	$\geq$ 15k x 15k
QE for 0.1 - 0.4 µm	> 15%	> 25%	30%	> 80%
QE for 0.4 - 1.0 µm	> 15%	> 25%	> 60%	> 80%
Well capacity (e⁻) @ pixel size (µm)	30,000 @ 15	40,000 @ 7	40,000 @ 7	100,000 @ 5
Read noise (e⁻ rms)	10	2	0.4	0.1
Read rate (pixels s⁻¹) @ read noise (e⁻ rms)	50,000 @ 10	50,000 @ 2	50,000 @ 0.4	100,000 @ 0.1
Operating temperature	- 95 °C	- 60 °C	- 20 °C	20 °C
Mosaic capability	No	No	Buttable for line array	Buttable for 2-D mosaic

Table 3. Capabilities and requirements for high-gain MCPs (from Timothy *et al.*, 1991).

Developed:	Diameter – 100 mm Spatial uniformity – 25 to 50 μm (multi-fiber defects) Channel diameter 10 μm Dark count rate < 0.3 counts cm⁻² s⁻¹ Maximum count rate – 50 counts channel⁻¹ s⁻¹ (12 μm channels) Lifetime – 10 C cm⁻²
Under development:	Channel diameter 8 μm Square channels (60-μm to 25-μm channels) Curved plates Dark count rate < 0.03 counts cm⁻² s⁻¹ Maximum count rate – 100 counts channel⁻¹ s⁻¹ (12 μm channels) Lifetime TBD
Required:	Diameter – 100 mm No spatial distortion (AT MCPs) Square channels (6-μm channels) Dark count < 0.01 counts cm⁻² s⁻¹ (anti-coincidence) Maximum count rate > 10² counts channel⁻¹ s⁻¹ (6-μm channels) Lifetime > 30 C cm⁻²

Table 4. Capabilities and requirements for MCP read-out systems (from Timothy *et al.*, 1991).

Developed:	~1 k × 1 k Spatial resolution 14 μm to 25 μm Position sensitivity – 1 μm Maximum count rate – 10⁶ counts s⁻¹
Under development:	~2 k × 2 k Spatial resolution 14 μm to 25 μm Position sensitivity – 1 μm Maximum count rate – 2 × 10⁶ – 10⁷ counts s⁻¹
Required:	~4 k × 4 k Spatial resolution 10 μm Position sensitivity < 1 μm Maximum count rate >> 10⁷ counts s⁻¹ Suitable for mosaics

5. ACKNOWLEDGMENTS

6. REFERENCES

Barstow M A Fraser G W and Milward S R 1985 *SPIE X-ray Instrumentation in Astronomy* 697 pp 352-361

Brandt J C and the GHRS Science Team 1979 *SPIE Instrumentation in Astronomy III* 172 pp 254-263

Carruthers G R Heckathorn H M Opal C B Jenkins E B and Lawrence J L 1988 *Advances in Electronics and Electron Physics* 74 pp 181-200

Eck H J Beaver E A and Shannon J L 1985 *Advances in Electronics and Electron Physics* 64A pp 141-152

Fraser G W Pearson J F Lees J E and Feller W B 1988 *SPIE Instrumentation in Astronomy II* 982 pp 98-107

Fraser G 1989 *X-ray Detectors in Astronomy* Cambridge University Press pp 208-228

Garmire G P Nousek J Burrows D Ricker G Bautz M Doty J Collins S Janesick J Mountain R W and Burke B E 1988 *SPIE X-ray Instrumentation in Astronomy II* 982 pp 123-128

Gonsiorowski T 1986 *SPIE Instrumentation in Astronomy VI* 627 pp 626-630

Harms R J and Fitch J E 1991 *SPIE Space Astronomical Telescopes and Instruments* 1494 pp 49-65

Janesick J E Elliott T Bredthauer R Chandler C and Burke B 1988 *SPIE X-ray Instrumentation in Astronomy II* 982 pp 70-75

Janesick J E Elliott T Dingizian A Bredthauer R Chandler C Westphal J and Gunn J 1989 *CCDs in Astronomy* Astronomical Society of the Pacific Conference Series 8 pp 18-39

Kellogg E Henry P Murray S and Van Speybroeck L 1976 *Review of Scientific Instruments* 47 pp 282-290

Lapington J S Breeveld A A Edgar M L Tandy J A and Trow M W 1990 *SPIE EUV, X-ray and Gamma-ray Instrumentation for Astronomy* 1344 pp 324-332

Lawrence G 1991 private communication

Lawrence J L and Joseph C L 1988 *Advances in Electronics and Electron Physics* 74 pp 465-473

Lumb D H and Holland A D 1988 *SPIE X-ray Instrumentation in Astronomy II* 982 pp 116-122

Martin C Jelinsky P Lampton M Malina R F and Anger H O 1981 *Review of Scientific Instruments* pp 1067-1074

McClintock W E Barth C A Steele R E Lawrence G M and Timothy J G 1982 *Applied Optics* 21 pp 3071-3079

Murray S S and Chappell J H 1988 *SPIE X-ray Instrumentation in Astronomy II* 982 pp 48-63

Norton T J Airey R W Morgan B L Read P D Powell J R 1988 *Advances in Electronics and Electron Physics* 74 pp 41-53

Roberts E H Tuohy I R and Dopita M A 1988 *Advances in Electronics and Electron Physics* 74 pp 297-313

Siegmund OHW Coburn K and Malina R F 1985 *IEEE Transactions in Nuclear Science* NS-32 pp 443-447

Siegmund OHW Hailey C J Stewart R E and Lupton J H 1988 *Advances in Electronics and Electron Physics* 74 pp 97-105

Siegmund OHW Lampton M L and Raffanti R 1989 *SPIE EUV, X-ray and Gamma-ray Instrumentation* 1159 pp 476-485

Siegmund OHW and Gaines G A 1990 *SPIE EUV, X-ray and Gamma-ray Instrumentation in Astronomy* 1344 pp 217-227

Siegmund OHW Cully S Warren J Gaines G A Priedhorsky W and Bloch J 1990 *SPIE EUV, X-ray and Gamma-ray Instrumentation for Astronomy* 1344 pp 346-354

Slater D C Morgan J S and Timothy J G 1989 *SPIE Ultraviolet Technology III* 1158 pp 118-126

Timothy J G 1981 *Review of Scientific Instruments* 52 pp 1131-1142

Timothy J G Morgan J S Slater D C Kasle D B Bybee R L and Culver H E 1989 *SPIE Ultraviolet Technology III* 1158 pp 104-117

Timothy J G 1991 *SPIE Space Telescopes and Instruments* 1494 pp 394-402

Timothy J G Blouke M Bredthauer R Kimble R Lee T -H Lesser M Siegmund OHW and Weckler G 1991 *Astrotech 21 Workshops Series III* JPL Publication 91-24 pp 27-33

Troeltzsch J R Ebbetts D C Garner H W Tuffli A Breyer R Kinsey J Peck C Lindler D and Feggans J 1991 *SPIE Space Astronomical Telescopes and Instruments* 1494 pp 9-15

Van Geest L K and Stoop KWJ 1985 *Advances in Electronics and Electron Physics* 64A pp 93-10

Wiza J L 1979 *Nuclear Instruments and Methods* 162 pp 587-601

Williams J T and Weistrop D 1983 *SPIE Instrumentation in Astronomy V* 445 pp 204-211

Woodgate B E 1989 *CCDs in Astronomy* Astronomical Society of the Pacific Conference Series 8 pp 237-257

FAR-ULTRAVIOLET MAMA DETECTOR IMAGERY AND EMISSION-LINE CCD IMAGERY OF NGC 6240

ANDREW M. SMITH

Laboratory for Astronomy and Solar Physics, Code 681, NASA/Goddard Space Flight Center, Greenbelt, MD 20771

ROBERT S. HILL

Hughes STX Corporation, 4400 Forbes Boulevard, Lanham, MD 20706

FREDERICK J. VRBA

U.S. Naval Observatory, Box 1149, Flagstaff Station, Flagstaff, AZ 86002

AND

J. GETHYN TIMOTHY

Center for Space Science, Stanford University, ERL 315, Stanford, CA 94305

Received 1991 November 13; accepted 1992 March 19

ABSTRACT

We have obtained an image of the luminous infrared galaxy NGC 6240 at 1480 Å using a multianode microchannel array (MAMA) detector with a rocket-borne telescope. At distances greater than 12″ from the nucleus the measured ultraviolet luminosity implies intensive star formation activity equal to 2–3 times that of a spiral galaxy such as M83. Optical images in the $H\beta$ and [O III] $\lambda 5007$ emission lines reveal a region of high excitation east of the nucleus between the centers of disks 1 and 2 as described by Bland-Hawthorn et al.

Subject headings: galaxies: interactions — galaxies: peculiar — galaxies: photometry — stars: formation

1. INTRODUCTION

The morphologically peculiar galaxy NGC 6240, a possible collision of at least two galaxies, has attracted much study in recent years, primarily because of the high far-IR luminosity revealed by the *IRAS* survey (Wright, Joseph, & Meikle 1984) and the development of ground-based infrared (IR) spectroscopic techniques. This object exhibits two pointlike nuclei separated by 1″8 (Fried & Schulz 1983) located approximately in the center of a chaotic array of plumes, loops, and dust lanes. Most of the spectroscopic work carried out on NGC 6240 to date has been confined to a region within 5″ of the double nucleus, which shows strong near-IR emission, strong H_2 quadrupole emission (see Lester, Harvey, & Carr 1988 and references therein), and from which the very strong far-IR emission is presumed to emanate. Imagery of NGC 6240 extending out to several arcminutes from the double nucleus has been obtained in visual and IR bandpasses (Fosbury & Wall 1979; Fried & Schulz 1983; Thronson et al. 1990; Keel 1990). Images in $H\alpha$ + [N II] have been obtained by Heckman, Armus, & Miley (1987) and Keel (1990). We distinguish three morphological components of the central system (Fig. 1): (1) a butterfly-shaped filamentary complex surrounding the double nucleus to a distance of ~10″; (2) a double loop ~40″ long to the west of the nucleus, aligned roughly north and south; and (3) fairly bright spiral arm fragments or tidal tails extending to ~30″ from the nucleus, also in a north-south direction. Recently, Bland-Hawthorn, Wilson, & Tully (1991) have delineated two disk systems in NGC 6240, centered at the double nucleus and at a point ~12″ to the northeast, respectively. The center of the second disk is not prominent in IR or CO 2.6 mm emission (Wang, Scoville, & Sanders 1991).

In this *Letter*, we report imaging observations made in the far-ultraviolet (FUV), B, and V bandpasses, and in the $H\alpha$, $H\beta$, and [O III] $\lambda 5007$ emission lines. The FUV image is discussed in relation to components 2 and 3. In particular, we show that these components have an FUV luminosity at least as great as that of a normal giant spiral. Our ground-based visual emission-line images are discussed in relation to component 1, within which we find a region of high excitation. Throughout we assume $H_0 = 67$ km s^{-1} Mpc^{-1} (Rowan-Robinson 1985), which locates NGC 6240 at a distance of 112 Mpc.

2. OBSERVATIONS

Sounding rocket 36.043GG, a Terrier/Black Brant, was flown 1989 June 27 6:00:01 GMT from White Sands Missile Range, New Mexico. The instrument was a 39 cm Ritchey-Chretian telescope (Bohlin et al. 1982) refitted with a 256 × 1024 pixel Multianode Microchannel Array (MAMA) a detector with cesium iodide photocathode. The MAMA time-tags and centroids the electron cloud emitted from the back of a microchannel plate in response to each detected photon. Because flux is not integrated on the detector itself, the flight observation can be reconstructed photon by photon in time order. Image blurring in this observation had two components: a jitter of ±8″ removed by applying an attitude offset returned in telemetry; and a smooth drift of 0″7 s^{-1} removed by following the motion of a point source (HD 152497) in the dejittered data. NGC 6240 was observed for a total of 210 s through CaF$_2$ and SrF$_2$ filters (identical for the purposes of this paper) yielding $\lambda_{\rm eff} = 1480$ Å and $\Delta\lambda = 410$ Å. The plate scale is 1″5 pixel^{-1} for a field of 6.4 × 25.6. *IUE* spectra of HD 152497, together with laboratory-measured filter curves and flat fields, were used for absolute calibration. From the 2200 Å feature in the HD 152497 spectrum, foreground reddening was estimated to be $E(B-V) = 0.15$ [the estimate from the map of Burstein & Heiles (1982) is $E(B-V) \lesssim 0.09$].
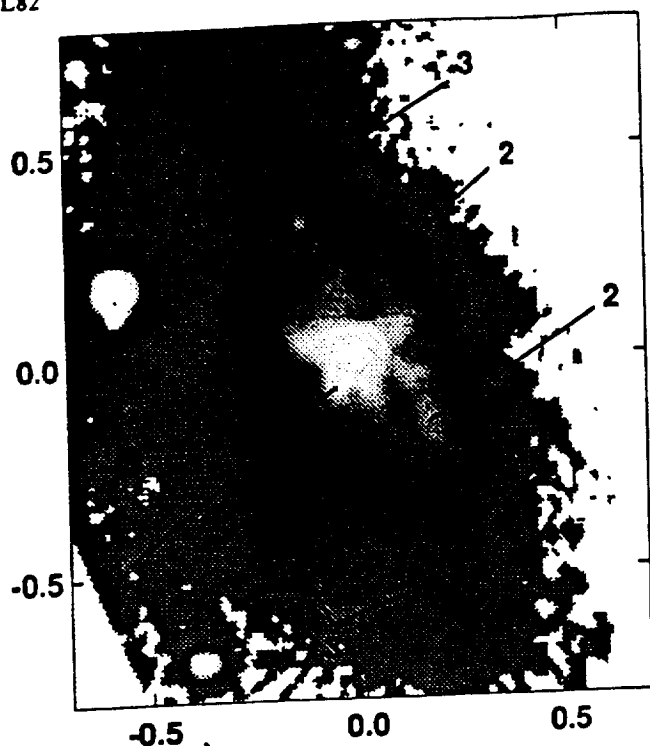
FIG. 1.—CCD image of NGC 6240 in Hα + [N II] + continuum. North is up, and east to the left. Axis labeled in arcminutes. Numerals distinguish three morphological components (see text).

TABLE 1

[O III]/Hβ RATIOS OF NGC 6240 FEATURES

FEATURE (1)	AVERAGE[a]		CENTER[b]	
	[O III]/Hβ (2)	Relative Error[c] (3)	[O III]/Hβ (4)	Relative Error[c] (5)
a.........	2.1	0.5	...	...
b.........	3.3	0.6	...	...
c.........	4.3	0.3	5.2	0.8
d.........	3.3	0.1	3.2	0.4
e.........	2.5	0.1	2.5	0.3
f.........	1.0	0.1	0.9	0.2
g.........	2.7	0.4	...	...
i.........	1.1	0.1	1.1	0.3
j.........	1.0	0.2	1.0	0.6
k.........	2.7	0.5	...	...

[a] Square aperture 1″2 on a side, centered on position marked in Fig. 2.
[b] Single pixel marked in Fig. 2.
[c] 1 σ/r, where r is center or average line ratio.

resulting monochromatic [O III] and Hβ images are shown in Figures 2a and 2b. An image of the ratio, [O III]/Hβ, is shown in Figure 2c.

Specific values of the [O III]/Hβ ratio corresponding to features marked in Figure 2 are given in Table 1. The values in column (2) correspond to a 3 × 3 pixel square aperture, for which the formal random errors are listed in column (3). The ratio [O III]/Hβ at the central pixel of each aperture is listed in column (4), with the random error in column (5), in those cases where the relative error is less than 1.0 (i.e, the result is significant at the 1 σ level).

3. DISCUSSION

Figure 3a (Plate L7) shows the 1480 Å image with B continuum contours superposed. Shown as well are the centers of disks 1 and 2 and the line of nodes of each disk (Bland-Hawthorn et al. 1991). The inner parts of the galaxy are too obscured to be seen in the short FUV exposure. However, the spiral armlike structures are obvious. Although they appear smooth at visual wavelengths, the FUV image indicates that they contain distinct star-forming regions or clusters. This effect may be produced in the FUV by uneven distribution of dust within the arms. In the northern arm, star formation seems to be occurring or has recently occurred as far as 30″ (16 kpc) from the nucleus. In Figure 3b we show a differentially masked visual picture overlaid with the contours of the FUV image. The visual picture shows a nearly vertical feature, usually interpreted to be a dust lane, which does not seem to correlate with either the presence or the absence of FUV emission.

The FUV emission is not correlated with any optical emission within 12″ (6.3 kpc) of the nucleus, or with the line of nodes of either disk 1 or 2. On the other hand, the FUV is well correlated with optical emission in the armlike or tidal-tail regions outside that radius, particularly to the north and the southwest. However, such structures cannot be excluded from interior parts of the galaxy, where they could be blocked from view by extinction. It is likely that these regions are Population I structures similar to the arms of normal spirals (but given the disrupted appearance of the galaxy, it is plausible that they are material arms rather than density waves).

We have measured the FUV luminosity at 1480 Å of seven of the cluster-like objects in Figure 3, and the results are listed in

Two new UV point sources were serendipitously discovered at $\alpha_{1950} = 16^h51^m6\overset{s}{.}37$ $\delta_{1950} = +2°31'40\overset{''}{.}0$ and $\alpha_{1950} = 16^h51^m1\overset{s}{.}40$ $\delta_{1950} = +2°26'50\overset{''}{.}7$. The second source was confirmed as a white dwarf using a visual spectrum kindly obtained by Craig Foltz at Kitt Peak National Observatory (Hintzen 1989).

Ground-based images of NGC 6240 were obtained by FJV on 1989 June 27, 1989 June 29, and 1990 June 28 with the 40 inch (1.016 m) telescope at the United States Naval Observatory Flagstaff Station using a UV-flooded Texas Instruments 816 × 816 CCD. The plate scale is 0″4 pixel⁻¹ for a field of 5″7 × 5″7. These images were reduced by bias subtraction and flat-fielding using standard site procedures.

The visual images were co-aligned to less than 1 pixel (using centroided coordinates of field stars) and smoothed by 3 pixels. The bandpass response functions of the emission-line filters (Δλ = 30 Å) were such that intercalibrated monochromatic images could be computed in instrumental units, provided that a way was found of interpolating continuum from B and V band data. The internal reddening of NGC 6240 varies on several spatial scales (Keel 1990), making a simple scaling of B or V inappropriate. Our method is based on the assumption that the northern arm (in our component 3) represents "normal spiral arm" material dominated by continuum, and with minimal line emission compared to the more energetic parts of the galaxy; the features of interest in our component 1 are then regarded as showing a line-emission excess above that norm. From the northern-arm data, we derived empirically (by matching histograms of certain instrumental flux ratios) a function relating continuum at the wavelengths of [O III] and Hβ to the instrumental broad-band fluxes b and v. The
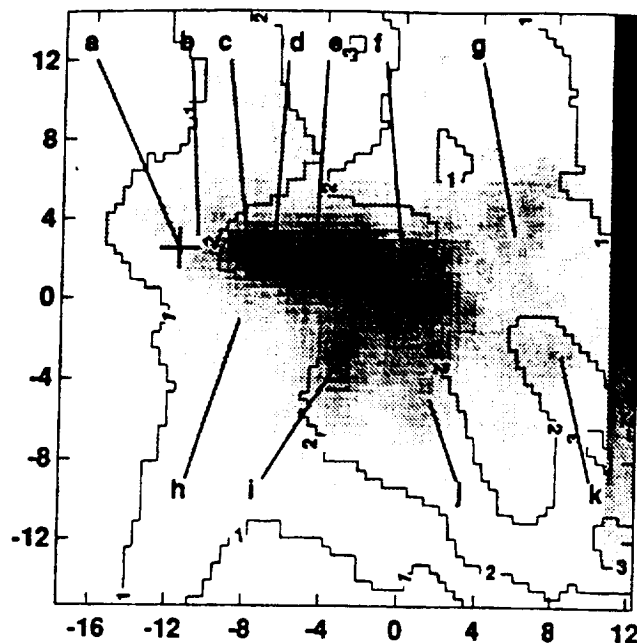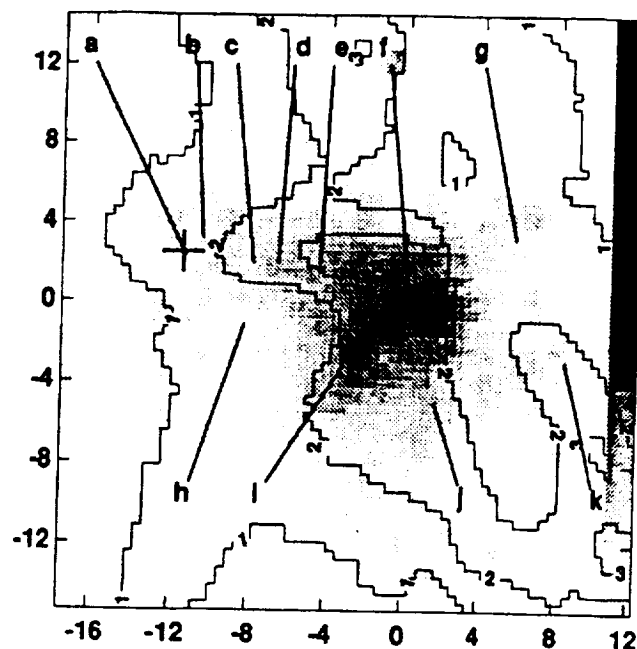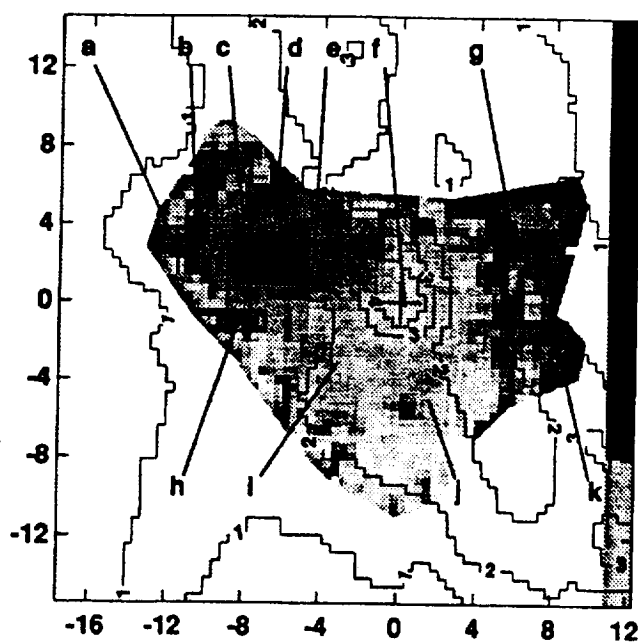
FIG. 2a

FIG. 2b

FIG. 2c

FIG. 2—CCD narrow-band images of NGC 6240 in emission lines. North up, east to the left. Axes labeled in arcseconds. B-band contours equally spaced in flux are superposed (same levels as in Fig. 3). (a)–(b) [O III] and Hβ, respectively (density wedges show equally spaced intensities). (c) [O III]/Hβ (density wedge shows measured flux ratios at integral values from 1–4). Areas of very low S/N have been masked out of the ratio image, but some noise still shows as dark "break-up" around the edge of the displayed portion. Labels a–k indicate features discussed in Table 1 and the text. Crosses or line segments indicate the centers of disks 1 and 2 of Bland-Hawthorn et al. (1991).

Table 2. They have been corrected for Galactic extinction, but not for extinction in NGC 6240. A typical source measurement comprises ~25 counts, of which ~10 are background. We note that UV 5 and UV 6 are about twice as bright as the fainter clusters and that the average cluster FUV luminosity uncorrected for internal extinction is ~29 times that of a typical bright H II region in M83 (Bohlin et al. 1990).

Assuming that the FUV image is evidence for bursts of star formation, we can estimate the initial mass of the clusters UV 1–UV 7 using the analysis of Lequeux et al. (1981) as developed by Landsman (1990; see Bohlin et al. 1990). In this scheme a set of evolutionary tracks in the $\log L$, $\log T_{\text{eff}}$ plane is selected for a discrete set of initial masses. Model atmospheres are then used to convert each $\log L$, $\log T_{\text{eff}}$ value into an FUV flux. At a given age, fluxes from stars of different masses are added together, weighted by an assumed initial mass function (IMF). In our calculations the IMF took the form $\Psi(M) = dn(M)/d(\ln M) \propto M^{-2}$ for 1.8 $M_\odot < M < 120$ $M_\odot$ and $M^{-0.6}$ for 0.007 $M_\odot < M < 1.8$ $M_\odot$ (Lequeux et al. 1981). We have assumed solar abundances. For a working model we follow

TABLE 2

CLUSTER LUMINOSITIES AND INITIAL MASSES

UV Cluster Identification Number	Luminosity[a]	SFR[b]	M_{total}[c]
1	6.4	0.34	6.8
2	7.0	0.36	7.3
3	1.9	0.10	1.9
4	7.7	0.40	8.1
5	11.6	0.61	12.1
6	12.1	0.66	12.6
7	9.2	0.49	9.6

[a] 10^{-38} ergs s^{-1} Å^{-1}, corrected only for Galactic extinction $E(B - V) = 0.15$.

[b] Star formation rate in $M_\odot$ yr^{-1}.

[c] 10^6 $M_\odot$, lower limit (see text).

Tanaka, Hasegawa, & Gatley (1991) and asume that star formation has taken place at a constant rate over a period of 20 Myr, and that we observed the FUV emission 10 Myr after the star formation has stopped. Inspection of our Hα image and that of Heckman et al. (1987) shows no correlation between Hα and FUV emission, from which we conclude that the clusters have aged sufficiently to no longer produce significant ionizing flux. This is consistent with our working model, which shows a decrease in ionizing flux by two orders of magnitude in a 10 Myr span following the cessation of star formation. Our calculation yields a luminosity per unit star formation rate in (ergs s^{-1} $Å^{-1})/(M_\odot$ Myr^{-1}), from which we derive the star formation rates and integrated cluster masses listed in Table 2. The results imply moderate star formation rates and total cluster masses of $0.5-1 \times 10^7 M_\odot$. Reasonable variations of the model parameters can change the numerical values by up to a factor of 3, but the results are likely to be minimum values since we have not corrected for extinction internal to NGC 6240. These cluster masses are about a factor of 30 less than the mass of stars produced at the center of NGC 6240 in a starburst as described recently by Tanaka et al. (1991). The total cluster mass derived from FUV data, i.e., from regions located more than 12″ from the center, is about a factor of 2 less than the central starburst mass.

About 45% of the total observed FUV comes from the listed clusters (the rest, probably, being from fainter clusters and from diffuse reflection off dust). In Table 3 the total FUV flux of NGC 6240, representing ∼270 net counts, is compared with the FUV fluxes for several spirals obtained with other sounding rocket observations. NGC 6240 emits FUV flux ∼2 times that of M83, roughly equal to that of M51 or M101, and ∼4 times that of M33. In other words, in its outlying arms alone, NGC 6240 exhibits an FUV luminosity comparable to that of a giant spiral with very active star formation and much greater than that of a relatively quiescent spiral. (All these results are uncorrected for extinction internal to the target galaxies.) This is consistent with the finding of Thronson et al. (1990) and Lester, Harvey, & Carr (1988) that the bolometric stellar luminosity of NGC 6240 is ∼2 times that of a giant spiral (see especially Fig. 10 of Thronson et al.).

The most noteworthy feature found in our visual imagery is a bar-like structure, resolved into two localized subregions, appearing between points a and f in Figure 3a, our [O III] image. (For conciseness, we simply call this feature the "bar," without implying any similarity to barred spirals.) Broad-band imagery also shows the bar, as indicated by the B bandpass contours superposed on the same figure. The east-west extent of the bar is ∼4″ (2.1 kpc). It appears to be closely aligned with the dynamic center of disk 2 and reasonably well aligned with the southern nucleus of the galactic core. It is exhibited, faintly, by the Hβ image (Fig. 2b) and is definitely present in the Hα pictures of Heckman, Armus, & Miley (1987) and Keel (1990). The [O III]/Hβ ratio image shows varying degrees of excitation within the bar. For example, at point c the average value in a 1″2 square aperture is 4.3 ± 0.3. At points d and e the average

TABLE 3
COMPARISON OF UV LUMINOSITY OF NGC 6240 WITH THOSE OF OTHER GALAXIES

GALAXY	OBSERVED		AT 112 Mpc	
	f_{1500}[a]	f_{2300}[a]	f_{1500}[a]	f_{2300}[a]
6240	9.1(−15)	...	9.1(−15)	4.2(−15)[b]
M31[c]	...	2(−11)	...	0.7(−15)
M33[d]	2.4(−11)	1.4(−11)	1.4(−15)	0.8(−15)
M51[c]	...	5.5(−13)	...	4.1(−15)
M83[c]	3.8(−12)	1.8(−12)	4.4(−15)	2.0(−15)
M101[c]	...	1.1(−12)	...	4.6(−15)

[a] In ergs s^{-1} cm^{-1} $Å^{-1}$, corrected for foreground extinction only: $E(B−V) = 0.15$ for NGC 6240, values from Burstein & Heiles 1982 for others.
[b] Extrapolated from f_{1500} using f_{2300}/f_{1500} of M83.
[c] Hill 1990.
[d] Landsman 1990.

values are 3.3 ± 0.1 and 2.5 ± 0.1, respectively. The shape of the bar in the ratio image differs from that in the [O III] image, very likely due to the nonuniform morphology of Hβ emission arising in other gas along the line of sight. In any case, an extensive region of high ionization does appear to be present between the center of disk 2 and the double nucleus.

At points corresponding to the centers of disks 1 and 2 and in the extended features of our component 1, the [O III]/Hβ ratio is characteristically low. However, at point b, ∼2″ away from the center of disk 1, the [O III]/Hβ ratio appears to be significantly elevated (3.3 ± 2.1). Point h shows high excitation ([O III]/Hβ = 3.6), but this value is not statistically significant. The derived [O III]/Hβ ratios are likely to be minimum values, since we cannot separate the Hβ emission contributed by the [O III] emitting gas from other Hβ emission along the line of sight.

The [O III]/Hβ ratios can easily be produced by shocks or through photoionization by thermal or nonthermal sources. Clearly, it would be useful to obtain spectra of the high-excitation regions in a diverse selection of emission lines in order to distinguish between these energizing mechanisms. Until more data are forthcoming, we simply note that the location of the high [O III] emission, seen clearly against a lower emission background, is suggestive of an association with the double nucleus or the center of disk 2.

REFERENCES

Bland-Hawthorn, J., Wilson, A. S., & Tully, R. B. 1991, ApJ, 371, L19
Bohlin, R. C., Cornett, R. H., Hill, J. K., & Stecher, T. P. 1990, ApJ, 363, 154
Bohlin, R. C., Hill, J. K., Stecher, T. P., & Witt, A. N. 1982, ApJ, 255, 87
Burstein, D., & Heiles, C. 1982, AJ, 87, 1165
Fosbury, R. A. E., & Wall, J. V. 1979, MNRAS, 189, 79
Fried, J. W., & Schultz, H. 1983, A&A, 118, 166
Heckman, T. M., Armus, L., & Miley, G. K. 1987, AJ, 93, 276
Hill, J. K. 1990, private communication
Hintzen, P. M. N. 1989, private communication
Keel, W. C. 1990, AJ, 100, 356

Landsman, W. B. 1990, private communication
Lequeux, J., Maucherat-Joubert, M., Deharveng, J. M., & Kunth, D. 1981, A&A, 103, 305
Lester, D. F., Harvey, P. M., & Carr, J. 1988, ApJ, 329, 641
Rowan-Robinson, M. 1985, The Cosmological Distance Ladder (New York: W. H. Freeman)
Tanaka, M., Hasegawa, T., & Gatley, I. 1991, ApJ, 374, 516
Thronson, H., Majewski, S., Descaries, L., & Hereld, M. 1990, ApJ, 364, 456
Wang, Z., Scoville, N. Z., & Sanders, D. B. 1991, ApJ, 368, 112
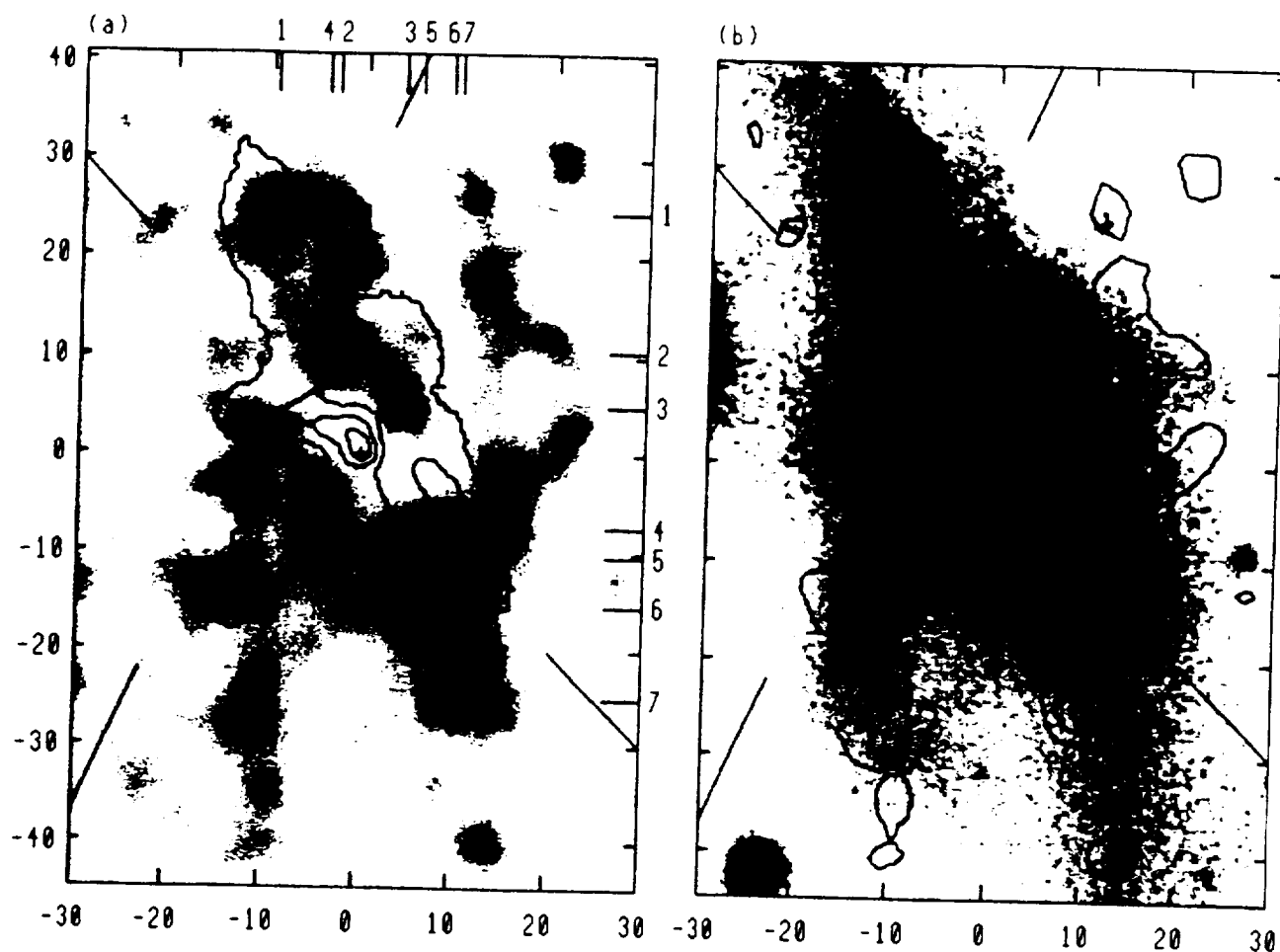Wright, G. S., Joseph, R. D., & Meikle, W. P. S. 1984, Nature, 309, 430

FIG. 3.—(a) MAMA detector image of NGC 6240 at 1480 Å. Superposed are B band contours equally spaced in flux (same levels as in Fig. 2). Indicators 1–7 along the axes identify the sources described in Table 2. (b) Differentially masked V-band image with equally spaced FUV contours superposed. North up, east to the left. Axes labeled in arcseconds. Crosses indicate the centers of disks 1 and 2 of Bland-Hawthorn et al. (1991), and oblique line segments show orientation of lines of nodes.

SMITH et al. (see 391, L82)

A New Speckle Interferometry System for the MAMA Detector

E. HORCH

Department of Applied Physics, Stanford University, Stanford, California 94305
Electronic mail: elliott@kilohoku.stanford.edu

J. S. MORGAN

Department of Astronomy, FM-20, University of Washington, Seattle, Washington 98125
Electronic mail: morgan@bluto.astro.washington.edu

G. GIARETTA

Department of Electrical Engineering, Stanford University, Stanford, California 94305
Electronic mail: giorgio@kilohoku.stanford.edu

D. B. KASLE

NASA Goddard Space Flight Center and Department of Electrical Engineering, CSSA, ERL 262, Stanford University,
Stanford, California 94305
Electronic mail: kasle@kilohoku.stanford.edu

ABSTRACT. We have developed a new system for making speckle observations with the multianode microchannel array (MAMA) detector. This system is a true photon-counting imaging device which records the arrival time of every detected photon and allows for reconstruction of image features near the diffraction limit of the telescope. We present a description of the system and summary of observational results obtained at the Lick Observatory 1-m reflector in 1991 September. The diffraction limit of the 1-m telescope at 5029 Å is about 0.125 arcsec and we have successfully resolved the catalogued interferometric binary HD 202582 with a separation of 0.157±0.031 arcsec. A pair of stars in the open cluster χ Persei separated by 2.65±0.22 arcsec with approximate V magnitudes 8.6 and 11.5 has also been successfully analyzed with the speckle technique.

1. INTRODUCTION

In conventional astronomy, the limit of angular resolution is not set by the size of the telescope aperture as diffraction theory predicts but instead by the size of the "seeing disk" of a point source, which is typically 1–2 arcsec at full width half-maximum (FWHM). The broad character of the seeing disk is due to inhomogeneities in the refractive index in the air above the telescope aperture. These inhomogeneities have the effect of breaking the aperture up into cells that have a typical length scale of 10 cm and evolve on a typical time scale of 10 ms. Within a cell, the refractive index is roughly uniform, but different cells have different values of the refractive index. It is the size of these cells which ultimately determines the width of the seeing disk.

One technique for obtaining angular resolution considerably better than the seeing is speckle interferometry. Speckle interferometry consists of taking many short integration images (frames) of a particular object of interest. In each frame, the turbulent effects of the atmosphere are approximately frozen and the frame image may be described as the interference pattern obtained by considering different pairs of subregions in the telescope aperture defined by the cells arising from nonuniformities in the refractive index. Each pair of subapertures considered independently would produce fringes in the image plane whose spacing is determined by the distance between the two subapertures. Taken together, the various fringes form a complicated interference pattern known as a speckle pattern. The speckles (or regions of constructive interference) fill a region in the image plane defined by the seeing disk, but have a characteristic width similar to that of the diffraction-limited point spread function of the telescope. To the extent that individual speckles can be resolved by the detector at the image plane, a frame contains high angular resolution information about the object.

For example, if the object of interest is a binary star, then the speckle patterns will exhibit speckle pairs at the vector separation of the two companions. Of course, these speckle pairs will occur at various places on the image plane, but they may be collected together by considering the autocorrelation function of a frame, which, up to a normalization factor, is equivalent to the histogram of the distance vectors between photon pairs. The Fourier transform of the image autocorrelation is the image power spectrum (the modulus squared of the Fourier transform of the frame image). The frame image $I(x)$ is the convolution of the point spread function $S(x)$ with the actual object intensity distribution $O(x)$:

$$I(x) = S(x) * O(x), \qquad (1)$$

where "*" denotes convolution. In the Fourier domain, a convolution becomes an ordinary product so that

$$\hat{I}(u) = \hat{S}(u) \cdot \hat{O}(u), \qquad (2)$$

where " $\hat{\ }$ " denotes Fourier transform and the spatial frequency variable conjugate to x is u. Taking the modulus square of this expression and averaging over many frames, we obtain the result that the average image power spectrum is the product of the true object power spectrum and the average point-spread function power spectrum:

$$\langle |\hat{I}(u)|^2 \rangle = \langle |\hat{S}(u)|^2 \rangle \cdot |\hat{O}(u)|^2, \qquad (3)$$

where $\langle \ \rangle$ denotes the average over many frames. If a speckle experiment is performed on the binary star, $\langle |\hat{I}(u)|^2 \rangle$ can be obtained by Fourier transforming the average autocorrelation of many frames of data. The same process performed on a point source yields $\langle |\hat{S}(u)|^2 \rangle$. As Eq. (3) shows, the true binary power spectrum can then be obtained by division, where such a division is valid in the region where $\langle |\hat{S}(u)|^2 \rangle$ is nonzero. In fact the average point-spread function power spectrum is nonzero out to the diffraction limit of the telescope and the method works not only for binary stars but also for general objects (Labeyrie 1970). The true object autocorrelation is then obtained by Fourier inversion. In the case of a binary system, reconstructing the object autocorrelation is sufficient to retrieve the separation, position angle (up to a 180° ambiguity), and the relative magnitudes of the two companions.

To have a successful speckle experiment, the image detector must have several special characteristics. First it must be capable of reading frames out at the rate of the evolution of the speckles; a minimum requirement is about 10 ms. The detector must have relatively high quantum efficiency so that speckles in a single frame will have sufficient contrast. Low read noise is important because the number of detected photons per frame is usually small (typically 1 to a few hundred). Since the goal is to obtain very-high-resolution information inside a comparatively large seeing disk, excellent geometric fidelity and fairly large formats are necessary.

While other detectors have been very successfully used in speckle interferometry, there are several motivations for building a system based on a MAMA detector. Unlike intensified-CCD speckle systems, the MAMA records the arrival time of every detected photon with a timing resolution of 400 ns. This allows for maximum flexibility in the analysis phase of a speckle experiment since the frame integration time that maximizes the signal-to-noise ratio may be identified and set in software after the observations have been completed. The flat-field response of current MAMA detectors has improved significantly over the past six years so that now it is possible to obtain 10% rms variations over the entire field of view. This is in contrast to earlier MAMA and PAPA detectors which commonly had 30% rms sensitivity variations across the field of view (Papaliolios et al. 1985). Resistive anode microchannel plate (MCP) readouts typically use stacks of MCPs to produce large charge clouds on the anodes, but this arrangement results in poorer position sensitivity than with the MAMA detector. The Caltech system, e.g., has a spatial resolution of 60 μ FWHM (Nakajima et al. 1989) compared with
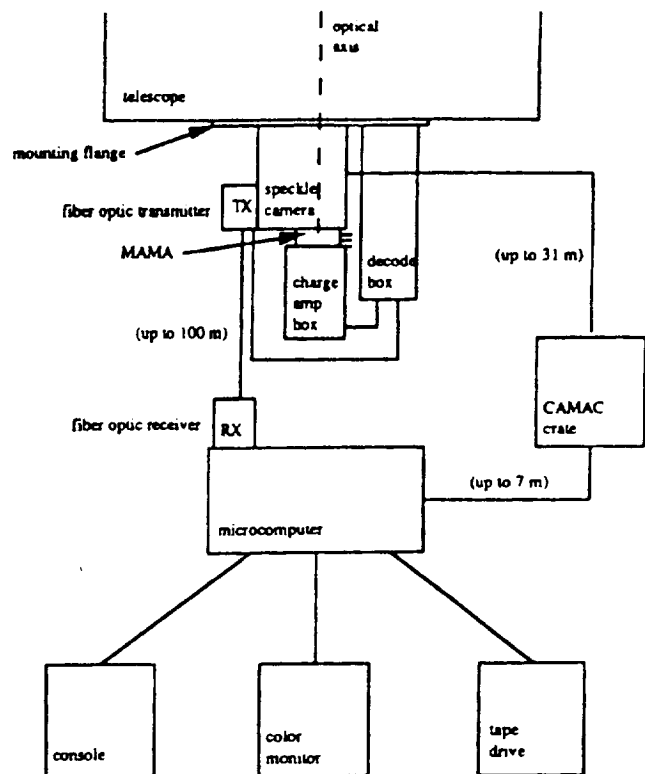
FIG. 1—The primary components in the Stanford speckle-interferometry system.

about 14 μ for the system described in this paper, which uses a single curved-channel MCP. In addition, stacked MCP detectors are susceptible to MCP saturation at lower count rates than curved-plate MAMA detectors. This is a phenomenon which increases the dead time of the detector. MAMA detectors are available in large formats (1024 $\times$ 1024 pixels), usually have a dark current under 20 Hz, and have excellent geometric fidelity (Morgan et al. 1989). Based on these characteristics, a MAMA-based speckle-interferometry system is a powerful instrument for high angular resolution astronomy.

2. SYSTEM DESCRIPTION

Starting from the telescope, the main components of the Stanford speckle system are (see Fig. 1): (1) a mounting flange which holds the detector and the speckle camera to the telescope so that the optical axes of the detector and telescope are matched; (2) the speckle camera which contains optical elements necessary for a speckle experiment; (3) the MAMA detector tube; (4) the charge amplifier box; (5) decode circuitry for assigning pixel addresses to output from the MAMA; (6) the fiber-optic link which allows for transmission of decoded data to a remote site; (7) the microcomputer, which operates the speckle camera and stores data; and (8) the CAMAC interface, which allows the microcomputer to issue commands to the speckle camera.
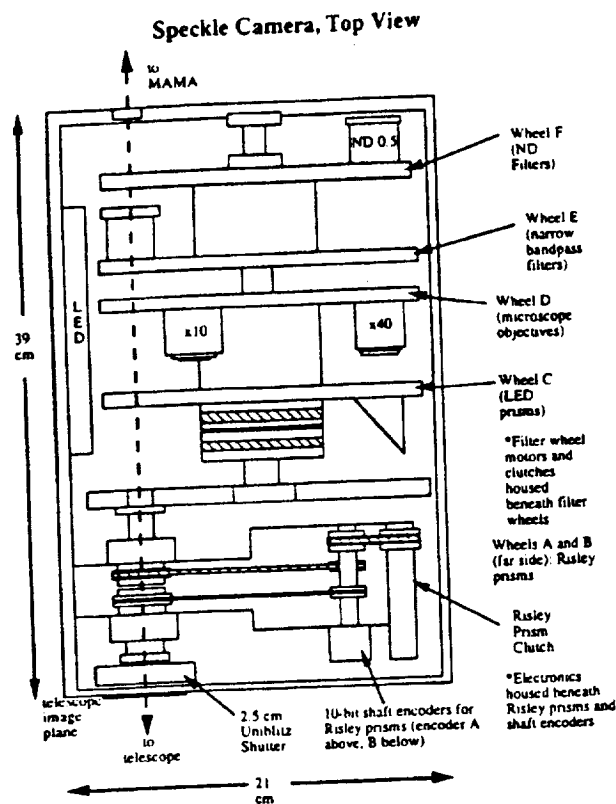
FIG. 2—Top view of the Stanford University speckle camera.

(a)

(b)

FIG. 3—(a) Block diagram of the MAMA detector operation; (b) an illustration of two sets of interleaved anodes with different sized electron clouds.

2.1 The Speckle Camera

The speckle camera sits between the telescope and the MAMA detector. A detail of this instrument is shown in Fig. 2. The optical and mechanical layouts of the camera were designed by Nate Hazen and Costas Papaliolios at Harvard University; this portion of our system is essentially a copy of the camera used at Harvard. The camera contains two Risley prisms to correct for atmospheric dispersion each of which may be rotated to an absolute position by its own 10-bit shaft encoder. It also contains four large wheels that hold filters and microscope objective lenses. The wheels and prisms are moved by issuing commands from the microcomputer, thus bringing the desired optical element into the optical axis. There are eight positions on each wheel. The two wheels closest to the MAMA detector are used for narrow-bandpass filters and neutral density filters while the second wheel from the telescope is used for microscope objectives. The wheel closest to the telescope can hold filters, but also has two prisms which can be used to illuminate the detector with light from a small LED, allowing for intensity calibration of the detector. The LED brightness can be controlled remotely. A reticle is etched on one of the prisms to give absolute spatial calibration. The camera has a 2.5 cm Uniblitz shutter which can be opened and closed by issuing a command from the microcomputer.

The microcomputer communicates to the camera via a CAMAC interface. This interface consists of a GPIB interface unit, a relay register, and an input/pulsed output
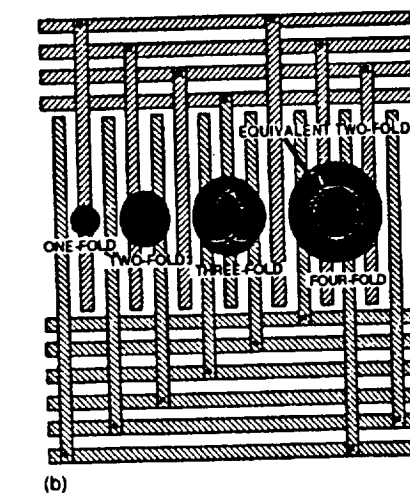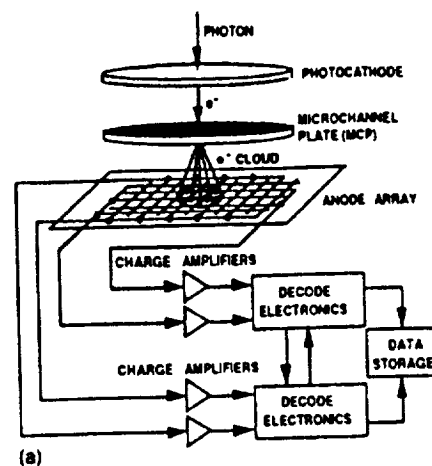
(I/PO) port. Commands issued from the microcomputer are addressed to individual registers in the relay and I/PO units. The output is then fed into a small driver board on the speckle camera. Status bits can be read out from the driver board so that the current positions of the wheels and prisms can be polled from the microcomputer.

2.2 The MAMA Detector and Event Decoding

The MAMA detector and decoding MAMA output have been discussed at length in the literature (Timothy et al. 1989; Kasle 1988), so we will give only a brief description here. There are two parts to the active surface of the detector, the microchannel plate (MCP) and the photocathode (PC). Photons which strike the photocathode may liberate one or more electrons which then cascade down through a microchannel in the MCP, freeing electrons at each contact made with the channel wall until a cloud of 10^5–10^6 electrons exits the channel and strikes an anode array beneath the MCP. Each anode is connected to a charge amplifier which takes this small deposit of charge

and outputs a signal level appropriate for the digital decoding electronics. Figure 3(a) illustrates how the MAMA works.

The current generation of MAMA detectors employs an anode array which consists of two sets of interleaved anodes in a repeating series [see Fig. 3(b)]. For historical reasons these are called "fine–fine" anode arrays. The first set of anodes consists of n anodes (which repeats for $n+2$ cycles) and the second set consists of $n+2$ anodes (which repeats for n cycles), resulting in a total of $n*(n+2)$ pixels, where n must be even to ensure unique decoding over the entire array. The interleaving of the two sets of anodes is analogous to two waves of slightly different frequency beating against each other over many cycles for one complete beat cycle. Another pair of anode sets [not shown in Fig. 3(b)] of m and $m+2$ anodes run underneath and perpendicular to the first pair of anode sets, resulting in a total of $m*(m+2)$ pixels in the perpendicular axis. A pixel is defined as spanning from one anode's center line to the next.

The configuration of a fine–fine array requires a complex algorithm involving coincidence discrimination for determining the position of a given photon event. Coincidence discrimination is the process of taking two or more anodes which experience electron pulses which are coincident in time and inferring the pixel location of the event in the anode array from the combination of anodes. While coincidence discrimination requires a more complex position decoding algorithm than would be needed for a configuration of discrete anodes, it requires far fewer charge amplifiers.

Recently, a technique has been developed which improves the resolution of MAMA images by utilizing a different encoding algorithm. The number of adjacent anodes hit is known as the order of the fold of the event. In the previous algorithm, an odd-fold event could be assigned to one of two pixels as illustrated in Fig. 3(b); however in the new algorithm, the event is assigned to a new pixel whose center lies directly on an anode center, as shown in Fig. 4. Thus, in high-resolution mode, the number of pixels in each direction is doubled. The improvement in resolution is determined by several factors including the distribution of folds, the voltage difference between anode layers, and the spacing of microchannels in the MCP, but has been shown to be as high as 55% with some MAMAs (Kasle and Morgan 1991). Our speckle observing system uses a decoder with the option for high resolution. The decoder is capable of processing raw data from the MAMA at a rate of 6.25 MHz in both normal and high-resolution modes.

2.3 Data Transfer and Storage

The detection and decoding functions are accomplished at the telescope while the accumulation of data and real-time display are carried out by the microcomputer, which in most observing situations is a large distance from the detector. The need to transfer the data from the detector to the computer requires a long-range (100 m), fast, reliable means to transmit the data. These requirements have been
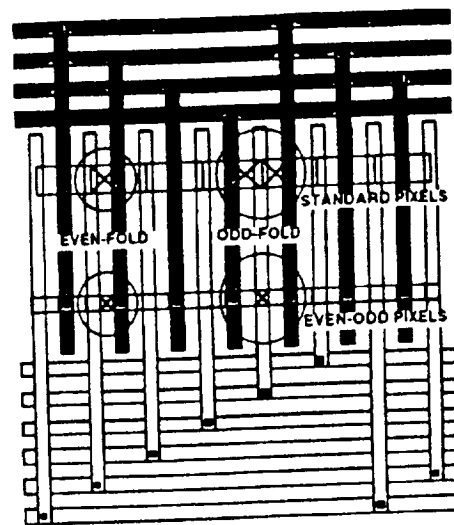

FIG. 4—An illustration of the high-resolution decoding algorithm which incorporates centroiding of the electron cloud striking the anode array to add an extra least-significant bit to the pixel address. Even-fold high-resolution pixels are centered between anodes and odd-fold high-resolution pixels are centered on anodes.

met by a fiber optic link that is currently able to transmit at a data rate of 3.3 Mevent/s for a total of 120 Mbits/s. (Each event is 32 bits long.) A very simple error detection system that rejects events with a double bit error has also been implemented. The detection efficiency of these errors is 50%.

The events arriving through the fiber optic link are processed by a custom computer interface designed at Stanford and shown in Fig. 5. The interface has five different modes of operation: calibrate, speckle, integrate, read, and clear. The calibrate mode is for setting the proper axis proportions in the real-time data display which is most often just an oscilloscope in $X-Y$ mode. The read and clear modes are for clearing and transferring data to the computer. In integration mode, pixel addresses in the memory are incremented as each event arrives, so that a direct image is built up over time. The memory allocated for each pixel is 16 bits allowing a maximum of 65,535 events to be accumulated in each pixel.

In the speckle mode, the pixel address and time of arrival are recorded in memory for each incoming event. To reduce the amount of data stored, the time of arrival is divided into two parts: a coarse time and a fine time tag which represent upper and lower parts of a 26-bit clock register. The fine time tag is attached to the address of every event while the coarse time is added only when an event arrives after the upper bits of the clock have been incremented by one or more. The clock frequency can be set in software at several different speeds ranging from tick intervals of 25–208 μs. For the observations we will describe, it was incremented every 208 μs. This mode of operation maximizes the data bandwidth by minimizing the amount of time spent writing coarse time tags. At this frequency, events had a time resolution of 3.25 μs. The storage format of speckle data in memory follows the structure shown in Fig. 6. The two top bits in each word

FIELD PROGRAMMABLE GATE ARRAY
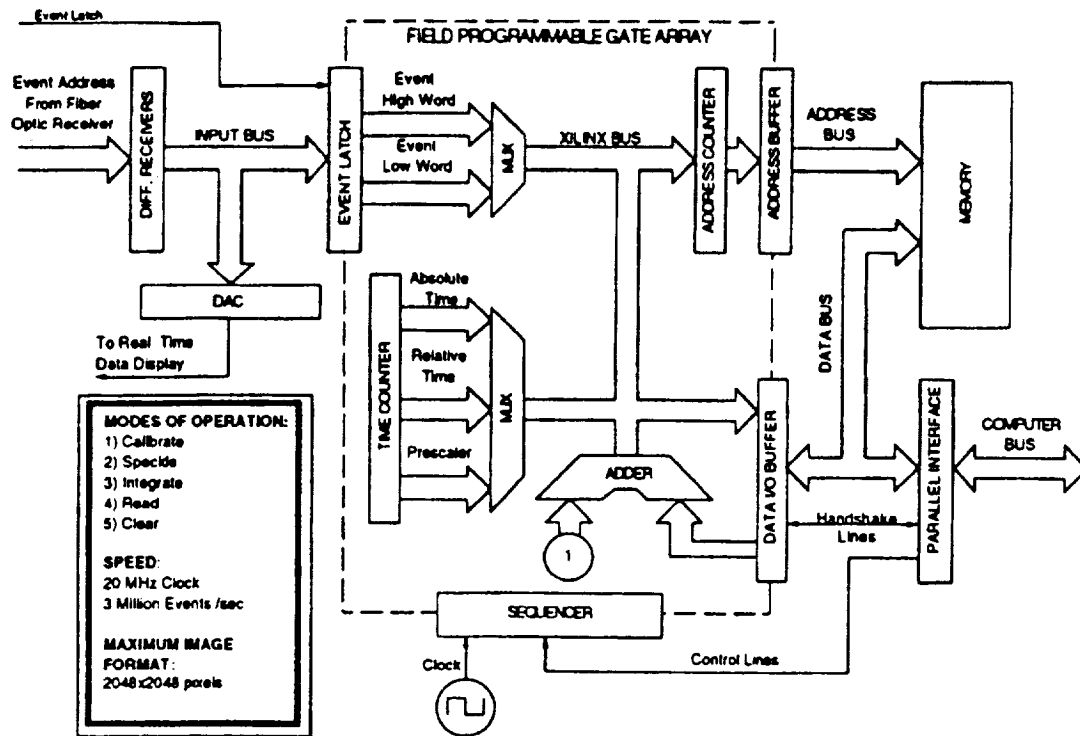
Event Latch

Event Address
From Fiber
Optic Receiver

DIFF. RECEIVERS

INPUT BUS

EVENT LATCH

Event
High Word

Event
Low Word

MUX

XILINX BUS

ADDRESS COUNTER

ADDRESS BUFFER

ADDRESS
BUS

MEMORY

DAC

To Real Time
Data Display

TIME COUNTER

Absolute
Time

Relative
Time

Prescaler

MUX

ADDER

1

DATA I/O BUFFER

DATA BUS

PARALLEL INTERFACE

COMPUTER
BUS

Handshake
Lines

MODES OF OPERATION:
1) Calibrate
2) Speckle
3) Integrate
4) Read
5) Clear

SPEED:
20 MHz Clock
3 Million Events /sec

**MAXIMUM IMAGE
FORMAT:**
2048 x 2048 pixels

SEQUENCER

Clock

Control Lines

FIG. 5—Block diagram of the MAMA speckle interface.

(called the word type) have been added to allow for detection of errors in the data stream. The prescaler portion of the coarse time tag encodes the frequency selected for the clock.

In the current system, data is dumped to nine-track tape every megabyte, and so there is no dead time in the data between dumps. The TS05 tape drive can write data at the rate of 24 kHz, and the interface can be reset and restarted while data is being dumped to tape. For bright objects (count rates >24 kHz), the interface fills with data faster than it can be written to tape, and the observation time for a given number of events is controlled by the tape drive. For dim objects (count rates <24 kHz), data is written to tape faster than the next data buffer is filled in the interface, and the integration time is controlled by the count rate of the object. With fewer counts per second, more events will have absolute time tags written with them, so that a file of 2 Mevent will be larger in terms of bytes for a dim object than for a bright object.

b15	b14	b13	b12	b11	b10	b9	b8	b7	b6	b5	b4	b3	b2	b1	b0
00		Y Coordinate							X Coordinate						
01		Fine Time Tag							Y Coordinate						
10		Coarse Time Tag														
11		Prescaler							Coarse Time Tag						

FIG. 6—The bit structure of MAMA time-tagged events. Each event is 2 words of 16 bits each containing the word type (bits 14 and 15), the x and y coordinates of the events, and a fine time tag. If the event occurs just after a tick on the coarse clock, a coarse time tag of two words is written after the event.

3. OBSERVATIONAL RESULTS

The first observations with this system were made on the 16th, 17th, and 18th of 1991 September, at the Lick Observatory 1-m reflector. The skies were clear and the seeing was between 1″ and 1.″7 all three nights. All of the data that we will discuss in this section was taken in low-resolution mode.

We used a sealed MAMA detector tube with a thermoelectrically cooled bialkali photocathode and 14 μ pixels. The average gain from a photoevent was measured in the lab to be 3.2×10^5 electrons/pulse which means that the distribution of multifolds was dominated by twofold events. We estimate that the quantum efficiency of the telescope/detector combination was on the order of 0.5%–1.0%. The low-gain MCP caused a substantially structured flat-field response. The detector also had a high dark current, roughly 100–300 Hz over the entire area of the anode array. This introduces a noise component into the speckle signal which is especially noticeable for dim objects.

Despite these detector deficiencies, it was an adequate tube to test the speckle system. We obtained speckle data of two point sources and three binary stars which illustrate the capabilities of our system in recovering high angular resolution information, substantially higher than the seeing limit. In Fig. 7, we have plotted the radially averaged spatial frequency power spectrum for two point sources. These graphs have the expected form of a narrow peak at low spatial frequency due to the seeing disk, and then a broad

Radially Averaged Power Spectra, HR 7734 and Fried Model
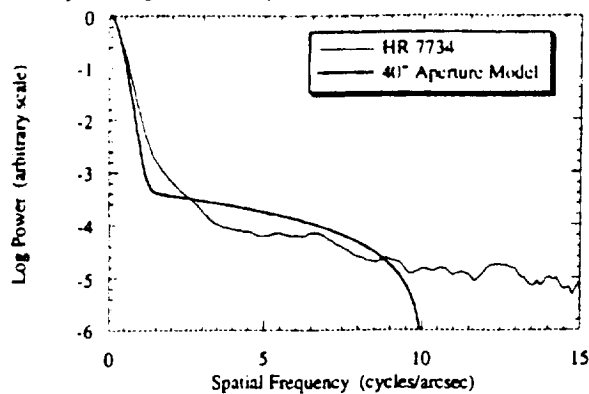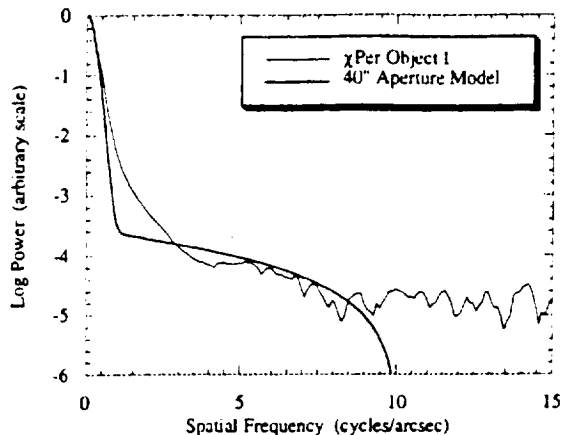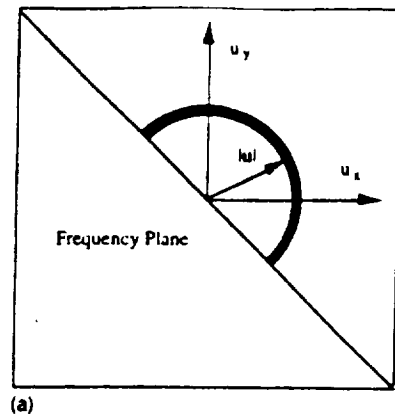

Radially Averaged Power Spectra
χ Per and Fried Model

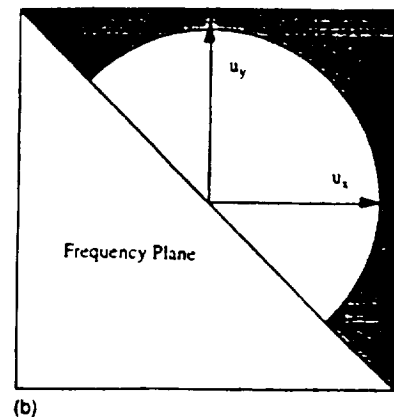FIG. 7—Radially averaged power spectra for two point sources and Fried models for the 1-m aperture.

(a)

(b)

FIG. 8—To make the signal-to-noise measurement in the power spectra of point sources, we considered the average inside a thin annulus of average radius $|u|$ as the signal at $|u|$ cycles/arcsec as shown in (a). The noise measurement was obtained by taking the standard deviation of values in all pixels lying outside the diffraction limit as shown in (b). Since the power spectrum is symmetric about the line $u_y = -u_x$, only points above this line are considered.

shoulder out to the diffraction limit. The power in this shoulder is generated by individual speckles (which are roughly the size of the diffraction-limited point-spread function of the telescope) so the detection of this speckle shoulder indicates that diffraction-limited information is contained in the data. Power beyond the diffraction limit is generated by the dark current and Poisson noise. Also plotted in these figures is a two-component Fried model for the power spectrum of a point source where we have matched the low-frequency peak widths.

It is important to characterize the signal-to-noise ratio in the power spectra in order to understand the limits of the detector system. We define the signal-to-noise ratio at a spatial frequency u as being the value of the power spectrum at u divided by the standard deviation of the values outside the diffraction limit, where little signal is expected. Since we will be working with the power spectra of point sources, which are radially symmetric, it is convenient to consider the average value inside a thin annulus of average radius $|u|$ centered at 0 frequency as the signal at a spatial frequency $|u|$. Figure 8 illustrates how the signal-to-noise measurement is made.

Using this method, we developed curves of S/N as a function of frame time at a fixed spatial frequency for two

point sources, HR 7734 and χ Per. Since the MAMA detector time tags photoevents, it is possible to analyze the same data at various frame times. The expected character of the S/N curve as a function of frame time is for the S/N to be low at small frame times, where Poisson noise dominates, to peak at the frame time corresponding to the time scale of fluctuations in the atmosphere, and then to return to lower values for longer frame times due to the loss of contrast in individual speckles on the image plane. Figure 9 shows the curves we obtained for our two point sources. These graphs indicate that S/N is maximized at a frame time of about 10 ms for HR 7734 and 30 ms for χ Per, which is consistent with the seeing estimate for those observations, about 1.6 arcsec in the case of HR 7734 and 1.0 arcsec in the case of χ Per.

At the telescope we measured the plate scale by moving a stellar image from one side of the active area of the detector to the other and recording the change in direction that the telescope was pointing. By moving the telescope direction only in declination, we were able to define a north–south vector on the detector field of view, and then

Signal-to-Noise Ratio, HR7734, 17Sept.

Legend:
—⊖— S/N @ 2 cycles/arcsec   — ♦ — S/N @ 4 cycles/arcsec
—⊡— S/N @ 3 cycles/arcsec   -- △ -- S/N @ 5 cycles/arcsec

Signal-to-Noise Ratio, χ Per

Legend:
—⊖— S/N @ 2 cycles/arcsec   — ♦ — S/N @ 4 cycles/arcsec
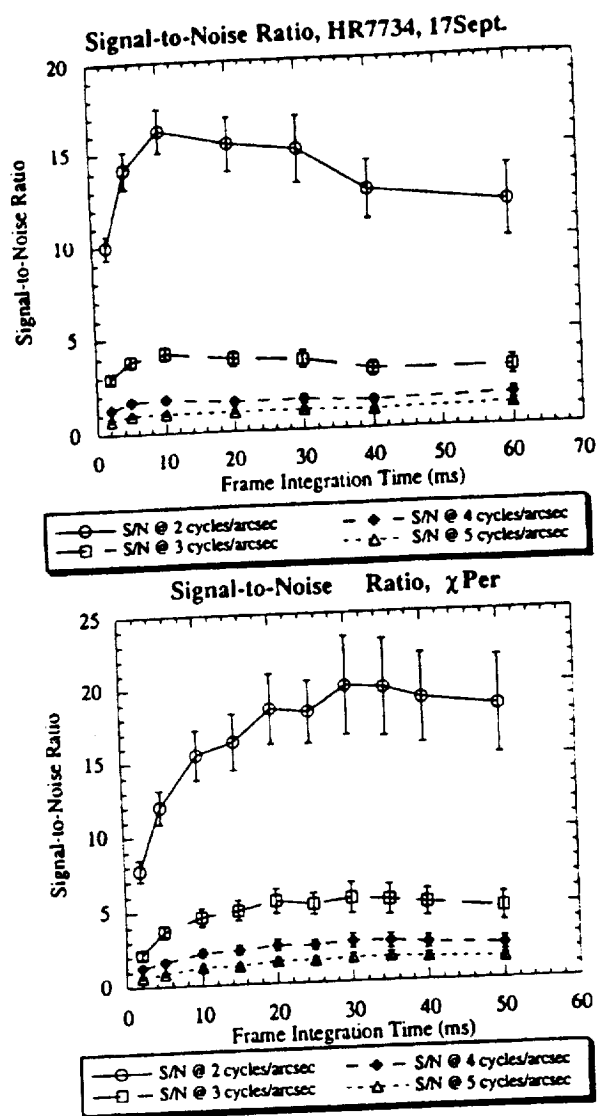—⊡— S/N @ 3 cycles/arcsec   -- △ -- S/N @ 5 cycles/arcsec

FIG. 9—Signal-to-noise ratio as a function of frame integration time for two point sources.

by repeating the measurement in RA, to obtain an east–west vector. This was converted into a detector pitch angle relative to the north–south orientation. The plate scale obtained from this method was 0.03918 ± 0.00327 arcsec/pixel and the pitch angle was $+2.4 \pm 0.84$ deg.

One object in our data set is a visually resolved pair of stars, shown in Fig. 10. This object lies in the field of the open cluster χ Per and the two stars have a magnitude difference of approximately 3. V magnitudes were estimated from a conversion curve derived from five standard stars observed with the same filter as the speckle observations. By using a two-dimensional Gaussian fit routine, we found the separation of the stars to be 2.65 ± 0.22 arcsec and the position angle to be 319.23 ± 0.86 deg. The object was then analyzed via the speckle-autocorrelation method where the separation was found to be 2.60 ± 0.22 arcsec and the position angle was 319.42 ± 0.94 deg. The main source of error in these measurements is the uncertainty in the plate factor, which is limited by the small number of
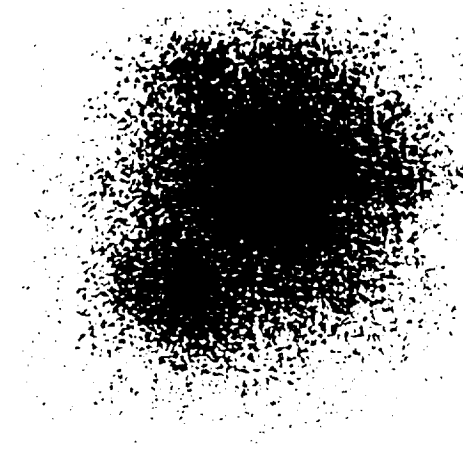

FIG. 10—A direct integration of a visually resolved star pair in the field of the open cluster χ Persei.

arcseconds on the detector field of view. We were also able to estimate the V magnitudes of the two stars from the reconstructed autocorrelation. Based on the amplitude of the central peak and the side lobes, the magnitudes of the two stars are approximately 8.6 and 11.4, very similar to the visual result of 8.6 and 11.5. The speckle analysis of this object gave a position angle, separation, and relative magnitude of the two stars in excellent agreement with the more conventional 2D fitting technique. This test case was chosen to verify the accuracy of the speckle astrometry and photometry when there is a significant difference in the brightness of the primary and companion. As shown in Table 1, only ten events per frame were recorded for the faint star. The power spectrum and a Wiener (optimal) filtered reconstructed autocorrelation for this object are shown in Fig. 11; observing parameters are shown in Table 1. Observational results are summarized in Table 2. We used a Wiener-filtering scheme as a first attempt at reconstructing autocorrelations of this object and the others described below. Though this method can produce oscillations in the reconstructions, we felt that this was an adequate technique for demonstrating the capabilities of the system. In the future, we will investigate the use of more sophisticated techniques.

We also observed two objects in the *CHARA Second Catalog of Interferometric Measurements of Binary Stars*, HD 199839 and HD 202582. Relevant data for these objects are shown in Table 3. A speckle-autocorrelation analysis was performed on the data at a frame time of 10 ms for

TABLE 1
Observing Parameters for a Visually Resolved Star Pair in χ Persei

Parameter	Bright Star	Faint Star
Approx. V Magnitude	8.6	11.5
Seeing Estimate	1.0″	1.0″
Count Rate	3.8 kHz	0.2 kHz
Events Recorded	1.10 Mevent	0.05 Mevent
Photons/Frame	190	10
Filter Wavelength	5029 Å	5029 Å
Filter Width	397 Å	397 Å

(a)
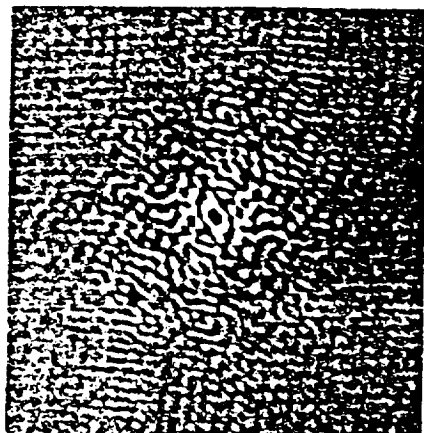
(b)

FIG. 11—(a) Power spectrum of a visually resolved star pair in the field of χ Persei obtained from 1.15 Mevent of MAMA speckle data; (b) Wiener-filtered reconstructed autocorrelation obtained from (a).

HD 199839 and 40 ms for HD 202582. Figures 12 and 13 show the result of the analysis, which is a Wiener-filtered reconstructed autocorrelation for each binary. Both binaries were successfully resolved.

Based on the plate scale and pitch angle discussed above, a separation of 0.360±0.041 arcsec and position angle of 320.0±3.4 deg was derived for HD 199839, and 0.157±0.031 arcsec with a position angle of 271.0±7.2 deg for HD 202582. This is very close to the diffraction limit of the 1-m telescope which is 0.125 arcsec at 5029 Å. In Fig. 14, we have plotted these results along with the earlier observations of each object given in the CHARA catalog. V magnitudes for the stars in each binary were estimated from the amplitudes of the central peaks and the side lobes of the reconstructed autocorrelation and we obtained values of 8.0 and 9.3 for HD 199839 and 6.5 and 8.1

TABLE 2
Observational Results for the Visually Resolved Pair

Parameter	Visual Result	Speckle Result
Separation	2.65 ± 0.22"	2.60 ± 0.22"
Position Angle	319.23 ± 0.85°	319.42 ± 0.94°
Primary V Mag	8.6	8.6
Companion V Mag	11.5	11.4

TABLE 3
Observing Parameters for Two Interferometric Binaries

| Parameter	HD 199839	HD 202582
V Magnitude	7.8	6.4
Spectral Class	A3	G0
Seeing Estimate	1.6"	1.0"
Count Rate	8.7 kHz	35 kHz
Events Recorded	1.56 Mevent	2.15 Mevent
Photons/Frame	87	1400
Filter Wavelength	5029 Å	5029 Å
Filter Width	397 Å	397 Å
Derived Separation	0.360 ± 0.041"	0.157 ± 0.031"
Derived Position Angle	320.0 ± 3.4°	271.0 ± 7.2°
Derived V Mag. Star 1	8.0	6.5
Derived V Mag. Star 2	9.3	8.1

for HD 202582. These observational results are shown in Table 3.

4. CONCLUSIONS AND FUTURE WORK

We have built a new system for taking speckle data with the MAMA detector. This system can transfer data to a remote site via a fiber optic link at the rate of 3 MHz, and
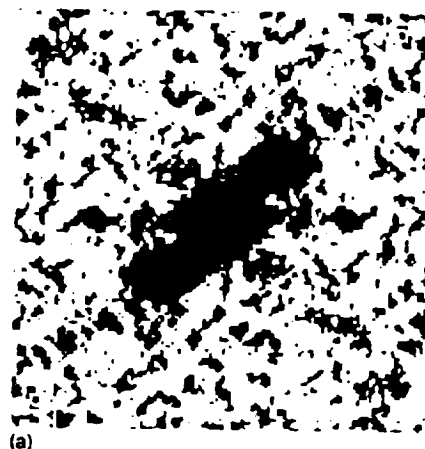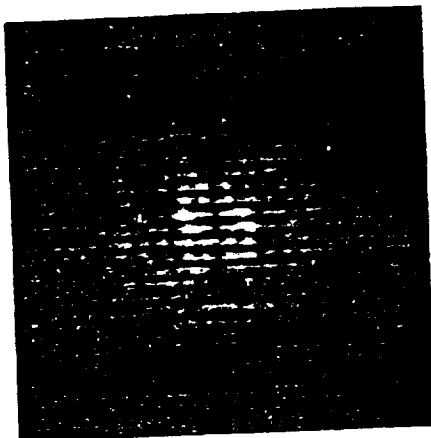

(a)
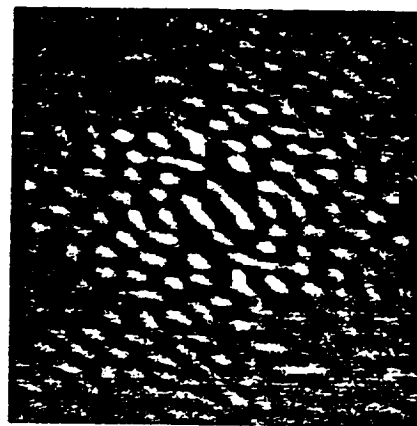
(b)

FIG. 12—(a) Power spectrum of HD 199839 obtained from 1.56 Mevent of MAMA speckle data; (b) Wiener-filtered reconstructed autocorrelation obtained from (a).

(a)

(b)

FIG. 13—(a) Power spectrum of HD 202582 obtained from 2.15 Mevent of MAMA speckle data; (b) Wiener-filtered reconstructed autocorrelation obtained from (a) shown at 2× magnification.

HD 199839, Separation Time History

HD 202582, Separation Time History

FIG. 14—Separation time histories for the two reconstructed binaries from the CHARA second catalog and our 1991.7 results.

can dump data to tape at the rate of 24 kHz. Continuous sections of data are dumped to tape every megabyte. We have tested this system at the 1-m reflector at Lick Observatory and successfully resolved two catalogued interferometric binary stars, one with a separation of 0.157 ± 0.031 arcsec. Since the diffraction limit of the telescope is ~0.125 arcsec, we have demonstrated that this system can recover image features near the diffraction limit. The system also recorded speckle data on a visually separated star pair where the companions had approximate visual magnitude of 8.6 and 11.5 and the speckle analysis of this object gave a position angle, separation, and approximate V magnitudes very similar to the visual analysis. This result demonstrates the accuracy of the speckle analysis of MAMA data at low light levels.

We are currently working on an identical computer interface to the one discussed here for the Macintosh, as well as building the next generation of visible light MAMAs, one of which will be a 1000×1000 (low-resolution) format detector with a trialkali (red-sensitive) photocathode. State-of-the-art charge amplifiers will be used to reduce the noise threshold and thereby increase the detective quantum efficiency of the M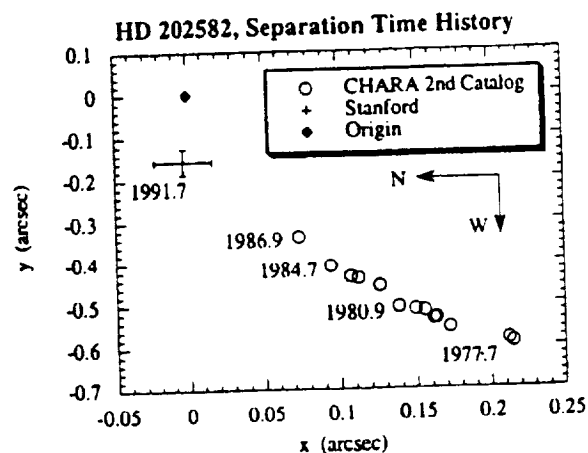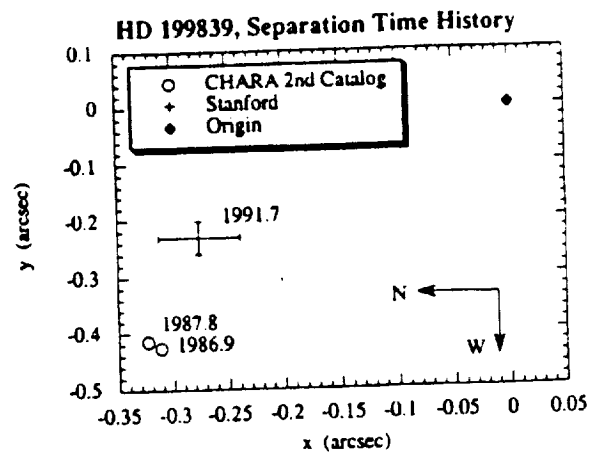AMA systems. Once these advances are in place, this should provide for an excellent speckle-interferometry system with no read noise, high quantum efficiency, low dark current, and outstanding geometric fidelity.

REFERENCES

Christou, J. C., Cheng, A. Y. S., Hege, E. K., and Roddier, C. 1985, AJ, 90, 2644

Fried, D. L. 1979, Opt. Acta, 26, 597

Gorham, P. W., Ghez, A. M., Kulkarni, S. R., Nakajima, T., Neugebauer, G., Oke, J. B., and Prince, T. A. 1989, AJ, 98, 1783

Hege, E. K., Hubbard, E. N., Strittmatter, P. A., and Cocke, W. J. 1982, Opt. Acta, 29, 701

Kasle, D. B. 1988, in SPIE Proc. Vol. 932, Ultraviolet Technology II, ed. R. E. Huffman (Bellingham, WA, SPIE), p. 280

Kasle, D. B., and Morgan, J. S. 1991, in SPIE Proc. Vol. 1549, EUV, X-Ray, and Gamma-Ray Instrumentation for Astronomy II, ed. O. H. Siegmund and R. E. Rothchild (Bellingham, WA, SPIE), p. 52

Labeyrie, A. 1970, A&A, 6, 85

McAlister, H. A., and Hartkopf, W. I. 1988, Second Catalog of Interferometric Measurements of Binary Stars, Georgia State University, Atlanta

Morgan, J. S., Slater, D. C., Timothy, J. G., and Jenkins, E. B. 1989, Appl. Opt., 28, 1178

Morgan, J. S., Timothy, J. G., Smith, A. M., and Kasle, D. B. 1990, in SPIE Proc. Vol. 1235, Instrumentation in Astronomy VII, ed. R. E. Huffman (Bellingham, WA, SPIE), p. 347

Nakajima, T. et al. 1989, AJ, 97, 1510

Papaliolios, C., Nisenson, P., and Ebstein, S. 1985, Appl. Opt. 24, 287

Roddier, F. 1987, Interferometric Imaging in Optical Astronomy, NOAO, Tucson

Timothy, J. G., Morgan, J. S., Slater, D. C., Kasle, D. B., Bybee, R. L., and Culver, H. E. 1989, in SPIE Proc. Vol. 1158, Ultraviolet Technology III, ed. R. E. Huffmann (Bellingham, WA, SPIE), p. 104

Performance of high resolution decoding with multi-anode microchannel array detectors

David B. Kasle
Stanford University CSSA, ERL 262
Stanford, CA 94305   (415)725-0438

Elliott P. Horch
Stanford University Center for Space Science and Astrophysics
Stanford University CSSA, ERL 262
Stanford, CA 94305   (415)725-0442

ABSTRACT

The Multi-Anode Microchannel Array (MAMA) is a microchannel plate based photon counting detector with applications in ground-based and space-based astronomy. The detector electronics decode the position of each photon event, and the decoding algorithm that associates a given event with the appropriate pixel is determined by the geometry of the anode array. The standard MAMA detector has a spatial resolution set by the anode array of 25 microns, but the MCP pore resolution exceeds this. The performance of a new algorithm that halves the pixel spacing and improves the pixel spatial resolution is described. The new algorithm does not degrade the pulse-pair resolution of the detector and does not require any modifications to the detector tube. Measurements of the detector's response demonstrate that high resolution decoding yields a 60% enhancement in spatial resolution. Measurements of the performance of the high resolution algorithm with a 14 micron MAMA detector are also described. The parameters that control high resolution performance are discussed. Results of the application of high resolution decoding to speckle interferometry are presented.

1. INTRODUCTION

The MAMA detector employs a photocathode for photon/electron conversion, a microchannel plate (MCP) for electron multiplication and an anode array combined with charge amplifiers for event detection. Digital decoding electronics interpret the charge amplifier outputs to determine the pixel position of an event. The block diagram of a MAMA detector is shown in Figure 1.

The current generation of MAMA detectors employ arrays that consist of two sets of interleaved anodes in a repeating series (see Figure 2). For historical reasons these are called "fine-fine" anode arrays. The first set of anodes consists of n anodes (which repeats for n+2 cycles) and the second set consists of n+2 anodes (which repeats for n cycles), resulting in a total of $n*(n+2)$ pixels. The interleaving of the two sets of anodes is analogous to two waves of slightly different frequency beating against each other for one complete cycle. Another pair of anode sets (not shown in Figure 2) of m and m+2 anodes run underneath and perpendicular to the first pair of anode sets, resulting in a total of $m*(m+2)$ pixels in the perpendicular axis. A pixel is defined as spanning from one anode's center line to the next.

The configuration of a fine-fine array requires a complex algorithm involving coincidence discrimination for decoding the position of a given photon event. Coincidence discrimination is the process of taking two or more anodes that experience electron pulses that are coincident in time and inferring the pixel location of the event in the anode array. While coincidence discrimination requires a more complex position decoding algorithm than would be needed for a configuration of discrete anodes (as opposed to the fine-fine-configuration), it requires far fewer anodes and therefore far fewer charge amplifiers.

The size of the electron cloud due to a single photon event varies depending on the MCP's characteristics as well as bias voltages applied to the photocathode, MCP and anode array. The electron cloud diameter is quantized by the total number of anodes illuminated in a given axis, also referred to as the order of the fold. For example, a three-fold designates the situation in which three contiguous anodes are struck by sufficient numbers of electrons to have voltages greater than some user-specified threshold. A subsection of a scaled-down version of one axis of a fine-fine anode array (n=4) with one-, two-, three-, and four-folds is shown in Figure 2. The electron cloud diameter must be sufficient to illuminate at least two anodes (a two-fold) in order to allow for the unique decoding of the position of the event. A saturated MCP pulse height distribution (PHD) is critical in this application because it allows the effective elimination of ambiguous one-fold events when the proper bias voltage is set on the anode array. Because of size variations in the electron cloud emanating from the MCP, the decoding algorithm must be capable of coping with higher-order folds. As Figure 2 illustrates, every higher-ordered fold can be reduced to an equivalent two-fold (that two-fold which occupies the same pixel as the higher-ordered fold). Notice that a three-fold (or any odd-fold) is ambiguous because it spans two equivalent two-folds. A decoder's function is to take an arbitrarily ordered fold and infer the corresponding pixel position of the event. Since there is one decoder input for each anode, a single axis requires 2n+2 inputs.
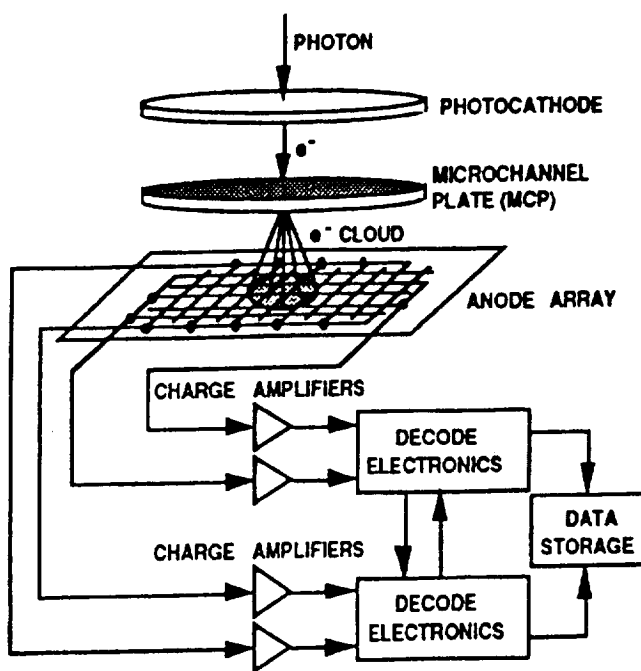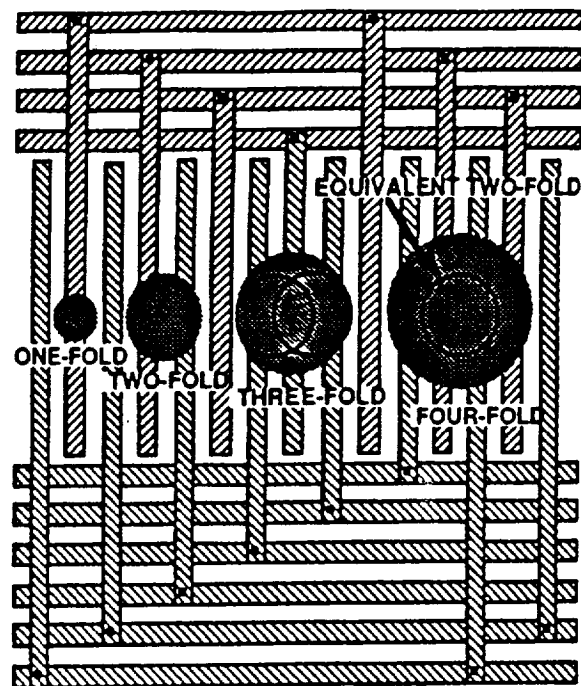
Figure 1. MAMA block diagram

Figure 2. Fine-fine array single axis with multi-folds

2. HIGH RESOLUTION DECODING

In a standard MAMA detector pixel size is equal to the spacing of the anodes, but the spatial resolution of the MCP is generally greater than that of the anode array. This implies that the detector is capable of spatial resolution greater than that achieved with the original fine-fine decoding scheme. It is possible to increase the resolution of the detector without changing the detector itself, but only by altering the readout electronics. One technique for improving resolution is called even-odd discrimination. This algorithm is incorporated into a new MAMA decoder as a user-selectable mode, which enabled testing of this technique as described below. Even-odd discrimination differentiates between even-folds and odd-folds to generate a single least significant bit (LSB), thereby halving the pixel spacing and doubling the number of pixels in each axis. Each pixel is characterized by 1) its separation from its nearest neighbors and 2) a gaussian shaped pixel response function, which is characterized by its width. In high resolution decoding, the pixel response width is determined primarily by the spatial resolution of the MCP. The detector spatial resolution is equal to whichever is greater, the pixel spacing or the pixel response width. In this case the pixel response width (which is the same as the MCP spatial resolution) is greater.

Even-odd discrimination can be performed in parallel with the standard decoding procedure with no loss of decoder speed and requires the addition of minimal hardware to the standard decoding circuitry (although the memory size must be quadrupled). Figure 3 illustrates normal resolution (top) versus high resolution achieved with even-odd discrimination (bottom). Standard pixels are twice the size of high resolution pixels, and span from the center of one anode to the next. By contrast, the even-fold pixels are centered between the anodes and the odd-fold pixels are centered on the anodes themselves, thereby resolving the ambiguous nature of odd-folds in normal resolution decoding. Figure 4 illustrates how each standard pixel is converted into four high resolution pixels in a two dimensional array. There are two possibilities: if odd-folds are always binned in the left hand standard-size pixel (the "throw left" option), then odd-fold pixels have an LSB of one and even-fold pixels have an LSB of zero. Conversely, if odd-folds are always binned in the right hand standard-size pixel (the "throw right" option), then odd-fold pixels have an LSB of zero and even-fold pixels have an LSB of one.

2.1 Experimental Procedure

The first imaging tests of high resolution decoding were performed with the experimental setup shown in Figure 5. The detector employed was an ultraviolet 25 micron 360x1024 pixel system with an opaque CsI photocathode. This detector has a microchannel plate with 12 micron diameter pores packed together as tightly as possible in a hexagonal lattice with 15 micron center-to-center spacing between the pores. There are 3.24 pores per low resolution pixel and 0.81 pores per high resolution pixel. The optical system employed an ultraviolet mercury pen ray lamp whose light was diffused by a diffusing lens placed in close proximity to the lamp. Neutral density filters were employed to decrease and control the photon flux, and the diminished
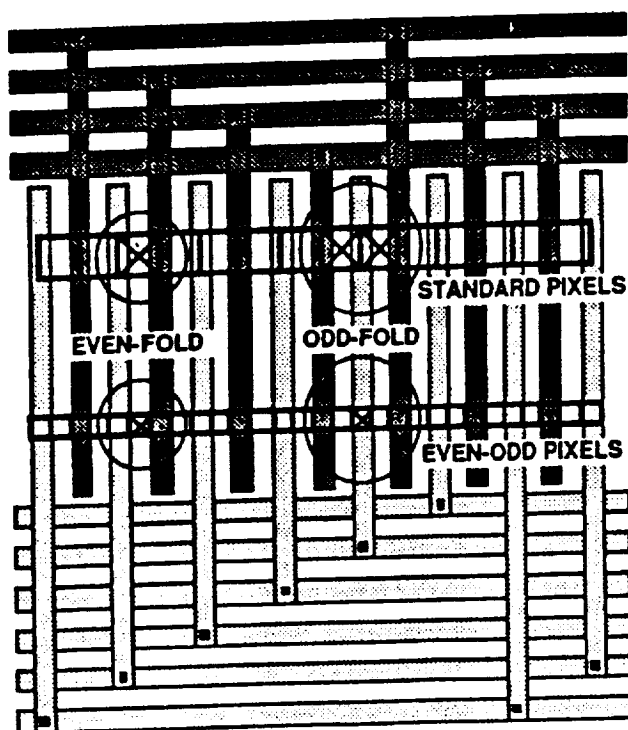
ONE STANDARD PIXEL = 4 HIGH RESOLUTION PIXELS

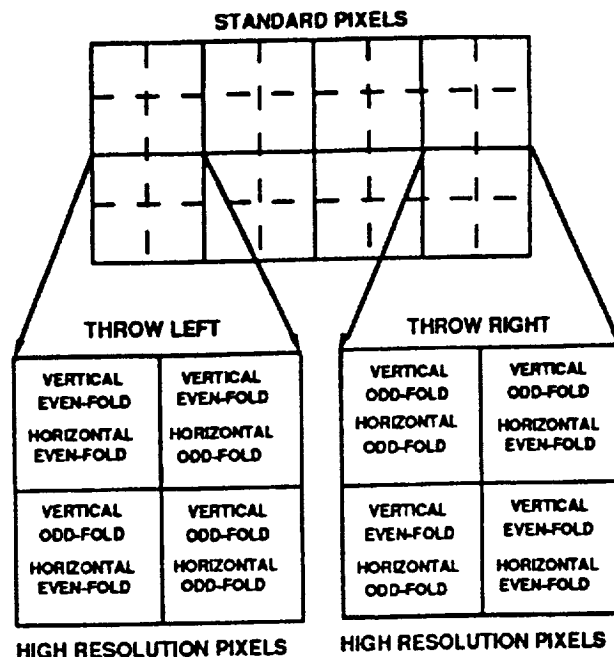Figure 3. High resolution : even-odd discrimination

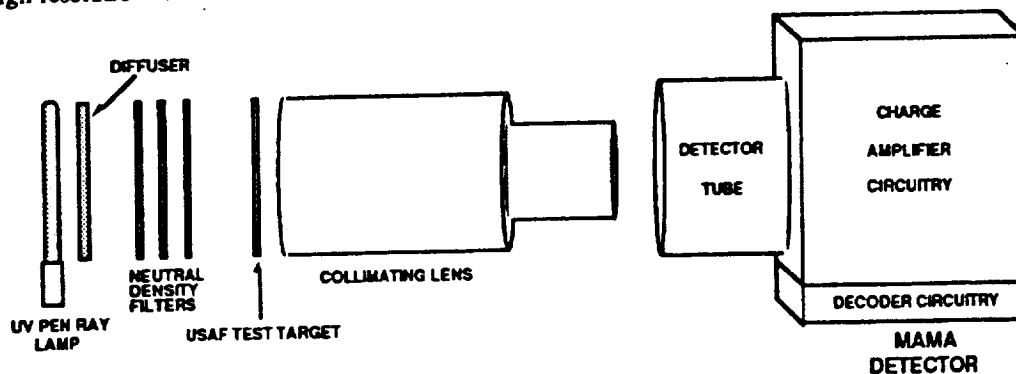Figure 4. High resolution : throw left vs. throw right

Figure 5. Optical arrangement for USAF test target imaging experiments.

photon flux illuminated an aluminized USAF test target. The light transmitted through the transparent portions of the USAF test target was collimated and focused by a UV collimating lens, which projected the focused target image onto the focal plane of the MAMA detector. Images were taken with the USAF test target in both low and high resolution mode. The images were then divided on a pixel-by-pixel basis by flat field exposures to normalize the pixel response. The low and high resolution images were taken under identical conditions.

It is important to note that there are two factors that complicate attempts to determine the upper limit to the resolution achieved with even-odd discrimination. Firstly, there is sampling error, which occurs whenever the edge of a feature in the image does not coincide with a pixel boundary. Secondly, all of the results shown here include the effects of aberrations in the input image caused by imperfections in the imaging optics. These aberrations tend to blur the smallest features in the image. Therefore the results shown here should be considered a lower limit to the performance of high resolution decoding.

2.2 25 Micron MAMA Detector Results

The USAF test target images shown in Figure 6 were taken with the photocathode voltage set at -2500 V and the MCP set at -2200V. In this case the demagnification factor of the optical system was -2.78. The low resolution exposure

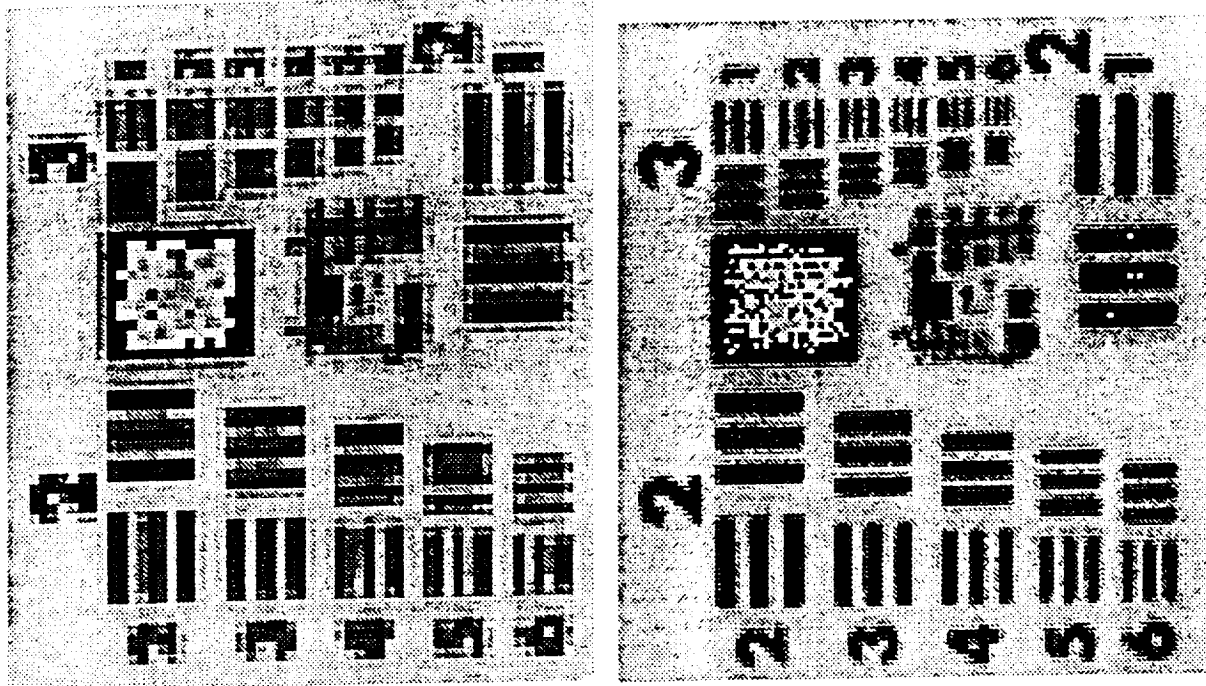**LOW RESOLUTION (2X MAGNIFICATION)** **HIGH RESOLUTION**

Figure 6. Normal resolution 25 micron MAMA image (2X magnification) of a portion of an USAF test target vs. high resolution image of the same target. The collimating lens aperture stop was set at f22 for the test target image.

consists of a 450 second f22 integration divided by a 6300 second flat field without the collimating lens. The high resolution exposure consists of a 1800 second f22 integration divided by a 25200 second flat field without the collimating lens.

Elements 2 through 6 of group 2 are clearly visible on the left side of both images, but the high resolution image obviously displays greater clarity. In addition, the low resolution image of elements 2 through 6 of group 3 are not resolved, whereas the high resolution image resolves individual bars down to group 3, element 6 for both horizontal and vertical elements. The digits in the high resolution image are again obviously clearer. And while neither image resolves the individual bars in the elements of group 4, high resolution is able to resolve each block of three horizontal bars from the adjacent block of three vertical bars. The images were recorded with a 16 bit depth, but they are displayed in Figure 6 in 8 bit mode. Therefore the brightest areas of the images, such as the inner portions of the largest rectangles, experience "roll-over" in the displayed image in Figure 6.

The quality of the USAF test target images can be displayed graphically by measuring the modulation of the image, i.e. the contrast between dark and light sections of the image as a function of the feature size. The desired data can be obtained by taking a swath of columns as wide as the smallest element (i.e. the smallest trio of bars) in the horizontal elements for a given group, usually the trio of bars that comprise element 6. The columns can then be added together and the data can be displayed as a modulation trace through the rows of pixels. Just such modulation traces are illustrated in Figure 7, which shows low resolution and high resolution traces through group 2 horizontal elements in the first graph and through group 3 horizontal elements in the second graph. In the case of the low resolution group 2 and group 3 elements, the swaths are six columns wide and three columns wide respectively. In the case of the high resolution group 2 and group 3 elements, the swaths are twelve columns wide and six columns wide respectively. A wider swath of columns generally leads to a greater signal-to-noise ratio in the data.

Each individual bar of the group 2 elements is clearly visible in the first graph of Figure 7 for both high and low resolution, although the peak-to-valley ratio is obviously greater in the high resolution data. The second graph of Figure 7 again demonstrates the superior resolving power of the even-odd discrimination high resolution algorithm. Low resolution is only able to resolve the vertical element 1 of group 3 whereas high resolution resolves down to element 6. The low resolution f8 and f22 images were both limited by the resolution of the pixel size. However, the smaller high resolution pixels made the input image quality the limiting factor to detectable resolution in the image. The high resolution trace in Figure 7 still demonstrates excellent modulation for element 6 of group 3. It is possible that a superior optical system could produce even
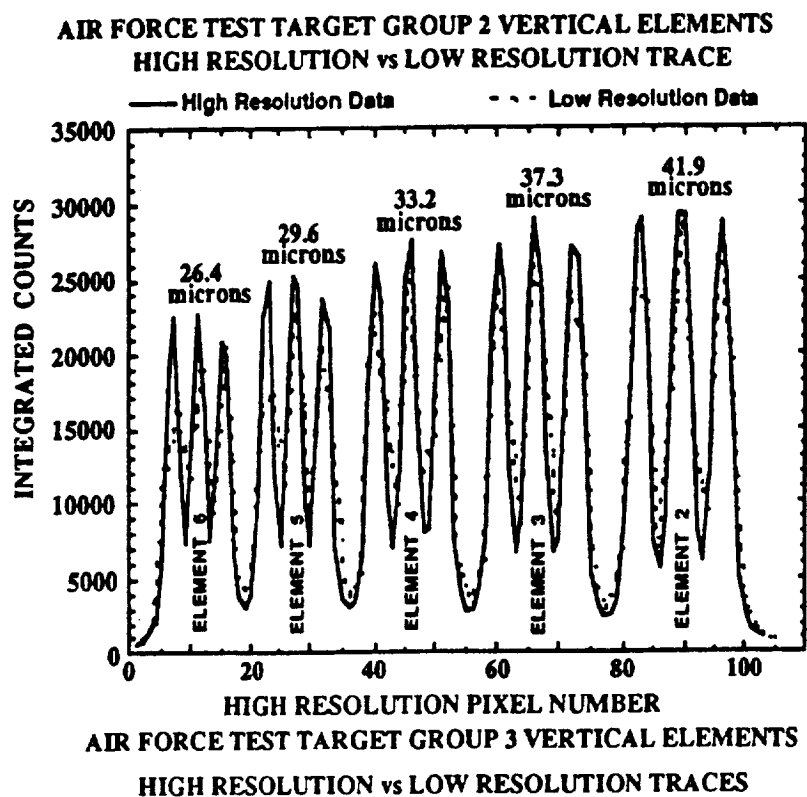
AIR FORCE TEST TARGET GROUP 2 VERTICAL ELEMENTS
HIGH RESOLUTION vs LOW RESOLUTION TRACE

——High Resolution Data   - - - Low Resolution Data

AIR FORCE TEST TARGET GROUP 3 VERTICAL ELEMENTS

HIGH RESOLUTION vs LOW RESOLUTION TRACES

——High Resolution Data   · · · Low Resolution Data

Figure 7. High and low resolution modulation traces through the Group 2 and Group 3 vertical elements shown in the USAF test targets from Figure 6. Feature size is shown in microns. Resolution of individual elements in units of line-pairs/mm is as follows: group 2 element 2: 11.94, element 3: 13.41, element 4: 15.06, element 5: 16.89, and element 6: 18.97 line-pairs/mm. Group 3 elements: element 1: 21.28, element 2: 23.89, element 3: 26.87, element 4: 30.06, element 5: 33.78, and element 6: 38.04 line-pairs/mm.

better results. Spatial sampling error and multi-fold displacement are the most likely causes of the difference between the high resolution group 3 vertical elements 5 and 6 and group 3 horizontal elements 5 and 6.

2.3 Modulation Transfer Function

The modulation between dark and light that a detector can recover from an input scene is primarily controlled by three factors. The first factor is the quality of the input image, which depends on the quality of the optical arrangement. The second is the resolution of the detector's pixels. And the third factor is the amount of spatial sampling error, i.e. the error incurred when the edge of a feature in the scene is not aligned with the edge of pixel. Spatial sampling error converts what might be sharp transitions between black and white into shades of gray.

The modulation is often measured by the *modulation transfer function (MTF)*, which is a function of the peaks, valleys and average background in the modulation traces in Figure 7. The MTF is defined by the equation:

$$MTF = \frac{PEAK \cdot VALLEY}{PEAK + VALLEY - (2 \times BACKGROUND)} \qquad (1)$$

The value of the MTF varies between zero and one, with higher values being most desirable. Figure 5-6 displays the average modulation transfer functions as a function of feature size for the low resolution group 2 and the high resolution group 3 horizontal elements. In both cases, the group with the smallest resolvable elements was used for computing the MTF in order to insure that the pixel size was the dominant factor. The trace through each element consists of three peaks and two valleys. The "PEAK" in equation 1 is defined as the average of the three peaks and the "VALLEY" in equation 1 is defined as the average of the two valleys. The "BACKGROUND" is defined as the valley between the element in question and the adjacent element. The triangles and squares in Figure 8 are the actual average MTFs for the low and high resolution images of Figure 6. The straight lines are linear least squares fits to the MTF data. The average difference between the low resolution and high resolution MTF least squares fits shows that high resolution has a 60% resolution enhancement over low resolution (i.e., a factor of 1.6).

2.4 14 Micron MAMA Detector Results

Similar tests to those described in the previous section were performed with a visible 14 micron MAMA detector. This detector has a bialkalai photocathode and a microchannel plate with 8 micron diameter pores packed together as tightly as possible in a hexagonal lattice with 10 micron center-to-center spacing between the pores. The anode array consists of 224x960 pixels with 14 micron spacing between the anodes. On average there are 2.27 pores for each pixel; therefore the spatial
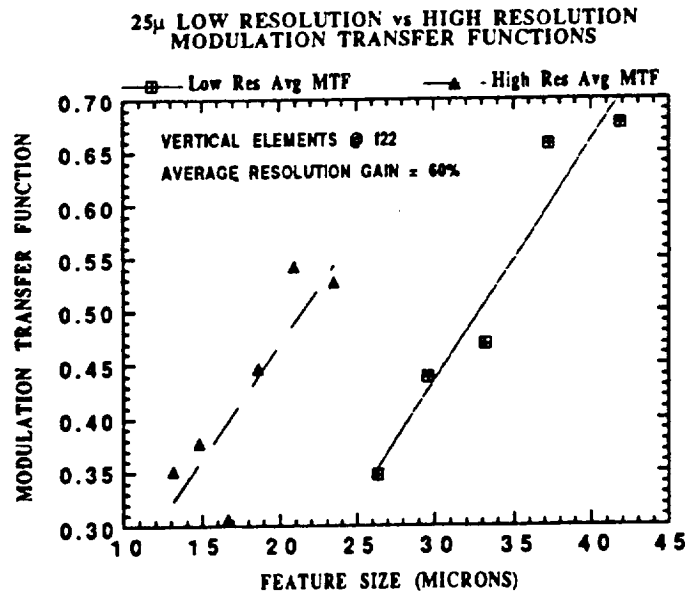

Figure 8. High and low resolution average modulation transfer functions. The high resolution MTF for the vertical group 3 elements is on the left and the low resolution MTF for the vertical group 2 elements is on the right. The straight lines are least squares fits to the MTF data.

resolution of the MCP is greater than that of the anode array, but not by as great a margin as is the case for the 25 micron MAMA detector previously described. In this case there are only 0.57 pores for each high resolution pixel. Thus the potential improvement of high resolution decoding is less with the 14 micron MAMA detector.

The USAF test target imaging experiment was repeated with the 14 micron MAMA detector. The differences between the 14 micron MAMA detector low resolution and high resolution images are not quite so obvious as was the case with the 25 micron MAMA detector. This is demonstrated more clearly in the group 3 low resolution versus high resolution modulation trace shown in Figure 9. The low resolution image resolves down to group 3, element 4 whereas the high resolution image resolves down to group 3 element 6. The high resolution trace clearly has superior resolution and high resolution modulation transfer functions in Figure 10 graphically show the resolution gain. The average difference between the MTF least squares fits reveals the resolution gain to be about 14% (i.e. a factor of 1.14).

It is somewhat surprising that high resolution decoding could result in any resolution enhancement for the 14 micron MAMA detector. Firstly, there are only 2.27 MCP pores for each low resolution pixel, which strictly limits the possible resolution gain. Secondly, the pixel size so small that any blur in the optical input image could dominate the results. And thirdly, the multi-fold distribution (MFD) is strongly skewed towards even-folds in the horizontal axis. The vertical axis has an even-fold to odd-fold ratio of 60% to 40%, but the horizontal axis has an even-fold to odd-fold ratio of 81% to 19%. Despite this circumstance, the vertical axis and the horizontal axis seem to have equal resolution. This result indicates that the high resolution decoding algorithm is robust in its ability to work over a range of conditions.

2.5   Factors Controlling High Resolution

Aside from external factors such as input image quality and spatial sampling error, the most critical factor in high resolution decoding performance is the resolution of the microchannel plate. This is true for any MAMA detector whose MCP pore resolution is less than twice that of its anode resolution, i.e. when the pores under sample the high resolution pixels. Under these circumstances, the MCP pore resolution is the limiting factor, and other parameters have only second order effects.

Most second order parameters affect the high resolution performance indirectly by modulating the multi-fold distribution. The multi-fold distribution for a single pore cannot be measured directly, but it determines which high resolution pixels the pore contributes counts to. A single pore can contribute counts to more than one pixel, and this in itself is a source of blurring in the image. In an ideal MAMA detector, each high resolution pixel would have at least one MCP pore delivering
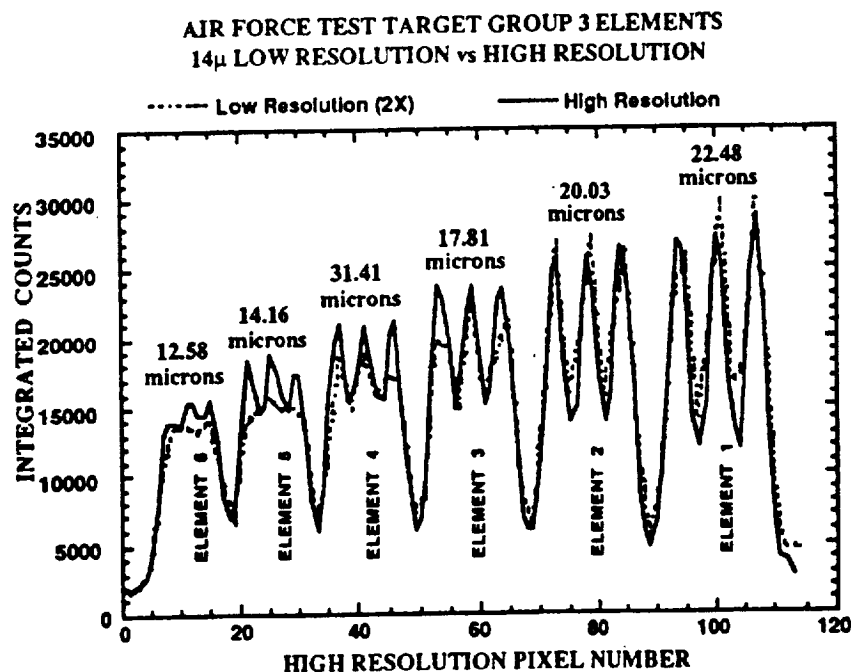

Figure 9. 14 micron high and low resolution modulation traces through the Group 3 vertical elements shown in the USAF test targets from Figure 5-13. Feature size is shown in microns. Resolution of individual elements in units of line-pairs/mm is as follows: group 3 element 1: 21.28, element 2: 23.89, element 3: 26.87, element 4: 30.06, element 5: 33.78, and element 6: 38.04 line-pairs/mm.

14 micron LOW RESOLUTION vs HIGH RESOLUTION MODULATION TRANSFER FUNCTIONS
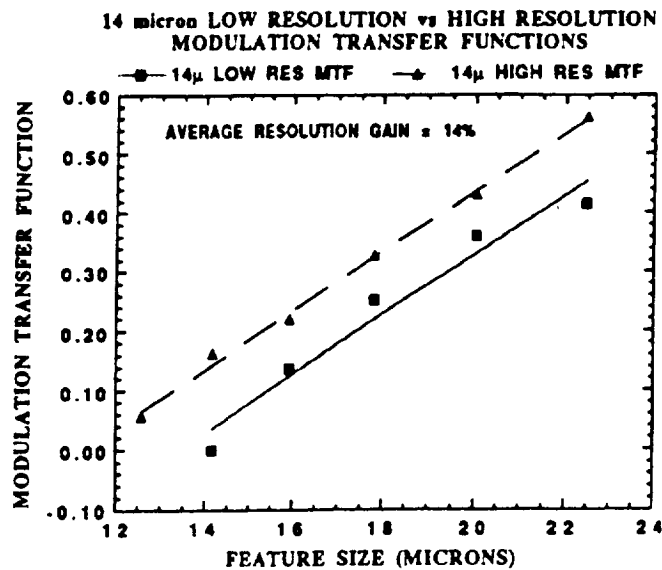
Figure 10. High and low resolution modulation transfer functions for the 14 micron MAMA detector. The high resolution MTF for the horizontal group 3 elements is on the left and the low resolution MTF for the horizontal group 3 elements is on the right. The straight lines are least squares fits to the MTF data.

counts to it alone. The higher the resolution of the MCP pores, the closer the detector comes to this ideal situation in which the achieved resolution is insensitive to the MFD and high resolution decoding actually doubles the resolution of the detector.

The MFD is controlled by several parameters. Increasing microchannel plate gain tends to increase the mean of the multi-fold distribution. In this context, increasing the mean of the MFD means changing the MFD so that it is weighted towards higher order multi-folds. The local MCP gain may vary, resulting in local variations in the MFD. Similarly the mean of the MFD increases with decreasing anode bias voltage or decreasing charge amplifier threshold.

The phenomenon in which a single MCP channel contributes counts to one high resolution pixel most of the time but then occasionally contributes counts to an adjacent pixel because the size of the multi-fold changes is called *multi-fold displacement*. The MFD for a given pore determines how frequently multi-fold displacement occurs. The position of the pore with respect to the anodes combines with the size of the output electron cloud to determine whether an even-fold or an odd-fold is produced. For example, a pore may produce predominantly three-fold events, thereby contributing counts to an odd-fold pixel. However, if the electron cloud size shrinks or grows, the pore will produce a two-fold or a four-fold, either of which would contribute a count to an adjacent even-fold pixel. Every time this happens, a slight amount of blur is introduced to the integrated image.

In an effort to explore the effect of varying the multi-fold distribution on high resolution image quality, imaging tests were performed while varying parameters of MCP voltage and charge amplifier threshold. Figure 11 illustrates the MFDs generated by the 25 micron 360x1024 pixel UV MAMA detector for MCP voltages of 2150 volts (high gain) and 2000 volts (low gain) while imaging the USAF test target. Both images were integrated with a charge amplifier threshold of 0.207 volts. The multi-fold distribution for 2150 volts is clearly biased towards higher ordered folds, peaking between three-folds and four-folds in the vertical axis. The MFD for 2000 volts peaks at two-folds in the vertical axis. At 2000 volts, the ratio of even-folds to odd-folds is 1.7 in the vertical axis, and at 2150 volts the ratio of even-folds to odd-folds is 1.06 in the vertical axis.

Despite the more optimal MFD at the higher voltage, the performance of high resolution as measured by the modulation transfer function was nearly the same for both MCP voltages. Modulation traces and the resulting modulation transfer functions were computed for the horizontal group 3 elements at both voltages, as shown in Figure 12. The modulation traces were performed in the vertical axis. Note that in the vertical axis, the high gain and low gain images have twin peaks of three- and four-folds and two- and three-folds respectively. The least squares linear fits for the two MTF functions are nearly equal, indicating that the high resolution performance is relatively insensitive to MCP gain in this operational regime.

Another set of USAF test target images were made with the same MAMA detector holding the MCP voltage constant and varying the charge amplifier threshold voltage. Images were integrated at three values of the threshold: 0.207 volts (regular threshold), 0.283 volts (midway threshold), and 0.322 volts (high threshold). The multi-fold distributions for these threshold cases are shown in Figure 13. The vertical axis MFD for the middle threshold of 0.283 volts is strongly peaked at three-folds, whereas the regular threshold and high threshold images have twin peaks of three- and four-folds and two- and three-folds respectively. The midway threshold MFD is narrower than either the regular threshold or the high threshold MFDs, therefore it is less likely to encounter multi-fold displacement. The result (illustrated in Figure 14) is that the least squares fits for the regular and high resolution MTFs are nearly equal, but the least squares fit to the midway threshold MTF indicates 6% better resolution than the regular threshold or the high threshold images. The performance of high resolution has some sensitivity to the multi-fold distribution in this operational regime, but the dominant factor in determining high resolution performance is still the resolution of the pore spacing in the microchannel plate.
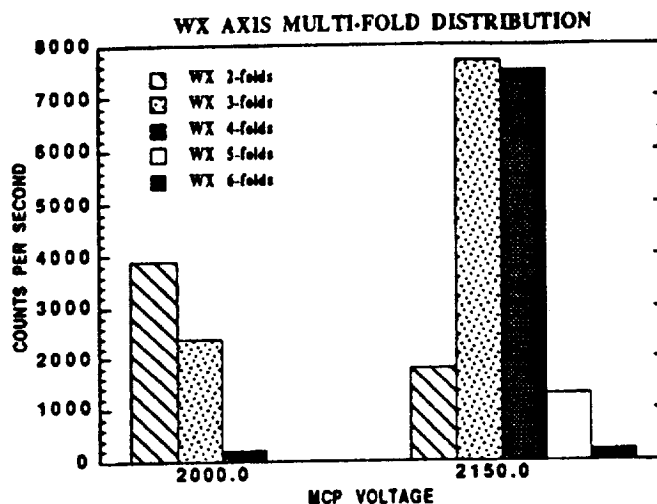

Figure 11. Vertical (WX) axis multi-folds for USAF test targets imaged at MCP voltages of 2000 volts and 2150 volts. The charge amplifier threshold was 0.207 volts.
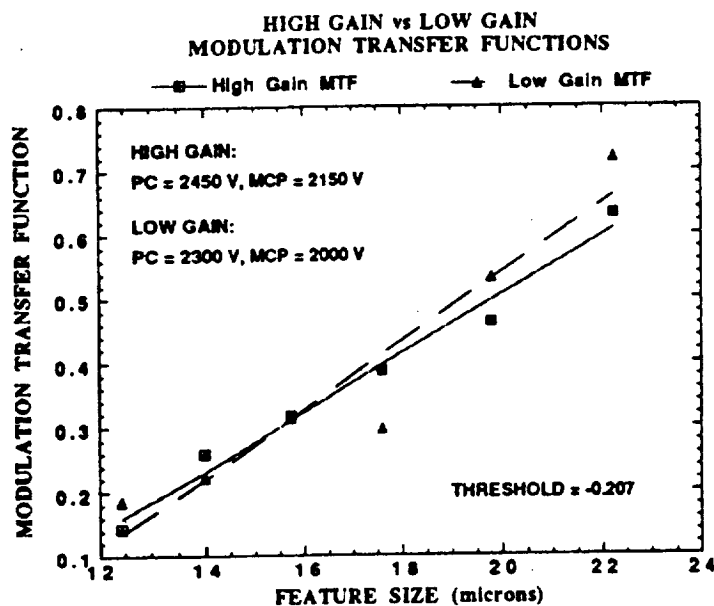

Figure 12. High resolution average modulation transfer functions for high MCP gain and low MCP gain. The MTF was computed from a high resolution modulation trace through the USAF test target horizontal group 3 elements. The straight lines are least squares fits to the MTF data. The least squares fits are nearly equal. The collimating lens aperture stop was at f22 and the demagnification factor was -2.78.

WX AXIS MULTI-FOLD DISTRIBUTION

12000

| □ WX 2-folds | ■ WX 4-folds | ■ WX 6-folds |
| ▣ WX 3-folds | □ WX 5-folds | |

COUNTS PER SECOND

10000

8000

6000

4000

2000

0

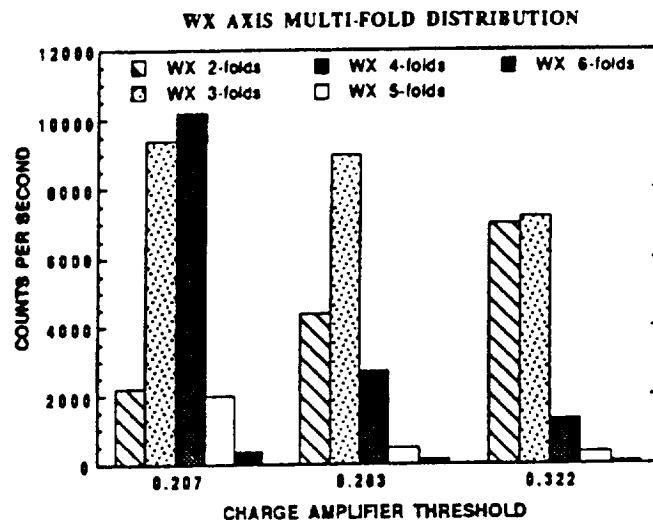0.207   0.283   0.322

CHARGE AMPLIFIER THRESHOLD

Figure 13. Vertical (WX) axis multi-folds for USAF test targets imaged at charge amplifier thresholds of 0.207 volts, 0.283 volts and 0.322 volts. The photocathode and the MCP were set to 2450 and 2150 volts, respectively.

HIGH RESOLUTION MODULATION TRANSFER FUNCTION AS A FUNCTION OF THRESHOLD

—○— Reg Threshold   —▲ ·Mid Threshold   — ■ ·High Threshold

MODULATION TRANSFER FUNCTION

0.7

0.6   Regular Threshold = 0.207
       Midway Threshold = 0.283
0.5   High Threshold = 0.322

0.4

0.3

0.2

0.1

0.0

-0.1

14   16   18   20   22   24   26
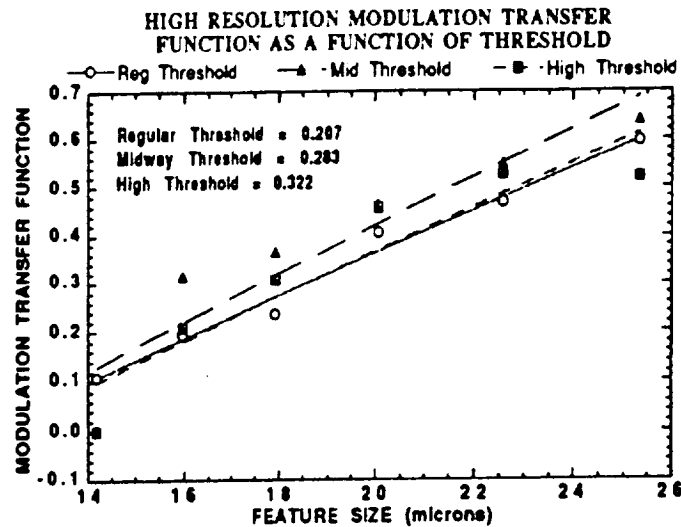
FEATURE SIZE (microns)

Figure 14. High resolution average modulation transfer functions for three different charge amplifier thresholds. The MTF was computed from a high resolution modulation trace through the USAF test target horizontal group 3 elements. The straight lines are least squares fits to the MTF data. The least squares fits are nearly equal for the regular threshold and the high threshold, but the midway threshold has 6% better resolution. The collimating lens aperture stop was set at f22 and the demagnification factor was -2.44. The photocathode and the MCP were set to 2450 and 2150 volts, respectively.

2.6 High Resolution Temporal Stability

Low resolution decoding is relatively insensitive to the multi-fold distribution, whereas high resolution is more sensitive to temporal variations in the MFD, since such variations will alternately increase or decrease the number of events in even-fold or odd-fold pixels. This can become a problem in the flat fielding process. If the original image and the flat field used to normalize the pixel response have significantly different MFDs, then the normalization will be imperfect, resulting in noise in the flat fielded image. The high resolution mode is therefore achieved at the expense of an increased sensitivity to the MFD. Both low resolution and high resolution have less temporal stability if the microchannel plate pulse height distribution (PHD) is not saturated or if the charge amplifier threshold is not located in the valley to the left of the PHD modal gain peak.

In order to test detector temporal stability, several high resolution flat field exposures were taken with the 360x1024 pixel UV MAMA detector. The flat field exposures were integrated long enough to average 10,000 counts per pixel in order to achieve 1% statistical noise. Given that in high resolution mode there are 1,474,560 pixels (720x2048), approximately 1.5×10^{10} photons were integrated in each exposure. Low resolution flat fields were constructed from the high resolution exposures by ignoring the least significant bit of the high resolution pixel addresses.

The first sets of flat field integrations were performed with a photocathode voltage of 2400 volts and an MCP voltage of 2100 volts. The initial flat field exposures were divided by subsequent flat field integrations in order to test the temporal stability of the detector response. The resulting histograms are shown for both low and high resolution in Figure 15. The narrow peak in both histograms indicates that both low and high resolution have good temporal stability. A second set of flat field integrations were performed with a photocathode voltage of 2450 volts and an MCP voltage of 2150 volts. These flat fields provided almost identical results, indicating that high resolution and low resolution decoding both provide temporal stability over a range of operational conditions. In theory, due to its greater sensitivity to MFD variations, high resolution decoding might have lower temporal stability than low resolution. In practice, the MFD can be kept sufficiently constant to negate any such effects. The conclusion of these results is that both high and low resolution decoding of MAMA detectors provide temporal stability of detector response when the detector's operating conditions and voltages are held constant.
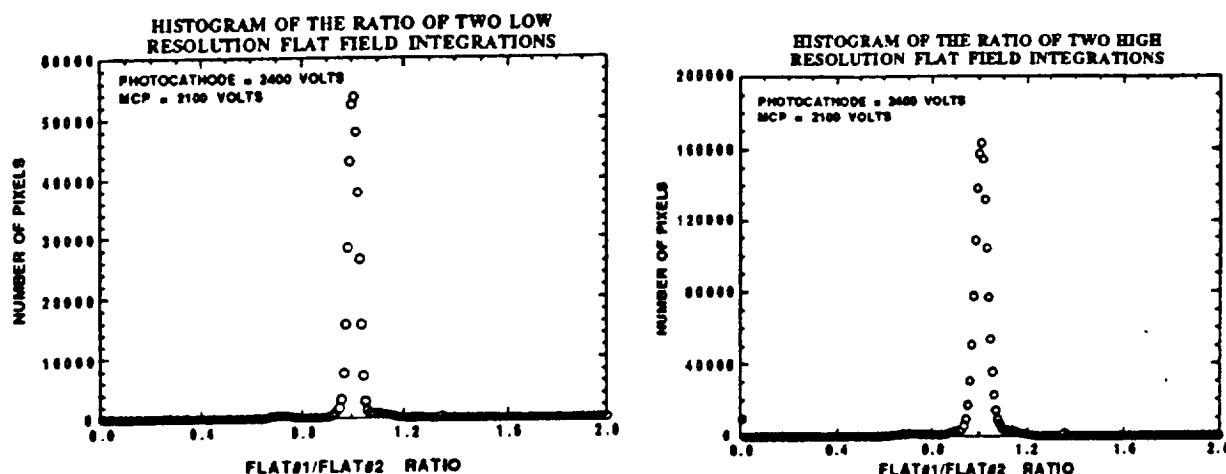

Figure 15. Histograms of low and high resolution ratios of two flat field integration. The photocathode and MCP voltages were 2400 and 2100, respectively. Both low and high resolution show good temporal stability.

3. SPECKLE INTERFEROMETRY WITH THE HIGH RESOLUTION ALGORITHM

3.1 The Method

In conventional ground-based visible light astronomy, the resolution of images is limited by the presence of turbulence in the air above the telescope aperture that blurs the image of a point source out into a patch of light roughly 1-2 arcsec at full width half maximum (FWHM). This point spread function, known as the "seeing disk," is some 50 times broader than the diffraction limit of the largest optical telescopes.

In speckle interferometry, it is possible to recover diffraction-limited resolution. If there were no atmospheric turbulence, light from an astrophysical point source would arrive at the telescope as a plane wave, and therefore have uniform phase and magnitude across the telescope aperture. It is well-known from optics that the point spread function is given by the modulus squared of the Fourier transform of the aperture function. Therefore, in the absence of turbulence, the uniform aperture function gives rise to an Airy pattern as the point spread function. In the real case of ground based observing, the turbulence in the telescope aperture disturbs the uniform phase of the aperture function. The effect of this is to produce an instantaneous point spread function that fills the area of the seeing disk but has a fine structure of bright regions which have a characteristic width similar to the diffraction-limited point spread function of the telescope. Such an instantaneous point spread function is known as a speckle pattern. Speckle patterns evolve on a typical time scale of 10ms, so that on an integration of significantly longer than this, the speckle nature of the image washes out and only the overall shape of the seeing disk remains. Because the individual speckles in a speckle pattern are the same size as the diffraction-limited point spread function, speckle patterns contain

high resolution information about astrophysical objects. One can hope to recover this information if the detector at the image plane can read out images at the rate of the time evolution of the speckles. The MAMA detector is capable of time-tagging photon events to a resolution of 400ns, so it is a good detector for this application.

Consider taking time-tagged data of a binary star. In a speckle experiment, photons can be binned into short integrations called "frames" where the integration time is short enough that the instantaneous point spread function does not change very much over the integration. If the object of interest is a binary star, frame images will exhibit speckle pairs at the vector separation of the companions, as illustrated in Figure 16. These speckle doublets will occur at various places on the image plane but may be collected together by considering the autocorrelation function of a frame, which is equivalent to the histogram of the distance vectors between photon pairs. Each frame image $I(x)$ may be described as a convolution of the true object intensity distribution $O(x)$ with the frame point spread function $S(x)$:

$$I(\mathbf{x}) = S(\mathbf{x}) * O(\mathbf{x}),$$ (2)

where "*" denotes convolution. In the Fourier domain, a convolution becomes an ordinary product so that

$$\hat{I}(\mathbf{u}) = \hat{S}(\mathbf{u}) \cdot \hat{O}(\mathbf{u}),$$ (3)

where "^" denotes Fourier transform and the spatial frequency variable conjugate to x is u. Taking the modulus squared of this and averaging over many frames, we obtain the result that the average image power spectrum is the product of the average point spread function power spectrum and the true object power spectrum:

$$\left\langle \left| \hat{I}(\mathbf{u}) \right|^2 \right\rangle = \left\langle \left| \hat{S}(\mathbf{u}) \right|^2 \right\rangle \cdot \left| \hat{O}(\mathbf{u}) \right|^2.$$ (4)

where $\langle\ \rangle$ denotes the average over many frames. If a speckle experiment is performed on the binary star, $\left\langle \left| \hat{I}(\mathbf{u}) \right|^2 \right\rangle$ can be obtained by Fourier transforming the average autocorrelation of many frames of data. The same process performed on a point source yields $\left\langle \left| \hat{S}(\mathbf{u}) \right|^2 \right\rangle$. The true binary power spectrum can then be obtained by division, where such a division is valid in the region where $\left\langle \left| \hat{S}(\mathbf{u}) \right|^2 \right\rangle$ is non-zero. In fact the average point spread function power spectrum is non-zero out to the diffraction limit of the telescope and the method works not only for binary stars but also for general objects (Labeyrie, 1970). The true object autocorrelation is obtained by Fourier inversion. In the case of a binary system, reconstructing the object autocorrelation is sufficient to retrieve the separation, position angle (up to a 180° ambiguity), and the relative magnitudes of the two companions. In practice, after forming the reconstructed power spectrum by division, the result is masked by a low pass filter before Fourier inverting to obtain a result uncontaminated by high frequency noise.
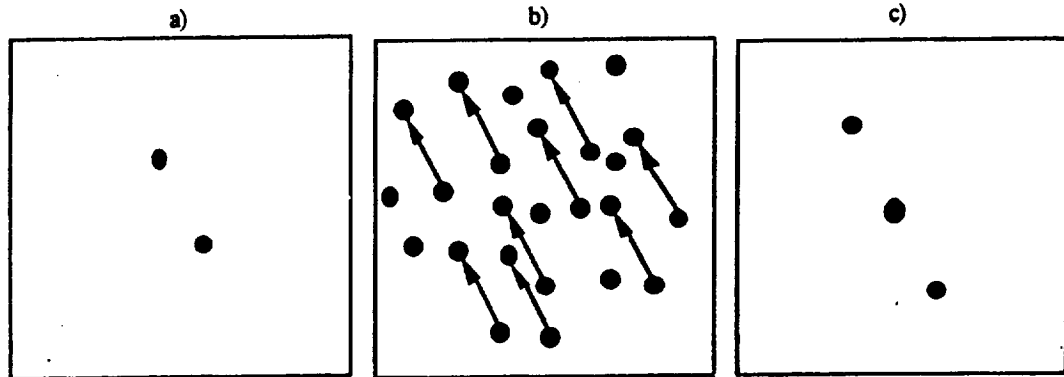

Figure 16. a) A binary star object function $O(x)$, b) illustration of a speckle pattern for a binary star where speckle doublets occur at the binary separation, c) the autocorrelation function of (a).

3.2 Observations with the High Resolution Decoding Algorithm

On May 22, 1992, the authors observed two binary stars and two point sources with the Lick Observatory 1-m reflector and a visible light MAMA detector operating in time tag mode. Data was recorded on each object using both the high resolution decoding algorithm and the old (low resolution) algorithm. The seeing estimate for these observations was about 1".5. We binned the data into 15ms frames and carried out the autocorrelation analysis described in the previous section.

Three separate autocorrelation reconstructions were completed for each binary. The first is based on the low resolution data, the second is also based on the low resolution data, but the reconstructed power spectrum was placed inside an array that was double the size of the low resolution arrays in both dimensions before Fourier inverting. Thus, it is the same data as the low resolution case, but oversampled by a factor of two in order to have the same pixel size in image space as the high resolution data. The third reconstruction is based on the high resolution data. In all cases, the same low pass filter was used to eliminate high frequency noise before Fourier inverting. The resulting autocorrelation reconstructions are shown in Figure 17.
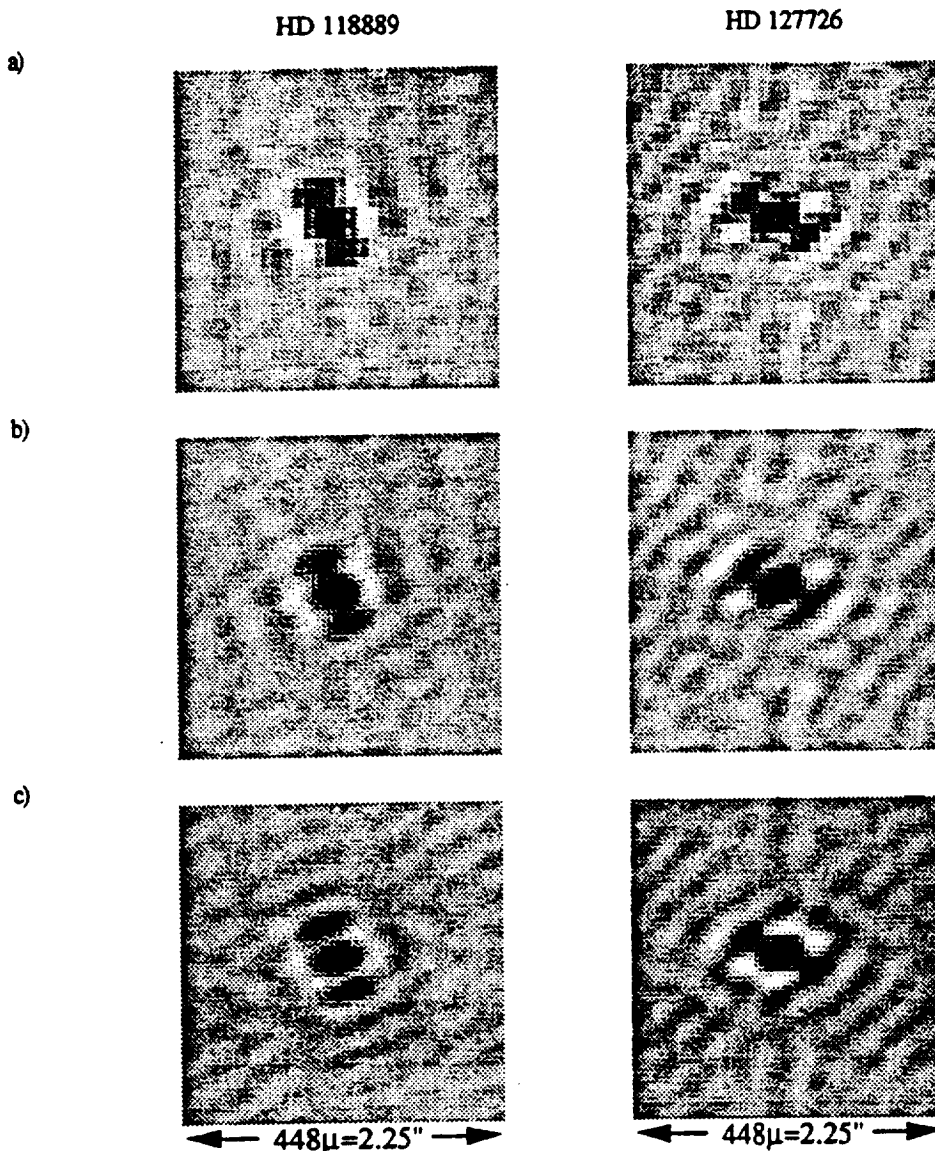

Figure 17. Low and high resolution autocorrelation reconstructions for the interferometric binary stars HD 118889 and HD 127726. a) Low resolution, b) Low resolution oversampled, and c) high resolution. The low resolution autocorrelations are 32x32 pixels, the high resolution oversampled low resolution results are 64x64 pixels.

TABLE 1

Observational Parameters of Two Binaries Derived from Low and High Resolution Data

| Parameter | HD 118889 | | HD 127726 | |
	Low Res.	High Res.	Low Res.	High Res.
Position Angle	286.3±9.1°	283.8±3.9°	144.2±8.0°	154.7±3.8°
Separation	0".22±0".04	0".26±0".02	0".25±0".04	0".27±0".02
Mag. Diff.	0.9	0.9	1.5	1.2

Notes: Error bars are derived from the assumption that the positions of the auto-correlation side peaks are known to ±0.5 pixels. Low resolution results are based on the autocorrelations shown in Figure 17a, high resolution results are based on Figure 17c.

These results clearly show that the high resolution algorithm is usable for speckle interferometry, since both binaries are resolved with high resolution data, and that the autocorrelation reconstructions in these two cases are at least as good as the low resolution data. Table 1 compares the values obtained for position angle, separation, and relative magnitudes of the two stars for the high and low resolution cases. They are in good agreement.

One other speckle study was performed using high resolution data. We took speckle data of a point source, HD 125019, in high and low resolution modes, and formed the power spectrum for each for a frame integration time of 15ms. Figure 18a shows the radially averaged power spectrum for both cases where it is evident that the high resolution power is higher in the region >2 cycles/arcsec. This is what would be expected if the pixel response function of high resolution data is narrower than that of low resolution data, since the power spectrum of the average pixel response function is incorporated into the overall point source power spectrum. Of course, power in this region is affected by the seeing conditions; in fact, the high frequency power goes as the inverse square of the seeing width. However, the seeing conditions in the low and high resolution data can be seen to be very similar by looking at the low frequency part of Figure 18a. While it is impossible to insure that all observing conditions were identical in both cases, this lends some evidence to the notion that the low resolution pixel response function is wider that for high resolution and that it is possible to obtain higher spatial resolution with the new algorithm.
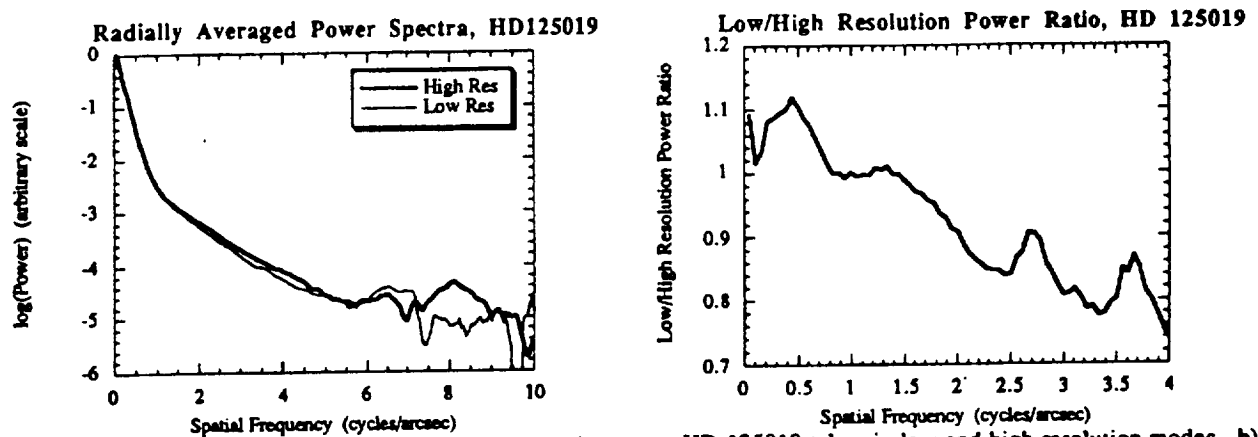

Figure 18. a) Radially averaged power spectra for the point source HD 125019 taken in low and high resolution modes. b) Radially averaged power ratio for the low frequency region of the power spectra.

4. SUMMARY

A new algorithm for decoding the output of MAMA detectors has been shown to enhance the detector spatial resolution by at least 60%. The exact degree of resolution depends primarily on the spatial resolution of the microchannel plate. The high resolution decoding algorithm shows excellent temporal stability and is relatively insensitive to variations in detector operating parameters. In preliminary tests at Lick Observatory, high resolution decoding appears to produce speckle interferometry results that are at least as good as the results obtained with low resolution decoding.

5. ACKNOWLEDGMENTS

6. REFERENCES

1. D.B. Kasle, "Decoding Techniques for fine-fine-geometry multi-anode microchannel arrays", *SPIE Ultraviolet Technology II*, Vol. 932, pp. 280-284, 1988.

2. D.B. Kasle, "High resolution decoding techniques and single chip decoders for multi-anode microchannel arrays", *SPIE Ultraviolet Technology III*, Vol. 1158, pp. 311-318, 1989.

3. D.B. Kasle and G. De Micheli, "An Image Decoding ASIC for Space-Based Applications", *Proceedings of EURO ASIC '91*, IEEE Computer Press, pp. 86-91, 1991

4. J.G. Timothy, "Electronic readout systems for microchannel plates," *IEEE Transactions on Nuclear Science*, Vol. NS-32, No. 1, pp. 427-432, 1985.

5. J.G. Timothy and R.L. Bybee, "High-resolution pulse-counting array detectors for imaging and spectroscopy at ultraviolet wavelengths," *SPIE Ultraviolet Technology*, Vol. 687, pp. 109-116, 1986.

6. J.S. Morgan, J.G. Timothy, A.M. Smith, R. Hill and D.B. Kasle, "High Time-Resolution Imaging with the MAMA Detector Systems," *SPIE Instrumentation in Astronomy VII*, Vol. 1235, pp. 347-356, 1990.

7. D.B. Kasle and J.S. Morgan, "High resolution decoding of multi-anode microchannel array detectors", *SPIE EUV, X-Ray, and Gamma-Ray Instrumentation for Astronomy II*, Vol. 1549, pp. 52-58, 1991.

8. Christou, J.C., Cheng, A.Y.S., Hege, E.K., & Roddier, C., "Seeing calibration of optical astronomical speckle interferometric data", *Astronomical Journal*, Vol. 90, pp. 2644-2651, 1985.

9. Fried, D.L., "Angular dependence of the atmospheric turbulence effect in speckle interferometry", *Optica Acta*, Vol. 26, pp. 597-613, 1979.

10. Labeyrie, A., "Attainment of diffraction limited resolution in large telescopes by Fourier analyzing speckle patterns in star images", *Astronomy & Astrophysics*, Vol. 6, pp. 85-87, 1970.

11. McAlister, H.A. & Hartkopf, W.I., *Second Catalog of Interferometric Measurements of Binary Stars*, Georgia State University, Atlanta, 1988.

12. Roddier, F., *Interferometric Imaging in Optical Astronomy*, NOAO, Tucson, 1987.

13. Horch, E., Morgan, J.S., Giaretta, G., & Kasle, D.B., "A new speckle interferometry system for the MAMA detector", *Publications of the Astronomical Society of the Pacific*, in press.

Microchannel plate modal gain variations with temperature

David C. Slater and J. Gethyn Timothy

Center for Space Science and Astrophysics, Stanford University, ERL 315B, Stanford, California 94305-4055

Measurements of the modal gain of two high-gain curved-channel microchannel plates (MCPs) at various operating temperatures are presented. Both MCPs were fabricated from Galileo Electro-Optics Corporation Long Life™ glass with 12-μm diam channels on 15-μm centers. The modal gain was found to decrease with increasing temperature at a rate of -0.1% $(^{\circ}C)^{-1}$. This reduction of gain with temperature is attributed primarily to an axial temperature gradient along each MCP channel creating a nonuniform electric field within the channel that lowers the effective output gain. A lowering of the secondary electron yield resulting from increased phonon scattering of secondary electrons released within the walls of the MCP channels was also assessed, but was found to have a negligible contribution to the drop in gain with temperature.

I. INTRODUCTION

The microchannel plate (MCP) is a thin (~ 0.5–1 mm) semiconducting glass plate composed of 10^5–10^7 small hollow channels each acting as an electron multiplier. The many closely spaced channels within the active area of the MCP allow it to be used in applications requiring high spatial resolution imaging and the bare MCP is routinely used as an image intensifier for the detection of UV and soft x-ray photons, electrons, and positive ions.[1] The MCP is the basic component of position sensitive detector systems that utilize one of a variety of position-encoding readout techniques, such as the resistive anode,[2] wedge-and-strip anode,[3] and the multianode microchannel array (MAMA)[4] systems.

The MCP, operating in a high-vacuum environment, acts as a continuous-dynode electron multiplier. When an incident photon or charged particle enters a channel and strikes the channel wall, one or more electrons are released which are drawn further down into the channel by the applied electric field across the MCP. These electrons eventually strike the channel wall and again cause the release of a number of electrons, the average of which is given by the value of the secondary electron yield. Provided the secondary electron yield is greater than one, a cascade of secondary electrons develops inside the channel. The number of electrons that exit the channel is referred to as the gain with units commonly expressed in terms of electrons per output pulse (electrons pulse^{-1}). Because of the random nature of the electron collisions inside a channel, the gain of each output electron cloud is randomly distributed. The statistical distribution of the gain is called the pulse-height distribution (PHD), known to take on various shapes depending primarily on the geometry of the channels and the magnitude of the applied MCP voltage. The MCPs operating under high-gain, space-charge saturated conditions, display quasi-Gaussian shaped PHDs.[1] Figure 1 shows the PHD of a curved-channel MCP with 12-μm diam channels and an L/D (channel length-to-diameter) ratio of 120:1 operating with an applied MCP voltage of 2000 V. The gain at the peak of the distribution is referred to as the modal gain, and the ratio of the full-width-at-half-maximum (FWHM) of the distribution to the modal gain is called the PHD resolution.

II. MODAL GAIN VERSUS TEMPERATURE MEASUREMENTS

Modal gain measurements of two high-gain curved-channel MCPs were made with the MCPs operating at various temperatures. Both MCPs employed 12-μm diam channels on 15-μm centers, and were fabricated by Galileo Electro-Optics Corporation (GEOC) using their Long-Life™ glass composition. The first MCP, designated MCP #1, had a rectangular active area of 327 mm^2, an L/D ratio of 125:1, and a plate resistance of 38.3 MΩ at 20 °C. The second MCP, designated MCP #2, had a rectangular active area of 203 mm^2, an L/D ratio of 146:1, and a plate resistance of 13.3 MΩ at 20 °C.

Both MCPs were operated under high vacuum ($< 10^{-7}$ Torr) in a demountable MAMA vacuum tube assembly with a linear (1×100)-pixel discrete-anode array used to detect the output pulses.[5] Figure 2 is a schematic showing how the MCP was mounted and biased within the MAMA tube assembly. The MCP was mounted above the (1×100)-pixel anode array using three raised ground pads that provided a 100-μm gap between the MCP output and the array. A negative high voltage was applied to the input side of the MCP, with the output at ground potential. The anode array was biased positively (~ 100 V) to attract the electron pulses from the MCP. Above the input surface of the MCP was an aperture plate that was biased more negative than the MCP input which provided enhanced detection efficiency by repelling those electrons that were photogenerated in the interchannel regions of the MCP back down into the MCP channels. Direct current high-voltage power supplies with a voltage stability of 0.005% (load regulation) were used to bias the MCP and the aperture plate in the MAMA tube assembly. A UV grade sapphire window was used at the front end of the MAMA tube to allow UV photons at a wavelength of 2537 Å from a mercury "penray" lamp to stimulate the MCP during these
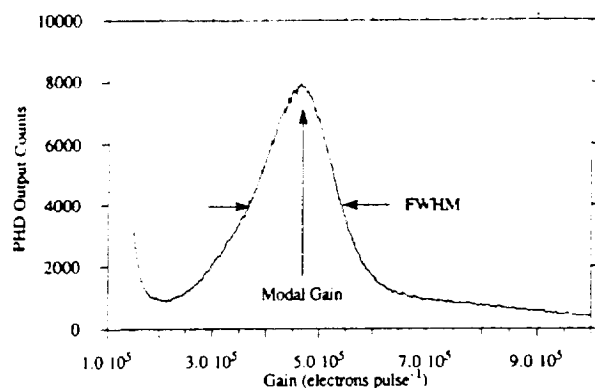
FIG. 1. Measured pulse-height distribution (PHD) of a curved-channel MCP operating in the space-charge saturated regime. Both the modal gain and the FWHM of the PHD are shown.

FIG. 3. The measured values of the modal gain ratioed to the normal operational value at $\Delta T = 0$ °C as a function of the change in the operational temperature, ΔT, of MCP #1 (circles), and #2 (triangles). The least-squares linear fit of the data is shown for both sets of data points. The error bars represent a ±2 channel resolution error in the determination of the modal gain with the multichannel analyzer.

tests. The output pulses from the MCP were amplified and sent to a calibrated multichannel analyzer used to display and record the PHDs.

The PHDs of MCP #1 and MCP #2 were measured and recorded at various operational MCP temperatures with 2537 Å photons. Prior resistance measurements of each MCP as a function of temperature, taken while baking each plate under vacuum in a temperature-controlled oven, provided a means to monitor the MCP's operational temperature. This was accomplished by recording the strip current through the MCP, converting the strip current to resistance, then converting the resistance value to temperature using the MCP resistance/temperature curves.

Microchannel plate #1 was operated with an applied MCP potential of 2200 V at three different temperatures— the normal operating temperature of 88 °C, and at 24 °C below and 64 °C above the normal operating temperature. The lower temperature was attained by passing nitrogen gas, adiabatically cooled by the Joule–Thomson effect, across the outside of the MAMA tube assembly. The higher temperature was attained by wrapping heater tape around the outside of the MAMA tube assembly creating a mini-oven. Thermocouples attached to the MAMA tube body were also monitored so that the measurements were made only after both thermocouples and MCP strip current had stabilized.

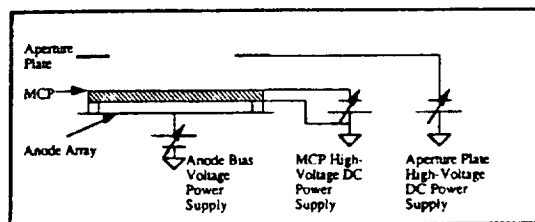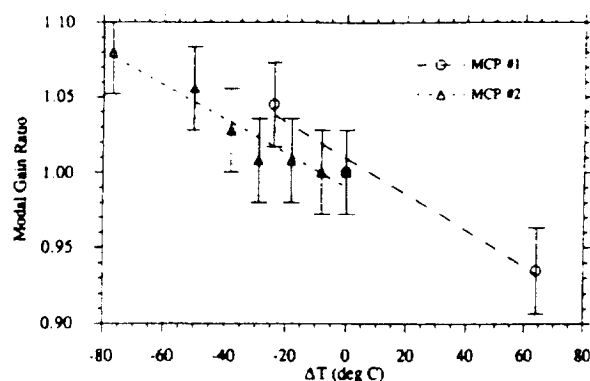A different approach was used to attain the temperature variation for MCP #2. Microchannel plate #2 was

operated with an applied MCP voltage of 2000 V. Because of the low resistance of MCP, the strip current through the plate at this voltage ranged from ~250 μA up to ~500 μA over a 10-min period from turn-on. This rise in strip current was due to the joule heating of the MCP.[6] The PHDs were recorded at specific intervals during warm-up of the MCP.

Figure 3 shows the measured values of the modal gain ratioed to the modal gain at the normal operating temperature. These data are plotted against the temperature difference from the normal operational value for both MCPs. The normal operating temperatures were 88 °C and 160 °C for MCP #1 and #2, respectively. The measured modal gain at these normal temperatures were 1.55×10^5 electrons pulse^{-1} for MCP #1, and 2.51×10^5 electrons pulse^{-1} for MCP #2. As is evident in Fig. 3, the modal gain was found to drop with increasing temperature at a rate of $-0.12 \pm 0.01\%$ (°C)$^{-1}$ for MCP #1 and $-0.11 \pm 0.02\%$ (°C)$^{-1}$ for MCP #2. The dashed lines in the figure are least-square linear fits to each data set.

III. DISCUSSION

The negative correlation of gain with temperature is postulated to be the result of two possible mechanisms: (i) the presence of an axial temperature gradient within each MCP channel which reduces the electric field within the MCP channels; and (ii) a negative temperature dependence of the secondary yield of the MCP glass.

A. Axial temperature gradient

Soul[7] was first to point out the existence of an axial temperature gradient within each MCP channel resulting from the dissipation of heat generated within the MCP during operation. Assuming that the heat is uniformly generated within the disklike volume of the MCP, and that the primary dissipation of the heat within the MCP is by conduction through the channel walls to both the input and

FIG. 2. Schematic showing the biasing arrangement of the aperture plate, MCP, and anode array inside the MAMA (1×100)-pixel tube assembly.

output surfaces of the MCP, the maximum temperature difference between the center of the MCP and the surface is given by

$$T_c - T_s = \frac{V_{MCP}^2 L}{8k_{th}R_{MCP}A(1-\eta)}, \qquad (1)$$

where T_c is the temperature at the plate center; T_s is the temperature at the plate surface; L is the plate thickness; V_{MCP} is the applied MCP voltage; k_{th} is the thermal conductivity of the channel walls; A is the plate active area; R_{MCP} is the plate resistance; and η is the open-area-ratio of the plate.[7] The actual temperature difference is probably somewhat less than that given by Eq. (1) since some of the energy is radiated away from the channel walls within the MCP. Of course, once the energy reaches the plate's surface, the energy is primarily dissipated by radiation since the only physical contact of the plate is at its edges, away from the active area where most of the heat is being generated.

Because the resistivity of the MCP glass is a temperature-dependent quantity, an axial temperature gradient along the channel axis causes a variation of the resistivity along the channel, which in turn leads to a non-uniform electric field between the input and output of the MCP. Feller[8] was first to point out that such a nonuniform axial field would cause a lowering of the output gain. The rate at which the output gain drops with temperature depends on the magnitude of the temperature difference within the channel, given by Eq. (1). The only quantity in Eq. (1) that is not known precisely, and has not been directly measured for both MCP #1 and #2, is k_{th}. Values of k_{th} quoted for unreduced lead-silicate glass range between 0.004 and 0.008 W cm^{-1} (°C)$^{-1}$.[7–9] However, independent measurements of MCP temperature as a function of applied MCP voltage were conducted on both MCP #1 and #2 which indirectly allowed a determination of k_{th} for both plates. For MCP #1, the value obtained for k_{th} was 0.008 W cm^{-1} (°C)$^{-1}$, which is within the range quoted for unreduced lead-silicate glass. For MCP #2 the value for k_{th} was found to be ~4 times greater at 0.031 W cm^{-1} (°C)$^{-1}$. The higher value may be a consequence of the higher lead dopant levels used to achieve the much lower plate resistivity compared with MCP #1. With these values for k_{th}, the predicted temperature differences based upon Eq. (1) for MCP #1 and #2 are, respectively, 0.44 °C and 0.92 °C. The relative closeness in magnitude between these two temperature differences for both of these plates may explain why the rate in gain drop with temperature was experimentally found to be so similar.

To understand in a more quantitative manner how the gain is affected by the axial temperature gradient, we put together a model to simulate the effects on the output gain in the presence of a nonuniform electric field along the channel axis. To keep the model simple we assumed the MCP to be a circular disk of radius r_0, with a constant (independent of temperature) thermal conductivity, k_{th}. The steady-state variation of temperature along the axis of the MCP can be found by solving the differential equation of heat conduction for a homogeneous, isotropic solid with heat generation within the body, given in cylindrical coordinates by the equation

$$\nabla^2 T(r,\phi,z) + (1/k_{th})g(r,\phi,z) = 0, \qquad (2)$$

where (r,ϕ,z) are the cylindrical coordinates, $T(r,\phi,z)$ is the temperature distribution, and $g(r,\phi,z)$ is the heat generated per unit time per unit volume. The channel input is defined at $z=0$.

To keep the problem of solving Eq. (2) tractable, we simplified the boundary conditions so that all boundaries (MCP input and output at $z=0$, $z=L$, and the MCP rim at $r=r_0$) maintain a constant temperature, T_s. More realistic boundary conditions would include the nonlinear effects of radiation transfer ($\sim T^4$) at the MCP input and output surfaces. With these simplified boundary conditions, the axial solution of Eq. (2) is given by the following equation:[10]

$$T(r,z) = T_s + \frac{g_0}{2k_{th}} z(L-z)$$

$$- \frac{4g_0 L^2}{\pi^3 k_{th}} \sum_{m=0}^{\infty} \frac{1}{(2m+1)^3} \frac{I_0(\xi_m r)}{I_0(\xi_m r_0)} \sin(\xi_m z), \quad (3)$$

where

$$\xi_m = \frac{\pi(2m+1)}{L},$$

g_0 is the heat generation at a constant rate, and I_0 is the modified Bessel function of order zero. The third term in Eq. (3) is small compared with the first two terms; hence, Eq. (3) reduces to the following at the center of the plate, with $g_0 = (V_{MCP}^2/R_{MCP})/$MCP volume):

$$T(r=0,z) \approx T_s + \frac{V_{MCP}^2}{2k_{th}R_{MCP}A(1-\eta)L} z(L-z). \quad (4)$$

Figure 4(a) shows how the temperature varies axially across MCP #2, according to Eq. (4), at surface temperatures of 80 °C and 160 °C.

The resistivity of the reduced lead-silicate glass behaves, as a function of temperature, in the same way as in a semiconductor; i.e., the resistivity decreases with increasing temperature. The plate resistivity as a function of temperature for MCP #1 and #2 was found to best fit a negative exponential equation of the form

$$\rho(T) = A \exp(-BT), \qquad (5)$$

where for MCP #1, $A = 7.28 \times 10^9$ Ω-cm, and $B = 0.00735$ (deg K)$^{-1}$; and for MCP #2, $A = 1.83 \times 10^9$ Ω-cm, and $B = 0.00844$ (deg K)$^{-1}$. Since the temperature along the channel is not a constant, but varies according to Eq. (4), the plate resistivity, given by Eq. (5), is no longer independent of the axial coordinate z.

The voltage drop along the channel, $V(z)$, is given by

$$V(z) = \frac{I_s \rho[T(z)]z}{A}, \qquad (6)$$

where I_s is the strip current flowing through the MCP. An axial temperature gradient across the channel implies a

AXIAL TEMPERATURE GRADIENT
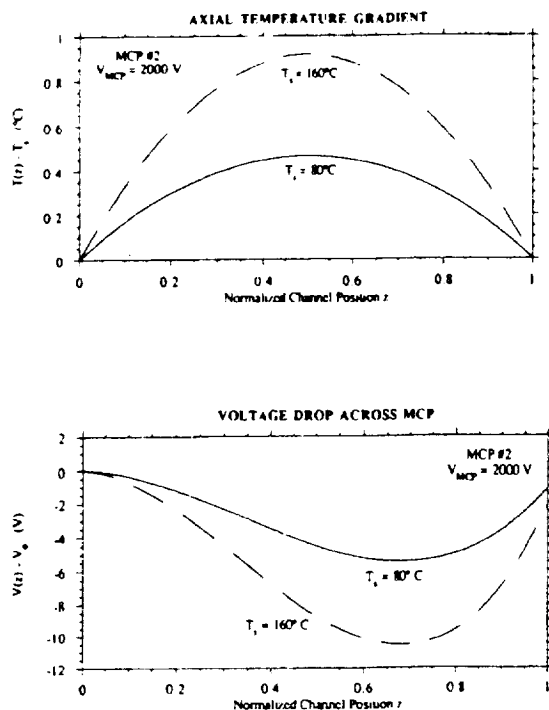

VOLTAGE DROP ACROSS MCP

FIG. 4. (a) The predicted temperature difference, $T(z) - T_r$ for MCP #2 as a function of position along the length of an MCP channel based on Eq. (4). The k_{th} value used for this calculation was 0.031 W cm^{-1} ($^{\circ}$C)$^{-1}$. The solid curve is the temperature profile at a surface temperature of 80 $^{\circ}$C; the dashed curve is the profile at 160 $^{\circ}$C. (b) The difference in the voltage, based on Eq. (6), along the MCP channel with $[V(z)]$ and without (V_0) an axial temperature gradient for MCP #2. The solid curve is for a surface temperature of 80 $^{\circ}$C; the dashed curve is for a surface temperature of 160 $^{\circ}$C.

nonlinear dependence with position for the voltage drop across the channel, given by substituting Eqs. (4) and (5) into (6). Figure 4(b) shows the difference between the voltage drop across MCP #2 with the axial temperature gradient shown in Fig. 4(a), and a linear voltage drop across the plate if no axial temperature gradient existed. The figure shows this voltage difference at the two surface MCP temperatures of 80 and 160 $^{\circ}$C. As is evident in the figure, the difference in the voltage drop with and without the axial temperature gradient across the channel is at a maximum about 7/10 down the length of the channel. At a surface temperature of 80 $^{\circ}$C the voltage differs from linearity by ~5 V; at 160 $^{\circ}$C it differs by more than 10 V.

The electric field across the MCP is found by taking the derivative of Eq. (6) with respect to z. In so doing, the electric field, $E(z)$, is given by

$$E(z) = \frac{-I_s\rho(z)}{A} [1 - B\gamma_l z (L - 2z)],$$ (7a)

where

$$\gamma_l = \frac{V_{MCP}^2}{2k_{th} R_{MCP} A (1 - \eta) L}$$ (7b)

and B is the coefficient in the argument of the exponential in Eq. (5). For both MCP #1 and #2, the second term in Eq. (7a) is negligible, reducing to

$$E(z) \approx \frac{-I_s\rho(z)}{A}.$$ (8)

Thus we see that the dependence of the electric field with position across the MCP thickness is nearly identical in form with that of the plate resistivity.

The model used to predict how the output gain changes with the temperature in the presence of an axial temperature gradient is based upon the MCP gain model derived by Adams and Manley.[11] The temperature distribution along the length of the MCP channel was first calculated using Eq. (4). The electric field distribution was then calculated using Eq. (8) in conjunction with Eq. (5) for the plate resistivity. The output gain of the channel, G, was computed by taking the product of the gain, Y_n of each dynode stage within the MCP:

$$G = \prod_{i=1}^{n} Y_n$$ (9)

where n is the number of dynode stages along the length of the channel. Here Y_n which represents the secondary electron yield of the reduced lead-silicate glass that makes up the MCP, is a linear function of the impact energy at energies less than 200 eV,[12] and is given by

$$Y_i = \alpha V_{ci} + Y_0,$$ (10)

where α is the slope of the secondary electron yield with impact energy, Y_0 is the zero intercept, and V_{ci} is the collision energy within dynode i, given by the following expression:[11]

$$V_{ci} = \frac{d^2}{4V_e} E_i^2.$$ (11)

In Eq. (11) E_i is the electric field within the ith dynode stage, d is the channel diameter, and V_e is the initial ejection energy of the secondary electrons. The values for α and Y_0 in Eq. (10) were taken from the secondary electron yield data published by Laprade et al.,[12] and the V_{ci} values were calculated using Eq. (8) substituted into Eq. (11). The electron ejection energy, V_e used was 1 eV.[1]

Figures 5(a) and 5(b) show the results of the model plotted with the measured gain values as a function of MCP surface temperature for both MCP #1 and #2, respectively. The model for MCP #1 shows two curves which span the reported values of k_{th} from 0.004 W cm^{-1} ($^{\circ}$C)$^{-1}$ (dashed curve) to 0.008 W cm^{-1} ($^{\circ}$C)$^{-1}$ (solid curve). The better fit is the dashed curve with a computed χ^2 value of 1.6 with 2° of freedom, compared with a χ^2 value of 1.9 for the solid line fit. The solid curve shows a flatter rate of gain change with temperature, as expected for a higher k_{th} value, which implies a lower axial temperature gradient.

The two curves shown in Fig. 5(b) for MCP #2 were computed with the k_{th} values of 0.03 W cm^{-1} ($^{\circ}$C)$^{-1}$ (dashed curve) and 0.08 W cm^{-1} ($^{\circ}$C)$^{-1}$ (solid curve). In
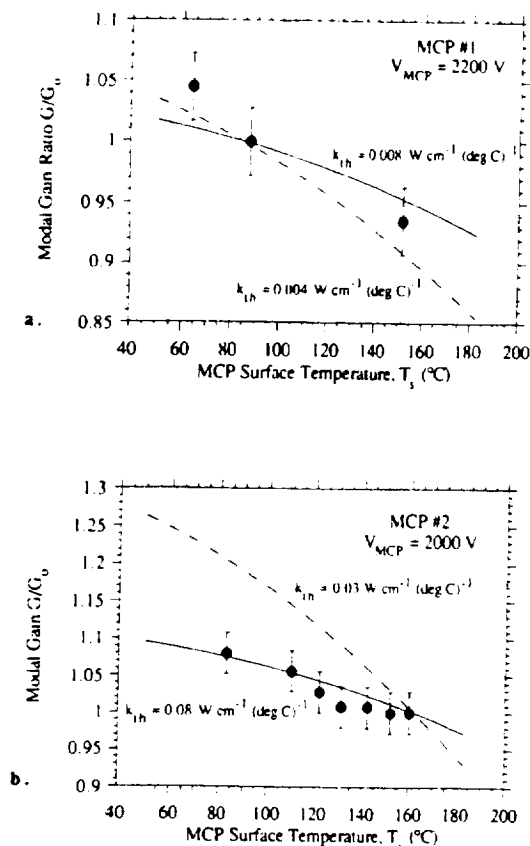
FIG. 5. (a) The measured modal gain values as a function of temperature for MCP #1 (filled circles). The solid curve is the predicted change in the gain with temperature, based upon the model described in the text, with $k_{th} = 0.008$ W cm^{-1} (°C)$^{-1}$. The dashed curve is the prediction with $k_{th} = 0.004$ W cm^{-1} (°C)$^{-1}$. (b) The measured modal gain values as a function of temperature for MCP #2 (filled circles). The solid curve is the predicted change in the gain with temperature, based upon the model described in the text, with $k_{th} = 0.08$ W cm^{-1} (°C)$^{-1}$. The dashed curve is the prediction with $k_{th} = 0.03$ W cm^{-1} (°C)$^{-1}$.

this case the better fit is with the larger k_{th} value. The smaller k_{th} value generates a curve that is greater than the measured data points and with a slope twice the magnitude.

The results of the modeling indicate that an axial temperature gradient due to the finite thermal conduction of the channels could account for the entire observed change in the modal gain with MCP temperature. The agreement between the model and the measured data for MCP #1 seems quite reasonable for the range of k_{th} values quoted for unreduced lead-silicate glass. The fit of the model for MCP #2, however, was less reasonable with respect to the assumed value of k_{th} [0.03 W cm^{-1} (°C)$^{-1}$]. The better fit for MCP #2 required a higher k_{th} value than either that quoted for unreduced lead-silicate glass or what was indirectly measured for MCP #2. These problems may result from the fact that the gain data values measured for MCP #2 were measured in a non-steady-state, nonequilibrium condition during the time the MCP was heating up to operational temperature. The gain values for MCP #1, on

the other hand, were measured after the plate had stabilized in temperature and therefore in a steady-state condition. Hence, more credence on the validity of the MCP #1 data and its model is thus afforded over that of MCP #2.

B. Changes in secondary yield

A second possibility that could cause a negative correlation of gain with temperature may result from a negative temperature dependence of the secondary yield of the MCP glass. Some insulators are known to display a negative dependence of the secondary yield with temperature.[13,14] Dekker[15,16] has shown that such a dependence could be explained by the increased scattering of secondary electrons with lattice vibrations at higher temperatures. The increased scattering lowers the mean-free path of the electron and hence lowers the effective yield. This effect on the yield is most noticeable for primary electron energies that produce penetration depths greater than the escape depth of the secondaries. This, in general, occurs at energies greater than where the secondary yield has already reached a maximum; for lead-silicate glass this occurs at energies exceeding 300 eV.[12] In this region of energy, Dekker predicts that the yield should go as $T^{-1/2}$.[15] For lower primary electron energies in the range of 50–100 eV, which are more representative of the primaries in an MCP, the drop in yield still exists, but is considerably less if not nonexistent.[15] Therefore, the relation that the secondary electron yield, Y, goes as $Y \sim T^{-1/2}$ can be thought of as an upper limit for a change in yield with temperature of an MCP, with the lower limit being no change.

Using the simplified discrete dynode model of an MCP channel,[11,17] the modal gain, G, goes as $G \sim Y^n$, where n is the average number of dynode stages along an MCP channel ($n \sim 20$–40). The proportional change in the yield, dY/Y, is given by

$$\frac{dY}{Y} = \frac{1}{n} \frac{dG}{G}.$$ (12)

With the average proportional change in modal gain per degree Celsius measured for both MCPs of $\langle dY/Y \rangle \sim 0.0011$, the proportional change in the secondary yield using Eq. (12) with $n = 20$ is $dY/Y \sim 5.5 \times 10^{-5}$ (°C)$^{-1}$. Using Dekker's result, the expected upper limit to the change in secondary yield based on the MCP #1 and #2 temperature data is $dY/Y \sim 1.3 \times 10^{-3}$ (°C)$^{-1}$. This value is some 20 times greater than measured. This discrepancy could be accounted for by the fact that the primary electron energies that exist in an MCP are low enough so that the penetration depth of the primaries during each collision in the MCP channel is less than the escape depth of the secondaries. For $n \sim 20$, and an applied MCP potential of 2000 V, the average primary electron energy is only ~ 100 eV. This is a value far below that which maximizes the secondary yield for MCP glass, which is known to occur above 300 eV.[18] Unfortunately, at this time there is no independent evidence that the secondary yield for lead-silicate glass is a function of temperature at these low primary electron energies. If such data existed,

one could then establish a more realistic lower bound to the expected change in the modal gain with temperature due to changes in the secondary yield with temperature.

IV. CONCLUSION

Our measurements of the dependence of the MCP modal gain on temperature indicate a slight drop in the modal gain of ~0.10% ($^{\circ}$C)$^{-1}$ over the operational temperature range of 60–160 $^{\circ}$C. We attribute this drop in gain with increasing temperature to a drop in the axial electric field strength due to the presence of an axial temperature gradient within the MCP channels. This effect was modeled and found to account for the entire change in modal gain over the temperature range measured.

A second possible contributor, that resulting from a drop in the secondary electron yield with temperature, was assessed but found at the upper limit to overestimate the rate of change in gain by a factor greater than 20. Because the temperature dependence of the secondary yield of lead-silicate glass at the collision energies representative of the cascading electrons within an MCP channel is unknown (and possibly nonexistent), it is uncertain whether or not this effect contributes at all to the drop in MCP gain with temperature. Therefore, it is more likely that the observed changes in the output gain with temperature is a result of the presence of a nonuniform axial electric field throughout the MCP channels resulting from an axial temperature gradient, and not of changes in the secondary electron yield with temperature.

ACKNOWLEDGMENTS

We would like to acknowledge the efforts of Bruce Laprade and Bruce Feller of GEOC, Sturbridge, MA, for

[1] J. L. Wiza, Nucl. Instrum. Methods 162, 587 (1979).
[2] M. Lampton and F. Paresce, Rev. Sci. Instrum. 45, 1098 (1974).
[3] C. Martin, P. Jelinsky, M. Lampton, R. F. Malina, and H. O. Anger, Rev. Sci. Instrum. 52, 1067 (1981).
[4] J. G. Timothy and R. L. Bybee, Solid State Imaging Devices, SPIE Proc. 116, 24 (1977).
[5] D. C. Slater, J. G. Timothy, and J. S. Morgan, Electron Image Tubes and Image Intensifiers, SPIE Proc. 1243, 35 (1990).
[6] J. F. Pearson, G. W. Fraser, and M. J. Whiteley, Nucl. Instrum. Methods A 258, 270 (1987).
[7] P. B. Soul, Nucl. Instrum. Methods 97, 555 (1971).
[8] W. B. Feller, Development of Microchannel Plates in Advanced Wind-Tunnel Instrumentation, NASA Contractor Report 181947 (February 1990).
[9] Y. S. Touloukian, Thermal Conductivity: Nonmetallic Solids (IFI/Plenum, New York, 1970).
[10] M. Necati Ozisik, Heat Conduction (Wiley, New York, 1980), pp. 133–136.
[11] J. Adams and B. W. Manley, IEEE Trans. Nucl. Sci. NS-13, 88 (1966).
[12] B. N. Laprade, S. T. Reinhart, and M. Wheeler, Electron Image Tubes and Image Intensifiers, SPIE Proc. 1243, 162 (1990).
[13] G. Blankenfeld, Ann. Phys. 9, 48 (1951).
[14] J. B. Johnson and K. G. McKay, Phys. Rev. 91, 582 (1953).
[15] A. J. Dekker, Physica 21, 29 (1954).
[16] A. J. Dekker, Solid State Physics—Advances in Research and Applications (Academic, New York, 1958), Vol. 6, pp. 251–311.
[17] E. H. Eberhardt, Appl. Opt. 18 (9), 1418 (1979).
[18] G. E. Hill, Photo-Electronic Image Devices (Academic, New York, 1976).

Time-Tag Photon Detection with the MAMA Detector System

G. Giaretta, E. Horch, J. G. Timothy and J. F. Heanue

Center for Space Science and Astrophysics, ERL313, Stanford University,
Stanford, CA 94305

and

David B. Kasle

Silicon Engines Inc., 955 Commercial St., Palo Alto, CA 94303

ABSTRACT

The Multi-Anode Microchannel Array (MAMA) detector system is a true photon-counting imager which records the position and arrival time of each detected photon *for post facto* image reconstruction analysis. Imaging by time-tag photon detection with the MAMA is being used for image stabilization on sounding rockets, and for speckle interferometry and speckle image reconstruction at ground-based telescopes using the Stanford University Speckle Interferometer System (SUSIS). This paper describes the construction and mode-of-operation of the MAMA time-tag photon-detection system, including recent improvements to the data-handling system which permit a data-recording rate in excess of 1M event s^{-1}. The intrinsic time resolution of the MAMA detector system is < 300 ns and the time resolution of the SUSIS used to date is 3.2 μs for each detected photon. A number of examples of both laboratory data and visible-light speckle interferometric deconvolutions and two-dimensional speckle image reconstructions are presented.

1. INTRODUCTION

We have recently developed and tested a new photon-counting detector system particularly suited for speckle interferometry applications, the Stanford University Speckle Interferometry System (SUSIS). A speckle interferometry system must be capable of reading from several tens, to hundreds of frames per second and must have low read-out noise because each frame generally is composed of one to a thousand photons. Since the goal of speckle interferometry is to obtain very-high-resolution information inside a comparatively large seeing disk large formats and high geometric fidelity are required. SUSIS meets all these requirements and because of its true photon counting capabilities and timing flexibility can also be successfully applied in situations where image drift compensation is required.

2. SYSTEM DESCRIPTION

In the SUSIS, the detection of the incoming photons has been divided among several components, each optimized for a particular function (Fig. 1a). A physical block diagram of the system is also shown for comparison (Fig. 1b).

The optical signal collected from the telescope is first conditioned by the speckle module. This module magnifies the speckles enough to make them spatially resolvable by the detector and at the same time a narrow band filter determines the spectral bandpass and corrects for atmospheric dispersion. Next, in a MAMA tube, the photons are converted to electrons by a bialkali photocathode and are subsequently amplified in a curved-channel Microchannel Plate (MCP). The single curved-channel MCP provides high gain for pulse counting and a low level of ion feedback. Quantum efficiencies of 1% at 5000 Å and gains on the order of 10^5-10^6 are obtained in the current MAMA detector tube[1]. A 14 μm fine-fine anode array is used to collect the cloud of electrons coming from the pores of the MCP and to encode the spatial information (this is necessary to reduce the number of subsequent data channels). Very large bandwidth charge-sensitive amplifiers convert the electron signal to a voltage and a thresholding scheme that exploits the saturation characteristic of the MCP gives a zero readout noise for the detector. Subsequently a VLSI decode chip generates the address of each event (detected photon) and quantizes its arrival time in intervals of 0.16 μs. Using a high-resolution decoding algorithm the pixel size can be reduced from 14 μm to 7 μm simply with a turn of a switch increasing the spatial resolution to 10 μm[2,3]. The overall spatial resolution of SUSIS is limited to 10 μm from the pore size of the MCP.

(a)
SUSIS Functional Block Diagram

(b)
SUSIS Physical Block Diagram
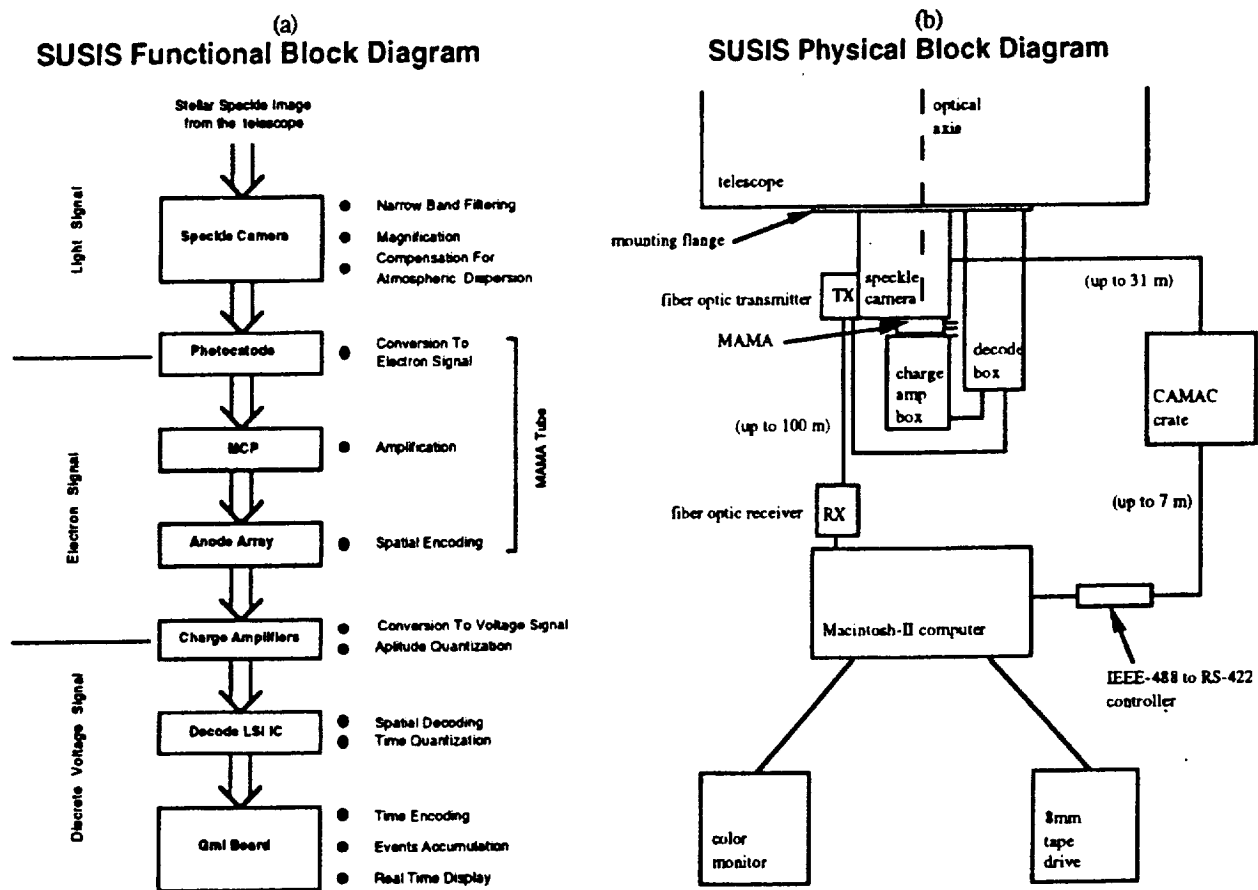
Figure 1. Functional (a) and physical (b), block diagrams of SUSIS.
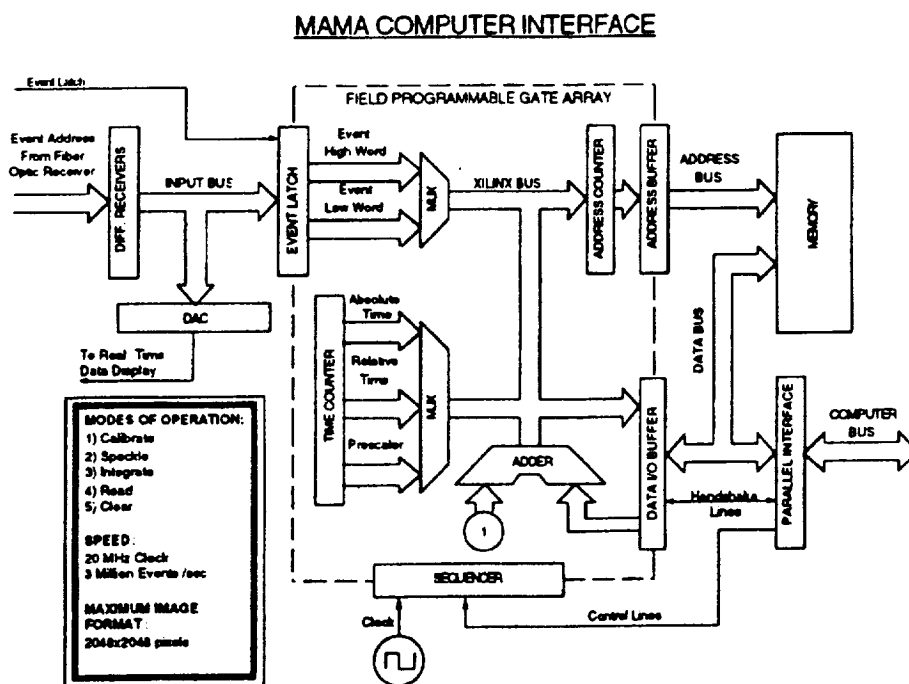
MAMA COMPUTER INTERFACE

Figure 2. Block diagram of the MAMA speckle interface.

Through a high-speed 120 MHz fiber-optic data link the event address arrives to a custom computer data acquisition board (Fig. 2) where each event is time tagged (speckle mode) or is accumulated to form an image (integration mode). The optical link has been chosen for its long distance high-data-rate capabilities and also for the high immunity to radio frequency noise typical of a telescope environment where electric motors are continuously operating. The high-speed data link together with a control data link for the speckle camera allows remote operation of the system (30 meters). A remote real-time display of the incoming photons is also available on an oscilloscope. The remote operation of the detector is very useful both for astronomical applications where the control room of the telescope is far from the telescope itself and for laboratory testing were the detector is generally operated in a dark room.

A complex scheme of time encoding has been implemented in this computer interface to almost double the number of events acquired in a single continuous 8 Mbytes memory buffer for typical observing conditions. First the time information is split into coarse and fine portions as shown in Table 1. The fine time-tag is kept with each event spatial information (Words 0-1) while the coarse time (Words 2-3) is stored only when the fine counter overflows and a new event comes in. A prescaler is used to change the base clock frequency of the fine time tag counter in order to keep the average number of events between coarse time tags constant with changing illumination conditions. SUSIS time resolution can be varied from 0.4 μs to 3.2 μs (prescaler set to 0 and 3 respectively).

Table 1. Format of the time-tag data of the SUSIS.

Bit:	15	14	13	12	11	10	9	8	7	6	5	4	3	2	1	0
Word 0:	0	0	Y Coord.			X Coordinate										
Word 1:	0	1	Fine Time Tag						Y Coordinate							
Word 2:	1	0	Coarse Time Tag													
Word 3:	1	1	Presc.		Coarse Time Tag											

If a Poissonian model of photon arrival times is assumed, the average number of photoevents stored in the 8 Mbyte buffer may be calculated as follows. The number of events in a given short interval of time will be given by the Poisson distribution

$$W(n) = \frac{\lambda^n}{n!} e^{-\lambda},$$ (1)

where W is the probability of obtaining n events and λ is the mean number of events per interval. If the interval is chosen to be the same as the coarse clock tick, then the probability W_n that an interval will have a coarse time tag associated with it is

$$W_n = 1 - W(0), \text{ or }$$ (2)

$$W_n = 1 - e^{-\lambda},$$ (3)

since all intervals which contain one or more events receive coarse time tags at the end of the first event. The average number of bytes B taken up in memory by an interval is then

$$B = 4\lambda + 4(1 - e^{-\lambda}),$$ (4)

and therefore the number of intervals stored in memory is constrained by the relation

$$4\lambda n_i + 4(1 - e^{-\lambda})n_i = 8 Mbytes,$$ (5)

where n_i is the number of intervals stored. This number is also related to the number of photo events n_{ph} stored in the interface by

$$n_{ph} = 25.6\mu s \cdot R \cdot 2^p \cdot n_i,$$ (6)

where R is the count rate and p is the value of the prescaler. Using both Eq. 5 and Eq. 6, one may solve for the number of photons stored and obtain

$$n_{ph} = \frac{2 \times 10^6}{1 + \dfrac{1 - e^{-25.6\mu s \cdot 2^p \cdot R}}{25.6\mu s \cdot 2^p \cdot R}}.$$ (7)

This relationship is shown graphically in Fig. 3 for a time between absolute time-tags of 204.8 μsec (prescaler value of 3), along with test data taken with the interface in the laboratory at various count rates.
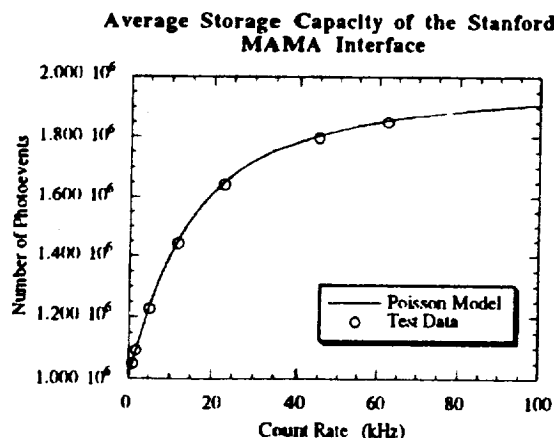

Average Storage Capacity of the Stanford
MAMA Interface

Figure 3. The average storage capacity of the Stanford MAMA computer interface as a function of count rate.

3. TIMING TESTS WITH THE SYSTEM

3.1 Poisson Tests of the Interface Timing Information

As a first test of the speckle interferometry system built at Stanford, the timing information that the computer interface assigns to incoming MAMA events was tested using two different data sets, one taken in the laboratory and the other taken at the telescope. Calculation of the reduced chi squared gives a quantitative evaluation of how well both data sets match a Poisson distribution. In particular, a section of a time-tagged data file was binned into exposures (or frames) of a given length of time. The number of counts in each frame was recorded. Then, a histogram of the number of events per frame was formed, and compared to a Poisson distribution of the same mean. Chi squared (for a Poisson distribution) is computed according to the formula

$$\chi^2 = \sum_{j=1}^{n} \frac{[f(x_j) - NP(x_j)]^2}{NP(x_j)}. \tag{8}$$

where N is the number of frames, $f(x_j)$ is the number of frames with x_j events, and $P(x_j)$ is the Poisson probability for a frame with x_j events. The reduced chi squared, denoted χ_ν^2, is calculated by dividing chi squared by the number of degrees of freedom, ν, of the system. For a Poissonian distribution, $\nu = n-1$, where n is the number of bins in the histogram of the data. The reduced chi squared is then given by

$$\chi_\nu^2 = \frac{\chi^2}{\nu}. \tag{9}$$

If a distribution is Poissonian, the reduced chi squared should be near 1, meaning that the predicted and actual deviations from the expected value of the histogram were nearly the same. Whatever the value of the reduced chi squared, it is possible to assign a probability that the observed distribution is drawn from a Poisson distribution based on this value[4]. In the following analysis, care was taken to insure the correct application of the chi squared method as described by Meyer[5]. The chi squared test is useful in many cases in determining if a given distribution is probably drawn from a given parent distribution.

The chi squared test of the timing information is useful in two ways for the MAMA-based speckle interferometry system. If a source with a known harmonic time signature is put on the detector, the recorded time tag data from the system should exhibit a non-Poissonian character, or a high value of the reduced chi squared. Also, if one forms the power spectrum of the time series of counts per exposure, a spike at the frequency of the harmonic signal should be observed. These features would be fairly convincing that the interface is not simply assigning times randomly. On the other hand, if a true Poisson source is imaged on the MAMA detector, then the reduced chi squared from the binned data should be near 1, indicating that the probability is high that the parent distribution is a Poisson distribution. If this is true, then the interface is not generating any large harmonic or other non-random signals in the timing information.

The speckle interferometry system was set up in the laboratory to be illuminated by a small incandescent light bulb. The light from the bulb was sent directly into the speckle camera. At the first focal plane inside the speckle camera, a pinhole mask was attached, so that only a small spot of light reached the active area of the detector. The experimental setup is shown in Fig. 4a. An example of an integrated image of the spot is shown in Fig. 4b.

The light intensity in the incandescent light bulb is proportional to the energy dissipated in the filament. The energy in turn depends on the square of the voltage applied which in our case was the 60 Hz 110V sinusoid from a wall power outlet. This indicates that the MAMA detector should see a variation in the source with a frequency of 120 Hz. If we can see harmonic behavior in a laboratory light source at this frequency, this is a good indication that the timing information assigned to events by the computer interface is at least good enough to do speckle interferometry at the frequencies characteristic of atmospheric turbulence.

(a)

(b)
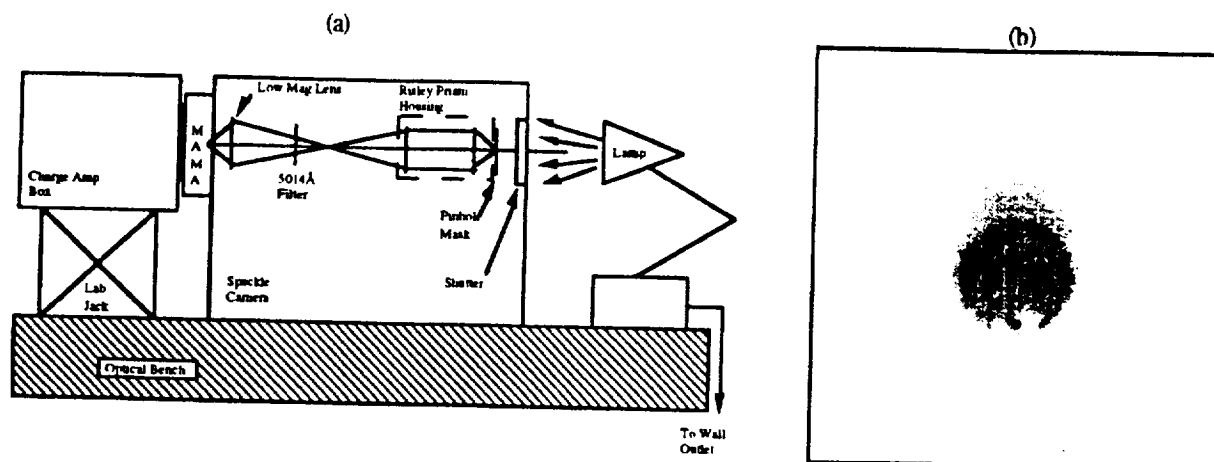
Figure 4. Experimental setup for laboratory spot tests (a) and typical integrated image (b).

The chi squared test described above was performed for spot data taken at 62.6 kHz in the laboratory. The detector sees the lamp as a non-Poissonian source. The reduced chi squared is 2.823, corresponding to a probability of much less than 0.1% that a distribution drawn from a Poisson parent distribution would have a reduced chi squared larger than that of the lab spot source. Fig. 5a shows a portion of the raw data stream. The data are binned in 0.2 ms exposures. Fig. 6a compares the histogram of the number of events per frame with a Poisson distribution of the same mean for the same data file. Fig. 7a shows a portion of the power spectrum for this file which includes the 100-200 Hz region; a large peak at 120 Hz can clearly be seen. This peak has a signal-to-noise ratio of 38.3. The detector system is able to see the harmonic signature of the laboratory light source.

The measured value of the frequency of the oscillation shown in Fig. 7a is 121.6 ± 1.8 Hz. This number was obtained by measuring the number of absolute time tags written in a data file and comparing it to the number of events obtained per second as recorded by a counter. The number of time tags per second can then be derived; providing an absolute measure of the tick interval of the fine time tag. The intensity variation detected by the MAMA system can also be estimated from the relative peak values at the 120 Hz peak and the peak at 0 frequency. The ratio of the maximum intensity to the minimum intensity in the cycle is about 1.1. This corresponds to a difference in instrumental magnitude of about 0.1 magnitudes.

Chi squared tests were also performed on astronomical data taken with the SUSIS. Unless the astronomical object is known to be variable, it is expected that the timing information will be Poissonian in character. Observations for these chi squared tests were taken at the Lick Observatory 1-m reflecting telescope on May 21 through the 23, 1992.

As with the laboratory data, the first set of data considered was 4096 frames long with an exposure time of 0.2 ms. Fig. 5b shows a portion of the raw data stream for a particular astrophysical source, the star HD 171994. Fig. 6b shows a histogram of the number of events recorded per frame for this same object, and Fig. 7b shows the power spectrum of the same data. These three figures may be directly compared with Figs. 5a, 6a and 7a. Together they indicate that the source HD171994 is indistinguishable from a Poisson source.
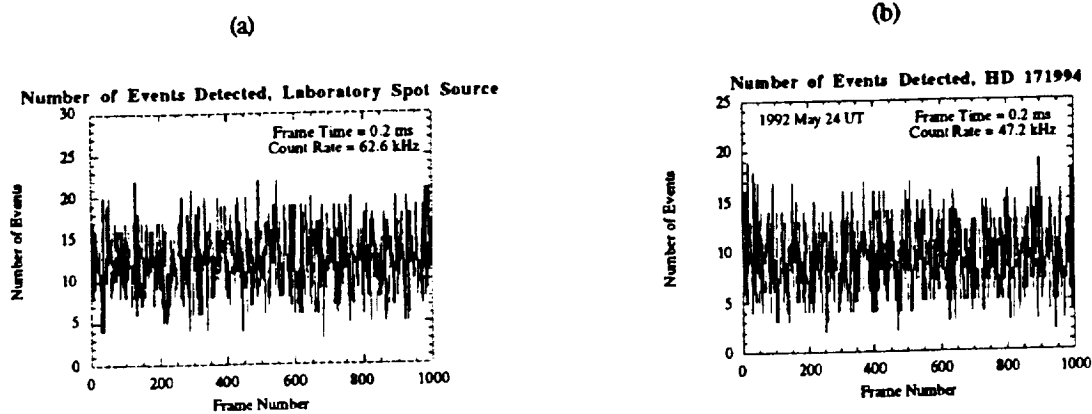
(a)

(b)

Number of Events Detected, Laboratory Spot Source

Frame Time = 0.2 ms
Count Rate = 62.6 kHz

Number of Events Detected, HD 171994

1992 May 24 UT   Frame Time = 0.2 ms
Count Rate = 47.2 kHz

Figure 5. A portion of the raw data stream for a laboratory spot source (a) and the star HD171994 (b).

(a)

(b)

Number of Events per Frame for a Laboratory Spot

Laboratory Spot
Poisson Distribution of Same Mean

Mean = 12.516 events/frame
Frame Time = 0.2 ms
Number of Frames = 4096
$\chi^2_\nu = 2.823$

Number of Events per Frame for HD171994

HD171994
Poisson Distribution of Same Mean

Mean = 9.435 events/frame
Frame Time = 0.2 ms
Number of Frames = 4096
$\chi^2_\nu = 0.945$
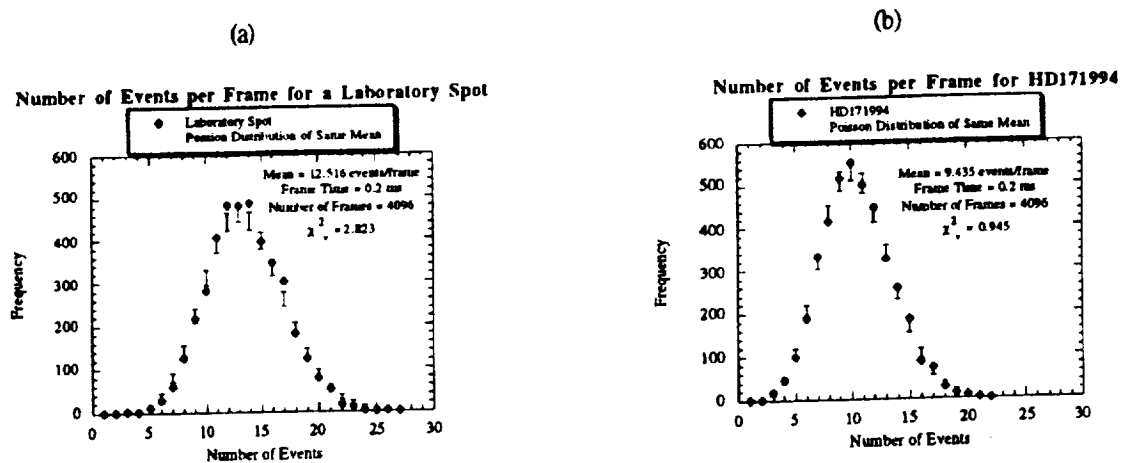
Figure 6. Histogram of the number of events detected for laboratory spot source (a) and the star HD171994 (b). The value of the reduced chi squared is significantly larger than one for (a). There is less than a 0.1% chance that a Poisson distribution would have a larger value of reduced chi squared.

(a)

(b)

Power Spectrum of a Laboratory Spot Source

Power Spectrum of HD171994 (1992 May 24 UT)
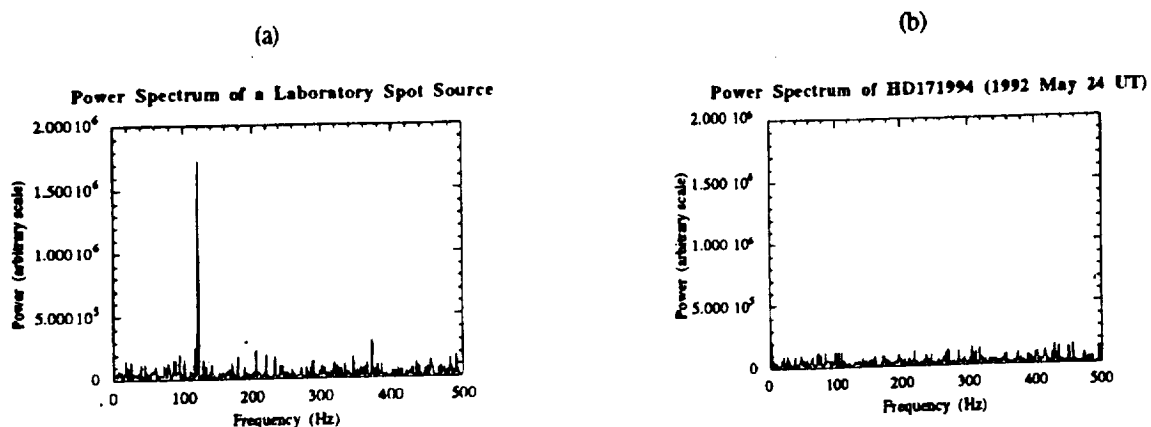
Figure 7. This figure shows the frequency content of the laboratory spot source (a) and the star HD171994 (b). There is a strong peak at 0 Hz which has not been shown. The only other feature in the spectrum is a sharp peak at 120 Hz, as expected for the light source (a). The same peak is not present in the astronomical source data (b).

The chi squared test was also performed for several different astronomical sources; all have reduced chi squared near 1. These results are shown in Table 2 where the rightmost column shows the approximate probability that a Poisson distribution would have a higher value of the reduced chi squared. The last object listed is a point source in the vicinity of the HII region I1369. The value of reduced chi squared was computed for various frame times on three different astronomical sources, and these results are shown in Fig. 8. In this case, the timing information deviates from a Poisson distribution on small time scales. For sources under about 50 kHz, a Poissonian response is obtained down to a frame integration time of about 50 μs, corresponding to the bottom four bits in the timing address of the events. For brighter sources, the non-Poissonian character of the event stream sets in at longer time scales.

Table 2. Results of the chi squared test $P_\chi(\chi^2, v)$ on several astronomical sources.

Reduced Chi Squared for Several Different Astronomical Sources		
Object	χ^2_v	*Approx.* $P_\chi(\chi^2, v)$
HD 171994	0.949	0.5
HD 119126	1.354	0.1
HD 129712	0.743	0.7
HD 161833 (binary)	1.204	0.2
HD 170109 (binary)	0.889	0.6
I1369.1	1.076	0.4
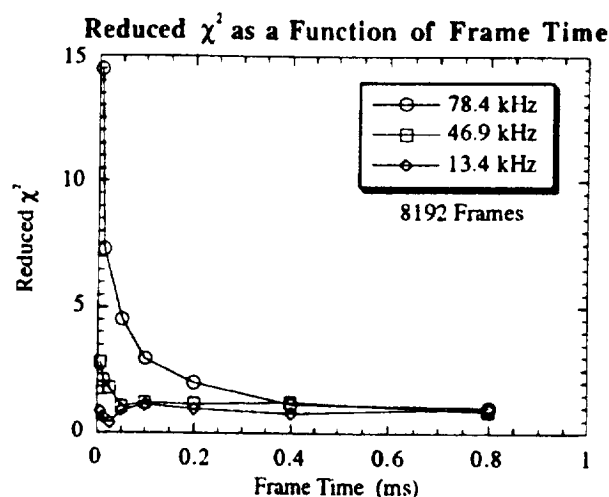
Figure 8. Reduced chi squared as a function of frame integration time for three different count rates: 78.4 kHz (HD119126), 46.9 kHz (HD171994), and 13.4 kHz (HD129712).

The fact that the timing information deviates from a Poisson distribution may be related to a loss of detective quantum efficiency (DQE) at high count rates. For the observational setup used to take these data, a loss in DQE is possible due to the speckle nature of short astronomical exposures. Such a loss in DQE affects the timing analysis performed here by leading to fewer frames where the number of counts obtained was higher than the true mean value expected from the source. In terms of system performance, the timing information will be limited only by the photon flux when searching for time-dependent phenomena on time scales above 50 μs and count rates below 50 kHz for astronomical observations. The system should therefore be able to detect time-dependent astrophysical phenomena with frequencies below 20 kHz. Higher frequencies may be

detected, but the results will not be flux-limited since the interface itself has a non-Poissonian response as these frequencies, and the analysis of such data on smaller time scales should reflect this.

3.2 Reconstruction of a Moving Image

As a second test of the timing information obtained with the MAMA-based speckle interferometry system, an image was focused onto the MAMA detector and moved in a linear fashion across the long axis of the active area during a time-tag integration. A small portion of a standard Air Force test target served as the image; the rest of the target was masked off with heavy construction paper. Light from the target passed through a collimating lens and formed an image on the active area of the detector. The lens was mounted on an x-y stage so that focusing could be accomplished by variation in the position in one direction prior to taking an exposure and motion across the long axis of the detector could be accomplished by manual variation in the other direction during the exposure. Figure 9 shows the experimental set up.
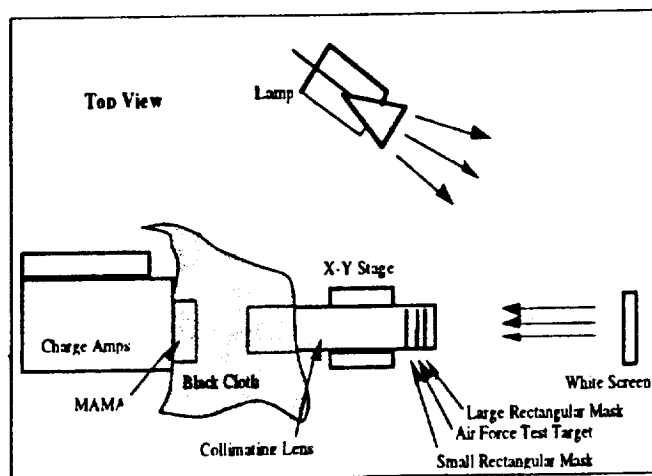
Figure 9. Experimental set up for the moving image study.
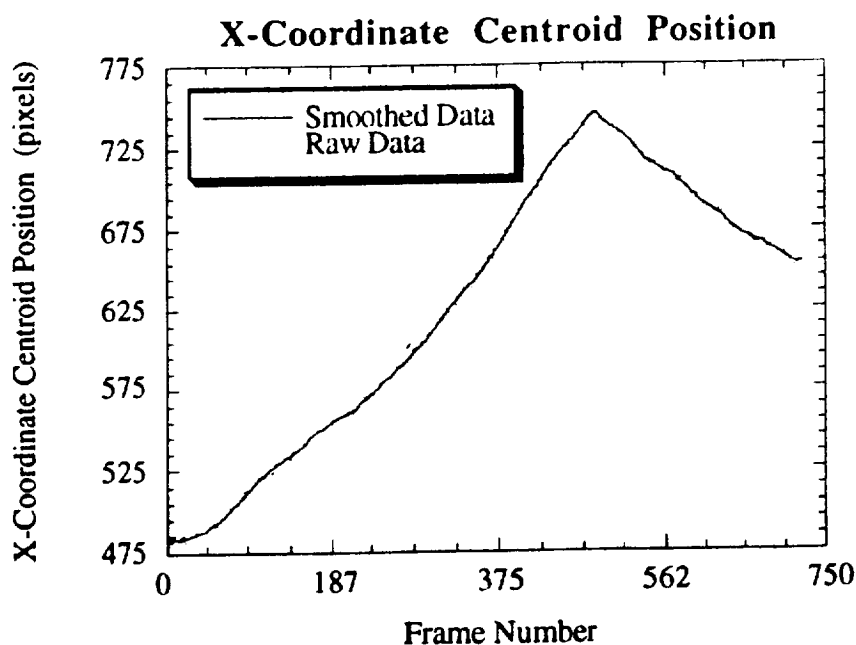
Figure 10. X-position centroids for the time-tagged data for the moving image study

The experiment consisted of three exposures. The first was a 1 minute exposure of the target in a fixed position at a count rate of 20 kHz. The second was the time-tagged data file at the same count rate where the image was moved across the detector by some 350 pixels. The total exposure time was again 1 minute. The integrated image obtained from this data file is shown in Fig. 11a. The motion blurs the resulting image in the horizontal direction. The third data file was a flat field image taken in the same configuration as the first exposure but without the Air Force test target. A flat-fielded image of the target can then be obtained by dividing the first exposure by the third one. Figure 11c shows this result.

To obtain a reconstructed image, the time-tagged data file was divided into frames of 0.1 s. This exposure time corresponds to an image shift within the exposure of about 0.6 pixels, indicating that within a frame, no significant image shift should be detectable. The centroid position of each frame was computed; Fig. 10 graphs the x-coordinate of the centroid as a function of frame number. Because of the random scatter in this function, an 11-point running mean to these centroid values was computed, and is shown in the same figure. This "smoothed" version of the centroid positions for both x and y coordinates was then used as a feducial to co-add the frames. The resulting reconstructed image is shown in Fig. 11b.
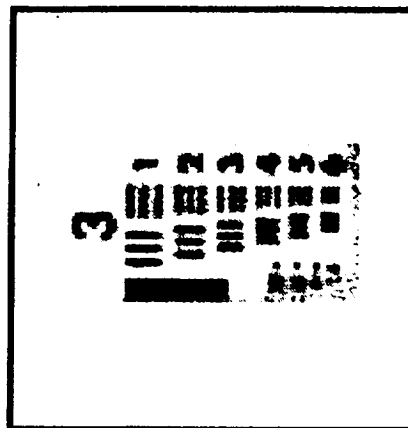
(a)
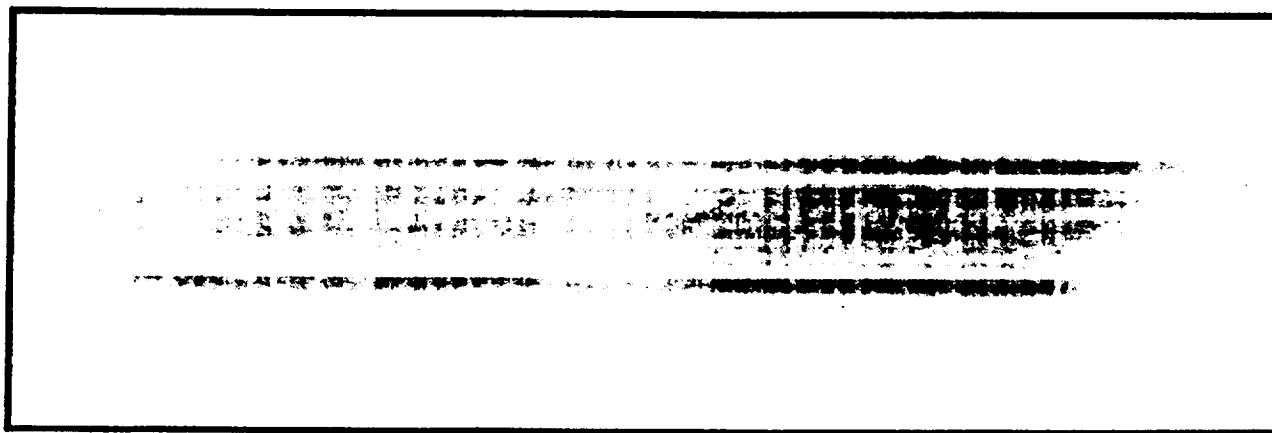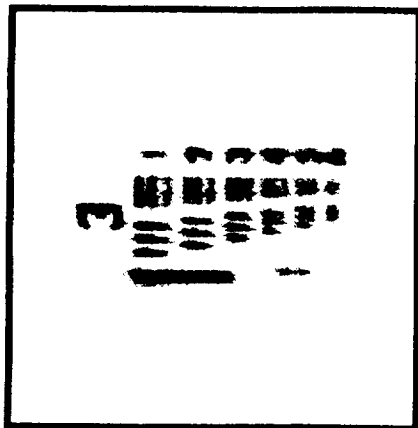
(b)   (c)

Figure 11. Image reconstruction of a moving image. a) Integrated image made from the raw time tagged data of a portion of an Air Force test target while was moving across the detector. b) Reconstructed image made by dividing the time tagged data of the moving target into 0.1 s frames and centroiding each frame before coadding. c) Flat fielded image of a stationary Air Force test target. The scale of Figs. (b) and (c) is 128x128 pixels.

Though some loss of resolution is apparent when comparing this image to Fig. 11c, even this simple reconstruction technique clearly gives a successful result. A more sophisticated image reconstruction technique has previously been used to reconstruct the image of NGC6240 acquired during a sounding rocket flight[6]. There the image was blurred from the drift of the sounding rocket during acquisition.

4. SPECKLE INTERFEROMETRY

4.1 The Method

In conventional ground-based visible-light astronomy, the resolution of images is limited by the presence of turbulence in the air above the telescope aperture that blurs the image of a point source out into a patch of light roughly 1-2 arcsec at Full Width Half Maximum (FWHM). This point spread function, known as the "seeing disk," is some 50 times broader than the diffraction limit of the largest optical telescopes.

In speckle interferometry, it is possible to recover diffraction-limited resolution. If there were no atmospheric turbulence, light from an astrophysical point source would arrive at the telescope as a plane wave, and therefore have uniform phase and magnitude across the telescope aperture. It is well-known from optics that the point spread function is given by the modulus squared of the Fourier transform of the aperture function. Therefore, in the absence of turbulence, the uniform aperture function gives rise to an Airy pattern as the point spread function.

In the real case of ground-based observing, the turbulence in the telescope aperture disturbs the uniform phase of the aperture function. The effect of this is to produce an instantaneous point spread function that fills the area of the seeing disk but has a fine structure of bright regions which have a characteristic width similar to the diffraction-limited point spread function of the telescope. Such an instantaneous point spread function is known as a speckle pattern. Speckle patterns evolve on a typical time scale of 10ms, so that on an integration of significantly longer than this, the speckle nature of the image washes out and only the overall shape of the seeing disk remains. Because the individual speckles in a speckle pattern are the same size as the diffraction-limited point spread function, speckle patterns contain high resolution information about astrophysical objects. One can hope to recover this information if the detector at the image plane can read out images at the rate of the time evolution of the speckles. It has been shown in the previous section that the timing resolution with the MAMA detector system is much better than the 10 ms figure which is s typical time scale for the evolution of speckle patterns on the image plane.

Consider taking time-tagged data of a binary star. In a speckle experiment, photons can be binned into short integrations called "frames" where the integration time is short enough that the instantaneous point spread function does not change very much over the integration. If the object of interest is a binary star, frame images will exhibit speckle pairs at the vector separation of the companions, as illustrated in Fig. 12. These speckle doublets will occur at various places on the image plane but may be collected together by considering the autocorrelation function of a frame, which is equivalent to the histogram of the distance vectors between photon pairs. Each frame image I(x) may be described as a convolution of the true object intensity distribution O(x) with the frame point spread function S(x)

$$I(\mathbf{x}) = S(\mathbf{x}) * O(\mathbf{x}),$$ (10)

where "*" denotes convolution. In the Fourier domain, a convolution becomes an ordinary product so that

$$\hat{I}(\mathbf{u}) = \hat{S}(\mathbf{u}) \cdot \hat{O}(\mathbf{u}),$$ (11)

where "^" denotes Fourier transform and the spatial frequency variable conjugate to x is u. Taking the modulus squared of this and averaging over many frames, we obtain the result that the average image power spectrum is the product of the average point spread function power spectrum and the true object power spectrum

$$\left\langle \left| \hat{I}(\mathbf{u}) \right|^2 \right\rangle = \left\langle \left| \hat{S}(\mathbf{u}) \right|^2 \right\rangle \cdot \left| \hat{O}(\mathbf{u}) \right|^2,$$ (12)

where ⟨ ⟩ denotes the average over many frames. If a speckle experiment is performed on the binary star, $\left\langle \left| \hat{I}(\mathbf{u}) \right|^2 \right\rangle$ can be obtained by Fourier transforming the average autocorrelation of many frames of data. The same process performed on a point source yields $\left\langle \left| \hat{S}(\mathbf{u}) \right|^2 \right\rangle$. The true binary power spectrum can then be obtained by division, where such a division is valid in the region where $\left\langle \left| \hat{S}(\mathbf{u}) \right|^2 \right\rangle$ is non-zero.

In fact the average point spread function power spectrum is non-zero out to the diffraction limit of the telescope and the method works not only for binary stars but also for general objects[7]. The true object autocorrelation is obtained by Fourier inversion. In the case of a binary system, reconstructing the object autocorrelation is sufficient to retrieve the separation, position angle (up

to a 180° ambiguity), and the relative magnitudes of the two companions. In practice, after forming the reconstructed power spectrum by division, the result is masked by a low pass filter before Fourier inverting to obtain a result uncontaminated by high frequency noise.
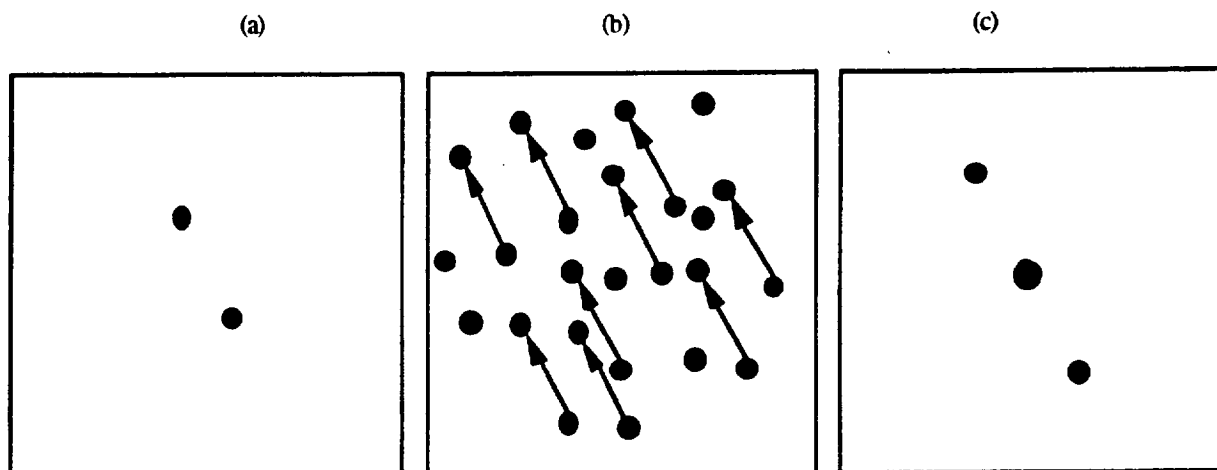
(a)	(b)	(c)

Figure 12. a) A binary star object function $O(x)$, b) illustration of a speckle pattern for a binary star where speckle doublets occur at the binary separation, c) the autocorrelation function of (a).

4.2 Speckle Autocorrelation Reconstructions of Binary Stars

The MAMA detector has been used to take speckle interferometry data of some 20 binary stars to make position angle and separation determinations. Some of these objects have been previously discussed[1,3,8,9]. Here we present two examples of autocorrelation reconstructions which have not previously been published made from data taken with the MAMA system described in this paper. Observations were carried out in May of 1992 at the Lick Observatory 1-m telescope. The seeing conditions for this run were approximately 1.5 arc seconds. Figure 13 shows the reconstructed autocorrelation functions of the two objects; comparing these functions with that of Fig. 12c, the binary signature of the objects can be clearly seen.

(a)	(b)
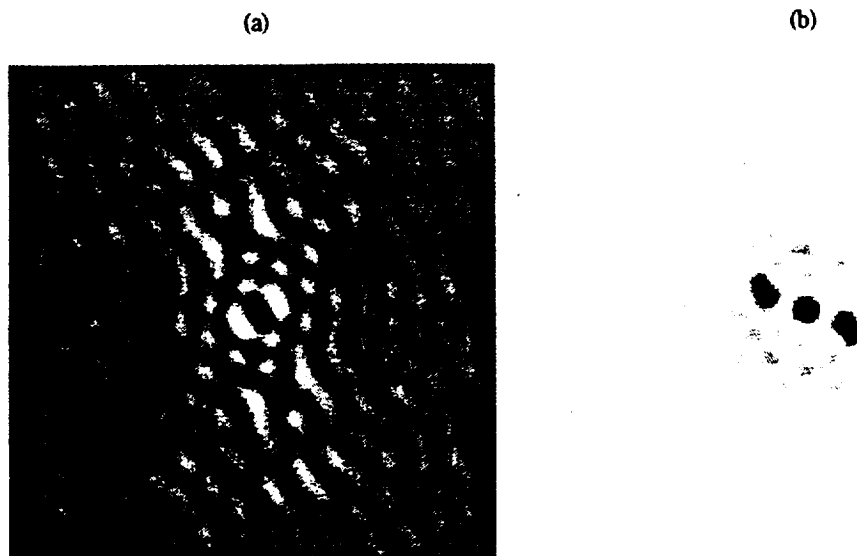
Figure 13. Autocorrelation reconstructions of the binary stars (a) HD136176 and (b) HD170109. HD136176 had a measured separation of 1.48±0.061 arc seconds and HD170109 had a measured separation of 0.716±0.047 arc seconds.

5. SPECKLE IMAGING

Speckle imaging is a term used to describe an extension of speckle interferometry where the final result is a reconstructed image rather than a reconstructed power spectrum or autocorrelation function. There are several variations on how the reconstructed image is obtained, but for the results in this section we have followed the method of Lohmann et al[10]. This method utilizes the triple correlation function of the speckle data frames, an object which is similar to the autocorrelation function, but retains the extra information necessary to reconstruct an image. While the power spectrum of many frames of data does not contain the phase information of the image Fourier transform, the Fourier transform of the triple correlation, known as the bispectrum, does contain this. By combining the modulus of the image Fourier transform (obtained from taking the square root of the power spectrum) with the phase derived from the bispectrum, a quasi-diffraction limited estimate of the image Fourier transform can be produced.

(a)   (b)
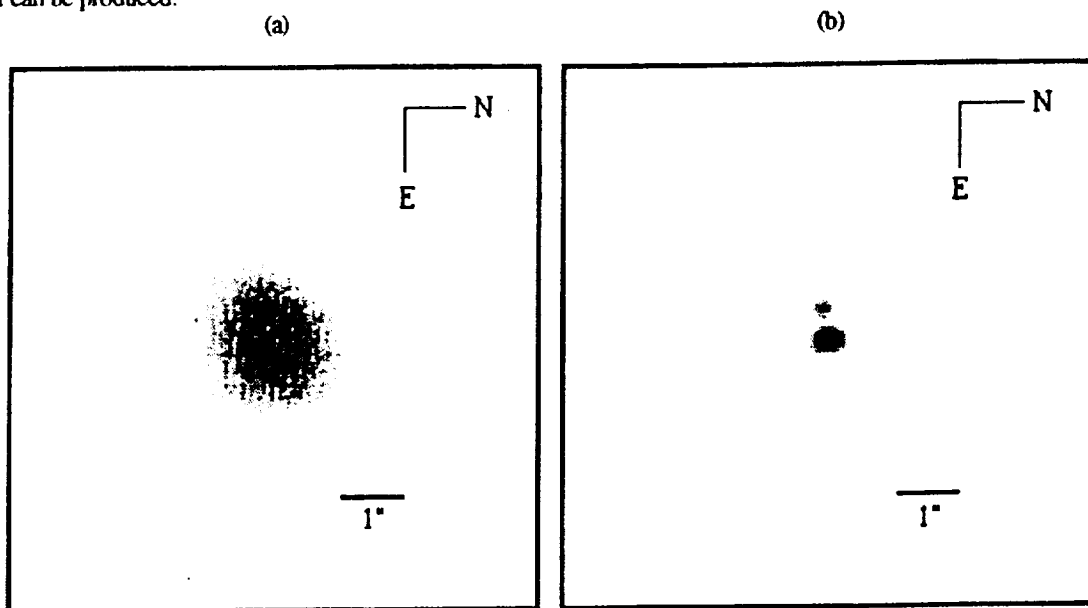
Figure 14. Image reconstruction of the binary star HD161833. (a) Integrated image showing the seeing-limited resolution (about 1.5 arc seconds). (b) Reconstructed image, where the resolution is about 0.3 arc seconds. The separation of the two stars was measured to be 0.556±0.072 arc seconds.

The reconstructed image is then the Fourier inversion of this function. Fig. 14a shows the integrated (seeing-limited) image of a close binary taken with the MAMA detector. Fig. 14b shows the reconstructed image using the Lohmann algorithm where the binary nature of the object is quite clear. Again the observations were carried out at the Lick Observatory 1-m telescope, where the diffraction limit for the wavelength of observation (5029Å) is about 0.125 arc seconds.

6. SUMMARY

The performance of a new time-tagging data acquisition system for the MAMA detector has been investigated both with laboratory and observational data. In the laboratory, the MAMA system was able to see the intensity variation from an incandescent bulb at a frequency of 120 Hz. A moving image was also successfully reconstructed from the time-tagged data. Using stars as Poisson sources of photons, it has been shown that the timing information of the MAMA detector system is Poissonian down to times scales less than about 0.4 ms for a wide range of count rates. This indicates that the system timing is more than adequate for the application of speckle interferometry. Speckle interferometry data of binary stars has been presented including successful autocorrelation and preliminary image reconstructions of binary stars.

7. ACKNOWLEDGMENTS

8. REFERENCES

1. E. Horch, J.S. Morgan, G. Giaretta and D.B. Kasle, "A new speckle interferometry system for the MAMA detector", *Publications of the Astronomical Society of the Pacific*, Vol. 104, pp. 939-948, 1992.

2. D. B. Kasle and J. S. Morgan, "High resolution decoding of multi-anode microchannel array detectors", *SPIE EUV, X-Ray, and Gamma-Ray Instrumentation for Astronomy II*, Vol. 1549, pp. 52-58, 1991.

3. D. B. Kasle and E. P. Horch, "Performance of high resolution decoding with multi-anode microchannel array detectors," *SPIE Ultraviolet Technology IV*, Vol. 1764, pp. 202-216, 1993.

4. P. R. Bevington, *Data Reduction and Error Analysis for the Physical Sciences*, McGraw-Hill, New York, 1969.

5. S. L. Meyer, *Data Analysis for Scientists and Engineers*, John Wiley and Sons, 1975.

6. J.S. Morgan and J. G. Timothy and A. M. Smith, B. Hill, D. B. Kasle, "High time-resolution imaging with the MAMA detector systems", *SPIE Instrumentation in Astronomy VII*, Vol. 1235, pp. 347-357, 1990.

7. A. Labeyrie, "Attainment of diffraction limited resolution in large telescopes by Fourier analyzing speckle patterns in star images", *Astronomy & Astrophysics*, Vol. 6, pp. 85-87, 1970.

8. E. Horch, J.S. Morgan, G. Giaretta, J. G. Timothy and D. B. Kasle, "Speckle observations of binary stars with the MAMA detector," *Complementary Approaches to Double and Multiple Star Research*, H. A. McAlister and W. I. Hartkopf, eds., pp. 549-551, 1992.

9. E. Horch and J. G. Timothy, "New speckle observations of catalogued binaries", *Bulletin of the American Astronomical Society*, Vol 24, p. 1169, 1992.

10. A. W. Lohmann, G. Wiegelt and B. Wirnitzer, "Speckle masking in astronomy: triple correlation theory and applications", *Applied Optics*, Vol. 22, pp. 4028-4037, 1983.

Speckle Imaging with the MAMA Detector:
Preliminary Results

E. HORCH

Department of Astronomy, Yale University, P.O. Box 208101, New Haven, Connecticut 06520-8101
Electronic mail: horch@sparx.astro.yale.edu

J. F. HEANUE

Department of Applied Physics, Stanford University, Stanford, California 94305
Electronic mail: john@shadow.stanford.edu

J. S. MORGAN

Department of Astronomy, University of Washington, Seattle, Washington 98195
Electronic mail: morgan@bluto.astro.washington.edu

J. G. TIMOTHY

Center for Space Science and Astrophysics, Stanford University, Stanford, California 94305
Electronic mail: gethyn@kilohoku.stanford.edu

ABSTRACT. We report on the first successful speckle imaging studies using the Stanford University speckle interferometry system, an instrument that uses a multianode microchannel array (MAMA) detector as the imaging device. The method of producing high-resolution images is based on the analysis of so-called "near-axis" bispectral subplanes and follows the work of Lohmann et al. (1983). In order to improve the signal-to-noise ratio in the bispectrum, the frame-oversampling technique of Nakajima et al. (1989) is also employed. We present speckle imaging results of binary stars and other objects from V magnitude 5.5 to 11, and the quality of these images is studied. While the Stanford system is capable of good speckle imaging results, it is limited by the overall quantum efficiency of the current MAMA detector (which is due to the response of the photocathode at visible wavelengths and other detector properties) and by channel saturation of the microchannel plate. Both affect the signal-to-noise ratio of the power spectrum and bispectrum.

1. INTRODUCTION

Speckle interferometry has been successfully used to gain high angular resolution information about astrophysical objects since its inception by Labeyrie (1970). In conventional astronomy, fluctuations in the atmosphere above the telescope aperture blur images so that the resolution is typically 1 to 2 arcsec, much worse than the diffraction-limited resolution of large telescopes. Speckle interferometry allows for the reconstruction of image features on a much smaller scale by taking many short (typically ~0.01 s) exposure images (frames) of an object, where over the exposure time the atmospheric fluctuations are effectively frozen. Labeyrie realized that the spatial frequency power spectrum of an object, averaged over many frames, retains high angular resolution information that can be retrieved by way of Fourier deconvolution. The method he developed fell short of producing full image reconstructions because the power spectrum contains no phase information about the object's Fourier transform.

Extensions on Labeyrie's technique that retain phase information (in the general case where no isolated point source exists in the field of view) were developed as early as 1974 by Knox and Thompson. They suggested an analysis technique involving the image cross spectrum, a mathematical object that retains a derivative of the phase on the frequency plane. Many investigators have reported results using other methods, some of which worked in special cases, some of which were borrowed from radio astronomy (see e.g., Rod-

dier 1987 for a review). Several years later, Lohmann et al. (1983) developed a technique of retrieving phase information from the image bispectrum. The analysis of the bispectrum has generally been acknowledged to be one of the best ways to derive a phase estimate in speckle imaging because the bispectral signal-to-noise ratio is high and because the bispectrum is relatively insensitive to telescope aberrations. Like the cross-spectral analysis of Knox and Thompson, the bispectrum can be used to derive a phase derivative estimate over the spatial frequency plane.

There are several different kinds of speckle interferometry systems currently in use. One type of system that has enjoyed great success is the intensified charge-coupled device (ICCD), favored by the U.S. Naval Observatory speckle interferometrists (Worley and Douglass 1992) and the Center for High Angular Resolution Astronomy (CHARA) group at Georgia State University (McAlister et al. 1987). In the 1980s, another kind of speckle interferometry device became available in the form of photon-counting cameras such as PAPA detectors (Papaliolios et al. 1985), resistive anode position sensing detectors (Nakajima et al. 1989), wedge and strip detectors (Barnstedt et al. 1987), and MAMA detectors (Morgan 1989; Timothy et al. 1989). These detectors all offer the advantage of time tagging each detected photon, allowing the frame rate to be set in software after the observations are completed. Also, they allow for the accurate subtraction of the so-called "photon noise bias" term in correlation func-

TABLE 1
Properties of Some Photon-Counting Speckle Systems Currently in Use

Imaging detector	Reference	Pixel format	Photocathode	Detector QE	Timing Res.	Spatial Res.
PAPA	Papaliolios et al. 1985	256×256	S-20	~3%	1 ms	25 μm
Wedge and Strip	Barnstedt et al. 1987	512×1024	S-20	~3%?	1 μs	50 μm
Res. Anode	Nakajima et al. 1989	1024×1024	MA-2	~2%	<1 μs	60 μm
MAMA	Horch et al 1992; Timothy et al. 1989	224×960 or 448×1920	Bialkali	~1%	0.4 μs	11 μm

tions, and give a data stream that is much more compact than nonphoton-counting devices.

The first speckle interferometry system for the MAMA detector was built in the mid-1980s by Morgan and Timothy and their collaborators at Ball Aerospace Systems Group. The device was used to take some preliminary speckle data of double stars and planetary objects (Morgan 1989; Meng et al. 1990; Morgan et al. 1990). From this experience, a new speckle system was built and was described in an earlier paper (Horch et al. 1992). Initial data taken with the new system showed that it was capable of retrieving nearly diffraction-limited information under good seeing conditions, but the studies by Horch et al. were limited to the power spectrum of objects, and speckle image reconstructions were not considered. In this paper, we show the first speckle imaging results with this system and make a study of the quality of these images. Two detector effects are discussed in detail, detective quantum efficiency and channel saturation of the microchannel plate. Our results can be compared to the work of other groups to give a clearer picture of how well the Stanford system works as a speckle imaging device and how it may best be used in the future for projects of scientific merit.

Some properties of the current Stanford system and several other photon-counting speckle imaging systems are shown in Table 1. While the Stanford system offers some advantage in spatial and temporal resolution, its detector quantum efficiency is lower than the other devices due mainly to the response of the bialkali photocathode at visible wavelengths. Since the signal-to-noise ratio (SNR) of the bispectrum is proportional to $n^{3/2}$ at low light levels, where n is the number of photons detected per frame, we can expect that the quality of speckle imaging results obtained with the current MAMA detector will be lower than those of other investigators.

2. INSTRUMENTATION

Although the Stanford speckle interferometry system has been previously described, it is useful to explain the basic operation of the system here, especially since we have made some recent system modifications. Figure 1 shows a block diagram of the current system. Light entering the telescope is imaged onto a plane at the front end of the "speckle cam-

era," a box that contains Risley prisms, microscope objective lenses, and narrow bandpass filters (in addition to some other optical elements). The speckle camera corrects for atmospheric dispersion, magnifies the image to a size appropriate for speckle interferometry, and filters the light so that the image received at the detector is quasimonochromatic.

The imaging detector is a MAMA detector with a bialkali photocathode and a single curved-channel microchannel plate (MCP) with 8 μm diameter channels on 10 μm centers. Current generation MAMA detectors have been described in detail by Timothy et al. (1989), so only a brief description of the detection process will be given here. Beneath the MCP is an anode array which collects the charge cloud from the output side of the microchannels. The charge on each anode
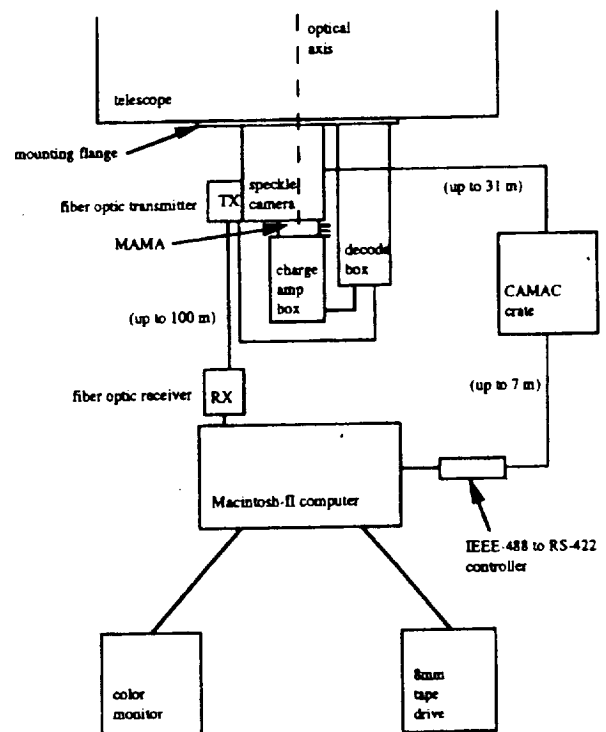

FIG. 1—The primary components of the Stanford University speckle interferometry system.

is amplified and positional information is determined by co-incidence electronics housed in a separate box called the "pixel decoder." The decoder was built by David Kasle (now of Kubota Pacific, Inc.) and is equipped with the high-resolution decoding algorithm which has been successfully used with MAMA detectors for the past three years (Kasle and Morgan 1991). This feature gives the Stanford speckle interferometer 7 μm square pixels and an intrinsic resolution of about 11 μm on the image plane (Kasle and Horch 1992).

Decoded photoevent data are transferred to a Macintosh computer by means of a fiber optic link. The receiving unit of the link is connected directly to a NuBus™ interface card that sits inside the computer. Both the fiber optic system and the computer interface were built by Giorgio Giaretta at Stanford University. The computer interface time tags the incoming data and stores the information in a file on the hard disk which is then transferred to 8 mm magnetic tape by means of an Exabyte tape drive. The computer also controls the speckle camera through a computer automated measurement and control (CAMAC) interface, so that filter selection and Risley prism orientation can be accomplished remotely.

3. THE RECONSTRUCTION METHOD

The construction of a high-resolution image from speckle data has three main steps: (1) the modulus of the object's Fourier transform is obtained via analysis of the image power spectrum, (2) the phase of the object's Fourier transform is obtained via analysis of the image bispectrum, and (3) the two pieces are combined to give an estimate of the object's (complex) Fourier transform and the result is Fourier inverted. In order to obtain the power spectra and bispectra of all of the objects discussed in the next section, the over-sampled frame technique of Nakajima et al. (1989) was used. In this case, the second frame in a sequence of frames starts halfway through the first frame, the third frame starts at the end of the first frame and halfway through the second frame, and so on. This has been shown to improve the SNR of the Fourier objects by 30%–40%.

Frames are also flat fielded in the following way. With an ideal photon-counting device, each detected event would be a delta function of unit weight and a frame would consist of the sum of such delta functions. However, there are in general nonuniformities in detector response across the image plane. Following Beletic (1989), we flat field frame images $I(x)$ by weighting the events depending on where they occur on the image plane, so that

$$I(x) = \sum_{i=1}^{N} w_i \delta(x - x_i).$$ (1)

The weights w_i are proportional to $1/f(x_i)$, where $f(x_i)$ is the number of counts at x_i in the flat-field image. To form the autocorrelation function $\gamma(x) = \int I^*(x')I(x'+x)dx'$ for a frame image, we substitute the right side of Eq. (1) in for I and obtain

$$\gamma(x) = \sum_{k=1}^{N} \sum_{\substack{l=1 \\ l \neq k}}^{N} w_k w_l \delta(x + x_k - x_l).$$ (2)

The photon noise bias is explicitly removed from each frame by requiring $l \neq k$. The result is then averaged over many frames and Fourier transformed to obtain the power spectrum. To compute the bispectrum, we use the subplane method of Northcott et al. (1988) (where the inverse transform of a particular bispectral subplane is calculated in image space), but again we use frame images of the form of Eq. (1). Define the Fourier transform of a function $g(x)$ on the image plane as

$$FT\{g(x)\} = \hat{g}(u) = \int g(x)\exp(-2\pi i u \cdot x)dx.$$ (3)

The bispectrum $\hat{C}(u_1, u_2)$ of $I(x)$ can be expressed as

$$\hat{C}(u_1, u_2) = \hat{I}(u_2)\hat{I}(u_1)\hat{I}^*(u_1 + u_2).$$ (4)

Consider a subplane of the bispectrum defined by u_2 fixed. The second two factors in the right side of Eq. (4) can be expressed as

$$\hat{I}(u_1)\hat{I}^*(u_1 + u_2) = FT\{[I(x)\exp(2\pi i u_2 \cdot x)] \otimes I(x)\},$$ (5)

where $\otimes$ denotes cross correlation and the Fourier transform frequency variable is u_1. The first factor is just

$$\hat{I}(u_2) = \int I(x)\exp(-2\pi i u_2 \cdot x)dx.$$ (6)

Substituting the right hand side of Eq. (1) for $I(x)$ in Eqs. (5) and (6), we obtain

$$\hat{C}(u_1, u_2) = \left(\sum_{\substack{m=1 \\ m \neq k, m \neq l}}^{N} w_m \exp(-2\pi i u_2 \cdot x_m) \right)$$

$$\times FT\left\{ \sum_{k=1}^{N} \sum_{\substack{l=1 \\ l \neq k}}^{N} w_k \exp(2\pi i u_2 \cdot x_k) \right.$$

$$\left. \times w_l \delta(x + x_k - x_l) \right\}.$$ (7)

Again the photon noise bias subtraction is done explicitly in these summations by removing the self-correlation terms and it can be shown that this is equivalent to the method of Beletic (1989). The first sum is simply a complex factor and may be placed inside the Fourier transform. Using the linearity of the transform, we can then average over many frames in image space and Fourier transform just once at the end

$$\langle \hat{C}(u_1, u_2) \rangle = FT\left\{ \sum_{\substack{m=1 \\ m \neq k, m \neq l}}^{N} w_m \exp(-2\pi i u_2 \cdot x_m) \right.$$

$$\times \left\{ \sum_{k=1}^{N} \sum_{\substack{l=1 \\ l \neq k}}^{N} w_k w_l \exp(2\pi i u_2 \cdot x_k) \right.$$

$$\left. \left. \times \delta(x + x_k - x_l) \right\} \right\},$$ (8)

where $\langle \rangle$ denotes the average over many frames. Equation (8) is the basic relation that we use to calculate flat-fielded, bias-subtracted subplanes.

The method of phase reconstruction used for the data presented below is that of Lohmann et al. (1983), where the phase map is built up recursively starting at the origin in the frequency plane. Although it is possible to construct the phase map with only two subplanes from the (four-dimensional) image bispectrum, using more subplanes can be beneficial depending on observing parameters (Nakajima 1988). In general, the highest signal-to-noise subplanes lie close to the $u_2 = 0$ subplane, where as above the bispectrum is of the form $\tilde{C}(u_1, u_2)$, and u_1 is the spatial frequency variable of the phase map. These are often called the "near-axis" subplanes. The recursive method used here is a very simple phase reconstructor with the main disadvantage that as the phase is built up away from the origin, errors begin to increase. There are now more sophisticated methods for the development of the phase map, such as the relaxation technique used by Meng et al. (1990). A new phase reconstruction program based on this method is currently being written for the Stanford system.

Once the phase map is combined with the modulus estimate, the result must be inverse transformed to yield a reconstructed image. We have found that with our data, the high-frequency portion of the reconstructed object Fourier transform must be attenuated before inverse transforming to give a high dynamic range reconstructed image. We have attempted a couple of different schemes for doing this, but for the images presented in this paper, the reconstructed transform was multiplied with a circular Gaussian filter of the form

$$\varphi(\mathbf{u}) = \exp\left[-\frac{1}{2}\left(\frac{|\mathbf{u}|}{\sigma}\right)^2\right], \tag{9}$$

where σ is a constant. This type of filter gives a fairly smooth reconstructed image with roughly Gaussian reconstructions for point sources and has the considerable advantage of simplicity. The effect of varying the filter width, σ, on image properties is discussed in the next section.

4. OBSERVATIONS

All of the observations discussed below were taken in 1992 May at the Lick Observatory 1-m reflector. Seeing for this run varied between 1″4 and 2″0. All observations were taken in low-resolution decoding mode (14 μm square pixels in a 224×960 format) with a 5029 Å filter that was 397 Å wide. At this wavelength, we estimate that the telescope-filter-detector combination has a quantum efficiency of about 0.5%.

The plate scale was measured by taking an image of a point source on one side of the active area of the detector and then moving the telescope until the star was on the other end of the field of view. The change in the direction that the telescope was pointing between the two images then leads to an estimate of the number of pixels per arcsecond. Since our MAMA detector has a large format, even with speckle optics, we were able to measure the plate scale within a couple
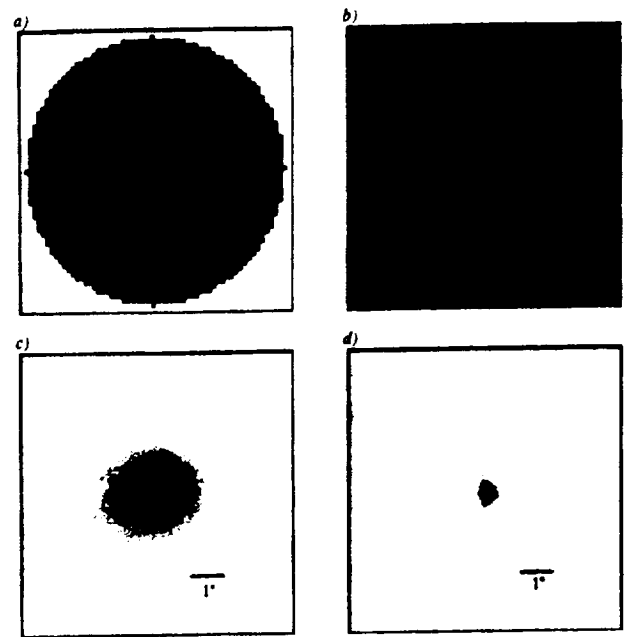

FIG. 2—Image reconstruction of the point source HD 125019. Linear grey scales are used in all plots. (a) The modulus of the Fourier transform where the grey scale goes from 0 (white) to 255 (black). Dark regions near the center are caused by a slight mismatch between the object and point source seeing conditions. (b) The phase of the Fourier transform, where the grey scale goes from $-\pi$ (white) to π (black). Both (a) and (b) have been shown out to the $1/e$ radius of the circular Gaussian filter used before inverse transforming to obtain the reconstructed image. (c) The integrated image of HD 125019. (d) The reconstructed image.

of percent using this technique. For the Lick observations, we obtained a plate scale of 0.06857 ± 0.0022 arcsec pixel^{-1}. The same technique also gives the angle between the detector long axis and true north (the detector pitch angle), where the result was $2°10 \pm 0°57$.

The first object that we analyzed was a point source, HD 125019. Figures 2(a) and 2(b) are the Fourier space representations of the reconstructed modulus and phase as obtained by the image reconstruction program prior to Gaussian filtering in the frequency domain. The origin (where spatial frequency is zero) is in the center of the diagram. The modulus estimate for a point source should be a constant while the phase should be a linear function of u, accounting for the arbitrary position of the object in image space. While the recovered phase map does appear to be roughly linear, the modulus estimate is not constant since there are dark peaks near the center of Fig. 2(a). These are caused by a mismatch in the seeing conditions between HD 125019 and the object used as a point source (HD 119126) to obtain the modulus. Even with this deficiency, a narrow reconstructed point spread function is obtained and shown in Fig. 2(d). Figure 2(c) shows the integrated (seeing-limited) image of the same data for comparison. Both Figs. 2(c) and 2(d) are normal image space representations of the data. A 1 arcsec bar is shown in these figures to illustrate the scale. Figure 3 shows surface plots of Figs. 2(c) and 2(d). As mentioned earlier, a Gaussian filter was applied to the data in Fourier space prior to transforming back to image space in order to
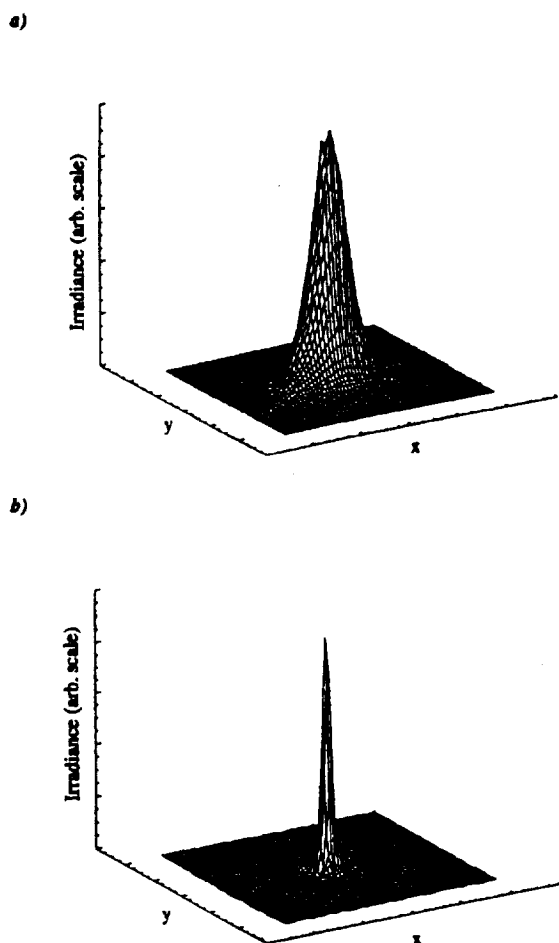
a)

b)

FIG. 3—Surface plots of (a) the integrated image and (b) the reconstructed image of HD 125019. The integrated image FWHM is 1″58 while the reconstructed image FWHM is 0″33.

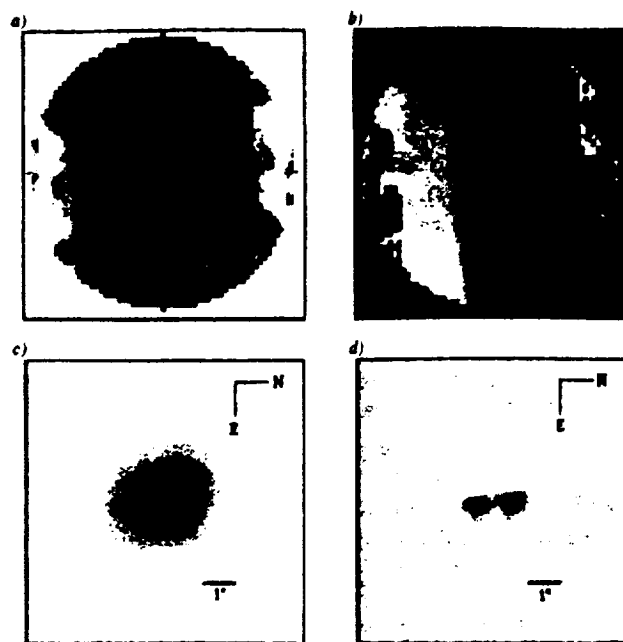*a)*   *b)*

c)   *d)*

FIG. 4—Image reconstruction of the binary star HD 115995. Linear grey scales are used in all plots. (a) The modulus of the Fourier transform where the grey scale goes from 0 (white) to 255 (black). Dark regions near the center are caused by a slight mismatch between the object and point source seeing conditions. (b) The phase of the Fourier transform, where the grey scale goes from −π (white) to π (black). Both (a) and (b) have been shown out to the 1/e radius of the circular Gaussian filter used before inverse transforming to obtain the reconstructed image. (c) The integrated image of HD 115995. (d) The reconstructed image. The star images appear elongated because the Risley prism positions were slightly in error for the observation, and did not fully compensate for the atmospheric dispersion.

produce Fig. 2(d) and all subsequent reconstructions shown here. The full width at half maximum (FWHM) of the integrated image is 1″58 while for the reconstructed image the result was 0″33. The dynamic range of the reconstructed image, defined to be the maximum value in the array divided by the value of largest spurious peak (positive or negative), is about 26.

Next we analyzed data taken of four objects from the *CHARA Second Catalog of Interferometric Measurements of Binary Stars* (McAlister and Hartkopf 1988). We present the data for two of these objects in the same form as for HD 125019. Figures 4 and 5 show the reconstruction of the binary star HD 115995 obtained with the image reconstruction software and the integrated image for comparison. The dynamic range for the reconstructed image is 14. Figures 6 and 7 show the result of the analysis for HD 161833, where the reconstructed image has a dynamic range of 35. A two-dimensional Gaussian fitting program was used to obtain the best fit positions of the two peaks in the reconstructed images of these and two other binaries analyzed the same way. These results are summarized in Table 2. Finally, the Stanford results for HD 161833 and HD 130188 have been com-

pared with the previous position measures found in the *CHARA Second Catalog* and one other source (Hartkopf et al. 1992) in Fig. 8. The relative movement of the components is real and the measurements are in good agreement with the previous observations. This is true for all the binaries in Table 2, where the uncertainty in the separation is typically a couple of hundredths of an arcsecond. The main contributor to this uncertainty is the measure of the plate scale.

Several other unresolved point sources and binaries were analyzed in the same way to determine how the dynamic range of the reconstructed images behaves as a function of the Gaussian filter width and as a function of V magnitude. As the width of the filter is increased in frequency space, the point spread function of a reconstructed image will become narrower, but at the cost of dynamic range, as shown in Fig. 9 for the binary HD 161833. This behavior reflects the fact that the SNR is lower in the high-frequency portion of the recovered object Fourier transform than in the low-frequency portion. Figure 10 shows how the dynamic range diminishes as the source brightness decreases. In this plot, the width of the Gaussian filter is fixed at 1.7 cycles arcsec^{-1}, the same width as for the reconstructed images shown in this section. By 11th magnitude, the reconstructed images show typical dynamic ranges of only about 5 (for 10^6 events analyzed). From Fig. 10, we can currently expect to obtain reconstructed images with dynamic ranges of 10 or better for ob-
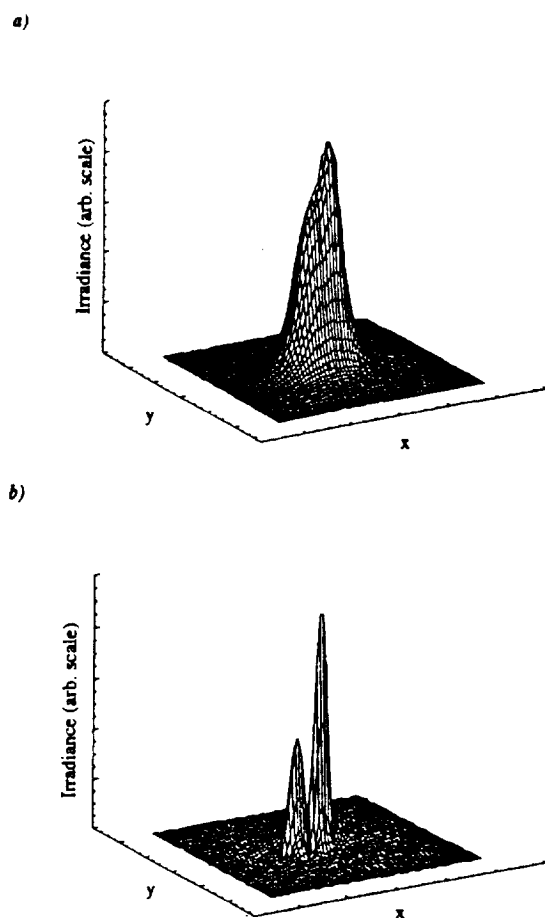
a)

b)

Fig. 5—Surface plots of (a) the integrated image and (b) the reconstructed image of HD 115995. The separation of the components is approximately 1.1 arcsec. North is in the positive *x* direction and east is in the negative *y* direction.

jects brighter than about 8th magnitude on a 1-m class telescope under normal observing conditions.

5. DETECTOR EFFECTS

When the above results are compared to some other speckle imaging studies, the Stanford system appears to give reconstructed images of lower quality. Recall from the previous section that the dynamic range of a reconstructed image is defined as the maximum value in the image divided by the largest spurious component. Hofmann and Weigelt (1986) have resolved a quadruple star system where the components are all about 12th magnitude with the 1.5-m Danish telescope at the European Southern Observatory, and while no dynamic range estimate is given for the image, the resolution of the reconstruction is about $0.\!''1$. Nakajima et al. (1989) obtain a dynamic range of 30 on a reconstructed image of a double star with $V = 4.2$. The object was observed using the Hale 5-m telescope and the reconstructed image had a beam FWHM of $0.\!''03$, which is diffraction limited. While the Stanford system at the Lick 1-m telescope gave a dynamic range of 35 for the binary HD 161833 (with $V = 5.6$) under similar seeing conditions, this image has a resolution
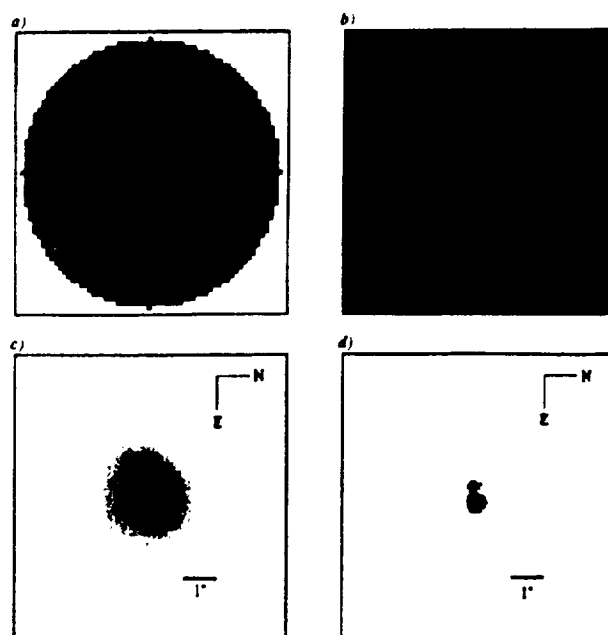

Fig. 6—Image reconstruction of the binary star HD 161833. Linear grey scales are used in all plots. (a) The modulus of the Fourier transform where the grey scale goes from 0 (white) to 255 (black). Dark regions near the center are caused by a slight mismatch between the object and point source seeing conditions. (b) The phase of the Fourier transform, where the grey scale goes from $-\pi$ (white) to π (black). Both (a) and (b) have been shown out to the $1/e$ radius of the circular Gaussian filter used before inverse transforming to obtain the reconstructed image. (c) The integrated image of HD 161833. (d) The reconstructed image.

of over twice the diffraction limit, with a beam FWHM of $0.\!''35$. A quasidiffraction-limited image of our HD 161833 data has dynamic range of less than 8. This again illustrates the trade-off between resolution and dynamic range; in the results above, we have chosen to present reconstructed images of lower resolution in order to maintain a standard of dynamic range. Therefore the current limitations of the Stanford system are realized in the lack of diffraction-limited resolution.

5.1 Detective Quantum Efficiency

The quality of the speckle imaging results is determined in part by the performance of the image device. In the case of the Stanford system, the MAMA detector currently used is not optimal for speckle interferometry for two reasons. First, as already mentioned, the photocathode material does not have as high a quantum efficiency in the visible as the S-20 and MA-2 photocathodes used with other systems. Secondly, properties of the MCP of this MAMA detector are not outstanding. It has a low gain, giving an average output of about 3×10^5 electrons pulse^{-1}. When the electronic threshold for event detection is set at a reasonable level to limit the dark current, this results in a lower gain-to-threshold ratio than most MAMA detectors have, about 1.2 compared with more typical values of 2 to 4. This ratio is important in determining both the detective quantum efficiency and the linearity of the device.
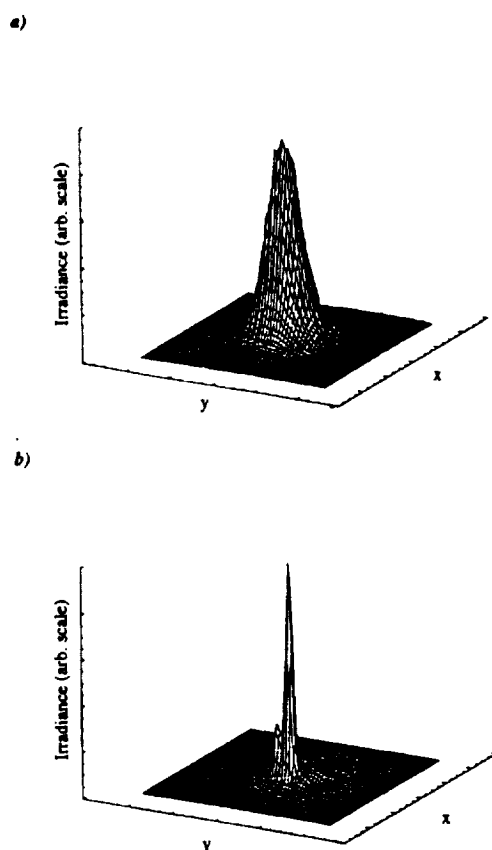
a)

b)

FIG. 7—Surface plots of (a) the integrated image and (b) the reconstructed image of HD 161833. The separation of the components is approximately 0.5 arcsec. North is in the positive x direction, east is in the negative y direction.

Figure 11 illustrates the effect of a low-gain MCP on MAMA detector quantum efficiency by showing the histogram of individual event gains, known as the pulse height distribution (PHD) of the detector, for the high- and low-gain cases. When the peak in the PHD (called the modal gain) is not very much higher than the threshold, more photoevents in the distribution fall below the threshold and go uncounted, thereby decreasing the detector's quantum efficiency. Even if a photoelectron is generated at the photocathode, it will not be counted if the MCP does not produce a large enough electron cloud.

TABLE 2
Stanford Speckle Imaging Results for Four Binary Systems[a]

Object	Position angle (°)	Separation (arcsec)	(Total) V Mag.[b]	Reconstr. image dynamic range
HD 115995	176.6±0.7	1.070±0.038	6.2	14.2
HD 128941	64.7±2.9	0.645±0.033	6.8	5.3
HD 130188	303.6±2.7	0.363±0.017	7.2	12.2
HD 161833	260.9±0.9	0.536±0.018	5.6	35.3

[a]All measures are for epoch 1992.39.
[b]From the *SAO Star Catalog*.

a)

b)
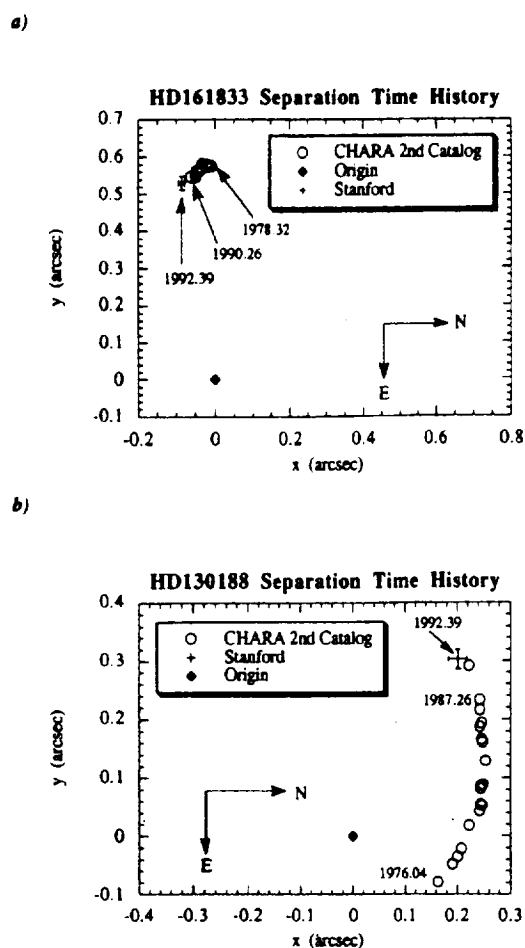
FIG. 8—Separation time histories for (a) HD 161833 and (b) HD 130188. Except for the indicated points, the data were taken from the *CHARA Second Catalog of Interferometric Measurements of Binary Stars* and subsequent work by the CHARA group.

5.2 Speckle Signal-to-Noise Ratios and Channel Saturation

Miller (1977) gave an expression for the power spectrum SNR of a point source
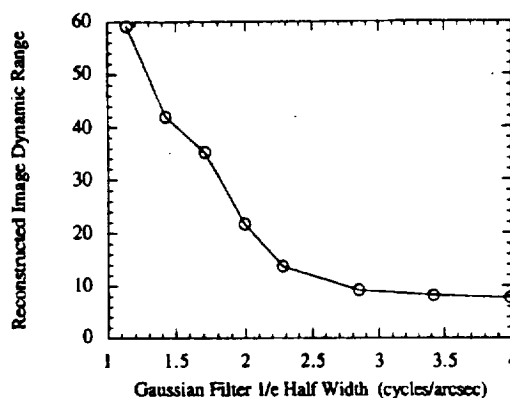

FIG. 9—The effect of varying the width of the Gaussian frequency filter on the reconstructed image dynamic range for the binary star HD 161833.
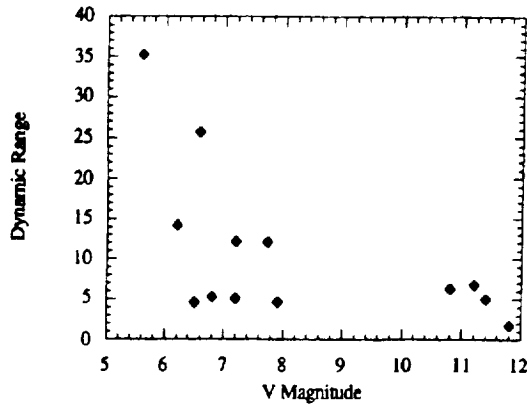
FIG. 10—Reconstructed image dynamic range as a function of V magnitude for several objects observed with the Stanford system.

$$\frac{S}{N}(u) = \sqrt{M} \; \frac{n \cdot T_{hf}(u)}{1 + n \cdot T_{hf}(u)}, \qquad (10)$$

where $u \equiv |u|$ is the spatial frequency, n is the number of photons per frame, M is the number of frames averaged. $T_{hf}(u)$ is the high-frequency expression for the speckle transfer function given by, e.g., Dainty (1984) as

$$T_{hf}(u) = 0.435 \left(\frac{r_0}{D}\right)^2 T_{tel}(u), \qquad (11)$$

where r_0 is the Fried parameter, D is the diameter of the telescope, and $T_{tel}(u)$ is the (diffraction-limited) transfer function of the telescope. We can compare Eq. (10) to MAMA speckle data taken at Lick Observatory by measuring the value of r_0 appropriate for the observation from the

a)

b)

a)

b)
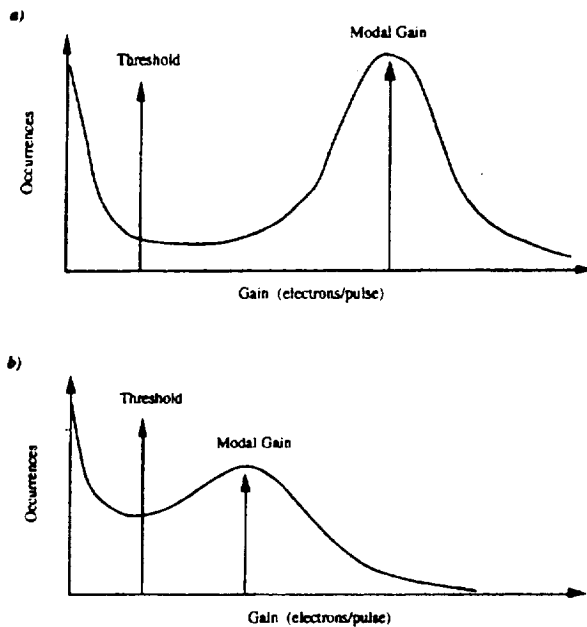
FIG. 11—(a) Typical high-gain MCP pulse height distribution. (b) typical low-gain MCP pulse height distribution. The threshold for event detection must be set above the low-gain tail, which is caused by charge amplifier noise.
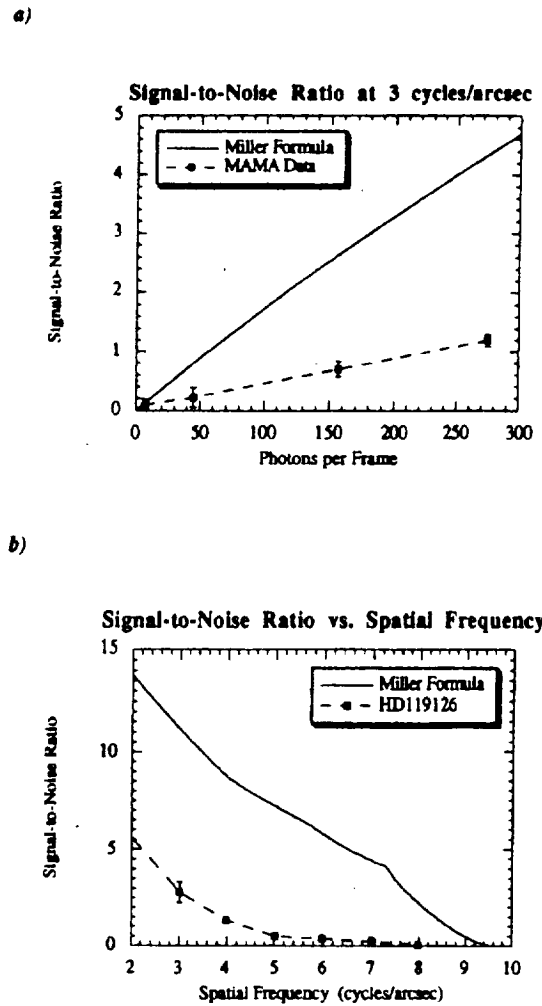
FIG. 12—(a) Stanford system SNR as a function of the number of photons per frame (or equivalently, count rate) for four point sources of different brightness observed under similar seeing conditions (1000 frames analyzed in each case), (b) Stanford system SNR as a function of spatial frequency for HD 119126, a point source of 78 kHz (6675 frames analyzed). Both are compared to the value expected from Eq. (10).

low-frequency portion of the power spectrum and assuming the Lick 1-m telescope has diffraction-limited optics. This gives $T_{hf}(u)$. The variables M and n are also matched with the observational values, and this leads to an expected value of the SNR based on photon statistics.

The SNR in a MAMA data point source power spectrum can be measured by considering a thin annulus centered on a spatial frequency of interest. The signal is given by the average value inside the annulus and the noise measurement is the standard deviation of values that lie inside the annulus. The division of these two quantities gives the observed SNR. Since the power spectrum is symmetric about the line $u_y = -u_x$ in frequency space, only the half annulus above the line is used for the measurements. Figure 12 shows a typical result for the signal-to-noise observed with the Stanford system. It currently gives SNRs that are well below the expected value from photon statistics, especially for higher count rates. This result is not connected with the low detective
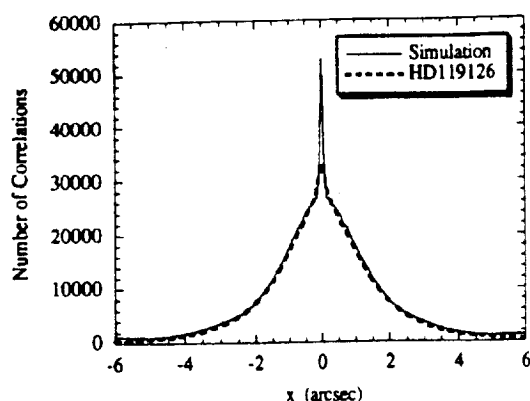
FIG. 13—X-axis cuts through point source autocorrelations for real and simulated data. The real data show fewer correlations at zero separation.

quantum efficiency of the system, since that is folded into Eq. (10) by way of the variable n.

In order to investigate why the Stanford system performs below the level of speckle photon statistics, we constructed a computer program to model the speckle process and photo-event detection with a MAMA detector. The portion of the code that models the formation of speckles operates under the assumption that the aperture function may be described as a simple random phase screen that is linearly translated across the telescope aperture as a function of time. The size of coherent phase regions within the aperture is set by convolving the phase screen with an input kernel. The shape and width of the kernel are determined by requiring that the seeing distribution is similar to that of real data. We also assume monochromaticity and perfect optics. For the model of the MAMA detector, we assume that 2.25 microchannels on average feed each detector pixel (the actual number for our current detector is 2.26 in low-resolution decoding mode), and that a microchannel takes some characteristic time τ_{ch} to recharge after an event has passed through it. This well-known feature of MCPs leads to a phenomenon called channel saturation which depletes the charge available on a channel wall in the MCP at high light levels and lowers the average gain of events. The program assumes that after an event has passed through a channel, it is dead for a time τ_{ch}. This assumption accounts for the physics of the MCP in a very simple way which is only reasonable in the case of a detector with a low gain-to-threshold ratio. If a detector has a high gain-to-threshold ratio, then even though two events may enter a channel very close in time and the second event produces a lower gain output charge cloud, this may still fall above the threshold level and be counted as an event. If the detector has a low gain-to-threshold ratio, the likelihood that the second count falls below the threshold is much higher. Because our current MAMA detector has a very low modal gain-to-threshold ratio (about 1.2), this assumption is a reasonable first attempt to estimate the effect of channel saturation on Stanford speckle data.

When the program is run with input parameters of no motion of the phase screen within a frame, observing parameters similar to Lick Observatory data discussed above, and
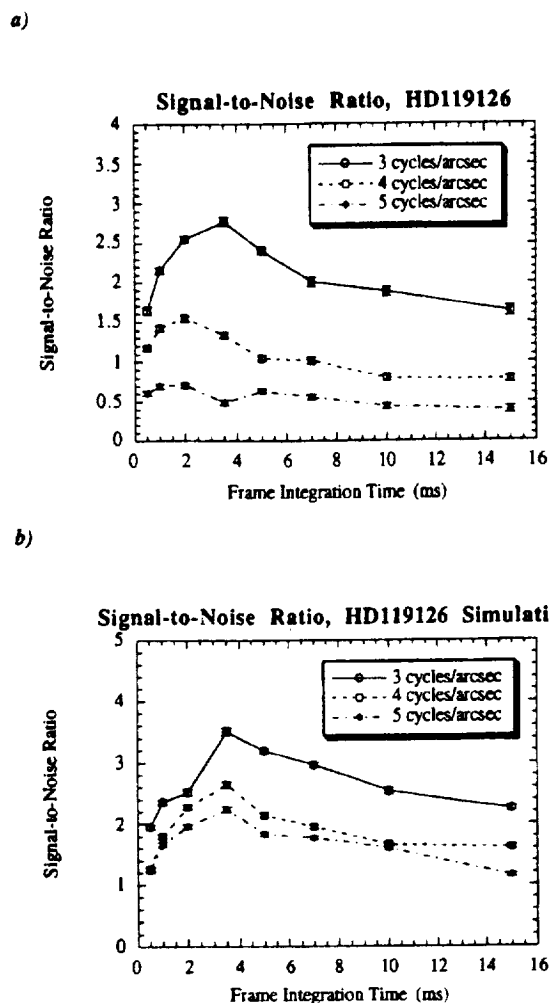

a)

b)

FIG. 14—Power spectrum signal-to-noise ratio as a function of frame integration time. (a) Real data of HD 119126, 6675 frames analyzed, (b) simulated data for observing parameters similar to those of HD 119126, 1000 frames analyzed.

assuming a perfect detector with zero channel recharge time, it produces simulated speckle data with SNRs that follow Eq. (10) within statistical errors. When we compare a MAMA data autocorrelation for a particular point source (HD 119126) with a simulated data autocorrelation with the same observational parameters including count rate (78 kHz), the only significant difference between the two is at very small separations, where there are more correlations in the simulated data. This is shown in Fig. 13. There are probably several contributing factors to this effect, including the non-monochromaticity of the MAMA data and slight misalignment of the Risley prisms during the MAMA observation. Two other contributors, which we shall discuss in more detail, are finite exposure time (which leads to motion of the phase screen within a frame) and channel saturation of the MCP.

Finite exposure time and optimal SNR have been discussed by, e.g., Dainty (1984). A finite frame exposure time spreads speckles out over more pixels on the image plane, decreasing the coherence of the speckle pattern. In an auto-
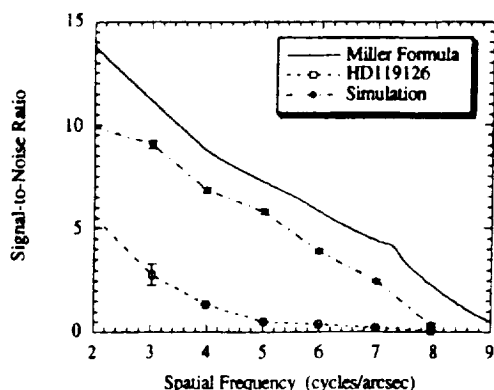
FIG. 15—Signal-to-noise ratio as a function of spatial frequency for the simulation of Fig. 14, normalized to 6675 frames. The real data values and Miller formula values are plotted for comparison.
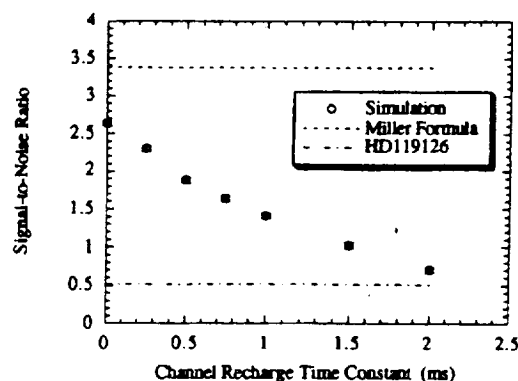

FIG. 16—The power spectrum signal-to-noise ratio (at 1/2 the diffraction limit) as a function of channel recharge time for the simulation of HD 119126. The Miller formula value and real data value are plotted for comparison.

correlation function, this will result in fewer correlations at zero or very small separations, which in turn will suppress the high-frequency wing of the power spectrum. This indicates that the frame integration time for a speckle observation should be chosen so that the speckle motion is small, but if too short a frame time is chosen, frames become photon starved and this also leads to a loss of SNR. The competition between these two effects results in a particular frame time that maximizes the SNR. When phase screen motion is added into the above simulation of HD 119126, it decreases the SNR in the power spectrum below the value predicted by Eq. (10). Figure 14 shows real and simulated data SNR as a function of frame integration time while Fig. 15 compares the result for the simulation's maximal SNR with the Miller formula [Eq. (10)]. The effect probably contributes to the loss of SNR in the MAMA data discussed above, but the simulation indicates that it is not large enough to fully explain the discrepancy between the MAMA data and the Miller formula.

Channel saturation is also a mechanism that can decrease the number of correlations at small separation. If two counts enter a particular microchannel one after the other, the second count will have a low-gain output pulse if it enters the channel before it has had sufficient time to recharge. The count may fall below the electronic threshold of event detection, and the loss of the such counts means the loss of correlations at zero separation. By taking our simulation of HD 119126 and varying the channel recharge time, we were able to study how this loss of counts affects the power spectrum SNR for the Lick observing parameters. The result is shown in Fig. 16. The reason that the simulation results do not match the Miller formula at zero channel recharge time is because of phase screen motion within frames. What is clear from Fig. 16 is that even channel recharge time constants of 1 ms or less significantly decrease the signal-to-noise of the power spectrum. Figure 17 shows the percentage of counts lost as a function of the channel recharge time. Only a few percent of the counts are lost, but the effect on the SNR of the high-frequency region of the power spectrum is substantial since the mechanism selectively throws out counts that would be recorded in the same pixel as detected events.

We have measured the channel recharge time for our current MAMA detector in the laboratory using the saturation detection efficiency method described in Slater (1991), and the value we obtained was 0.683 ± 0.165 ms. According to the simulation results, we can expect that the SNR in the power spectrum of HD 119126 is decreased by about a factor of 1.5–2.0 due to this detector effect alone. HD 119126 had an observed count rate in between those of HD 161833 and HD 115995, the binaries discussed in detail in Sec. 4. We have completed several other simulations, all of which suggest that channel saturation is a major contributor to the loss of SNR in MAMA detector data of the brighter Lick sources (>50 kHz).

6. CONCLUSIONS

We have presented some of the first speckle image reconstructions made from data taken with the Stanford University speckle interferometry system. On subarcsecond binary stars, we have obtained separations and position angles that are in excellent agreement with the measurements of other investigators and have typical astrometric uncertainties of a couple of hundredths of an arcsecond. The main component of these uncertainties is due to the plate scale measure.
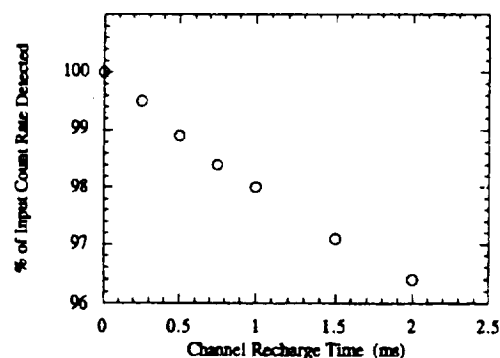

FIG. 17—The percentage of counts detected as a function of the channel recharge time from model data.

The reconstructed images presented here are severely limited by two detector effects. First, the quantum efficiency of the photocathode used with the current Stanford system is a factor of 2 to 3 lower than other speckle imaging systems currently in use. Secondly, due to the inferior properties of the MCP in the current MAMA detector, it is susceptible to channel saturation even at count rates under 100 kHz. A simple model predicts that an MCP with low gain-to-threshold ratio and channel recharge time similar to that of our MAMA detector lowers the SNR of a 78 kHz point source by a factor of 1.5 to 2.0, even though the percentage of counts missed by the detector is less than 4%.

REFERENCES

Barnstedt, J., Neri, R., and Grewing, M. 1987, Mitt. Astron. Ges., 68, 240

Beletic, J. W. 1989, Opt. Comm., 71, 337

Dainty, J. C. 1984, in Laser Speckle and Related Phenomena, ed. J. C. Dainty (Berlin, Springer), p. 255

Hartkopf, W. I., McAlister, H. A., and Franz, O. G. 1992, AJ, 104, 810

Hofmann, K.-H., and Weigelt, G. 1986, A&A, 167, L15

Horch, E., Morgan, J. S., Giaretta, G., and Kasle, D. B. 1992, PASP, 104, 939

Kasle, D. B. and Morgan, J. S. 1991, in EUV, X-Ray, and Gamma Ray Instrumentation for Astronomy II, SPIE Proc. Vol. 1549 (Bellingham, WA, SPIE), p. 52

Kasle, D. B., and Horch, E. P. 1993, in Ultraviolet Technology IV, SPIE Proc. Vol. 1764 (Bellingham, WA, SPIE), p. 202

Knox, K. T., and Thompson, B. J. 1974, ApJ, 193, L45

Labeyrie, A. 1970, A&A, 6, 85

Lohmann, A. W., Weigelt, G., and Wirnitzer, B. 1983, Appl. Opt., 22, 4028

McAlister, H. A., and Hartkopf, W. I. 1988, Second Catalog of Interferometric Measurements of Binary Stars (Atlanta, Georgia State University)

McAlister, H. A., Hartkopf, W. I., Hutter, D. J., and Franz, O. G. 1987, AJ, 93, 688

Meng, J., Aitken, G. J. M., Hege, E. K., and Morgan, J. S. 1990, J. Opt. Soc. Am. A, 7, 1243

Miller, M. G. 1977, J. Opt. Soc. Am., 67, 1176

Morgan, J. S. 1989, in High Resolution Imaging by Interferometry (Garching, European Southern Observatory), p. 381

Morgan, J. S., Timothy, J. G., Smith, A. M., Hill, R., and Kasle, D. B. 1990, in Instrumentation in Astronomy VII, SPIE Proc. Vol. 1235 (Bellingham, WA, SPIE), p. 347

Nakajima, T., Kulkarni, S. R., Gorham, P. W., Ghez, A. M., Neugebauer, G., Oke, J. B., Prince, T. A., and Readhead, C. S. 1989, AJ, 97, 1510

Nakajima, T. 1988, J. Opt. Soc. Am. A, 5, 1477

Northcott, M. J., Ayers, G. R., and Dainty, J. C. 1988, J. Opt. Soc. Am. A, 5, 986

Papaliolios, C., Nisenson, P., and Ebstein, S. 1985, Appl. Opt., 24, 287

Roddier, F. 1987, Interferometric Imaging in Optical Astronomy (Tucson, NOAO)

Slater, D. C. 1991, Dynamic Range Improvement Study of Multianode Microchannel Array Detector Systems, Ph.D. Thesis, Stanford University

Timothy, J. G., Morgan, J. S., Slater, D. C., Kasle, D. B., Bybee, R. L., and Culver, H. E. 1989, in SPIE Proc. Vol. 1158, Ultraviolet Technology III, ed. R. E. Huffman (Bellingham, WA, SPIE), p. 104

Worley, C. E., and Douglass, G. G. 1992, in Complimentary Approaches to Double and Multiple Star Research (IAU Colloquium 135), ed. Harold A. McAlister and William I. Hartkopf (San Francisco, Astronomical Society of the Pacific), p. 583

[This page is intentionally left blank.]
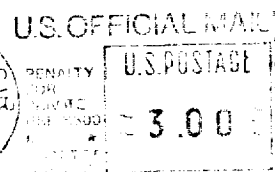
OFFICE OF THE UNDER SEC. OF DEFENSE (ACQUISITION & TECH.) DEFENSE TECHNICAL INFORMATION CENTER 8725 JOHN J KINGMAN RD STE 0944 FT BELVOIR, VA 22060-6218					
OFFICIAL BUSINESS - PENALTY FOR PRIVATE USE, $300 POSTMASTER: DO NOT FORWARD					
AD Number	Pages	Quantity	Type Copy	Source	Priority
ADB224215	216	1 of 1	H	E	

Received Date: 06-FEB-98

To: 15941

Requested By: CYNTHIA BARNES
Attn: R M RIDGEWAY

NATL. AERONAUTICS & SPACE ADMIN LINTHICUM HTS
AEROSPACE INFO CTR
800 ELKRIDGE LANDING RD
LINTHICUM HEIGHTS, MD 21090-2903

514544001

Distributed By

DTIC

Information For The Defense Community